FUEL OXIDATION MODEL VALIDATION AND APPLICATION TO THE MITIGATION OF STRESS CORROSION CRACKING IN FUEL SHEATHING

VALIDATION D'UN MODÈLE D'OXYDATION DU COMBUSTIBLE ET APPLICATION À L'ATTÉNUATION DE LA CORROSION SOUS CONTRAINTE DU GAINAGE DE COMBUSTIBLE

A Thesis Submitted to the Division of Graduate Studies
of the Royal Military College of Canada

by

Aaron D. Quastel

In Partial Fulfillment of the Requirements for the Degree of
Doctor of Philosophy

Kingston, Ontario, Canada

May 2016

Author's Declaration

I hereby declare that I am the sole author of this thesis. This is a true copy of the thesis, including any required final revisions, as accepted by my examiners.

I understand that my thesis may be made electronically available to the public.

Acknowledgements

I would like to acknowledge my RMC supervisors Dr. Brent Lewis and Dr. Emily Corcoran for helping me complete this work. Without their unwavering support, guidance, availability, and patience this thesis would not have been possible. I would also like to acknowledge Dr. Bill Thompson for his mentoring on chemical thermodynamics and on use of related software tools. I'd also like to acknowledge Tim Nash for his glass blowing work and expertise and for Clarence McEwen for his invaluable machine shop expertise. A special thanks to Brent Ball for providing IT support and computer related advice (and our engaging conversations). I want to also thank Bob Whitehead for his help with XRD scans. I'd also like to thank Katherine Nielsen and Kristine Mattson for their assistance in NAA analysis and Dave Ferguson for his appreciated assistance and allowing me the use of the Slowpoke lab space.

Special acknowledgements to Bernie Surrette from Chalk River Laboratories for providing some of the experimental materials used in this thesis and for his advice. I want to also thank Cathy Thiriet from Chalk River Laboratories and Farzin Abbasian from Stern Laboratories for providing preliminary lab results that was helpful in the model development. I would also like to acknowledge the National Science and Engineering Research Council (NSERC), the Canadian Nuclear Safety Commission (CNSC), the Canadian Nuclear Laboratories (CNL), and the University Network of Excellence in Nuclear Engineering (UNENE) for their financial support of this work.

Finally I wish to thank my fellow grad students and colleagues at the college for their friendship, comradery and good times.

Abstract

Quastel, Aaron D., PhD (Nuclear Engineering) Royal Military College of Canada. May 2016. Fuel Oxidation Model Validation and Application to the Mitigation of Stress Corrosion Cracking in Fuel Sheathing, Supervisors: Dr. Brent J. Lewis and Dr. Emily C. Corcoran.

Light and heavy water cooled reactors typically use uranium dioxide ceramic fuel contained and sealed in zirconium alloyed sheath or clad fuel rods or elements. Normally the sheath or clad fuel remains intact throughout its duration in the reactor core. In rare occurrences, (<0.1 %) sheath or clad breaches can form exposing the fuel to the coolant leading to fuel oxidation. Fuel oxidation can affect reactor safety and operation by reducing thermal conductivity of the fuel leading to increased fuel temperatures in normal and accident conditions. Further, the oxidized fuel can have a lower melting point, and fission products release can be enhanced.

A mechanistic fuel oxidation model for defective UO_2 fuel to predict oxygen/uranium (O/U) ratios was developed at RMC, which included coupling fuel oxidation kinetics, solid state oxygen diffusion in the fuel, gas phase diffusion in the fuel cracks and in the fuel-to-sheath gap, and heat transfer. To validate the model an *out-reactor instrumented defected fuel experiment* was designed and built. The fuel oxidation model was modified to represent this experiment. Two fuel oxidation models representing the *out-reactor instrumented defective fuel experiment* were analyzed: A 2D r-θ model and 3D model. Both models included discrete radial fuel cracks for gas phase diffusion, where hydrogen and hyperstoichiometric oxygen generation were provided by flux terms on common gas and solid domain boundaries in the fuel. The 2D r-θ model provided an estimate of the radial temperature distribution and the 3D model provided an estimate of fuel oxidation in the out-reactor experiment. Since fuel cracking plays a central role in fuel oxidation the conditions for fuel crack propagation using the J integral and predictions for radial fuel crack geometry in thermally expanded UO_2 fuel were studied in a plane strain 2D r-θ solid mechanics model.

In the experimental work of this thesis it was shown that hyperstoichiometric oxygen in the presence of graphite (CANLUB) in CANDU fuel can have mitigative properties against stress corrosion cracking in fuel sheathing. Experimental results provided a first estimate of how much hyperstoichiometric oxygen needs to be added to the fuel to provide and repair a protective oxide layer on the internal sheath surface against iodine corrodant. The fuel oxidation model was modified to compute suitable conditions in the fuel pellet sintering process in order to introduce a thin layer of oxygen on the outside surface of the fuel while ensuring that the bulk O/U ratio of 2.00 for the fuel pellet was not disturbed.

Résumé

Quastel, Aaron D., PhD (Génie atomique) Collège militaire royal du Canada. Mai 2016. Validation d’un modèle d'oxydation du combustible et application à l'atténuation de la corrosion sous contrainte du gainage de combustible, Superviseurs: Dr. Brent J. Lewis et Dr. Emily C. Corcoran.

Les réacteurs refroidis à l'eau légère ou lourde utilisent généralement du combustible céramique de dioxyde d'uranium contenu et scellé dans une gaine en alliage de zirconium ou dans des barres ou des éléments de combustibles chemisés. Normalement, la gaine ou le chemisage du combustible reste intacte tout au long de son séjour dans le cœur du réacteur. Dans de rares cas (<0,1 %), des brèches peuvent se former dans la gaine ou le chemisage et exposer le combustible au liquide réfrigérant, provoquant ainsi une oxydation du combustible. L'oxydation du combustible peut affecter la sécurité et le fonctionnement du réacteur en réduisant la conductivité thermique du combustible, qui à son tour provoque des températures de combustible plus élevées dans des conditions normales et accidentelles. En outre, le combustible oxydé peut avoir un point de fusion plus bas et le rejet de produits de fission peut augmenter.

Un modèle mécaniste d'oxydation du combustible pour les combustibles défectueux afin de prédire les rapports O/U a été développé au CMRC, et celui-ci incorpore le couplage des cinétiques d'oxydation du combustible, la diffusion d'oxygène dans le combustible, la diffusion en phase gazeuse dans les fissures du combustible et dans l'intervalle qui sépare le combustible à la gaine, et du transfert de chaleur. Pour valider ce modèle, une *expérience hors-réacteur de combustible intentionnellement défectueux et instrumenté* a été planifiée, préparée, et effectuée. Le modèle d'oxydation du combustible a été modifié pour représenter cette expérience. Deux modèles d'oxydation du combustible représentant l'*expérience hors-réacteur de combustible intentionnellement défectueux et instrumenté* ont été développés : un modèle r-θ en 2D et un modèle en 3D. Les deux modèles comprennent des fissures dans le combustible séparées et radiales permettant de prendre en considération la diffusion en phase gazeuse d’hydrogène et d’oxygène hyper stœchiométrique, provenant du gaz interstitiel et des parties du combustible adjacentes aux fissures. Le modèle r-θ en 2D fournit une estimation de la distribution radiale de la température et le modèle en 3D fournit une estimation de l'oxydation du combustible dans l'expérience hors-réacteur. Parce que le réseau de fissures radiales dans le combustible influence de manière significative l'oxydation du combustible, les conditions de leur propagation utilisant l'intégrale J et les prédictions de leur géométrie et de leur nombre dans le combustible UO_2 thermiquement dilaté ont été étudiées dans un modèle mécanique à contrainte plane r-θ en 2D.

Dans les travaux de recherche de cette thèse, il a été constaté que l'oxygène hyper stœchiométrique en présence de graphite (CANLUB) dans le combustible CANDU pourrait atténuer la corrosion sous contrainte du gainage de combustible. Les résultats expérimentaux ont fourni une première estimation de la quantité d'oxygène hyper stœchiométrique devant être ajoutée au combustible pour fournir et réparer une couche d'oxyde protectrice contre l’effet corrosif de l'iode à la surface interne de la gaine. Le modèle d'oxydation du combustible a été modifié pour prédire les conditions nécessaires lors du frittage des pastilles de combustible pour produire une fine couche de combustible hyperstœchiométrique à leur surface tout en veillant à ce que le rapport O/U de 2,00 soit conservé dans leur volume.

Dedication

This thesis is dedicated to my Mom and Dad, Eva and Michael Quastel.

Table of Contents

Section **Page No.**

List of Figures

List of Tables

List of Abbreviations and Symbols

Abbreviations	Meaning
a	crack length
a_c	critical crack length
a_{lat}	atomic lattice distance or spacing
a_o	empirical constant
a_{pellet}	fuel pellet radius
A	crack area
A	relative crack lengths
A_{area}	cross sectional area
A_n	electrical conductor cross section of conductor n
AECL	Atomic Energy of Canada Limited
ALE	Arbitrary Lagrangian Eulerian
b	initial unstressed slotted ring opening dimension
B	specific burnup
B_{th}	body thickness
BWR	boiling water reactor
C	a unitless ratio of areas used in $E_{\alpha\ Zirc}$
CANDU	Canadian Deuterium Uranium
C_{CG}	Cauchy-Green deformation tensor
c_g	molar concentration of the steam gas
$c_\mathrm{g}D_\mathrm{g}$	steam diffusivity quantity
C_{ijkl}	forth order elasticity tensor
CNSC	Canadian Nuclear Safety Commission
COG	Candu Owners Group
COMSOL Muliphysics®	Commercial software package for solving multi-physics problems using the finite element technique
C_p	specific heat capacity
CRL	Chalk River Laboratories
CT	Coulometric Titration
c_U	molar density of uranium in UO_2
D	chemical diffusion coefficient for interstitial oxygen diffusion and general diffusion coefficient
D_f	fraction from theoretical density
D_s	stiffness tensor
d_a	mass damping coefficient
d_{hkl}	interatomic spacing
DNGS	Darlington Nuclear Generating Station
ds	increment length along the integration contour Γ
D_y	specimen deflection (displacement) in y (vertical) direction

Abbreviations	**Meaning**
d_x, d_y	prescribed displacement in x and y directions
e_a	mass coefficient
EDX	energy-dispersive X-ray spectroscopy
E, E'	isotropic Young's modulus
E_{α_Zirc}	Young's modulus of α Zircaloy
E_{Ir}	Young's modulus of iridium
Eq. and Eqs.	Equation and Equations
E_{UO2}	Young's modulus of UO_2
f	hydrogen pickup fraction
$\bar{f}$	body force vector
F	source term in general PDE
F_c	Zircaloy surface corrosion enhancement factor
F_{cv}	column vectors of nodal boundary conditions
F_{d}	fractional change in porosity
F_{dg}	deformation gradient matrix
F*A*C*T and FactSage	Facility for the Analysis of Chemical Thermodynamics software
FEA	finite element analysis
FES	fuel element simulator (the out-reactor instrumented fuel element). Two FES's are discussed: FES1 and FES2.
F_{vol}	fuel volume
ftsg	fuel-to-sheath gap
g and g_0	combined temperature jump distance
G	Gibbs energy
G^{o}	Gibbs energy at standard conditions
G_c	critical strain energy release rate
G^E	excess Gibbs energy
G_r	energy release rate
G_{s}	scalar
G_{sh}	shear modulus
h_{solid}	solid heat transfer coefficient
h_{gas}	fluid heat transfer coefficient
H	Meyer hardness
I	centroidal moment of inertia
I_z	centroidal moment of inertia about the z axis
I_e	total electrical current
I_n	electrical current running through conductor n
$\mathbf{I}$ and $\bar{\mathrm{I}}$	identity matrix or tensor
I_0 and I_1	zeroith and first order modified Bessel functions

Abbreviations	Meaning
I-SCC	Iodine Induced Stress Corrosion Cracking
J	J integral
J^*	J integral in a thermal gradient
J_d	diffusion flux vector
k	thermal conductivity
k_e	thermal conductivity electron hole movement contribution
k_f	fluid thermal conductivity component
k_m	harmonic mean thermal conductivity
k_{ph}	thermal conductivity lattice vibration contribution (phonons)
k_{rad}	thermal conductivity radiative contribution
K	stress intensity factor
K_{1_Zirc}	component of E_{α_Zirc} that accounts for oxidation effects
K_{2_Zirc}	component of E_{α_Zirc} that accounts for the effect of cold work
K_{3_Zirc}	component of E_{α_Zirc} that accounts for fast neutron fluence
K_c	fracture toughness
K_{ec}	equilibrium constant
K_I, K_{II}, K_{III}	mode I, II and III stress intensity factors
K_{Ic}	mode I fracture toughness
K_s	element property or stiffness matrix
ℓ	fuel element length
l_{ec}	electrical conductor length
l_{rw}	slotted ring width
n	mole number
n_{or}	order of reflection
$\mathbf{n}$, n	unit normal vector
n_O	oxygen moles
N	index of refraction
$\mathbf{N}$	flux vector
N_A	Avogadro's number
$\mathrm{N_o}$	scalar
N_O	oxygen number density
M	molecular/molar mass and bending moment
p	pressure
p_{ip}	crack healing interface pressure
p_o	ambient pressure
p_t	total system/coolant pressure in atm
P_f	force
P_{gap}	pressure in the fuel-to-sheath gap

Abbreviations	Meaning
P_i	interfacial pressure
P_{linear}	fuel element linear power
P_{or}	fuel porosity
P_{vol}	electrical power
PDE	partial differential equation
PDF	powder diffraction file
PIE	post irradiation examination
ppg	pellet-pellet gap
PWR	pressure water reactor
q	hydrogen or deuterium mole fraction
q_c	hydrogen or deuterium mole fraction dissolved in the coolant
Q	molar effective heat of transport
Q_f	heat of fracture
Q_r	reaction quotient
Q_v	fuel heat source
r	radial coordinate
r_{is}	internal sheath radius
r_m	molecular radius
R	ideal gas constant and reaction rate
R_1 and R_2	surface roughness of surfaces 1 and 2
R_i	inside radius
R_n	electrical resistance of conductor *n*
R_o	outside radius
R_{rms}	root mean square surface roughness
R_s	source term (reaction rate)
R_{sr}	slotted ring radius
R_T	equivalent remaining electrical resistance
RMC	Royal Military College of Canada
R_f^{react}	reaction rate for fuel
$R_f^{react,ox}$	reaction rate for fuel oxidation
$R_f^{react,red}$	reaction rate for fuel reduction
$R_{Zirc\_sheath}^{ox}$	reaction rate for sheath oxidation
SCC	stress corrosion cracking
STP	standard temperature and pressure
t	time
t_{cc}	crack closure time
t_g	fuel-to-sheath gap distance

Abbreviations	**Meaning**
t_s	sheath thickness
t_{sr}	slotted ring thickness
T	temperature
TC	thermocouple
TC1, TC2, TC3	thermocouples at three radial positions
T_{gap}	average temperature in the gap
T_i	traction vector components
T_{ref}	reference temperature
T_{surf}	surface temperature
TGA	thermo gravimetric analyzer
$\mathbf{u}$	displacement vector
u	displacement in x direction
u_{cv}	column vector of unknowns at the nodes
u_i	displacement vector components
$\bar{u}$, $\mathbf{U}_{\mathrm{trans}}$, $\mathbf{u}_t$	velocity field
v	displacement in y direction
w	displacement in z direction
w_e	elastic strain energy density
w_f	final stressed slotted ring opening dimension
w_i	width or thickness
w_s	strain energy density
W	weight
x, Xdev	oxygen stoichiometry deviation
$\mathbf{x}$	spacial coordinate
$\mathbf{X}$	material coordinate
x_e	equilibrium stoichiometric deviation
x_{fs}	stoichiometric deviation at fuel surface
XRD	X-ray diffraction
Y	dimensionless correction factor
Y_s	sheath yield stress

Symbol	**Meaning**
α	surface exchange coefficient for fuel oxidation
α_e	isotropic thermal expansion coefficient
α_{Ir}	thermal expansion coefficient of iridium
α_R	term used in k_{rad} (thermal conductivity radiative contribution)
α_{th}	thermal accommodation coefficient
α_{UO2}	thermal expansion coefficient of UO_2
$\alpha_{\mathrm{Zircaloy}}$	thermal expansion coefficient of Zircaloy
β	fractional fuel burnup
β_{T}	paramter that accounts for temperature effects
γ	ratio of specific heats
γ_s	surface energy
$\Gamma, \mathbf{\Gamma}$	flux vector
Γ_{c}	integration contour
δ_{corr}	delta correction quantity
δ_{kl}	Kronecker delta
δ_{ts}	time scale coefficient in Comsol®
ΔG	Gibbs energy change
ε	strain and the ratio of crack volume to fuel volume (or porosity)
ε_{ij}^{e}	elastic strain tensor
ε_{inel}	inelastic strain tensor
ε_{ij}^{p}	plastic strain tensor
ε_{ij}^{t}	thermal strain tensor
ε_{kl}, ε_{ij}	strain tensor
ε_o	initial strain tensor
ζ	log of the hydrogen-to-steam partial pressure ratio
θ	wave incidence angle
κ	inverse neutron diffusion length
κ_{1d}	correction factor for dissolved fission products
κ_{1p}	correction factor for precipitated fission products
κ_{2p}	correction factor for porosity
κ_{4r}	correction factor radiation damage
λ	wave length
λ_{fp}	mean free path
μ	dynamic viscosity of a gas or fluid
ν	Poisson’s ratio
ν_{Ir}	Poisson’s ratio of iridium
ν_{UO2}	Poisson’s ratio of UO_2
$\nu_{\_Zirc}$	Poisson’s ratio of Zircaloy

Symbol	Meaning
Π	potential energy
σ	stress
σ_{AB}	combined collision cross section
σ_c	failure stress or critical remote stress
σ_{cs}	collision cross section
σ_{f}	pellet average surface-to-volume ratio
σ_f	fracture stress
σ_{ij}	stress tensor
σ_{kk}	principle stress tensor
σ_n	electrical conductivity of conductor n
σ_o	initial stress tensor
σ_r	radial stress
σ_t ,σ_θ	tangential/transverse/azimuthal stress
σ_x	stress in the x direction
σ_y	stress in the y direction
σ_{y_axis}	maximum tensile stress in slotted ring specimen
σ_{ys}	yield stress
σ_{ys0}	initial yield stress of Zircaloy
σ_z	stress in the z direction
τ	tortuosity factor
ρ	integration contor radius
ρ_g	gas or fluid density
ρ_s	fuel density
ρ_{TD}	fuel theoretical density
ϕ	fast neutron fluence
Ω_{AB}	collision integral

CHAPTER 1 INTRODUCTION

1.1 The State and Contribution of World Power Reactors

In 2001 there were 405 operating power reactors worldwide, of these 213 were pressure water reactors (PWR), 85 were boiling water reactors (BWR), 36 were CANDU and other types of pressure heavy water reactors and 15 were Russian RBMK type reactors. This number comprises about 86% of all power reactors that are all light or heavy water cooled [1]. Today there are 434 reactors in operation and more are under construction, especially in the developing world. The total world electricity generation by nuclear power was 11.94% in 2011 and in Canada was 16.14% in 2014 [2]. It is conceivable that in future nuclear energy will play a larger part in world energy generation in order to reduce the detrimental effects of pollution and carbon dioxide emissions from fossil fueled power plants on Earth's climate.

1.2 The CANDU Reactor and CANDU Fuel

In 2010 about 50% of Ontario's electrical energy (≈12,000 MWe installed capacity) was provided by CANDU nuclear power plants. In the future, the Ontario Ministry of Energy's long term energy plan [3] has stated that by 2030 nuclear reactors will remain the primary providers of electrical energy for the province, just under 50%. This will be equivalent to about 12,000 MWe of installed nuclear capacity, which is much the same as today.

Hence to meet this objective some current reactor installations will have to refurbished and modernized, while others will have to be retired, and new reactors will have be built. The major change to Ontario's energy makeup currently taking place is the reduction in the dependence on fossil fuels like coal in exchange for cleaner sources energy like solar wind and natural gas. Since nuclear power is essentially a zero emission energy source and provides a stable and reliable supply for base-line load, it will remain an important source of energy for the province in the future.

Historically the Canadian power reactor program started in 1962 with the commissioning of the 25-MWe Nuclear Power Demonstration (NPD) Reactor in Rolphton in Ontario, which was a prototype CANDU reactor. The program continued with the first 200

MWe CANDU reactor, beginning with Douglas Point on Lake Huron commissioned in 1967. This reactor design was exported later to India with the first Rajasthan reactor being commissioned in 1973. The power output from CANDU reactors was continuously increased to 515 MWe with the Pickering units in 1971, 640 MWe with Gentilly-2 in Quebec in 1982, 805-840 MWe in 1976 and 1985 with the Bruce reactors, and finally to 880 MWe with the Darlington reactors in 1990 [4].

The CANDU reactor

The CANDU (Canada Deuterium Uranium) reactor has three unique designs compared to pressure water reactors (PWRs) and boiling water reactors (BWRs), the latter two being the most prevalent in the world. In particular the CANDU reactor has:

i.) An online fueling ability; unlike BWRs and PWRs, CANDU reactors do not undergo batch refueling but are refueled during normal operation of the reactor, which decrease costly down times;

ii.) Uses natural uranium for fuel instead of more expensive enriched fuel used in PWRs and BWRs; and

iii.) Uses pressure tubes to contain the fuel bundles, which are relatively easy to manufacture instead of pressure-vessels as used in PWRs and BWRs that are costly to manufacture.

Figure 1 depicts the main components of the CANDU reactor, which include: (1) the fuel bundles, (2) the calandria, (3) the shutoff and adjuster rods, (4) the coolant reservoir, (5) the steam generators, (6) the secondary coolant pump, (7) the primary coolant and pump, (8) the fueling machines, (9) the heavy water moderator in the calandria between the calandria tubes, (10) the pressure tubes located in each calandria tube, which contains the fuel bundles and primary coolant, connected outside the calandria to the fuel channels, (11) the secondary loop steam exiting to the steam generator, (12) the secondary loop condensed water returning to steam generator, and (13) the reactor containment building [5].

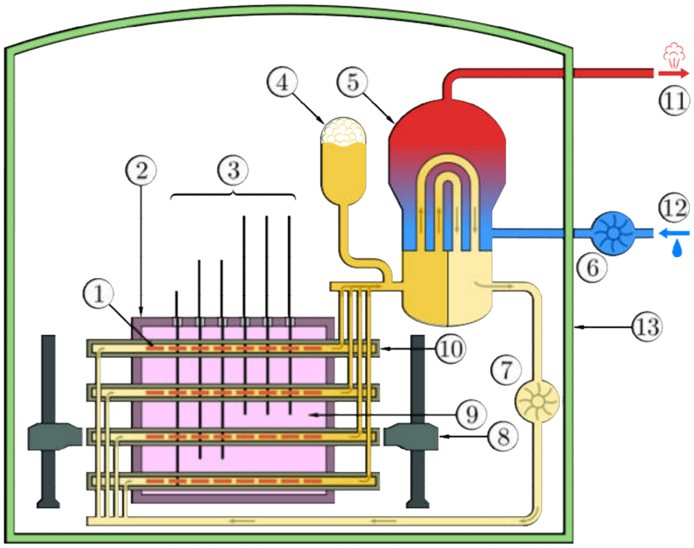

Figure 1: A general schematic of a CANDU reactor depicting its main components, some of which include: (1) the fuel bundles, (9) the reactor moderator, (10) the pressure tubes encased in calandria tubes positioned in (2) the calandria. Connected to each pressure tube outside the calandria is a fuel channel (10), which is fueled by (8) the fueling machine [5]**.**

A key component of this reactor is the heavy water for moderator (located in the calandria) and coolant (flowing though the pressure tubes). The heavy water (i.e., D_2O) is composed of a hydrogen isotope (deuterium) rather than ordinary protium. Deuterium is naturally occurring in nature and is <0.02 atom% abundant in the hydrogen makeup of ordinary water. Heavy water is used in CANDU reactors for its good neutron moderating ability (though not as good as light water) but especially for its good neutron economy (i.e., its ability to absorb less neutrons than light water). When the D_2O coolant enters the reactor, it is at a temperature of 266°C and when it exits the channel it is at 310°C. During this time the water is pressurized at 10 MPa and does not boil, noting that the saturation temperature of steam at this pressure is 311.06 °C [1][6].

A series of improvements to the basic Pickering design led to the CANDU-6 design. The CANDU-6 is essentially a version of the Pickering power plant but was re-designed to be able to be built in single-reactor units. CANDU-6 type reactors in Canada include the Gentilly-2 reactor in Quebec (now shutdown) and the Point Lepreau reactor in New Brunswick. Also, the CANDU-6 forms the majority of foreign CANDU systems, including the Wolsong reactors in South Korea in 1983, the Embalse reactor in Argentina in 1984, the Cernavodă reactors in Romania in 1996, and the Qinshan reactors in China in 2003 [5].

CANDU fuel

In natural uranium (where no enrichment is performed) the isotopic abundance of U-235 is 0.72 atom%, while the remaining is mostly U-238. The fissile portion of the fuel is U-235, while the fertile portion of the fuel is U-238. For any reactor to sustain a stable nuclear chain reaction it must have a certain amount of fissile nuclei [1]. A nuclear fission reaction begins when a neutron impacts a U-235 nuclei and is captured. The resulting U-236 is unstable and splits into two particles (fission fragments), see Figure 2. Within a very short period of time after fission occurs ($<10^{-15}$ s) several neutrons are emitted (i.e., 2-3 neutrons on average for fissile U-235) causing further fissioning and thereby establishing a chain reaction.

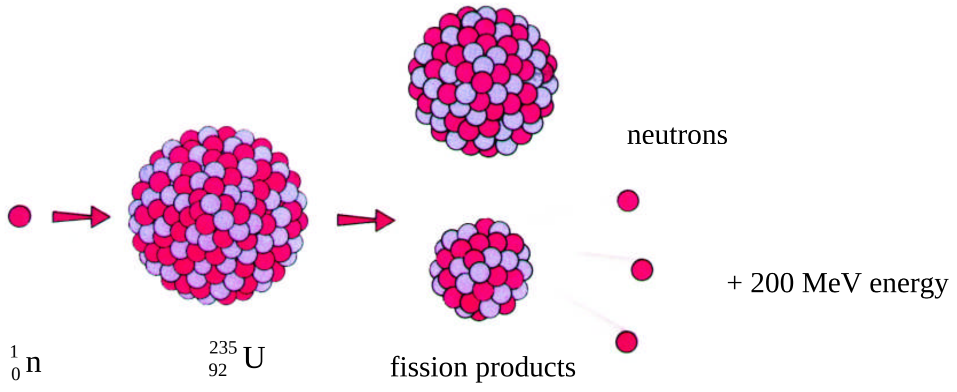

Figure 2: The basic mechanism of nuclear fission, adapted from [4]

The total energy liberated per fission reaction is about 200 MeV (or about $3.2\text{x}10^{-11}$ joules), which is about 3 million times the amount of chemical energy released by the combustion of a carbon atom [7].

In the CANDU reactor, the natural uranium used in the fuel is in the form of a uranium dioxide ceramic (UO_2). This ceramic is formed into uranium dioxide fuel pellets that are about 12 mm in diameter and about 16 mm long. About 30 pellets are inserted in a 482 mm long Zircaloy-4 tubing/sheathing that is 0.4 mm thick. The Zircaloy tube sheathing is back filled with mostly helium gas at atmospheric pressure and is then sealed with resistance welded Zircaloy end caps. This assembly is called a fuel element as shown in Figure 3.

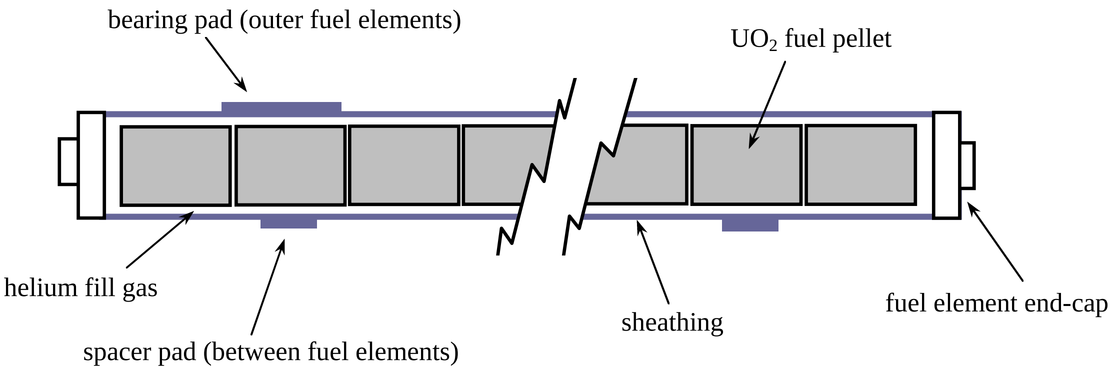

Figure 3: Axial cross section of a CANDU fuel element. Dimensions are not to scale.

These fuel elements are then resistance welded to Zircaloy end plates to form 28 and 37 fuel element bundles (Pickering and Bruce bundles, respectively), as shown in Figure 4.

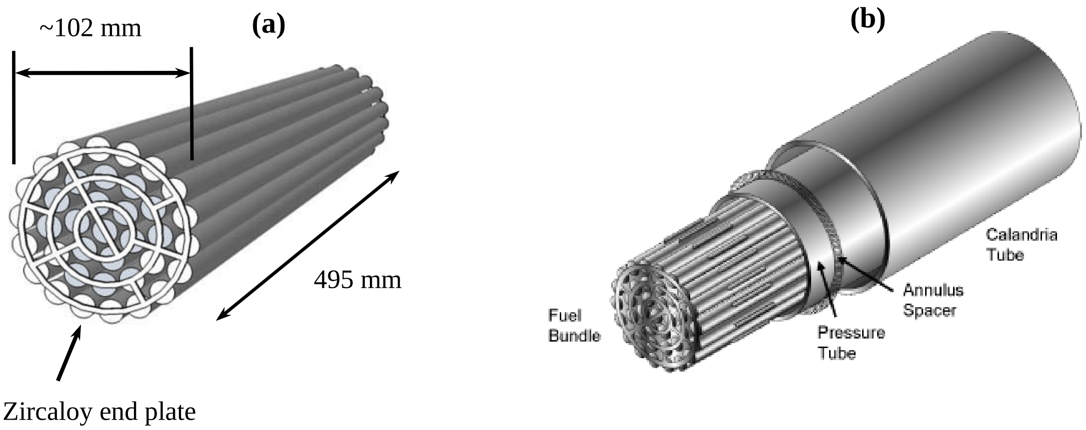

Figure 4: (a) 37-element CANDU fuel bundle and (b) a fuel bundle positioned in a pressure tube situated in a calandria tube [8][9][10]

The spacer pads and bearing pads in Figure 3 are attached by beryllium brazing in order to provide the right clearances between the fuel elements in the bundle and pressure tube so that the coolant can flow efficiency between the fuel elements to remove the generated heat.

Twelve fuel bundles reside in a pressure tube (see again Figure 1, item 10) for a duration of about six months. During refueling, eight of the down stream fuel bundles will be removed by inserting eight fresh fuel bundles from the upstream fueling machine. The average fission energy released per unit mass of the fuel is termed the specific fuel burnup. For a CANDU 37-element fuel bundle this value is about 7800 MWd $(\text{tonU})^{-1}$ [10].

There are other types of solid nuclear fuel besides UO_2 such as uranium carbide (UC) and uranium nitride (UN) [11][12], which are also high melting point ceramic materials. Liquid nuclear fuels like aqueous uranyl sulfate fuels or uranium/plutonium fluorides fuels in molten salt possibly mixed with breading materials such as thorium fluoride [13] also show promise in future applications. However, the fuel that is used in most nuclear power reactors today is uranium dioxide (UO_2) and still remains the fuel of choice in the near future.

1.3 Chemistry of Uranium Dioxide Fuel

UO_2 possesses the cubic fluorite lattice structure (named after the CaF_2 compound). The solid UO_2 is held together by ionic bonds. An ionic bond is the attraction between a positive and a negative ion resulting from the complete (or nearly complete) transfer of one or more valence electrons from one atom to another. Crystalline UO_2 consists of U^{4+} and O^{2-} ions to maintain charge neutrality. The UO_2 crystal structure can be described in two different ways. In the first description, Figure 5 (a), the oxygen ions are arranged in eight simple-cubic lattice cubes where the uranium atoms reside at the centre of the oxygen cubes but only in four out of the eight available interstitial sites. In the second representation, Figure 5 (b), the uranium ions form a face centred cubic lattice with an oxygen sublattice in the centre. Both representation unit cells in Figure 5 (a) and (b) have the same unit cell side length of a_o equal to 5.460 Å [14] or 5.470 Å [15] when O/U stoichiometry ratio is 2.

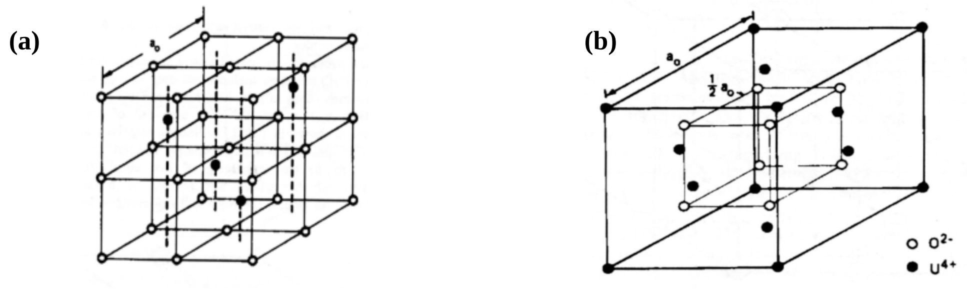

Figure 5: The uranium dioxide unit cell represented by a simple cubic anion lattice structure – the fluorite structure (a) and a face centred cubic cation lattice structure (b), taken from [15]

Since uranium has many valence states (U^{4+}, U^{5+}, and U^{6+}) deviations from stoichiometry are possible. To ensure electrical neutrality when oxygen ions are added or removed from a stoichiometric UO_2 matrix requires that some of the uranium cations change valence states. For example with the addition of one O^{2-} ion to the UO_2 matrix requires that two U^{4+} ions be converted to U^{5+} ions [15]. Although one might expect that any interstitial oxygen ion entering the fluorite structure to make hyperstoichiometric UO_2 would occupy one of the four empty uranium ion interstices, this situation does not occur. Instead, in hyperstoichiometric UO_2 fuel, the oxygen ions can occupy two other types of interstitial sites in the simple cubic structure sublattice formed by eight oxygen atoms (i.e., ⅛ of the fluorite unit cell), which is illustrated in Figure 6. There are two types of interstitial oxygen sites within the simple cubic sublattice. Type I sites lie along six diagonals at the edge centres of the cube.

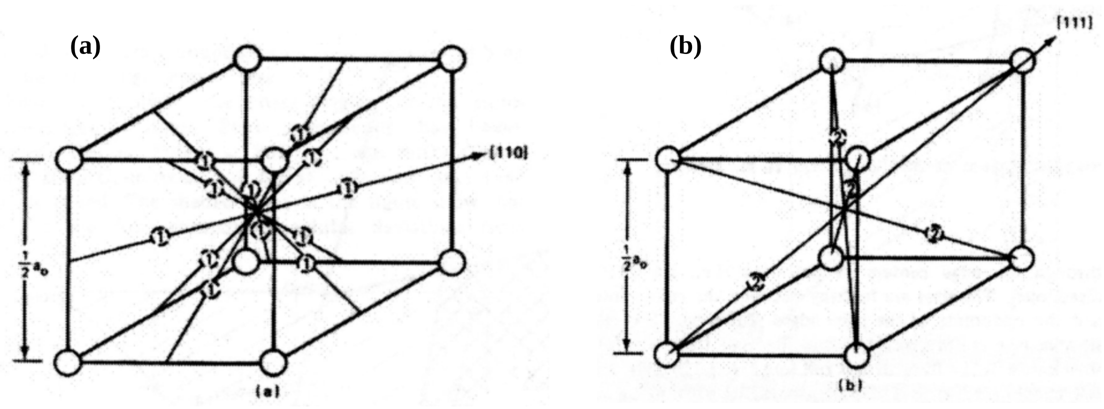

Figure 6: Possible sites for interstitial oxygen atoms; Type I interstitial oxygen sites (a) and Type II interstitial oxygen sites (b), taken from [15]

Each diagonal offers two possible oxygen interstitial sites, one between the cube centre and the cube edge. Hence Type I sites can provide 12 possible sites per simple cube sublattice or 48 sites in the fluorite unit cell. This is illustrated in Figure 6 (a). A Type II interstitial oxygen site is illustrated in Figure 6 (b), which is comprised of four empty simple cubes (i.e., no uranium atom) with four body diagonals each providing a maximum of one interstitial oxygen site. Hence there is a maximum of 16 Type II interstitial sites per fluorite unit cell [15]. In slightly hyperstoichiometric fuel a 'defect complex' can consist of two Type I interstitials, two Type II interstitials, two vacant normal oxygen lattice sites and four U^{5+} on nearby normal cation sites (also known as the 2:2:2 clusters [16]) to neutralize the charge. The two vacant sites with the two interstitial oxygen anions are known as Frenkel defect pairs. In higher stoichiometric deviation *x* in UO_{2+x}, when more and more of the fluorite unit cell contains a defect complex, and when a ratio of nine oxygen anions to four uranium cations is achieved, a new phase of U_4O_9 appears. This phase has the same fluorite structure of UO_2 but it also has a 'super-lattice' formed by the ordered structure of defect complexes [15].

If cation and anion defects are compared, the metal vacancies and metal interstitials are minority defects in UO_2. Their mobility is much smaller than that of oxygen. For example, at 1400 K, the diffusion coefficient of oxygen anions is 10^5 times greater than that of uranium cations in the UO_2 matrix, depending on the deviation from stoichiometry. As a result, the low mobility of U cations is rate-determining for important effects such as creep, grain growth, sintering, densification and swelling in UO_2 [17].

Early phase diagrams of the UO_2 - U_4O_9 system were established in the 1960's [18][19] by analyzing UO_2 samples in Vycor tubes, which were then heated to temperatures over 1000 K, depending on what phase was being studied and oxidized in a steam or oxygen environment. The Vycor tubes where then quenched to 'freeze' in the phase of interest. The metalographic determination of phases were then determined with microscopy. This analysis included diffraction, reflection or refraction techniques using electromagnetic radiation or electron beams. Figure 7 shows the quenched sample data over a range of compositions for O/U ratios between 2.008 and 2.248.

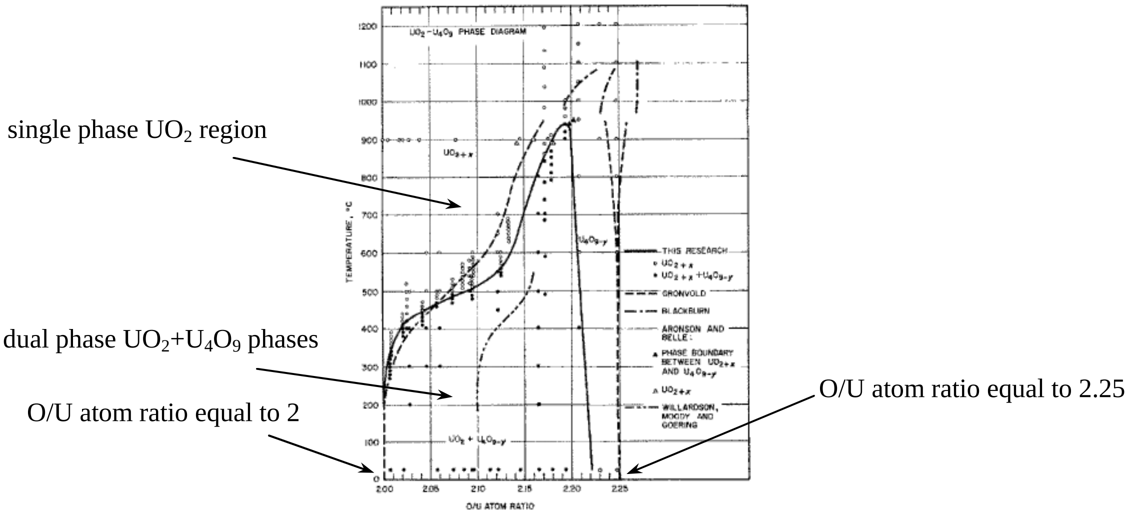

single phase UO_2 region

dual phase UO_2+U_4O_9 phases

O/U atom ratio equal to 2

O/U atom ratio equal to 2.25

Figure 7: Early phase diagram of the UO_2-U_4O_9 by Schaner [18]

The departure from stoichiometry for the uraninite phase (UO_2) can be expressed as an atom fraction of O or U, O/U ratio or with the value x in the subscript UO_{2+x}. A value of x greater than zero, as seen in Figure 7, is termed hyper-stoichiometry and a value less than zero is termed hypo-stoichiometry (not shown in Figure 7 but shown in Figure 9).

With the advent of computers it became possible to build more complete and accurate phase diagrams using thermodynamic computations based on temperature, pressure and concentration conditions using the Gibbs free energy minimization principle, which is a basis for chemical thermodynamics. This powerful tool is also used to compute chemical reactions, i.e., if a chemical reaction is spontaneous (product favored) or not. The Gibbs free energy minimization principle was an important discovery in chemistry by J. Willard Gibbs in 1876 [20]. As some Gibbs energy minimization software computations are included in this thesis, its basis is briefly explained below.

Gibbs energy minimization technique

The 2nd law of thermodynamics states that the total entropy of the universe is continuously increasing. In other words, a product-favored chemical reaction for example, is accompanied with an increase in entropy of the universe $\Delta S_{\text{universe}}$, which is always positive. The entropy change due to the dispersal of matter in the course of the reaction is called the entropy change of the system ΔS_{system}. This change occurs when reactants are converted completely to products. Lastly the entropy change to the surroundings, $\Delta S_{\text{surroundings}}$, is created by the dispersal of energy by its chemical reaction or process. Thus entropy change of the universe is the summation of the entropy change of a system plus the entropy change in the surroundings, and it is always greater than zero, as stated in Eq. (1) [20]. The superscript ^{o} indicates the standard state, typically at 1 atm and 25 °C.

$$\Delta S^o_{universe} = \Delta S^o_{system} + \Delta S^o_{surroundings} \geq 0 \qquad (1)$$

In an isothermal process, when the temperature is constant and the energy transfer is slow, the change in entropy for the surroundings is defined by Eq. (2) [20]. This equation states that for an exothermic reaction, where ΔH_{system} is negative, there will be an increase in entropy of the surroundings:

$$\Delta S^o_{surroundings} = \frac{q_{surroundings}}{T} = \frac{-\Delta H_{system}}{T} \qquad (2)$$

Substituting Eq. (2) into Eq. (1) and multiplying by -T we obtain:

$$-T\Delta S_{universe} = -T\Delta S_{system} + \Delta H_{system} \qquad (3)$$

Gibbs called the change in the free energy of the system (the LHS of Eq. (3)) ΔG_{system}, and at standard conditions it is written as:

$$\Delta G^o_{system} = \Delta H^o_{system} - T\Delta S_{system} \qquad (4)$$

The $\Delta G^o_{\text{system}}$ free energy change for a chemical reaction is an increase or a decrease in the free energy as the reactants (in their standard states) are converted completely to the products (in their standard states). This full conversion process though does not quite happen in reality. Instead some reactants are always present at equilibrium [20]. Under these circumstances, the free energy change of the system is not equal to the free energy change at standard conditions, $\Delta G^o_{\text{system}}$, but equal to the free energy change at non-standard conditions, ΔG_{system}. The relationship between the two is given by Eq. (5), where R is the universal gas constant and T is the temperature in Kelvin.

$$\Delta G_{system} = \Delta G^o{}_{system} + RT\ln Q_r \qquad (5)$$

Here Q_r is the reaction quotient. For example, for the reaction:

$$a\text{A} + b\text{B} \Leftrightarrow c\text{C} + d\text{D} \qquad (6)$$

the reaction quotient can be given by Eq. (7) [20].

$$Q_r = \frac{[\text{C}]^c[\text{D}]^d}{[\text{A}]^a[\text{B}]^b} \qquad (7)$$

At chemical equilibrium the reaction is neither product favored nor reactant favored. As such ΔG=0 and Q_r=K_{ec}, where K_{ec} is the familiar thermodynamic equilibrium constant, so that Eq. (5) becomes:

$$\Delta G^{o} = -RT \ln K_{ec} \qquad (8)$$

Figure 8 illustrates the relationship between the Gibbs free energy and the reaction progression direction. We say that products are favored over reactants when $\Delta G^{0}<0$ and $K_{ec}>1$ and that the reactants are favored when $\Delta G^{0}>0$ and $K_{ec}<1$.

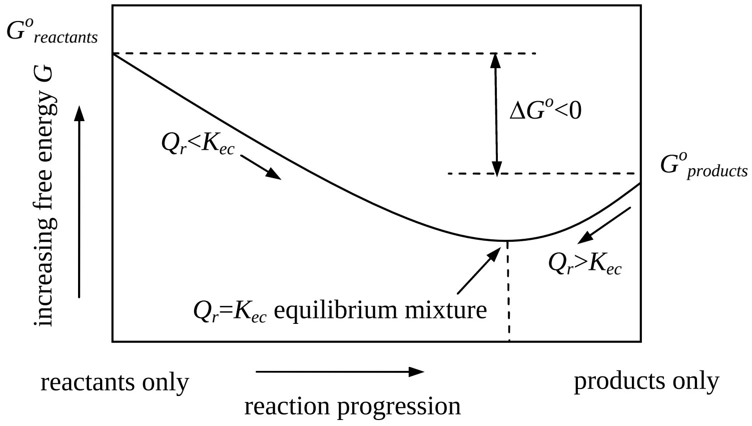

Figure 8: Gibbs free energy versus reaction progression for product favored reactions, adapted from [20]

For the use of Eq. (4) in Gibbs energy minimization software such as F*A*C*T® or FactSage® version 6.1 [21], the enthalpy and entropy of the elemental constituents of a compound need to be defined as a function of temperature. Absolute Gibbs energy functions, Eq. (9) [22], which are later converted to a Gibbs energy of formation functions, are used for this purpose [22].

$$\begin{aligned} H_T &= \Delta H^{o}_{298K} + \int_{298K}^{T} C_p(T)\,dT \\ S_T &= S^{o}_{298K} + \int_{298K}^{T} \frac{C_p(T)}{T}\,dT \end{aligned} \qquad (9)$$

Where $C_p(T)$ is the heat capacity at constant pressure as a function of temperature in phase equilibria in a system of interest, as usually studied at isobaric conditions.

Briefly, the Gibbs free energy equation in Eq. (4), is used to calculate the free energy of the elemental, compound, or phase constituents possible at a specified composition and temperature. Computer programs are used to iteratively compare the free energy of these constituents and isolate the most stable constituent or a combination of constituents that possess the lowest Gibb's free energy [23]. In order to assess all the phase boundaries of a system, as partially given in Figure 7 through experiment, the Gibb's free energy of all possible phases can be calculated at a given temperature and constant pressure as a function of composition. In this manner, it is possible to theoretically determine the composition limits over which a phase is stable. By repeating this analysis for various temperatures, the phase boundaries of a system can be determined [23].

For the mixing of two components within a phase, the change in Gibbs energy is expressed as a combination of ideal and excess terms. The ideal solution expresses ideal mixing of two components, where there is no interaction between the components of the mixture [24]. Excess functions are thermodynamic properties of solutions which are departures of an ideal solution at the same conditions of temperature and composition. Excess Gibbs energy G^E can be expressed by Eq. (10):

$$G^E \equiv G_{\left(\substack{\text{actual solutions} \\ \text{at } T, P \text{ and } x}\right)} - G_{\left(\substack{\text{ideal solutions at} \\ \text{same } T, P \text{ and } x}\right)} \qquad (10)$$

where $G_{\text{actual solutions}}$ is the change in the Gibbs energy of the mixed phases or solutions, which can also be written as $\Delta G_{\text{mixed phases}}$ [25]. $G_{\text{ideal\_solutions}}$ can also be written as $G_{\text{ideal\_mix}}$ and is expressed by Eq. (11) [26]:

$$G_{\text{ideal\_mix}} = \sum_i x_i RT \ln x_i \qquad (11)$$

where x_i is the molar fraction of component i, R is the universal gas constant 8.314 J mol^{-1} K^{-1} and T is in K.

Thus, for a binary system Eq. (11) can be substituted into Eq. (10). Solving for $G_{\text{actual\_solutions}}$ (or $\Delta G_{\text{mixed phases}}$), Eq. (10) can be rewritten as Eq. (12) [24][27]:

$$\Delta G_{\text{mixed phases}} = x_A RT \ln x_A + x_B RT \ln x_B + G^E \qquad (12)$$

If the two mixed components easily dissolve together, the resultant mixture is more stable than the collection of separate components and $\Delta G_{\text{mixed phases}} < 0$. Conversely, if neither component dissolves into the other, then $\Delta G_{\text{mixed phases}} > 0$ [24].

Hyperstoichiometric uranium dioxide, UO_{2+x} (where x is the deviation from stoichiometry), can be thought of as a solvent of UO_2 particles in which a solute of UO_3 particles is dissolved in. Thus, for hyperstoichiometric UO_2 [24]:

$$UO_{2+x} = (1-x)UO_2 + xUO_3 \qquad (13)$$

Here the Gibbs energy terms can use a Margules recursive formulation [26], with the activity coefficients expressed as a power series. Thus, the change in Gibbs energy for the binary O-U phase diagram can be written as Eq. (14), where p_0, p_1, p_2, p_3 are constants or simple functions of temperature and X_{UO_2} and X_{UO_3} are the mole fractions of UO_2 and UO_3 in the solid solution mixture, respectively. Lastly, it is noted that X_{UO_3} is equivalent to the stoichiometric deviation x in UO_{2+x} [24].

$$\begin{aligned}\Delta G_{\text{mixed phases hyper}} &= X_{\text{UO}_2} RT \ln X_{\text{UO}_2} + X_{\text{UO}_3} RT \ln X_{\text{UO}_3} + \\ &X_{\text{UO}_2} X_{\text{UO}_3}\left[p_o + p_1 X_{\text{UO}_3} + p_2 X^2_{\text{UO}_3} + p_3 X^3_{\text{UO}_3}\right]\end{aligned} \qquad (14)$$

In a similar manner hypostoichiometric uranium dioxide, UO_{2-x}, can be thought of as a solvent of UO_2 particles in which a solute of UO particles is dissolved in. So hypostoichiometric UO_2 can be expressed as [22]:

$$UO_{2-x} = (1-x)UO_2 + xUO \qquad (15)$$

Where the change is Gibbs energy for this binary O-U phase diagram can be written as:

$$\begin{aligned}\Delta G_{\text{mixed phases hypo}} &= X_{\text{UO}_2} RT \ln X_{\text{UO}_2} + X_{\text{UO}} RT \ln X_{\text{UO}} + \\ &X_{\text{UO}_2} X_{\text{UO}}\left[p_o + p_1 X_{\text{UO}} + p_2 X^2_{\text{UO}} + p_3 X^3_{\text{UO}}\right]\end{aligned} \qquad (16)$$

Both equations (14) and (16) form the $UO_{2\pm x}$ phase.

In the O-U phase system, the binary oxides U_4O_9, U_3O_7, U_3O_8, and UO_3 are present, and $UO_{2\pm x}$, liquid and gas phases are represented by solution phases. This system is one of the more complex oxide systems known. Most of these oxides are polymorphic (i.e., an ability for the oxide to exist in more than one crystal structure) and are oxide phases with different ranges of composition rather than as stoichiometric compounds [28]. With Gibbs energy minimization computations, a more complete phase diagram of the O-U system can be generated [29]. Figure 9 covers the stoichiometry ratio O/U between 1.4 to 3.0 within a temperature range of 25°C at 3000°C.

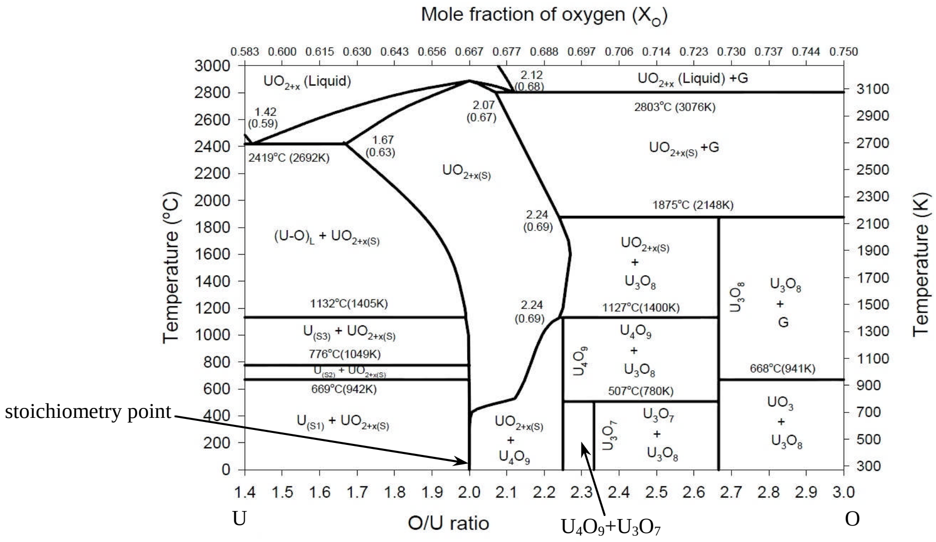

Figure 9: Phase diagram for the U-O system, taken from [29]

The melting point of the uranium oxide when the O/U ratio is close to 2 (i.e., UO_2) is approximately 2865°C (3138 K). As can be seen in Figure 9, the uraninite phase appears on either side of the O/U ratio of 2 at various temperatures. One can also observe that on either side of the O/U ratio of 2, the melting point decreases at thermodynamic equilibrium conditions. UO_2 is a dark brownish ceramic material and its theoretical density is 10.96 g cm^{-3}. Natural uranium dioxide used in CANDU fuel has an actual density of 10.6 g cm^{-3}. The difference comprises the fuel porosity (of a few percent), which provides the primary containment for fission products.

1.4 Defective Fuel Behavior

Oxidized Fuel

In a fuel element, the Zircaloy sheathing, which is an alloy of zirconium, is used as a barrier between the fuel and the water coolant flowing in the reactor core. Zircaloy is used rather than other metals or alloys due to its superior neutron economy characteristics, corrosion resistance, and heat transfer properties. The sheath (or cladding in BWRs and PWRs) allows the transport of fission heat to the coolant and prevents the release of fission products into the coolant. Its primary function is to protect the fuel from being oxidized by the coolant. However, on rare occasions, a small primary hole or crack can occur in the sheathing during reactor operation as a result of debris fretting (mechanical damage), pellet-cladding interaction (PCI), which includes iodine and possibly cadmium induced stress corrosion cracking (SCC) [30], or by manufacturing defects. An example of a clad defect due SCC in BWR fuel [31] is given in Figure 10 (a). Note a large radial fuel crack originating from the pellet centre reaching the pellet surface and the failed cladding at the 3 o’clock position, the fuel crack believed to be a passageway for corrosive fission products. An example of debris fretting damage in BWR fuel rods bottom section [32] is given in Figure 10 (b).

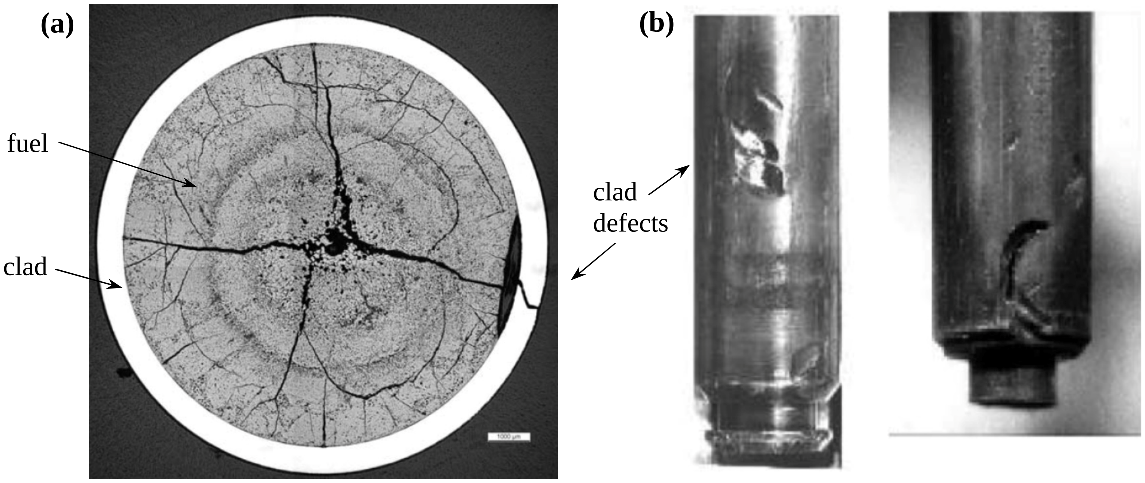

Figure 10: (a) An example of SCC clad defect in BWR fuel and (b) an example of debris fretting in BWR fuel rods bottom section. Images taken from [31] and [32], respectively.

The debris in the coolant can lead to fretting damage can typically include turnings, shavings from machining work and objects such as tools, screws, bolts, nuts, metal clips, electrical connectors, pieces of wires, parts of gaskets, and saw blades have been found in damaged fuel [32].

A primary sheath defect can lead to the formation of secondary sheath defects due to deuteriding blister formation [33], as shown in this pressurized heavy water reactor (PHWR) defective fuel pin in Figure 11: (a) one blister close to the fuel element (or pin) end-cap and (b) one perforated blister close to the fuel element central bearing pad. The primary sheath defect for this case was an incomplete end-cap weld (no shown in Figure 11).

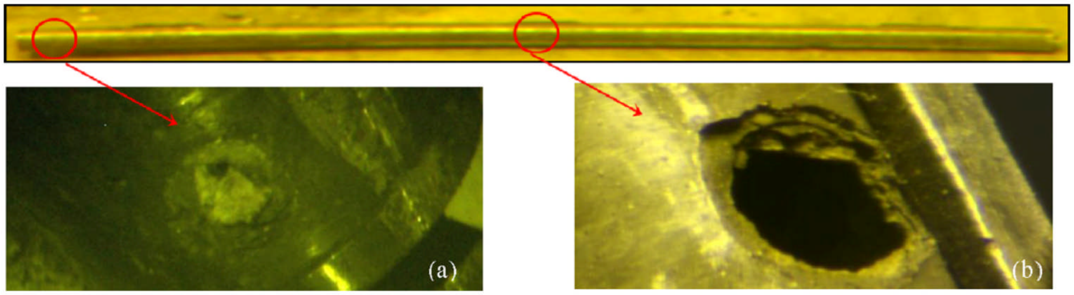

Figure 11: Images (a) and (b) show two secondary sheath defects in a PHWR defective fuel element (or pin), taken from [33]

Generally the performance of CANDU fuel has been excellent. In the 1970's the failure rate for fuel bundles loaded into the Douglass Point demonstration CANDU reactor and the first Pickering CANDU reactor in Ontario was under 1%. In more recent times the failure rate for individual fuel elements has been about 0.1% [34]. Interestingly, the main failure mechanism in PWR's and BWR's is currently related to debris fretting and grid-to-rod fretting [35]. In CANDU-6 reactors, according to the 1997 annual fuel bundle defect rate, about half of the fuel bundles that were found to be defective were attributed to debrid fretting. This was true of newer CANDU units that were recently comissioned, where in older CANDU units the debris fretting failue frequency was lower, possibly due to the coolant being continuously filtered out over time [36].

Sheath or clad breaches allow coolant (heavy water or light water) to enter the fuel element and make direct contact with the fuel [37][38], which can lead to fuel oxidation. As the fuel is oxidized, the fuel thermal conductivity will be degraded (i.e., reduced) resulting in higher fuel temperatures. Thermal conductivity dependence was first shown by Goldsmith and Douglas [39]. Figure 12 by Lucuta *et al.* [40] provides measurements of thermal conductivity of UO_{2+x} vs. temperature for various levels of fuel oxidation (for 100% dense fuel).

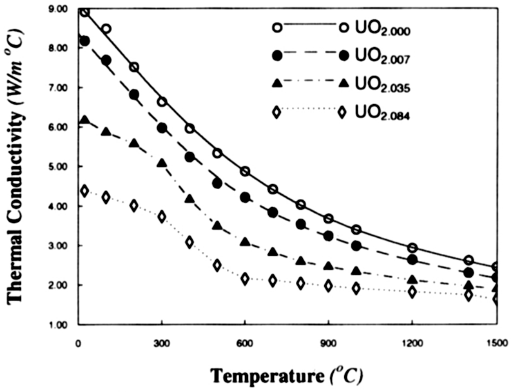

Figure 12: The thermal conductivity normalized to 100% theoretical density for UO_2 and UO_{2+x} for various *x* values vs. temperature, taken from [40]

As can be seen in Figure 12 increases in fuel oxidation leads to a decrease in fuel thermal conductivity. It is important to note though that these measurements are not thermal conductivities of actual in-reactor or out-reactor fuel pellets but homogeneously oxidized 1 mm thick UO_2 disk specimens with almost theoretical density. As will be discussed later actual defective fuel will oxidize in a non-homogeneous manner.

With the reduction in thermal conductivity in hyper-stoichiometric fuel, the fuel melting temperature will be reduced due to the reduction of the liquidus and solidus temperatures possibly by 100-200 degrees (see the region near O/U of 2 and a temperature of 2800 °C in U-O phase diagram in Figure 9). This effect could lead potentially to centreline fuel melting in high-powered elements, particularly during accident conditions [41][42][43][44]. Fission product release will also be enhanced by a greater mobility in the hyper-stoichiometric fuel [45][46]. The fission product release from a defective fuel element into the reactor primary coolant also means that fuel management could be disrupted and regular reactor maintenance could also be affected as a result of imposed radiation safety limits.

In the early 1970’s the failure rate of CANDU fuel elements was noticed to increase substantially, specifically during power ramps. Fortunately, with the ability of the CANDU reactor to locate and replace defective fuel bundles without having to shut down, the economic penalty was minimal. Nevertheless, since this increased failure rate reflected negatively on plant operation, a short but intensive research and development program to identify and eliminate the problem was launched. The problem was identified as stress corrosion cracking and the solution that showed the most promise (out of 17 proposed solutions) was the inclusion of a thin layer of graphite on the internal surface of the fuel sheathing [34]. This remedy significantly reduced the effects of stress corrosion cracking phenomena at typical CANDU reactor burnups during refueling operations. This graphite coating was named CANLUB for its then perceived lubrication properties. The first ‘CANLUB fuel’ was loaded into the Pickering reactors by December 1972 [34][47].

Over the years, the CANDU fuel element and fuel bundle design have matured and is well established. The failure rate has been generally quite low. This has been attributed to a robust design, high manufacturing quality, built-in safety margins and prudent operation assuring compliance with strict limits [48]. However, the Canadian Nuclear Safety Commission (CNSC) has observed that the condition of certain fuel bundles irradiated in CANDU reactors differed from that as predicted and accounted for in design, operation, and safety analysis documentation. As a result, the CNSC has activated a Generic Action Item 94G02 “Impact of Fuel Bundle Condition on Reactor Safety”. To achieve the closure of Generic Action Item GAI 94G02, one of the issues that has received priority has been the behavior of oxidized fuel in CANDU reactors. This action called for the generation of experimental data on fuel oxidation in defective fuel at reactor pressures and temperatures to help validate a model that would predict fuel oxidation in defective fuel with sufficient accuracy [48].

Various experiments with intact fuel at reactor temperatures and pressures have been conducted to measure the fuel thermal conductivity and fuel-to-sheath gap conductance

[49][50]. For the investigation of defective fuel behavior, past experiments have also been conducted. Lewis *et al.* [38] and Hüttig *et al.* [51] investigated the fission product release from defective fuel while Une *et al.* [44] measured the post irradiation fuel oxidation behavior. Karlsson *et al.* [52] performed pellet erosion experiments on BWR fuel with a pre-designed cladding breach. Limbäck *et al.* [53] and Cheng *et al.* [54] investigated secondary fuel degradation with in-situ centreline fuel temperature measurements and hydrogen gas pressure measurements in the latter experiment. Nevertheless, no instrumented experiments to date (primarily instrumented temperature measurements) have been conduced on defective fuel at reactor temperatures and pressures specifically to study the fuel oxidation phenomenon.

Simple models have been developed in the past to describe fuel oxidation kinetics in operating fuel rods but these models typically ignored the axial migration of the steam and hydrogen mixture in the fuel-to-sheath gap or through the fuel cracks. Also these models failed to treat interstitial oxygen migration in the UO_2 matrix by considering both concentration driven diffusion as well as thermal diffusion in a temperature gradient as present in operating fuel elements [37][41][42][46].

To address the CNSC active Generic Action Item 94G02 priority, a mechanistic fuel oxidation model was developed at the Royal Military College of Canada (RMC) [24][29], to predict fuel oxidation behavior and thermal performance in operating defective fuel in normal operating conditions. This fuel oxidation model was extended and improved in this work to assist in the design of an *out-reactor instrumented fuel oxidation experiment* to help address this Generic Action Item. These out-reactor test data can be further used for model validation. An *out-reactor instrumented fuel oxidation experiment* built by Stern Laboratories in Hamilton under the guidance of AECL-CRL (Atomic Energy of Canada Limited - Chalk River Laboratories), now CNL (Canadian Nuclear Laboratories) and RMC has been proposed to the industry and designed for this purpose.

The possible relation between oxidized fuel and stress corrosion cracking of Zircaloy sheathing in CANDU fuel

The role of CANLUB in CANDU fuel elements has been debated over the last three and a half decades. Generally there are two camps of thought:

i.) The first group argue for the emphasis on the mechanical causes of stress corrosion cracking in Zircaloy sheathing [55][56]. They claim that graphite (CANLUB) acts as a lubricant or friction layer interface, which reduces the coefficient of friction, μ, between the expanding fuel pellets and the collapsing sheathing, from μ=0.7-0.9 for bare Zircaloy to μ=0.2-0.3 with CANLUB [57]. Hence it was believed that the local stresses in the Zircaloy sheath are reduced with the graphite, mitigating SCC. In reality though the ‘lubrication’ afforded by the CANLUB had a very marginal effect on the stress intensity in the Zircaloy cladding (a ≈5% reduction) [57], which questions the importance of this SCC mitigation explanation alone. An indirect observation though made by Wood *et al.* [57] was that a smaller number of peripheral fuel cracks appeared in the fuel pellet when CANLUB was used, which could in turn reduce the fission product availability at the inside surface of the Zircaloy sheathing.

ii.) The second group argue the benefits provided by the graphite layer are more chemical in nature and its true function may be two fold: a) The dried graphite layer possesses chemical gettering properties (absorption and/or adsorption) for the corrosive fission product species from the fuel and/or b) It has the ability to act as a physical barrier between the corrosive fission product species and the Zircaloy sheath [58][59].

One of the reasons that support the latter hypothesis is the observation that the SCC failure rate is still reduced even when the graphite layer has come off the Zircaloy surfaces at various locations in fuel elements [58]. Considering these two hypotheses, the question arose could there be another role of CANLUB graphite in mitigating SCC in CANDU fuel?

It has been shown that the naturally occurring oxide layer formed on the Zircaloy surface when exposed to oxygen or air plays a protective role against various corrodants [60]. Penetrating cracks in the fuel sheathing typically occur where the oxide layer is absent or has been damaged. In particular, it is reported that the sheath is nearly immune to stress corrosion cracking if the oxide layer remains intact [61]. Une [60] has demonstrated that when a thin sub micron thickness oxide layer is formed on a Zircaloy surface by introducing a low partial pressure of oxygen at temperatures typical of the fuel-to-sheath gap it acts as a protective barrier from iodine corrodant attack. However when very low strains (<0.5%) are imparted onto the Zircaloy sheath, the zirconium oxide protective layer can break and crack [61], allowing corrodants access to the bare sheath metal below. Thicker zirconium oxide layers do not necessarily mean added protection from a corrosive environment. Yang *et al.* [62] showed that pressurized Zircaloy-4 tubes sealed with iodine corrodant (which were pre-oxidized internally to various zirconium oxide thicknesses) did not fail when the oxide layer was 0.2 μm thick but did fail when the oxide layer was >0.2 μm thick. Lastly it is mentioned that the protective oxide layer can dissolve into the zirconium α matrix at temperatures above 800 °C due to a higher oxygen diffusion coefficient in α_{Zr} in Zircaloy-4 ($D_o \cong 1.5\times10^{-10}$ cm^2 s^{-1} [63]). But at temperatures of the fuel-to-sheath gap, around 623 K (350 °C) during NOC (normal operating conditions), the diffusion coefficient of oxygen in the Zircaloy is much lower ($D_o \cong 2\times10^{-17}$ cm^2 s^{-1} [64][65]) meaning the oxide layer is present while in the reactor.

The oxygen in the zirconium oxide layer in CANDU fuel could come from a few sources. One such source could be available when CANDU fuel pellets are manufactured in the factory. In the final manufacturing stage the pellets are reduced from UO_3 to UO_2 by exposing them to H_2 gas in a furnace at a temperature >2000 K as shown in Eq. (17). The hydrogen reduces the UO_3 and UO_{2+x} (where x is the deviation from stoichiometry) so that an O/M ratio of exactly 2 is achieved [66].

$$UO_{2+x} + xH_2 \rightarrow UO_2 + xH_2O \qquad (17)$$

However, if the reducing process during the fuel pellet manufacturing process is incomplete and/or if the sintered and reduced fuel pellets are stored in air for long durations they may pick up some oxygen from the air, reversing the reaction above to an oxidation reaction so that the O/M ratio becomes greater than 2. The CANLUB coating (or graphite carbon) may act as a reducing agent for the oxygen in the hyperstoichiometric UO_{2+x} fuel (as similar to the hydrogen in Eq. (17) [14]). This process would allow oxygen to travel in gaseous form as carbon monoxide or carbon dioxide to exposed areas of the zirconium surface and oxidizing those sensitive areas (possibly with the aid of radiolysis of the carbonaceous gases near the sheath). Thus, there may be a chemical relationship between CANLUB graphite, the fuel, and the Zircaloy sheath internal surface, which mitigates the SCC phenomena in Zircaloy sheathing. This proposed process is discussed further in Chapter 5.

Another source of oxygen that can be mentioned is from the excess oxygen generated in irradiated fuel. From the fission yield and valence states of the fission products, the excess oxygen per atom percent burnup can be estimated. For example, a 1 atom% burnup can theoretically cause a change from 2.000 to 2.009 in the O/M ratio in UO_2 fuel [40]. In practice though, in post irradiation examinations, the oxygen balance in irradiated fuel appears to be near the stoichiometric region, i.e., an O/M ratio of 2.000 [40][67]. Lucuta *et al.* [40] and Matzke [67] suggested that some of the fission yielded oxygen may be buffered by metallic molybdenum (given its high yield [68]), but that the Zircaloy clad (or sheath) can also act as an oxygen getter [67].

It then can be asked if the excess oxygen in UO_2 fuel, introduced either during manufacturing of the pellets or during the fission process, is liberated or can thermally desorb on its own, to reach the sheath and oxidize it. It would seem that thermal decomposition of the higher uranium oxides like U_3O_8 and UO_3 to UO_2 and O_2 would be possible at elevated temperatures and at reduced pressures based on the average free energy of decomposition. Biltz and Müller in [14] showed though that the decomposition of U_3O_8 usually stops at $UO_{2.15}$ when in vacuum of at least 20 mtorr or above and at temperatures up to 1300 °C. This result occurs because the true or differential free energy of decomposition increases far above the average free energy of decomposition in the solid-solution stoichiometry range below $UO_{2.30}$ [14]. This suggests that in order to remove the hyperstoichiometric oxygen from UO_{2+x}, a reducing agent is necessary.

Reduction of the higher uranium oxides with graphite was shown in work by Lawrence *et al.* [69]. Here uranium carbide fuel was produced by reducing UO_{2+x} and U_3O_8 uranium oxides with graphite. The equilibrium constants of these reactions were more or less known at the time but not their reaction rates. In these tests, compacts of uranium oxides and graphite were prepared by mixing crushed UO_{2+x} samples ($UO_{2.008}$, $UO_{2.14}$, $UO_{2.33}$) and U_3O_8 and crushed graphite at molar ratios of 1:1 and lower and sealing them in evacuated silica tubes. The tubes were heated to temperatures of 700 °C, 800 °C, 900 °C, 1000 °C and 1250 °C, and the tube contents were then analyzed with a mass spectrometer. It showed that CO and CO_2 gases evolved from the reduction of uranium oxides with graphite for heating durations of about 300 minutes. The evolved gases were mostly CO_2 when the temperature was held at 700 °C and mostly CO when the temperature was held at 800 °C and above.

In related work, Campbell [70] studied the effects of graphite discs inserted between adjacent UO_2 pellets in CANDU fuel as an additional heat path. Specifically, Campbell wanted to see if significant amounts of CO and CO_2 gases would be liberated by the reduction of UO_{2+x} with carbon (i.e., graphite), where x in his experiments was set to 0.015, to stoichiometric $UO_{2,}$ and possibly to UC and to U in order to assess if a large gas pressure would be generated in the fuel element (>10 MPa). It was found that CO and CO_2 gases were indeed formed but at levels below 10 MPa. It was found also that the dominant reaction was the reduction of UO_{2+x} with carbon to form stoichiometric UO_2, while the formation of UC and U was much less favorable.

Thus, some carbothermal (or carbothermic) reduction of hyperstoichiometric fuel may be occurring in CANDU fuel, which may have mitigating effects on stress corrosion cracking of CANDU fuel Zircaloy sheathing.

1.5 Fuel Oxidation Model

In the original fuel oxidation model, Higgs [24][29] solved three time dependent and coupled partial differential equations: (1) a gas phase diffusion transport equation occurring in the thermally induced fuel cracks and in the fuel-to-sheath gap, (2) an interstitial oxygen diffusion equation occurring in the fuel matrix, and (3) a heat conduction equation applied to the solid fuel matrix. The gas phase equation solves for the hydrogen mole fraction. The interstitial oxygen diffusion equation solves for the solid state oxygen migration concentration in the fuel matrix and the heat conduction equation provides for an estimate of the temperature distribution in the fuel matrix. In the fuel oxidation model, the rate of reaction for either oxidation or reduction depends on temperature, oxygen stoichiometry deviation in the fuel and the hydrogen mole fraction. Since both the hydrogen gas diffusion equation in the fuel cracks and solid state oxygen diffusion equation in the fuel have the same reaction rate term then both of these mass balance equations are fully coupled. Furthermore, the thermal conductivity of uranium dioxide depends on the oxygen stoichiometry deviation and temperature. Hence, this problem is highly nonlinear and was best solved with multiphysics software such as COMSOL Multiphysics® [71].

Higgs [24][29] solved these three governing differential equations in an axial-symmetric 2D *r*-*z* model. This was a convenient way to approach the problem if the problem is considered symmetric. Figure 13 (a) shows the representation of the axial-symmetric 2D *r*-*z* model and Figure 1 (b) shows the same model and a 2D *r*-*θ* model representation but in 3D. From the figure below it becomes clear that the sheath defect represented in the Higgs model is actually a ‘ring defect’ of a defined width as seen as a purple band. However this geometry does not fully describe the problem as further discussed in Section 1.6.

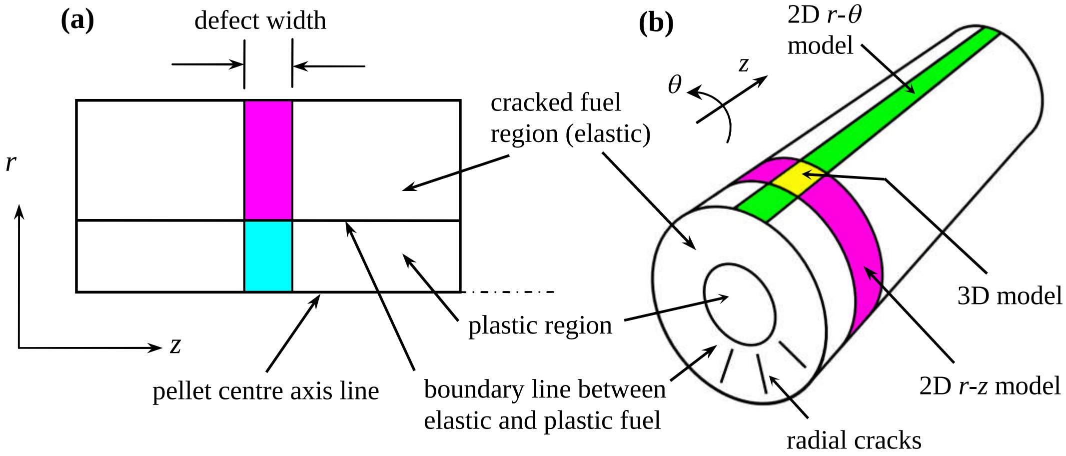

Figure 13: (a) 2D representation of the axial-symmetric [29] in-reactor fuel element model and (b) an equivalent 3D representation of the 2D axial-symmetric model with a sheath ring defect indicated by the purple band. The green band represents a sheath defect in a 2D *r*-*θ* model and the yellow patch represents a sheath defect in a 3D model (most realistic).

Two regions exist in the fuel pellet; an elastic outer region which is brittle with thermally-induced cracks, and an inner plastic region that is ductile and free of cracks (boundary line in Figure 13). The brittle-to-ductile transition temperature is illustrated in Figure 14 (a) [72]. A transition temperature occurs between 1200°C and 1400°C, but this point also depends on the strain rate (where a higher strain rate tends to increase the brittle-to-ductile transition temperature). The fracture stress increases in the elastic region of the fuel and is grain size dependent. A larger grain size tends to decrease the fracture strength. Figure 14 (b) illustrates the elastic, elastic-plastic transition and plastic domains in a cross section of an in-reactor fuel element.

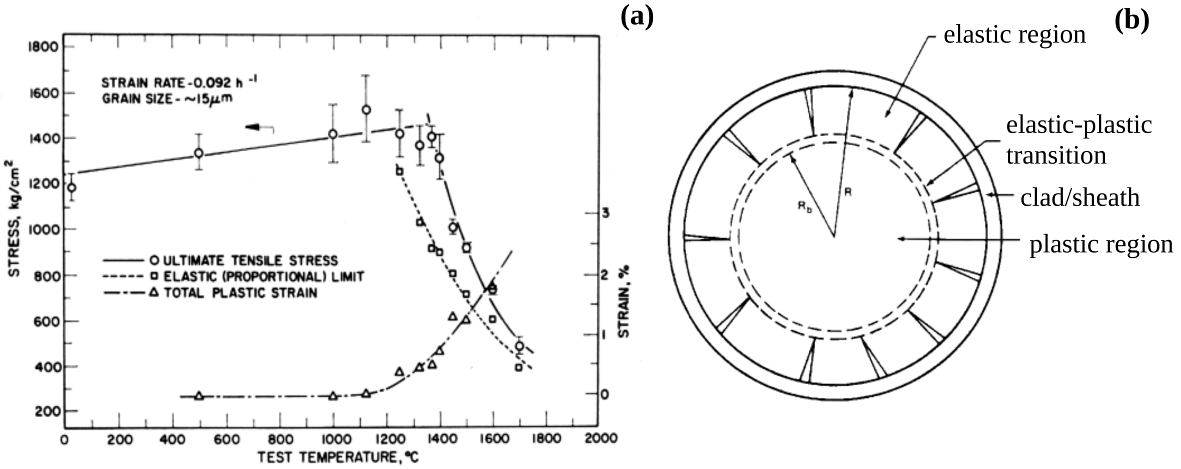

Figure 14: (a) Fracture stress versus temperature in UO_2 with 15 μm grain size, taken from [72] and (b) an in-reactor fuel element cross section showing the characteristic elastic and plastic regions in the fuel pellet, taken from [15]

Fuel cracking in the elastic part of the fuel is an important phenomenon, which is considered in the fuel oxidation model. This phenomenon is important because the fuel cracks allow access of the gas phase to the hotter regions of the fuel where the chemical reactions are accelerated, specifically, for the hydrogen gas diffusion equation and the reaction rate between the fuel and the coolant. With fission heat generation in the fuel pellets during normal operating conditions, thermally induced stresses result in the fuel pellets due to the large radial temperature gradient (over a thousand degrees K) between the pellet centre and the pellet surface (near the coolant). It can be noted that fuel oxidation in defective fuel can potentially increase (in extreme cases) these thermal stress due to the increase in fuel temperature. These stresses are relieved by fuel cracking when these thermal stresses typically exceed 80-150 MPa [15][73]. Figure 15 (a) shows a schematic of pellet cracking, which is intentionally exaggerated to emphasize the crack geometry.

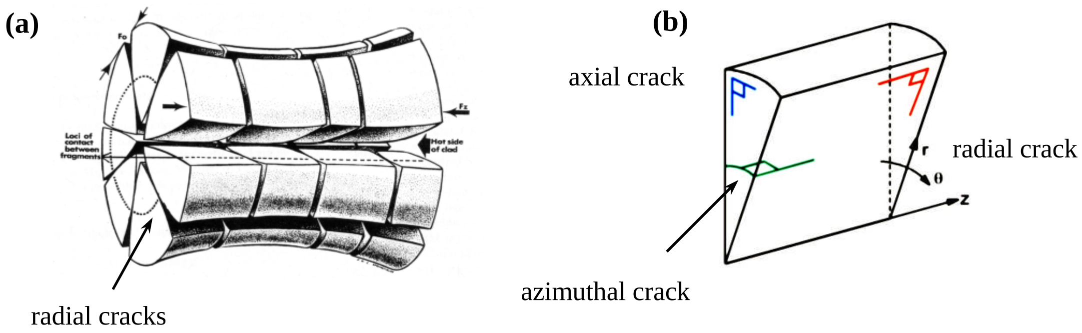

Figure 15: (a) Fuel pellet thermally induced cracking schematic with exaggerated crack widths, taken from [74] and (b) crack type orientations and their designations

Also shown in Figure 15 (a) is the thermal bambooing or hourglassing effect at the pellet edges, as discussed in [55][75]. In Figure 15 (b), three types of fuel cracks are identified in UO_2 nuclear fuel pellets: radial cracks, axial cracks, and azimuthal cracks. Out of these three types of cracks, it is believed that the radial and the axial cracks provide the dominant access paths for steam and hydrogen transport to and from the highest temperature regions of the fuel.

In modeling work by Williford [76] it is suggested that for various initial fuel-to-clad gaps (in BWR fuel) and various fuel linear powers, an appropriate radial fuel crack width develops. Figure 16 shows that for a larger initial diametral gap (fuel-to-clad gap) and smaller linear power, a larger fuel crack width develops. Also, the plot suggests that for higher linear powers, the fuel cracks may be closing and that the fuel cracks may be reaching a common fuel crack width value of $\approx 20\ \mu$m.

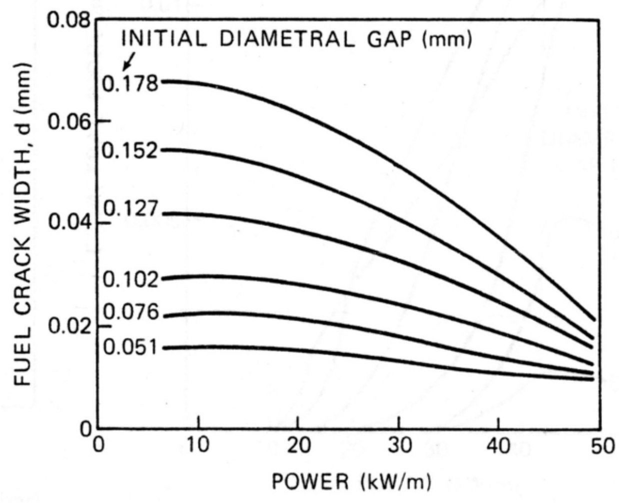

Figure 16: Fuel crack widths vs. linear power and initial diametral gap, taken from [76]

1.6 Limitations of the Higgs Model

The previous 2D axial-symmetric (*r*-*z*) fuel oxidation model [24][29] was able to predict the extent of fuel oxidation for defective fuel elements located in-reactor. Nevertheless, when this model was modified to a more representative 3D geometry, the model under predicted the extent of fuel oxidation. When the sheath defect surface area defined in the 2D axial-symmetric model was compared to actual defect sizes on the sheathing of defective fuel elements irradiated in the Bruce Nuclear Generating Stations and Pickering Nuclear Generating Stations, a substantial difference in defect surface area was noted. This is so because the sheath defect geometry in the 2D axial-symmetric model is actually representative of a band defect completely around the sheath circumference, instead of the actual sheath defect surface area, which is a point defect. This approach also assumes the hydrogen mole fraction in the defective fuel is azimuthally symmetric where in reality it is not.

The Higgs model makes an assumption that the transport of hydrogen in the fuel-to-sheath gap was more of an effective path compared to that in the fuel cracks in the axial direction, so that only the radial transport direction (the *r* direction in Figure 13 (a)) for hydrogen diffusion in the cracks needed to be considered. This assumption may be over simplistic. From the work of Wood and Oguma [57][73], the number of radial cracks that appear in fuel pellets is approximately equal to the fuel element linear power divided by two, or P_{linear}[kW m^{-1}]/2. Also, from Williford [76], who modeled BWR fuel pellet cracking at 40 kW m^{-1}, a fuel rod with an initial 0.06-0.13 mm fuel-to-clad gap (similar to CANDU fuel) would result in a radial fuel crack that is ≈20-30 μm in width. Thus, with sheath creep-down in CANDU fuel, the fuel-to-sheath-gap may be only ≈1 μm [15][77] in thickness, so that it is expected that gas diffusion in the radial fuel cracks would also occur, if not more so than in the fuel-to-sheath gap.

To account for fuel cracking in the fuel oxidation model, Higgs used empirical scaling parameters (or equation coefficients) [24]. Specifically, σ_{f} (where f stands for fuel) was used as a scaling parameter for the reaction rate terms used in both the oxygen diffusion equation in the fuel and in the hydrogen diffusion equation in the fuel cracks. The term was defined as the average ratio of the total surface area of the fuel cracks to the total volume of the fuel. For the hydrogen diffusion equation, a scaling parameter ε was used, which was the ratio of the crack volume to the total fuel volume. These artificial scaling parameters were used, since only a single domain was used for the two transport equations, i.e., a separate discrete fuel crack region was not modeled. This approach (which is analogues to some extent to the 'smeared crack' technique [78] that uses a fictitious crack model and not actual discrete fuel cracks) simplified the model construction considerably but ignored the true crack volume and crack surface area directly under the sheath defect zone. Hence, the ε ratio at the local scale may be quite different from the globally-assumed values for the fuel element.

Another limitation of Higgs model [24][29] was the simplification of the hydrogen gas diffusion equation in the fuel-to-sheath gap in the 2D axial-symmetric geometry. This model was simplified by reducing the transport equation to one dimension by using the Green's Theorem (e.g., integration by parts). In COMSOL Multiphysics®, this simplification approach was referred to as using the *weak* and *dweak* form. In this case, the equation was reduced from two dimensions to a single dimension. By applying this simplification the diffusion occurs over a line but since the model is axial-symmetric the diffusion can be imagined actually occurring in the fuel-to-sheath-gap in two dimensions (as a very thin cylinder) with no fuel-to-sheath gap thickness. In reality, though the fuel-to-sheath gap thickness is quite thin, it has a finite dimension, so that model results differed between using these two approaches.

Lastly, the elastic-to-plastic transition boundary seen in Figure 13 (a) (i.e., where fuel oxidation is thought to occur in the purple zone but not in the light blue zone) was previously accounted for by applying a function that produced a value between zero and one to the scaling parameters σ_f and ε [24]. However, in certain circumstances, the model became unstable using this technique.

Summary of Chapter 1:

- The CANDU reactor main features and CANDU fuel were introduced and discussed.
- The chemistry of uranium dioxide was discussed, which included: Its crystal structure, its oxygen interstitial sites due to the various uranium valence states, its oxygen stoichiometric deviation state - being either hyper or hypostoichiometric, as determined at equilibrium using the Gibbs energy minimization technique.
- Defective nuclear fuel in water cooled reactors and accompanying fuel oxidation and its effect on fuel thermal conductivity was introduced.
- Next, the reasoning for the development and validation of the mechanistic fuel oxidation model, to predict fuel oxidation behavior and thermal performance of operating defective fuel during normal operating conditions, was given.
- A link was then made between oxidized fuel, CANDU graphite, and stress corrosion cracking of Zircaloy sheathing in CANDU fuel (the latter being one of the fuel failure mechanisms).
- Lastly, the importance of the fuel oxidation model geometry selection (i.e., 2D and 3D) was explained in relation to observed sheath defect surface areas, and the importance of modeling discrete fuel cracks was discussed. Both of these aspects of the model were related to the limitations of the Higgs fuel oxidation model [24][29].

CHAPTER 2 GOALS OF RESEARCH

A mechanistic fuel-oxidation model for defective fuel has been developed at the Royal Military College of Canada (RMC) [29] and a controlled experiment was designed and built to validate the current model with discrete fuel cracks. The motivation for the *out-reactor instrumented defected fuel experiment* is that fuel oxidation has never been investigated experimentally at both high coolant pressure (≈10 MPa) and reactor temperatures while simultaneously measuring in-situ fuel temperature changes (and hence, the effect of reduced thermal conductivity due to fuel oxidation). Also, the experiment incorporates highly controlled test parameters such as the onset of a sheath defect (of a specific size), heating duration and power settings (related to temperature). These test results will therefore assist in the benchmark of the RMC fuel oxidation model. The model will then be incorporated into fuel performance codes for defective fuel assessment [48]. A validated model is applicable not only to CANDU reactors but also to pressure water and boiling water reactors, as they are UO_2 fuelled and water-cooled.

The additional models developed in this thesis therefore address two goals. The first goal was to extend the fuel oxidation model so that it could be used to provide guidance for the design of the *out-reactor instrumented defected fuel experiment*. This out-reactor experiment was led and technically supported by CNL (Canadian Nuclear Labs) formally AECL-CRL (Atomic Energy of Canada Limited - Chalk River Laboratories), was funded by COG (CANDU Owners Group), and was constructed and operated by Stern Laboratories Incorporated. At the time of this thesis was being written an initial commissioning test and final test were conducted. Post test oxygen measurements were being completed. In this test fuel element temperatures were measured in real-time at various radial and axial locations. All tests were conducted at reactor pressures and temperatures without a radiation flux. The second goal of this thesis was to address the previously discussed limitations of the Higgs fuel oxidation model [24][29].

This thesis work provides a 2D r-θ and 3D model simulations, which include discrete fuel cracks. Figure 17 shows the three different types of 2D r-θ models, where the purpose of these models was to provide justification for the parameters used in the 3D fuel oxidation model in order to predict the extent of oxidation in the *out-reactor instrumented defected fuel experiment*.

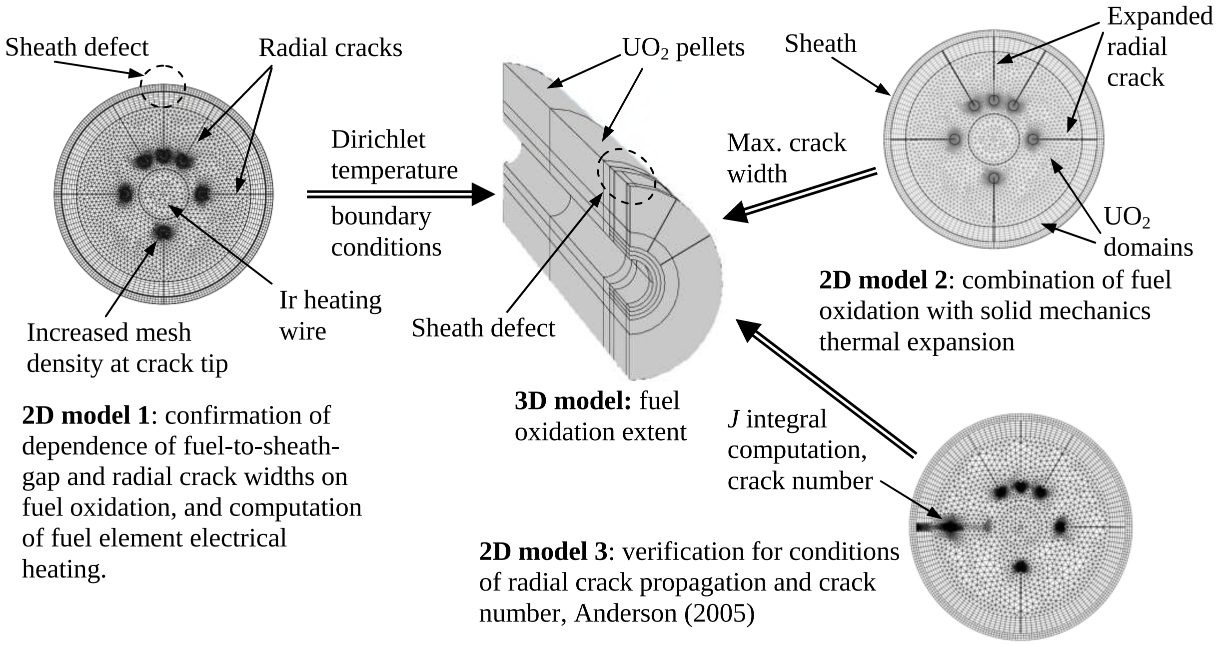

Figure 17: 2D r-θ models with the corresponding mesh to predict the temperature and stress distribution (as well as geometry displacement) used as input parameters for the 3D model

The first type of model ('2D model 1' in Figure 17) predicted the temperature distribution, the hydrogen mole fraction in the infiltrating steam in the fuel cracks (which is a result of fuel oxidation due to contact between the fuel and the coolant), and the resulting UO_{2+x} distribution in the fuel matrix. This model also computed the fuel element electrical heating and provided temperature bondary condtions to the 3D model. The second type of 2D r-θ model ('2D model 2' in Figure 17) computed fuel oxidation coupled to a solid mechanics model. With this model the stress field due to thermal expansion, the geometry of radial fuel cracks (such as crack width), and contact pressure of the sheath on the fuel was computed. A third 2D r-θ model ('2D model 3' in Figure 17) was based on the second model but neglected fuel oxidation. Its purpose was to investigate the conditions for the onset of radial fuel crack growth and the number of possible radial fuel cracks formed due to thermal expansion in the out-reactor fuel pellet. This was conducted by computing the J integral, which provided the stress intensity factor at crack tips, assuming linear elastic fracture mechanics [79].

Before tackling a full length 3D model of the out-reactor fuel element, two additional models were constructed and computed for validation purposes. The first was a 2D r-θ model that computed the temperature distribution as well as mechanical stress due to electrical heating in the out-reactor fuel element, but where no fuel oxidation was computed. This temperature modelled result was compared to the temperature measurements obtained in the first prototype test (FES1) at the Stern Laboratories. The second model attempted to estimate the extent of fuel oxidation for an actual defective fuel element in an operating power station. This model was constructed in 3D as a full length model (0.48 m long) to compare actual PIE (post irradiation examination) O/U ratio measurements in a defective fuel element to model results.

With the above model simulations and comparison to previous actual measurements, a model geometry was defined for a full length 3D fuel simulation of an out-reactor fuel oxidation experiment. Boundary conditions were provided by the 2D r-θ models (Figure 17). The improved geometry construction toolkit of the COMSOL® 4 version platform made the building of the more complex 3D model much easier. This model provided for a more realistic simulation of the element used in the out-reactor experiment. In this work, the radial fuel cracks were modeled as well as a pellet-pellet interface gap (that acts as a crack) - both near the defected sheath site. The sheath and most of the fuel-to-sheath gap were neglected to reduce model complexity. The results of this model also provided design support for the *out-reactor instrumented defected fuel experiment*.

Finally, since uranium dioxide can be oxidized by water or oxygen (i.e., to absorb oxygen atoms in an exothermic reaction), and since hyperstoichiometric uranium dioxide may be reduced by carbon (i.e., the CANLUB graphite, see again Section 1.4), the experimental part of this thesis also focused on the effect of oxidized UO_2 in the presence of graphite to determine its impact on iodine induced stress corrosion cracking in the Zircaloy sheathing. This investigation specifically examined if there was any benefit of excess oxygen potential in UO_2 fuel in contact with graphite to mitigate this corrosion process. Based on these experimental results, the fuel oxidation model was used to compute the necessary heating temperature and heating time needed to ‘load’ the required hyperstoichiometric oxygen onto the external surfaces of a fuel pellet, while not altering the overall stoichiometric O/U ratio in the bulk of the manufactured fuel pellet.

Summary of Chapter 2:

- Some of the models developed in this thesis will address two goals: The first goal is to extend the fuel oxidation model so that it can be used to provide guidance for the design of the *out-reactor instrumented defected fuel experiment*. The second goal is to address the previously discussed limitations of the Higgs fuel oxidation model.

- An explanation was given for the development of three 2D r-θ models. The first model will show the dependence of fuel crack width and fuel-to-sheath gap on the extent of fuel oxidation. A second model will compute fuel oxidation while being coupled to a solid mechanics model to provide the expected fuel crack geometry during the test. A third model will compute the onset and number of fuel cracks using the J integral.

- With the supporting 2D r-θ models, and an additional 3D in-reactor fuel oxidation model, a 3D out-reactor defective fuel model will be developed to initially validate the fuel oxidation model.

- Lastly, the experimental part of this thesis will investigate the effect of oxidized UO_2 in the presence of graphite to produce carbonaceous gases that can have mitigative properties against stress corrosion cracking in Zircaloy sheathing. The fuel oxidation model will also be used to compute the necessary conditions to introduce a small amount of hyperstoichiometric oxygen to s fuel pellet.

CHAPTER 3 MODEL DEVELOPMENT

Section 3.1 discusses the out-reactor test setup at Stern Laboratories, as needed for the model design parameters. The model in turn provided feedback to the designer of the test. Section 3.2 provides the background and governing equations for the updated fuel-oxidation model, as needed for the simulation of the *out-reactor instrumented defected fuel experiment*.

3.1 Out Reactor Experiment Setup

The out-reactor test facility at Stern Laboratories includes a small self-contained coolant loop capable of operating at CANDU reactor conditions. This loop is designed to run at up to 10 MPa inlet pressure and normal coolant temperatures of 280°-310°C. A laboratory data acquisition system is used to monitor the loop and test-fuel simulator instrumentation. Electrical current is used as the heating source for the out-reactor fuel element.

The fuel element simulator has 29 fuel pellets, with an axial clearance of 1 to 3 mm. Typical primary fuel sheath defect surface area in defective fuel has been observed to be 1-2 mm^2 [43][80][81], while sheath defects as large as 35 mm^2 have been observed [29]. Sheath defects are usually identified as secondary defects (due to hydriding or deuteriding damage) [33][81]. The designed sheath defect surface area for this test is targeted to be 5-15 mm^2 though smaller sheath defect sizes are acceptable as well. At a chosen time after a conditioning heating period, an artificial slit defect is initiated in-situ in the sheath. The breached sheath exposes the fuel to the coolant water at a temperature of approximately 260-295°C and a pressure of 7.5-10 MPa.

Each test pellet is about 16 mm in length and 12 mm in diameter. The test pellets include a central hole to accommodate an electrical iridium (Ir) heating bar about 2.9 mm (2.87 mm) in diameter. Temperature measurements of the test fuel are performed in real time with thermocouples at three radial positions in the test pellet as indicated in Figure 18. Thermocouple holes were ≈0.66 mm in diameter. Thermocouple holes (1) and (3) were originally positioned 0.5 mm from the pellet edges and thermocouple (2) was positioned equally spaced between the two. The actual pitch circle radii of the thermocouples were

TC1=2.74±0.13 mm, TC2=3.83±0.13 mm, and TC3=4.98±0.13 mm [82]. The electrical heating bar is made to run through the entire central length of the fuel element so that the fuel pellets are heated from the central diameter.

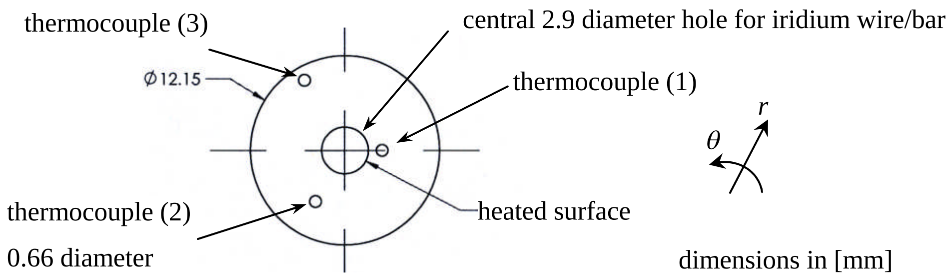

Figure 18: Radial cross section of UO_2 test pellet with drilled holes. The 2.9-mm diameter central hole is for the iridium electrical heating bar. The smaller holes provide access for thermocouples and thermocouple wires. Thermocouple sites were located at: (1) close to the pellet centre and near the heating element, (2) between the pellet centre and pellet outer surface and (3) near the outer surface of the pellet.

This heating technique has been successfully employed in the past by Oguma [73] using a tungsten bar to heat UO_2 fuel pellets to study cracking and relocation behaviour. The UO_2 fuel pellet material after it has been sintered was extremely hard and it was found that drilling the small holes into the finished pellet proved to be too difficult. As such, it was decided to first drill the compacted UO_2 pellets and then sinter them. Figure 19 shows the compacted and drilled UO_2 pellet on the left and a sintered UO_2 pellet on the right.

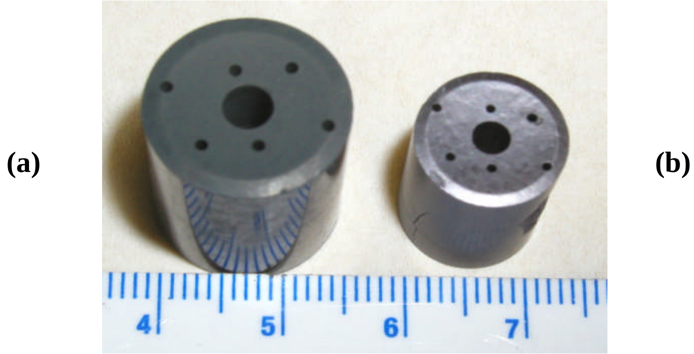

Figure 19: (a) Compacted and drilled (unsintered) pellet and (b) a finished pellet after sintering (manufactured at CRL-CNL)

The technique for making the in-reactor fuel pellets was not without problems. Some pellets cracked when drilled and some pellets experienced unacceptable distortion during the sintering process. Nevertheless, there were enough satisfactory pellets manufactured by the Fuel Engineering Branch and the Fuel and Fuel Channel Safety Branch at CNL (formally AECL-CRL) to build two complete out-reactor fuel elements.

Iridium (Ir) was chosen for making the central heater bar, since it is a noble metal and has a high melting temperature (2466 °C) so that it can withstand the hot and oxidizing environment. The limiting factor when using the iridium bar as a heater in the UO_2 pellets is the iridium-zirconium eutectic point, which is 1240 °C [83]. Other metal pairs such as tungsten-zirconium or tantalum-zirconium have good (high) eutectic points and good weldability, but tungsten and tantalum are not noble metals. The eutectic point occurring at welded junctions between the iridium bar heater and the Zircaloy end-caps in the fuel element could have been a problem, but the temperature at these locations are lower due to edge effects, so this problem was mostly avoided.

The out-reactor fuel element is heated by passing electrical current through the central iridium bar as well as the Zircaloy sheath (i.e., the two conductors are connected in parallel). This is because Stern Laboratories experience has shown that if only the central electrical heating bar is biased to the current voltage and the sheath is grounded, electrical arching and shorting can occur between the heater bar and sheath, leading to damage and failures. In order to prevent this from happening, the Zircaloy sheathing is connected in parallel to the iridium bar conductor (instead of being grounded). Figure 20 provides part of a drawing [84] of the fuel element simulator. The sheath defect in the figure is just above pellet number 8 from the downstream end cap (at item #6). SECTION B-B shows an axial view of the pellet number 4 and the first set of three thermocouples at three radial and azimuthal positions (TC-1, TC-2 and TC-3). SECTION C-C shows the second set of thermocouples at a second axial position (TC1, TC2 and TC3), which is located at pellet number 8 from the downstream end cap. Note that the second set of thermocouples pass through pellet number 4 in SECTION B-B. The iridium bar is fixed (screwed and welded) at the outlet end (left) but is free to axially expand at the inlet end (right). Silver powder, item #2, is used to ensure electrical contact throughout the test.

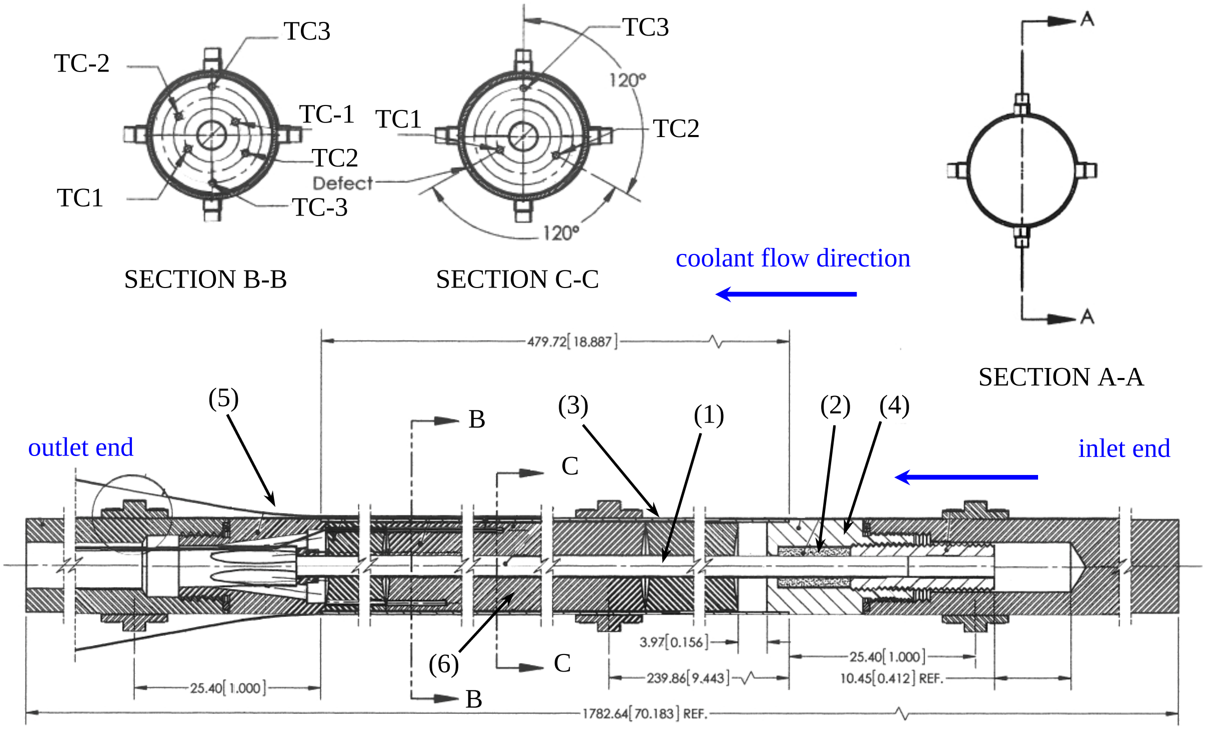

Figure 20: Fuel element simulator assembly drawing [84]. The key parts are (1) the iridium bar (heater), (2) the silver powder packing section for electrical conduction and expansion allowance, (3) the sheath, (4) the upstream end cap, (5) the downstream end cap, and (6) pellet at location of the sheath defect.

Before the test is started, the fuel element is heated (under pressure) by electrical power for a few hours in order to allow for both fuel cracking and sheath creep down to occur. Once the fuel and sheath are conditioned, the sheath is defected by helium gas injection into the fuel element to induce an internal pressure of ≈10-12 MPa while the pressure of the coolant loop is lowered from 10 MPa to ≈7 MPa. With a pre-machined axial groove (located between pellets 8 and 9) where the sheath wall is ≈1/10 of the original wall thickness and with the high internal pressure, a sheath defect occurs. Figure 21 (a) shows the design and location of the defect groove on the sheath. Figure 21 (b) shows a picture of an initial sheath rupture test performed in air at room temperature, with no pellets installed, conducted at Stern Laboratories.

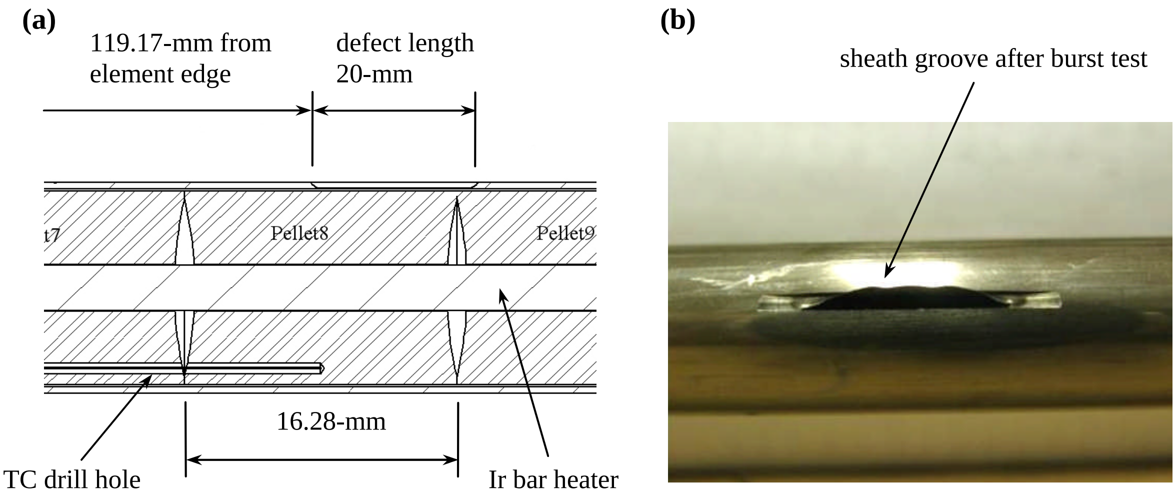

Figure 21: (a) Sheath defect design and location on the fuel element simulator (not to scale) [85] and (b) a sheath groove after a burst test in air with no pellets installed [86]

Bursting the fuel element filled with equivalent sized fuel pellets, with a sheath defect described in Figure 21, at coolant temperature and pressure, yielded a smaller sheath defect surface area than 1 mm^2 (figure not shown). As a result a modified 3-cut sheath defect design was developed. Figure 22 shows a sheath burst test result using this improved design (designed at the Fuel and Fuel Channel Safety Branch at CNL by the author, B. Leitch, and C. Thiriet and tested at Stern Laboratories).

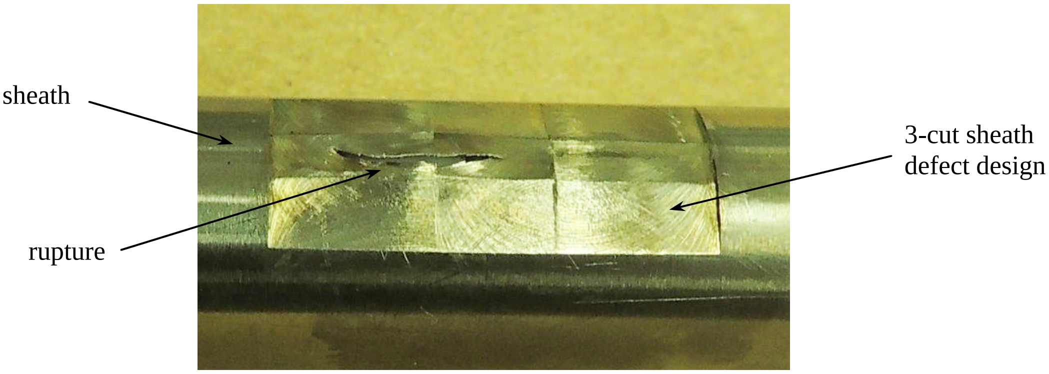

Figure 22: Sheath defect after rupture test at loop temperature and pressure. Test was conducted with equivalent sized fuel pellets.

With this 3-cut sheath defect design a satisfactory defect surface area was achieved, which was ≈4 mm^2 in this case, approaching the original defect size requirement [87].

Post experiment measurement of the oxygen potential, or the O/M ratio, at several axial and radial locations in the fuel stack will be required for validation of the fuel oxidation model. The first method is based on a Coulometric Titration (CT) method [80] employed previously at CNL (formally AECL-CRL) to measure the average O/M ratio of spent CANDU fuel. This O/M ratio measurement technique has a detection limit of ≈2.01 and a maximum uncertainty of ±0.011 in irradiated and unirradiated UO_{2+x} fuel [87][88]. Generally in this technique powdered UO_{2+x} samples for coulometric titration (CT) analysis are prepared from 1.4, 1.6, and 1.8 mm diameter drilled-out holes (using diamond tipped drill bits) that are ≈5 mm deep in the oxidized fuel pellet. These UO_{2+x} samples are then heated to 1273 K in a reducing atmosphere provided by a known H_2 in Ar (carrier gas). When the CT apparatus operates in the reduction mode (for determining x in the samples), only the down stream CT electrolysis cell is used. When the carrier gas flows over the sample in the furnace some of the H_2 will reduce the UO_{2+x} to produce water vapour. The remaining hydrogen in the gas (that is not picked up by the specimen) is oxidized by oxygen from the downstream CT cell. The hyperstoichiometric oxygen content in the samples is then determined by knowing the precise quantity of hydrogen that was coulometrically titrated in the downstream cell [22][80]. The second method involves taking X-ray diffraction scans [18][89] of the oxidized fuel specimens and working out the material lattice parameter. Using a relationship between the lattice parameter and the O/U ratio, the oxygen stoichiometric deviation can be deduced [89]. The uncertainty of this method can be as high as $\pm\Delta x=0.015$ when $x=0.050$, according to a lattice parameter vs. O/M ratio plot given in [89].

3.2 Fuel-Oxidation Model Development

The following section provides the governing equations of the fuel-oxidation model as applied to the out-reactor experiment. The subsequent subsections provide the thermal physical properties of the materials involved.

In the mechanistic model [29], a treatment is required for both gas phase and solid-state oxygen diffusion, which are controlled by temperature-dependent reactions. This necessitates knowledge of the temperature distribution in the fuel element. Hydrogen (H_2) and steam (H_2O) are specifically considered in this treatment rather than deuterium and heavy water.

Figure 23 depicts an axial cross section schematic of the test fuel element without thermocouples or the central electrical heating element. In the schematic, fuel cracks appear in the fuel pellets as a result of fuel thermal expansion [75][90].

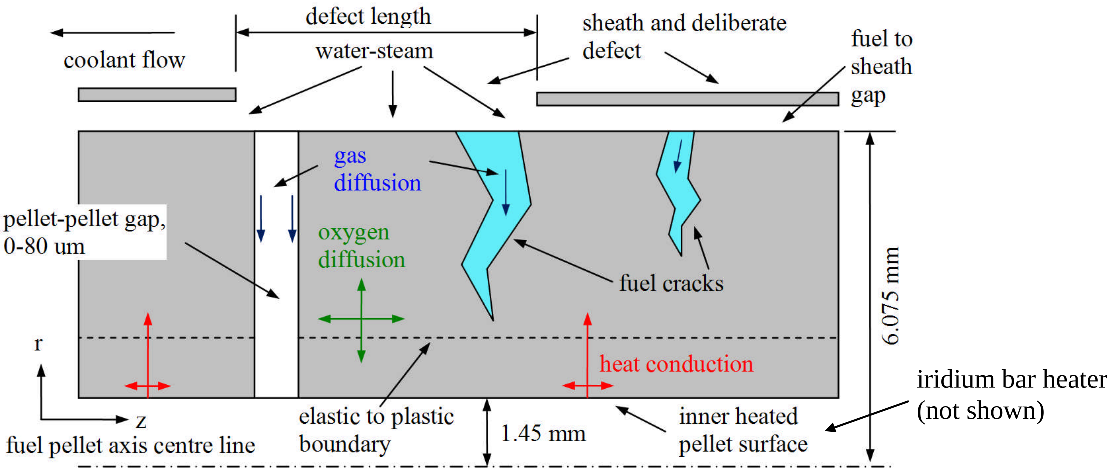

Figure 23: A 2D *z-r* representation of out-reactor fuel element. Heat conduction occurs over all domains, gas transport occurs in fuel cracks and in a pellet-pellet gap, and solid state oxygen diffusion occurs in the fuel. The defect length is ≈5-15 mm with a width of 0.1-1.0 mm (the latter in the azimuthal direction not shown).

Below the elastic-plastic boundary, cracks will initially appear but will later self heal [15][91]. The temperature at which this transition occurs in the model was set at 1523 K, yielding an *effective* crack tip depth. In reality though this transition occurs over a range of temperatures [15][73]. Figure 23 depicts a deliberate sheath defect, which is 1 mm wide (into the page) and 5-15 mm long in the axial *z* direction. Actual sheath defects can be less than 1 mm wide. Elevated oxidation occurs when the coolant/steam makes contact with the hotter regions of the fuel, via the fuel cracks and the pellet-pellet gap near the sheath defect.

The hydrogen mole fraction, q, at the defect location and in the volume of the radial cracks directly under the defect site, is assumed to be 4.1×10^{-6} moles m^{-3}. This value is the hydrogen mole fraction of the coolant in reactor [29] referred to as q_c. The generalized mass balance equation for oxygen transport in the fuel matrix is given by Eq. (18):

$$c_{\mathrm{U}} \frac{\partial x}{\partial t} = c_{\mathrm{U}} \nabla \cdot \left(D \left(\nabla x + x \frac{Q}{RT^2} \nabla T \right) \right) + R_f^{react} \qquad (18)$$

where x is the oxygen deviation from stoichiometry in the uranium oxide matrix (UO_{2+x}), c_{U} is the molar density of uranium in mol m^{-3}, R is the universal or ideal gas constant equal to 8.205×10^{-5} atm m^3 mol^{-1} K^{-1}, T is the temperature in K, D is the chemical diffusion coefficient for oxygen interstitials, which is a function of temperature (T in K) [29] as given by Eq. (19). It can be noted that Eq. (18) considers both normal diffusion in a concentration gradient and diffusion in a temperature gradient (the Soret effect).

$$D = 2.5 \times 10^{-4} \cdot \exp(-16400 / T) \quad \mathrm{m^2\ s^{-1}} \qquad (19)$$

For the temperature gradient diffusion, Q is the molar effective heat of transport and is provided by Eq. (20) (where x again is the stoichiometric deviation value):

$$Q = -3.5 \times 10^{34} \exp(-17(4 + 2x)) \quad \mathrm{J\ mol^{-1}} \qquad (20)$$

In Eq. (18) R_f^{react} is the rate of reaction for either fuel oxidation or reduction in moles O or H_2 m^{-2} s^{-1}. For oxidation the reaction rate is given by:

$$R_f^{react,ox} = c_{\mathrm{U}} \alpha \sqrt{(1-q) p_t} \, (x_e - x) \ \text{ for } \ x < x_e \qquad (21)$$

where α is the rate coefficient for the surface-exchange of oxygen, which is given by Eq. (22) [29][92], where T is in K and α has the units of m s^{-1}.

$$\alpha = 0.365 \exp\left(\frac{-23500}{T} \right) \qquad (22)$$

Generally, Eq. (22) has the form of the Svante Arrhenius equation, which relates the rate constant of a chemical reaction and the temperature at which the reaction takes place [93]. In Eq. (21), p_t is the total system pressure in atmospheres (of the coolant), q is the hydrogen mole fraction in the fuel cracks and in the fuel-to-sheath gap, x (or ‘Xdev’ is the notation used in the simulation models) is the stoichiometric deviation, and x_e is the equilibrium stoichiometry deviation based on the local oxygen potential of the gas in the fuel cracks using thermodynamic analysis [29]. The kinetic reaction rate in Eq. (18) can also represent chemical reduction in moles O or H_2 m^{-2} s^{-1} as given in Eq. (23) [29].

$$R_f^{react,red} = c_{\mathrm{U}}\alpha\sqrt{qp_t}\left(x_e - x\right) \text{ for } x > x_e \tag{23}$$

The equilibrium stoichiometry deviation x_e is given by [24][29]:

$$x_e = \frac{a_\aleph + c_\aleph\zeta + e_\aleph T + g_\aleph T^2 + m_\aleph T^2 + k_\aleph \zeta T}{1 + b_\aleph\zeta + d_\aleph T + f_\aleph\zeta^2 + p_\aleph T^2 + n_\aleph\zeta T} \tag{24}$$

where ζ is the log of the hydrogen-to-steam partial pressure ratio equal to $\zeta = \log\left(\frac{q}{1-q}\right)$, and the coefficients are given by:

Table 1: Coefficient values used in the equilibrium stoichiometry deviation x_e equation

coefficient	value
$a_\aleph$	0.033107007
$b_\aleph$	0.268984735
$c_\aleph$	0.008679485
$d_\aleph$	-0.000622197
$e_\aleph$	-5.18804E-05
$f_\aleph$	0.020038397
$g_\aleph$	0.000450165
$k_\aleph$	-7.83442E-06
$m_\aleph$	1.84196E-08
$n_\aleph$	-7.45197E-05
$p_\aleph$	1.39057E-07

The condition statement for either fuel oxidation or fuel reduction is provided by [24]:

$$R_f^{react} = \left\{ \begin{matrix} R_f^{react,ox} & x_{e\_fix} \geq x \\ R_f^{react,red} & x_{e\_fix} < x \text{ and } x > x_{fs} \end{matrix} \right\} \tag{25}$$

where x_{fs} is the stoichiometric deviation at the pellet surface equal to 1×10^{-4} and x_{e_fix} is another condition statement provided by [24]:

$$x_{e\_fix} = \begin{cases} x_{fs} & x_e < x_{fs} \\ x_e & x_e \geq x_{fs} \end{cases} \tag{26}$$

A zero flux boundary condition for the oxygen stoichiometric deviation is taken as zero at all external geometric boundaries in the model, except for crack and pellet-pelled surfaces. See Sections 3.5.2, 3.5.5, and 3.5.6 for more details.

It is worth mentioning that Eq. (23) representing chemical reduction kinetics of the fuel may be conservative. This is because experiment data [94][95] suggests that interstitial diffusion alone is not rate-limiting and that, alternatively, one can consider a combined diffusion/mass transfer model [94][95]. In terms of the time scale of the *out-reactor instrumented defected fuel experiment* or with defective fuel residence time in a reactor there is no significant change over longer times as the fuel will go to the equilibrium value of x_e in Eq. (24).

Hydrogen is contributed to the gas environment in the fuel cracks by the fuel-oxidation reaction and to a lesser extent by sheath oxidation. The mass balance for the hydrogen molar concentration, qc_g, in the fuel cracks and in the fuel-to-sheath gap is provided by Eq. (27) as a general form time-dependent diffusion equation. This equation is applicable only in the domain outside fuel elastic-to-plastic boundary in the radial direction (see again Figure 23) where the fuel cracks reside, in the fuel-to-sheath gap, and in the pellet-pellet gap.

Eq. (27) is essentially the same equation used by Higgs [29] but here the diffusion equation is used for all gas domains (fuel cracks and the fuel-to-sheath gap in a 2D model, and the pellet-pellet gap in a 3D model).

$$c_g \frac{\partial q}{\partial t} = \nabla \cdot \left(c_g D_g \nabla q \right) + R_f^{react} + \left(1 - f \right) R_{Zirc\_sheath}^{ox} \tag{27}$$

However, it neglects axial bulk-flow. Here c_g in Eq. (27) is the total molar concentration of the steam gas in mol m^{-3} and it is calculated using the ideal gas law:

$$c_g = \frac{p_t}{RT} \qquad (28)$$

where p_t is the total system pressure in atmospheres and R is the universal gas constant of 8.205×10^{-5} atm m^3 mol^{-1} K^{-1} and T is the gas temperature in the fuel cracks, the fuel-to-sheath gap and pellet-pellet gap. The parameter c_gD_g is the steam diffusivity quantity that has the units of mol m^{-1} s^{-1} and is calculated from Chapman-Enskog gas kinetic theory in Eq. (29) [24][43]. This equation is solved for light water steam in the out-reactor test:

$$c_g D_g = 2.2646\times10^{-3}\frac{\sqrt{T\left(M_{H_2}^{-1}+M_{H_2O}^{-1}\right)}}{\sigma_{AB}^2\Omega_{AB}} \qquad (29)$$

where M_{H_2} and M_{H_2O} are the molecular weights of hydrogen and water molecules equal to 2.0159 g mol^{-1} and 18.0153 g mol^{-1}, respectively. σ_{AB} is the combined collision diameter of hydrogen and water equal to $0.5\left(\sigma_{H_2}+\sigma_{H_2O}\right)$, where $\sigma_{H_2} = 2.827$ Å and $\sigma_{H_2O} = 2.641$ Å. Ω_{AB} is the collision integral given by [24]:

$$\Omega_{AB} = 0.45776 + 0.80674\left(0.004549T\right)^{-0.45859} \qquad (30)$$

Zircaloy sheath oxidation/corrosion with resulting hydrogen generation and pickup by the sheathing is also considered in the 2D r-θ fuel oxidation model. Hence the source term $R_{Zrc\_sheath}^{ox}$ for hydrogen production in mol H$_2$ m^{-2} s^{-1} in the fuel-to-sheath gap is also added in Eq. (27). The source term $R_{Zrc\_sheath}^{ox}$, which is a function of temperature, is provided by [29]:

$$R_{Zirc\_sheath}^{ox} = 160\exp\left(-14192/T_{sheath\_inner}\right)F_c \qquad (31)$$

where T_{sheath_inner} is the inner surface temperature of the sheath and $F_c \approx 3$ [38] is the enhancement factor for out-reactor Zircaloy surface corrosion. It is worth noting that the internal Zircaloy sheath surface corrosion due to steam exposure is enhanced by fission product bombardment for in-reactor conditions, where $F_c \approx 49$ in comparison. The parameter f in Eq. (27) is the hydrogen pickup fraction by the sheath and was set to 0.05

[29][38]. Lastly it is noted that the sheath/water oxidation reaction competes with fuel oxidation. This effect was applied in only one of the 2D *r-θ* fuel-oxidation models (with the closed fuel-to-sheath gap, Section 4.2.1 results), since its contribution was found to be small.

The temperature profile in the fuel element is obtained from the solution of a time-dependent heat conduction equation given by:

$$\rho_s C_p \frac{\partial T}{\partial t} = \nabla \cdot \left(k \nabla T\right) + Q_v \tag{32}$$

where ρ_s is the density in mol m^{-3} (or kg m^{-3}), C_p is the specific heat capacity at constant pressure in kJ mol^{-1} K^{-1} or kJ kg^{-1} K^{-1} and k is the thermal conductivity in kW m^{-1} K^{-1} of all constituent materials in the fuel element. The parameter Q_v is the volumetric heat source term of the fuel. In the current 2D *r-θ* out-reactor fuel oxidation model, the Q_v term is the ohmic heating generated in the iridium bar heater and in the Zircaloy sheath (and to a small extent in the UO_2 pellets). In the 3D out-reactor fuel-oxidation model, this term is set to zero. Instead Dirichlet temperature boundary conditions were used to describe this heat source. For an in-reactor defective fuel element, the Q_v term is set to a fission heat source term given by:

$$Q_v = \frac{P_{\mathrm{linear}}}{\pi a_{pellet}^2} \left[\frac{\left(\kappa a_{pellet}\right)}{2 I_1\left(\kappa a_{pellet}\right)} \right] I_o\left(\kappa r\right) \tag{33}$$

where P_{linear} is the linear power of the fuel element in kW m^{-1}, a_{pellet} is the pellet radius in m, κ is the inverse neutron diffusion length in m, r is the radial distance from the pellet centre, I_o and I_1 are the zeroith and first order modified Bessel function, which are provided in Eq. (34) [96].

$$\begin{aligned} &I_n\left(x\right) = \sum_{k=o}^{\infty} \frac{1}{k!\left(n+k\right)!} \left(\frac{x}{2}\right)^{n+2k} \text{ where } n = 0,1 \\ &\text{e.g., } I_0\left(x\right) = 1 + \frac{x^2}{2^2} + \frac{x^4}{2^2 \cdot 4^2} + \frac{x^6}{2^2 \cdot 4^2 \cdot 6^2} + .. \end{aligned} \tag{34}$$

The thermal conductivity k of UO_{2+x} as seen in Eq. (32) is evaluated using:

$$k = \kappa_{1d}\kappa_{1p}\kappa_{2p}\kappa_{4r}\left(k_{ph} + k_{e} + k_{rad}\right) \tag{35}$$

as proposed by Lucuta *et al.* [97] and employed by Higgs [24][29]. Generally the thermal conductivity of UO_2 in Eq. (35) is comprised by three terms: The conductive heat transfer k_{ph} term via lattice vibration (or phonons), the electron hole movement k_e term (or polarons), and the radiative thermal effects k_{rad} term. The heat transfer via lattice vibration k_{ph} term is given by Eq. (36), provided from the Ellis-Porter-Shaw model [29][98], where T is in K, and where Eq. (36) is correlated to experimental data and is valid over an oxygen stoichiometry deviation range from $x = 0$ to ≈0.2 for fully dense fuel. k_{ph} has the units of kW m^{-1} K^{-1}.

$$k_{ph} = \frac{1}{A(x) + B(x)T} \tag{36}$$

The values *A(x)* and *B(x)* are given by Eq. (37a) and (37b), respectively [29], where x is the oxygen stoichiometry deviation value as solved for in Eq. (18).

$$A(x) = 14 - 10.763\sqrt{x} - 2381.4x + 12819.86\left(\sqrt{x}\right) \tag{37a}$$

$$B(x) = \begin{cases} 0.2218 + 0.2562\sqrt{x} - 0.64x - 3.6764\left(\sqrt{x}\right)^3, & x < 0.155 \\ 0, \quad x \geq 0.155 \end{cases} \tag{37b}$$

The electron hole movement k_e term is given by Eq. (38) [29] where T is in K, and where k_e and has the units of kW m^{-1} K^{-1}.

$$k_e = \left(0.871 + 2.9 \times 10^{-5} T\right)^{-1} \frac{2.024 \times 10^{8}}{T^{5/2}} \exp\left(\frac{-16350}{T}\right) \tag{38}$$

At normal operating fuel temperatures, the radiative term k_{rad} contributes less than 0.01% to the overall thermal conductivity and so is neglected in the in-reactor models [29][42]. Since the heating technique in the *out-reactor instrumented defected fuel experiment* utilizes a central electrical heating element the temperature at the element centre (in the plastic region of the fuel) can be relatively high ($T > 1900$ K), as compared to in-reactor operating fuel at normal/medium linear powers [77]. Hence, the radiative term is considered [97] and its contribution to fuel thermal conductivity is given by [42]:

$$k_{\mathrm{rad}} = 1.5\times10^{-10}\left(\frac{N^2}{\alpha_R(T)}\right)T^3 \quad \text{using} \qquad (39)$$
$$\alpha_R(T) = C_1 \exp(C_2 T)$$

where k_{rad} has the units of kW m^{-1} K^{-1} and T is in K, and where N is index of refraction (set to 2.25) with C_1 = 8750 m^{-1} and C_2 = 7.5971×10^{-4} K^{-1} [42].

The correction or contributing factors (κ) in Eq. (35) account for burnup, porosity, and radiation damage effects. Although in the out-reactor fuel oxidation test there will be no burnup or radiation damage, the model includes these terms for completeness, since it is applied later for in-reactor conditions. The first factor $\kappa_{1\mathrm{d}}$ is a correction factor for fully dense fuel for dissolved fission products at fractional burnup β in atom% and is given by Eq. (40) [24][29].

$$\kappa_{1\mathrm{d}} = \left(\frac{1.09}{\beta^{3.265}} + \frac{0.0643}{\sqrt{\beta}}\sqrt{T}\right)\cdot \arctan\left(\frac{1}{1.09/\beta^{3.265} + \left(0.0643/\sqrt{\beta}\right)\sqrt{T}}\right) \qquad (40)$$

The correction factor $\kappa_{1\mathrm{p}}$ for precipitated fission products is given by Eq. (41) [29].

$$\kappa_{1\mathrm{p}} = 1 + \frac{0.019\beta}{(3-0.019\beta)(1+\exp(-(T-1200)/100))} \qquad (41)$$

where again β is the fractional burnup in atom%. Both Equations (40) and (41) take on a value of unity when β approaches zero. The correction factor, $\kappa_{2\mathrm{p}}$, accounts for fuel porosity and is given by Eq. (42a):

$$\kappa_{2\mathrm{p}} = (1-\beta_{\mathrm{T}} P_{\mathrm{or}}) \qquad \text{using} \qquad (42a)$$
$$P_{\mathrm{or}} = (1-\rho_{\mathrm{s\_new}}/\rho_{\mathrm{TD}})\cdot(1-F_{\mathrm{d}}) \qquad (42b)$$

where β_{T} accounts for temperature effects and is equal to 2.6-0.5×10^{-3}T where T is in K, P_{or} is the fuel porosity, $\rho_{\mathrm{s\_new}}$ is the density of the fuel when it is newly sintered/manufactured, and ρ_{TD} is the maximum theoretical density of the fuel. F_{d} in Eq. (42b) is the fractional change in porosity with specific burnup B in MWh kgU^{-1}:

$$F_{\mathrm{d}} = 0.6 - \exp\left(-0.506 - 8.67\times10^{-10}T^{3}\left(1-\exp\left(-2.87\times10^{-2}B\right)\right)\right) \qquad (43)$$

Here B can be replaced by the fractional burnup β by multiplying by 225 MWh kgU^{-1} per atom %.

It is important to point out a significant difference in the thermal conductivity calculation of the UO_2 fuel pellets for out-reactor and in-reactor conditions [29]. The difference lies with the last factor in Eq. (35), which is the radiation damage factor, κ_{4r}, given by:

$$\kappa_{4\mathrm{r}} = 1 - \frac{0.2}{1+\exp\left(\left(T-900\right)/80\right)} \qquad (44)$$

For an in-reactor environment, the effects of radiation damage is important only for temperatures below 1100 K due to annealing effects above this temperature [29]. Since there is no radiation damage in the *out-reactor instrumented defected fuel experiment* this factor is set to unity. Lucuta *et al.* [97] provides the estimated effect of radiation damage on the thermal conductivity of the fuel (Figure 24). As can be seen in the figure below, the reduction in thermal conductivity is significant in the low-temperature regions of the fuel where radiation damage occurs and that persists in the fuel, especially around 700-800 K.

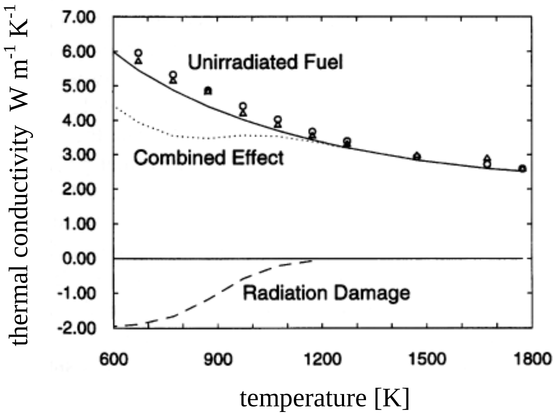

Figure 24: The estimated effect of radiation damage on thermal conductivity as a function of temperature, taken from [97]

Since κ_{4r} is set to 1 in the out-reactor fuel oxidation model, the thermal conductivity of the out-reactor fuel will be greater in the outer regions of the fuel pellet as compared to the outer regions for in-reactor defective fuel as simulated by Higgs [24][29]. Hence, with radiation, this term tends to increase the temperature for in-reactor fuel so that fuel oxidation will increase. Thus, with the radiation damage factor set to unity, there is predicted to be a marked decrease in fuel oxidation in out-reactor fuel compared to in-reactor fuel at similar powers.

The density ρ_s of the UO_2 fuel in Eq. (32) (named cu_UO2 in the model implementation) is given by Eq. (45) [29] and has the units of mol m^{-3}:

$$\rho_s = 40588\rho_f\left(1 - P_{or}\right) \tag{45}$$

where P_{or} is the fuel porosity given by Eq. (42b), ρ_f is a unit less temperature dependent function formulated for UO_2 thermal expansion [99] and converted to a volume thermal expansion [24][100] to assess the UO_2 density change as a function of temperature in Eq. (46). The number 40,588 is the maximum theoretical mole density of UO_2 per m^3.

$$\rho_f = \left(4.391\times10^{-13}T^3 - 2.705\times10^{-10}T^2 + 9.802\times10^{-6}T + 0.99734\right)^{-3} \qquad 273 < T < 923\,\mathrm{K} \tag{46a}$$

$$\rho_f = \left(1.219\times10^{-12}T^3 - 2.429\times10^{-9}T^2 + 1.179\times10^{-5}T + 0.99672\right)^{-3} \qquad T \ge 923\,\mathrm{K} \tag{46b}$$

The specific heat capacity of stoichiometric and hyperstoichiometric uranium dioxide is given by Eq. (47), where C_p has the units of kJ mol^{-1} K^{-1} (named Cp_UO2 is the fuel-oxidation model), T is in K, and x is the stoichiometry deviation [29].

$$C_p = 1000^{-1}\begin{pmatrix} 52.174 + 45.806x + \left(87.951\times10^{-3} - 7.3461\times10^{-2}x\right)T \\ + \left(1 - x\right)\left(-84.241\times10^{-6}T^2 + 31.542\times10^{-9}T^3 - 2.6334\times10^{-12}T^4\right) \\ - \left(713910 + 295090x\right)T^{-2} \end{pmatrix} \tag{47}$$

It is worth noting here, as explained earlier, that in the previous Higgs model [29], scalar parameters σ_f and ε (defined as the ratio of the total pellet crack surface area to the total fuel volume and the ratio of the total volume of cracks in the fuel to the total volume of fuel, respectively) were used in Eq. (18) and (27). However, in the current model, these parameters are eliminated, since discrete radial fuel cracks are specifically modeled near the sheath defect.

Finally, the uranium dioxide specific heat C_p and thermal conductivity k are both functions of temperature T and stoichiometry deviation x. The source term R_f^{react} is a function of the temperature, oxygen stoichiometry deviation, and hydrogen mole fraction q. Thus, since this latter term appears in both the solid state oxygen diffusion equation (Eq. (18)) and in the hydrogen mole fraction diffusion equation (Eq. (27)) this problem is highly non-linear and coupled.

Before defining the thermal properties of the remaining materials constituting the out-reactor fuel element, a few words are added concerning the elastic-to-plastic transition temperature and location in the fuel. As previously explained in Section 1.5 and at the beginning of Section 3.2, the elastic-to-plastic transition occurs over a range of temperatures (1200-1400 °C). An *effective* crack tip was positioned in the current model at a location where the temperature was 1250 °C. Below the elastic-to-plastic boundary (Figure 23) the model assumed the fuel cracks were fully healed at the onset of the simulation (i.e., no cracks). However, crack healing between the temperatures 1400-1700 °C is governed by time dependent diffusion processes, and above 1700 °C cracks self heal by vapour transport phenomena [101]. In other words, fuel crack healing occurs over time so that during the planned two week *out-reactor instrumented defected fuel experiment* the fuel cracks (in the plastic region) may still be healing (i.e., the plastic region fuel cracks may still be present). In fact, Ainscough *et al.* [102] showed (in a lab setting) that crack healing does occur in UO_2 given sufficient time and provided that the plastic fuel is under compression, where crack healing takes place in two stages: crack closure followed by sintering. The following equation [102] can be used to estimate the fuel crack healing (or closure) time:

$$t_{cc} = \frac{1.8\times10^{-6}\exp\left(32000/T\right)}{p_{ip}} \tag{48}$$

where T is in K, p_{ip} is in MPa, and t_{cc} is in hours. For example, if the interface pressure acting on a crack in the plastic fuel is 1 MPa [102] and the fuel temperature is 1500 °C (1773 K) then the crack healing (or closure) time would be just over five days. Thus, it is possible that fuel cracks will be present in the plastic region of the fuel during the *out-reactor instrumented defected fuel experiment*. This could potentially accelerate fuel oxidation, since the steam could access the plastic (i.e., hotter) regions of the fuel. Depending on the outcome of the experiment, this point can be considered later in the model, but it was not in this work.

3.2.1 Thermal and Density Properties of Steam

In the current fuel oxidation model separate domains were considered for the discrete fuel cracks, the fuel-to-sheath gap, and a pellet-pellet gap. When the fuel is defective or is defected these domains become occupied by steam (and hydrogen). Hence the steam thermal conductivity is specifically defined by Eq. (49) [103] at a pressure of 10 MPa:

$$\begin{aligned} k_{\mathrm{steam}} &= 0.0001 && T \leq 573.15\,\mathrm{K} \\ k_{\mathrm{steam}} &= \frac{-9.3878\times10^{-6} + 1.5569\times10^{-7}(T-273.15) - 5.4523\times10^{-10}(T-273.15)^2}{1 - 3.7241\times10^{-3}(T-273.15) - 2.1893\times10^{-8}(T-273.15)^2} && T > 573.15\,\mathrm{K} \end{aligned} \tag{49}$$

where k_{steam} has the units of kW m^{-1} K^{-1} and T is in K. Note that Eq. (49) was corrected from its form in reference [103] and now agrees with the steam table data provided by Grigull *et al.* [104] and Haar *et al.* [105]. In the interior of the fuel, where steam-filled radial cracks reside, the steam thermal conductivity is less than the thermal conductivity of the uranium dioxide fuel by more than an order of magnitude at typical fuel temperatures. Since the modeled radial cracks are very thin (only 15-25 μm wide), and the temperature gradient is primarily in the radial direction, the overall affect of the radial cracks on the heat transfer is quite small. On the other hand, in the fuel-to-sheath gap, heat has to traverse across a steam gap, which will cause a temperature drop. Section 3.3.2 discusses the assessment of the effective thermal conductivity in an open and closed fuel-to-sheath gap, the latter scenario being when the sheath has fully crept down to the pellet surface and the pellets are fully thermally expanded and cracked.

It is important to assess the steam thermal conductivity in the fuel-to-sheath gap in the *out-reactor instrumented defected fuel experiment* because coolant entering the fuel element at 10 MPa is in a liquid phase and only becomes saturated and super heated at 584.18 K (or at 311.03°C) [104]. The steam thermal conductivity as a function of temperature given by

Eq. (49), is plotted in Figure 25. The superheated steam has a minimum thermal conductivity value of 6.9×10^{-5} kW m^{-1} K^{-1} at T=653 K. Above this temperature k_{steam} rises due to an increase in the kinetic energy of water molecules. In fact, the thermal conductivity of gases generally rises as a square root of the absolute temperature [106]. Conversely, below T=653 K, k_{steam} also rises as the temperature decreases nearing the steam saturation temperature. Superheated steam turns into saturated steam (liquid and gas phases) just below 584.18 K and its thermal conductivity can increase to 5.27×10^{-4} kW m^{-1} K^{-1} (almost ten times higher than its minimal value) when the steam quality reaches zero (i.e., the fluid is a liquid phase). This sudden increase is seen as the dashed line in Figure 25. To avoid this modeling complication k_{steam} is set to a constant value of 1×10^{-4} kW m^{-1} K^{-1} at $T \leq 573.15$ K.

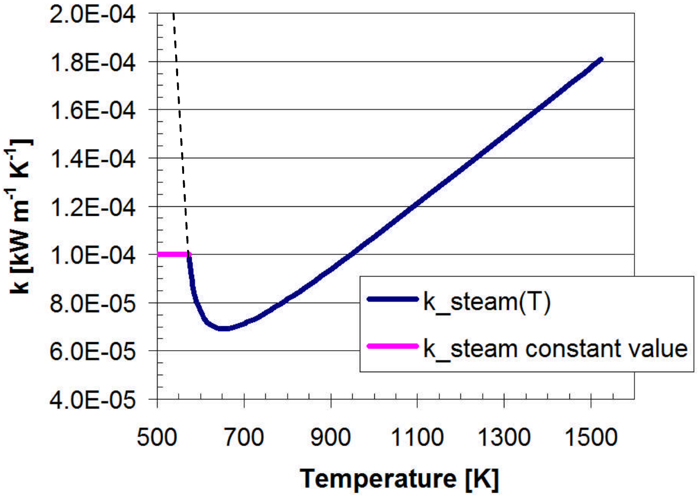

Figure 25: Steam thermal conductivity as a function of temperature at 10 MPa [103][104][105]

When the power in the out-reactor fuel element and the coolant temperature in the test loop are sufficiently high, the water entering the breached fuel element will flash into steam, and k_{steam} will be at a low value in the fuel-to-sheath gap (as also expected in a defective in-reactor fuel element). But if this is not the case, the water may be in a liquid or saturated state thereby cooling the fuel element. Since fuel oxidation is a temperature-dependent phenomenon this can retard fuel oxidation.

The specific heat capacity of the steam at 100 atm is given by Eq. (50), which is divided up into four spline equations and three constants from steam data tables (reference [104]),

$$
\begin{array}{ll}
C_{p\_\mathrm{steam}} = 21.612 - 5.024\times10^{-2}\left(T \text{ - } 273.15\right) & 584.18 < T \le 640.45 \\
C_{p\_\mathrm{steam}} = 3.159 & 640.45 < T \le 648.15 \\
C_{p\_\mathrm{steam}} = 3.7211 - 2.274\times10^{-3}\left(T - 273.15\right) + 1.381\times10^{-5}\left(T - 773.15\right)^2 - 3.8565\times10^{-8}\left(T - 773.15\right)^3 & \\
 & 648.15 < T \le 918.15 \\
C_{p\_\mathrm{steam}} = 2.42 & 918.15 < T \le 973.15 \\
C_{p\_\mathrm{steam}} = 2.134 + 4\times10^{-4}\left(T - 273.15\right) & 973.15 < T \le 1573.15 \\
C_{p\_\mathrm{steam}} = 2.66 & 1573.15 < T \le 1673.15 \\
C_{p\_\mathrm{steam}} = 2.7089 + 2.255\times10^{-5}\left(T - 273.15\right) - 8.4387\times10^{-7}\left(T - 1973.15\right)^2 & 1673.15 < T \le 2273.15
\end{array}
\qquad (50)
$$

where C_{p_steam} has the units of kJ kg^{-1} K^{-1} and T is in K.

The density of the steam at 100 atm is given by Eq. (51), which is divided up into five spline equations from steam data tables (reference [104]), where ρ_{steam} has the units of kg m^{-3} and T is in K. The last equation is the ideal gas law where P is in atm.

$$
\begin{array}{ll}
\rho_{\mathrm{steam}} = 91.38 - 0.1349\left(T - 273.15\right) + 8.88\times10^{-4}\left(T - 648.15\right)^2 & 584.15 < T \le 673.15 \\
\rho_{\mathrm{steam}} = -8.842\times10^{-2}\left(T - 273.15\right) + 73.343 & 673.15 < T \le 723.15 \\
\rho_{\mathrm{steam}} = 57.8 - 0.0546\left(T - 273.15\right) + 1.294\times10^{-4}\left(T - 773.15\right)^2 & 723.15 < T \le 873.15 \\
\rho_{\mathrm{steam}} = -3.892\times10^{-2}\left(T - 273.15\right) + 49.686 & 873.15 < T \le 923.15 \\
\rho_{\mathrm{steam}} = 44.674 - 3.121\times10^{-2}\left(T - 273.15\right) + 4.304\times10^{-5}\left(T - 923.15\right)^2 & 923.15 < T \le 1073.15 \\
\rho_{\mathrm{steam}} = \dfrac{101325P}{461.52T} & 1073.15 < T \le 2273.15
\end{array}
\qquad (51)
$$

3.2.2 Thermal and Density Properties of Iridium

The thermal conductivity of the iridium bar is provided by Savitskii [107]:

$$
k\_\mathrm{Ir} = 1000^{-1}\left(-0.0259T + 154.76\right) \qquad 300 \le T \le 2000 \qquad (52)
$$

where k_Ir has the units of kW m^{-1} K^{-1} and T is in K. Generally the thermal conductivity of iridium is quite high relative to the UO_2, even though k_Ir drops from 0.147 kW m^{-1} K^{-1} to 0.103 kW m^{-1} K^{-1} over a span of 1700 degrees K.

The specific heat capacity of Ir is provided by the PGM Database [108]:

$$C_p\_\mathrm{Ir} = 1000^{-1}(0.027T + 122.33) \qquad 300 \le T \le 2000 \tag{53}$$

where C_p_Ir has the units of kJ kg^{-1} K^{-1} and T is in K.

The density of iridium is given as ρ_Ir = 22500 kg m^{-3} [109].

3.2.3 Thermal and Density Properties of Zircaloy

The thermal conductivity of the Zircaloy sheath is provided by [110] and is given by Eq. (54), where k_Zirc has the units of kW m^{-1} K^{-1} and T is in K.

$$k\_\mathrm{Zirc} = 1000^{-1}\left(7.67\times10^{-9}T^3 - 1.45\times10^{-5}T^2 + 2.09\times10^{-2}T + 7.51\right) \qquad 300 \le T \le 2098 \tag{54}$$

The specific heat capacity of Zircaloy-2 is provided by Eq. (55), tabulated from data from [110]. C_p_Zirc has the units of kJ kg^{-1} K^{-1} and T is in K. The specific heat capacity of Zircaloy-4 was not provided in [110] but it was assumed in this study that C_p values for Zircaloy-2 and Zircaloy-4 up to 1090 K are similar. It can be noted that these two alloys are quite similar in composition. Zircaloy-2 is composed of Zr with 1.5%Sn, 0.13%Fe, 0.1%Cr, and 0.05%Ni, whereas Zircaloy-4 is composed of Zr with 1.5%Sn, 0.2%Fe, and 0.1%Cr (no Ni) on average [111].

$$C_p\_\mathrm{Zirc} = 1000^{-1}\left(-6.492\times10^{-5}T^2 + 0.207T + 226.7\right) \qquad 300 \le T \le 1090 \tag{55}$$

The density of Zircaloy is given as ρ_Zirc = 6490 kg m^{-3} [110].

3.2.4 Thermal and Density Properties of Thermocouple Materials

Generally there are three internal thermocouples at two axial positions in the out-reactor fuel element for a total of six. The thermocouple used is a Type-R thermocouple for all three internal radial positions in the pellet for its good tolerance value (0.25%) and temperature range (-50 to 1768° C). The design of the thermocouples used is an ungrounded type as depicted as a cross section view in Figure 26. The effect of the three radially and azimuthally positioned thermocouples on the resultant temperature distribution in the pellet directly under the sheath defect in the out-reactor fuel element is not significant. Nevertheless, its effect is noticeable in the local temperature distribution and for the applied power. CNL and Stern Laboratories have thus requested that this contribution be included in the 2D r-θ fuel oxidation model.

In an ungrounded thermocouple, the thermocouple junction is separated from the thermocouple sheath by a layer of insulating material, in this case magnesium oxide (magnesia).

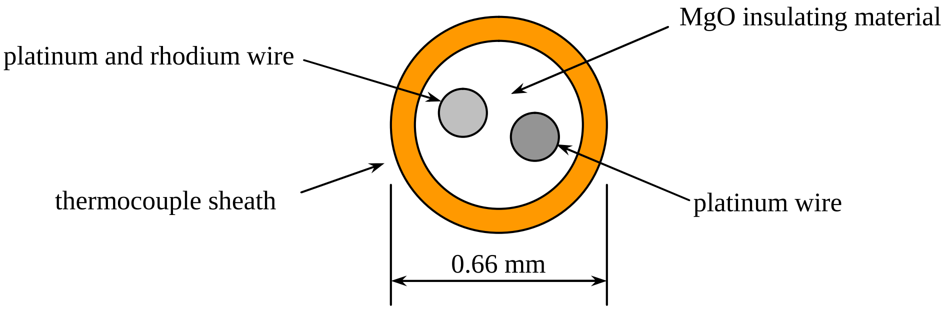

Figure 26: A radial cross section schematic of an ungrounded thermocouple used in the out-reactor fuel element

Generally the sheath of the thermocouple and thermocouple wires are good conductors of heat so that there will not be a large temperature drop in the radial direction. At the locations where there is no thermocouple, but only the 0.66 mm diameter thermocouple hole, the opposite effect can occur because the fill gas in the drilled hole is a poor conductor of heat.

The thermal conductivity of the Type-R thermocouple wires was assessed as a combination of the thermal conductivity properties of platinum and rhodium as given by Eq. (56), with units in kW m^{-1} K^{-1}.

$$k_{\mathrm{Type\_R}} = 1000^{-1}\left(0.935k_{\mathrm{Pt}} + 0.065k_{\mathrm{Rh}}\right) \qquad 300 \leq T \leq 1090 \tag{56}$$

The thermal conductivity of pure platinum and pure rhodium as a function of temperature is given by Equations (57) and (58) [108], with units in W m^{-1} K^{-1} and T is in K.

$$k_{\mathrm{Pt}} = 0.0091T + 70.282 \qquad 300 \le T \le 2000 \tag{57}$$

$$k_{\mathrm{Rh}} = \begin{cases} -0.0520T + 167.60 & 300 \le T \le 800 \\ -0.0183T + 140.67 & 800 < T \le 2000 \end{cases} \tag{58}$$

The composition of the thermocouple sheath is 80% platinum and 20% rhodium so the thermal conductivity composition of the two is given by Eq. (59), in units of kW m^{-1} K^{-1}.

$$k_{\mathrm{Type\_R\_sheath}} = 1000^{-1}\left(0.8k_{\mathrm{Pt}} + 0.2k_{\mathrm{Rh}}\right) \qquad 300 \le T \le 2000 \tag{59}$$

The thermal conductivity of the magnesium oxide insulator (magnesia) in the thermocouple is given by Eq. (60) [109] where the units are in kW m^{-1} K^{-1} and T is in K.

$$k_{\mathrm{magnesia}} = \begin{cases} 1000^{-1}\left(-0.06T + 58.389\right) & T < 673 \\ 1000^{-1}\left(-0.0153T + 28.266\right) & 673 \le T < 1473 \\ 1000^{-1}\left(0.0068T - 4.2174\right) & 1473 \le T \le 1973 \end{cases} \tag{60}$$

The specific heat capacity of magnesia is given by Eq. (61) as a function of temperature where the units are in kJ kg^{-1} K^{-1} and T is in K [109][112].

$$C_{p\_\mathrm{magnesia}} = \begin{cases} \left(-2.464\times10^{-11}T^4 + 5.076\times10^{-8}T^3 - 4.024\times10^{-5}T^2 + 1.503\times10^{-2}T - 1.132\right) \\ \qquad 300 \le T < 600 \\ 0.8643T^{0.0478} \qquad 600 \le T \le 1100 \end{cases} \tag{61}$$

The heat capacity of platinum is 0.133 kJ kg^{-1} K^{-1} and of rhodium is 0.243 kJ kg^{-1} K^{-1} at 298 K and 100 kPa [109]. The specific heat capacity combination of the two is given as:

$$C_{p-\mathrm{Type\_R}} = \left(0.935C_{p-\mathrm{Pt}} + 0.065C_{p-\mathrm{Rh}}\right) = 0.140 \text{ kJ kg}^{-1}\text{ K}^{-1} \tag{62}$$

The specific heat capacity of the Type-R thermocouple sheath is given as:

$$C_{p-\mathrm{Type\_R\_sheath}} = \left(0.8C_{p-\mathrm{Pt}} + 0.2C_{p-\mathrm{Rh}}\right) = 0.155 \text{ kJ kg}^{-1}\text{ K}^{-1} \tag{63}$$

The density of platinum is 21450 kg m^{-3} and of rhodium is 12420 kg m^{-3} [108]. The density of the combined two in the Type-R thermocouple wire in kg m^{-3} is given by:

$$\rho_{\text{Type\_R}} = \left(0.935\rho_{\text{Pt}} + 0.065\rho_{\text{Rh}}\right) = 20863 \tag{64}$$

The density of the Type-R thermocouple sheath in kg m^{-3} is given by:

$$\rho_{\text{Type\_R\_sheath}} = \left(0.8\rho_{\text{Pt}} + 0.2\rho_{\text{Rh}}\right) = 19644 \tag{65}$$

The density of magnesia is ρ_{MgO} is 3580 kg m^{-3} [113].

3.3 Fuel-Oxidation Model For 2D *r*-θ and 3D Geometries

The governing equations that describe the fuel oxidation phenomena discussed in Section 3.2 are solved using both 2D *r*-θ and 3D geometries. Unlike the work by Higgs [24][29], which used a *r*-*z* axisymmetric coordinate system for a 2D model, here a 2D *r*-θ and 3D coordinate system is used instead to capture the discrete radial fuel cracks. These models include centrally-heated fuel (using an iridium bar heater), three ungrounded thermocouples at three radial and azimuthal positions (only in the 2D *r*-θ model), a collapsed fuel sheath with a fuel-to-sheath gap (only in the 2D *r*-θ model), and an axial sheath defect. Thus, these models simulate defected fuel with sheath defects illustrated in Figure 27 (a), as green area in the 2D *r*-θ model and yellow area in the 3D model.

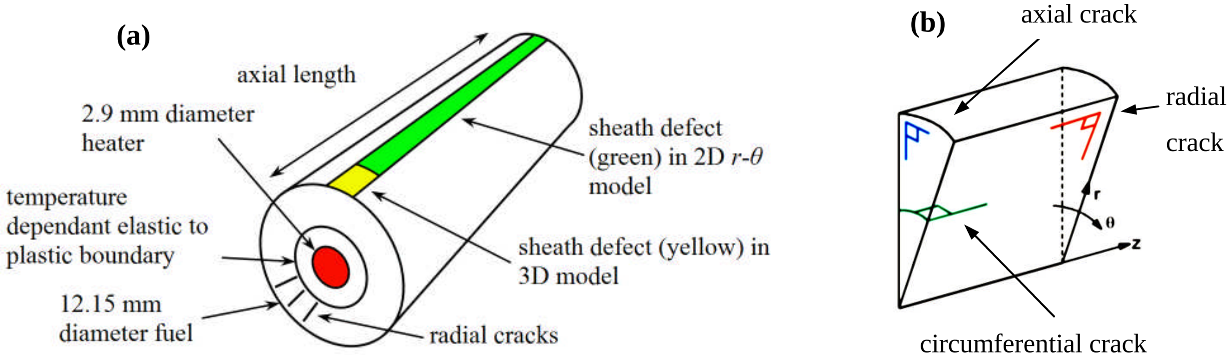

Figure 27: (a) 2D *r*-θ and 3D model defect representations; the green area represents a sheath defect equal to the length of the fuel element and the yellow area represents a finite sheath defect in the 3D model. (b) The schematic gives the representation of the three types of fuel cracks.

The radial cracks and fuel-to-sheath gap are modelled as conduits for hydrogen gas diffusion. Figure 27 (b) shows the three different fuel cracks that can occur in UO_2 fuel where the z axis is the axial direction of the fuel rod or element. The radial cracks are considered the most relevant type of fuel cracks for the current study. In reality though, cracks can be a combination of these three crack types.

In the 3D and 2D r-θ fuel oxidation models (the 3D and 2D models depicted in Figure 17), the general form for the oxygen diffusion equation, in Eq. (18), is written as Eq. (66), where for the 2D r-θ model the z coordinate term is neglected.

$$c_{\mathrm{U}}\frac{\partial x}{\partial t}=c_{\mathrm{U}}\left[\frac{1}{r}\frac{\partial}{\partial r}\left(rD\left(\frac{\partial x}{\partial r}+x\frac{Q}{RT^2}\frac{\partial T}{\partial r}\right)\right)+\frac{1}{r}\frac{\partial}{\partial\theta}\left(D\left(\frac{1}{r}\frac{\partial x}{\partial\theta}+x\frac{Q}{RT^2}\frac{1}{r}\frac{\partial T}{\partial\theta}\right)\right)+\frac{\partial}{\partial z}\left(D\left(\frac{\partial x}{\partial z}+x\frac{Q}{RT^2}\frac{\partial T}{\partial z}\right)\right)\right]+R_f^{react} \qquad (66)$$

It is noted that if temperature was independent of θ then the second term in Eq. (66) could also be neglected. However, the θ term does not cancel out in the vicinity of the thermocouples and thermocouple drilled-holes. Also, the z term will not cancel out when consideration is made for the varying fuel thermal conductivity, which depends on the degree of fuel oxidation.

Hydrogen gas diffusion in the radial fuel cracks, the fuel-to-sheath gap, and in the pellet-pellet gap is considered in the radial, azimuthal, and axial directions in the 3D model (whereas in the Higgs model [29] only the radial and axial directions were considered). The differential equation for the hydrogen mole fraction q in Eq. (27) can be rewritten as:

$$c_g\frac{\partial q}{\partial t}=\frac{1}{\tau^2 r}\left[\frac{\partial}{\partial r}\left(rc_g D_g\frac{\partial q}{\partial r}\right)+\frac{\partial}{\partial\theta}\left(\frac{c_g D_g}{r}\frac{\partial q}{\partial\theta}\right)+\frac{\partial}{\partial z}\left(rc_g D_g\frac{\partial q}{\partial z}\right)\right]+R_f^{react} \qquad (67)$$

where τ is the path tortuosity factor for gas diffusion in the cracked fuel. Here the fuel cracks are assumed to be straight so $\tau=1$ (though in reality $\tau>1$ is expected). In the 2D r-θ model, the axial component is neglected. The azimuthal term in Eq. (67) is included in the 2D r-θ model and 3D model. This term is necessary, since as the distance increases in the azimuthal direction from the sheath defect site, the hydrogen mole fraction in the fuel changes, which affects fuel oxidation. The Higgs model [29] used a 2D axisymmetric geometry without separate domains for fuel cracks.

The general form of the heat equation, Eq. (32), in the 3D model becomes:

$$\rho_s C_p \frac{\partial T}{\partial t} = \frac{1}{r}\frac{\partial}{\partial r}\left(rk\frac{\partial T}{\partial r}\right) + \frac{1}{r}\frac{\partial}{\partial \theta}\left(\frac{k}{r}\frac{\partial T}{\partial \theta}\right) + \frac{\partial}{\partial z}\left(k\frac{\partial T}{\partial z}\right) + Q_v \tag{68}$$

In the 2D r-θ model, the heat equation is simplified by removing the axial component in Eq. (68). As mentioned, in the 3D model of the out-reactor fuel element, the heat source term Q_v is removed and replaced by boundary conditions provided by the solution of the 2D r-θ model.

3.3.1 Modeling of the Fuel Cracks and Gap

The interaction of the steam and the cracked fuel occurs in the model at the boundary separating these two substances, which is an example of a heterogeneous (gas and solid) chemical reaction [114]. In the current models, the oxygen diffusion equation, Eq. (18), and the gas diffusion equation, Eq. (27), occur in separate domains where the source term, R_f^{react}, has a value of zero. Nevertheless $R_f^{react}(x,q)$ can be expressed so that Eqs. (18) and (27) are coupled together at the fuel-to-gas (steam) interface. This is accomplished in the models using flux terms at domain common boundaries. Table 2 gives the flux terms for the two coupled equations, which are simply the source terms at the end of Equations (18) and (27).

Table 2: Flux term definitions at the gas-to-fuel crack surface boundaries

Applied in	Inward flux term	Equivalent weak form term
Oxygen diffusion equation, Eq. (18)	$R_f^{react}\frac{1}{c_\mathrm{U}}$	$x_{test}R_f^{react}\frac{1}{c_\mathrm{U}}$
Gas diffusion equation, Eq. (27)	R_f^{react}	$q_{test}R_f^{react}$

Note that the flux term in Eq. (18) includes the reciprocal of uranium molar density c_U. This is because Eq. (18) is divided by c_U so that the coefficients in front of the time derivative and the del operator in Eq. (18) are inputted as unity in COMSOL Multiphysics® equation entry. As mentioned earlier the source term has the units of moles O or H_2 m^{-2} s^{-1}.

For the reader’s interest, the equivalent ‘weak’ form terms [115] are provided in Table 2 (third column from left) for the flux terms, which can be used in COMSOL®’s weak form contribution nodes instead of the flux terms to yield the same result. If all terms of Eq. (27) were recast on the boundary of a fuel crack in the weak form (using the Green's Theorem and integrating by parts) then the PDE on the boundary could be written as:

$$x_{test} \cdot x_{time} = -x_{r\_test} \cdot D\left(x_r + x\left(\frac{Q}{RT^2} \right) T_r \right) + x_{test} \cdot R_f^{react} \frac{1}{c_{\mathrm{U}}} \tag{69}$$

where the subscripts *time* and *r* indicate derivatives of *x* with respect to time and in the radial direction. The subscript *test* indicates a test function. For further reading on the ‘weak’ and ‘dweak’ form see [24][71][115].

The weak form was previously used by Higgs in a axisymetric 2D *r-z* fuel oxidation model [24][29]. Revisiting this model it was found that the contribution of gas diffusion in the fuel-to-sheath gap in the axial direction (with no separate fuel-to-sheath gap domain), did not have a significant effect on fuel oxidation. As such, this technique was not used in the current fuel oxidation models presented here. Instead, the gas diffusion equation was defined in the fuel-to-sheath gap domain. This was made possible in COMSOL® version 4 (and higher) with its improved capability for dealing with very thin and long geometry domains.

An additional flux term (or source term) in Eq. (27) is shown in the following table:

Table 3: Flux term used in the fuel-to-sheath gap at the Zircaloy sheath internal surface for hydrogen generation by sheath oxidation

Applied in	Inward flux term
Hydrogen diffusion equation, Eq. (27)	$R_{Zirc\_sheath}^{ox}$, Eq. (31)

which was used on the internal Zircaloy sheathing surface in the 2D r-θ fuel oxidation model. This source term, provided by Eq. (31), contributes to the production of hydrogen in the fuel-to-sheath gap from sheath oxidation, in addition to the hydrogen produced by fuel oxidation with the steam in the fuel cracks.

3.3.2 Heat Transfer in the Gap

When a fresh fuel bundle is inserted in the fuel channel of a CANDU reactor there exist a gap between the fuel pellets and fuel sheathing. This gap is approximately 0.02-0.13 mm [38][116]. In this situation fission heat is primarily transported from the fuel surface to the sheath inner surface via heat transfer through the helium fill gas layer. Since the CANDU fuel sheath thickness is only ≈0.4 mm [37][116], and because of fuel thermal swelling/expansion and cladding creepdown due to a high external coolant pressure, the fuel-to-sheath gap will close after a conditioning period. When this gap closes, heat will be transported by both solid conduction, where there is physical contact (when the two materials touch within the surface roughness under a load), and by heat conduction via the gas film that fills the domains of the interface where contact is not made [15]. In the *out-reactor instrumented defected fuel experiment* a similar process will occur. Thus, it is necessary to simulate the fuel-to-sheath gap of the fuel element.

The solid heat transfer coefficient h_{solid} in kW m^{-2} K^{-1} is given by Eq. (70) using the treatment of Campbell *et al*. [50]:

$$h_{solid} = \frac{k_m P_i^{1/2}}{a_0 R_{rms}^{\ \ 1/2} H} \tag{70}$$

where k_m is the harmonic mean thermal conductivity of the fuel and sheath solids in kW m^{-1} K^{-1}. The interfacial pressure P_i between the fuel and the sheath surfaces can be derived by solving for pressure in the hoop stress equation [117] and setting the hoop stress equal to the yield stress in MPa:

$$P_i = Y_s * t_s / r_{is} \tag{71}$$

where Y_s is the sheath yield stress in MPa as a function of temperature where T is in K given by Eq. (72), as interpreted from the work by Talia *et al.* [118]. In (71) t_s is the sheath thickness and r_{is} is the internal sheath radius.

$$Y_s = -1.008 \times 10^{-6} T^3 + 0.0026 T^2 - 2.4337 T + 849.28 \tag{72}$$

In Eq. (70) a_o is an empirical constant equal to 8.6×10^{-3} $\mathrm{m}^{0.5}$ $\mathrm{MPa}^{-0.5}$ [50], R_{rms} is the root-mean-square (rms) surface roughness of the fuel pellet and sheathing surfaces equal to $\sqrt{\left(R_1{}^2 + R_2{}^2\right)/2}$ where R_1 and R_2 are the rms surface roughnesses of each surface, respectively. Lastly H is the Meyer hardness of the Zircaloy sheath given as H=4.4*Y_s [50] in MPa. The Meyer hardness can also be given by a more precise expression in MPa [119]:

$$H = 1x10^{-6}\exp\left\{26.034 + T\left(-2.6394x10^{-2} + T\left(4.3504x10^{-5} - T\left(2.5621x10^{-8}\right)\right)\right)\right\} \qquad (73)$$

The fluid heat transfer coefficient h_{gas} (of the steam gas) in kW m^{-2} K^{-1} is given by Eq. (74) [37][50][120]:

$$h_{gas} = \frac{k_f}{1.5\left(R_1 + R_2\right) + t_g + g_0\left(T_{gap}/273\right)^{1.2405}\left(0.101/P_{gap}\right)} \qquad (74)$$

where k_f is the fluid thermal conductivity component in the gap, R_1 and R_2 are again the rms surface roughnesses of the fuel surface and inner surface sheath in m, t_g is the fuel-to-sheath gap thickness in m, g_0 is the combined temperature jump distance (for both the fuel and sheath surfaces [50]) at standard temperature and pressure for H_2O in m [37], T_{gap} is the average temperature of the gap in K and P_{gap} is the pressure in the gap in MPa. With the derived values for both the solid and the fluid heat transfer coefficient, an effective thermal conductivity value can be derived for the fuel-to-sheath gap [77]:

$$k_{gap\_effective} = \frac{h_{solid} + h_{gas}}{h_{gas}} k_{gas} \qquad (75)$$

If in a defective fuel element the combined temperature jump distance for H_2O at standard conditions is 3.4 μm according to [37], the average temperature in the gap is 577 K (assuming a ≈1 μm gap) and the pressure in the gap is 10 MPa, then the combined temperature jump distance for conditions in the gap (the right hand term in the denominator of Eq. (74)) would be 8.45×10^{-8} m.

For a closer look at the heat transfer coefficient in the gap, for validity confirmation purposes, an alternative to Eq. (74) can be written as [15]:

$$h_{gas} = \frac{k_f}{t_g + g_c + g_f} = \frac{k_f}{t_g + g} \qquad (76)$$

where g_c and g_f are the temperature jump distances of the clad and the fuel, respectively, and the rms surface roughnesses (R_1 and R_2) are momentarily neglected. Denoting the combined temperature jump distance for these two surfaces as g, its value is given by [15]:

$$g = 2\left(\frac{2-\alpha_{th}}{\alpha_{th}}\right)\left(\frac{\gamma}{1+\gamma}\right)\left(\frac{k}{\mu C_p}\right)_g \lambda_{fp} \qquad (77)$$

where α_{th} is the thermal accommodation coefficient, γ is the ratio of specific heats of the gas (C_p/C_v), the quantity $(k/(\mu C_p))_g$ is the reciprocal of the dimensionless Prandtl number (where μ is the dynamic viscosity of the gas), and λ_{fp} is the mean free path of the gas. If the thermal accommodation coefficient is taken as unity (meaning the scattered gas molecules are completely equilibrated after colliding with the substrate walls) [15], γ and 1/Pr for steam are 1.327 and 1.041 [121], respectively, then the product of the first four terms in Eq. (77) is equal to 1.187 (or close to unity). Thus, the determining component of the temperature jump distance in the mean free path λ_{fp} of the gas.

Kinetic theory can be used to find the mean free path of an H_2O molecule as steam at normal fuel-to-sheath gap temperatures and gas pressures. The mean free path of a molecule (that is, the average distance it can travel between collisions) is given by the following [122]:

$$\lambda_{fp} = \frac{1}{\sqrt{2} n \sigma_{cs}} \qquad (78)$$

where λ_{fp} is in m, n is the number density of the gas, and σ_{cs} is the collision cross-section of the molecule. The number density of the steam can be calculated using [1]:

$$n = \frac{\rho_g N_A}{M} \qquad (79)$$

where n is in m^{-3}, ρ_g is the density of the gas, N_A is the Avogadro number and M is the gas molar mass. The density of the steam at 10 MPa and 600 K is 36.11 kg m^{-3} (using the ideal gas law where R_{steam} is equal to 461.52 J kg^{-1} K^{-1}). If the steam molar mass is 18.015 g mol^{-1}

then using Eq. (79) the steam number density is 1.207×10^{27} molecules m^{-3}. The collision cross section of a water molecule using the hard-sphere model is [123]:

$$\sigma_{cs} = 4\pi r_m^2 \qquad (80)$$

where σ_{cs} is in m^{-2}, and r_m is the molecular radius (or the distance between the hydrogen and oxygen atom in the water molecule). If r is $\approx1\times10^{-10}$ m [20] then σ_{cs} is 1.256×10^{-19} m^2 and so the mean free path λ_{fp} of the steam molecule in the fuel-to-sheath gap, using Eq. (78), is expected to be 4.662×10^{-9} m. Thus, the combined temperature jump distance for both the fuel and sheath surfaces, Eq. (77), is $g = 1.187*4.662\times10^{-9} = 5.534\times10^{-9}$ m. Table 4 provides the temperature jump distance values for these two calculation methods.

Table 4: Temperature jump distance comparison of steam at ≈600 K and 10 MPa

Equation used	**Temperature jump distance *g* [m]**
Eq. (74)	8.45×10^{-8}
Eq. (77) and (78)	5.53×10^{-9}

It is noted that the latter value using Eq. (77) is slightly more than an order of magnitude smaller than the previously calculated value using Eq. (74). It is possible that taking the thermal accommodation coefficient α_{th} as unity in Eq. (77) was overly simplistic and that the actual value is probably < 1. For example, if $\alpha_{th} = 0.4$ then $g = 2.21\times10^{-8}$ m, which approaches the value g in Eq. (74). Hence these two temperature jump distances may be realistic. If the rms surface roughnesses are considered as well (R_1=0.5 μm for the fuel and R_2=1 μm for the sheath), as in Eq. (74), and t_g is taken as 1 μm, then the contribution of the calculated temperature jump distance to the effective width of the fuel-to-sheath gap (the denominator of Eq. (74)) may be only ≈2.5%. Thus the contribution of the combined temperature jump distance to the fluid heat transfer coefficient in the out-reactor defected fuel element fuel-to-sheath gap is expected to be small.

When the fuel-to-sheath gap is greater than 1 μm (i.e., the gap is considered to be open), or the effective gap is greater than 1.79 μm (when including the inside sheath and fuel surface roughnesses, R_{rms}, as used in Eq. (70)) then the temperature jump distance becomes insignificant. Hence in this work, in 2D r-θ fuel oxidation models where the fuel-to-sheath gap is open (>≈1 μm), the effective thermal conductivity in the gap is taken simply as the thermal conductivity of the gas k_{gas} (or of the steam).

3.3.3 Electrical Power Computation

In the out-reactor experiment, the 2D r-θ fuel oxidation model also takes into consideration the varying electrical conductivities of the iridium bar and the Zircaloy sheath as a function of temperature. It calculates the varying electrical current flowing through each conductor using a current divider equation. Also, the uranium oxide pellets were included in the electrical current calculation, even though its contribution to ohmic heating is very low. This calculation was completed in order to obtain a better estimation of the electrical power distribution in the fuel element. With the derived calculated parallel electrical currents, the volumetric power was assessed in each conductor domain for the heat conduction equation (refer to Eq. (32) and (68)). It is assumed here that the resistivity calculated for each conductor is homogeneous throughout the whole length of the conductor. In reality though this may be an oversimplification, since the electrical resistivity of the conductors at the out-reactor fuel element ends can be different from that in the whole due to lower temperature edge effects. Figure 28 shows the basic electrical heating circuit of the out-reactor fuel element, which uses DC voltage.

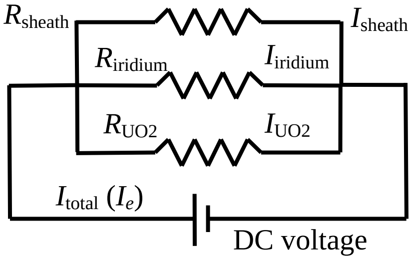

Figure 28: Basic electrical heating circuit of the out-reactor fuel element

The resistance of each conductor is calculated using the conductance equation [123]:

$$R_n = \frac{l_{ec}}{\sigma_n(T) \cdot A_n} \qquad (81)$$

Where l_{ec} is the length of the electrical conductor in m or in this case the out-reactor fuel element, R_n is the resistance in Ω, σ_n is the electrical conductivity in Ω^{-1} m^{-1}, and A_n is the cross section of the conductor n in m^{-2}, respectively.

The electrical conductivity of the iridium bar [108] as a function of temperature is given by Eq. (82), where σ_{Ir} has the units of Ω^{-1} m^{-1} and T is in K. In iridium, as the temperature increases the electrical conductivity decreases, which in turn increases the total electrical resistance.

$$\begin{aligned} \sigma_{Ir} &= 1.6297x10^{10}T^{-1.1797} \quad (273 < T < 2400\,\mathrm{K}) \\ \sigma_{Ir} &= 1.66x10^{6} \quad (\mathrm{T >= 2400\,K}) \end{aligned} \qquad (82)$$

The electrical conductivity used for the Zircaloy sheathing can be initially taken as the electrical conductivity of pure zirconium [109]:

$$\begin{aligned} \sigma_{zirconium} &= 3.527\times10^{9}T^{-1.284} && (200 \le T < 400\ \mathrm{K}) \\ \sigma_{zirconium} &= 3.527\times10^{9}T^{-1.284} + 496T - 198400 && (400 \le T < 900\ \mathrm{K}) \\ \sigma_{zirconium} &= 8.12\times10^{5} && (T \ge 900\,\mathrm{K}) \end{aligned} \qquad (83)$$

where $\sigma_{zirconium}$ has the units of Ω^{-1} m^{-1} and T is in K. Since it was found that the temperature distribution in the out-reactor fuel element, due to electrical heating, was sensitive to the electrical conductivities of the iridium bar and the Zircaloy sheathing, three additional equations are given for the electrical conductivities of Zircaloy as a function of temperature. Eq. (84) is the electrical conductivity of Zircaloy-2 according to data by Price [124]:

$$\begin{aligned} \sigma_{Zircaloy\_Price} &= 3.772\times10^{7}T^{-0.5865} && 295 \le T < 668 \\ \sigma_{Zircaloy\_Price} &= 8.361\times10^{5} && T \ge 668 \end{aligned} \qquad (84)$$

where $\sigma_{Zircaloy\_Price}$ has the units of Ω^{-1} m^{-1} and T is in K. The electrical conductivity of Zircaloy composed of zirconium with 1.65% tin (which approximates Zircaloy-2 and -4) is given by Eq. (85) based on data provided by Benedict *et al.* [125]:

$$\begin{aligned} \sigma_{Zircaloy\_Ben} &= 1.887\times10^{7}T^{-0.4848} && 273 \le T < 873 \\ \sigma_{Zircaloy\_Ben} &= 7.22\times10^{5} && T \ge 873 \end{aligned} \tag{85}$$

where $\sigma_{Zircaloy\_Ben}$ has the units of Ω^{-1} m^{-1} and T is in K. The last equation provided for the electrical conductivity of Zircaloy is given by Stern Laboratories [126]:

$$\begin{aligned} \sigma_{Zircaloy\_Stern} &= \frac{1}{-9.283\times10^{-13}T^{2} + 1.6869\times10^{-9}T + 0.6553\times10^{-6}} && 273 \le T < 1000 \\ \sigma_{Zircaloy\_Stern} &= 7.073\times10^{5} && T \ge 1000 \end{aligned} \tag{86}$$

where $\sigma_{Zircaloy\_Stern}$ has the units of Ω^{-1} m^{-1}. For the expected temperatures in the Zircaloy sheath, the electrical conductivity values are highest in Eq. (83) and lowest in Eq. (86) (a difference of ≈31% at 600 K). A lower electrical conductivity of the Zircaloy sheath yields a higher electrical resistivity thereby forcing more of the electrical current to flow through the Ir conductor (i.e., acting as an electrical shunt). Hence, this result causes more of the total electric power to be generated in the Ir conductor, which has the effect of increasing the out-reactor fuel element temperature and thus the amount of fuel oxidation. Alternatively, the higher the electrical conductivity of the Zircaloy sheath, the lower is the electrical resistivity. This promotes more electrical current to flow in the sheath and thus more power is generated in the sheath with less generated in the Ir bar heater conductor. Since the coolant effectively removes the heat generated from the sheath, the sheath electrical power provides very little contribution to the out-reactor fuel element heating. Hence, with higher sheath electrical conductivity, less fuel oxidation will occur.

UO_2 is a good semiconductor that has the intrinsic electrical conductivity of silicon but less than that of gallium arsenide. Its electrical conductivity of UO_2 is given by Eq. (87), which was based on data by [127], using a MATLAB software spline function. The electrical conductivity σ_{UO2} has the units of Ω^{-1} m^{-1}. Generally, as the temperature of UO_2 increases the electrical conductivity increases, which decreases the UO_2 electrical resistance.

$$\begin{aligned}
\sigma_{UO_2} &= -3.4385 + 9.765\times10^{-3}T + 3.0542\times10^{-5}(T-454.5)^2 && (287 =< T < 833\,\text{K}) \\
\sigma_{UO_2} &= -6.75209 + 1.90017\times10^{-2}T && (833 =< T < 1250\,\text{K}) \\
\sigma_{UO_2} &= -1514/3 + (313/750)T && (1250 =< T < 2000\,\text{K}) \\
\sigma_{UO_2} &= -5084.1772 + 2.70709T && (2000 =< T < 3355\,\text{K})
\end{aligned} \tag{87}$$

For reference purposes, the electrical conductivities of the three constituent materials used to construct the out-reactor fuel element are compared in Table 5. The UO_2 material has the lowest electrical conductivity of the three materials by at least three orders of magnitude. This means that it has a much greater electrical resistivity than the two metallic conductors. Hence, no significant electrical conduction is expected to pass through the UO_2 pellets in normal operation.

Table 5: Electrical conductivity comparison between the three different materials in the out-reactor fuel element

	Zircaloy†	**Iridium**	**UO_2**
Electrical conductivity [Ω^{-1} m^{-1}]	7.5×10^5 at 600 K	2.07×10^6 at 2000 K	330 at 2000 K

†The electrical conductivity of Zircaloy using Eq. (86).

Although the electrical resistance in the UO_2 fuel is expected to be relatively high, it is modeled in one of the 2D r-θ fuel oxidation models (at the request of the Stern Laboratories) to assess the fuel ohmic heating contribution. Lastly, it is important to note that the electrical conductivity of UO_2 can increase rapidly with temperature. For example, at a temperature of ≈3400 K, the electrical conductivity of UO_2 can rise to 4000 Ω^{-1} m^{-1}. Thus, conditions for electrical failures (i.e., electrical arcing and shorting) in the current test with conductors connected in parallel are expected to be avoided.

A current divider equation, Eq. (88) [128] is used to calculate the electrical current in each conductor in parallel where I_1 is the current flowing through conductor 1 in Amps, R_1 is the resistance of conductor 1 in ohms, R_T is the equivalent remaining resistances of the circuit and I_e is the total electrical current flowing through the circuit.

$$I_1 = \frac{R_\mathrm{T}}{R_1 + R_\mathrm{T}} I_e \qquad (88)$$

To simplify the derivation of I_Ir I_Zr and I_UO2 the following notation is used:

$$\begin{aligned} I_\mathrm{Ir} &= I_1 \quad I_\mathrm{Zr} = I_2 \quad I_\mathrm{UO2} = I_3 \\ R_\mathrm{Ir} &= R_1 \quad R_\mathrm{Zr} = R_2 \quad R_\mathrm{UO2} = R_3 \end{aligned} \qquad (89)$$

For I_1 we calculate the remaining resistances R_T in Eq. (88) using R_2 and R_3 in parallel (where $\frac{1}{R_\mathrm{T}} = \frac{1}{R_2} + \frac{1}{R_3}$) so that $R_T = \frac{R_2 R_3}{R_2 + R_3}$. Substituting this expression into Eq. (88) one obtains the expression for the current I_1 passing through resistance R_1:

$$\begin{aligned} I_1 &= \frac{R_2 R_3}{R_1 R_3 + R_2 R_3 + R_1 R_2} I_e \quad \text{hence:} \\ I_\mathrm{Ir} &= \frac{R_\mathrm{Zr} R_\mathrm{UO2}}{R_\mathrm{Zr} R_\mathrm{UO2} + R_\mathrm{Zr} R_\mathrm{UO2} + R_\mathrm{Ir} R_\mathrm{Zr}} I_e \end{aligned} \qquad (90)$$

Similar expressions are derived for I_Zr and I_UO2. The electrical power dissipated in the fuel-element conductors in kW m^{-3} can now be calculated using Joule's law for thermal power as written in Eq. (91), where I_n is the current running through conductor n.

$$P_\mathrm{vol} = \frac{I_n^2 R_n}{A_n l_{ec}} 10^{-3} \qquad (91)$$

Using Eq. (90), R_n is the resistance of conductor n using Eq. (81), A_n is the cross section of the conductor n and l_{ec} is the length of the heating conductor.

The true electrical conductivities of the Zircaloy sheath and Ir bar are not known with complete certainty. Also it is difficult to know the electrical joint resistance between the Ir bar and the Zircaloy end-cap or the resistance between the Ir bar to the silver packing at the inlet (see Figure 20). The fuel-to-sheath gap also plays an important role on the temperature distribution in the out-reactor fuel element, which in turn affects the electrical conductivities of the various materials. Only the thermocouple temperature measurements in the fuel pellets can provide this necessary information.

3.4 The Fuel Solid Mechanics Model

In the 2D *r-θ* and 3D fuel oxidation models, both heat and diffusion equations are solved. Pre-defined geometries of radial fuel cracks provide conduits for steam ingress and surfaces for the steam and fuel chemical interaction. The geometry (length and width) and number of these radial fuel cracks in the non solid mechanics models in this thesis was initially based on experimental results from others [57][73][76] (see Section 1.6). The objective of this section is to determine with solid mechanics modeling if radial fuel cracks will occur and the crack geometry. Section 3.4.1 provides a theory on solid mechanics and Section 3.4.2 discusses conditions for crack propagation in fuel.

3.4.1 Solid Mechanics Theory

In the COMSOL Multiphysics® software package, the physical space of the solid is known as the 'special frame' and the positions in the physical space are identified by the lower case 'special coordinates' x, y and z. Continuum mechanics theory also uses a second set of coordinates known as the 'material (or reference) coordinates' denoted by upper case variables X, Y and Z. Each solid particle is uniquely defined by the initial or reference coordinates. As long as the particle in the solid does not change position, the spatial and material coordinates coincide and displacements $\mathbf{u}$ are equal to zero. When the solid deforms each material particle maintains its material coordinate $\mathbf{X}$, which represents a coordinate vector, while the spatial coordinate $\mathbf{x}$ can change with time and applied force, as expressed by:

$$\mathbf{x} = \mathbf{x}(\mathbf{X},t) = \mathbf{X} + \mathbf{u}(\mathbf{X},t) \qquad (92)$$

where $\mathbf{u}$ is the particle displacement vector that has the components u, v and w [129][130]

The stress field is related to the displacement field in the solid by Hooke's Law [130][131] as expressed by:

$$\sigma_{ij} - \sigma_o = C_{ijkl}\,(\varepsilon_{kl} - \varepsilon_o - \varepsilon_{inel}) \qquad (93)$$

where σ_{ij} is the stress tensor in Pa, σ_o is the initial stress tensor in Pa, C_{ijkl} is the forth order elasticity or elastic stiffness tensor in Pa, ε_{kl} is the strain tensor, ε_o is the initial stress tensor. The inelastic strain tensor ε_{inel} in Eq. (93) due to thermal expansion is provided by:

$$\varepsilon_{inel} = \alpha_e \left(T - T_{ref} \right) \delta_{kl} \tag{94}$$

where α_e is the isotropic thermal expansion coefficient, T is the temperature in K, T_{ref} is the strain reference temperature, typically set to room temperature and δ_{kl} is the Kronecker delta, applied to the solid particle at spatial coordinates x, y and z. The Kronecker delta takes the value of:

$$\delta_{kl} = \begin{cases} 1, i = k \\ 0, i \neq k \end{cases} \tag{95}$$

The gradient of the displacement vector **u**, which is used repeatedly, is always computed with respect to the material coordinates **X**. In 2D, the displacement gradient vector in m can be written as Eq. (96). Note that the gradient of the displacement vector field notation can be written in two equivalent ways [130].

$$\nabla \mathbf{u} = \mathbf{u} \otimes \nabla = \begin{bmatrix} \frac{\partial u}{\partial X} & \frac{\partial u}{\partial Y} \\ \frac{\partial v}{\partial X} & \frac{\partial v}{\partial Y} \end{bmatrix} \tag{96}$$

For small deformations, the infinitesimal strain tensor in Eq. (93) can be written in terms of the displacement gradient as expressed by:

$$\varepsilon = \frac{1}{2} \left(\nabla \mathbf{u} + \left(\nabla \mathbf{u} \right)^T \right) \tag{97}$$

Eq. (97) is also known as the infinitesimal rotation tensor [130], which can also be written in component form:

$$\varepsilon_{mn} = \frac{1}{2} \left(\frac{\partial u_m}{\partial x_n} + \frac{\partial u_n}{\partial x_m} \right) \tag{98}$$

For modeling large deformations, a deformation gradient F_{dg} can be defined when an infinitesimal line element $d\mathbf{X}$ is mapped to the corresponding deformed line element $d\mathbf{x}$, as expressed in Eq. (99) [129][130]. The deformation gradient F_{dg} contains the complete information about the local straining and rotation of the material.

$$d\mathbf{x} = \frac{\partial \mathbf{x}}{\partial \mathbf{X}} d\mathbf{X} = F_{dg} d\mathbf{X} \qquad (99)$$

In terms of the displacement gradient, the deformation gradient F_{dg} can be written as Eq. (100), where $\mathbf{I}$ is the identity matrix.

$$F_{dg} = \nabla \mathbf{u} + \mathbf{I} \qquad (100)$$

The right Cauchy-Green deformation tensor [130] for elastic deformation is defined by applying Eq. (100) and is written as Eq. (101), where F_{dg}^{T} is the transpose of matrix F_{dg}.

$$C_{CG} = F_{dg}^{T} F_{dg} = (\nabla \mathbf{u})^{T} + \nabla \mathbf{u} + (\nabla \mathbf{u})^{T} \nabla \mathbf{u} + \mathbf{I} \qquad (101)$$

The Green-Lagrange strain tensor is then given by Eq. (102) [131], which can be used for applications of large deformations.

$$\varepsilon = \frac{1}{2}(C_{CG} - \mathbf{I}) = \frac{1}{2}\left[(\nabla \mathbf{u})^{T} + \nabla \mathbf{u} + (\nabla \mathbf{u})^{T} \nabla \mathbf{u}\right] \qquad (102)$$

The elasticity tensor C_{ijkl} in Eq. (93), which is also referred to as the stiffness tensor D_s, can be written in 2-dimensions as Eq. (103) [132]:

$$[D_s] = \frac{E}{(1+\nu)(1-2\nu)} \begin{bmatrix} 1-\nu & \nu & 0 \\ \nu & 1-\nu & 0 \\ 0 & 0 & \frac{(1-2\nu)}{2} \end{bmatrix} \qquad (103)$$

where E is the isotropic Young's modulus and ν is the Poisson's ratio. The elasticity tensor C_{ijkl} in 3-dimensions or 2-dimensions for a plane strain case is a 6-by-6 matrix. The Hooke law, Eq. (93), can now be expressed for a plane strain case:

$$\begin{bmatrix}\sigma_x\\ \sigma_y\\ \sigma_{xy}\end{bmatrix}=\begin{bmatrix}\sigma_x\\ \sigma_y\\ \sigma_{xy}\end{bmatrix}_o+D_s\left[\begin{bmatrix}\varepsilon_x\\ \varepsilon_y\\ 2\varepsilon_{xy}\end{bmatrix}-\begin{bmatrix}\varepsilon_x\\ \varepsilon_y\\ 2\varepsilon_{xy}\end{bmatrix}_o-\left(T-T_{ref}\right)\begin{bmatrix}\alpha_x\\ \alpha_y\\ 0\end{bmatrix}\right] \qquad (104)$$

where $\varepsilon_z = \varepsilon_{yz} = \varepsilon_{xz} = 0$ and with Eq. (105):

$$\sigma_z=\frac{E\nu\left(\varepsilon_x+\varepsilon_y\right)}{\left(1-2\nu\right)\left(1+\nu\right)}-\frac{E\alpha_z\left(T-T_{ref}\right)}{1-2\nu},\ \sigma_{xz}=\sigma_{yz}=0 \qquad (105)$$

If the stresses are defined, the strains can be solved for by taking the inverse relationship of Eq. (104) providing Eq. (106) [130], where D_s^{-1} can also be called S_{ijkl}, the elastic compliance tensor.

$$\begin{bmatrix}\varepsilon_x\\ \varepsilon_y\\ \varepsilon_{xy}\end{bmatrix}=\begin{bmatrix}\varepsilon_x\\ \varepsilon_y\\ \varepsilon_{xy}\end{bmatrix}_o+D_s^{-1}\left[\begin{bmatrix}\sigma_x\\ \sigma_y\\ 2\sigma_{xy}\end{bmatrix}-\begin{bmatrix}\sigma_x\\ \sigma_y\\ 2\sigma_{xy}\end{bmatrix}_o+\left(T-T_{ref}\right)\begin{bmatrix}\alpha_x\\ \alpha_y\\ 0\end{bmatrix}\right] \qquad (106)$$

The criteria for either plane strain or plane stress solid mechanics case is defined in Section 3.4.2. The computation of Eq. (106) provides the solution to the solid mechanics displacements of the model.

3.4.2 Crack Geometry and Crack Propagation Conditions Theory

In order to investigate the phenomena of thermally (non-isothermal) expanded fuel cracks and the conditions for fuel pellet crack propagation, the following section provides the theory for the solid mechanics treatment. The model considers thermal expansion in all modeled materials: the Ir bar heater, the fuel pellet, and the Zircaloy sheathing. It also includes the mechanical contact between the fuel pellet surface and internal Zircaloy sheathing surface due to pellet expansion and external coolant pressure on the sheath outer surface. Heat transfer between the fuel pellet and the Zircaloy sheath through the steam filled gap considers only the thermal conductivity of the steam (see Section 3.3.2). Conditions for crack propagation are assessed by computing the *J* integral (discussed in this section) solved with a steady state solver, applied in a geometric parameterization problem (i.e., a parametric stationary analysis). Dynamic and time dependent fractures, which consider inertia effects, rate-dependent material behavior, and reflected stress waves, were not considered in this analysis since it was found that the current version of COMSOL® software is not sufficiently advanced to handle this task. Zircaloy sheath plasticity leading to stress relaxation is considered when the Zircaloy yield stress is reached. However, Zircaloy creep is not considered in this model.

The theoretical normal stress that is required to fracture a solid can initially be given by Eq. (107) [15][79]. If this equation is applied to a UO_2 ceramic, where Young's modulus E is about 2×10^{11} Pa, the surface energy γ_s is 1 J m^{-2} and the atomic lattice distance or spacing a_{lat} is about $3x10^{-10}$ m, then the predicted fracture stress is about 2.3×10^{4} MPa (or about $0.1E_{UO2}$).

$$\sigma_f = \sqrt{\frac{E\gamma_s}{a_{lat}}} \qquad (107)$$

In reality though, brittle fracture occurs in the UO_2 ceramic at much lower stress values at around 140 MPa (Figure 14). This discrepancy is due to the presence of surface and bulk defects in the fuel. Griffith first showed [15][79] that the stress around the tip of a surface or internal crack can be very much higher than the applied remote tensile stress that acts on the unflawed solid. For a penny-shaped crack embedded in a solid under a remote stress σ, as depicted in Figure 29, which represents a 'plane strain' problem where $\sigma_z = \nu(\sigma_x + \sigma_y)$, the fracture stress can be expressed by Eq. (108) [79].

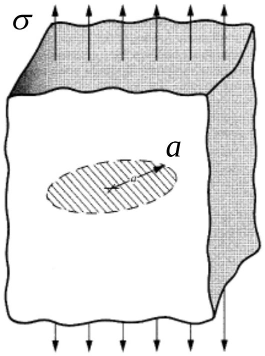

Figure 29: A penny-shaped crack embedded is a solid subjected to a remote tensile stress, adapted from [79]

where here a is a half crack length.

$$\sigma_f = \sqrt{\frac{\pi E \gamma_s}{2\left(1-\nu^2\right)a}} \tag{108}$$

If the penny-shaped crack (pore) is equal to about 40 μm across, the crack radius a is 20 μm. The Poisson's ratio ν in UO_2 fuel is given by Eq. (109) [15]:

$$\nu_{\mathrm{UO2}} = 1.32\left(1-0.26P_{or}\right)-1 \tag{109}$$

where P_{or} is the fuel porosity (equal to ≈0.0328). Thus the Poisson's ratio is equal to 0.3087. Calculating σ_f using Eq. (108), one obtains a value of 137.9 MPa, which agrees very well with experimental values as indicated in Figure 14 (where for example in the figure 1400 kg cm^{-2} is equivalent to 140 MPa).

A more commonly used expression for the actual fracture stress in the UO_2 ceramic as a function of temperature is given by [110]:

$$\sigma_f = \begin{cases} 1.7\times10^8\left(1-2.62\left(1-D_f\right)\right)^{1/2}\exp\left(\dfrac{-Q_f}{RT}\right) & 273 < \mathrm{T} \le 1000\,\mathrm{K} \\ \sigma_f\left(1000\mathrm{K}\right) & \mathrm{T} > 1000\,\mathrm{K} \end{cases} \tag{110}$$

where D_f is the fraction of theoretical density of the fuel, Q_f is the heat of fracture equal to 1590 J mol^{-1}, R is the universal gas constant equal to 8.314 J mol^{-1} K^{-1} and T is the temperature of the fuel in K. Eq. (110) gives fracture stress values approaching experimental measurements as shown in Figure 14. For temperatures above 1000 K, a constant value is used for the in-pile fracture strength of plastic UO_2. For example, typical values are: $\sigma_f\,(D_f=0.97, T=298\text{ K})=84.9$ MPa, $\sigma_f\,(D_f=0.97, T=600\text{ K})=118.64$ MPa, and $\sigma_f\,(D_f=0.97, T=1000\text{ K})=134.77$ MPa.

To assess whether a fracture occurs in a material in a traditional structural design approach, the applied stress is compared to the material's strength (yield/tensile strength). If the former is smaller than the latter the material will remain intact. One typically includes a safety factor on stress combined with minimum tensile elongation requirements on the material. Yet, as seen in Eq. (107), this approach does not consider that the stress intensity increases near material flaws. The fracture mechanics approach, on the other hand, considers three variables rather than just two. It considers the applied stress, the material flaw size and the material fracture toughness, which replaces the material strength as the relevant material property [79].

In the energy approach used by Irwin [133], a crack occurs when the energy available for crack growth is sufficient to overcome the material resistance. Irwin defined the energy release rate G_r as indicated by Eq. (111), where Π is the potential energy and A is the crack area, for a linear elastic material.

$$G_r = -\frac{d\Pi}{d\mathrm{A}} \tag{111}$$

The term 'rate' does not refer to a derivative with respect to time but to the rate of change in potential energy with respect to a crack area. For an infinite plate under a tensile load with an internal $2a$ crack length, the strain energy release rate is given by:

$$G_r = \frac{\pi\sigma^2 a}{E} \tag{112}$$

When catastrophic fracture occurs, $G_r \geq G_c$, the latter being the critical strain energy release rate, which is a measure of the material fracture toughness given by [79]:

$$G_c = \frac{\pi\sigma_c^2 a_c}{E} \tag{113}$$

where σ_c is the critical or failure stress that varies as the reciprocal squre root of the critial half-crack length a_c.

The critical energy release rate expressed in Eq. (113) still does not provide a practical means to assess conditions for fracture propagation. Hence using elastic theory principles, the tensile and shear stresses near the crack tip, which are functions of both radial distance r and angle θ from the crack tip in polar coordinates, can be expressed. For example, the tensile stress in the x principle direction can be evaluated from Eq. (114). Similar expressions can be written for σ_y and τ_{xy}.

$$\sigma_x = \frac{K}{\sqrt{2\pi r}} f_x(\theta) \quad \text{where} \quad f_x(\theta) = \cos\frac{\theta}{2}\left(1 - \sin\frac{\theta}{2}\sin\frac{3\theta}{2}\right) \tag{114}$$

The parameter K is termed the stress intensity factor and it is a central and important concept in fracture mechanics [79][133]. There are three modes by which a load can operate on a crack. Mode I is an opening or tensile stress, Mode II is a sliding (or in-plane) shear stress and Mode III is a tearing (or out-of-plane) shear stress, as seen in Figure 30. Mode I is the most typical and it is the mode of cracking treated in this thesis, which is written with the Mode I notation as K_I.

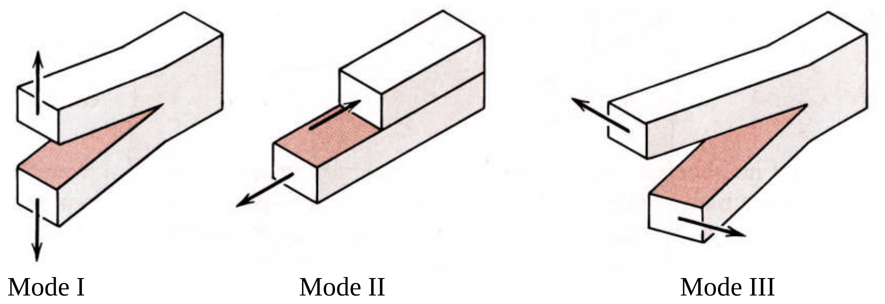

Figure 30: The three modes of loading that can be applied to a crack, adapted from [133]

When θ=0, the trigonometric function in Eq. (114) disappears, which means that the crack plane is a principle plane for a pure Mode I loading and it provides a useful specification of the stress around a flaw. Using the Westergaard Stress Function, the stress intensity factor is related to the applied stress σ and the crack length a by [79][133]:

$$K_I = Y\sigma\sqrt{\pi a} \tag{115}$$

where Y is a dimensionless correction factor that depends on the geometry and the mode of loading (refer to Figure 29 as an example). Y is also sometimes called the configuration correction factor. The typical unit of K is MPa m$^{0.5}$.

Since the stress in the vicinity of the crack tip can be defined in terms of the stress intensity factor, a critical value of K exits, which can be used to specify conditions for brittle fracture. This critical value is termed the fracture toughness of the material, K_c [133]:

$$K_c = Y\sigma_c\sqrt{\pi a} \qquad (116)$$

where σ_c is the critical remote stress to cause fracture specific to the crack length. In other words K_c is a value of K at which a crack begins to grow.

The fracture toughness of material becomes constant when the body thickness reaches a minimal value at which point plane strain conditions are said to exist. For determining if plane strain conditions preside, the following condition must be true [133]:

$$B_{th} \geq 2.5\left(\frac{K_{Ic}}{\sigma_y}\right)^2 \qquad (117)$$

where B_{th} is the body thickness in m. In our case B_{th} is taken as the length of a CANDU fuel pellet, which is about 16 mm long, and σ_{ys} is the yield stress of uranium dioxide. The yield stress of UO_2 at temperatures less than 1173 K is around 275 MPa [134]. This yield stress value is more than the fracture stress calculated using Eq. (110) at the same temperatures. This is typical of brittle materials [15]. One can use an experimental value measured for the UO_2 fracture toughness at room temperature as provided by Kutty *et al.* [135], who used the Vikers Indentation Crack Length Method [136], for a fuel porosity of 0.053 and a critical crack length of 856 μm, K_{Ic} = 0.88 MPa $m^{0.5}$. In other work compiled by Ganguly and Jayaraj [137] a fracture toughness of ≈0.83 MPa $m^{0.5}$ was reported using a similar measurement technique. Using Eq. (117) with the former K_{Ic} value, yields a B value of $2.5\text{x}10^{-5}$ m, which is less than 0.016 m (the pellet length). As such the applicable fracture study case is plane strain.

Thus for mode I (Figure 30) plane strain fracture toughness, Eq. (116) can be written as:

$$K_{Ic} = Y\sigma\sqrt{\pi a} \qquad (118)$$

Eq. (118) indicates that for a specific applied remote stress σ there exists a specific crack length a that yields a plane strain fracture toughness that causes fracture.

K_I is the driving force for fracture and K_{Ic} is the measure of the material resistance and is essentially a material property. Thus, if the following is true, fracture can occur:

$$K_I \geq K_{Ic} \qquad \text{crack propagates} \tag{119}$$

There are various loading and crack geometries for which the configuration correction factor Y as well as the stress intensity factor in Eq. (115) has been pre-calculated based on applied forces, moments, stresses, pressures and geometry. Depending on the type of crack and its geometry, Y can have varying values. For example for an infinite plate with a through-thickness crack, see Figure 31(a), Y will be close to unity. For a semi-infinite plate width that has an edge crack, see Figure 31(b), Y is given as $1.12-0.23(a/w_i)+10.6(a/w_i)^2-21.7(a/w_i)^3+30.4(a/w_i)^4$ [138] and when $w_i >> a$ then $Y \cong 1.122$. Generally, in this case, Y is a function of a and w_i [139].

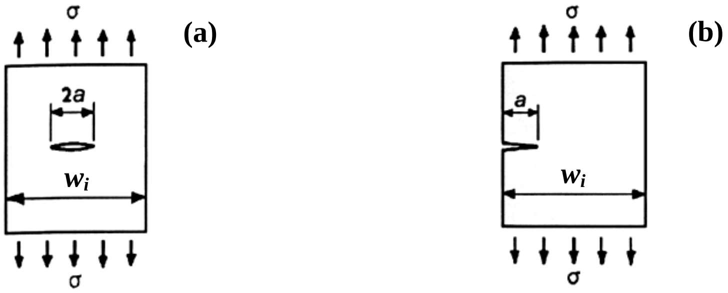

Figure 31: Schematic representation of (a) an interior crack in a plate and (b) and an edge crack in a plate, adapted from [139]

The basic crack loading examples shown in Figure 31 are not directly comparable to out-or-in reactor thermally expanded (and stressed) fuel pellets with a surface crack or flaw. The logical next question was were there analytically derived expressions for the stress intensity factors for bodies similar to the out-reactor fuel pellet so that Eq. (115) and Eq. (118) could simply be used to predict conditions for fuel crack propagation/extension.

A slightly more representative configuration to an out-reactor fuel pellet is provided in Figure 32, for which K has been calculated [140]. Here a cylinder body has an external radial edge crack, which is subjected to a uniform internal pressure. The stress intensity factor is a function of the pressure, the cylinder internal and external radii and the crack length. E.g., for a crack length of a=0.5 mm and R_1=1.5 mm and R_2=6.075 mm (similar to the out-reactor pellet) the configuration correction factor Y is equal to 1.12 [140].

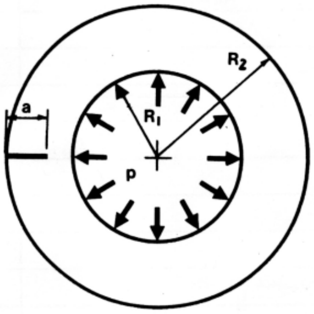

Figure 32: An external radial edge crack in a cylinder subjected to a uniform internal pressure, taken from [140]

This though is not equivalent to the thermally stressed out-reactor fuel pellet. According to Kam and Lu [141] who analytically studied an internally-heated cylinder (similar to the out-reactor fuel pellet) stresses are generally compressive (negative) at the cylinder inner surface and tensile (positive) at the outer surface. Conversly, in the cylinder subjected to a uniform internal pressure in Figure 32 the azimuthal (hoop) stress is always tensile.

Existing stress intensity factors that consider thermal loading are very limited in the literature as compared to mechanical load cases, the latter as shown in Figure 31 and Figure 32. This lack of information is mostly the result of the added complexity of the thermal crack problem. Wu [142] provides some illumination on this topic. For a steady state thermal gradient across the wall thickness of a hollow cylinder with an external radial crack, where the temperature of the internal surface is held at T and the external surface is held at $T+\Delta T$ (where ΔT may be positive or negative), the analytical solution to the azimuthal stress in the out-reactor fuel pellet geometry as a function of radial position can be given by [142]:

$$\sigma_t(r) = \frac{E\alpha_e \Delta T}{2(1-\nu)\ln\zeta_r}\left[1+\ln\left(\frac{r}{R_o}\right)+\frac{\zeta_r^2\ln\zeta_r}{1-\zeta_r^2}\left(1+\left(\frac{r}{R_o}\right)\right)\right] \tag{120}$$

where E is the Young's modulus, α_e is the thermal expansion coefficient, ν is the Poisson's ratio, and ζ_r is the ratio of the internal-to-external pellet radii or R_i/R_o. Eq. (120) is given here only as a reference. The 2D r-θ model numerically computes the stress distribution in the pellet with the added ability to input mechanical properties that are dependent on temperature. Configuration correction factors, Y, are provided by Wu [142] in Figure 33 for various relative crack lengths A, equal to a/w_i, where a is the actual crack length and w_i is the thickness of the cylinder, or R_o-R_i.

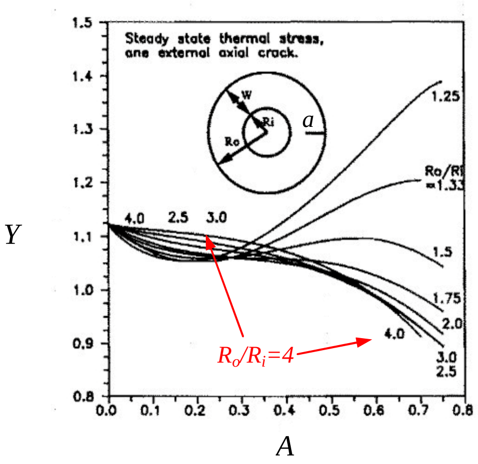

Figure 33: Stress intensity factors for an external radial crack in a hollow cylinder with a steady state thermal stress, taken from [142]

For the out-reactor pellet geometry, the curve of interest in this figure is indicated by red arrows in Figure 33 and Eq. (121) gives the polynomial trendline for the R_o/R_i=4 curve.

$$Y = -0.836A^3 + 0.359A^2 - 0.149A + 1.125 \tag{121}$$

As can be observed the configuration correction factor decreases gradually as the external radial crack length a increases for the indicated curve. The Y values in Figure 33 were derived using a closed-form weight function method [143].

The stress in the out-reactor thermally expanded fuel pellet is not homogeneous in direction or in magnitude nor is the Young's modulus, given that it is a function of temperature. Also, since the analytically calculated correction factor shown in Figure 33 considers only one surface crack and not more than one, it is hard and essentially impossible to analytically assess the stress intensity factor K_I in Eq. (115) for a thermally expanded fuel pellet.

To resolve his problem, a relationship between the stress intensity factor K_I and the energy release rate G_r can be derived by substituting Eq. (115) into Eq. (112), which shows that the stress intensity factor and the energy release rate are directly related for linear elastic materials:

$$G_r = \frac{K_I^2}{E'} \tag{122}$$

where E' is the Young's modulus given by:

$$E' = \left\{ \begin{matrix} E & \text{for plane stress conditions} \\ \dfrac{E}{\left(1-\nu^2\right)} & \text{for plane strain conditions} \end{matrix} \right\} \tag{123}$$

where the Poisson's ratio ν for UO_2 for plane strain conditions is provided by Eq. (109).

A more general version of the strain energy release rate (Eq. (112)) is the J contour integral formulated by Rice [144]. For the special case of linear elastic materials, $J = G_r$. Substituting this value into Eq. (122) and solving for K_I the following result is obtained:

$$K_I = \sqrt{JE'} \tag{124}$$

The J integral is a path independent line integral around the tip of a crack and it is the measure for the intensity of stresses and strains at the tip of cracks and notches. The J integral can be viewed as both an energy parameter equivalent to an energy release rate G_r and a stress intensity parameter comparable to K. Also, the J integral is useful for calculating the energy release rate in nonlinear elastic bodies (where the load is not linear with displacement) that contain a crack. It can be used to idealize elastic-plastic deformation for non-linear elastic materials. The *J* integral effectively extends the limits of the linear elastic fracture mechanics [79][139].

The *J* integral [139] is provided by the following:

$$J = \int_{\Gamma_c} \left(w_s dy - T_i \frac{\partial u_i}{\partial x} ds \right) = \int_{\Gamma_c} \left(w_s n_x - T_i \frac{\partial u_i}{\partial x} \right) ds \qquad (125)$$

where w_s is the strain energy density, T_i are components of the traction vector, u_i is the displacement vector components, and *ds* is the length increment along the contour Γ_c. The right hand side of Eq. (125) is an alternative description of the *J* integral that is a little more intuitive to use. This alternative description can be explained by showing that if the increment $d\underline{s} = (dx,dy)$ is a vector coinciding with part of the contour Γ_c, then $dx = -n_y ds$ and $dy = n_x ds$, where $\underline{n} = (n_x,n_y)$ is the outward directed unit vector normal to the contour [139].

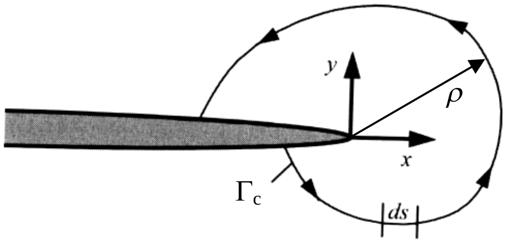

Figure 34: An arbitrary contour Γ_c around a crack tip [79]

Thus, substituting $dy = n_x ds$ into the first expression on the left in Eq. (125) yields the second expression on the right in Eq. (125). The strain energy density w_s is provided by Eq. (126) in 2D where σ_{ij} and ε_{ij} are the stress and strain tensors.

$$w_s = \int_0^{\varepsilon_{ij}} \sigma_{ij} d\varepsilon_{ij} = \frac{1}{2}\left(\sigma_x \cdot \varepsilon_x + \sigma_y \cdot \varepsilon_y + 2 \cdot \sigma_{xy} \cdot \varepsilon_{xy}\right) \qquad (126)$$

The traction vector is a stress vector acting on the contour Γ_c and has the unit N m^{-2}. In other words, if a free body diagram is drawn of the immediate crack domain in the contour, T_i would be the stresses acting on the body in the outward direction. The components of the traction vector T_i are provided by Eq. (127), where n_j are the components of the unit vector normal to the contour Γ_c.

$$\overline{T_i} = \sigma_{ij} n_j \tag{127}$$

If we expand Eq. (127) in the *x* and *y* coordinates one obtains:

$$\overline{T} = \left[\left(\sigma_x \cdot n_x + \sigma_{xy} \cdot n_y \right), \left(\sigma_{xy} \cdot n_x + \sigma_y \cdot n_y \right) \right] \tag{128}$$

Thus, expanding the 2nd term on the RHS of Eq. (125), and using Eq. (128):

$$T_i \frac{\partial u_i}{\partial x} = \left[\left(\sigma_x \cdot n_x + \sigma_{xy} \cdot n_y \right) \cdot \frac{\partial u_1}{\partial x} + \left(\sigma_{xy} \cdot n_x + \sigma_y \cdot n_y \right) \cdot \frac{\partial u_2}{\partial x} \right] \tag{129}$$

The resulting *J* integral has the units of work or energy per fracture surface area, in J m^{-2} (or N m^{-1}). Thus, assessing Eq. (124) for the stress intensity factor *K* around a propagating crack tip (by computing the *J* integral Eq. (125)) and comparing this result to a measured fracture toughness K_{Ic} [135][137] the condition for crack propagation in a UO_2 ceramic can be determined.

The above described *J* integral computation assumes a path independent line integral (i.e., arbitrary line integration paths around the crack tip yield the same *J* value, refer to Figure 34) and is applicable for bodies for isothermal, steady state temperature distributions. Yet when a temperature gradient exists (parallel to the crack growth direction), inducing thermal stresses in the body (due to thermal expansion), the computed *J* integral can become path dependent, which is undesirable. To overcome this problem Wilson and Yu [145] modified the conventional *J* integral to include an area integral that compensates for the temperature gradient in thermal stress problems. The modified equation is referred to here as the J^* integral and it describes the energy release rate to crack extension, which is given by Aoki *et al.* [146] and also by [147][148]:

$$J^* = \int_{\Gamma_c} w_e dy - \int_{\Gamma_c} T_i \frac{\partial u_i}{\partial x} ds + \iint_A \sigma_{ij} \frac{\partial \left(\varepsilon_{ij}^t + \varepsilon_{ij}^p \right)}{\partial x} dA \tag{130}$$

where w_e is the elastic strain energy density, σ_{ij} is the stress tensor, ε_{ij}^{t} is the thermal strain tensor, and ε_{ij}^{p} is the plastic strain tensor. Also, the elastic strain energy density w_e is similar to w_s in Eq. (126) but considers only the mechanical elastic strain, as follows.

$$w_e = \int_0^{\varepsilon_{ij}^{e}} \sigma_{ij} d\varepsilon_{ij}^{e} = \frac{1}{2}\left(\sigma_x \cdot \varepsilon_x^{e} + \sigma_y \cdot \varepsilon_y^{e} + 2 \cdot \sigma_{xy} \cdot \varepsilon_{ij}^{e}\right) \qquad (131)$$

It is noted that the total strain tensor ε_{ij} is a composition of the elastic ε_{ij}^{e} strains and the thermal and plastic strains, as written:

$$\varepsilon_{ij} = \varepsilon_{ij}^{e} + \varepsilon_{ij}^{t} + \varepsilon_{ij}^{p} \qquad (132)$$

The thermal strain ε_{ij}^{t} is also refered to as the inelastic strain ε_{inel} earlier in the text. Recalling Eq. (94) and rewriting this equation with the present terms:

$$\varepsilon_{ij}^{t} = \alpha_e \Delta T \delta_{ij} \qquad (133)$$

where α_e is the thermal expansion coefficient, ΔT is the temperature increment from the reference temperature and δ_{ij} is the Kroneker Delta. If the thermal strain in Eq. (133) is substituted into Eq. (130) in the area integral and the plastic strain is ignored then Eq. (130), for a homogeneous material, becomes [146][148]:

$$J^{*} = \int_{\Gamma_c} w_e dy - \int_{\Gamma_c} T_i \frac{\partial u_i}{\partial x} ds + \alpha_e \iint_A \sigma_{kk} \frac{\partial T}{\partial x} dA \qquad (134)$$

where α_e is outside the integral if constant and inside if temperature dependent, and σ_{kk} is the principle stress tensor. If the material properties are temperature dependent (i.e., $E(T)$, $\alpha_e(T)$, and $\sigma_Y(T)$, the latter if plasticity is investigated) and the temperature distribution in the material is not uniform then the material can be considered as not homogeneous. For this case the J^{*} integral can be written as [146]:

$$J^{*} = -\int_{\Gamma_c} T_i \frac{\partial u_i}{\partial x} ds + \iint_A \sigma_{ij} \frac{\partial \varepsilon_{ij}}{\partial x} dA \qquad (135)$$

where the area integral on the RHS of Eq. (135) can be expressed as a combination of thermal and elastic area integrals, and plasticity is ignored, as follows:

$$\iint_A \sigma_{ij} \frac{\partial \varepsilon_{ij}}{\partial x} dA = \iint_A \alpha_e \sigma_{kk} \frac{\partial T}{\partial x} dA + \iint_A \sigma_{ij} \frac{\partial \varepsilon_{ij}^{e}}{\partial x} dA \qquad (136)$$

Lastly, as the integration contour radius decreases (Figure 34) in length, the area integrals of equations (134) and (135) (the third and second terms, respectively, which include thermal strains) vanish, since the thermal strains (ε_{ij}^{t}) in these small contours is small. Hence, at small contour radii (or size) the J^* integral (Eq. (134) and Eq. (135)) and the regular J integral (Eq. (125)) are equivalent [146]:

$$J^{*} = \lim_{\rho \to 0} J \qquad (137)$$

It remains to provide the mechanical properties, specifically, the thermal expansion coefficient α_e, Young's modulus E, and the Poisson's ratio ν of the relevant materials for the out-reactor fuel element.

The thermal expansion coefficient of solid UO_2 is provided by Eq. (138) from the work of Martin [99] and has the units of K^{-1}.

$$\alpha_{\mathrm{UO2}} = 9.828x10^{-6} - 6.390\times10^{-10}T + 1.330\times10^{-12}T^2 - 1.757\times10^{-17}T^3 \qquad 273\mathrm{K} \le T \le 923\mathrm{K} \qquad (138a)$$

$$\alpha_{\mathrm{UO2}} = 1.1833\times10^{-5} - 5.013\times10^{-9} + 3.756\times10^{-12}T^2 - 6.125\times10^{-17}T^3 \qquad 923\mathrm{K} \le T \le 3120\mathrm{K} \qquad (138b)$$

The Young's modulus of elasticity for stoichiometric UO_2 is given by [110] with units of Pa:

$$E_{\mathrm{UO2}} = 2.334\times10^{11}\left(1 - 2.752\left(1 - D_f\right)\right)\cdot\left(1 - 1.0915\times10^{-4}T\right) \qquad \text{for } 300\,\mathrm{K} < T < 3113\,\mathrm{K} \qquad (139)$$

where D_f is the fraction from theoretical density, which is equal to $\rho_{\mathrm{UO2}}/\rho_{\mathrm{TD}}$. Here the fuel density ρ_{UO2} is a function of temperature and ρ_{TD} is the maximum theoretical density of UO_2. The Poisson's ratio for UO_2 is provided by Eq. (109) as shown previously.

The linear thermal circumferential expansion of Zircaloy-2 or -4 for the alpha phase used in the plane strain model is given by Eq. (140), where ε_{11} has the units of m m^{-1} [110].

$$\varepsilon_{11} = 4.95\times10^{-6}T - 1.485\times10^{-3} \qquad \text{for } 300\,\mathrm{K} < T < 1083\,\mathrm{K} \tag{140}$$

The thermal expansion coefficient of Zircaloy-2 or -4, in the circumferential direction, is:

$$\alpha_{\mathrm{Zircaloy}} = \frac{\varepsilon_{11}}{\left(T - T_{\mathrm{ref}}\right)} \qquad \text{for } 300\,\mathrm{K} < T < 1083\,\mathrm{K} \tag{141}$$

where T is in K and T_{ref} is the relative temperature from which the material is heated from (which was set to 300 K). The Young's modulus of elasticity in Pa of Zircaloy-2 or -4 in the alpha phase is provided by [110]:

$$E_{\alpha\_\mathrm{Zirc}} = \left(1.088\times10^{11} - 5.475\times10^{7}T + K_{1\_\mathrm{Zirc}} + K_{2\_\mathrm{Zirc}}\right)/K_{3\_\mathrm{Zirc}} \qquad \text{for } 300\,\mathrm{K} < T < 1083\,\mathrm{K} \tag{142}$$

where K_{1_Zirc} accounts for the effect of oxidation given by [110]:

$$K_{1\_\mathrm{Zirc}} = \left(6.61\times10^{11} + 5.912\times10^{8}T\right)\cdot\Delta_{\mathrm{Zirc}} \tag{143}$$

where Δ_{Zirc} is a unitless value of the average oxygen concentration minus the oxygen concentration of the as-received cladding given in (kg oxygen/kilogram Zircaloy). Its value can be set to an as-received value of 0.0012 (kg oxygen/kilogram Zircaloy). K_{2_Zirc} accounts for the effect of cold work given by Eq. (144), where C was set to 0.001 and is a unitless ratio of areas.

$$K_{2\_\mathrm{Zirc}} = -2.6\times10^{10}C \tag{144}$$

K_{3_Zirc} is a unitless value to account for the effect of a fast neutron fluence and is given by Eq. (145). When the fast neutron fluence ϕ, which is in n m^{-2}, is zero, K_{3_Zirc} takes on a value of unity.

$$K_{3\_\mathrm{Zirc}} = 0.88 + 0.12\exp\left(-\frac{\phi}{10^{25}}\right) \tag{145}$$

In the model, ϕ was set to zero. Computing Equations (142) through (145) for the expected temperatures in the out-reactor test yields a Zircaloy Young's modulus of about 77 GPa. The Poisson's ratio for Zircaloy-2 or -4 was taken as $\nu_{\_\mathrm{Zirc}}$=0.37 [149]. A similar Poisson's ratio value is provided by [150]. The Zircaloy density is given as ρ_{Zirc}=6.44 g cm^{-3}.

In the model when the fuel pellets thermally expand outward to the sheath and contact is made, the sheath will be pushed outward until the yield stress of the sheath is reached. The initial yield stress of Zircaloy in the transverse direction at the coolant temperature before work hardening ranges from 130-170 MPa. In this work, an approximate value is given by [118][151][152]:

$$\sigma_{ys0} = 150 \quad \mathrm{MPa} \tag{146}$$

The isotropic tangent modulus of Zircaloy (after yielding) is given by Eq. (147) [153] and is used for isotropic hardening during plastic deformation.

$$E_{\alpha\_iso\_T} = \frac{E_{\alpha\_Zirc}}{10} \tag{147}$$

Figure 35 shows the elastic modulus (dark blue line, from Eq. (142)) and isotropic tangent modulus graphically (red line, from Eq. (147)) for Zircaloy at *out-reactor instrumented fuel oxidation experiment* temperatures.

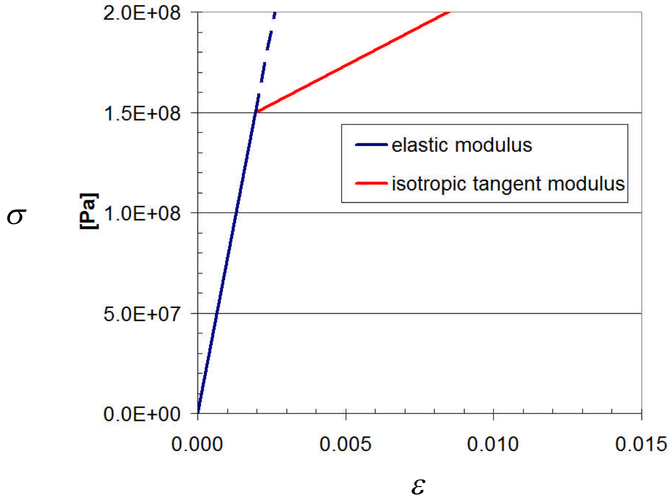

Figure 35: The stress-strain curve that shows the elastic and hardening regions in Zircaloy

The last material properties needed in the solid mechanics model is the iridium bar heater element. In the 2D *r*-*θ* model there is no gap between the iridium bar and the inside surface of the UO_2 fuel pellet. The thermal expansion coefficient of the iridium and the UO_2 are similar but not identical (the α_{UO2} being a little higher than $\alpha_{\_Ir}$ at the same temperature). Hence, the gap between the iridium bar heater and the UO_2 pellets may increase or decrease when heated in the experiment. This would depend on the temperature of each material and the original gap distance between these two materials.

The thermal expansion coefficient of iridium depends on temperature. According to the PGM database [108], $\alpha_{\_Ir}$ varies between 6.5×10^{-6} K^{-1} and 9×10^{-6} K^{-1} for temperatures between ambient and 1750 °C, respectively. A value of $6.4x10^{-6}$ K^{-1} [109] was selected in the current analysis (there is no difference in model result between using the selected value or 6.5×10^{-6} K^{-1}). Choosing the lower value for $\alpha_{\_Ir}$ will show that the thermal expansion of the pellets alone provides suitable conditions for fuel cracking.

The Young's modulus of iridium was set to E_{Ir}=$528x10^9$ Pa and the Poisson's ratio was $\nu_{\_Ir}$=0.26 [108].

3.5 Numerical Implementation of the Models

COMSOL Multiphysics$^{®}$ platforms versions 3.5a up to 4.3b were selected for computing the fuel oxidation model for the reasons explained in Section 1.5. It was also used for its flexibility and robustness in modeling the fuel stress and strains and fuel and sheath contact using COMSOL$^{®}$'s solid mechanics physics to predict fuel crack geometry and number. Six models are included in this thesis, which are numerically implemented in this section. The first three have 2D r-θ fuel cross section geometries that model fuel oxidation and fuel cracking separately. A third 2D r-θ model demonstrates coupling the fuel oxidation model with fuel thermally expanded fuel cracks. The forth and fifth models are full length 3D fuel oxidation models: one that models an in-reactor defective fuel element and one that models the *out-reactor instrumented fuel oxidation experiment*. The last model is a 2D model of a final stage in a fuel pellets sintering process.

The reason that multiple versions of COMSOL$^{®}$ were used in this thesis to generate the mentioned models was because COMSOL Inc. releases an updated version of their software twice a year. Working with the most up-to-date version of software allowed access to the latest COMSOL$^{®}$ tools sets and improved functionality, as well as software fixes. Each model numerical implementation sub-section mentions what specific version of COMSOL$^{®}$ was used.

3.5.1 COMSOL$^{®}$ and the Finite Element Analysis Method

COMSOL$^{®}$ uses what is called the *finite-element* analysis method to solve a partial differential equation (PDE) or a number of equations, sequentially or simultaneously. In this method the solution domain is divided into simply shaped regions called elements. An approximate solution for the PDE can be developed for each of these elements. The total solution is then generated by linking together the individual solutions [154][155]. Discretization involves dividing up the solution domain into finite elements. Figure 36 depicts model solution domains with examples of a line element in 1D and triangular and quadrilateral elements in 2D.

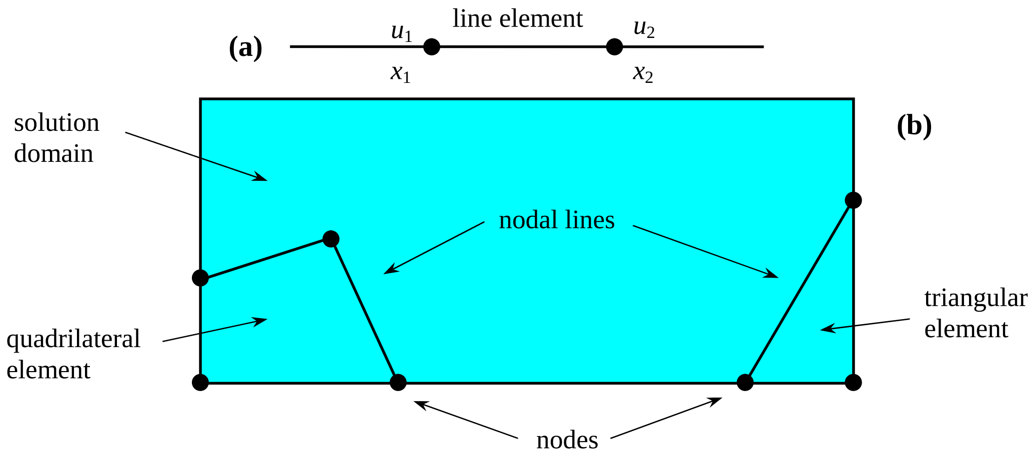

Figure 36: (a) A line element employed in one dimension and (b) quadrilateral and triangular elements employed in two dimensions. Adapted from [154]

Equations are developed to approximate the solution of each element. This involves two steps: (i) An appropriate function is selected with unknown coefficients that are used to approximate the solution and (ii) the coefficients are evaluated so that the function approximates the solution in an optimal fashion. Polynomials are often involved for this purpose, since they are easy to manipulate.

The finite-element analysis method using the direct approach is demonstrated when applied in the simple 1D element with two nodes (Figure 36 (a)). For the 1D case the simplest approximation function is the first-order polynomial or straight line, provided by:

$$u(x) = a_o + a_1 x \tag{148}$$

Where $u(x)$ is the dependent variable, a_o and a_1 are constants, and x is the independent variable. This function must pass the values of $u(x)$ at the end points of the element at x_1 and x_2 in Figure 36 (a), therefore:

$$\begin{aligned} u_1 &= a_o + a_1 x_1 \\ u_2 &= a_o + a_1 x_2 \end{aligned} \tag{149}$$

These equations can be solved using Cramer's rule [154].

$$a_o = \frac{u_1 x_2 - u_2 x_1}{x_2 - x} \qquad a_1 = \frac{u_2 - u_1}{x_2 - x_1} \tag{150}$$

Substituting these terms into Eq. (148), one gets [154]:

$$u = N_1 u_1 + N_2 u_2 \quad \text{where} \quad N_1 = \frac{x_2 - x}{x_2 - x_1} \text{ and } N_2 = \frac{x - x_1}{x_2 - x_1} \tag{151}$$

The equation for u in Eq. (151) is called an approximation or shape function, and equations N_1 and N_2 are called interpolation functions [155][155]. Eq. (151) provides a means to predict (or interpolate) intermediate values between given values u_1 and u_2 at the nodes. For example the general shape function u in Eq. (151) could be used to represent a concentration distribution in the finite element:

$$c = N_1 c_1 + N_2 c_2 \tag{152}$$

where c in the concentration shape function and c_1 and c_2 are the concentration values at nodes 1 and 2 . This equation amounts to a linear interpolation between two nodal points as shown in the following figure.

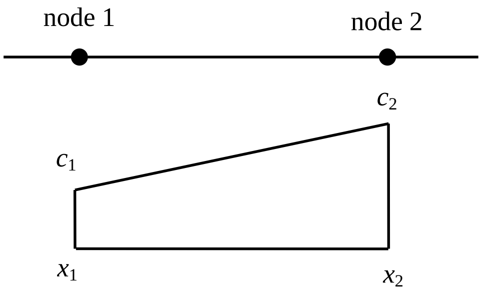

Figure 37: A linear approximation or shape function for a line element

The definition of the diffusion flux is the diffusion coefficient times the concentration gradient, which is Fick’s first law. It can be expressed in one dimension by:

$$J_d = -D\frac{dc}{dx} \tag{153}$$

If a linear approximation function is used to characterize the element's concentration c, the diffusion flux into the element through node 1 and 2 can be represented by:

$$J_{d1} = D\frac{c_1 - c_2}{x_2 - x_1} \quad \text{and} \quad J_{d2} = D\frac{c_2 - c_1}{x_2 - x_1} \tag{154}$$

These two equations express the relationship of the element's internal concentration distribution (nodal concentrations) to the diffusion flux at the finite element ends. These equations can be simplified further to express concentration gradients at the element boundaries [154]:

$$J_{d1} = -D\frac{dc(x_1)}{dx} \quad \text{and} \quad J_{d2} = D\frac{dc(x_2)}{dx} \tag{155}$$

The diffusion flux terms in Eq. (155) can be substituted into the element equations to give:

$$\frac{1}{x_2 - x_1}\begin{bmatrix} 1 & -1 \\ -1 & 1 \end{bmatrix}\begin{Bmatrix} c_1 \\ c_2 \end{Bmatrix} = \begin{Bmatrix} -\dfrac{dc(x_1)}{dx} \\ \dfrac{dc(x_2)}{dx} \end{Bmatrix} \tag{156}$$

Eq. (156) is a matrix equation that describes the behavior of the finite element and has the general form of [154][155]:

$$[K_s]\{u_{cv}\} = \{F_{cv}\} \tag{157}$$

where K_s is the element property or stiffness matrix, u_{cv} is the column vector of unknowns at the nodes (in this case c_1 and c_2), and F_{cv} is the column vector of external influences or boundary conditions (in this case the concentration gradients). The solution of Eq. (157) can be obtained with linear algebra techniques such as *Gauss elimination* or *LU decomposition*. In *LU decomposition* the idea is to replace the stiffness matrix in a system of linear equations by the product of two matrices *LU*, to form a diagonal matrix, and by doing so solving the unknowns [154][156]. If the stiffness matrix in square and is not ill-conditioned, a matrix inverse can be derived so that a formal solution of the column vector of unknowns, u_{cv}, in Eq. (157) can be solved [154]:

$$\{u_{cv}\} = [K_s]^{-1}\{F_{cv}\} \tag{158}$$

Solving Eq. (158) is often referred to as the direct method. For the solution of the models discussed in this work direct COMSOL® solvers such as PARDISO and MUMPS were used. PARDISO is a fast multi-core solver. Also, since the stiffness matrix and its inverse matrix can be large, the memory requirements using the PARDISO solver can be significant.

The solution time and memory requirements of a model simulation are strongly related to the *degrees of freedom* of the model. For most *physics interfaces* in COMSOL® 4.0 and up (*application modes* in COMSOL® 3.5a and previous) each dependent variable is present in all nodes of a mesh. First order shape functions in one dimensional elements will have two nodes and second order shape functions in one dimensional elements will have three nodes (one mid point node), etc. Hence, the shape function order contributes to the number of degrees of freedom of the model. In general the total number of degrees of freedom of a model is equal to the number of nodes multiplied by the number of dependent variables, where the number of nodes is dependent on the order of the shape function and model dimension (1D, 2D or 3D) [71][155].

3.5.2 The 2D r-θ Fuel Oxidation Model Numerical Implementation

Two variations of this model were considered in this simulation. (i) The first model assumed sheath contact with the UO_2 pellets, i.e., a closed fuel-to-sheath gap case. This modeled case was built on COMSOL® version 3.5a platform. (ii) The second model assumed that the Zircaloy sheath had not totally crept down onto the fuel pellets, i.e., an open fuel-to-sheath gap case. The reason why the sheath may not have fully crept down on the pellets in the *out-reactor instrumented fuel oxidation experiment* (as normally occurs in in-reactor CANDU fuel) is because of the short conditioning period in the test (only a few hours). Additionally, to defect the Zircaloy sheath, an internal differential pressure (≈2.7-6.2 MPa) in the out-reactor fuel element was applied until the sheath failed at the pre-machined sheath defect surface. During this time the sheath may have expanded and sheath ‘lift-off’ may have occurred due to the internal pressure, so that there ceased to be direct contact between the sheath and the pellets. Thus, for this second case various fuel-to-sheath gaps (as well as crack widths) were modeled, which was modeled with the later and more advanced COMSOL® version 4.2a platform.

(i) *2D r-θ Fuel Oxidation Model with a Closed Fuel-to-Sheath Gap*

The governing equations for fuel oxidation and electrical heating as applied to the *out-reactor instrumented fuel oxidation experiment* are outlined in Section 3.2 and Section 3.3. This 2D r-θ geometric representation assumes axial symmetry and allows for the investigation of radial cracks and a fuel-to-sheath gap geometry on the effect of fuel oxidation, the assessment of the expected electrical power for given temperature distribution, and the influence of the thermocouples on the local fuel temperature.

As can be seen in Figure 38, the model geometry contains several domains. In this model, twelve explicit radial cracks were defined based on the reasoning given by Oguma [73] for centrally and electrically heated fuel pellets at an applied power. Specifically, if the central linear heating power target is ≈24 kW m^{-1} then ≈12 radial fuel cracks may form in the out-reactor fuel pellets.

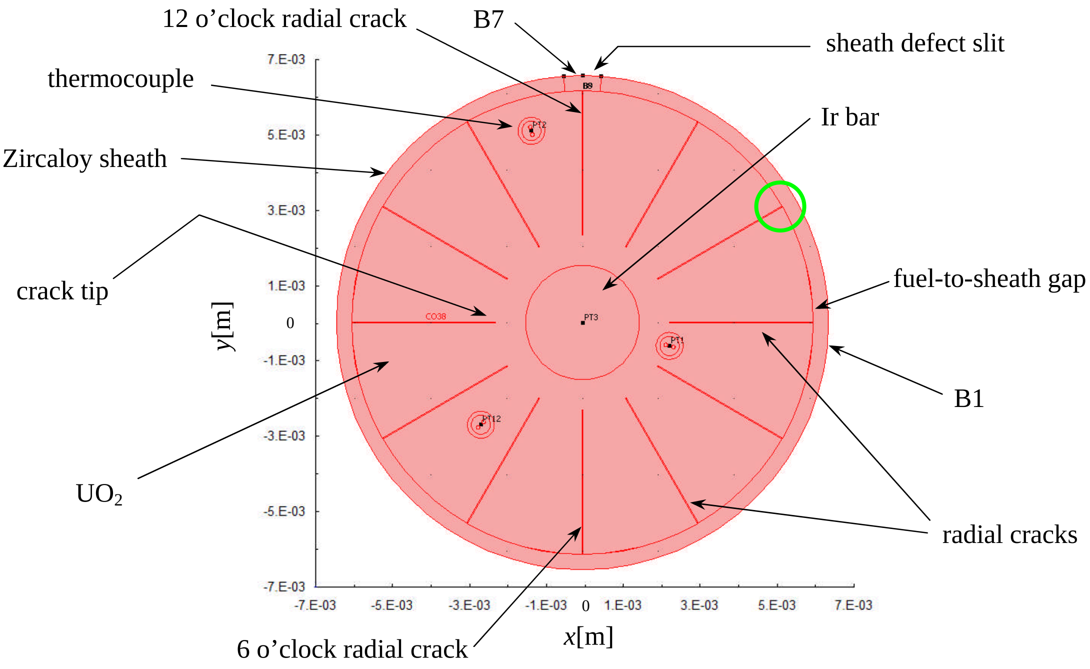

Figure 38: Geometry of the 2D *r*-*θ* model showing the different materials of the fuel element simulator and the 12 pre-defined radial fuel cracks.

The radial fuel cracks extend to the fuel-to-sheath gap as can be seen in a close-up view in Figure 39, of an area indicated by a green circle in Figure 38. The width of the radial cracks in this model was set to 15 μm based on the analysis of Williford [76].

The fuel-to-sheath gap was set to 1 μm that assumes the sheath has crept down with a 'closed' fuel-to-sheath gap, i.e., the sheath is considered to be in contact with the fuel pellet using the treatment discussed in Section 3.3.2. The *effective* crack dimension (specifically the crack root position) was determined by first applying an achievable electrical power to the out-reactor fuel element, which was set as high as possible without failing the out-reactor Ir bar heater (determined by experimentation). Then the crack tip (or crack root) radial dimension was set in the model so that the crack tip was positioned at the approximate temperature of 1250°C on the first simulated day. The discrete temperature of 1250°C was selected so that it fell within the 1200°C - 1400°C transition temperature for elastic to plastic fuel (refer to Sections 1.5 and 3.2, and Figure 13, Figure 14, and Figure 23). Also, this modeled transition temperature can justify the selection of a higher transition temperature, such as 1300 °C or 1350 °C, if higher fuel oxidation was measured in the test. Thus, the crack tip (or root of the crack) was set to 0.00229 m (2.29 mm) from the centre of the fuel element (to coincide with 1250 °C in the fuel) using a specific electric heating power.

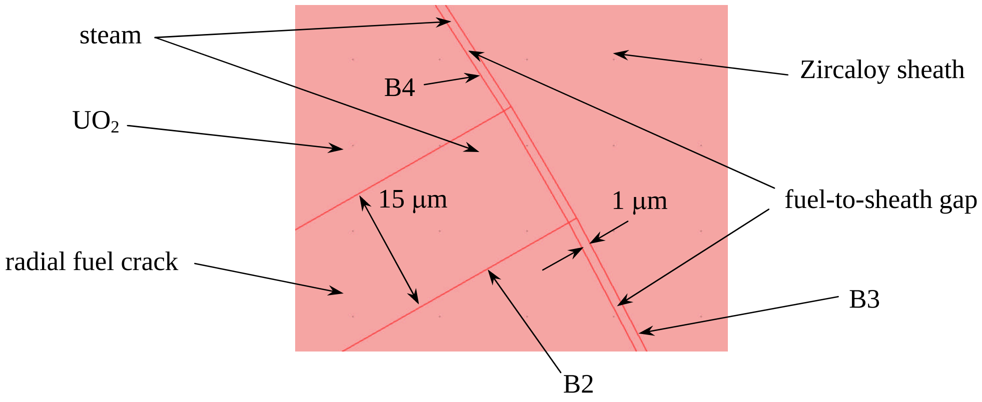

Figure 39: Close-up view of the fuel-to-sheath gap domain, a fuel radial crack domain, and UO_2 domains with boundaries

In this fuel oxidation model with a closed fuel-to-sheath gap a 'heat transfer by conduction' physics application mode was used for modeling the heat conduction, which in COMSOL® 3.5a format is given by the equation:

$$\delta_{ts}\rho C_p \frac{\partial T}{\partial t} - \nabla \bullet (k\nabla T) = Q + h_{trans}(T_{ext} - T) + C_{trans}\left(T_{ambtrans}{}^4 - T^4\right) \qquad (159)$$

The coefficients of Eq. (159) are provided in Table 6 by comparing to Eq. (32) and Eq. (68).

Table 6: Parameters used in heat conduction application mode in COMSOL® 3.5a

Parameter or coefficient	Description	Value or expression as used in model
δ_{ts}	Time scaling coefficient	1
k	Thermal conductivity	keff_UO2 k_Zirc k_Ir Cp_steam k_Rtype k_TC_sheath k_Magnesia
ρ	Density	cu_UO2 rho_Zircaloy rho_Ir

Table 6: Parameters used in heat conduction application mode in COMSOL® 3.5a

Parameter or coefficient	Description	Value or expression as used in model
		rho_steam rho_Rtype rho_Magnesia
C_p	Specific Heat Capacity	Cp_UO2 Cp_Zirc Cp_Ir Cp_steam Cp_Rtype Cp_Magnesia
Q	Heat source	Q_vol_UO2 Q_vol_Ir Q_vol_Zirc
h_{trans}	Heat transfer coefficient	0
T_{ext}	External temperature	0
C_{trans}	User defined constant	0
$T_{ambtrans}$	Ambient temperature	0

Note: All units are in SI units except for Cp_UO2 which is given in kJ mol^{-1} K^{-1} and cu_UO2 which is given in mol m^{-3}. All powers and energies are in kW and kJ.

For the closed fuel-to-sheath gap 2D r-θ model, only one temperature boundary condition was used. A Dirichlet boundary condition for Eq. (159) was applied to the model's outer surface (or the sheath), identified as boundary B1 in Figure 38, and is given in Table 7.

Table 7: Boundary condition for the heat transfer equation used in a closed fuel-to-sheath gap model

Boundary	Parameter	Value or expression as used in model
B1	Temperature	T = T_s_outer

The oxygen solid state diffusion equation was solved using COMSOL® 3.5a's 'PDE general form equation' application mode. This form was used (as it was also used in [24]), since it was possible to define regular diffusion (concentration driven) as well as thermo-diffusion (the Soret effect). With the dependent variable defined as Xdev for the oxygen stoichiometric deviation value x (in UO_{2+x}), the general form of the equation in COMSOL® 3.5a format is given by:

$$e_a \frac{\partial^2 Xdev}{\partial t^2} + d_a \frac{\partial Xdev}{\partial t} + \nabla \bullet \Gamma = F \tag{160}$$

The coefficients of Eq. (160) are provided in Table 8 by comparing to Eq. (18) and Eq. (66). The interstitial oxygen flux vector term, Γ, in Eq. (160) is given by:

$$\Gamma = -D\left(\nabla Xdev + Xdev \frac{Q}{RT^2} \nabla T \right) \tag{161}$$

The flux vector term Γ is written in Table 8 as it is entered in COMSOL®. Specifically, the oxygen diffusion coefficient D is called D_O2, Xdev is the deviation from stoichiometry, Xdevx is the gradient of Xdev in the x coordinate direction, Xdevy is the gradient of Xdev in the y coordinate direction, Tstar is the molar effective heat transport Q, divided by the ideal gas constant R, where Q is given by Eq. (20), and Tx and Ty are the temperature gradients in the x and y coordinate directions, respectively.

Table 8: Coefficients used in COMSOL® 3.5a PDE general form equation application mode (the interstitial oxygen diffusion equation)

Parameter or coefficient	Description	Value or expression used in model
e_a	Mass coefficient	0
d_a	Damping/mass coefficient	1
Γ	Flux vector	-D_O2*(Xdevx+Xdev*Tstar/T^2*Tx) -D_O2*(Xdevy+Xdev*Tstar/T^2*Ty)
F	Source term	0

The boundary conditions for Eq. (160) are described by Eq. (162):

$$G_s = -\mathbf{n} \cdot \mathbf{\Gamma} \text{ on } \partial\Omega \tag{162}$$

where **n** is the unit vector normal to the ∂Ω geometric boundary (or surface in 3D), **Γ** is the flux vector at the applicable geometric boundary (or surface), and G_s is a scalar.

Figure 40 shows an inner region of the fuel element simulator cross section that includes the iridium bar heater to UO_2 boundary, the UO_2 to radial crack boundary and the boundary between the UO_2 cracked surfaces and steam fill gas.

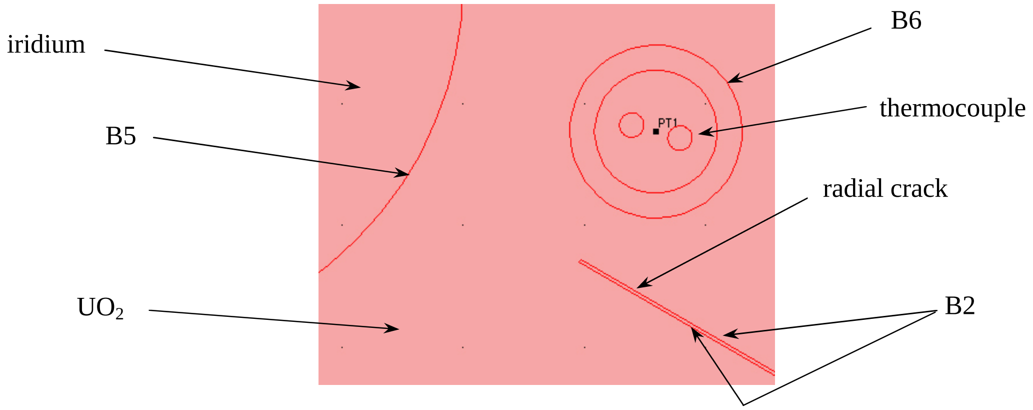

Figure 40: Inner region of a fuel element simulator with applicable boundaries

Table 9 provides the boundary conditions used in the oxygen diffusion equation. Refer to Figure 39 and Figure 40 for the identification of the relevant boundaries applicable to Eq. (160). In Table 9 the values of G_s is zero at all boundaries except for boundary B2, which is equal to the kinetic reaction rate R_f^{react} (see Eq. (25) and Section 3.3.1) divided by the molar density of UO_2, defined as Rreact_fuel and cu_UO2 in COMSOL® format, respectively.

Table 9: Boundary conditions for interstitial oxygen diffusion equation (Eq. (162))

Boundary	**Boundary condition type**	**G_s value as used in model**
B2	Neumann	Rreact_fuel/cu_UO2
B4	Neumann	0
B5	Neumann	0
B6	Neumann	0

With the solution of the oxygen diffusion equation, it is possible to create 2D distribution plots and radial plots of the oxygen stoichiometric deviation x. In this manner, the extent of fuel oxidation can be estimated and compared. Since x is the deviation from the O/U ratio of 2, it is possible to calculate the oxygen excess number density in the oxidized fuel pellet matrix by multiplying the average stoichiometry deviation value by the number density of UO_2, as shown in by:

$$N_{\mathrm{O}} = N_{\mathrm{UO}_2} \cdot x_{average} \tag{163}$$

where N_{UO_2} is equal to 2.444×10^{28} UO_2 particles m^{-3}, assuming a maximum theoretical fuel density and $x_{average}$ is calculated by integrating x over the fuel domain (in this case in 2D) as given by Eq. (164).

$$x_{average} = \frac{\int x dA}{A_{UO_2}} \tag{164}$$

With the average oxygen stoichiometric value calculated over the fuel element cross section A_{UO_2}, the total molar uptake of oxygen in the fuel can be calculated:

$$n_{\mathrm{O}} = \frac{N_{\mathrm{O}} \cdot F_{vol}}{N_{\mathrm{A}}} \tag{165}$$

where n_{O} is the excess (hyperstoichiometric) oxygen in moles, F_{vol} is the fuel element, fuel pellet, or other volume in m^3, and N_{A} is Avogadro's number. In a similar manner in a 3D model the $x_{average}$ is calculated over the volume of the fuel element model:

$$x_{average} = \frac{\int x dV}{V_{UO_2}} \tag{166}$$

and the excess oxygen in moles n_{O} (Eq. (165)) is similarly calculated.

The last PDE to be solved simultaneously in this model is the hydrogen diffusion equation in the radial fuel cracks and in the fuel-to-sheath gap. The 'diffusion application mode' in COMSOL® 3.5a was used for this purpose, where the dependent variable is the hydrogen mole fraction q as shown in the following equation:

$$\delta_{ts} \frac{\partial q}{\partial t} + \nabla \bullet \left(- D \nabla q \right) = R_s \tag{167}$$

Again, the coefficients of Eq. (167) can be determined on comparison to Eq. (27) and Eq. (67). Table 10 provides the coefficient parameters, where c_g (or cg used in the model) is the total molar concentration of the gas in the fuel cracks and in the fuel-to-sheath gap.

Table 10: Coefficients for the hydrogen mole fraction diffusion equation

Parameter or coefficient	Description	Value or expression used in model
δ_{ts}	Time scaling coefficient	cg
D	Diffusion coefficient	cDg/tau^2
R_s	Reaction rate	0

The boundary conditions for Eq. (167) are provided in Eq. (168), which includes the flux, insulation and concentration boundary conditions. Here **n** is the unit normal vector, **N** is the flux vector, N_o is the inward flux, k_c is the mass transfer coefficient, c_b is the bulk concentration, q is the hydrogen mole fraction, and q_c is the hydrogen mole fraction of the coolant.

$$\begin{aligned}&\text{Flux boundary condition: } -\mathbf{n}\cdot\mathbf{N} = N_o + k_c(c_b - q) \quad \text{where } \mathbf{N} = -D\nabla q\\ &\text{Insulation/symmetry boundary condition (Neumann): } \mathbf{n}\cdot\nabla q = 0 \qquad (168)\\ &\text{Concentration boundary condition (Dirichlet): } q_c\end{aligned}$$

In CANDU heavy water coolant q_c (defined as qdef in the COMSOL® model) is equal to 4.1×10^{-6} [29]. It can be added here that the q_c value is a factor of ≈3 less than the solubility of hydrogen gas in regular light water, which is $\approx1.4\times10^{-5}$ molar fraction at room temperature [109]. Thus, the hydrogen mole fraction in the out-reactor coolant should be close to or less than the hydrogen mole fraction in heavy water coolant. Referring again to Figure 38, Figure 39 and Figure 40, Table 11 provides the boundary conditions as entered in the model for the hydrogen mole fraction equation, where Rreact_fuel is the oxidation source term provided by Eq. (21) and Rox_sheath is the hydrogen source term due to a metal-water reaction provided by Eq. (31).

Table 11: Boundary conditions for the hydrogen mole fraction equation

Boundary	**Boundary condition type**	N_o	k_c	c_b	$\mathbf{n} \cdot \nabla q$	$q = q_c$
B2	Flux	Rreact_fuel	0	0	NA	NA
B3	Flux	Rox_sheath	0	0	NA	NA
B4	Neumann	NA	NA	NA	0	NA
B7	Dirichlet	NA	NA	NA	NA	qdef

For numerical stability in the diffusion application mode, the dependent variable q must be constrained between the values of 0 for pure steam and 1 for pure hydrogen. This constraint is provided by introducing the variable q_{fix} as a condition statement outlined in Eq. (169) [24]. q_{fix} is the variable used for the valiable q in Eq. (21) and (23),

$$q_{fix} = \left\{ \begin{array}{lll} q_c & \text{for} & q < q_c \\ q & \text{for} & q > q_c \quad \text{and} \quad q < 0.95 \\ 0.95 & \text{for} & q > 0.95 \end{array} \right\} \tag{169}$$

as written in the COMSOL$^{®}$:

qfix = (q<qdef)*(qdef)+(q>=qdef&&q<=0.95)*q+(q>0.95)*0.95 (170)

For a numerical solution of the fuel oxidation model with electrical heating, the model geometry illustrated in Figure 38 is subdivided into finite elements (see Figure 41). The easiest way to mesh a FEA model geometry is to select 'Free Mesh' parameters in the mesh generator. This approach however would create an excessive number of triangle or quadrilateral mesh elements in slender geometries like in the radial cracks. In other words, this would create models with large degrees of freedom that would typically increase the computation time and can lower the probability for solution convergence, which should therefore be avoided. Instead, in COMSOL$^{®}$ 3.5a, two types of meshing techniques were used: 1) 'Mapped Mesh Parameters' for meshing the slender radial crack and the fuel-to-sheath gap domains. This meshing technique was also used to set a distribution of mesh nodes along boundaries such as the iridium bar heater and UO_2 interface, in the thermocouple boundaries, along the Zircaloy sheath external surfaces, and in the sheath defect. Once this method was completed, the 2) ‘Free Mesh’ technique was used to mesh the remaining domains such as the fuel and iridium bar heater. In this model, there were 10,178 elements and 38,580 degrees of freedom.

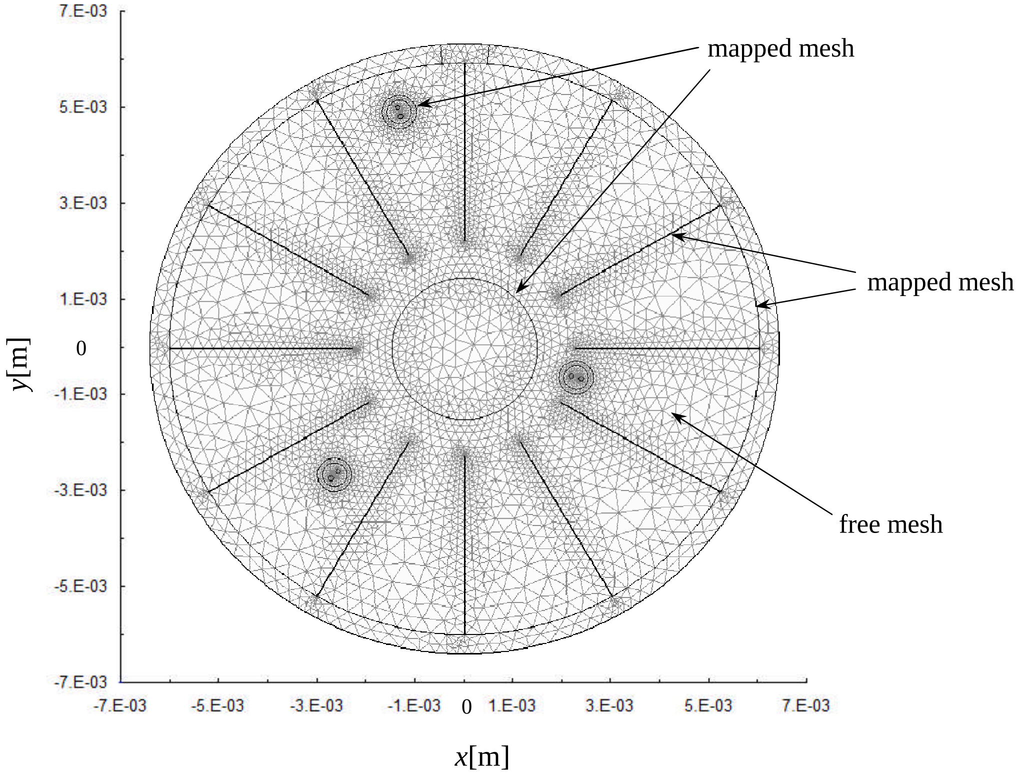

Figure 41: Finite element mesh distribution for the 2D *r*-*θ* model in COMSOL® 3.5a

This numerical model was run on a duo quad core (8 CPUs) 2.66 GHz Intel Xeon® HP work station operating on a Windows XP 64 bit Professional® platform. The solution time was 1-2 hours. The results of the simulation are detailed in Section 4.2. The constant values used for the model parameters are listed in the following table.

Table 12: List of constants used in the 2D *r*-*θ* fuel oxidation model

Symbol	COMSOL® constant name	Description	Value
ρ_{TD}	theoretical_density	the theoretical fuel pellet density	10.96 [g cm^{-3}]
ρ_{s_new}	density_manf	Manufactured fuel density	10.63 [g cm^{-3}]
NA	porosity_manf	Manufactured fuel porosity	$1-\frac{\text{density\_manf}}{\text{theoretical\_density}}$

Table 12: List of constants used in the 2D *r-θ* fuel oxidation model

Symbol	COMSOL® constant name	Description	Value
p_t	PT	Coolant pressure	100 [atm]
R	R	Universal gas constant	8.205×10^{-5} [atm m^3 $gmol^{-1}$ K^{-1}]
σ_{H2}	sigmaH2	H_2 collision diameter	2.827 [Å]
σ_{H2O}	sigmaH2O	H_2O collision diameter	2.641 [Å]
M_{H2}	MH2	H_2 molecular weight	2.0159 [g mol^{-1}]
M_{H2O}	MH2O	H_2O molecular weight	18.0153 [g mol^{-1}]
q_c	qdef	Hydrogen mole fraction in CANDU coolant	4.1×10^{-6}
x_{fs}	Xsurf	Stoichiometry deviation at pellet crack surfaces	1×10^{-4}
$\kappa/\sigma_{\mathrm{AB}}$	koverepsilon	Inverse of Lenard-Jones force constant	0.00454959 K^{-1}
τ	tau	Tortuosity factor	1
$a_\aleph$ $b_\aleph$ $c_\aleph$ $d_\aleph$ $e_\aleph$ $f_\aleph$ $g_\aleph$ $k_\aleph$ $m_\aleph$ $n_\aleph$ $p_\aleph$	a b c d e f g k m n p	Constant in polynomial fit for x_e	0.033107007 0.268984735 0.008679485 -0.000622197 -5.18804E-05 0.020038397 0.000450165 -7.83442E-06 1.84196E-08 -7.45197E-05 1.39057E-07
β	Beta	Burnup in atom %	0.00001
I	I_current	Total electrical current running through the fuel element	1085 [A]
NA	A_Ir	cross sectional area of Iridium wire	pi*0.0015^2 [m^2]
NA	A_Zirc	cross sectional area of Zircaloy sheath	1.5386e-5 [m^2]
A_{UO_2}	A_UO2	cross sectional area of Zircaloy sheath	pi*(0.006075^2-0.0015^2-3*0.000355^2) [m^2]
ℓ	l	Fuel element length	0.482 [m]
T_{s_outer}	T_s_outer	Outer sheath temperature	548 [K]
r_{is}	r_s_inner	Inner sheath radius	0.006076 [m]
NA	r_s_outer	Outer sheath radius	0.006476 [m]
t_s	ts	Sheath thickness	r_s_outer-r_s_inner [m]
R_1	R1	Fuel surface roughness	0.5×10^{-6} [m]

Table 12: List of constants used in the 2D *r*-*θ* fuel oxidation model

Symbol	COMSOL® constant name	Description	Value
R_2	R2	Zircaloy sheath surface roughness	1×10^{-6} [m]
g	g0	Temperature jump distance for steam at STP	3.27×10^{-6} [m]
t_g	g12	fuel-to-sheath gap distance	1×10^{-6} [m]
R_{rms}	Rough	Root-mean-squared roughness	sqrt((R_1^2+R_2^2)/2) [m]
f	f_pickup	hydrogen pickup by the sheath	0.05
F_c	F_crrs	enhancement factor for in-reactor corrosion (of the Zircaloy sheath)	3
N	N	refraction parameter for krad	2.25
N_A	N_Avogadro	Particles/molecules per mol	6.022×10^{23}
N_{UO_2}	N_UO2	number density of UO_2	2.444×10^{28} [particles m^{-3}]
F_{vol}	fuel_vol	Fuel element volume	pi*(0.006075^2-0.0015^2-3*0.000355^2)*ℓ [m^3]
ρ_Ir	rho_Ir	Density of iridium	22.5 [g cm^{-3}]
$\rho_\mathrm{B\_type}$	rho_Btype	Density of Type B thermocouple wire	19.53 [g cm^{-3}]
$\rho_\mathrm{R\_type}$	rho_Rtype	Density of Type R thermocouple wire	20.53 [g cm^{-3}]
ρ_Zirc	rho_Zircaloy	Density of Zircaloy	6.49 [g cm^{-3}]
ρ_Magnesia	rho_Magnesia	Density of magnesia	3.58 [g cm^{-3}]
NA	Cp_Btype	Specific heat capacity of Type B thermocouple wire	0.153 [kJ kg^{-1} K^{-1}]
NA	Cp_Rtype	Specific heat capacity of Type R thermocouple wire	0.140 [kJ kg^{-1} K^{-1}]

For further details on the 2D *r*-*θ* fuel oxidation model see the COMSOL® model report in Appendix A.

(ii) *2D r-θ Fuel Oxidation Model with an Open Fuel-to-Sheath Gap*

The 2D *r-θ* fuel oxidation model with an open fuel-to-sheath gap was very similar to the closed one but with the following differences:

1. Only six radial cracks were modeled (compared to the twelve in the closed fuel-to-sheath gap model); three in the vicinity of the sheath defect and another three in the pellet circumference.

2. A manual heat source in the iridium wire/bar was input (excluding Zircaloy sheath heating) rather than applying a total electrical current input
3. No thermocouples were included
4. A general extrusion coupling variable is used to define thermal continuity between the fuel pellet, fuel-to-sheath gap domains, and the Zircaloy sheath.

The objective of this model was to investigate the effect of the size of the fuel-to-sheath gap dimension and the size of the fuel crack width dimension on fuel oxidation. Both types of dimension changes can affect the hydrogen mole fraction diffusion rate, which in turn can affect fuel oxidation. The former case is pertinent to the scenario when the sheath has not completely crept down onto the fuel.

The reason only six radial cracks were included in the following 2D *r-θ* fuel oxidation model (rather than twelve cracks in the *Closed Fuel-to-Sheath Gap* case) was for the following reason. The preferred electrical current set to flow through the fuel element (≈1085 A in Table 12), producing a linear power in the iridium bar heater of about 24 kW m^{-1}, may have been hard to achieve in reality. This is partly due to the iridium and zirconium eutectic point, which pose temperature operation limits (refer again to Section 3.1). Hence, it was predicted that lower heating powers (<24 kW m^{-1}) may need to be used. Since the approximate number of radial cracks in the fuel pellets is equal to $P_{\text{linear}}[\text{kW m}^{-1}]/2$ [29][73] (see again Section 1.6), it was expected that less than 12 radial cracks would develop in the experiment. From a fuel oxidation point of view this does not change the modeled oxidation result substantially, since, as will become apparent in the result section, the radial cracks closest to the sheath defect contribute the most to fuel oxidation.

Figure 42 shows the basic geometry of the open fuel-to-sheath gap fuel oxidation model. This geometry is also used in the solid mechanical model discussed in Section 3.5.3 to investigate the conditions for crack propagation. The internal boundaries seen in the UO_2 domain, (as shown in Figure 42) are present for meshing purposes.

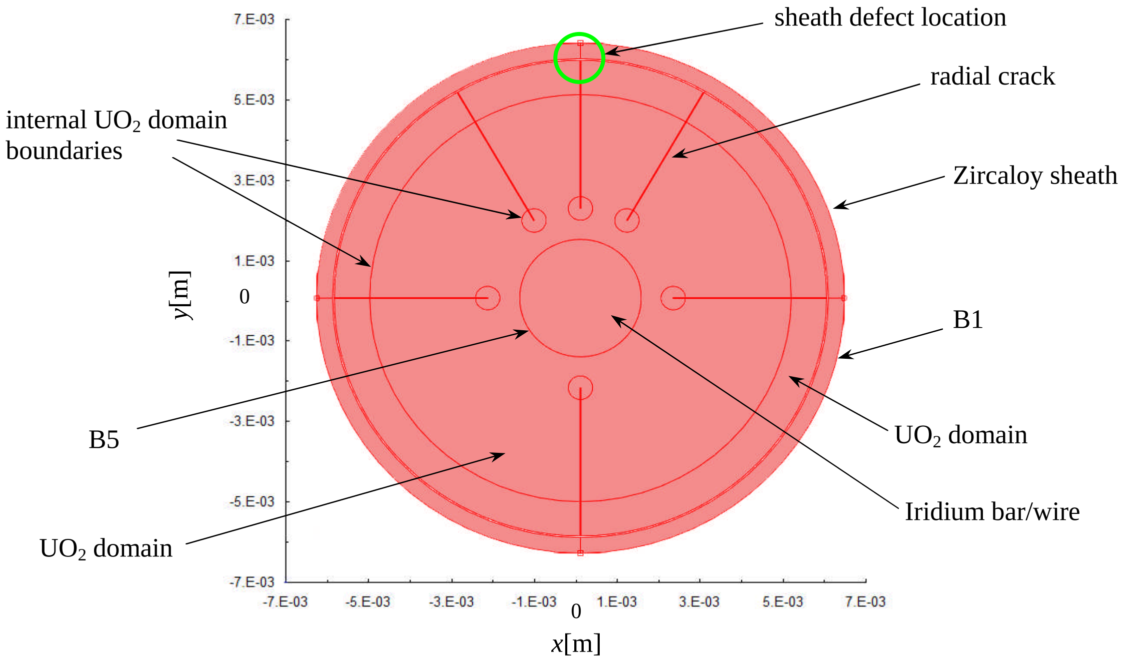

Figure 42: Geometry of the 2D *r-θ* fuel oxidation model showing the different materials of the out-reactor fuel element with six pre-defined radial fuel cracks

The green circle in Figure 42 gives a close-up view of the sheath defect location in Figure 43. The two domains (the Zircaloy sheath and the fuel pellet with the fuel-to-sheath gap) are separated by a 'geometry assembly' gap. These two geometries are linked together using an extrusion coupling variable that provides continuity for heat conduction between the two domains in the 'geometry assembly'. The use of a geometry assembly vs. a typical 'geometry union' in COMSOL® was performed to investigate sheath and fuel contact, which is discussed later in Sections 3.5.3 and 4.3. Hence for practical purposes, an almost identical geometry assembly is used here to study fuel oxidation. Inspection of Figure 43 shows that the sheath defect is not defined as an axial slit in the Zircaloy sheathing (as shown in Figure 38), since this extra detail was unnecessary. Instead, an appropriate Dirichlet boundary condition q_c is defined on the fuel-to-sheath gap boundary above the vertical radial crack indicated by a purple line B7, since the modeled hydrogen mole fraction gradient in the sheath slot in the previous model was very small and contributed little to the fuel oxidation.

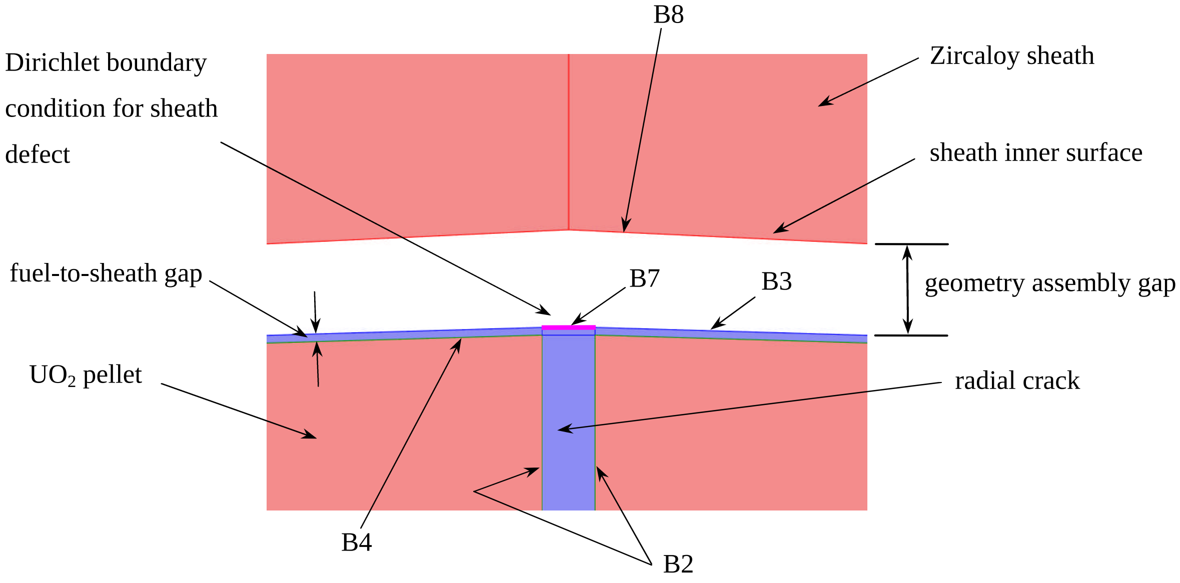

Figure 43: Close up view of the location of the sheath defect showing the various domains and boundaries as well as the fuel-to-sheath gap and the geometry assembly gap

The heat conduction equation is very similar to the general form time dependent equation, Eq. (159), used in the closed fuel-to-sheath gap fuel oxidation model and is specifically expressed as Eq. (171). Here $\mathbf{U}_{trans}$ is the velocity field for convection and it is set to zero. Q_v is the volumetric heat source term in kW m^{-3}.

$$\rho C_p \frac{\partial T}{\partial t} + \rho C_p \mathbf{U}_{trans} \bullet \nabla T = \nabla \bullet \left(k \nabla T\right) + Q_v \tag{171}$$

In this study, two simulations were computed: (i) where the radial cracks are varied in thickness and the fuel-to-sheath gap is held constant and (ii) where the fuel-to-sheath gap is varied while the radial crack widths are held constant. For case study (i) a constant Q_v power density term is used for the iridium bar heater defined in the COMSOL$^{®}$ model as Q_vol_Ir equal to 3.2×10^6 kW m^{-3}, as derived from the closed fuel-to-sheath gap 2D r-θ fuel oxidation model. This model achieves a fuel temperature at the radial crack tips of ≈1250°C during the first simulated day. For case study (ii) varying values of Q_v were used to achieve a fuel temperature at the radial crack tips of ≈1250°C during the first simulated day. In both cases the crack depth was the same, equal to 0.00229 m (2.29 mm) from the fuel element centre.

The boundary conditions for the heat conduction equation, Eq. (171), in the open gap model are similar to those stated in Table 7 except that here an integration coupling variable (i.e., a general extrusion in COMSOL®) is used to define thermal continuity between the outer surface of the fuel-to-sheath gap (gas domain) and the Zircaloy sheath inner surface. These boundary conditions are given in Table 13. Specifically, the temperature at boundary B3 is equal to the temperature at boundary B8 (Figure 43). Implementation of the general extrusion variable is discussed in Section 3.5.3.

Table 13: Boundary conditions for the heat transfer equation used in the open gap

Boundary	**Parameter**	**Value or expression used in model**
B1	Temperature	*T*=T_s_outer
B3 to B8	Continuity	*T*(B3) =*T*(B5)

The boundary conditions for the oxygen interstitial diffusion equation, Eq. (160), in the open fuel-to-sheath gap model are identical to boundary conditions stated in Table 9 for the closed fuel-to-sheath gap model except that here boundary B6 is not applicable.

The equation used for the hydrogen model fraction in the fuel cracks and fuel-to-sheath gap in COMSOL® 4.2a format has the form of the following equation:

$$\frac{\partial q}{\partial t} + \nabla \bullet \left(- D\nabla q\right) + \mathbf{u}_t \bullet \nabla q = R_s \qquad (172)$$

where q is the hydrogen mole fraction, D is the diffusion coefficient (in this case it is the diffusivity quantity $c_g D_g$ provided by Eq. (29)), $\mathbf{u}_t$ is the velocity field applicable to convection (which is set to zero), and R_s is the source term. To ensure that Eq. (172) has the same form as the general hydrogen mole fraction equation, Eq. (27) (and Eq. (167) used for the closed fuel-to-sheath gap model), i.e., so that the time scaling parameter δ_{ts} (equal to c_g) is in front of the time derivative, the source term R_s is substituted by Eq. (173). This also sets R_s to be zero in the gas domain.

$$R_s = \left(1 - c_g\right)\frac{\partial q}{\partial t} \tag{173}$$

The boundary conditions for the hydrogen mole fraction equation, Eq. (172), are provided by Table 14. The boundary conditions for the open fuel-to-sheath gap model are similar to those of the closed gap model stated in Table 11, but no hydrogen flux term from sheath oxidation is considered. At boundary B2 (the crack surfaces) the flux term is the reaction rate R_f^{react} as provided by Eq. (25) (and defined as Rreact_fuel in the COMSOL® model format) and at boundary B7 (the sheath defect) the Dirichlet boundary condition is defined as q_c (where q_c is defined as qdef in the COMSOL® model format).

Table 14: Boundary conditions for the hydrogen mole fraction diffusion equation for the open fuel-to-sheath gap fuel oxidation model

Boundary	**Boundary condition type**	N_o	$\mathbf{n} \cdot \nabla q$	$q = q_c$
B2	Flux	Rreact_fuel	NA	NA
B3	Flux	0	NA	NA
B4	Neumann	NA	0	NA
B7	Dirichlet	NA	NA	qdef

The mesh used in the open fuel-to-sheath gap fuel oxidation model, Figure 44, is very similar to that used in the 2D model described later in Section 3.5.3. In this model there is use of both a mapped mesh (quadrilateral mesh) and a free triangular mesh, similar to the mesh used in the closed fuel-to-sheath gap model. In this model's mesh though, the sheath and the outer fuel domain use quadrilateral mesh. The mesh is also made more dense near the crack tips where there is increased oxidation. This was made possible by including 0.6 mm diameter domains around each crack tip.

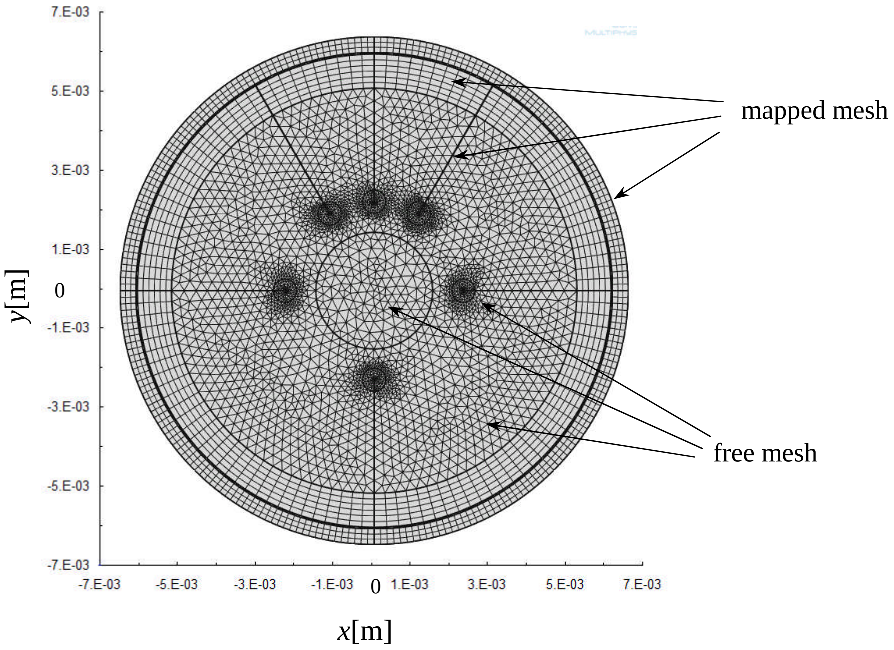

Figure 44: Finite element mesh distribution of the open fuel-to-sheath gap 2D r-θ fuel oxidation model generated on COMSOL® 4.2a

Note that for this open fuel-to-sheath gap fuel oxidation model an all-triangular mesh was used as well, which yielded the same result.

In this model, there were 7,430 mesh elements and 33,705 degrees of freedom. This numerical model was run on a 4 core, 2.80 GHz Intel i7 VAIO laptop with Turbo Boost Technology to 3.1 GHz operating with a Windows 7, 64 bit Professional® operating platform. The solution time was <1 hours. The results of the simulation are detailed in Section 4.2.2.

The mapped mesh prepared for the fuel-to-sheath gap and the radial cracks can be considered a 'high aspect ratio' mesh, where one edge is longer than the normal edge. Actually, one of the reasons for using mapped or swept mesh is to create mesh elements that are elongated in slender geometry domains in order to save computer resources but at the same time to adequately capture the applied physics. In COMSOL®, the 'mesh quality' ranges in values between 0 to 1. Generally a high mesh quality is closer 1. If the gradient is gradual enough, such as for that case of the hydrogen mole fraction concentration q, the aspect ratio of the mesh can be increased in the direction of the concentration gradient to reduce the degrees of freedom of the model. COMSOL® may identify such mesh as a low quality mesh even though it is quite adequate to use in the model.

In order to be sure the 2D models were meshed properly, a model with a higher mesh density and a higher mesh quality was prepared, as shown in Figure 45. This mesh is especially dense along the radial fuel cracks and along the fuel-to-sheath gap when compared to the low density mesh in Figure 44. Also, the mesh of the fuel domain in Figure 45 was changed to an all triangular mesh rather than partly quadrilateral, to ensure the model result was independent of mesh type.

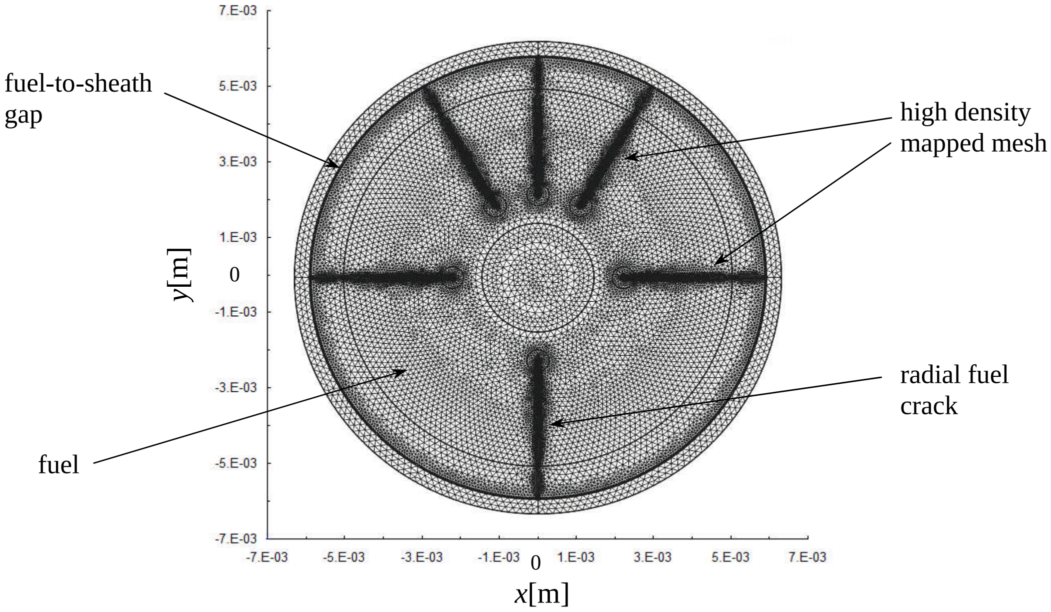

Figure 45: Higher density finite element mesh distribution used in the open fuel-to-sheath gap 2D *r-θ* fuel oxidation model to demonstrate mesh independence

Thus, in this higher mesh-density model the number of mesh elements was increased to 31,736, which in turn increased the number of degrees of freedom to 142,797. The results of this model simulation are detailed in Section 4.2.2.

3.5.3 The Fuel Solid Mechanics and Crack Propagation Model Numerical Implementation

To study the shape of the radial fuel cracks, considering only thermal expansion with linear elastic material properties, and to study the conditions for crack propagation also due to thermal expansion, a plane strain solid mechanics model was developed for two cases: (i) a model with five pre-set initially 3 μm wide radial fuel cracks and one ‘quasi-dynamic’ radial crack that starts as a surface flaw, and (ii) a model with one pre-set initially 3 μm wide radial fuel crack and one surface flaw. The quasi-dynamic model employed a steady state solver with a geometric parametric sweep (i.e., a parametric stationary analysis) where after each solution the geometry (i.e., the surface flaw crack length) was modified followed by a generation of a new mesh. This was done, since implementing a time-dependent moving mesh was not feasible with the applied version of software. The static radial fuel crack tips were located at the position of 1250°C, which is within the transition domain for plastic and elastic fuel behavior as shown in Figure 14.

As suggested earlier, the clad (or sheath) may contain to some degree the thermally expanded fuel pellet together (see again Figure 16), which may affect the crack widths and crack growth. Hence, in addition to the two modeling objectives stated above, the 2D model consisted of two independent geometries in a COMSOL® ‘assembly’: The first geometry consisted of the expanding fuel pellet and iridium bar heater, and the second geometry was for the Zircaloy sheath under coolant pressure. This representation allowed modeling the physical contact between the fuel pellet and Zircaloy sheath.

For this model, the ‘Thermal Stress’ interface (or module) was used in COMSOL® version 4.3a (the term ‘interface’ or ‘module’ is equivalent to the term ‘application mode’ as used in the earlier COMSOL® 3.5a version). The thermal stress interface combines a solid mechanics interface (or module) with the heat transfer interface. This application mode or interface has the equations for stress analysis for a solution displacement and equations for heat transfer. The coupling between these two physics takes place on the domain level where the temperature from the heat transfer interface acts as a thermal load for the solid mechanics interface causing thermal expansion.

Finally, as mentioned at the end of Section 3.4.2 the displacement of the UO_2 pellets due to thermal expansion at the inner pellet annulus (where the Ir bar heater is located), at the expected heating temperature, may or may not cause the gap between UO_2 and the Ir to close. Contact between the two (or a reduced gap) would reduce the operating temperature of the Ir bar, which would extend its life during the experiment. On the other hand, physical contact may affect the fuel cracking behavior (crack number and geometry). Since modeling contact (or a changing gap) between the Ir bar and the UO_2 pellet (as was done between the UO_2 and the sheath) was not attempted in the model due to the need for added model complexity. Instead, two model configurations were considered: (i) where the Ir bar and UO_2 pellets were modeled as a solid continuity (no Ir-UO_2 gap), and (ii) where the iridium bar was removed from solid mechanics modeling (no mechanical contact exists between the Ir and UO_2). It is mentioned that the second case neglects modeling the temperature jump across the Ir-UO_2 gap.

The geometry of the 2D *r-θ* plane strain solid mechanics model, depicted in Figure 46, is very similar to that shown in Figure 42 that was used for the 2D *r-θ* fuel oxidation model.

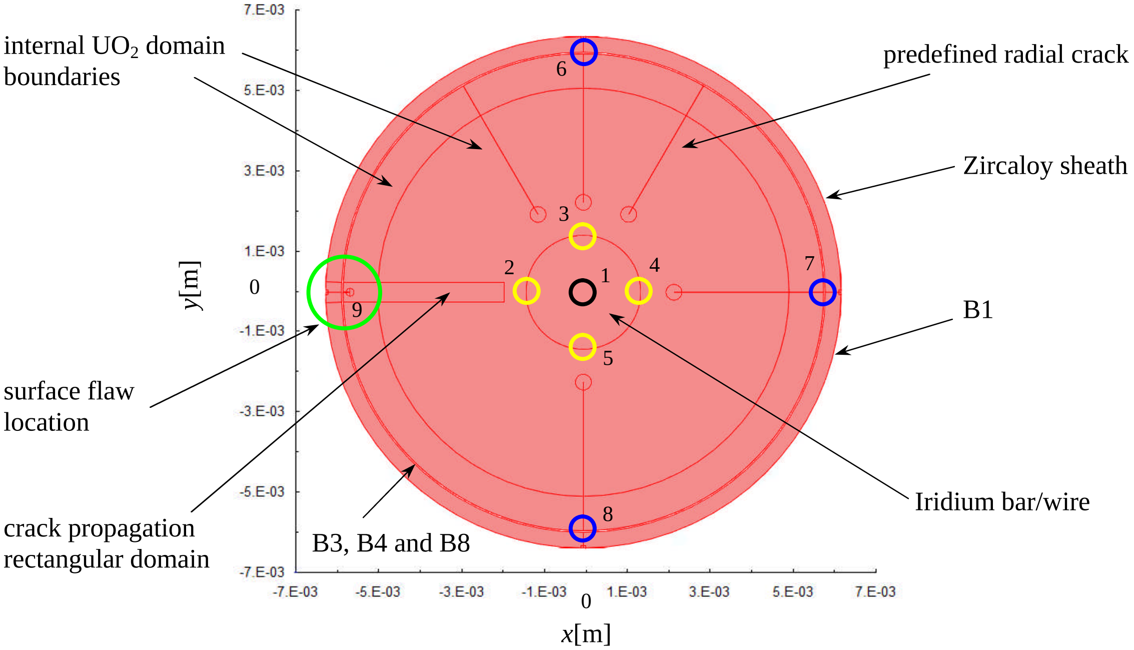

Figure 46: Geometry of the 2D *r-θ* solid mechanics model showing the different materials of the out-reactor fuel element and the five pre-set radial fuel cracks and one surface flaw

Included in this model is a separate rectangular domain for investigating conditions for pellet cracking, where the green circle indicates the location of a fuel pellet surface flaw.

The small blue, yellow, and black circles indicate locations where the model was constrained (discussed later in the section). Lastly, five pre-set radial cracks were included.

The steady state heat conduction equation in the COMSOL® 4.2a Thermal Stress interface has the general form given by:

$$\rho C_p \mathbf{U}_{trans} \bullet \nabla T = \nabla \bullet \left(k \nabla T\right) + Q_v \tag{174}$$

where ρ is the density, C_p is the specific heat capacity, $\mathbf{U}_{trans}$ is the velocity field for convection, k is the thermal conductivity, and Q_v is the heat source. Since heat transfer via convection is not relevant in this model the left hand side of Eq. (174) was set to zero. The temperature boundary conditions for the heat conduction equation are the same as indicated in Table 13. Heat generated in the iridium bar heater was provided by a constant Q_{Ir} power term (called Q_vol_Ir in the model) equal to 3.5×10^6 kW m^{-3}. This power value was provided by the fuel oxidation model discussed in Section 3.5.1.

For the gas domains where no solid mechanics physics was solved, specifically in the steam filled fuel cracks and in the fuel-to-sheath gap, only a heat conduction equation was applied. For this special case, a heat transfer sub-node (that is solid mechanics physics free, called ‘Heat Transfer in Solids 1’) was defined in the Thermal Stress interface node as shown in the following figure.

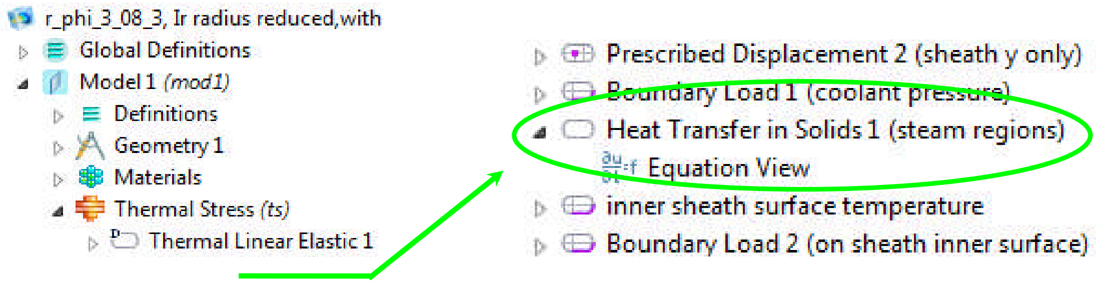

Figure 47: In the COMSOL® model builder, under the Thermal Stress node, the ‘Heat Transfer in Solids 1’ is defined

A ‘Heat Transfer in Fluids’ sub node could have also been selected (not shown here) if the accompanying velocity field terms were set to zero. Lastly, in order for these gas domain boundaries to be geometrically coupled with the changing thermally expanding solid pellet boundaries, an Arbitrary Lagrangian Eulerian (ALE) moving mesh was used. ALE is explained in more detail in Section 3.5.4.

In order to solve a solid mechanics model, it is necessary to provide boundary load conditions as well as kinematic constraints and symmetry constraints (if any). Applied loads can be point loads, moments, distributed loads or pressures. The applied boundary loads are provided by Table 15, with parameters or variables as used in the model. The contact_pressure value is computed in COMSOL® with a custom penalty method, which is explained later.

Table 15: Boundary loads applied to solid mechanics 2D *r-θ* plane strain model

Boundary	Surface name	Parameter/variable	Value
B1	Sheath outside surface	coolant_p	1×10^7 Pa
B4	Pellet surface	contact_pressure	Varies with azimuthal position
B8	Sheath inside surface	contact_pressure	Varies with azimuthal position

Kinematic constraints are equations that control the motion of solids, faces, edges, or points. A special constraint to keep an edge of a body straight or to make a boundary rotate, requires constraint equations. In COMSOL® 4.2a, a ‘prescribed displacement’ is used to define a constraint by entering a constraint expression. A ‘fixed’ constraint is used when translational motion in all three x, y and z directions is prevented.

The locations of ‘fixed’ and ‘prescribed displacement’ constraints are shown in Figure 46, indicated by the small circles at numbered locations. The black central circle indicates the location of a fixed constraint and the other small circles (yellow and blue) indicate the locations of prescribed displacement constraints. Table 16 defines the applied constraints and their locations. The vector displacement field is given by $\mathbf{u} = (u, v)$ where u is the displacement in the x direction and v is the displacement in the y direction.

Table 16: Fixed and prescribed displacement constraints used in the 2D r-θ plane strain model

Constraint type	Part of model	Location in model (Figure 46)	Expression
Fixed constraint	Iridium bar and pellet	1	$\mathbf{u} = 0$
Prescribed displacement	Iridium bar and pellet	2, 4	$v = v_o = 0$
Prescribed displacement	Iridium bar and pellet	3, 5	$u = u_o = 0$
Prescribed displacement	Sheath	7, 9	$v = v_o = 0$
Prescribed displacement	Sheath	6, 8	$u = u_o = 0$

For example, for the ‘iridium bar and pellet’, of locations 3 and 5 in Figure 46, the prescribed displacement constraint is set to zero in the x direction but movement is allowed in the y direction.

Included in this model is contact modeling between the expanding fuel pellet and the contracting Zircaloy sheath. A customized penalty method was prepared and used in the model to simulate solid contact rather than using COMSOL®’s built-in solid contact algorithms. The premises of the penalty method is that when two or more rigid bodies overlap and penetrate each other due to movement caused by external forces or thermal expansion, a force proportional to the penetration depth is applied to resist, and ultimately eliminate, the penetration. On the one hand, very low penalty values can improve convergence but can allow the boundaries to penetrate each other to some degree. Very large penalty values on the other hand allows for very little boundary penetration, which increases the displacement field accuracy. The disadvantage of a large penalty value is that convergence difficulties may arise.

The penalty method equations that are used in the COMSOL® 2D r-θ plane strain model are detailed in Table 17 and the method is explained with the aid of Figure 48. A ‘geometry assembly’ gap initially exists between the sheath inner surface (B8) and the fuel-to-sheath gap domain (blue area) outer surface (B3). When the model simulation is initiated, heat is generated in the iridium bar domain causing the fuel pellet to thermally expand as explained in Section 3.4.1. With an applied coolant force on the external sheath surface and the thermal expansion on the pellet, contact between the sheath and pellet is achieved within only a few minutes of heating. Hence, the initial geometry assembly gap is closed leaving only the fuel-to-sheath gap (slender blue domain) between the fuel and the sheath.

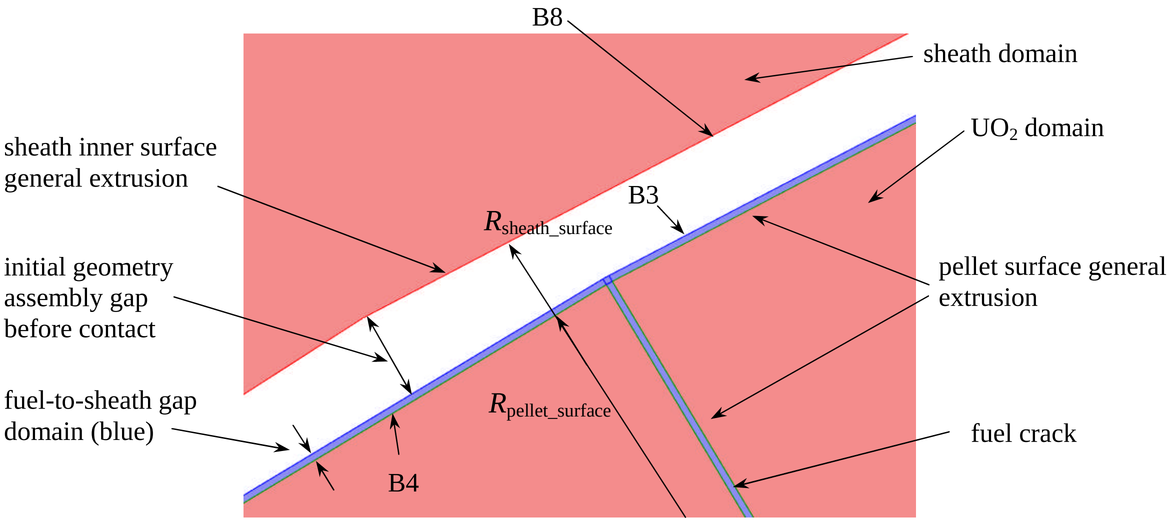

Figure 48: Close-up view of the fuel and sheath region before simulation initiation to explain contact modeling using the penalty method

At every time step the ‘relative_distance’ variable in Table 17, which is the distance between the sheath and the pellet surface, is computed over 2π radians of the sheath and pellet. This is achieved by using two ‘extrusion coupling variables’ in COMSOL® called the ‘sheath_inner_surface()’ and ‘pellet_surface()’, which are geometrically defined as the sheath inner surface and pellet surface, respectively. The difference between these two variables is the ‘relative_distance’.

Table 17: Variables used for general extrusion model coupling to apply the penalty method

Variable name	Expression used in COMSOL® model	Purpose
calangle	atan2(y,x)	Provides the angle at every specified coordinate.
sectorangle	((sin(calangle)>=0)*calangle + (sin(calangle)<0)*(2*pi+calangle))	Provides positive angles from 0 to 2π for coordinates *x* and *y*.
R1	sqrt(x^2+y^2)	Conversion from Cartesian *x* and *y* coordinate to radial coordinate
relative_distance	sheath_inner_surface(R1)-pellet_surface(R1)-ftsg_thickness	Calculates the relative distance between the sheath inner surface and the pellet surface over 2π.
contact_pressure	-(relative_distance<0)*relative_distance*2e14	If the pellet surface overlaps the sheath inner surface a proportional contact pressure is applied.

The ‘ftsg_thickness’ is the fuel-to-sheath gap thickness, which is set in this case to 3 μm. The ‘sectorangle’ equation ensures the angle is always positive on the sheath x and y coordinates and runs from 0 to 2π. When the pellet outer boundary with the fuel-to-sheath gap thickness (B3) passes the Zircaloy sheath inner boundary (B8), the relative_distance variable becomes negative. At this point, the ‘contact_pressure’ variable takes on a positive value in Pa, which is applied to the sheath inner surface (B8) and the fuel pellet outer surface. In this manner every azimuthal point on the sheath internal surface receives a specific value of pressure, which in this case, is linearly proportional to the penalty distance, i.e., the relative_distance.

To numerically assess whether conditions for linear elastic fracture occur as expressed in Eq. (119) in the out-reactor fuel pellet due to thermal expansion, the stress intensity factor K_I was computed. Figure 49 illustrates the circular J integral contour located around a pellet surface flaw tip. Also in the figure is a blue line that separates the 3 μm thick fuel-to-sheath gap domain (which is hard to discern in this figure) and the surface pellet flaw domain that is initially 0.175 mm deep into the pellet. It can be noted that the J integral contour could also have been rectangular or diamond shaped. The wedge shape of the surface flaw was selected for its simplicity.

The stress intensity factor equations used in the model in COMSOL® format are presented in Table 18. The numerical formulation for the J integral was taken from an example of an edge crack in a body under tensile stress [71], as illustrated in Figure 31 (b).The first term in Eq. (125) is the integrated value of $w_s n_x$ over ds, called W_1 in the model. It is calculated by taking the strain energy density w_s, defined by Eq. (126), called ts.Ws in the model, and multiplying it by the unit normal vector n_x, called Nx1 in the model, and integrating this variable over the circular contour Γ_c by applying the intop1 integration operator.

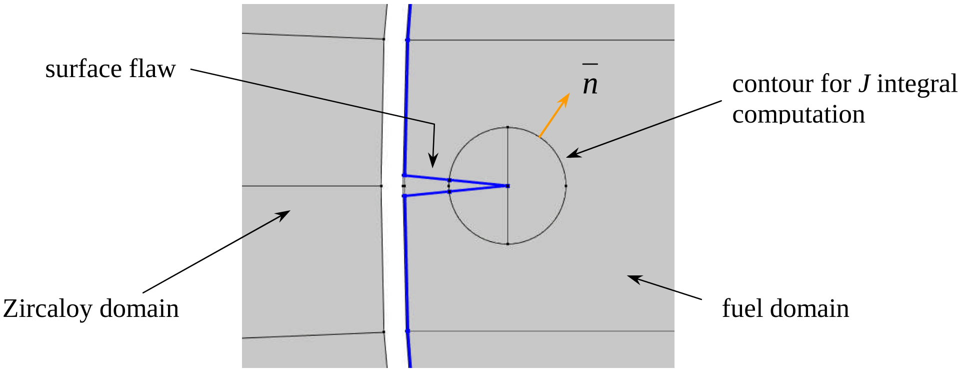

Figure 49: The pellet surface flaw and the *J* integral boundary used in the plane strain model

In a similar manner, the second term in Eq. (125) is the integrated value of $T_i(\partial u_i/\partial x)$ over *ds*, called Tdudx_1 in the model, where T_i is the traction vector and u_i is the displacement vector. The first component of the traction vector is $\sigma_x \cdot n_x$, called ts.sx*Nx1 in the model, where again n_x (or Nx1) is the unit normal vector of the circular contour around the crack tip. The derivatives of the displacement vector in the *x* direction, $\partial u_i/\partial x$, are called uX and vX in the model.

With the two terms of Eq. (125) computed their sum is equal to the *J* integral quantity, called J_1 in the model. The UO_2 modulus of elasticity at the crack tip, called ES_UO2_crack in the model, is estimated by calculating E_{UO2} given by Eq. (139) and the UO_2 Poisson's ratio ν_{UO2} given by Eq. (109). The division by $\left(1-\nu_{UO2}^2\right)$ is due to the plane strain condition, Eq. (123).

Table 18: *J* integral numerical equations in COMSOL® format

Symbolic name	Variable name used in model	Expression in COMSOL® format	Description/purpose
$\int_{\Gamma_c} (w_s n_x) ds$	W_1	intop1(ts.Ws*Nx1)	The integral of ts.Ws, the first term in Eq. (125)
w_s	ts.Ws	0.5*(ts.Sl11*ts.eel11+2*ts.Sl12*ts.eel12+ 2*ts.Sl13*ts.eel13+ts.Sl22*ts.eel22+ 2*ts.Sl23*ts.eel23+ts.Sl33*ts.eel33)	The elastic strain energy density (without initial strain terms) as defined in COMSOL® 4.3b. Similar to Eq. (126).

Table 18: *J* integral numerical equations in COMSOL® format

Symbolic name	Variable name used in model	Expression in COMSOL® format	Description/purpose
$\int_{\Gamma_c}\left(T_i \frac{\partial u_i}{\partial x}\right)ds$	Tdudx_1	intop1(-((ts.sx*Nx1+ts.sxy*Ny1)*uX + (ts.sxy*Nx1+ts.sy*Ny1)*vX))	The second term in Eq. (125). The quantity in the inner parenthesis is the traction vector and ts.sx is the stress in the *x* direction.
J	J_1	W_1+Tdudx_1	The *J* integral quantity
E_{UO2}	ES_UO2_crack	aveop2(ES_UO2/(1-nu_UO2^2))	Young's modulus at the crack tip, [N/m^2]. Eq. (123) and Eq. (139)
K_I	KI_1	sqrt(ES_UO2_crack*abs(J_1))	Stress intensity factor [Pa*m^0.5], Eq. (124)

The stress intensity factor K_I, given by Eq. (124), can then be calculated around the crack tip.

The absolute crack length, *a*, called crack_length_a in the model (Table 19), is calculated at each parametric crack length value increase, using two integration operators in COMSOL® called intop2() and intop3(); one at the pellet surface next to the crack opening and one at the crack tip, respectively.

Table 19: Absolute crack length

Symbolic name	Variable name	Expression	Description/purpose
a	crack_length_a	abs(intop3(x)-intop2(x))	length of crack

Using the parametric range defined in COMSOL® as range (0,8.75e-8,1.4e-6), where 8.75e-8 s in the time increment. The time values are converted to distance using the Raleigh wave speed in UO_2 equal to a velocity of 2580 m s^{-1} for a propagating crack [79][157]. It is noted here that including the velocity of a propagating crack was not necessary in this case, since the model is solved as a steady-state problem. Nevertheless, it is added for reference purposes only. If a time dependent solution were required in a different model then terms such as the dynamic stress intensity factor, the Raleigh surface wave speed, and the Freund crack speed could be considered [79].

As previously mentioned in Section 3.4.2, Kutty [135] used the Vickers indentation technique, commonly used for determination of fracture parameters of brittle and ceramic materials, to determine the fracture toughness and fracture surface energy of sintered UO_2 at room temperature. Extrapolating from experimental values [135] a fracture toughness applicable to CANDU fuel is provided in the following table:

Table 20: Experimental UO_2 fracture toughness K_{Ic} [135]

Volume fraction porosity P_{or}	**crack length a [μm]**	**Fracture toughness K_{Ic} [MPa $m^{0.5}$]**
0.03	879	0.822

For the specific case of the UO_2 pellet, the fracture stress σ_f provided by Eq. (110) and the correction factor Y provided by Eq. (121), can be used to calculate the fracture toughness near the pellet surface. The fracture stress at this location, which is temperature dependent, is about 120 MPa. The correction factor Y at the pellets surface is estimated to be 1.119. If a pore size in a fuel pellet is selected to be as high as $2a$ =40 μm [15] then the plane strain fracture toughness calculated using Eq. (118) is presented in Table 21.

Table 21: Calculated UO_2 fuel fracture toughness K_{Ic}

crack length a [μm]	**Fracture toughness K_{Ic} [MPa $m^{0.5}$]**
20	1.064

One reason that the measured fracture toughness of UO_2 [135][137] mentioned earlier is lower than the calculated value could be because the fracture stress of UO_2 (Eq. (110)) decreases with temperature and the measured results were taken at room temperature. Another reason could be due to the selected pore size (crack length a) given by Olander [15], which may be excessive in length. Song *et al.* [158] reports an upper pore size of only 10 μm in sintered and reduced UO_2 fuel, which may be more appropriate. Lastly, only a single calculated K_{Ic} point is presented, since only the fracture stress σ_f (Eq. (110)) for typical crack lengths in UO_2 (fuel pore sizes) is known (i.e., there is little information σ_f of UO_2 with varying crack lengths).

The fracture toughness values reported in Table 20 and Table 21 are the values that are compared in this work to the stress intensity factor (Eq. (124)) computed around the crack tip to determine if crack propagation is favored.

For computing the J^* integral (Eq. (134) and Eq. (135)), which ensures integration path independence in a material that is in the presence of thermal gradients, the implementation of the applicable equations in COMSOL® format is provided in Table 22.

Table 22: J^* integral numerical equation formulation

Symbolic name	Variable name in model	Expression in COMSOL® format	Description/purpose
$\alpha_e \iint_A \sigma_{kk} \frac{\partial T}{\partial x} dA$	area_integral	intop4(alpha_exp_UO2*(ts.Sl11+ts.Sl22+ts.Sl33)*ts.gradTX)	Third term in Eq. (134) used in homogeneous materials
J^*	J_star	J_1+area_integral	The J^* integral, Eq. (134)
$\iint_A \sigma_{ij} \frac{\partial \varepsilon_{ij}}{\partial x} dA$	area_integral_2	intop4((ts.Sl11+2*ts.Sl12+2*ts.Sl13+ts.Sl22+2*ts.Sl23+ts.Sl33)*d((ts.eel11+2*ts.eel12+2*ts.eel13+ts.eel22+2*ts.eel23+ts.eel33),X))	Second term in Eq. (135) used in non homogeneous materials
J^*	J_star_2	Tdudx_1+area_integral+area_integral_2	The J^* integral, Eq. (135)
K_I	KI_1_star	sqrt(ES_UO2_crack*abs(J_star))	Stress intensity factor, Eq. (124)
	KI_1_star_2	sqrt(ES_UO2_crack*abs(J_star_2))	Stress intensity factor, Eq. (124)

Note: The 'ts.Slij' in 'area_integral' and 'area_integral_2' integrals is the Second Piola-Kirchhoff stress tensor in the local coordinate system. 'ts.slij' stress tensor could have been used instead of 'ts.Slij' with only minor differences in results. The latter was used, since it is also used by COMSOL® ts.Ws in Table 18.

J^* is computed for an isotropic material with temperature gradients (or J_star) and computed for a non homogeneous material (J_star_2), as discussed in Section 3.4.2. In the current work both values of J^* are computed to see if they are both path independent.

The constants used in the 2D r-θ plane strain solid mechanics model are summarized in the following table:

Table 23: List of constants used in the 2D plane strain model

Symbol	COMSOL® constant name	Description	Value
ρ_{TD}	theoretical_density	the theoretical fuel pellet density	10.96 [g cm^{-3}]
$\rho_{\text{s\_new}}$	density_manf	Manufactured fuel density	10.63 [g cm^{-3}]
NA	UO2_frac_theo_dens	UO_2 fractional theoretical density	$\frac{\text{density\_manf}}{\text{theoretical\_density}}$
NA	porosity_manf	Manufactured fuel porosity	$1-\frac{\text{density\_manf}}{\text{theoretical\_density}}$

Table 23: List of constants used in the 2D plane strain model

Symbol	COMSOL® constant name	Description	Value
Δ_{Zirc}	delta_zirc	average oxygen concentration	1e-4
C	cold_work_zirc	unitless ratio of areas	0.001
ϕ	phi_fluence	fast neutron fluence	0 [n m^{-2}]
x	Xdev	Stoichiometric deviation value	0.000001
T_{ref}	T_ref	Strain reference temperature	300 [K]
NA	T_surf	Outside sheath surface temperature	573 [K]
β	Beta	Burnup in atom %	0.00001
R	R_gas	Gas constant	8.3144 [J mole^{-1} K^{-1}]
Q_f	Q_frack	Effective heat of cracking	1590 [J mole^{-1}]
NA	sheath_wall	Sheath wall thickness	0.0004 [m]
NA	sheath_R_inner	Sheath inside radius	0.006116 [m]
NA	sheath_R_outer	Sheath inside radius	sheath_R_inner + sheath_wall
R_o	pellet_radius	Pellet radius	0.006075 [m]
NA	ftsg_thickness	Fuel-to-sheath gap	3e-6 [m]
NA	Ir_radius	Iridium bar radius	0.00145[m]
ρ_{Zirc}	rho_zircaloy	Density of Zircaloy	6.44 [g cm^{-3}]
ρ_{Ir}	rho_Ir	Density of iridium	22.5 [g cm^{-3}]
ν_{UO2}	nu_UO2	UO_2 Poisson's ratio	1.32*(1-0.26*porosity_manf)-1
$\nu_{\_\mathrm{Ir}}$	nu_Ir	Iridium Poisson's radio	0.27
$\nu_{\_\mathrm{Zirc}}$	nu_zirc	Zircaloy Poisson's radio	0.37
$\alpha_{\_\mathrm{Ir}}$	alpha_Ir	Iridium coefficient of linear expansion	6.4e-6
σ_{ys0}	s_yield_zirc_initial	Initial yield stress of Zircaloy at 573 K	150e6 [Pa]
E_{Ir}	E_Ir	Young's modulus of Ir	528e9 [Pa]
Q_{Ir}	Q_vol_Ir	Volumetric electric heat source in iridium bar	3.5e6 [kW m^{-3}]
NA	coolant_p	Coolant pressure	10e6 [Pa]
NA	crack_depth	Crack tip radial position	0.00229 [m]

For further details on the 2D r-θ solid mechanics and crack propagation model see COMSOL® model report in Appendix B.

Mesh elements and contour shapes for regular J integral computation

Two types of mesh schemes were used to compute the solid mechanics crack investigation model: (i) A mesh consisting of a combination of quadrilateral and triangular mesh elements and (ii) a mesh consisting of mostly quadrilateral elements. For both cases the regular J integral Eq. (125) was computed (i.e., no thermal gradient consideration). In Figure 50, the first mesh scheme (generated on COMSOL® 4.2a) is used where the rectangular mesh is applied to the model peripheral regions, which is ideally suited for the solid-solid contact modeling between the sheath and fuel pellet where increased stability and accuracy is required. The Zircaloy lower stiffness (due to its Young's modulus and shape) was assigned a denser mesh (for most of the sheath circumference) than the stiffer UO_2 material with the larger Young's modulus and thicker dimensions. This afforded improved stability during solution convergence.

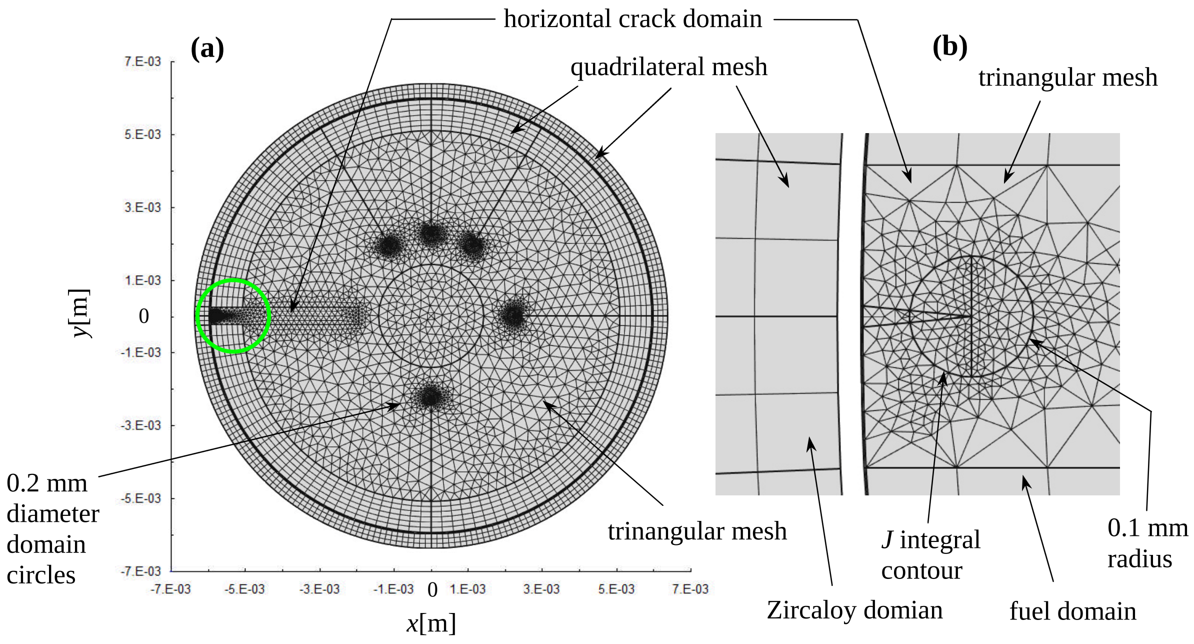

Figure 50: Finite element mesh of 2D r-θ plane strain solid mechanics model, where (a) is the general mesh at simulation start and (b) is the closeup region of the surface flaw

For the first mesh scheme, Figure 50, in the area where conditions for crack propagation were computed the mesh consisted of triangular elements due to the ease of generating a new mesh for every new geometric parametric sweep value. For this a separate horizontal rectangular crack domain was defined in the fuel domain so that a denser mesh could be defined in the vicinity of the ‘propagating’ crack tip (see Figure 50 (a) and (b)). The mesh was made especially dense in and around the circular *J* intergral contour. For the remainder of the crack tips that did not change position with the parametric sweep, a 0.4 mm diameter circle domain was included to increase the local mesh density.

To ensure the stress intensity factor computation, around the parametrically grown crack tip, was independent of the selected mesh type and the shape of the *J* integral contour, a second mesh configuration scheme was used. Here the ‘horizontal crack domain’ was widened. The domains of the *J* integral contour, the horizontal crack domain, and the remaining fuel domain (largest area) were filled with quadrilateral mesh elements, see Figure 51 (generated on COMSOL® 4.3a). Unlike when using the ‘free triangular’ mesher, which can mesh any domain, errors can occur when using the ‘free quadrilateral’ mesher.

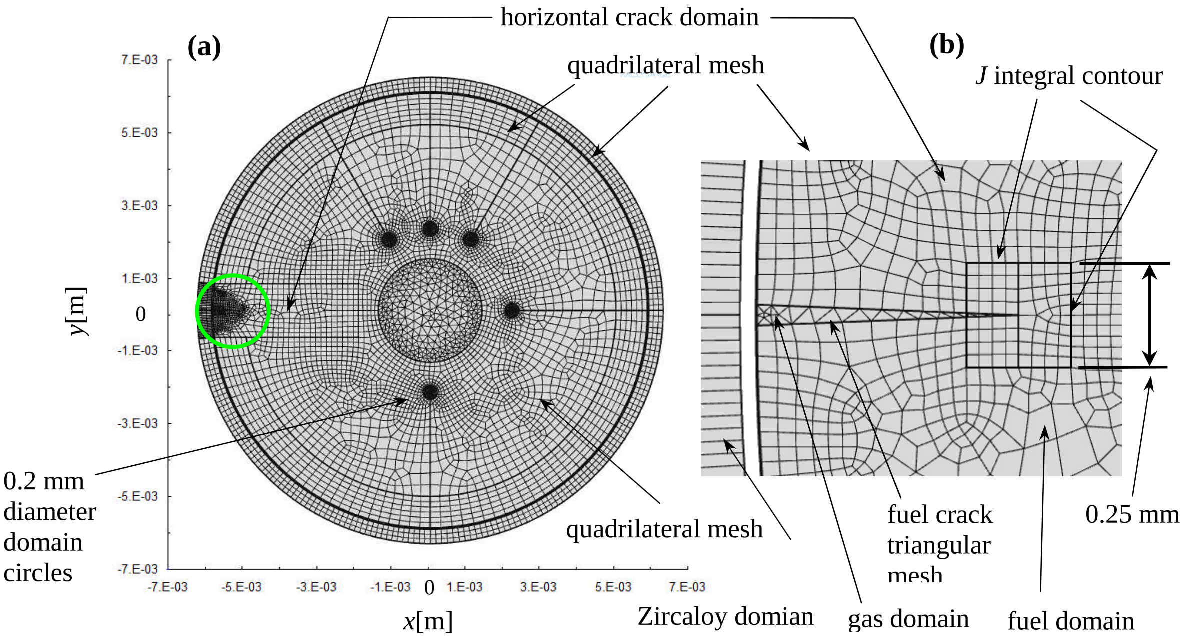

Figure 51: Finite element mesh of 2D *r-θ* plane strain solid mechanics model with quadrilateral mesh, where (a) is the general mesh at simulation start and (b) is the closeup region of the surface flaw

Errors such as: “failed to create an even number of edge elements” can occur. For this reason all meshes in the parametric sweep (17 in all) were first checked for proper generation, so that errors could be corrected before running the model. The only domains that were filled with triangular mesh elements were the small 0.4 mm diameter circles around the five unchanging crack tips, the iridium bar heater, and the developing fuel crack domain, where only the heat transfer equation was solved for. The last difference between the mesh shown in Figure 50 to the mesh shown in Figure 51 is the *J* integral contour, which is circular in the former and square in the latter. This was to show that the shape of the *J* integral contour does not affect the outcome of the computation.

Meshes and contour shapes of varying sizes for J and J^* integral computation

In Figure 50 and Figure 51 the *J* integral contour was approximately the same size; 0.1 mm radius for the circular contour and 0.25 mm side length for the square contour. To show contour shape independence as well as contour path independence, larger circular and square contours were also modeled. But first for computing the *J* integral, Eq. (125), and the J^* integral, Eq. (135) for a non homogeneous material (which also considers thermal gradients), it was noticed that the solution was sensitive to the type of mesh used (triangular elements vs. quadrilateral elements), especially when computing Eq. (135). Since it is usually the practice to use quadrilateral mesh in 2D (or hexahedron mesh in 3D) in solid mechanics problems, the following mesh configuration (Figure 52) included mostly quadrilateral mesh.

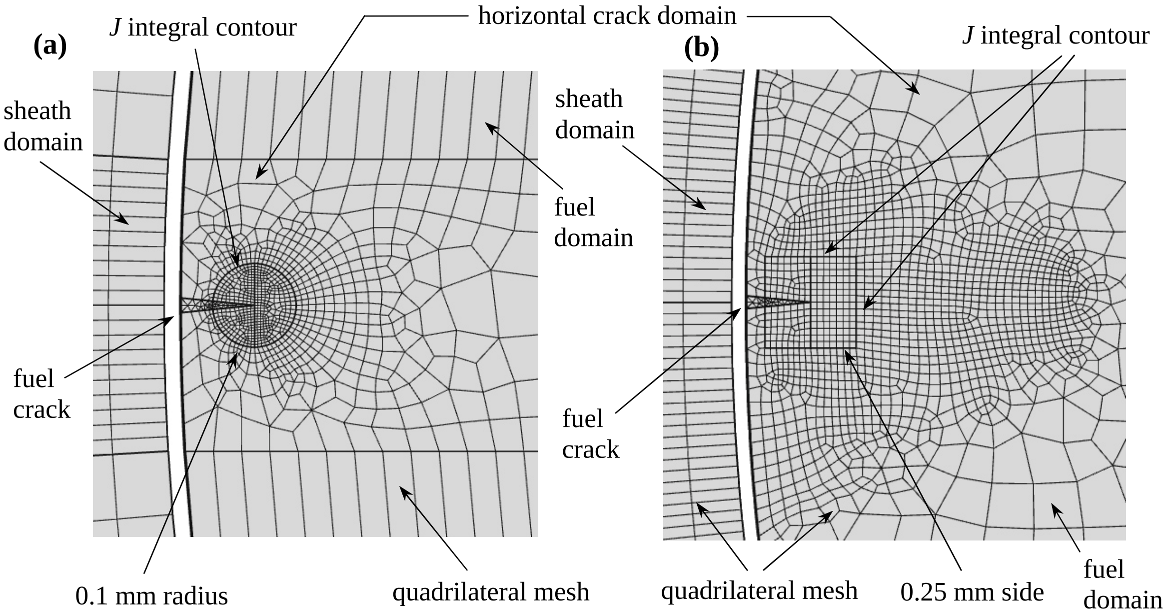

Figure 52: Smaller *J* integral contours, specifically: (a) 0.1 mm radius round contour and (b) 0.25 mm square contour, both with quadrilateral mesh

In these models the meshed fuel domains were similar to the previous meshed models (in Figure 50 and Figure 51) except that the ‘horizontal crack domain’ was made slightly wider in the vertical direction to accommodate the *J* integral contour and the mesh, the mesh was made denser, and all mesh elements were made quadrilateral.

For models with increased *J* integral contour sizes, Figure 53 (a) shows a 0.25 mm radius contour and Figure 53 (b) shows a 0.5 mm sided square contour, both having a quadrilateral mesh. As shown previously, the crack domains used a triangular mesh, since this domain was outside the solid mechanics physics domain and so did not require quadrilateral mesh.

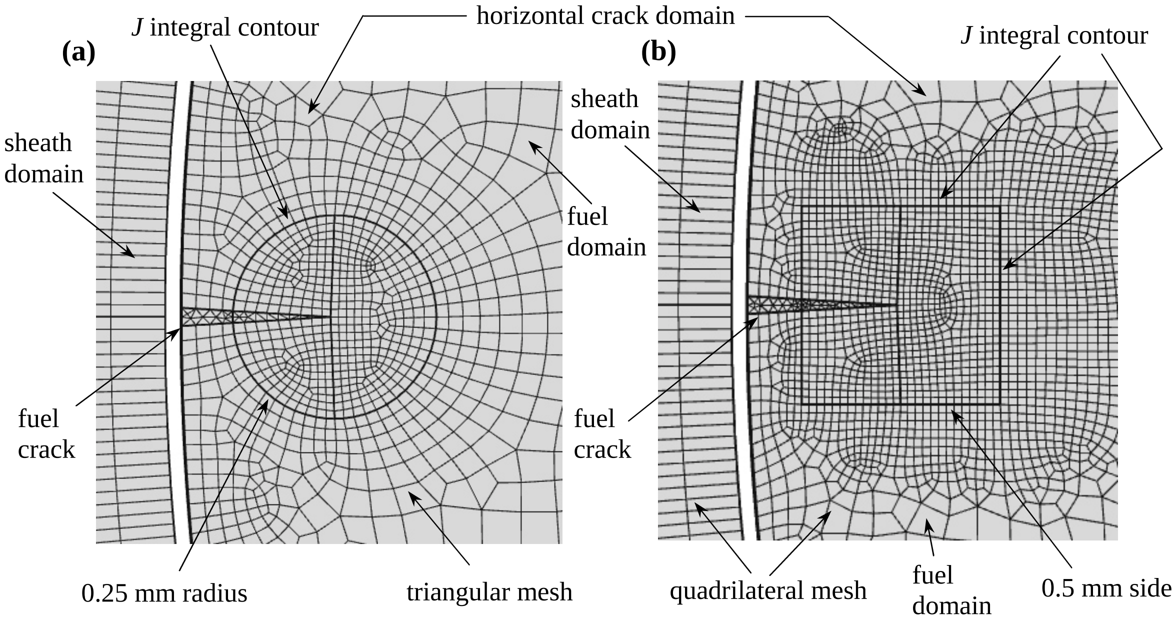

Figure 53: Larger *J* integral contours, specifically: (a) 0.25 mm radius round contour and (b) 0.5 mm square contour, both with quadrilateral mesh

For the model shown in Figure 53 (b) the model number of elements was 11,445 and the geometric discritization used in solving the heat conduction equation were 1st order polynomials, or linear shape functions. Setting the heat conduction equation polynomial shape function to linear was sufficient, since increasing it to quadratic shape function had a barely discernable improvement on the solution. For solving the solid mechanics physics the geometric discritization was set to 2nd order polynomial, or quadratic shape function. The resulting model degrees of freedom solved for was 205,959. A direct method solver, called MUMPS in COMSOL® was used to compute the model, also known as a Gaussian Elimination or LU decomposition solver (also called LU factorization). MUMPS is a fast multi-core capable solver, introduced in COMSOL® version 4.x and later. The remaining of the models in this section were solved with similar solver settings.

3.5.4 The Coupled 2D *r-θ* Out-Reactor Fuel Oxidation and Plane Strain Solid Mechanics Model Numerical Implementation

In the current *out-reactor instrumented defected fuel experiment* the power applied on the fuel element will not change substantially during the test. This means that the radial crack lengths and widths will not greatly change. Additionally, the amount of fuel oxidation achieved will be modest, but measurable, given the relatively short heating time (1-2 weeks) and the relatively low linear powers (17-23 kW total or 10-12 kW when only the central Ir heater is considered). It is expected this oxidation level will not substantially change the UO_2 fuel thermal conductivity. Hence coupling the fuel oxidation model with the solid mechanics model with thermally expanded fuel cracks, would seem to have limited benefits. However a similar model simulating an in-reactor high powered defective fuel element in normal and accident conditions may be quite useful, where crack number and crack geometry may change substantially during its time in the reactor core. This in turn could affect the fuel oxidation rate leading in certain cases to fuel melting. The following model numerical implementation describes how the fuel crack domains and solid fuel boundaries can be coupled together. Cracks lengths (or depths), which are dependent on fuel temperature, are fixed in this model, but could be made to vary as well.

For the gas domains, where no solid mechanics physics is solved, specifically in the steam filled fuel cracks and in the fuel-to-sheath gap, only the the heat conduction equation is solved for. But in this configuration the hydrogen mole fraction equation, Eq. (27), would be independent of the pellet radial crack dimensions, since the boundaries of the gas filled domains would not follow the pellet boundaries. Model results in Section 4.2.2 will show that there is an effect of the radial fuel crack width on the amount of fuel oxidation. Hence, in this section, the gas domain boundaries (of the steam filled fuel cracks and fuel-to-sheath gap) are geometrically coupled with the changing thermally-expanded solid pellet boundaries using an Arbitrary Lagrangian Eulerian (ALE) moving mesh (or a deformed mesh method) in COMSOL®.

Within the ALE moving mesh interface, the ‘Prescribed Mesh Displacement’ node is activated. For the ‘Prescribed *x* and *y* displacement’, or d_x and d_y inputs, the values in Eq. (175) are applied. The dependent dispalcement variables *u* and *v* are computed by solving the solid mechanics part of the model.

$$\begin{aligned} d_x &= u \\ d_y &= v \end{aligned} \tag{175}$$

The pellet boundaries highlighted in blue in Figure 54 indicate where the ‘prescribed mesh displacement’ values *u* (*x* coordinate displacement) and *v* (*y* coordinate displacement) are applied. In this manner the boundaries of the non-solid mechanics part of the model - the hydrogen mole fraction diffusion equation, active in the steam-filled cracks and fuel-to-sheath gap domains - follow the thermally expanding or contracting crack boundaries of the solid fuel.

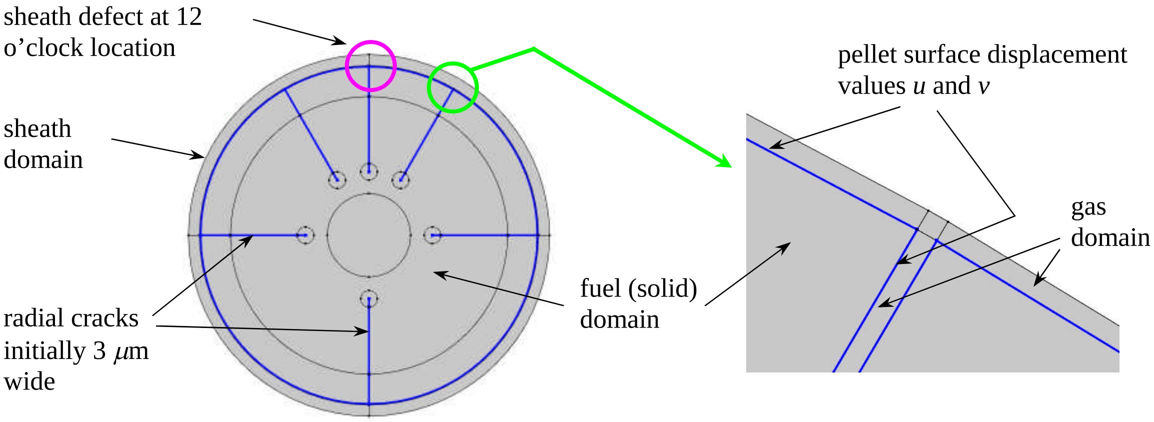

Figure 54: Boundaries used for ALE moving mesh fuel oxidation and plane strain solid mechanics model

Thus the fuel oxidation model becomes coupled with the plane strain solid mechanics model. COMSOL Multiphysics$^{®}$ Version 4.3b FEA software package was used for this purpose.

The six fuel cracks in Figure 54 are full length in the radial direction and are initially 3 μm wide. Sheath plasticity was not considered in this model to improve solution convergence. Quadratic shape functions were applied in all physics in this model. Triangular mesh elements (5,204 elements for internal fuel domains) and quadrilateral mesh elements (1,530 for external fuel domains and sheath domains for contact modeling) were used. Fuel oxidation, due to a sheath breach located at 12 o’clock position in the model, was allowed to occur at common interfaces between the fuel and gas domains in all six fuel cracks. The time dependent fully coupled model was solved for two weeks of simulated heating. The remaining model numerical implementation follows similar steps outlined in Section 3.5.1 for the fuel oxidation model and Section 3.5.3 for the plane strain solid mechanics model. In this model there were a total of 6,734 mesh elements and 90,889 degrees of freedom. The model was solved on an Intel Xeon® duo quad core (8 CPUs) HP work station operating at 2.66 GHz on a Windows XP 64 bit Professional® platform. 5-6 days of computer operation was required to solve this model. The results of the simulation are detailed in Section 4.4.

3.5.5 The In-Reactor 3D Fuel Oxidation Model Numerical Implementation

A 3D fuel oxidation model was constructed that simulates an in-reactor defective fuel element with similar operating parameters recorded for fuel element X5 (XC9179Z-5) from Darlington Nuclear Generating Station [29]. COMSOL® version 3.5a was used in this case. The purpose of this model was to compare model oxidation results to actual oxygen stoichiometric deviation measurements of an in-reactor defective fuel element (post irradiation examinations (PIE) that includes coulometric titration measurements [24]). The in-reactor defective fuel oxidation model includes fission heating and burn-up. This model contains discrete radial fuel cracks similar to the 2D r-θ fuel oxidation model discussed in Section 3.5.1 and generally discussed in Section 3.3.1, but only cracks immediately in the vicinity of the sheath defect are considered. Furthermore, the radial cracks only run a partial length of the fuel element. The reasoning for these two points will become clear in the results section. The sheath defect size in this model is specified to be similar in surface area to the sheath defect actually observed (see the yellow patch in Figure 27 (a)). Also included in this model is a single pellet-pellet gap beneath the sheath defect where steam ingress and additional surface oxidation is believed to occur [80].

The peak fuel element linear power, the approximated largest sheath defect size, the fuel burnup, and the estimated post defect residence time were provided by [24]. The largest sheath defect was estimated to be 8 mm^2 but more than one sheath defect was observed. Specifically, at one end of the fuel element an open blister was observed. At the fuel element mid section several blisters near bearing pads as well as a sheath crack were observed. Lastly, at the other end of the fuel element an incomplete endcap to sheath weld was observed [24]. Hence the actual total sheath defect surface area was larger than 8 mm^2. A single sheath defect may not be representative of multiple sheath defects, but for simplicity purposes a single 12 mm^2 sheath defect was selected and was positioned at the fuel element axial centre. The actual average bundle burnup was 45-139 MWh kgU^{-1} at the time the bundle (and the defective fuel element) was removed from the reactor, which is equivalent to a relative burnup of 0.200 to 0.617 atom%. For simplicity purposes a constant relative burnup value was used in the model equal to 0.5 atom%. Lastly, a post sheath defect residence time of 126 days was used, as determined by ^{131}I measurements [24]. Table 24 at the end of this section provides the remaining parameters used in the fuel oxidation model of the in-reactor defective fuel element XC9179Z-5.

A ¼ model was sufficient to represent a full length fuel element due to symmetry (i.e., the model is reflected about the $\tilde{z}$ axis in the axial direction, and reflected again about the $\tilde{z}$ axis but in the $\tilde{y}$ axis direction. Model reflection about the $\tilde{x}$ axis could not be done due to non symmetry of the defect surface in this direction, see Figure 55 (a). The sheath surface defect was defined by the silhouette of a circle equal to approximately 12 mm^2 in area (or a dashed circle with a radius of 2 mm), see Figure 55 (b).

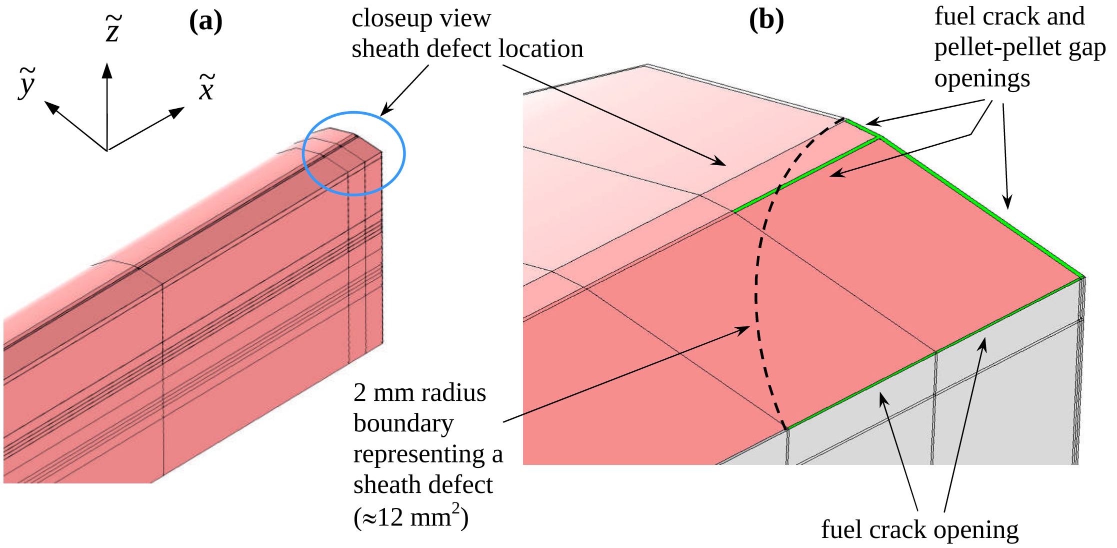

Figure 55: Sheath defect location and geometry in 3D in-reactor fuel oxidation model

The green thin surface areas Figure 55 (b) are the crack and pellet-pellet gap opening surface areas under the 2 mm radius sheath defect circle.

The fuel crack and pellet-pellet gap geometry location and identification in the model is provided in Figure 56. In this ¼ model only two radial cracks were created: one vertical crack (a) at the model $\tilde{z}$ axis of reflection and one crack (b) rotated 16.2° degrees from vertical crack (a). Again, since the model is reflected about the $\tilde{z}$ axis the number of radial cracks is this model is actually three. The width of crack (a) was set to 15 μm, but since the model is reflected this width is equivalent to 30 μm. The width of crack (b) was set to 30 μm. The pellet-pellet gap near the sheath defect, where in deuterium gas diffusion also occurs, was set to 25 μm and due to model reflection this gap is equivalent to 50 μm in width. The depth of the fuel cracks was set to 4.575 mm from the surface (or 1.5 mm from the centre of the fuel element). This dimension was chosen so that the root of the crack was positioned at a temperature of ≈1250°C (based on the applied fuel element power) for the reason explained in Section 1.5.

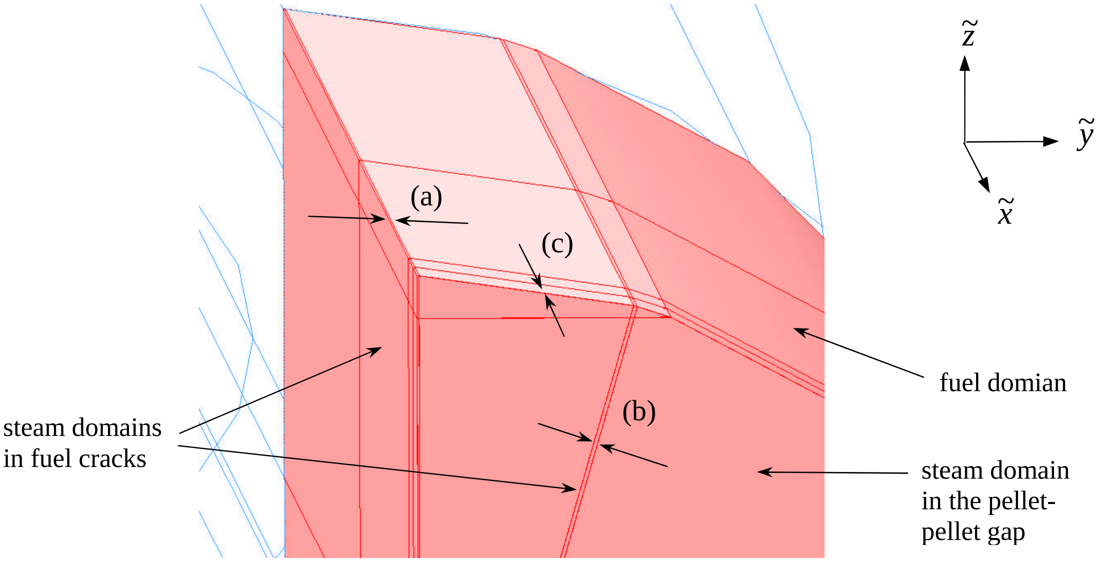

Figure 56: In-reactor fuel crack geometric locations and width identifications

The fuel element model consisted of two partial or sub geometry models - forming an ‘assembly model’. This was done so different meshes (that do not share common nodes at a common interface) could be used in each partial or sub-geometry. This allowed the modeling of the slender fuel cracks using swept mesh in the first sub-geometry and regular free tetrahedral mesh in the second sub-geometry. The reason why the entire length of the model was not meshed with swept mesh was because the generated prism and hexahedron cells in the swept mesh increases the model’s degrees of freedom from 1.4-8.5 times as compared to all tetrahedrons [159]. Hence, using this modeling approach conserved available computer resources (especially computer memory). To allow for physics continuity between the two sub model geometries an 'identity pair' was defined between model boundaries that occupied the same interfaces. This is shown in Figure 57. Sub geometry 1 contained the slender fuel cracks and pellet-pellet gap and sub geometry 2 contained only solid fuel with no cracks. In COMSOL® version 3.5a the identity pair was activated from the Options/Identity Conditions/Identity Boundary Conditions pull-down in the software toolbar. The dependent variables used in the identity pair are the temperature variable *T* and the solid state oxygen stoichiometry deviation variable Xdev (or *x*). The deuterium-to-steam ratio (deuterium and not hydrogen, since it's an in-reactor case) diffusion dependent variable *q* was not used in the identity pair, since its equation was not used in sub geometry 2. In the identity pair the dependent variables *T* and Xdev are applied as the 'source' expressions in sub geometry 2 and as 'destination' expressions in sub geometry 1.

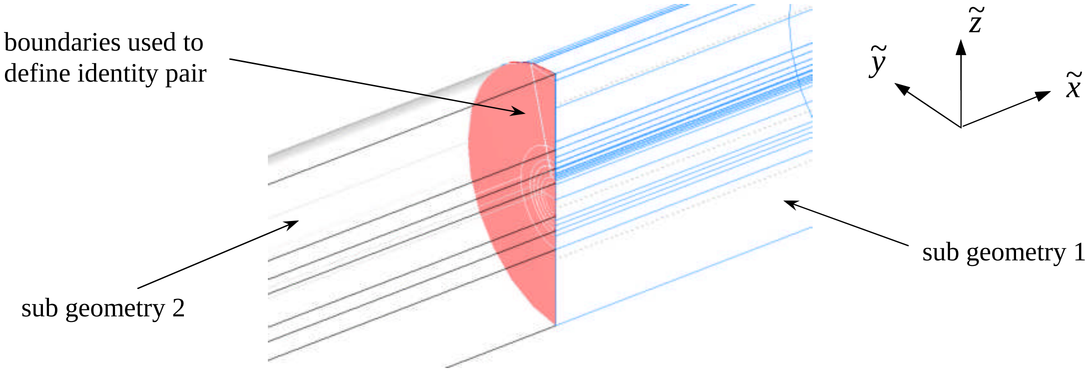

Figure 57: Identity pair boundaries used for physics continuity

Transport and generation of deuterium gas within the fuel cracks and pellet-pellet gap near the sheath defect is governed by the hydrogen (or in this case - deuterium) diffusion equation, Eq. (27), or in COMSOL® form in Eq. (167) and in expanded form in Eq. (67). Deuterium generation due to sheath oxidation by the steam is neglected. The initial deuterium mole fraction *q* in the fuel cracks and pellet-pellet gap is equal to constant q_c where ℓ is the model length (see Table 24):

$$q = q_c,\ \ell - 0.013\ [\mathrm{m}] < \tilde{z} < \ell,\ \text{at } t = 0 \tag{176}$$

The boundary conditions for the deuterium diffusion equation are similar to Eq. (168), with the difference that in this model fewer radial cracks are defined. The boundaries that participate in fuel oxidation and hydrogen generation are highlighted in red in Figure 58. These boundaries lie between the steam and fuel domains.

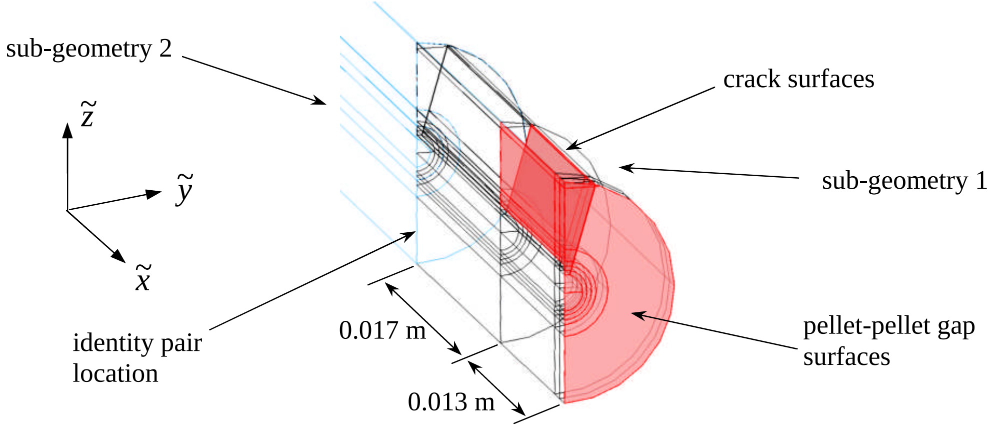

Figure 58: Flux surfaces active at fuel crack surfaces and at a pellet-pellet gap surface in an in-reactor fuel oxidation model

The inward fluxes N_o for the deuterium diffusion equation at the indicated surfaces is given by Eq. (177), where internal volume fluxes **N** are expressed as well.

$$\text{at the surface: } N_o = -\mathbf{n} \cdot \mathbf{N} = R_f^{react} \equiv \text{"} flux \text{"}$$

$$\text{and within the gas domain: } \mathbf{N} = -\frac{c_g D_g}{\tau^2} \nabla q \qquad (177)$$

For the surfaces that were very slender, such as crack edges or tips, or that did not share common interfaces between the steam and the solid domains, such as the crack surfaces at reflection boundaries, the inward flux was set to zero. The boundary condition for the sheath defect, see the green slender areas in Figure 55 (b), was set to value q_c.

For interstitial oxygen diffusion Eq. (18), expanded as Eq. (66), was applied. Before the onset of fuel oxidation (i.e., intact fuel and zero burnup) the fuel pellets were assumed to be essentially stoichiometric, where a_{pellet} (or a_pellet in model) is the pellet radius:

$$\begin{gathered} x \approx 0 \ (x = 1\times10^{-4}) \text{ , at } t = 0\text{, for} \\ 0 < \tilde{x} < \ell \\ -a_{pellet} < \tilde{y} < a_{pellet} \\ -a_{pellet} < \tilde{z} < a_{pellet} \end{gathered} \tag{178}$$

Boundary conditions for the solid state oxygen diffusion equation (Eq. (66)) is zero at all external boundaries of the model (i.e., zero flux) except for fuel crack and pellet-pellet gap boundaries where the fuel domains share gas domain boundaries (Figure 58). The inward fluxes G_s for the solid state interstitial oxygen diffusion equation, at these surfaces, are given by Eq. (179), where internal fluxes are expressed as well:

$$\begin{gathered} \text{at the surface: } G_s = -\mathbf{n}\cdot\mathbf{\Gamma} = \frac{R_f^{react}}{c_U} \equiv \text{"} flux \text{"} \\ \text{and within the solid domain: } \mathbf{\Gamma} = -D\left(\nabla x + x\frac{Q}{RT^2}\nabla T\right) \end{gathered} \tag{179}$$

The heat conduction equation, Eq. (32) (and in an expanded form in cylindrical coordinates as Eq. (68)), with a volumetric fission heating source term Q_v provided by Eq. (33) (which employs first order modified Bessel functions) was used in this model. The linear power P_{linear} was set to 44 kW m^{-1}. The boundary conditions for this equation are illustrated in the following figure:

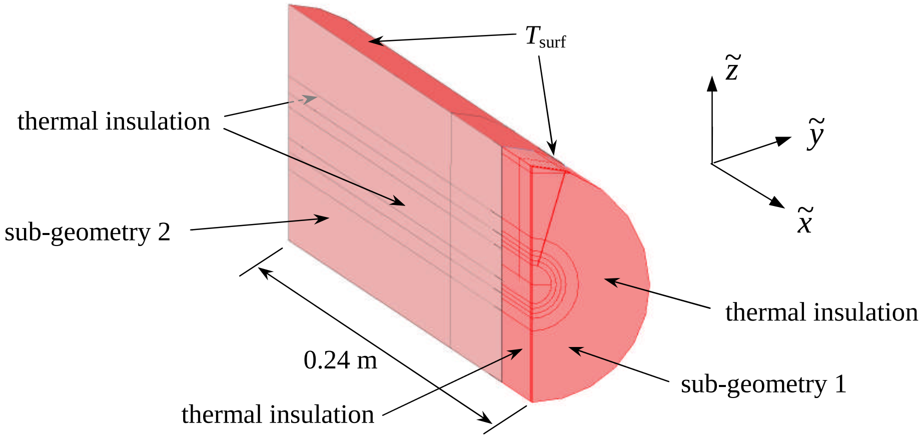

Figure 59: Heat conduction equation boundary conditions for in-reactor model

The fuel outer surface temperature is provided by the Dirichlet boundary condition:

$$\text{at the fuel surface: } T = T_{\text{surf}} \text{ (=645 K and 706 K)} \tag{180}$$

The former temperature boundary condition is an estimated value. See Table 24 at end of section for additional information on the latter value. The temperature gradient at the fuel element model ends as well as across the model reflected about the $\tilde{z}$ axis is given by the Neumann boundary conditions:

$$\frac{\partial T}{\partial x} = \frac{\partial T}{\partial y} = 0 \tag{181}$$

As explained earlier, an identity pair (Figure 57) was used in order to conserve computer memory during the computation. Specifically, the fuel element end, half-circle, outer surface (see Figure 60 (a)) was meshed in 2D using 'free' mesh triangles in the fuel domains and rectangles (also called quadrilaterals) in the slender fuel cracks domains using 'mapped' mesh.

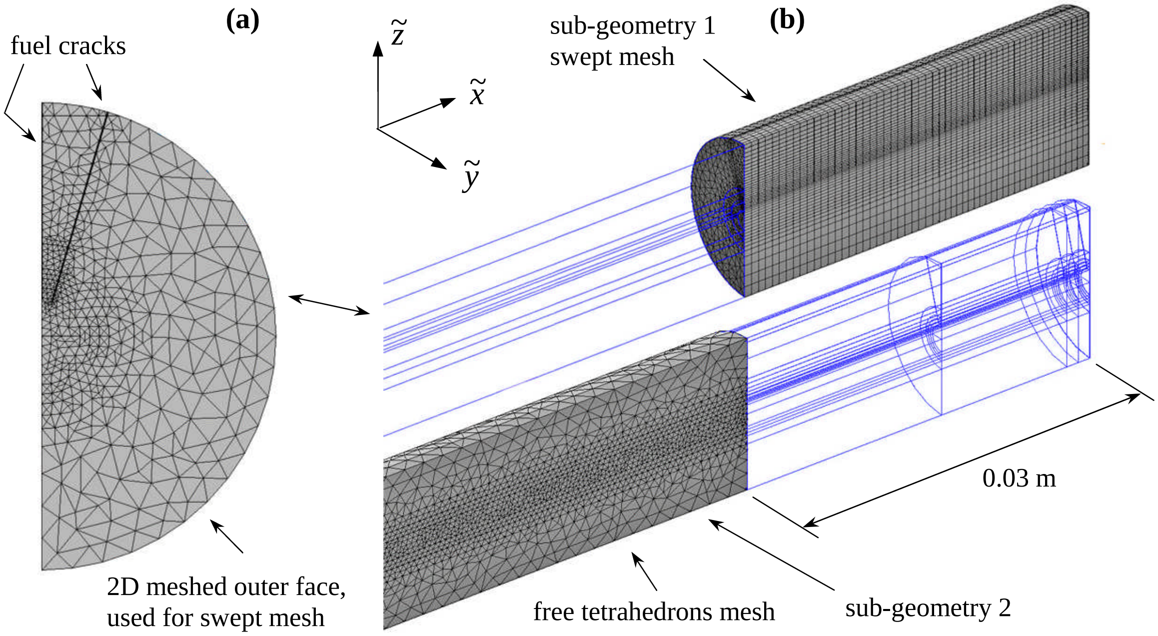

Figure 60: (a) 2D meshed surface used to sweep 3D sub-geometry 1 and (b) two meshed 3D sub-geometries where sub-geometry 1 consisted of prism and hexahedron cells and sub-geometry 2 consisted of tetrahedrons.

Once this was done this outer meshed surface was swept along the fuel element axis (Figure 60 (b)) producing prism mesh elements with triangular bases in the fuel domains and hexahedrons in the crack domains, which constituted sub-geometry 1. In sub-geometry 2 free tetrahedral mesh elements were used exclusively. In both sub-geometries the mesh at the centre of the fuel element was made denser than the mesh at the fuel element periphery (in the radial direction). This was done so that sufficient mesh was available to compute the solution at steep radial temperature gradients where accelerated reaction rates occur (near the fuel centre) but to conserve computer memory where gradients and reaction rates were relatively small (in the fuel periphery). In the axial direction a sufficient distribution of swept mesh and free tetrahedron mesh elements was generated to model concentration gradients and to achieve improved convergence.

The mesh used in the out-reactor model depicted in Figure 60 was designed to conserve computer resources. However, it was necessary to check if using an assembly model with an identity pair (combining the two fuel element domains) as well as a partial length crack domain in the axial direction (a 0.013 m long domain in Figure 58 rather than a full length crack domain), still achieved a reasonable prediction of oxidation in a defective fuel element. To do this the following single solid model and mesh was designed (i.e., not an assembly model as shown previously in Figure 60 (a)). In this model the same number of radial cracks was modeled (two actual, which is equivalent to three in total considering model reflection), except that in this case the cracks ran the full length of the model (i.e., 0.240 m long instead of only 0.013 m long). Figure 61 shows the full length meshed model consisting of prism and hexahedron mesh elements. As for axial mesh density, the mesh was made denser near the sheath defect and pellet-pellet gap location and less dense near the other end of the model.

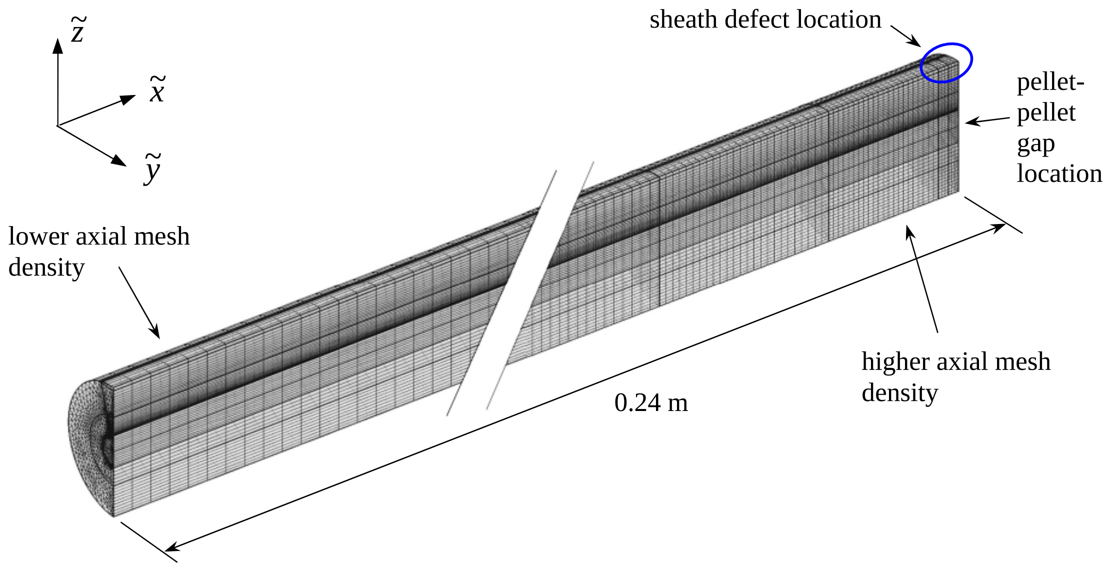

Figure 61: A 3D swept mesh geometry consisting of prisms with triangular bases and hexahedrons mesh elements

The geometric discritization (i.e., order of shape functions) used in solving the heat conduction equation, the solid state oxygen diffusion equation, and the hydrogen mole fraction diffusion equation, for both models shown in Figure 60 and Figure 61, was set to quadratic (i.e., 2nd order shape functions). For the model with mesh illustrated in Figure 60 a direct method solver called PARDISO was used, also known as a Gaussian Elimination or LU factorization solver. PARDISO is a fast multi-core capable solver, which also requires increased computer memory. A Spark-9000 mainframe computer at HPCVL (High Performance Computing Virtual Laboratory) at Queens University operating on a Linux platform was used to perform this computation with COMSOL® 3.5a finite element analysis software. The same direct solver (PARDISO) was used to compute the model with the mesh illustrated in Figure 61, except that here the model was solved on COMSOL® 4.3b software using a duo hex core (12 processors) Xeon, 96 GB RAM HP Z800 workstation computer operating on a Windows 7 platform.

The computer resource requirements to solve each model were markedly different. The degrees of freedom of the model shown in Figure 60 (using the identity pair) was $1.24{\times}10^6$ and the computer memory required was about 32 GB. The degrees of freedom of the model shown in Figure 61 was 3.11×10^6 and the computer memory required was about 95 GB. Hence the fully swept meshed model required more computer resources to solve.

Lastly, for the purpose of comparison a numerical implementation description for a model based on the Higg's modeling approach [24][29], as explained in Section 1.6 and Section 4.5.2, is briefly illustrated in Figure 62.

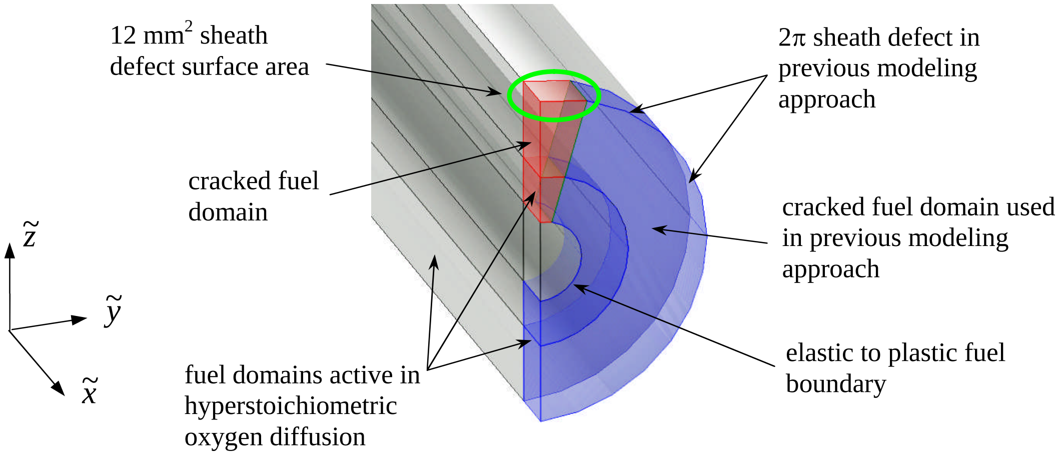

Figure 62: Using the previous modeling approach [24][29] in 3D where the red domain represents cracked fuel where radial gas diffusion occurs

The red domain in the figure represents cracked fuel where both solid state hyperstoichiometric oxygen diffusion (Eq. (18)) and hydrogen gas diffusion (Eq. (27)) occur. The blue domain in the figure is identical to the red domain - in the Higgs axisymmetric 2D *r*-*z* model for a sheath defect that is 2π in circumference – with the exception that the sheath is intact and only solid state oxygen diffusion is considered. To be consistent with the 2D *r*-*z* Higgs model [24][29] the gas diffusion in the figure was set to be anisotropic in the $\tilde{z}$ direction (i.e., approximately equivalent to the radial direction in cylindrical coordinates). It can be noted that allowing the gas diffusion in all principal directions in the red domain inceases the maximum Xdev result by ≈10%, which is not significant. The sheath defect area was set to be 12 mm^2 to be consistent with the current 3D in-reactor fuel oxidation model (representing fuel element XC9179Z-5) described in Figure 55 at the beginning of this section. Finally, the previous 2D *r*-*z* model approach [24][29] used what is called the *weak* and *dweak* form terms to simulate gas diffusion in the fuel-to-sheath gap but these terms were not used in this model. See explanations given in Section 1.6 and Section 3.3.1.

Table 24: List of constants used in the 3D In-Reactor Fuel Oxidation Model

Symbol	COMSOL® constant name	Description	Value
ρ_{TD}	theoretical_density	the theoretical fuel pellet density	10.96 [g cm^{-3}]
ρ_{s_new}	density_manf	Manufactured fuel density	10.63 [g cm^{-3}]
NA	porosity_manf	Manufactured fuel porosity	$1 - \frac{\text{density\_manf}}{\text{theoretical\_density}}$
p_t	PT	Coolant pressure	100 [atm]
R	Rgas	Universal gas constant	8.205×10^{-5} [atm m^3 gmol^{-1} K^{-1}]
κ	kappa	inverse neutron diffusion length	110 [1/m]
β	Beta	Fractional burnup (atom %)	0.5
σ_{H2}	sigmaH2	H_2 collision diameter	2.827 [Å]
σ_{H2O}	sigmaH2O	H_2O collision diameter	2.641 [Å]
M_{H2}	MH2	D_2 molecular weight	4.028204 [g mol^{-1}]
M_{H2O}	MH2O	D_2O molecular weight	20.020004 [g mol^{-1}]
τ	tau	Tortuosity factor	1
q_c	qdef	Hydrogen mole fraction in CANDU coolant	4.1×10^{-6}
x_{fs}	Xsurf	Stoichiometry deviation at pellet crack surfaces	1×10^{-4}
κ/σ_{AB}	koverepsilon	Inverse of Lenard-Jones force constant	0.00454959 K^{-1}
$a_{\aleph}$	a	Constant in polynomial fit for x_e	0.033107007
$b_{\aleph}$	b		0.268984735
$c_{\aleph}$	c		0.008679485
$d_{\aleph}$	d		-0.000622197
$e_{\aleph}$	e		-5.18804E-05
$f_{\aleph}$	f		0.020038397
$g_{\aleph}$	g		0.000450165
$k_{\aleph}$	k		-7.83442E-06
$m_{\aleph}$	m		1.84196E-08
$n_{\aleph}$	n		-7.45197E-05
$p_{\aleph}$	p		1.39057E-07
T_{surf}	Tsurf	Fuel surface temperature	645 [K] and 706* [K]
P_{linear}	P_density	Linear power	44** [kW m^{-1}]
ℓ	l	Fuel element length half	0.241 [m]
NA	a_pellet	Fuel pellet radius	0.006075 [m]

Table 24: List of constants used in the 3D In-Reactor Fuel Oxidation Model

Symbol	COMSOL® constant name	Description	Value
N_A	N_Avogadro	Particles/molecules per mol	6.022×10^{23}
N_{UO_2}	N_UO2	number density of UO_2	2.444×10^{28} [particles m^{-3}]
F_{vol}	fuel_element_vol_quart	Quarter fuel element volume	pi*(a_pellet^2)/2*ℓ [m^3]

Note: The fuel surface temperature* and linear power** of fuel element XC9179Z-5 was taken from [29].

3.5.6 The Out-Reactor 3D Fuel Oxidation Model Numerical Implementation

A 3D geometry for computing fuel oxidation is computationally more expensive than a 2D model (described in Section 3.5.1) but represents more accurately the extent of fuel oxidation for the actual size of sheath defect and the actual fuel element length. Incorporating all the 2D r-θ model features into the 3D model was not feasible with the available computer power and not really necessary. These extra features included: Fully cracked fuel pellets, solid mechanics thermal stress computations (described in Section 3.5.3), fuel and sheath contact force computations using the penalty method, and electrical (or Joule) heating computations. It will be seen in results Section 4.2.1, using the 2D r-θ fuel oxidation model, that modeling only a few of the radial cracks near the sheath defect yields a similar result when all the radial cracks are modeled. Thus, the 3D out-reactor fuel oxidation model included only some of the pre-defined radial fuel cracks near the site of the sheath defect (similar to the in-reactor model described in Section 3.5.5). Also included in the model was a fuel-to-sheath gap, covering only part of the fuel element near the sheath defect site. Electric-Joule heating was not included in the model, instead boundary temperature conditions were used at the fuel central annulus and the fuel outer surface, which are based on the 2D r-θ model results (refer to Sections 3.5.1 and 4.2.1). Two power cases were selected for simulating the out-reactor fuel oxidation experiment, a high powered case (23 kW total) and a low powered case (17 kW total). The high powered case was the ideal setting in order to accelerate fuel oxidation but in case this power was not feasible to achieve in the experiment a lower powered case was also modeled. Table 25 at the end of this section provides the model parameters used in the out-reactor fuel oxidation model. The two power cases are determined by the selection of parameters in Table 25: the fuel inner annulus surface temperature T_{heater} and the crack tip position dimension crack_tip_radius.

As in the in-reactor model described in Section 3.5.5, a ¼ model was sufficient to represent a full length fuel element due to symmetry. The sheath surface defect was defined by a slim surface strip 0.5 mm wide and 7.5 mm long, seen in blue in Figure 63. Due to the model's double reflections the actual sheath defect surface area is 1×15 mm^2.

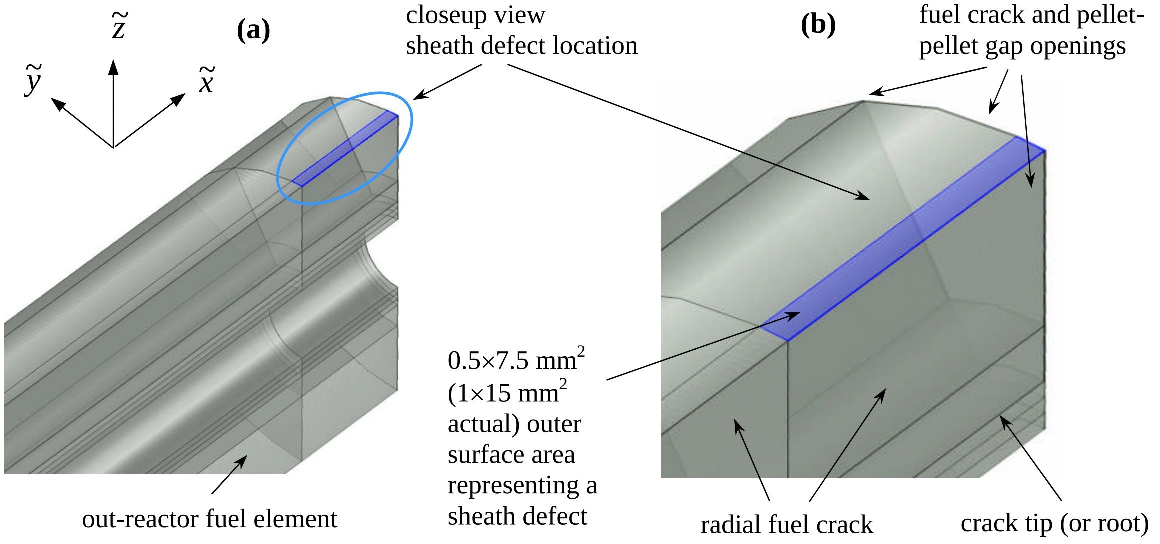

Figure 63: Sheath defect location and geometry in 3D out-reactor fuel oxidation model

The fuel crack and pellet-pellet gap geometry position and identification in the model is provided in Figure 64. In this ¼ model three radial fuel cracks were included: one vertical crack (a) at the model $\tilde{z}$ axis of reflection and two cracks (b) rotated 30° and 60° degrees from vertical crack (a). Again, since the model is reflected about the $\tilde{z}$ axis the number of radial cracks in this model is actually five. The width of crack (a) was set to 12.5 μm, but since the model is reflected, this width is equivalent to 25 μm (crack_width in Table 25). The width of cracks (b) was set to 25 μm. The pellet-pellet gap near the sheath defect, where hydrogen gas diffusion also occurs, was set to 25 μm (ppg in Table 25) and due to model reflection this gap is equivalent to 50 μm in width. The depth of the fuel cracks was set to 3.785 mm and 4.201 mm from the pellet surface (or 2.290 mm and 1.874 mm from the centre of the fuel element), for the two modeled power cases. These dimensions were chosen so that the tip (or root) of the crack was positioned at a temperature of ≈1250°C (based on the applied fuel element power) for the reason explained in Section 1.5.

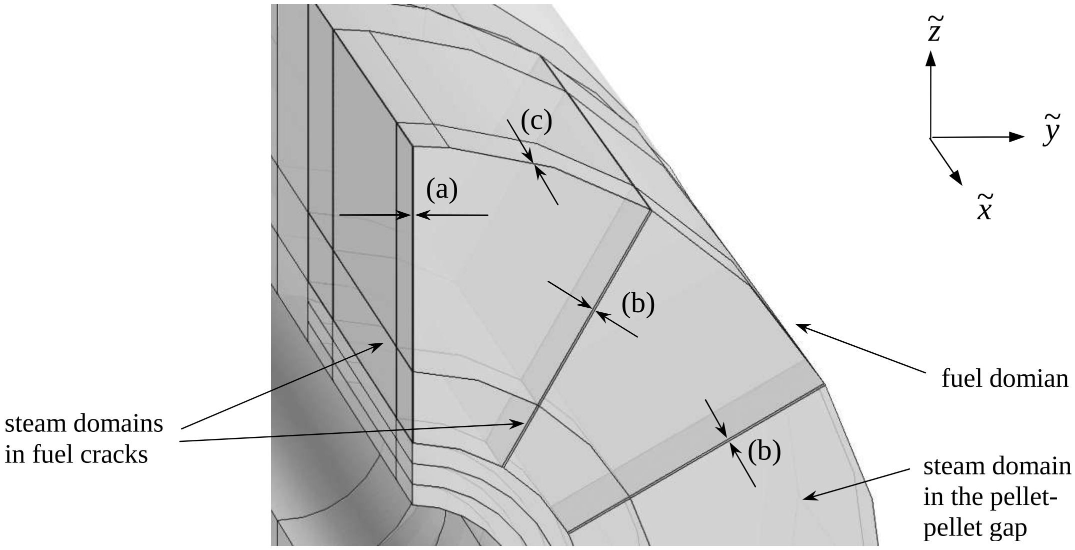

Figure 64: Out-reactor fuel crack geometric locations and width identifications

As in the in-reactor defective fuel element model in Section 3.5.5, the out-reactor model consisted of two partial or sub geometry models - forming an assembly model for the reasons explained earlier. To allow for physics continuity between the two sub models an identity pair was defined between the boundaries that occupied the same interface. This is shown in Figure 65. Sub geometry 1 contained the slender cracks and pellet-pellet gap and sub geometry 2 contained only solid fuel with no cracks. In COMSOL® Multiphysics version 4.2a the identity pair is activated by inserting in the ‘definitions’ an ‘identity boundary pair’. The dependent variables used in the identity pair are the temperature variable T and the solid state oxygen stoichiometry deviation variable Xdev (or x). The hydrogen-to-steam ratio diffusion dependent variable q is not used in the identity pair, since its equation is not used in sub geometry 2. In the identity pair the dependent variables T and Xdev are applied as the ‘source’ expressions in sub geometry 2 and as ‘destination’ expressions in sub geometry 1.

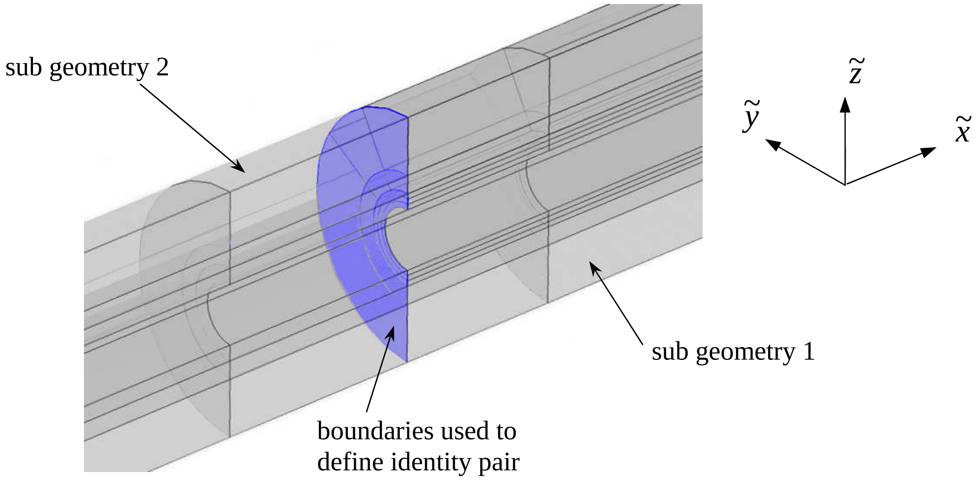

Figure 65: Identity pair boundaries used for physics continuity

Transport and generation of hydrogen gas within the fuel cracks and the pellet-pellet gap near the sheath defect is governed by the hydrogen diffusion equation, Eq. (27), or in expanded form in Eq. (67), or in COMSOL® form in Eq. (167). Hydrogen generation due to sheath oxidation by steam is neglected. The initial deuterium mole fraction q in the fuel cracks and pellet-pellet gap is equal to constant q_c where ℓ is the model length (see Table 25):

$$q = q_c,\ \ell - 0.025\ [\mathrm{m}] < \tilde{z} < \ell,\ \text{at } t = 0 \tag{182}$$

The boundary conditions for the hydrogen diffusion equation in the fuel cracks are similar to Eq. (168), with the difference, when compared to the 2D r-θ model, that in the 3D model there are fewer defined radial cracks. The boundaries that participate in fuel oxidation (and hence hydrogen generation) are highlighted in blue in Figure 66.

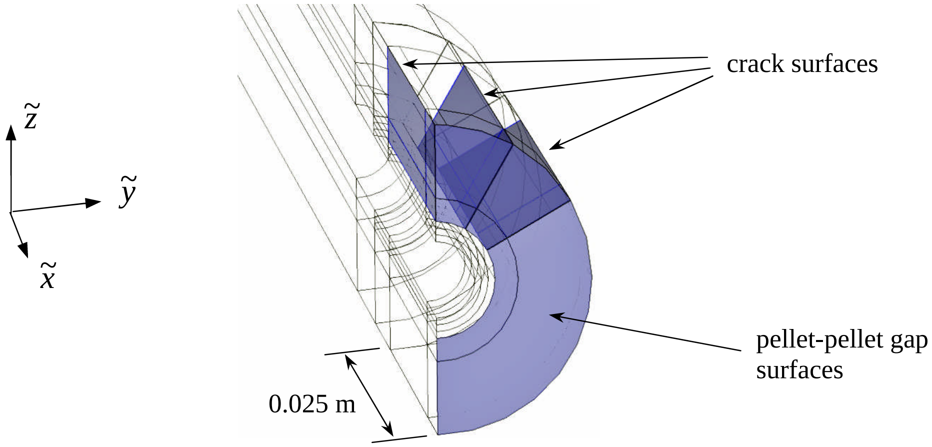

Figure 66: Out-reactor model flux surfaces active at fuel crack surfaces and at a pellet-pellet gap surface

The indicated boundaries in Figure 66 lie between the steam and fuel domains. The inward fluxes N_o for the hydrogen diffusion equation at these surfaces is given by Eq. (177). The inward fluxes were set to zero for those surfaces that were very small, such as crack edges or tips, or that did not share common interfaces between the steam and the solid domains, such as the crack surfaces at reflection boundaries. The boundary condition for the sheath defect itself, see the blue strip surface area in Figure 63 (b), was set to the value q_c, see Table 25.

For interstitial oxygen diffusion Eq. (18), expanded as Eq. (66), is applied. Before the onset of fuel oxidation (i.e., intact fuel and zero burnup) the fuel pellets are assumed to be essentially stoichiometric, specifically Eq. (178) is applied. Boundary conditions for the solid state oxygen diffusion equation (Eq. (66)) are zero at all external boundaries of the model (i.e., zero flux) except for fuel crack and pellet-pellet gap boundaries where the fuel domains share gas domain boundaries (Figure 66). The inward fluxes G_s for the solid state interstitial oxygen diffusion equation, at these surfaces, is given by Eq. (179).

In the out-reactor fuel element the UO_2 fuel is headed by a central electrical heater element. The power and expected temperature distribution in the fuel are computed with the 2D r-θ model, as explained in Chapter 2. Hence, in the heat conduction equation, Eq. (32) (or Eq. (68) expanded in cylindrical coordinates), the volumetric heating source term Q_v is neglected (is set to zero). Instead surface boundary conditions are utilized, which are derived from the results of the 2D r-θ model. The heat conduction equation boundary conditions are illustrated in the following figure:

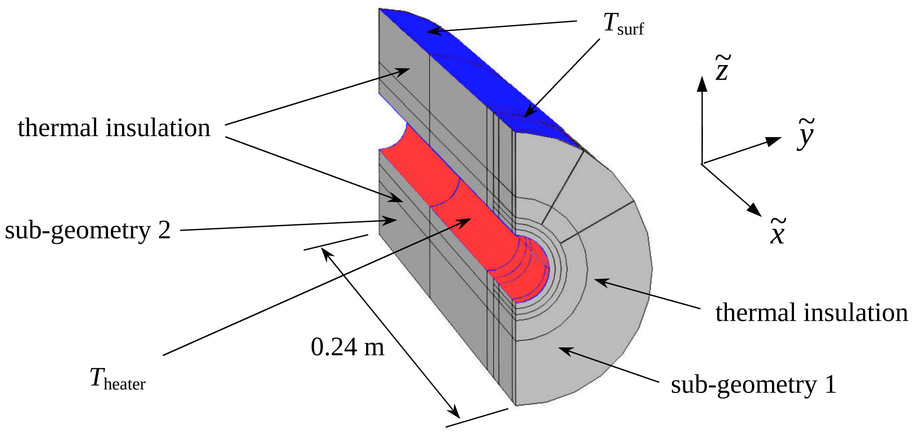

Figure 67: Heat conduction equation boundary conditions for the out-reactor model

The Dirichlet boundary conditions for the surface temperature at the iridium bar to inner UO_2 interface was set to T_{heater} (red) and the UO_2 to fuel-to-sheath gap interface was set to T_{surf} (blue), see Table 25 for the values used. The remaining of the model's exterior and interior surfaces were set to thermal insulation, or Eq. (181). However, it should be mentioned that ignoring the fuel element edge-effects at the fuel element ends (by setting there thermal insulation boundary conditions) is not quite representative. This is because the fuel element ends will be relatively cooler due to heat conductance through connected electrodes. Hence in reality the fuel stack end pellets are expected to oxidize less.

The applied mesh used in the out-reactor fuel oxidation model is shown in Figure 68. Since applying the swept mesh is more computationally expensive than using a free tetrahedral mesh the crack domain in the current model extends to only part of the axial length of the model. Like in the in-reactor fuel oxidation model, a fuel element end, half-circle, outer surface (see Figure 68 (b)) was initially meshed in 2D using ‘free’ triangle mesh elements in the fuel domains and quadrilaterals in the slender fuel cracks domains using ‘mapped’ mesh. Also meshed was a partial section of the fuel-to-sheath gap, between the fuel radial cracks, with quadrilaterals. To mesh sub-geometry 1 this outer 2D meshed surface was swept 3.3 cm along the fuel element axis (or a distance of 6.6 cm for the model with a reflected boundary condition) producing prisms with triangular bases in the fuel domains and hexahedrons in the crack and fuel-to-sheath gap domains.

For sub-geometry 2 (the remaining 20.7 cm length of the model) the mesh consisted entirely of tetrahedron mesh elements. Three concentric domains were created in sub-geometry 2 so that varying tetrahedral mesh densities could be defined: highest mesh density near the inner UO_2 annulus (or near the iridium bar heater) and lowest mesh density at the UO_2 outer regions. This was done in order to conserve computer resources, while at the same time providing enough mesh density to capture the steep radial temperature gradients, which in turn affects oxidation and diffusion rates, especially near the fuel centre. This configuration also provided sufficient distribution of swept and free tetrahedrons mesh elements in the axial direction so that oxidation gradients could be observed and stable convergence could be achieved.

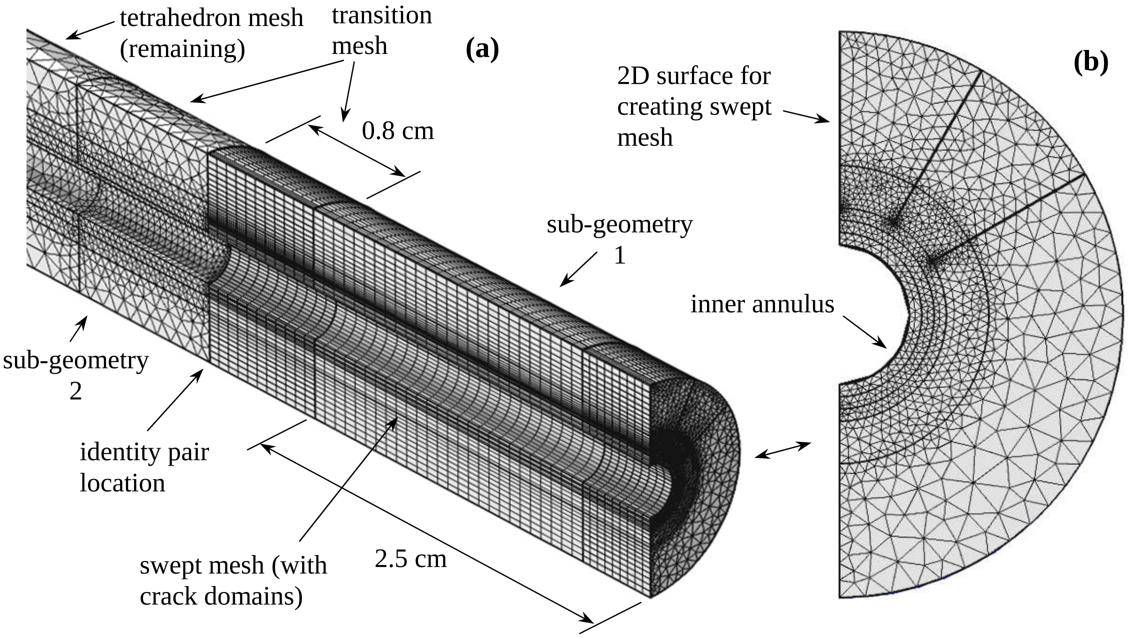

Figure 68: (a) Swept mesh in the 3D out-reactor model and (b) the original meshed 2D plane used for the 3D sweep in sub-geometry 1

A final feature to discuss in the applied mesh shown in Figure 68 is the transition mesh sections: one section being a swept mesh in sub-geometry 1 (that is 0.8 cm long) and one section being a free tetrahedral mesh in sub-geometry 2 (that is 1 cm long). Since the sub-geometries are not actually connected as single solid, as mentioned earlier, an identity pair was used to communicate the dependent variables across this common interface. Thus to reduce numerical errors the density of the two separate meshed surfaces at this common interface was increased. Also the hydrogen diffusion equation domain (of the fuel cracks) was not extended right up to the identity pair (at 3.3 cm from the model end) but only up to the beginning of the swept transition mesh (up to 2.5 cm from the model end). This was done in order to eliminate the additional physics (the hydrogen diffusion equation) at the identity pair to reduce numerical difficulties for the solver.

For the physics solved in this model the geometric discritization (or polynomial shape functions) were set to quadratic. This full length fuel element model was solved with COMSOL® 4.2a using a 12 core Xeon, 96 GB RAM HP Z800 workstation computer operating on a Windows 7 platform. The degrees of freedom of the model with the mesh shown in Figure 68 was 1.545×10^6 and the computer memory required was about 52 GB. The following table provides the model parameters used in the out-reactor fuel oxidation model.

Table 25: List of parameters used in the 3D out-reactor fuel oxidation model

Symbol	COMSOL® constant name	Description	Value
ρ_{TD}	theoretical_density	the theoretical fuel pellet density	10.96 [g cm^{-3}]
ρ_{s_new}	density_manf	Manufactured fuel density	10.6 [g cm^{-3}]
NA	porosity_manf	Manufactured fuel porosity	$1-\dfrac{\text{density\_manf}}{\text{theoretical\_density}}$
p_t	PT	Coolant pressure	100 [atm]
R	Rgas	Universal gas constant	8.205×10^{-5} [atm m^3 gmol^{-1} K^{-1}]
β	Beta	Fractional burnup (atom %)	0.00001
σ_{H2}	sigmaH2	H_2 collision diameter	2.827 [Å]
σ_{H2O}	sigmaH2O	H_2O collision diameter	2.641 [Å]
M_{H2}	MH2	H_2 molecular weight	2.01594 [g mol^{-1}]
M_{H2O}	MH2O	H_2O molecular weight	18.01594 [g mol^{-1}]
τ	tau	Tortuosity factor	1
q_c	qdef	Hydrogen mole fraction in CANDU coolant	$4.1\times10^{-6*}$
x_{fs}	Xsurf	Stoichiometry deviation at pellet crack surfaces	1×10^{-4}

Table 25: List of parameters used in the 3D out-reactor fuel oxidation model

Symbol	COMSOL® constant name	Description	Value
$\kappa/\sigma_{\mathrm{AB}}$	koverepsilon	Inverse of Lenard-Jones force constant	0.00454959 K^{-1}
$a_\aleph$	a	Constant in polynomial fit for x_e	0.033107007
$b_\aleph$	b		0.268984735
$c_\aleph$	c		0.008679485
$d_\aleph$	d		-0.000622197
$e_\aleph$	e		-5.18804E-05
$f_\aleph$	f		0.020038397
$g_\aleph$	g		0.000450165
$k_\aleph$	p		-7.83442E-06
$m_\aleph$	m		1.84196E-08
$n_\aleph$	n		-7.45197E-05
$p_\aleph$	k		1.39057E-07
T_{surf}	T_surf	Fuel outer surface temperature	583 [K]
T_{heater}	T_heater	Fuel inner surface temperature	$1816^{\dagger}$ [K] and $2176^{\ddagger}$ [K]
ℓ	l	Fuel element length half	0.241 [m]
NA	a_pellet	Fuel pellet radius	0.006075 [m]
NA	Ir_bar_radius	Iridium bar radius	0.00145 [m]
N_{A}	N_Avogadro	Particles/molecules per mol	6.022×10^{23}
N_{UO_2}	N_UO2	number density of UO_2	2.444×10^{28} [particles m^{-3}]
F_{vol}	fuel_element_vol_quart	Fuel element volume	2×pi×(a_pellet^2-Ir_bar_radius^2)*ℓ[m^3]
NA	crack_tip_radius	Crack tip distance from centre	$0.001874^{\dagger}$ [m] and $0.00229^{\ddagger}$ [m]
NA	crack_width	fuel crack width	25×10^{-6} [m]
NA	ppg	pellet-pellet gap	25×10^{-6} [m]

Note: The hydrogen mole fraction[*] of the coolant was set to the hydrogen mole fraction that occurs in CANDU heavy water coolant. In reality the hydrogen mole fraction in the test loop at Stern Labs is that of high purity light water, which is lower than CANDU heavy water coolant. A lower q_c value does not change the oxidation results as discussed in Section 4.6. The T_{heater} temperature and the crack_tip_radius for the low[†] power case and for the high[‡] power case.

For further details on the 3D out-reactor fuel oxidation model see COMSOL® model report in Appendix C.

3.5.7 The Fuel Oxidation Model Applied to a Modified UO_2 Fuel Pellet Sintering Process Numerical Implementation

It is shown in Section 5.5 how hyperstoichiometric oxygen in UO_2 fuel in powder form (mixed with graphite) can have a protective effect on Zircaloy-4 loaded slotted rings exposed to iodine corrodant. This section shows how the fuel oxidation model is modified in order to compute specific superficial oxygen uptake into fully reduced UO_2 fuel pellets as a mitigation approach to I-SCC in CANDU fuel. The reason that ‘superficial’ oxygen is desired, i.e., the hyperstoichiometric oxygen is deposited on the pellet outer surface rather than distributed evenly in the fuel pellet volume, is two fold: 1.) It is desired to have the hyperstoichiometric oxygen positioned as near as possible to the graphite layer on the sheath inner surface to utilize the carbon’s chemical reducing properties as explained in Sections 1.4 and 5.2, and 2.) It is desired to keep O/U stoichiometry of the inner regions of the fuel close to 2.00 in order to maintain optimal fuel thermal and mechanical properties. It will be shown though in model results (Section 4.5.2) that the stoichiometry deviation needs to be significant in order to degrade the thermal conductivity properties of the fuel in order to substantially raise its temperature. The following superficial pellet oxidation process adds only a minor amount of hyperstoichiometric oxygen to the fuel, which does not degrade the fuel thermal properties. Hence this pellet sintering process modification should not impact fuel safety.

In the experimental part of this work in Chapter 5 the amount of oxygen added to UO_2 powdered/granule batches, which was shown to have a mitigative effect on the I-SCC of Zircaloy-4 specimens (Figure 141 and Figure 144), ranged from $0.4\text{-}8.7\times10^{-6}$ moles O_2 per cm^2 of Zircaloy specimen surface area. If the quantity 2×10^{-6} mol cm^{-2} is selected as a starting point quantity for superficial molecular oxygen (O_2) to be added to CANDU fuel pellets to mitigate I-SCC, the total amount of hyperstoichiometric oxygen per pellet can be calculated. The total internal surface area of Zircaloy in a fuel element is: $A_{\mathrm{Zircaloy}}=2\pi rl=2\pi\cdot0.6115[\mathrm{cm}]\cdot48.2[\mathrm{cm}]=185.19\ [\mathrm{cm}^2]$, so the total atomic mole amount of oxygen added to a fuel pellet is:

$$n_O = 2\left[\frac{\mathrm{atom}}{\mathrm{molecule}}\right]\cdot 2\times10^{-6}\left[\frac{\mathrm{mol}}{\mathrm{cm}^2}\right]\cdot 185.19\left[\mathrm{cm}^2\right]\cdot\frac{1}{30[\mathrm{pellet}]} = 2.469\times10^{-5}\left[\frac{\mathrm{mol}}{\mathrm{pellet}}\right] \qquad (183)$$

The following model description uses the same techniques used to model the in-reactor and out-reactor fuel oxidation described in Sections 3.5.5 and 3.5.6. In this case the fuel oxidation model applied in Figure 69 describes a reflected fuel pellet cross section (red domain) exposed to steam flow from left to right (grey domain). Eq. (18) in Section 3.2 describes the solid state diffusion of oxygen in the fuel pellet domain. The pellet O/U stoichiometry initial condition is that it is fully reduced and is equal to 2 (or x or Xdev ≈ 0). Eq. (27) describes the hydrogen mole fraction diffusion in the steam gas domain, where the Zircaloy oxidation source term $R^{ox}_{zirc\_sheath}$ in the equation equals zero (i.e., not applicable in this model). A Dirichlet boundary condition for the hydrogen mole fraction, q_{def}, is applied on boundary 1, which was determined using Gibbs energy minimization FactSage 6.4 software knowing T_{heating} and p of the water vapour. Eq. (32) describes the temperature distribution in the steam gas domain as well as in the solid pellet domain, where the heat source term Q_v equals zero. A Dirichlet temperature boundary conditions, equal to T_{heating}, is applied on boundary 1 while Neumann temperature boundary conditions equating to zero are applied on boundaries 2, 3 and 4. The inward flux terms acting in Equations (18) and (27) (for the production of hyperstoichiometric oxygen in the fuel domain and the production of hydrogen in the superheated steam domain), active on the fuel-to-steam boundary in the Figure 69, is given by Table 2.

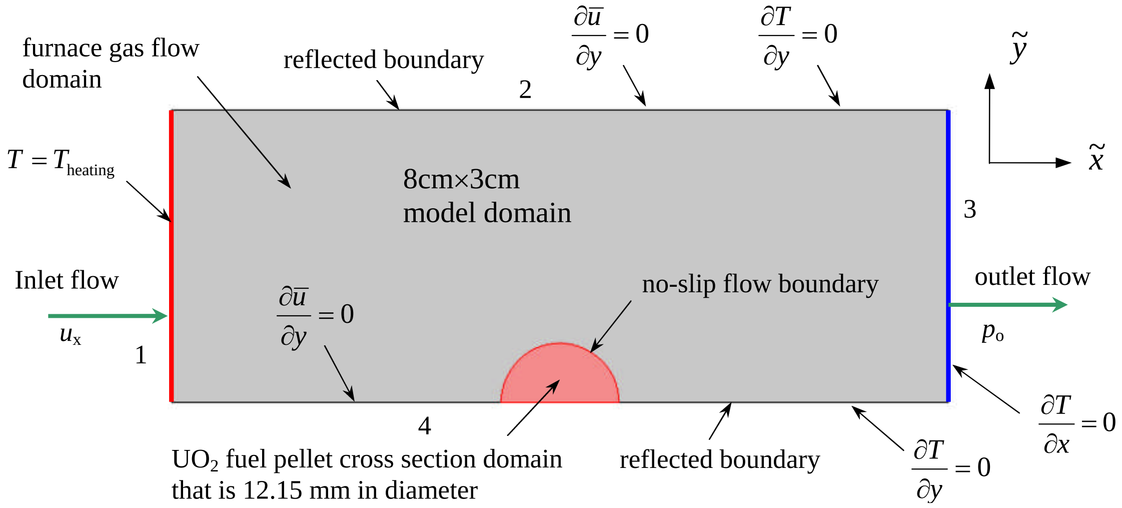

Figure 69: Schematic of the modified UO_2 sintering process model

In the typical pellet sintering process a flow of reducing gas passes over the pellets. In the presented model this is simulated by including laminar flow physics. Laminar flow was selected (rather than turbulent flow) based on the dimensionless Reynolds number calculation for water vapour flow over a flat plate, knowing the water vapour density, the viscosity, the velocity and the flow length [160].

The momentum transport of the flow is described by the weakly compressible Navier-Stokes equation, applicable for flow velocities less than Mach 0.3 (or 0.3 times the speed of sound at sea level - approximately 100 m s^{-1} in atmospheric air). Below this speed pressure expansion work done by the gas is negligible [160]. The Navier-Stokes equation (also the momentum balance equation) is given by the following:

$$\rho_g \frac{\partial \bar{u}}{\partial t} + \rho_g (\nabla \bar{u}) \bullet \bar{u} = -\nabla p + \mu \nabla \bullet (\nabla \bar{u}) + \bar{f} \tag{184}$$

where $\bar{u}$ is the velocity vector field, ρ_g is the density of the fluid, p is the pressure, μ is the viscosity, and $\bar{f}$ is a body force (typically gravity). The first term on the LHS of Eq. (184) is the unsteady acceleration term, the second term on the LHS is the convective acceleration term, the first term on the RHS is the pressure gradient, and the second term on the RHS is the viscosity term [161]. In COMSOL Multiphysics® [71] this equation is expanded somewhat and is given as:

$$\rho_g \frac{\partial \bar{u}}{\partial t} + \rho_g (\bar{u} \bullet \nabla)\bar{u} = \nabla \bullet \left[-p\bar{I} + \mu\left(\nabla \bar{u} + (\nabla \bar{u})^T\right) - \frac{2}{3}\mu(\nabla \bullet \bar{u})\bar{I} \right] + \bar{f} \tag{185}$$

where $\bar{I}$ is the identity tensor. If the flow was considered incompressible the second viscosity term with the 2/3 factor would disappear. Lastly the flow mass balance is expressed as:

$$\frac{\partial \rho_g}{\partial t} + \nabla \bullet (\rho_g \bar{u}) = 0 \tag{186}$$

Neumann velocity boundary conditions equating to zero are applied on boundaries 2 and 4. A Dirichlet velocity boundary condition, equal to u_x, is applied at the inlet of the model on boundary 1, and an ambient pressure boundary condition, p_0, is applied at the outlet of the model on boundary 3.

The oxygen mole upatake into the fuel pellet is calculated using Eq. (163), (164), and (165).

The applied mesh used in the modified UO_2 pellet sintering process model, which is composed of triangular mesh elements, is presented in Figure 70

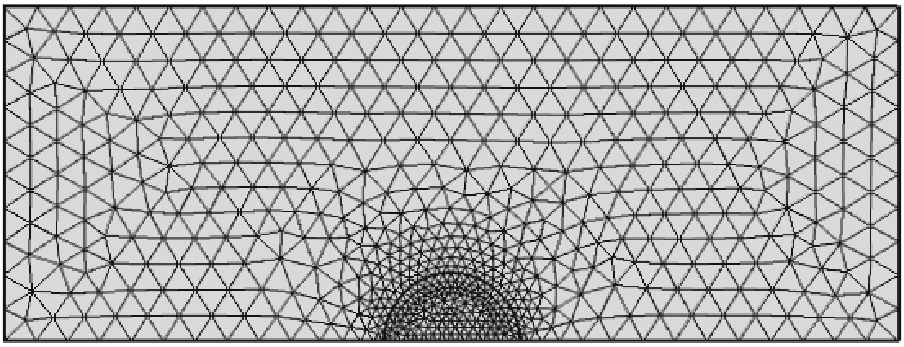

Figure 70: Applied mesh in modified UO_2 pellet sintering process model

where the number of triangular elements is 1,202. The simulated time in this model was 1000 s. The direct solver in COMSOL$^{®}$ called PARDISO was used.

The geometric discritization (or polynomial shape functions) applied to all computed physics in this model were set to quadratic. COMSOL$^{®}$ 4.3b finite element analysis software operating on a Windows 7 platform on a Sony VIAO laptop with an Intel i7-2640M CPU at 2.8 GHz with 8 GB RAM was used for this simulation. The model degrees of freedom with the mesh shown in Figure 70 was 9,873 and the computer memory required was about 882 MB.

The following table provides key model parameters used in the modified UO_2 fuel pellet sintering process:

Table 26: Parameters used in the modified UO_2 fuel pellet sintering process

Symbol	COMSOL® constant name	Description	Value
ρ_{TD}	theoretical_density	the theoretical fuel pellet density	10.96 [g cm^{-3}]
$\rho_{\mathrm{s\_new}}$	density_manf	Manufactured fuel density	10.6 [g cm^{-3}]
NA	porosity_manf	Manufactured fuel porosity	$1-\dfrac{\text{density\_manf}}{\text{theoretical\_density}}$
p_t	PT	Gas pressure	1 [atm]
p_0	p0	Ambient pressure	101325 [Pa]
R	Rgas	Universal gas constant	8.205×10^{-5} [atm m^3 $gmol^{-1}$ K^{-1}]
NA	Rsteam	Steam gas constant	461.52 [J kg^{-1} K^{-1}]
β	Beta	Fractional burnup (atom %)	0.00001
σ_{H2}	sigmaH2	H_2 collision diameter	2.827 [Å]
σ_{H2O}	sigmaH2O	H_2O collision diameter	2.641 [Å]
M_{H2}	MH2	H_2 molecular weight	2.01594 [g mol^{-1}]
M_{H2O}	MH2O	H_2O molecular weight	18.01594 [g mol^{-1}]
q_c	qdef	Hydrogen mole fraction in the oxidizing steam	$2.4\times10^{-4*}$
x_{fs}	Xsurf	Stoichiometry deviation at pellet surface	1×10^{-4}
$\kappa/\sigma_{\mathrm{AB}}$	koverepsilon	Inverse of Lenard-Jones force constant	0.00454959 K^{-1}
$a_\aleph$	a	Constant in polynomial fit for x_e	0.033107007
$b_\aleph$	b		0.268984735
$c_\aleph$	c		0.008679485
$d_\aleph$	d		-0.000622197
$e_\aleph$	e		-5.18804E-05
$f_\aleph$	f		0.020038397
$g_\aleph$	g		0.000450165
$k_\aleph$	k		-7.83442E-06
$m_\aleph$	m		1.84196E-08
$n_\aleph$	n		-7.45197E-05
$p_\aleph$	p		1.39057E-07
T_{heating}	T_heating	Steam inlet temperature	1523 [K]
γ	ratio_steam	Specific heat ratio	1.327
N_{A}	N_Avogadro	Particles/molecules per mol	6.022×10^{23}
$N_{\mathrm{UO_2}}$	N_UO2	number density of UO_2	2.444×10^{28} [particles m^{-3}]

Table 26: Parameters used in the modified UO_2 fuel pellet sintering process

Symbol	COMSOL® constant name	Description	Value
u_x	u_flow	Fluid velocity	0.4 [m s^{-1}]
NA	pellet_radius	Fuel pellet radius	0.006075 [m]
NA	pellet_length	Fuel pellet length	0.016 [m]
F_{vol}	pellet_vol	Fuel pellet volume	1.855×10^{-6} [m^3]

Note: The hydrogen* mole fraction of the oxidizing steam was determined by using Gibbs energy minimization software FactSage 6.4 with parameters T_{heating} and p_t.

Summary of Chapter 3:

- The out-reactor experimental set-up at Stern Laboratories and the design of the out-reactor defected fuel element were described and discussed (Section 3.1).

- The fuel oxidation model, adapted to the out-reactor defected fuel experiment, was then discussed (Sections 3.2 and 3.3). The thermal properties of the out-reactor fuel element were defined and details of the 2D r-θ and 3D model geometries were provided. Information on modeling the discrete fuel cracks and fuel-to-sheath gap was given. Also, the ohmic heating theory applied in one of the 2D r-θ models was explained.

- Next, a solid mechanics model with discrete fuel cracks was discussed (Section 3.4). The theory of the J integral was explained, and was used as a way to assess the stress intensity factor around a fuel crack tip. By comparing to the fracture toughness of the fuel material (a material property), conditions suitable for crack propagation could be determined.

- Lastly, the finite element analysis theory was briefly introduced and explained (Section 3.5). Each model (six models in all) was numerically implemented using COMSOL Multiphysics®.

CHAPTER 4 MODEL RESULTS

4.1 Modeled and Measured UO_2 Thermal Conductivity

The thermal conductivity of the fuel is an important parameter to accurately model the temperature distribution in the fuel. The amount of fuel oxidation is to a great extent temperature dependent and so temperature distribution in the fuel is important. As such, for reference purposes and as a ‘sanity check’ the model used for the uranium dioxide thermal conductivity is compared to the experimental data shown in a review by Carbajo *et al.* [100] in Figure 71. A similar plot is provided in a review by Fink [162].

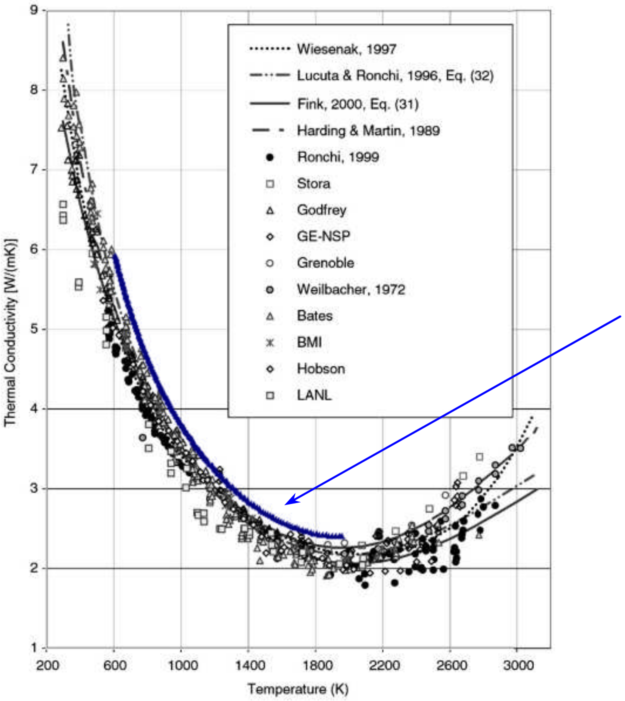

modeled UO_2 thermal conductivity

Figure 71: Comparison of UO_2 thermal conductivity in the fuel oxidation model with no burnup to experimental data as a function of temperature, at 95% theoretical density and with no burnup, taken from [100]

It can be seen from the plot that the modeled thermal conductivity (blue curve), as taken from the work of Higgs *et al.* [29] and Lucuta *et al.* [97], is ≈8-10% above the thermal conductivity provided by other workers. The modeled blue curve was generated from the fuel oxidation model when the UO_2 fuel theoretical density was set at 95% with zero fuel burnup.

A comparison was made between the Higgs formulation for UO_2 thermal conductivity [29] (that considers temperature, oxygen stoichiometric deviation, fuel burnup, and fuel porosity) and the MATPRO formulation [110] (that considers only temperature and fuel porosity). Generally, MATPRO is a report that describes the material properties, correlations, and computer sub codes developed for use with various light water reactor accident analysis computer programs. MATPRO is often referred to as an 'industry standard' though it was not formally developed as such. In using the Higgs approach (which is based on the work by Lucuta *et al.* [97] and Ellis *et al.* [98]) the UO_2 fraction from theoretical density was set to ≈ 0.97 and the fractional burnup was set to 1×10^{-8} (≈ 0). The linear power of the fuel element was set to 75 kW m^{-1} and the fuel surface temperature was set to 580 K. The latter two values are not necessarily realistic in CANDU fuel but were used in a model similar to that in [29], or that described in Section 3.5.5, to plot UO_2 thermal conductivity as a function of temperature with an extended temperature range.

As can be seen in Figure 72 the thermal conductivity of unirradiated UO_2 is slightly higher at the cooler end of the graph (near 580 K) using the Higgs formulation (blue curve) compared to using the MATPRO formulation (yellow curve); a difference of about 10%. At the warmer end of the graph both formulations for UO_2 thermal conductivity agree quite well in the temperature range of 1500-1800 K. At a higher temperatures range between 1800 K and 2300 K the Higgs and MATPRO formulations start to diverge from one another. Furthermore, when the UO_2 thermal conductivity (Eq. (35)) includes k_{rad} (Eq. (39)), which is the radiative contribution to the fuel thermal conductivity, there is an increase in the fuel thermal conductivity between $\approx$1200-2300 K, as shown by the red curve. Thus, the fuel thermal conductivity, which considers the Higgs formulation and k_{rad} (the latter previously neglected by Higgs [29]), is slightly higher than the MATPRO formulation and the experimental measurements (Figure 71), through the whole temperature range (580-2300 K). Although this thermal conductivity curve (used in the fuel oxidation models presented in this work) may be higher than in reality, this difference is not substantial and is not expected to substantially affect the outcome of the fuel oxidation computation.

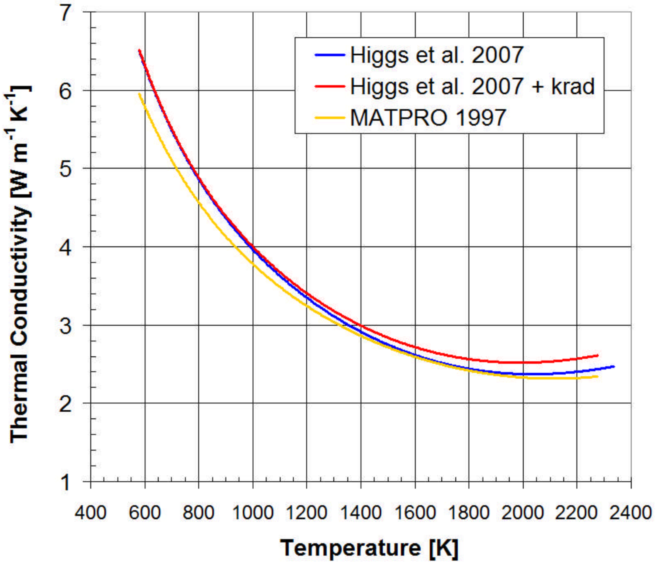

Figure 72: Thermal conductivity of UO_2 using Higgs [29] formulation (blue curve) and MATPRO [110] formulation (red curve) for fuel at 97% theoretical density

Nevertheless, the following correction quantity δ_{corr} in kW m^{-1} K^{-1} can be subtracted from k for UO_2 (Eq. (35)) so that the red curve matches the MATPRO formulation more closely in Figure 72 for the temperature range of 535-2300 K. This correction quantity is added for reference purposes only and was not used in this work.

$$\delta_{\text{corr}} = -2.784\times10^{-10}T^3 + 1.637\times10^{-6}T^2 - 2.963\times10^{-3}T + 1.82 \qquad (187)$$

4.2 Fuel Oxidation Model Results

The following simulation solves for the fuel oxidation in a 2D r-θ geometry. This geometry was less computationally expensive than a 3D one, however it tends to over-predict the extent of fuel oxidation as the defect length is not specified in the axial direction (where in the 2D representation, it is a slit as long as the simulated element length).

4.2.1 Closed Fuel-to-Sheath Gap 2D *r-θ* Fuel Oxidation Model Results

The temperature distribution and oxygen stoichiometric deviation (x or Xdev) predictions using the 2D r-θ model, after 2 weeks of heating, are shown in Figure 73 (a) and (b), respectively. The radial gradient in the temperature and Xdev plots can be observed in these 2D plots as well as small azimuthal variations. As can be seen the maximum oxygen stoichiometry deviation occurs in the fuel that is nearest the iridium bar heater (red area), while near stoichiometric fuel results in the coolest regions away from the fuel centre (dark blue area).

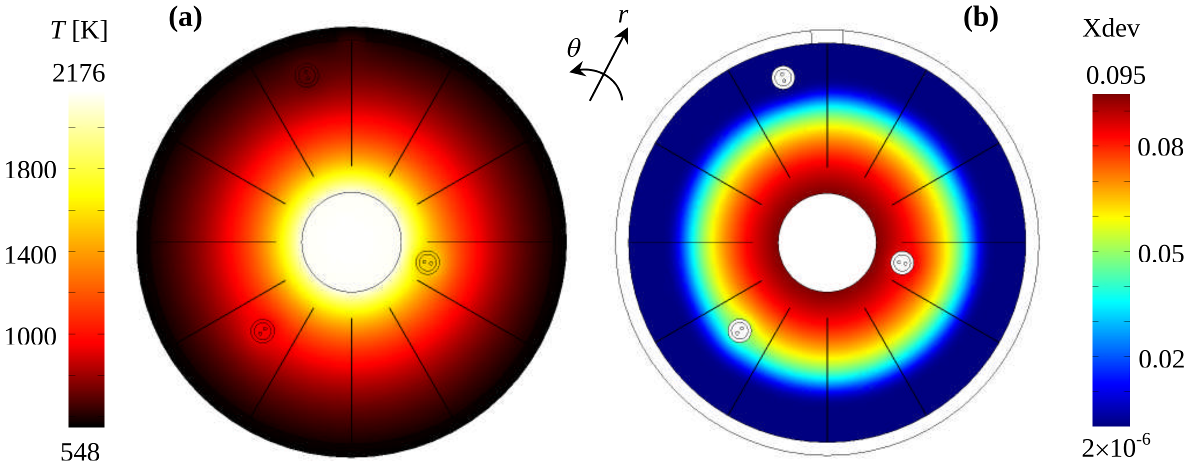

Figure 73: Temperature distribution plot (a) and oxygen stoichiometry deviation distribution plot (b) at 2 weeks of simulated heating time in the 2D *r-θ* closed fuel-to-sheath gap fuel oxidation model

Two temperature radial plots, after two weeks of heating, are provided in Figure 74. The purple dashed line runs through the ungrounded Type-R thermocouple nearest the iridium bar heater (TC1 in Figure 18) and the solid blue line runs through the fuel element without the presence of a thermocouple. The plot demonstrates a nearly homogenous temperature distribution in the iridium bar heater, a steep temperature gradient in the UO_2 fuel and a small temperature drop in the sheath. Observing the sheath location more carefully one notices the slight concave facing down temperature profile, which is due to the modeled sheath electrical power generation.

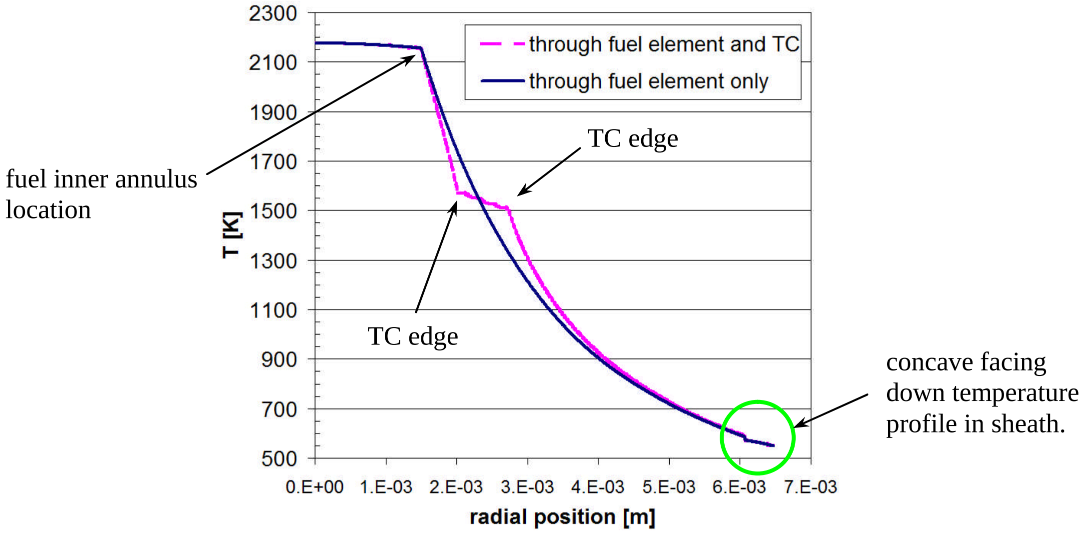

Figure 74: Radial temperature profile running though the fuel element with a thermocouple (dashed purple line) and without a thermocouple (solid blue line) in the 2D *r-θ* closed fuel-to-sheath gap fuel oxidation model

The small but steep temperature drop in the fuel-to-sheath gap is depicted more closely in Figure 75 (a). The temperature drop is small, less than 15 degrees, due to the fuel-to-sheath gap being considered closed, or set to 1 μm wide, and filled with 100 bar steam. In this situation the heat conductivity of the gap is a combination of both solid and fluid heat transfer, as explained in Section 3.3.2. The temperature through the thermocouple is presented in a close-up plot in Figure 75 (b), where there is a stepwise drop through the thermocouple. The thermocouple sheath is a combination of platinum and rhodium, which conduct heat relatively well so there is only a slight drop in temperature. MgO is used to electrically isolate the thermocouple from the UO_2 material, which is a requirement of the experiment. This creates the steeper temperature drop in this material than in the metallic regions of the thermocouple. The temperature difference of the two thermocouple wires is over 20 degrees in this configuration. This may be important to consider when analyzing the experimental temperature measurements because the temperature increase due to fuel oxidation can be less than this temperature difference for the given duration of the experiment.

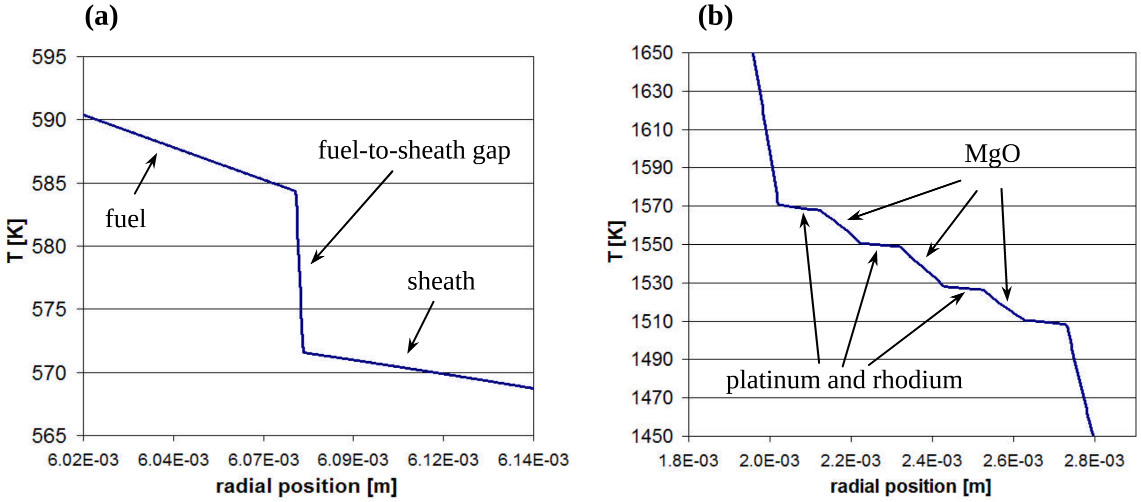

Figure 75: Closeup view of (a) fuel-to-sheath gap temperature profile and (b) thermocouple temperature profile nearest the iridium bar heater in the 2D *r*-*θ* closed fuel-to-sheath gap fuel oxidation model

Before completing the description on the fuel element radial temperature profile model results, the effect of the gap between the fuel pellets and the iridium bar heater is briefly discussed. The temperature distribution and profile model results shown in Figure 73 (a) and Figure 74, respectively, assume there is no gap between the iridium bar heater and the fuel pellets. In reality though, a gap does exist. Based on the engineering dimensions and tolerances between these two manufactured parts, a maximum possible gap was estimated to be ≈60 μm, without considering thermal expansion effects (i.e., in its room temperature state with a change in the component dimensions). Figure 76 shows the radial temperature profile in the fuel element when this gap is included in a model that considers heat transfer by conduction only. In the plot it can be observed that there is a >400 degree increase from the fuel inner annulus surface to the iridium bar heater surface. This though does not have a substantial impact on the 2D r-θ fuel oxidation model described in Section 3.5.1 that does not include this gap. This is because the temperature of the fuel inner annulus in the model that does include this gap (Figure 76) is similar to the temperature of the fuel inner annulus in the model that does not consider this gap (Figure 74). Since it is the fuel temperature (and not the iridium bar heater temperature) that determines the extent of oxidation in the fuel, the fuel-to-iridium gap was neglected in the numerical implementation of the 2D r-θ fuel oxidation model (Section 3.5.1) as well as in the fuel solid mechanics and crack propagation model (Section 3.5.3).

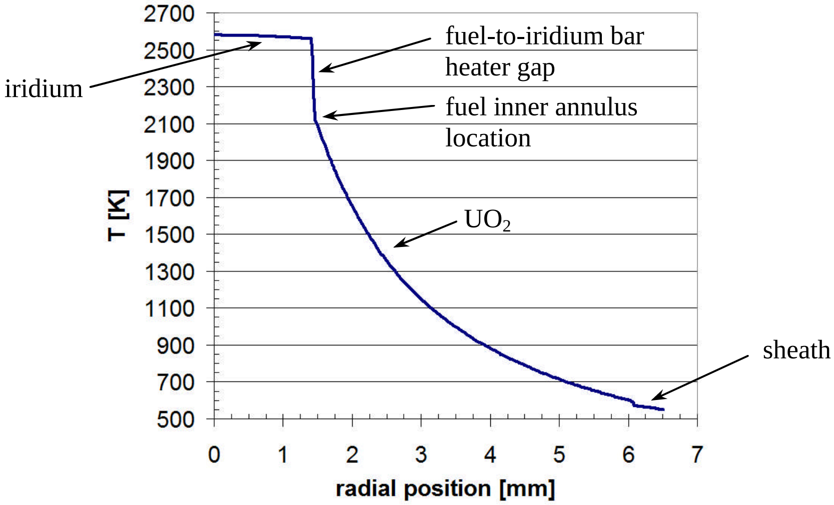

Figure 76: Radial temperature profile in the 2D r-θ closed fuel-to-sheath gap that considers a 60 μm fuel-to-iridium heater bar gap

Nevertheless modeling the iridium bar heater and the fuel-to-iridium gap may be very important from an engineering standpoint of the experiment. Allowing the Ir central heater to reach such high temperatures can shorten its lifespan, which is undesirable. The computation of this temperature jump in the gap was achieved using COMSOL® 4.3b heat transfer with surface-to-surface radiation physics, since at high temperatures a greater fraction of the heat is transported via radiation (without which the modeled temperature of the iridium bar heater would be higher than that shown in Figure 76).

Recall that Figure 73, Figure 74 and Figure 75 show the radial temperature profiles in the out-reactor fuel. The radial temperature is plotted at three different times in Figure 77: 6 hours, 1 day, 4.6 days, and 2 weeks of heating. In Figure 77 (a), the temperature varies slightly with time, especially in the fuel element interior, while the temperature in the peripheral region is steady due to a constant coolant boundary condition. Figure 77 (b) is a closeup plot near the location of the thermocouple (TC1 in Figure 18 and Figure 20) nearest the iridium bar heater indicated by the vertical dotted line.

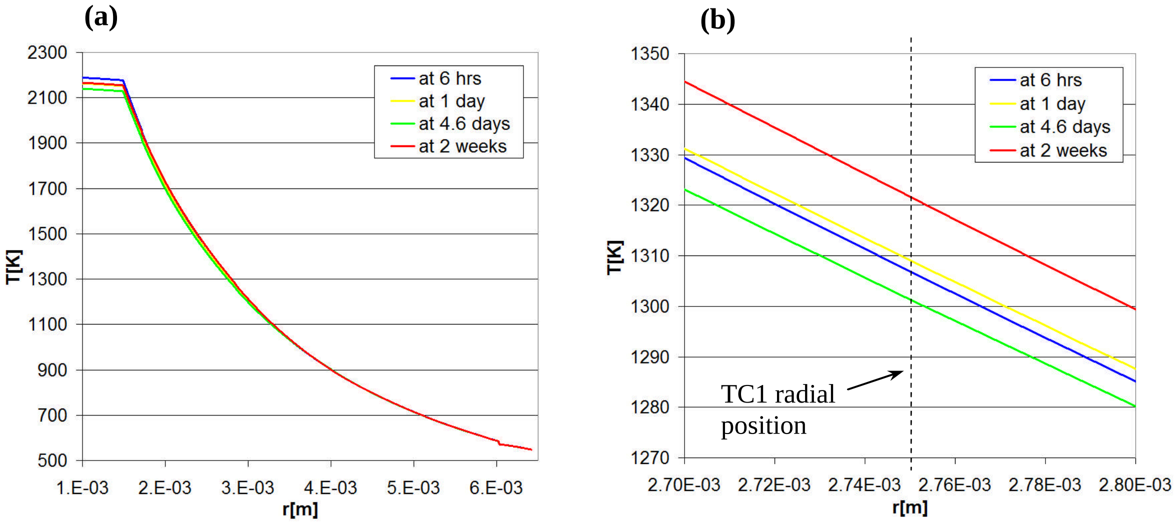

Figure 77: Radial temperature plots at different times

During the first 6 hours to one day of heating, the temperature at the first thermocouple position reaches 1310 K (blue and yellow curves) but then drops to just above 1300 K (green curve) after four days. As the simulation continues to two weeks, the temperature rises again to just above 1320 K (red curve). The initial drop in temperature is not expected when considering that the fuel is being oxidized throughout the simulation. However, this behavior can be explained where Figure 78 shows the UO_{2+x} thermal conductivity and oxygen stoichiometric deviation at a radial location (where the innermost thermocouple is positioned at a ≈2.75 mm radius) versus a 2-week heating simulation. As can been seen, the thermal conductivity in the UO_2 pellet at this location (solid blue curve) initially rises to 3.16×10^{-3} kW m^{-1} K^{-1} for 3.5 heating days but then starts to decay after this time. The oxygen stoichiometric deviation is also plotted (dashed purple curve), which shows that the oxygen deviation content in this location continuously increases, faster in the beginning but then slower at the end of 14 days of simulation. The reason the thermal conductivity initially rises and then falls is due to the nature of the phonon contribution (lattice vibration) equation (see Eq. (36)).

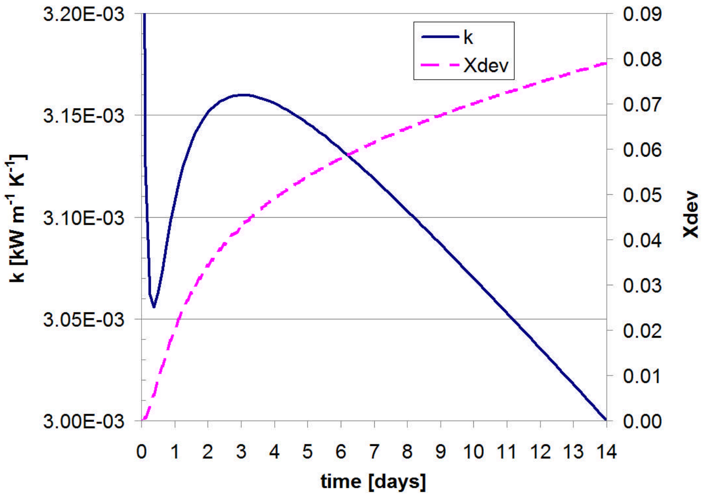

Figure 78: The thermal conductivity and stoichiometric deviation at the inner most thermocouple location in the fuel for a heating time up to 2 weeks

In Figure 73 (b) it appears that the stoichiometric oxygen deviation is symmetric in the azimuthal direction but a closer look shows some variation. This small azimuthal non-symmetry is shown Figure 79, where the solid blue line represents the radial oxygen stoichiometry deviation in the fuel and the dashed purple line represents the radial oxygen stoichiometry deviation in the fuel while passing through a thermocouple nearest the iridium bar heater. Interestingly, the results show higher oxygen deviation values in the vicinity of the thermocouple, away from the pellet centre, due to the higher thermal conductivity of the thermocouple causing higher local fuel temperatures.

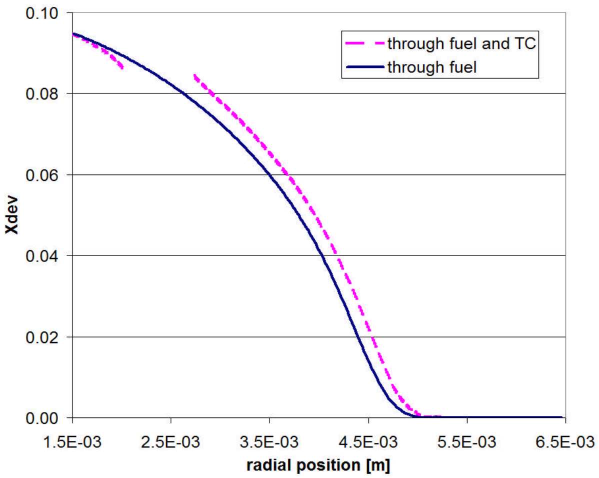

Figure 79: Oxygen stoichiometry deviation radial plot, through fuel only and through the thermocouple and fuel

The amount of fuel oxidation after two weeks of heating is summarized in Table 27. Here the maximum stoichiometric deviation is provided as well as the molar number of oxygen atoms that have been taken up by the fuel in Eq. (165). The maximum temperature at the iridium bar heater is also indicated at 1 day, 4.6 days, and 2 weeks of heating.

Table 27: Closed fuel-to-sheath gap 2D *r-θ* fuel oxidation model result at 2 weeks of heating providing maximum Xdev and *T* values

Xdev$_{max}$ at 2 weeks	n_O [mol] at 2 weeks	T_{max} at 1 day [K]	$T_{UO2\text{-}Ir}$ at 1 day [K]	T_{max} at 4.6 days [K]	T_{max} at 2 weeks [K]
$0.095\pm^{0.005}_{0.003}$	$0.068\pm^{0.010}_{0.009}$	$2170\pm^{10}_{300}$	$2150\pm^{10}_{300}$	$2150\pm^{10}_{300}$	$2180\pm^{10}_{300}$

As can be seen there is a ≈20 degree drop in the max temperature at the iridium bar centre between 1 day and 4.6 days of heating. The temperature then rises by ≈30 degrees at 2 weeks. This change in temperature, due to fuel oxidation, was also seen in the vicinity of the innermost thermocouple as plotted in Figure 77 (b). The computed mole uptake of oxygen atoms into the fuel matrix of the full length out-reactor fuel element is also indicated in the table (which is equivalent in mass to ≈1 g).

The computed electrical powers generated in all three conductors (where UO_2 is considered as an electrical semi-conductor at the planned operating temperatures of the test) is provided in Table 28. The electrical power is indicated as the total power in kW and power density in kW m^{-3} (for a 0.482 m fuel element length) after 2 weeks of electrical heating.

Table 28: Computed electrical power used to heat the modeled fuel element simulator

P_{Iridium} [kW]	P_{UO2} [kW]	P_{Zircaloy} [kW]	P_{Iridium} [kW m^{-3}]	P_{UO2} [kW m^{-3}]	P_{Zircaloy} [kW m^{-3}]
$12.0 \pm^{0}_{1.7}$	< 0.1	$10.5 \pm^{1.1}_{0}$	$(3.5 \pm^{0}_{0.5})\times10^{6}$	$< 0.1\times10^{6}$	$(1.4 \pm^{0.2}_{0})\times10^{6}$

For comparison to in-reactor fuel element linear powers, the electrical power is indicated for each conductor separately and as a total linear power in Table 29. Generally the heating power levels were stable throughout the simulation though there was a slight increase in the Zircaloy sheath electrical power as the model simulation progressed.

Table 29: Electrical power in fuel-element expressed as linear power

$P_{\text{linear\_total}}$ [kW m^{-1}]	$P_{\text{linear\_iridium}}$ [kW m^{-1}]	$P_{\text{linear \_UO2}}$ [kW m^{-1}]	$P_{\text{linear\_Zircaloy}}$ [kW m^{-1}]
$47 \pm^{2}_{4}$	$25 \pm^{0}_{4}$	< 0.1	$22 \pm^{2}_{0}$

From the above tables, the expected heat generation in the UO_2 fuel is negligible and the main heating power occurs in the iridium bar and Zircaloy sheath. Since the power generated in the Zircaloy sheath is mostly released to the coolant, the main heating of the UO_2 fuel is provided by the iridium bar heater. The actual linear power of the out-reactor fuel element is thus expected to be ≈25 kW m^{-1} and not the total linear power of ≈47 kW m^{-1}. It should be noted here that the model assumed a constant electrical current input of 1085 A. In reality this may vary somewhat.

Before continuing on with the model results a few words are given on model result uncertainties. There can be many sources of uncertainties in the out-reactor fuel oxidation model, such as the uncertainties in the thermal properties of the modelled materials (such as the fuel thermal conductivity) or the uncertainties in the fuel oxidation equations, some of which are not known or not published. As a result best estimate model results are presented. Nevertheless, two sources of error were quantified to provide the uncertainties in the 2D r-θ fuel oxidation model results shown in Table 27, Table 28, and Table 29. (i) The first source of error considered was the Zircaloy electrical conductivity. In Section 3.3.3 three equations were presented for this quantity (Eqs. (83), (85), and (86)). Eq. (86) provided the lowest electrical conductivities for the Zircaloy sheath, which promoted increased electrical current flow through the iridium bar heater and thus increased the inner fuel temperature and hence fuel oxidation. To derive a lower-bound for fuel oxidation Eq. (83) (for zirconium) was selected instead, which provided the highest electrical conductivities for the sheath. (ii) The second source of error considered was the crack depth, which was used to derive an upper-bound uncertainty for fuel oxidation. In the regular model the crack depth was set so that crack tips were located in the fuel at a temperature equal to 1250 °C. To increase fuel oxidation the crack depth was modified so that the crack tips were located at the increased temperature of 1300 °C. This can be justified, since the transition between elastic fuel (where there are fuel cracks) to plastic fuel (where no cracks are believed to exist) occurs between 1200-1400 °C (refer to Sections 1.5, 3.2, and 3.5.1).

For the results presented in Table 27, all of the radial fuel cracks in the model provide a pathway for fuel oxidation; specifically, the flux terms, specified in Table 2 in the solid state oxygen diffusion equation Eq. (18) and in the gas diffusion equation Eq. (27), are active at all of the fuel-to-gas interfaces in the twelve radial cracks. But to define all the radial cracks in the model is labor intensive and can be complicated to mesh and to compute in a 2D model, and even more so in a 3D model. The question then arose what would be the extent of fuel oxidation in the 2D r-θ model if only some of the radial cracks near the sheath defect participated in fuel oxidation. Figure 80 provides the oxygen stoichiometry deviation distribution result using the 2D r-θ fuel oxidation model when only five of the 12 radial cracks were included.

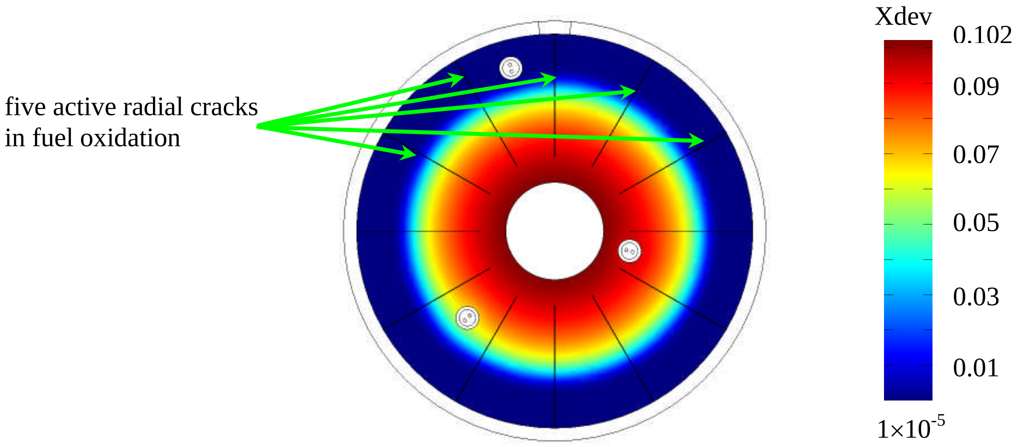

Figure 80: The oxygen stoichiometry deviation distribution plot after 2 weeks of simulated heating in a closed fuel-to-sheath gap fuel oxidation model with only five active radial fuel cracks in the fuel oxidation

Table 30 provides the oxidation and maximum temperature results for this 2D r-θ model. As can be seen, when compared to the results in Table 27, the maximum stoichiometry deviation was 7.4% higher and the average oxygen molar uptake was 22.1% higher than the case where all radial fuel cracks were included in the model (i.e., that included flux terms).

Table 30: Closed fuel-to-sheath gap 2D r-θ fuel oxidation model results when only five radial cracks near the sheath defect include oxidation flux terms

Xdev_{max} at 2 weeks	n_O [mol] at 2 weeks	T_{max} at 1 day [K]	T_{max} at 4.6 days [K]	T_{max} at 2 weeks [K]
$0.102\pm^{0.005}_{0.003}$	$0.083\pm^{0.010}_{0.009}$	$2160\pm^{10}_{300}$	$2140\pm^{10}_{300}$	$2200\pm^{10}_{300}$

Also observed was that the maximum temperature after 2 weeks of heating was ≈20 degrees higher than the case where all 12 radial cracks were included in the model (Table 27), due to the increased fuel oxidation. Initially this result may seem counter intuitive. But when consideration is made that the UO_2 fuel is being reduced as well as being oxidized, it can be shown that more oxidation is occurring in this case, since there are no active cracks in the hydrogen rich domain away from the sheath defect. The following elaborates on this observation.

The kinetic reaction rate for either fuel oxidation or reduction is computed by solving Eq. (25), which can be compared graphically at different azimuthal locations and at different times. Figure 81 (a) shows the computed reaction rate in the radial fuel crack right under the sheath defect at the 12 o'clock location (refer to Figure 38) at two different times. At 6 hours of heating (blue solid line), the maximum reaction rate was as high as 1.12×10^{-3} moles O or H_2 m^{-2} s^{-1} at the pre-set crack tip.

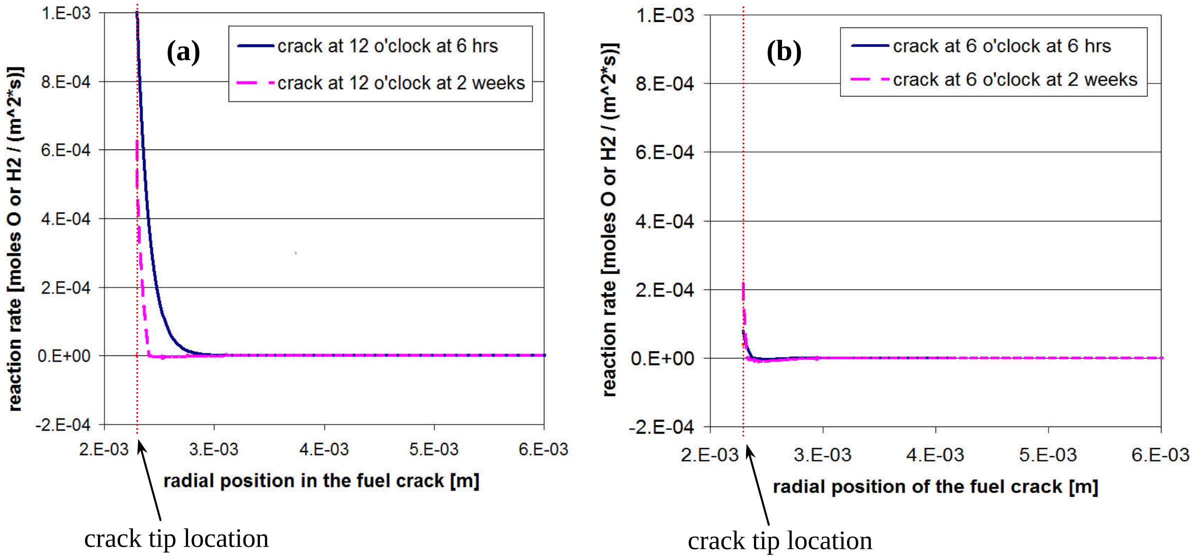

Figure 81: Reaction rate comparison in the fuel element at two different times in the radial crack positioned at (a) 12 o'clock near the sheath defect and at (b) 6 o'clock

The reaction rate decays quickly to values approaching zero as the distance increases along the radial crack away from the fuel element centre. The reason for this drop off is due to the steep radial temperature gradient in the out-reactor fuel element and due to the nature of the reaction rate, which is an Arrhenius exponential decay function in Eq. (22). At two weeks of heating at the 12 o'clock radial crack over a radial distance of only 0.36 mm away from the crack tip, there was >200° degree drop, which reduces the oxygen surface exchange rate coefficient α by about 90%.

Referring again to Figure 81 (a), as the simulation heating time increases to 2 weeks (purple dashed line), the maximum reaction rate drops to only 6.24×10^{-4} moles O or H_2 m^{-2} s^{-1}

and the radial distance in the crack over which oxidation is occurring (positive values) becomes more limited to the immediate crack tip location. This can be compared with the reaction rate at the 6 o’clock location in Figure 81 (b) (refer again to Figure 38). It can be noticed at this remote crack location (the most distant radial crack from the sheath defect) the reaction rate is almost an order of magnitude lower than at the 12 o’clock location (Figure 81 (a)), for both 6 hours and 2 weeks of heating.

To illustrate the reducing reaction rates, which were not as clear as the oxidation rates plotted in Figure 81, the reaction rates in the radial cracks at the 12 and 6 o’clock positions for 2 weeks of heating are plotted in Figure 82. The *y* axis range was reduced in order to emphasize reducing reaction rates, which are negative in value. As expected, the reaction taking place in the 12 o’clock position (solid blue curve) is a combination of two reaction zones: a thin but relatively sharp oxidation rate zone very close the crack tip and a broader reducing rate zone further away from the crack tip indicated by a local minimum.

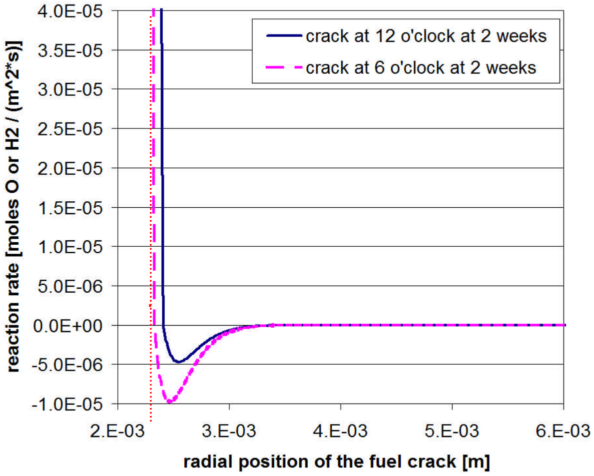

Figure 82: Comparison of reaction rates at two different locations in the radial cracks positioned at 12 o’clock near the sheath defect (blue curve) and at 6 o’clock away from the sheath defect (purple dashed curve)

The 6 o’clock crack (dashed purple curve) shows similar behavior to the 12 o’clock but the 6 o’clock crack shows a broader and deeper reducing reaction zone. In other words more fuel reduction is occurring in the more distant 6 o’clock position radial crack. Thus the 2D r-θ model shows that the fuel oxidation reaction rates are azimuthal and radial crack position dependent in relation to the defect location.

The reason for the reduced oxidation / increased reduction reactions away from the sheath defect is due, in part, to the high hydrogen mole fraction. When the q value (or the hydrogen mole fraction in the cracks) is high the reaction rate for fuel oxidation in Eq. (21) is low and for fuel reduction in Eq. (23) is higher. In Figure 83 q is plotted along the 12 o’clock and 6 o’clock positioned radial cracks at 6 hours and 2 weeks of heating times. In Figure 83 (a) the hydrogen mole fraction in the 12 o’clock position, at the crack tip, is generally 2-4 orders of magnitude greater than the boundary condition q_c (see Table 12) at the sheath defect location. In the 6 o’clock position in Figure 83 (b) the hydrogen mole fraction is relatively high and is constant along the crack length. In both figures the hydrogen mole fraction is also higher at the start of the simulation (at 6 hours) than at the end of the simulation (at 2 weeks).

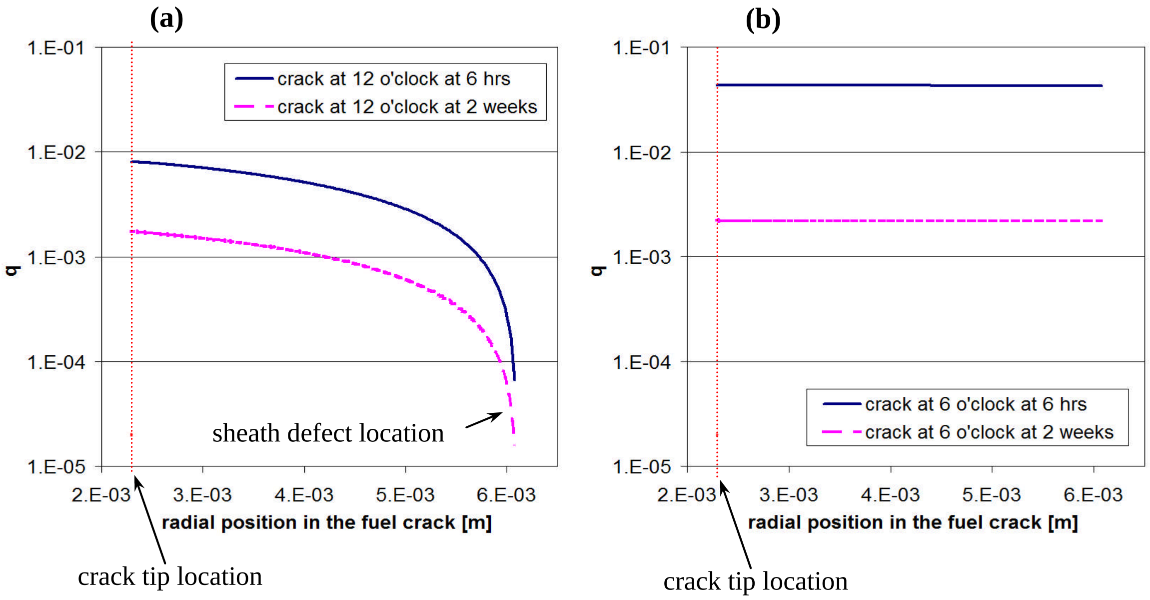

Figure 83: The hydrogen mole fraction plotted along the radial cracks at positions (a) 12 o’clock and (b) 6 o’clock in the 2D r-θ (closed fuel-to-sheath gap) fuel oxidation model

This is because the oxidation process is faster in the beginning of the simulation and so the hydrogen production is also increased. Although the model does not reach steady-state equilibrium in two weeks of heating, the oxidation rates do slow down as was observed in Figure 81 (a).

The effect of the non-azimuthal symmetric reaction rate can be demonstrated by plotting the oxygen deviation distribution during the first few minutes of the heating/oxidation simulation. Figure 84 provides the oxygen stoichiometric deviation after 135 seconds into the simulation. As can be seen the oxygen deviation is at a maximum near the sheath defect (at the 12 o’clock position) where Xdev=4.3×10^{-4}.

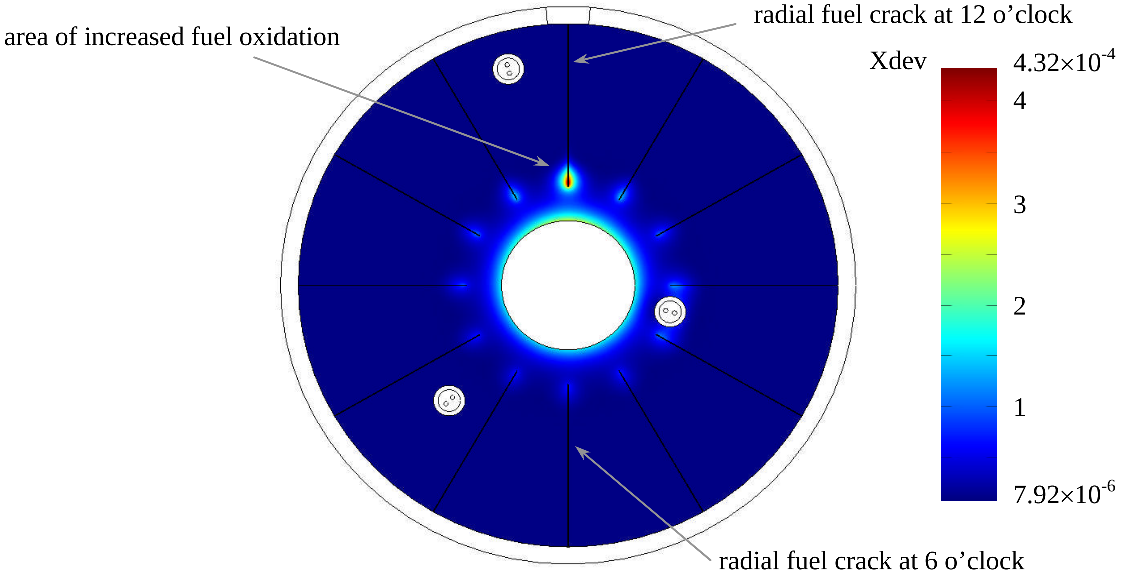

Figure 84: Oxygen stoichiometry deviation distribution result after 135 seconds of heating time in the 2D *r-θ* (closed fuel-to-sheath gap) fuel oxidation model

The model simulation provides the temperature distribution in the out-reactor fuel element while predicting the required electrical power distribution in the element that will ensure a measureable fuel oxidation in the test. With the fuel-to-sheath gap closed, the thermal resistance between the fuel and the sheath will be at its lowest level requiring an optimal electrical heating power ($25\pm^{0}_{4}$ kW m^{-1}, see Table 29). The amount of fuel oxidation is over-predicted, since the sheath defect in the 2D r-θ model extends over the element length (as an artifact of the 2D r-θ representation). Nevertheless, this model provides an upper-bound assessment and it is useful in showing the azimuthal effects in relation to the sheath defect location. The effect of fuel oxidation on the thermal conductivity of the fuel is demonstrated in the radial-temperature plots. As the fuel oxidizes, the thermal conductivity is reduced, resulting in an increase in the fuel temperature. Lastly, it is shown that if only part of the radial cracks near the sheath defect participate in the fuel oxidation, the overall outcome is a slight increase in the amount of fuel oxidation.

4.2.2 Open Fuel-to-Sheath Gap 2D *r-θ* Fuel Oxidation Model Results

For the open gap model, two parametric case studies were performed:

(i) A study case including four different fuel-to-sheath gap (ftsg) dimensions with a common crack width dimension was modeled.

(ii) A study case including four different crack width dimensions and a common fuel-to-sheath gap dimension was modeled.

Both study cases change the geometry of the steam domains, and hence the hydrogen diffusion rates are changed. This in turn can affect fuel oxidation. The radial temperature distribution and resulting oxidation are presented for these two cases.

The purpose of case study (i) is to compare the effect of different gap sizes on the amount of fuel oxidation, since the gap size affects hydrogen gas diffusion. In this case, the radial crack dimension was pre-set to 20 μm wide (as compared to the 15 μm wide fuel cracks in the closed gap model in Section 4.2.1). The ftsg was set to 1, 3, 10, and 20 μm, the crack depth was set to 2.29 mm (the distance from the pellet centre and the crack tip), and the iridium bar heater power was set to various powers. Figure 85 (a) shows the temperature and (b) the oxygen stoichiometric deviation results after two weeks of heating for the case where the ftsg was set to 3 μm and the Ir heater power was set to 3.26×10^{6} kW m^{-3}.

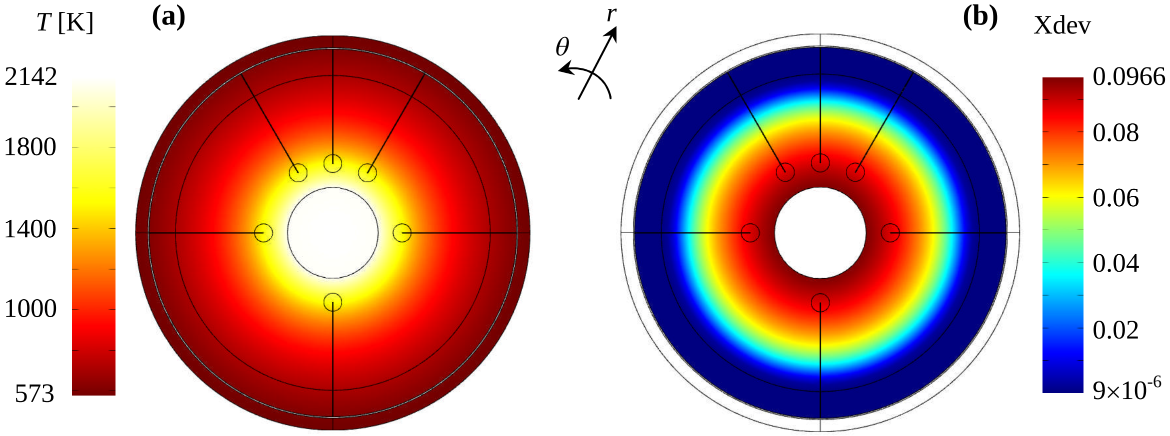

Figure 85: (a) Temperature distribution plot and (b) oxygen stoichiometry deviation distribution plot at 2 weeks of simulated heating time in a 2D *r-θ* fuel oxidation model with a 3 μm open ftsg

The radial temperature plot of the above mentioned model with a 3 μm ftsg is given by the purple curve in Figure 86. The vertical dotted line in the plot shows the location of the common radial crack tips and the horizontal dotted line indicates the common crack tip temperature. The remaining 1, 10, and 20 μm ftsg modeled radial temperatures for this case study are also plotted in Figure 86. Oxidation and reduction reactions occur to the right side of the vertical dotted line where the radial cracks exist, where the temperature is approximately the same in the immediate vicinity of the crack tip (≈1523 K). However, further away from the crack tip (nearer the fuel pellet surface) the fuel temperature changes. In the 20 μm ftsg model (yellow curve) the temperature is higher in the pellet outer regions compared to the 1 μm ftsg model (blue curve). But this change in temperature in the fuel outer regions is not significant as far as fuel oxidation is concerned, which is discussed in Section 6.1. On the left side of the vertical dotted line in Figure 86, no reactions occur (due to a lack of fuel cracks), except for solid state oxygen diffusion in the fuel.

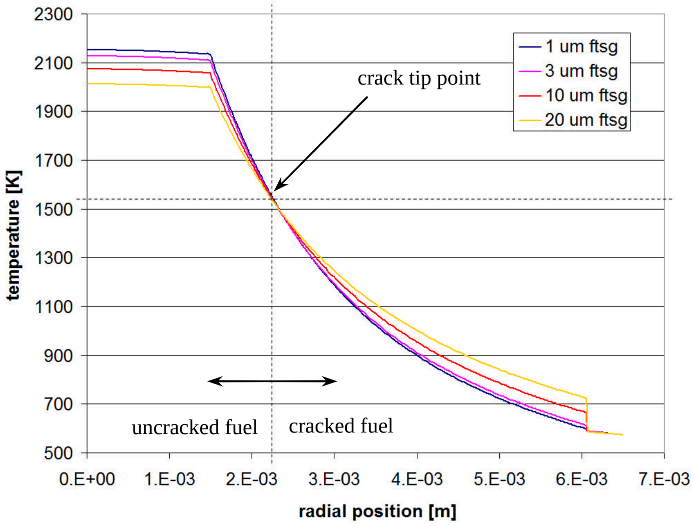

Figure 86: Radial temperature plots for four fuel-to-sheath gaps, all considered open gaps except for the 1 μm gap

The results of case study (i) are summed up by Table 31, which provides the maximum fuel oxidation value and the average oxygen molar uptake after two weeks of heating.

Table 31: Results of a 2D *r*-*θ* fuel oxidation model when varying the open ftsg dimension while maintaining a similar crack tip depth and temperature

ftsg [μm]	P_{Iridium} [kW m^{-3}]	Xdev$_{\text{max}}$ $\pm^{0.005}_{0.003}$ at 2 weeks	n_O $\pm^{0.010}_{0.009}$ [mol] at 2 weeks
1	3.355×10^6	0.094	0.0684
3	3.260×10^6	0.097	0.0772
10	2.990×10^6	0.103	0.1041
20	2.686×10^6	0.107	0.1294

Note: The crack width was maintained at 20 μm for the four models. In these models the iridium bar heater radius was set at 1.5 mm.

As seen in Table 31 when the fuel-to-sheath gap is at its minimum value (i.e., 1 μm), the oxygen stoichiometric deviation is also at its lowest value. On the other hand the oxygen molar uptake doubles when the fuel-to-sheath gap is at its maximum value (i.e., 20 μm).

For case study (ii), the ftsg dimension was pre-set to 3 μm and the radial crack width was varied. The purpose in this case was to compare the effect of fuel crack widths on the amount of fuel oxidation, since this dimension also affects the hydrogen gas diffusion mass transport. Since the ftsg was maintained at the same value for the four crack width models, the applied power density was the same in each crack width simulation. The crack tip was positioned at 2.29 mm from the element radial centre so that the crack tip temperature was ≈1523 K. Table 32 provides the maximum oxygen stoichiometric deviation and the average oxygen molar uptake results after two weeks of fuel heating and oxidation. A plot of Table 32 data is also given in Figure 87, which shows that as the radial fuel crack width was increased from 1 μm to 20 μm, so did the maximum oxygen stoichiometric deviation (blue diamonds). This was more clearly demonstrated when the average oxygen molar uptake into the fuel element was plotted against the radial fuel crack widths (magenta squares).

Table 32: Results of a 2D *r-θ* fuel oxidation model when varying the crack width dimension while maintaining a common fuel-to-sheath gap dimension

Crack width [μm]	P_{Iridium} [kW m^{-3}]	Xdev$_{\max}$ $\pm^{0.005}_{0.003}$ at 2 weeks	n_O $\pm^{0.010}_{0.009}$ [mol] at 2 weeks
1	3.2×10^6	0.072	0.030
3	3.2×10^6	0.077	0.037
10	3.2×10^6	0.086	0.053
20	3.2×10^6	0.094	0.070

Note: The fuel-to-sheath gap dimension was maintained at 3 μm in the four modeled cases.

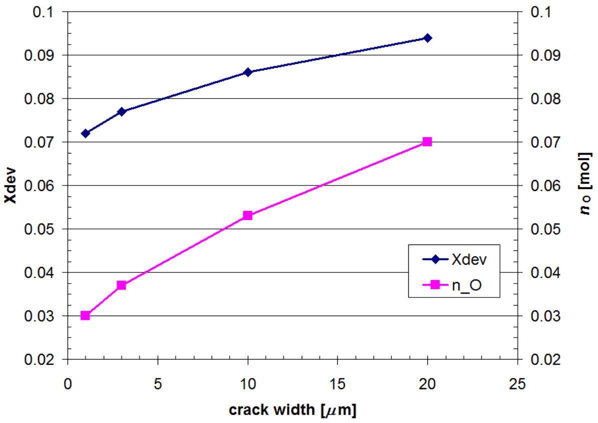

Figure 87: Maximum oxygen stoichiometric deviation Xdev and oxygen mole uptake versus radial fuel crack width

For the testing of the mesh and mesh-type independence, the second simulation case in Table 32 was repeated with a difference mesh; changed from the from a ‘hybrid’ mesh (quadrilateral and triangular mesh) shown in Figure 44, to an all-triangular one shown in Figure 45 in Section 3.5.1 (except for the radial fuel cracks and the fuel-to-sheath gap domains that used a quadrilateral mesh). Additionally, the mesh density was increased on average by a factor of >4, with an emphasis of mesh density increases in the radial fuel cracks and the fuel-to-sheath gap. Table 33 provides the fuel oxidation result for the increased mesh-density model.

Table 33: Results of a 2D *r-θ* fuel oxidation model with increased mesh density

Crack width [μm]	P_{Iridium} [kW m^{-3}]	Xdev$_{max}$ $\pm^{0.005}_{0.003}$ at 2 weeks	n_O $\pm^{0.010}_{0.009}$ [mol] at 2 weeks
3	3.2×10^{6}	0.076	0.037

Note: The fuel-to-sheath gap dimension was maintained at 3 μm.

As observed, the fuel oxidation results between these two meshed models were very similar (the second row results in Table 32 and the result in Table 33). Specifically, there was a 1.3% decrease between the maximum oxygen stoichiometry deviation and a 0.0% decrease in the average oxygen molar uptake into the fuel, between the all-triangular (high density) model and the hybrid (lower density) one. The results varied only within a small percentage so that the results are independent of the mesh structure.

These model results show that the fuel-to-sheath gap dimension and radial crack width dimension can have an effect on the extent of fuel oxidation, which is elaborated on further in discussion Section 6.1. With this point made the following results section assesses the expected radial crack geometry (crack width dimensions) due to thermal expansion of the fuel and the assessment of conditions for radial crack propagation.

4.3 The 2D r-θ Plane Strain Solid Mechanics Model Results

The radial fuel crack geometries used in the 2D r-θ fuel oxidation model, described in the Section 3.5.1, with the results discussed in Sections 4.2.1 and 4.2.2, were simple pre-defined slender rectangles that did not change shape throughout the simulation (i.e., did not expand due to thermal stresses). The following 2D r-θ plane strain models considers these geometries while investigating thermal stress (providing the crack geometry) and conditions for fuel crack propagation.

In order to study a few possible scenarios, the following results section is divided into two parts:

i.) In the first scenario, a model with five (5) pre-set radial cracks that were initially 3 μm in width and with one surface pellet flaw that was initially 0.175 mm deep was considered. Also, the model assumed the iridium bar heater and the UO_2 pellet inner annulus were in contact. Thus, these two materials were modeled as a solid continuity in the solid mechanics physics module.

ii.) In the second scenario, two models were considered:

  a) A model that had five (5) pre-set radial cracks that were initially 3 μm in width with one surface flaw that was initially 0.175 mm deep.

b) A model that had one (1) pre-set radial crack that was initially 3 μm in thickness with one surface flaw that was initially 0.175 mm deep.

In both models a) and b) of scenario ii.) the iridium bar heater domain was not included in the model solid mechanics physics computation, i.e., in this case it was assumed there is no physical contact between the iridium bar heater and UO_2 pellet annulus (i.e., the iridium bar heater expansion and contraction forces are neglected). This scenario was considered in order to investigate the case of no physical contact between the iridium bar heater and the UO_2 pellet and how this effects fuel crack growth conditions. The effect on the number of pre-existing fuel cracks on fuel crack growth conditions was also investigated.

Simulation Results

Part i.)

The following figure provides the calculated von Mises stress distribution based on the 2D r-θ plane strain model using COMSOL's steady state numerical solver. In this plot, the surface flaw is 0.175 mm deep. As observed, all five radial fuel cracks have thermally expanded.

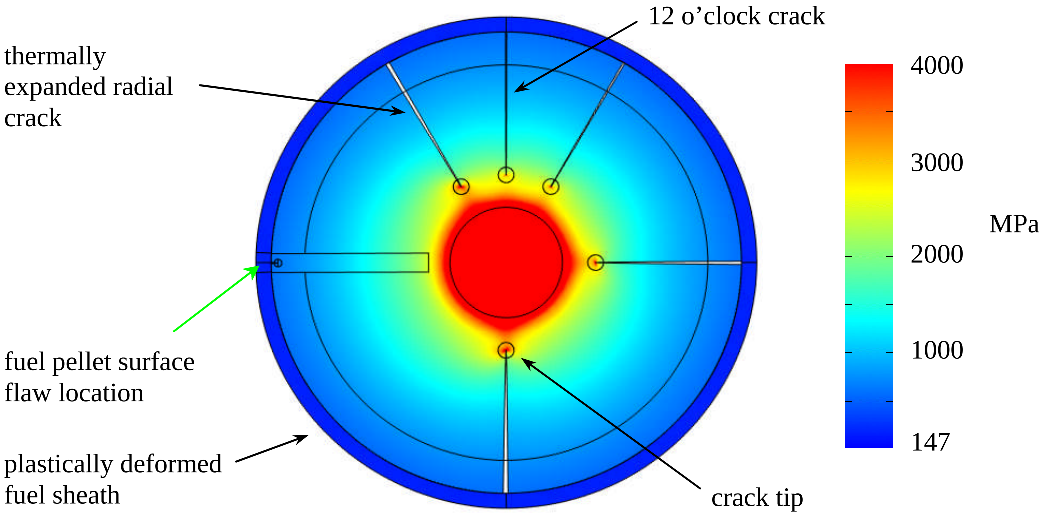

Figure 88: von Mises stress distribution in a thermally expanded out-reactor fuel pellet

The von Mises stress, also known as the equivalent tensile stress, is an expression that includes all principle stresses. Generally it is used to predict the yielding of materials under multiaxial loading conditions. In this case though it is used to visualize the stresses present in the pellet. The von Mises stress is provided by Eq. (188) for plane strain conditions [79].

$$\sigma_{\text{von\_Mises}} = \sqrt{\frac{1}{2}\left(\left(\sigma_x - \sigma_y\right)^2 + \left(\sigma_x - \sigma_z\right)^2 + \left(\sigma_y - \sigma_z\right)^2\right)} \tag{188}$$

It can be observed in Figure 88 that the regions of highest von Mises stress are at the fuel element centre (red areas) and this stress gradually subsides as the pellet surface and sheath (blue areas) are approached. Also observed is that the five expanded radial cracks are wedge shaped and at their crack tips higher von Mises stresses are present. A closeup view of the radial crack opening and crack tip of the 11 o'clock crack is provided in Figure 89 (a). The crack opening after thermal expansion is shown to be ≈100 μm wide, which is 5 times wider than the widest radial crack modeled in the 2D r-θ fuel oxidation model in Section 4.2. This would suggest that the 1-20 μm radial crack widths used previously (Section 4.2) may have been conservative values. Figure 89 (b) shows the von Mises stress concentration at the 11 o'clock crack tip, which is observed to be non symmetrical about the crack tip, due to the non symmetry of the local stresses.

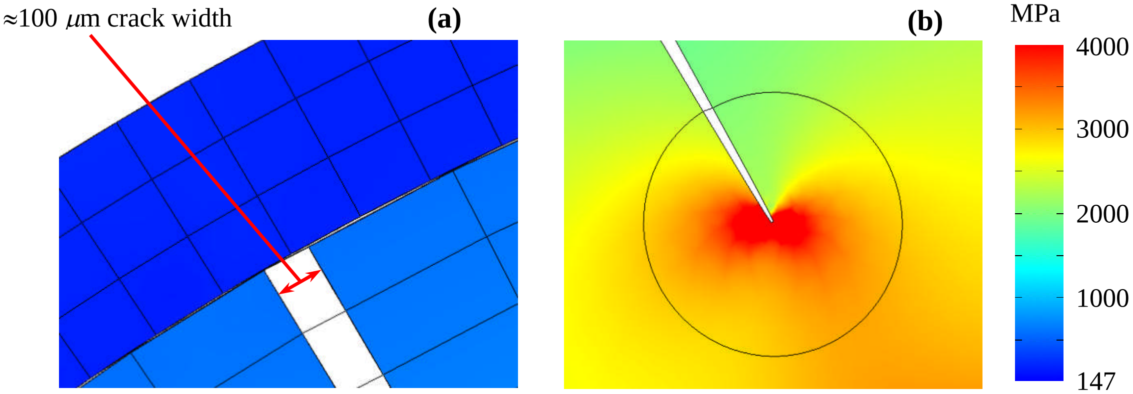

Figure 89: von Mises stress distribution in closeup view of (a) crack opening and (b) crack tip of the 11 o'clock radial crack before the 9 o'clock radial crack has opened

The horizontal ‘figure eight’ area in Figure 89 (b), which is red colored indicating areas of high stress at the crack tip, is characteristic of crack tip stress fields as discussed by Anderson [79].

There was a substantial difference in the von Mises stress between the inner and outer fuel element regions as seen in Figure 89 (a) and (b). This was partly because the outer fuel regions were at a lower temperature and because the sheath was allowed to plastically deform upon contact with the fuel pellet after the sheath transverse stress reached 150 MPa. The contact pressure that acted as a boundary condition on the internal sheath surface and fuel pellet outer surface was computed with the penalty method as explained in Section 3.5.3. Figure 90 shows the contact pressure plotted as a function of azimuthal position on the pellet-sheath interface, and it ranges between 1×10^5 to 2×10^8 Pa. Hence, every point on the circumference of the sheath received a different pressure based on how much the sheath and pellet surfaces/boundaries penetrated each other. The average contact pressure was computed as 7.78×10^7 Pa and is indicated in the figure by the red dashed line.

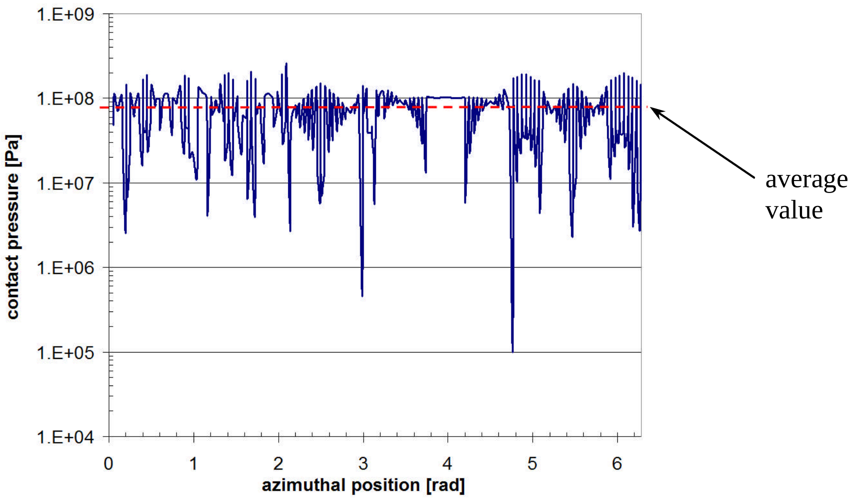

Figure 90: The simulated contact pressure between the sheath and the fuel pellet vs. the azimuthal position of the contact surface

Since the current model has a 2D r-θ geometry, it is more intuitive to express the stresses acting in the plane strain model in cylindrical coordinates. Furthermore, the von Mises stress only gives the absolute combined stress field, and not the principle stresses. Thus, Eq. (189) provides the conversion of stresses from Cartesian to cylindrical coordinates [138], where σ_x and σ_y are the stresses in the x and y directions and τ_{xy} is the shear stress perpendicular to the x direction and parallel to the y direction.

$$\begin{aligned} \sigma_r &= \sigma_x \cos^2\theta + \sigma_y \sin^2\theta + 2\tau_{xy} \sin\theta\cos\theta \\ \sigma_\theta &= \sigma_x \sin^2\theta + \sigma_y \cos^2\theta - 2\tau_{xy} \sin\theta\cos\theta \end{aligned} \tag{189}$$

In a classic crack analysis problem, one can consider a remote stress acting on a surface crack of length a (i.e., see the Mode I loading in Figure 30). Compressive stresses can also create conditions for crack propagation, called ‘wing cracks’ [163], but a specific treatment is needed for this analysis, which is not included in this work. Using Eq. (189), the radial and azimuthal stresses are plotted in Figure 91. The vertical dashed orange line in the figure represents the inner UO_2 annulus. Due to thermal expansion, the radial stress (blue curve) starts at zero and is then compressive (negative) throughout until it arrives at the pellet surface flaw.

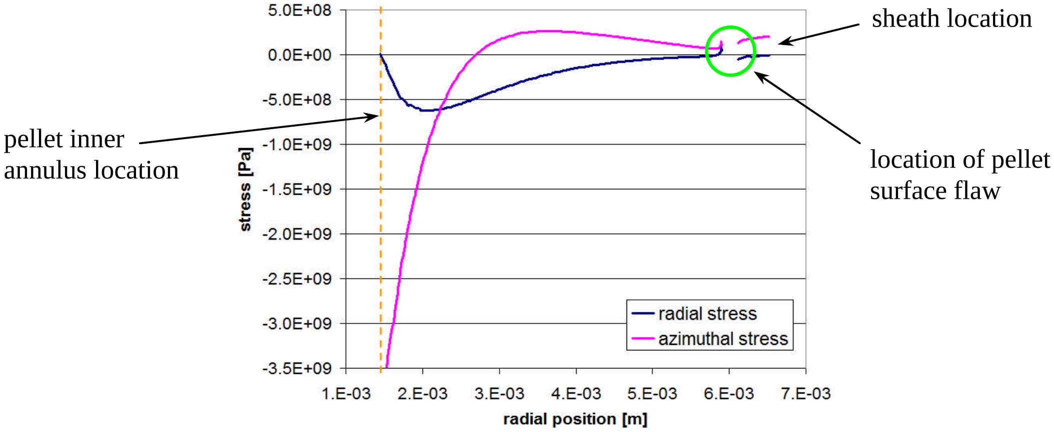

Figure 91: Radial and azimuthal stresses vs. radial position through the fuel pellet, fuel pellet surface flaw, and sheath

The azimuthal stress (purple curve) on the other hand is initially compressive at the pellet inner annulus with a calculated stress as high as 3.5 GPa. The azimuthal stress then becomes tensile (positive) when at the radial position of ≈2.65 mm from the fuel element centre and rises to a maximum value of 260 MPa. The stress then decreases but remains in the tensile state all the way to the surface flaw, which is 0.175 mm from the pellet surface. The gap in the stress plot (green circle) is due to the presence of the pellet surface flaw. The stress in the sheath is basically a hoop stress, which reaches a maximum value of ≈200 MPa after strain hardening from an initial pre-defined Zircaloy yield stress σ_{ys0} of 150 MPa.

For the case when the developing radial crack is at full length (i.e., it is as long as the remaining radial cracks) the radial and azimuthal stresses are plotted in Figure 92. At this point the crack has grown to a length in the fuel pellet where the crack tip temperature reaches 1473-1673 K (i.e., at a temperature range where fuel cracks self heal), at which point the parametric solver stops. The final crack tip is set to a distance of 2.29 mm from the fuel element centre (where the fuel element temperature reaches ≈1523 K, see Section 3.5.1). Here the azimuthal stress (purple curve) is compressive at the pellet inner annulus as before but quickly changes to tensile stress as the crack tip is approached. The change from compressive to tensile stress occurs at 2.2 mm from the fuel element centre rather than at 2.7 mm when the crack is only a surface flaw, as shown in Figure 91. At the region near the crack tip the azimuthal stress jumps substantially to ≈10 GPa, which is about three times above the theoretical fracture stress of UO_2.

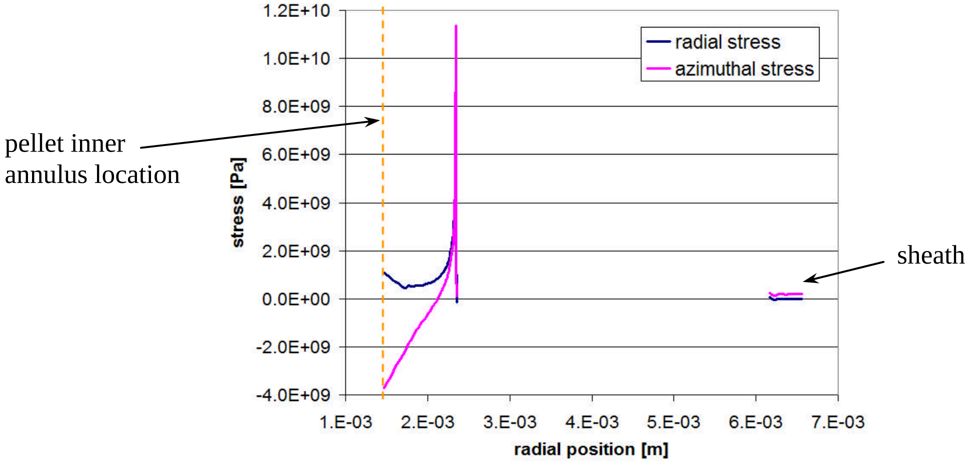

Figure 92: Radial and azimuthal stresses vs. radial position through the fuel pellet, fuel pellet radial crack, and sheath when the crack is fully extended

For analyzing the conditions for crack propagation in the sixth crack that starts as a pellet surface flaw, the stress intensity factor K_I is computed and compared to the calculated fracture toughness K_{Ic} of the UO_2 ceramic (Eq. (118)), as provided from Table 21. It is also compared to an experimental measured fracture toughness by Kutty [135], as provided from Table 20. Figure 93 plots K_I as a function of the crack length a. The crack length increases from a surface flaw length of 0.175 mm to 3.36 mm in length, the computed stress intensity factor K_I around the crack tip increases from 3.00×10^6 Pa $m^{0.5}$ to 4.46×10^7 Pa $m^{0.5}$. After this point, K_I decreases somewhat to 3.82×10^7 Pa $m^{0.5}$, at which point the parametric solver is pre-set to stop where fuel plasticity is believed to occur (i.e., at about 2.29 mm from the pellet centre where the temperature is ≈1250°C).

Comparing the computed K_I curve to the fracture toughness K_{Ic} values in Figure 93 for a surface flaw similar in size to a pellet pore (yellow triangle provided by Table 21 in Section 3.5.3), or to a measured value (green square [135]), the stress intensity factor K_I is always greater than the fracture toughness of the material. This result would indicate that crack propagation conditions are favored throughout the length of the crack.

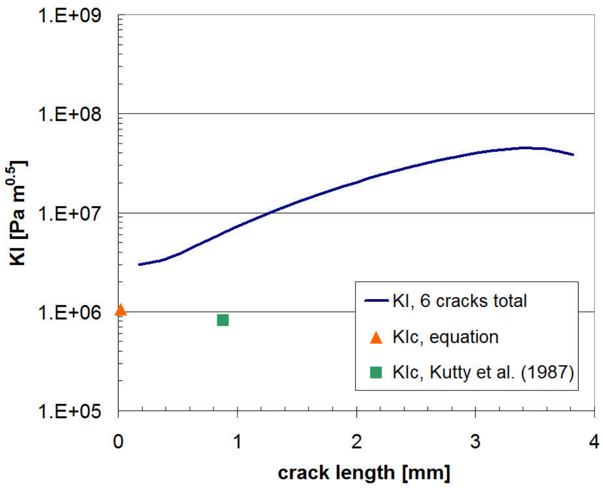

Figure 93: The stress intensity factors around crack tip vs. crack length in a model with six cracks total with iridium bar and UO_2 domain mechanical continuity, and UO_2 fracture toughness

In Figure 94 (a), the width of the 11 o'clock crack is shown to be 44.7 μm (at the crack opening), which is less than half as wide as it was in Figure 89 (b) when the 9 o'clock crack was still a surface flaw (i.e., a short crack). It is observed that the 11 o'clock crack tip in Figure 94 (b) has similar maximum von Mises stress of 4000 MPa as in Figure 89 (b) but has greatly reduced its surface area. Thus, the growth of an extra radial crack, specifically a 6th radial crack at the 9 o'clock location, is accompanied by a reduction in the local stresses in neighboring fuel crack tips and a reduction in crack width openings.

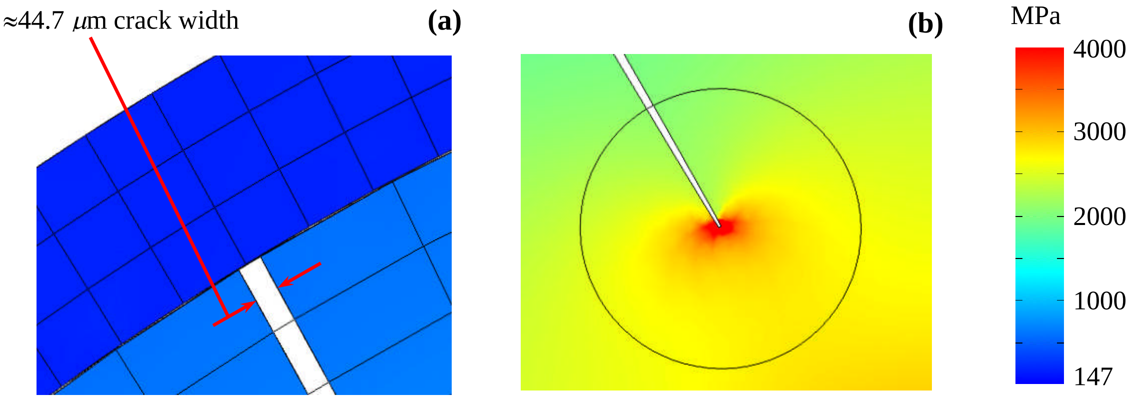

Figure 94: von Mises stress distribution in closeup view of (a) crack opening and (b) crack tip of the 11 o'clock radial crack after the 9 o'clock radial crack has fully opened

The radial stress in Figure 92 was not zero or compressive (negative in sign) at the inner UO_2 pellet annulus surface as would otherwise be expected. This result is because in this 2D r-θ plane strain model, the iridium bar and the UO_2 fuel pellet surrounding it were modeled as solid continuity between these two domains. In reality, the UO_2 pellet central annulus and the iridium bar surfaces, when heated in the experiment, can slip and slide and possibly separate from each other (i.e., the initial gap between these two materials may increase), thereby reducing any stress build up in the pellet. In other words, modeling these two materials with solid continuity may over simplify the problem. This in turn can affect conditions for fuel cracking. Hence, the following *Results Part* ii.) sub-section addresses this issue.

Part ii. a.)

In this section the iridium bar was excluded from the solid mechanics computation. Instead, only heat transfer physics was solved-for in the iridium bar domain. In this manner, the UO_2 pellet was free to expand without being 'tethered' or 'pushed' by the iridium bar. Figure 95 provides the von Mises stress distribution for the 2D r-θ plane strain model where five pre-set radial cracks are allowed to open due to thermal expansion. A sixth radial crack opens up parametrically at the 9 o'clock position from a surface flaw that is 0.175 mm deep.

As one observes, the areas of highest von Mises stress in the pellet are near the UO_2-to-iridium interface and at the pre-set crack tips.

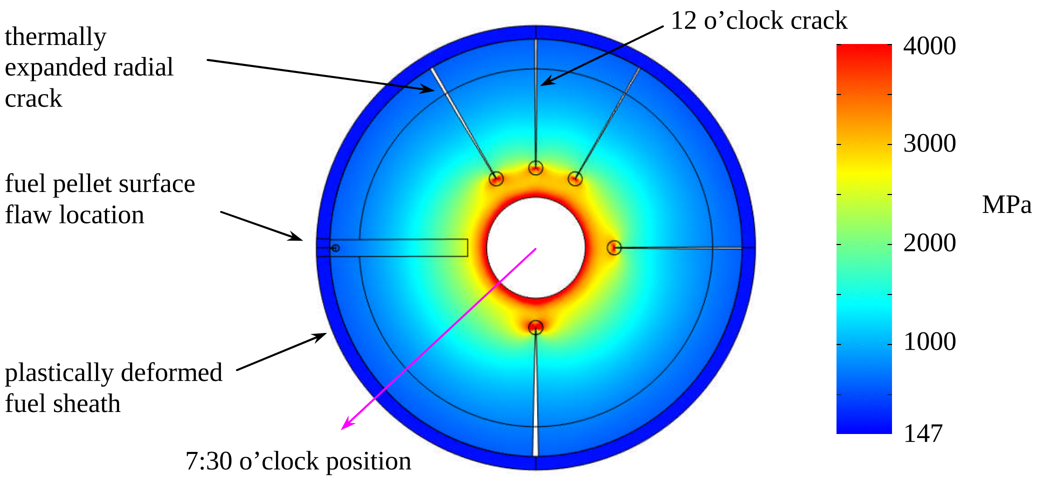

Figure 95: von Mises stress distribution in a thermally expanded out-reactor fuel pellet where the iridium bar is excluded from the solid mechanics computation

If these results are compared with those in Figure 88, it is possible to discern slight differences in the von Mises stress distribution, however clearer differences can be distinguished when plotting the radial and azimuthal stresses in two different azimuthal locations (or clock positions). The azimuthal stress is plotted as light blue and blue curves in Figure 96. The light blue curve is the azimuthal stress in the pellet plotted at the 9 o’clock position from the centre of the pellet, through the pellet, pellet surface flaw, and the sheath. The blue curve is the azimuthal stress plotted at the 7:30 o’clock position (i.e., a 45° angle away from the developing radial crack as indicated in Figure 95). Similarly, the red and orange curves are the radial stresses plotted at the 7:30 and 9 o’clock positions, respectively. The green dashed vertical line indicates the pellet inner annulus location. Generally, the stress plots at the two different clock positions were similar, except at the crack tip where there was a stress riser.

The radial stress at the inner pellet annulus is zero as expected (as compared to the previous model result in Figure 92 that considered solid continuity between the Ir and UO_2).

The red curve is less smooth due to the coarser mesh at this location. These stress profiles can be compared with those of Figure 91, where the iridium bar heater was included in the stress computation. It is also noticed that the light blue and orange curves for the azimutahl and radial stresses, respectively, rise sharply in magnitude and were highly compressive (i.e., negative in sign) near the surface flaw crack tip region (in the green ellipse). This stress concentration behavior, as was seen earlier in Figure 92, is typical when discontinuities such as a void or crack are present in a loaded material.

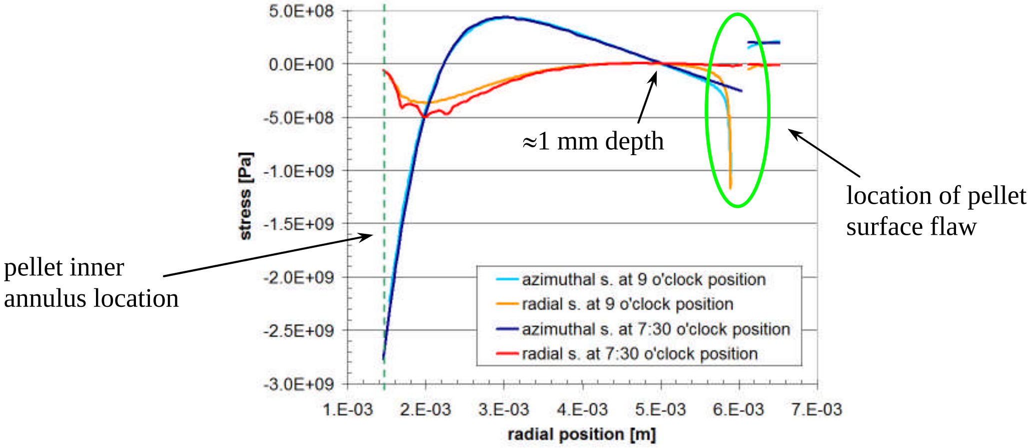

Figure 96: Radial and azimuthal stresses vs. radial position through the fuel pellet, fuel pellet surface flaw and sheath, in a model with five preset radial cracks and one surface flaw

As discussed in Section 3.4.2 the type of cracking investigated in this thesis was Mode I cracking (Figure 30) where a material is forced apart by applying a tensile stress normal to the plane of a crack. However, the plot in Figure 96 shows that when the surface crack or flaw is only 0.175 mm in length the azimuthal stress (light blue curve) is compressive (negative in value) down to a depth of ≈1 mm below the pellet surface. Hence, Mode I cracking acting on a surface flaw is not represented in this case. In other words, the surface flaw may not develop into a full length fuel crack with five pre-set radial cracks already present. The azimuthal stress though becomes tensile at a depth greater than 1 mm into the pellet, which can promote Mode I internal cracks. However, this was not considered in this work.

Part ii. b.)

The following results consider the case when there is only one pre-set radial crack and one surface flaw in the out-reactor fuel pellet. The other pre-set radial cracks, at 11, 12, 1, and 6 o'clock positions, as indicated Figure 97, were disabled and not allowed to open.

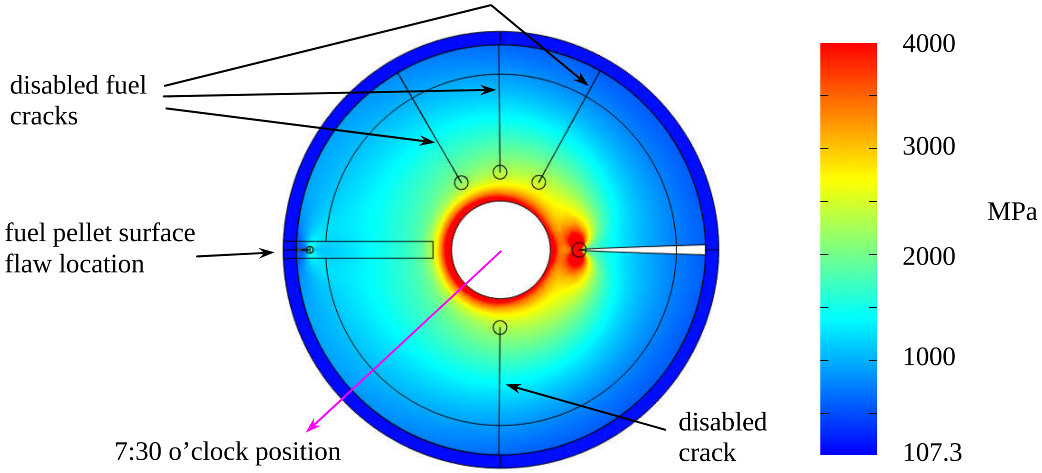

Figure 97: von Mises stress distribution in a thermally expanded out-reactor fuel pellet where the iridium bar is excluded from the solid mechanics computation. Only one pre-set radial crack (right) and one surface flaw (left) are allowed to open

As before, the radial and azimuthal stresses are plotted in Figure 98. The dashed green vertical line in the figure represents the inner UO_2 annulus surface. The blue and light blue curves represent the azimuthal stress in the pellet plotted at the 7:30 and 9 o'clock positions, respectively, were generally similar except at the crack tip where there is a stress riser. Furthermore, the radial and azimuthal stresses in Figure 98 are similar to the previous radial and azimuthal stress results in Figure 96 (from a model with five pre-set radial cracks and one surface flaw) except that in this case the azimuthal stress near the pellet surface is tensile, including the stress riser at the surface flaw crack tip.

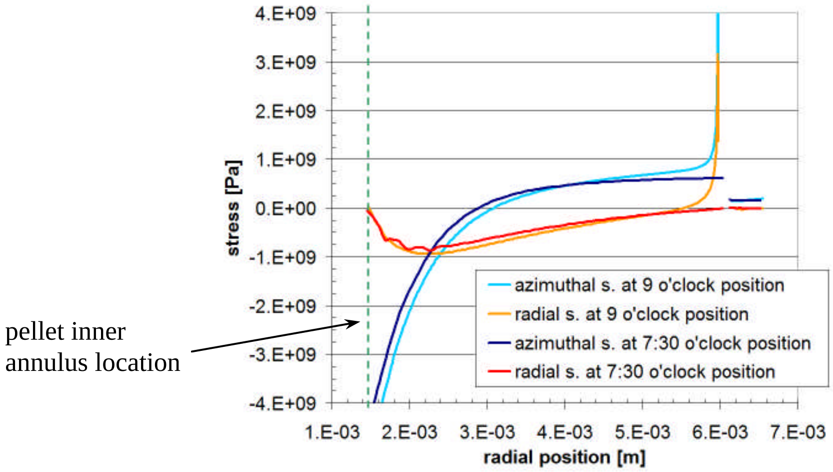

Figure 98: Radial and azimuthal stresses vs. radial position through the fuel pellet, fuel pellet surface flaw, and sheath, in a model with one pre-set radial crack and one surface flaw, when the iridium bar is excluded from solid mechanics computation

The stress intensity factor K_I was computed for the second scenario case where the iridium bar heater was neglected from the solid mechanics computation. Figure 99 presents K_I values for the two cracked fuel configurations: (a) a model with five pre-set radial cracks and one surface flaw (six cracks in all) represented by the purple curve and (b) a model with one pre-set radial crack and one surface flaw (two cracks in all) represented by the blue curve. As can be seen the stress intensity factor around the crack tip of the developing fuel crack is higher when fewer pre-existing radial cracks are present. Additionally, the stress intensity factor K_I is well above the fracture toughness K_{Ic} of the UO_2 ceramic (the calculated value indicated by the orange triangle provided by Table 21 in Section 3.5.3 and the green square value provided by Kutty *et al.* [135]). Since the stress at the pellet surface was shown to be tensile (Figure 98) in a model with one pre-set radial crack and one surface flaw, it can be deduced that conditions for crack propagation are favored.

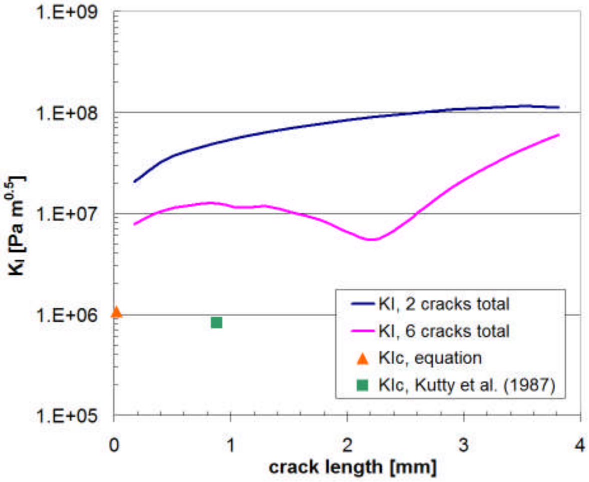

Figure 99: The stress intensity factor around crack tip vs. crack length for two crack number cases, when the iridium bar is mechanically neglected in the model. The analytical and measured fracture toughness of UO_2 ceramic is given for specific crack lengths.

A comparison can be made between the computed K_I curves from models with six radial cracks in total (five pre-set radial cracks with one growing crack from a surface flaw), when including and excluding the iridium bar as solid continuity with the fuel. Specifically the K_I curve in Figure 93 with solid continuity and K_I curve in Figure 99 without solid continuity (purple curve), show that former stress intensity factor curve is generally lower at the pellet surface and higher in the pellet interior where the crack is ≈2.2 mm in length. Since there is an initial gap between the iridium bar and the UO_2 pellet (refer to Section 4.2.1) the purple curve in Figure 99 may be more representative of the out-reactor fuel oxidation test conditions (i.e., no intimate contact between the iridium bar and the UO_2 pellet). Assuming cracking is initiated only from the pellet surface the purple K_I curve in Figure 99 shows more favorable conditions for crack initiation if the azimuthal stress in this location is also tensile.

From these results it seems that between one and <five radial cracks will develop from pellet surface flaws. Cracks can also grow from internal pellet pores/flaws, which could lead to a higher number of cracks. This though was not modeled in this work.

Before continuing further, a comparison is made between the stress intensity factors computed with two mesh types: A mesh consisting of 77% triangular elements and 23% quadrilateral elements (Figure 50) and a mesh consisting of 24% triangular elements and 76% quadrilateral elements (Figure 51). From Figure 100 there does not seem to be a difference in the stress intensity factor values computed using the regular *J* integral (Eq. (125)) with these two different mesh configurations.

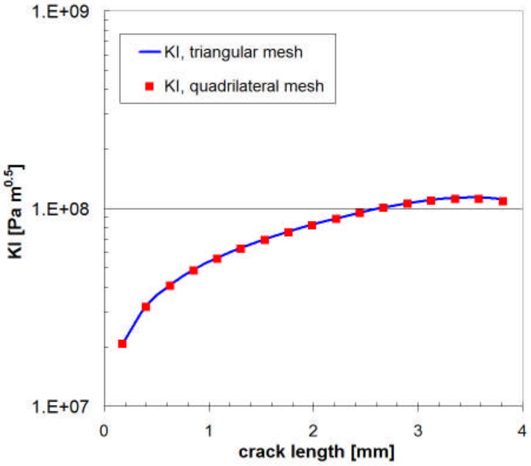

Figure 100: The K_I computed values for a model with mostly triangular mesh (blue curve) and a model with mostly quadrilateral mesh (red squares)

Furthermore, the *J* integral contour for the triangular meshed model was circular and for the quadrilateral meshed model it was rectangular, of approximately the same size. These results indicate contour shape independence, as expected.

Analysis of the J and J^* integrals considering two contour shapes of two sizes

Previously the *J* integral was computed and the stress intensity factor K_I was determined by solving Eq. (124). This was then compared to the fracture toughness values K_{Ic} of the UO_2 ceramic for the purpose of determining fracture propagation conditions. But for situations where there is a temperature gradient in the material parallel to the crack growth direction J^* is also computed, as explained in Section 3.4.2.

A comparison is made between the J and J^* integral (for J^* using Eq. (134) for a homogeneous material and Eq. (135) for a non-homogeneous material) using two contour shapes and sizes. The reason this is done is to see if the computation of J is sufficient in assessing conditions for fuel cracking or if J^* provides additional information that needs to be taken into consideration. Testing different contour shapes and sizes verifies computation path independence.

As was seen earlier in Figure 100 the stress intensity factors using the conventional J integral, seemed to be independent of contour shape and size as well as mesh type. Yet the J^* computation was a little sensitive to mesh type, as explained at the end of Section 3.5.3. Hence, the mesh type used for the following plots was all quadrilateral mesh elements. For the case that the integration contour was a 0.1 mm radius contour and a small 0.25 mm sided square contour, i.e., essentially the same contour size but different shapes (see applied mesh and contours in Figure 52 (a) and (b)), Figure 101 shows the stress intensity factors as a function of crack length a. K_I assessed by computing the J integral is identified as KI in the plot legend and the purple squares. K_I assessed by computing the J^* for homogeneous materials (Eq. (134)) is identified as KI_1_star in the plot legend and the blue diamonds. And lastly K_I assessed by computing the J^* for non-homogeneous materials (Eq. (135)) is identified as KI_1_star_2 in the plot legend and the yellow triangles. As can be observed in the figure KI_1 and KI_1_star are essentially the same, with a maximum value of $\approx 1.1\times10^8$ Pa $m^{0.5}$ occurring at a crack length of ≈3.5 mm. KI_1_star_2 though (yellow triangles) was higher and had a maximum value of $\approx 1.6\times10^8$ Pa $m^{0.5}$. In Figure 101 (a) it is observed that the KI_1_star_2 curve is a little less smooth when the small round contour was used as compared to Figure 101 (b) where a square contour was used. It was not concluded what led to this result difference.

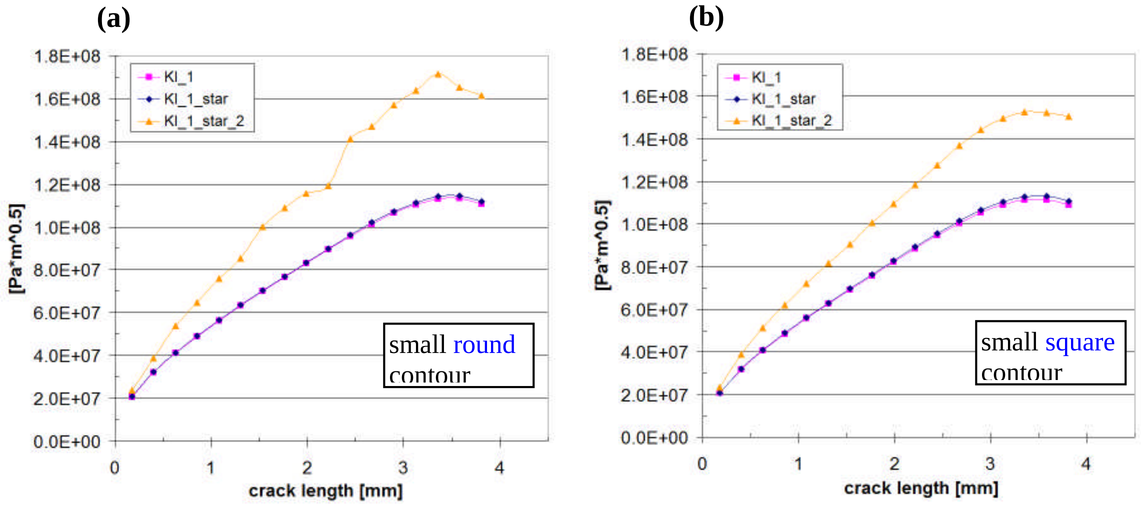

Figure 101: Stress intensity factors K_I computed using (a) a 0.1 mm radius contour and (b) a 0.25 mm sided square contour

For the larger integration contours shown in Figure 53 (a) and (b) the stress intensity factors K_I (KI_1, KI_1_star and KI_1_star_2) are plotted in a similar fashion as a function of the crack length a in Figure 102. In this case the integration contours were increased in size: from 0.1 mm to 0.25 mm radius contour and from 0.25 mm to 0.5 mm sided square contour. It can be observed that the K_I plots using the larger round contour, Figure 102 (a), or the larger square contour, Figure 102 (b), yielded similar values, specifically, the maximum KI_1 and KI_1_star values were $\approx 1.2\times10^8$ Pa $m^{0.5}$ and the maximum KI_1_star_2 values were $\approx 1.5\times10^8$ Pa $m^{0.5}$. I.e., the J or J^* computations are independent of contour shape, as they should be.

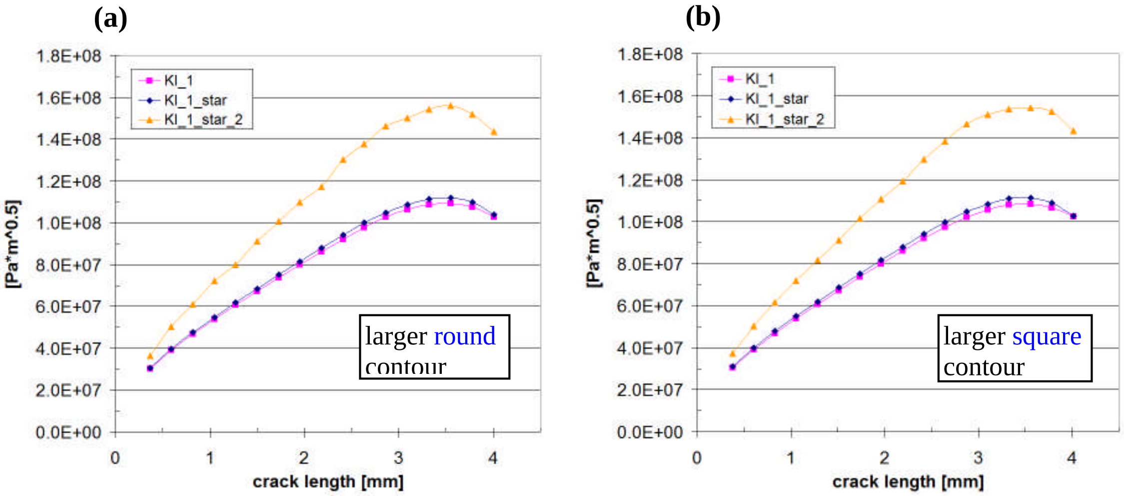

Figure 102: Stress intensity factors K_I computed using (a) a 0.25 mm radius contour and (b) a 0.5 mm sided square contour

If the K_I plots (KI_1, KI_1_star and KI_1_star_2) in Figure 101 using the small integration contours, are compared to K_I plots in Figure 102 using the larger integration contours, it is noticed that the curves are generally very similar as well. This would indicate that the J and J^* computations, in a centrally heated (electrical heating) UO_2 fuel pellet with thermal expansion, with one fully developed radial crack and one surface flaw that develops into a full length radial crack, are independent of integration contour shape and size.

Thus the computed stress intensity factors K_I presented in figures Figure 101 and Figure 102 (KI_1, KI_1_star) show the J and J^* integrals (the latter for homogeneous materials) produce similar result and are independent of integration contour shape and size. The assessment of the stress intensity factor K_I (KI_1_star_2) by computing J^* for non-homogeneous materials yielded somewhat greater stress intensity factors compared to the previous two cases. Although the assessment of K_I using J^* for non-homogeneous materials is more applicable in the out-reactor fuel pellets, the use of the J integral gave K_I values over an order of magnitude greater than the fracture toughness K_{Ic} of UO_2. In other words the J integral (Eq. (125)) should be sufficient for assessing K_I for predicting conditions suitable for crack propagation from a surface flaw of a thermally expanded UO_2 fuel pellet. Also, the J

integral is easier to numerically implement than J^*. However, if a more conservative estimate is required for the onset of crack propagation conditions in a non homogeneous material, the J^* integral (Eq. (135)) should be used, since it yields a higher K_I value.

4.4 The 2D *r-θ* Fuel Oxidation Model Coupled with the Solid Mechanics Plane Strain Model Results

In this model results section the 2D r-θ fuel oxidation model was coupled to the solid mechanics plane strain model using the Arbitrary Lagrangian Eulerian (ALE) moving mesh method (or a deformed mesh method). Since the solid mechanics part of the model included fuel-to-sheath contact modeling (as explained in Section 3.5.3) the solid mechanics model was configured to the first model scenario described in Section 4.3. Specifically the iridium bar heater and the fuel pellet were modeled as a solid continuity (with no gap). This approach ensured better convergence. Figure 103 provides the model results for: (a) the temperature distribution, (b) the oxygen stoichiometric deviation distribution and (c) the von Mises stress distribution, after two weeks of heating. The hydrogen mole fraction distribution (q in Eq. (27)), in the fuel cracks and in the fuel-to-sheath gap, is not shown here, since the solution distribution it is too slender to present as a 2D plot but it would show a minimal value at the sheath breach area and an increasing value (in hydrogen fraction) in the fuel cracks and fuel-to-sheath gap as the distance from the sheath breach is increased. The maximum crack opening expansion was about 100 μm (bottom 6 o’clock crack in Figure 103) due to its more remote azimuthal location with respect to the other radial cracks. The oxygen deviation from stoichiometry in Figure 103 (b) is highest near the centre of the fuel, $x = 0.088$, where it is hottest and lowest at the fuel periphery where it is coolest, keeping in mind that crack widths can affect the extent of fuel oxidation (as was shown in Section 4.2.2). This maximum x result is similar to the maximum oxidation result ($x = 0.095$) in the solely 2D r-θ fuel oxidation model shown in Figure 73 (b) though here it is a little lower. This result is possibly due to the smaller number of modeled radial cracks and their azimuthal distribution in the fully coupled model (6 versus 12 radial cracks), and because in the fully coupled model the iridium bar heater volumetric power was 3.19×10^{6} kW m^{-3} whereas in the solely 2D r-θ fuel oxidation model in Section 4.2.1 the volumetric power was higher at 3.52×10^{6} kW m^{-3}.

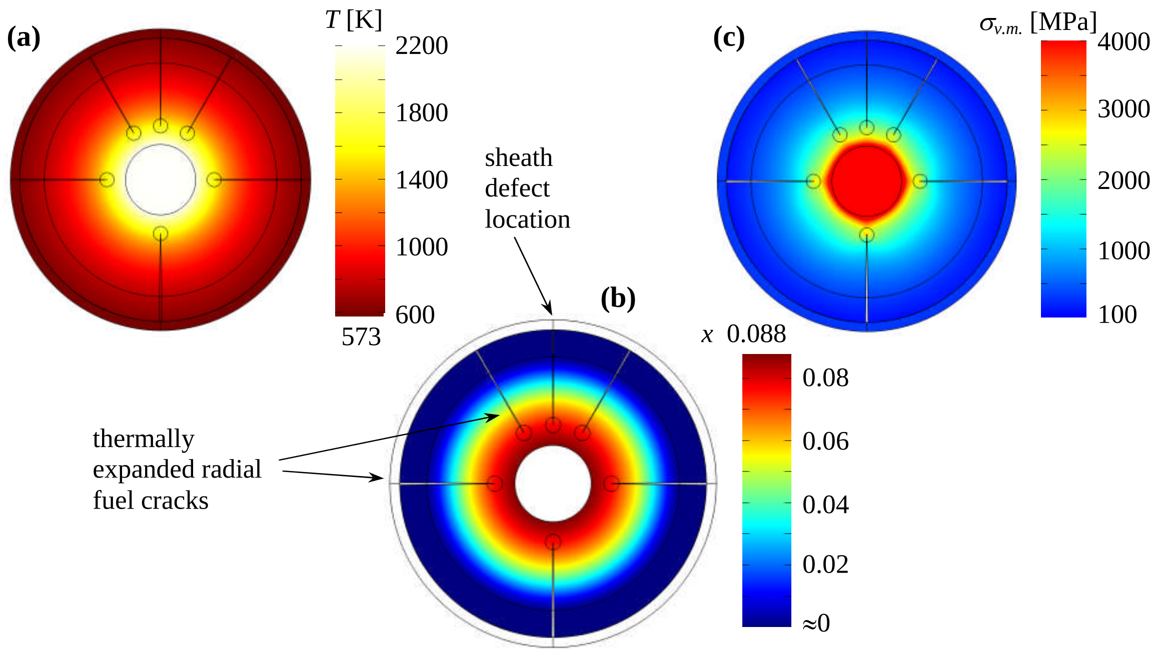

Figure 103: Coupled fuel oxidation and solid mechanics model results that includes: (a) temperature distribution, (b) oxygen stoichiometric deviation distribution and (c) von Mises stress distribution

The contact pressure between the sheath and the thermally expanded fuel pellet (using the penalty method explained in Section 3.5.3) can be compared between this model and the solely solid mechanics model computed in Section 4.3. Figure 104 shows the contact pressure versus the azimuthal position on the pellet-sheath interface in this fully coupled fuel oxidation model and the solid mechanics model after two weeks of simulated heating. The pressure acting on the sheath and pellet is not numerically smooth but varies from nearly zero to as high as 3×10^{8} Pa. The contact pressure on the other hand computed for the solely solid mechanics model, shown in Figure 90 in Section 4.3, is smoother and ranges between 1×10^{5} to 2×10^{8} Pa. The average contact pressure here was 1.25×10^{8} Pa, which is slightly more than the solely solid mechanics model's 7.78×10^{7} Pa average contact pressure. This was because in this model the sheath was not allowed to mechanically yield as was done in Section 4.3, causing the contact pressure to increase and vary more using the penalty method.

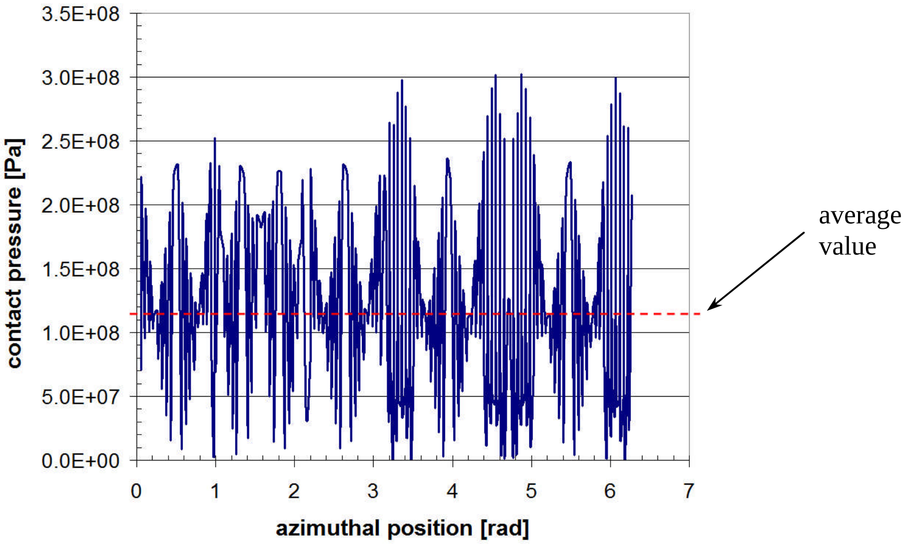

Figure 104: The simulated contact pressure between the sheath and the fuel pellet versus the azimuthal position of the contact surface in the coupled fuel oxidation and solid mechanics model after 2 weeks of heating

In this time dependent model the fuel is heated from coolant temperature, set in this case to 573 K, which rises in the interior to 2200 K as shown in Figure 103 (a). Since the radial cracks thermally expand and Arbitrary Lagrangian Eulerian (ALE) moving mesh ensures the crack boundaries follow the fuel boundaries it was possible to compute the total radial cracks cross sectional surface area as a function of time. Figure 105 shows that after 40 seconds of simulated heating the total radial cross section surface area of the fuel cracks stabilizes at just under 1 mm^2. This is an important observation because this value is about 25 times greater than the fuel-to-sheath gap cross section surface area (assuming a closed 1 μm fuel-to-sheath gap). Hence, this model result supports the idea that gas diffusion in the expanded fuel cracks is a more dominant pathway than in the fuel-to-sheath gap in CANDU fuel element (the latter as suggested by Higgs [24][29]). This gas diffusion passageway is utilized in the 3D fuel oxidation models dicussed later.

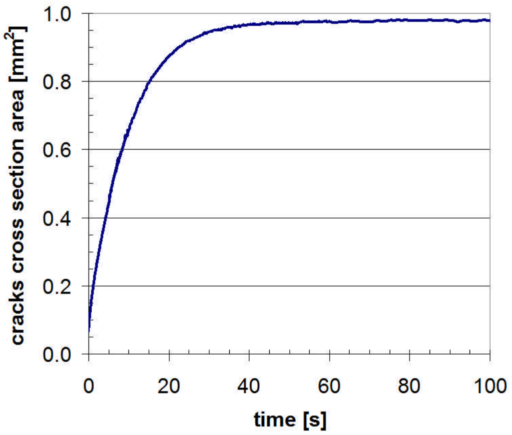

Figure 105: Total radial fuel cracks cross section surface area vs. time in the coupled fuel oxidation and solid mechanics plane strain model

The model results show that the time dependent solid mechanics model with the thermally expanded fuel cracks can be coupled with the time dependent fuel oxidation model in a 2D r-θ model configuration. The computation time though was relatively long. Specifically, for solving this model having a 90,889 degrees of freedom model it took about 5-6 days to converge to a solution. Considering that the time it took for the 2D r-θ fuel oxidation model (on its own) to converge was only 1-2 hours (Sections 3.5.1 and 4.2) and the time it took for converging a similar but steady state 2D r-θ solid mechanics model (on its own) was about 30 minutes, the convergence time for the fully coupled model is considerably longer. This is partly due to the nature of solid mechanics contact modeling in the current model where the solver continuously computes the contact pressure that ensures minimal sheath and fuel domain penetration. The model never actually converges to a final contact pressure in the simulated time. Instead the contact pressure varies with time. In other words the contact pressure, plotted in Figure 104 after two weeks of heating, would be different if plotted after one hour, one day or one week of simulated heating. Changes in fuel and sheath displacement on the other hand would be hardly discernable.

4.5 Fuel Oxidation Model Validation

The following section provides a benchmark of the fuel oxidation model against two experimental results. Section 4.5.1 compares the model to the first out-reactor commissioning test where modeled and measured temperatures and heating powers are compared. Section 4.5.2 makes a comparison between fuel oxidation model results to an in-reactor defective fuel element measurements.

4.5.1 Comparison of Model to the Stern Laboratories Commissioning Test

A 1st FES (fuel element simulator, from here on refered to as FES1) commissioning test was performed on May 7, 2012 at Stern Labroratories in Hamilton Ontario. In this test a full length out-reactor fuel element (UO_2 pellet filled, thermocouple instrumented, and heated with a central iridium bar heater), as detailed in Figure 20, was used. The purpose of the FES1 commissioning test, was to learn how the iridium bar heater and the Type-R thermocouples would behave in the planned out-reactor fuel oxidation experiment and if the intended test parameters (such as the applied electrical power) would be suitable for a successful test.

Since this fuel element was instrumented with thermocouples the temperature measurements of this test were used to validate part of the fuel oxidation model. Specifically, the model's thermal properties such as the thermal conductivity of the UO_2 pellets and the Zircaloy sheathing, as well as the thermal resistance across the fuel-to-sheath gap were modeled. This was done so that modeled temperatures could be compared to thermocouple temperature measurements.

Experimental Measurements

During the FES1 test the electrical power was increased to a maximum of 17 kW (total) and held at steady state. Temperature readings were then taken over a180 s duration. The power was then reduced and turned off. The logged temperature and power readings are presented in Figure 106. Plane A represents the thermocouples plane at SECTION C-C in Figure 20 (i.e., at the 8th pellet from FES1 outlet side) and plane B represents the thermocouples plane at SECTION B-B in Figure 20 (at the 4th pellet from FES1 outlet side) [164]. One can observe that the temperature measurements at these two axial planes were not identical. For example TC1 (the inner most thermocouple) at plane A and B differed on average by 41.85 degrees Kelvin. Nevertheless the reading of each thermocouple was quite stable with time. For example the mean temperature and error due to noise, at three standard deviations (99.7% confidence of the mean) of TC1, plane A, was 1154.50±0.45 degrees Kelvin. Thermocouple reading uncertainty is discussed further later in this section.

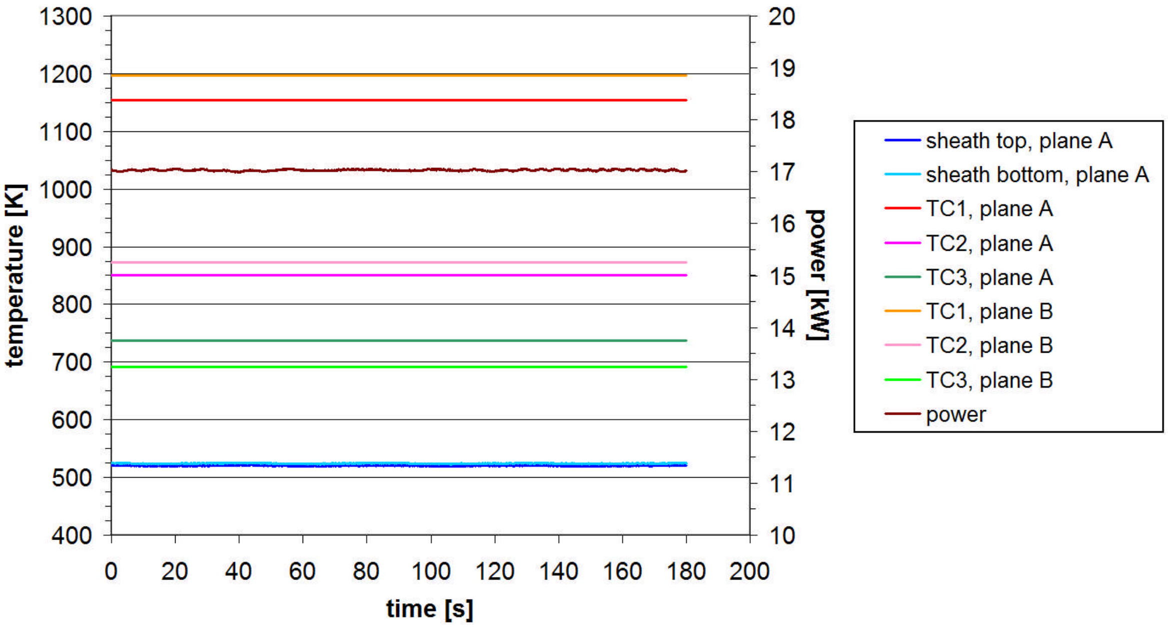

Figure 106: Thermocouple temperature measurements in FES1 at two axial planes A and B. Data provided by Stern Labs.

There are a few reasons the thermocouple temperature reading at the same radial position but at different axial planes read noticeably different temperatures. The first reason could be because the radial positions were not exactly identical and differed slightly in dimensions. This could be expected given that the thermocouple drill holes were made prior to the pellet sintering process. Since the pellets shrink in the sintering process (Figure 19) it is possible that uneven shrinking occurred, which could potentially shift the final radial position of the thermocouple holes. A second possible reason could be that the fitted thermocouple in the pellet drill hole itself (even though very small) may have been positioned closer to a specific side of the hole. Based on the dimensions of the thermocouples and drill holes a shift of 20-30 μm of the thermocouple either towards or away from the pellet centre of the pellet or away from the pellet centre was possible, which in turn could cause a change in the temperature reading.

Model Comparison

The model used to validate the heat transfer properties of the fuel oxidation model included the heat transfer equation, Eq. (174) (used previously in Section 3.5.3), and the solid mechanics equation, Eq. (93) (also used previously in Section 3.5.3), using COMSOL's Thermal Stress interface (or module), were solved with a steady state solver. The level of fuel oxidation was pre-set to a near zero constant. Included in the model are the thermal properties of the thermocouples as discussed in Section 3.2.4 and electrical heating of the fuel element model using the electrical power computations discussed in Section 3.3.3. In this model though only the electrical current flowing through the iridium bar heater and the Zircaloy sheath were considered. The fuel pellet electrical conduction was neglected, since its contribution to ohmic heating is negligible at the designed heating temperatures. Solid mechanics physics was implemented in this model, since it was already set up in the crack propagation model in Section 3.5.3 and also because it computed the small changes in the thermocouples' positions (for TC1 and TC2) due to pellet thermal expansion (for reference purposes).

The constants (COMSOL$^{®}$ parameters) used in this Thermal Stress steady state model that represents the FES1 test are provided in Table 34. Two important constants (or parameters) in the table need to be mentioned. The first constant was the total electrical current set to flow through the fuel element, I_e, which was set to 990 A (near the 930 A actual measurement). The second constant was the fuel-to-sheath gap distance (ftsg_thickness in COMSOL$^{®}$ model), which was set to 5.1 μm. The higher the electrical current I_e (or the voltage applied on the FES) the more power will be generated and the hotter the fuel will get.

Conversely the fuel-to-sheath gap dimension is also very important. The greater this dimension the higher the thermal resistance across this gap, and the higher the fuel temperature will become. In CANDU fuel the coolant pressure and the ability of the sheath to creep down eventually causes the fuel-to-sheath gap to close. Since the FES1 test ran for a relatively short period of time (2-3 hours for heating up the system and another 0.5 hours for steady state heating operation) and since the outside coolant pressure (loop pressure) was 5.9 MPa and inside element pressure was 5.3 MPa (i.e., only 0.6 MPa differential pressure was applied onto the sheath) [164], the fuel-to-sheath gap was expected to have remained open. This would mean a gap greater than 1 μm. The electrical current and the fuel-to-sheath gap parameters used in the model were determined by trial and error to simulate as close as possible the FES1 temperature readings shown in Figure 106. This was done by running several model cases of increasing fuel-to-sheath gap dimensions. As this dimension was increased the fuel element temperature increased for the same applied electrical current (electrical power). This was followed by lowering the electrical current in the model, which caused a drop in the fuel element temperature, especially near the fuel centre. The temperature of the fuel periphery however was higher compared to the previous model result. In this manner the model temperature profile was made to fit the three thermocouple readings and the total FES1 power reading as close as possible.

Table 34: List of selected constants used in the validation of the Thermal Stress model

Symbol	**COMSOL® constant name**	**Description**	**Value**
ρ_{TD}	theoretical_density	The theoretical fuel pellet density	10.96 [g cm^{-3}]
$\rho_{\mathrm{s\_new}}$	density_manf	Manufactured fuel density	10.63 [g cm^{-3}]
NA	UO2_frac_theo_dens	UO_2 fractional theoretical density	$\frac{\text{density\_manf}}{\text{theoretical\_density}}$
NA	porosity_manf	Manufactured fuel porosity	$1-\frac{\text{density\_manf}}{\text{theoretical\_density}}$
Δ_{Zirc}	delta_zirc	Average oxygen concentration	1e-4
C	cold_work_zirc	Unitless ratio of areas	0.001
ϕ	phi_fluence	Fast neutron fluence	1 [n m^{-2}]

Table 34: List of selected constants used in the validation of the Thermal Stress model

Symbol	COMSOL® constant name	Description	Value
x	Xdev	Stoichiometric deviation value	0.000001
T_{ref}	T_ref	Strain reference temperature	300 [K]
NA	T_surf	Outside sheath surface temperature	523 [K]
β	Beta	Burnup in atom %	0.00001
NA	sheath_wall	Sheath wall thickness	0.0004 [m]
NA	sheath_R_inner	Sheath inside radius	0.006116 [m]
NA	sheath_R_outer	Sheath inside radius	sheath_R_inner + sheath_wall
R_o	pellet_radius	Pellet radius	0.006075 [m]
NA	ftsg_thickness	Fuel-to-sheath gap	5.1e-6 [m]
R_i	Ir_radius	Iridium bar radius	0.00145[m]
ρ_{Zirc}	rho_zircaloy	Density of Zircaloy	6.44 [g cm^{-3}]
ρ_{Ir}	rho_Ir	Density of iridium	22.5 [g cm^{-3}]
ν_{UO2}	nu_UO2	UO_2 Poisson's ratio	1.32*(1-0.26*porosity_manf)-1
$\nu_{\mathrm{\_Ir}}$	nu_Ir	Iridium Poisson's radio	0.27
$\nu_{\mathrm{\_Zirc}}$	nu_zirc	Zircaloy Poisson's radio	0.37
$\alpha_{\mathrm{\_Ir}}$	alpha_Ir	Iridium coefficient of linear expansion	6.4e-6
E_{Ir}	E_Ir	Young's modulus of Ir	528e9 [Pa]
NA	coolant_p	Coolant pressure	10e6 [Pa]
I_e	I_current	Total fuel element electrical current	990 [Amp]

A value for stoichiometric deviation (x) and fractional burnup (β) is also given in Table 34, since they are called for in Eq. (42a) for porosity and in Eq. (36) for k_{ph} (heat transfer via lattice vibration). These values were set close to zero, since in FES1 no fuel oxidation or fuel burnup occurred. Note: The x and β values could also have been set to zero achieving the same result.

The fuel element back-fill gas used in the FES1 test was not helium (or steam) but argon. The thermal conductivity of argon at 10 MPa pressure was derived from tabulated data [165] and is given as a function of temperature and has the units of kW m^{-1} K^{-1}:

$$k_{\mathrm{argon}} = 7.078 \times 10^{-7} T^{0.5988} \tag{190}$$

It is noted that although the FES1 experiment coolant and fuel element pressure were at ≈5 MPa, the difference in argon thermal conductivity at 10 MPa at fuel-to-sheath gap temperatures is very small. So Eq. (190) remains applicable.

Expressions for density and specific heat at constant pressure for argon are not needed for models solved in steady state, unless momentum terms are included in the heat transfer treatment (which is not the case here). Nevertheless they are added here for completeness. Using the ideal gas law the density of argon in kg m^{-3} at 10 MPa as a function of temperature is given by Eq. (191) where T is in K.

$$\rho_{\mathrm{argon}} = \frac{48680}{T} \tag{191}$$

The specific heat of argon in kJ kg^{-1} K^{-1} at constant pressure at 10 MPa in the temperatures range $280 \leq T \leq 500$ K is given by [166]:

$$C_{p\_\mathrm{argon}} = -1.775 \times 10^{-8} T^3 + 2.356 \times 10^{-5} T^2 - 1.063 \times 10^{-2} T + 2.196 \tag{192}$$

and in the temperature range $500 < T \leq 1000$ K is given by:

$$C_{p\_\mathrm{argon}} = 1.154 \times 10^{-7} T^2 - 2.24 \times 10^{-4} T + 0.6364 \tag{193}$$

The 2D r-θ heat transfer and solid mechanics steady-state FES1 commissioning test model that considered applied electrical power, coolant temperature, fuel-to-sheath gap, and thermocouples TC1 and TC2, was prepared on COMSOL® 4.3a platform. The following plot, Figure 107, provides a temperature solution distribution plot.

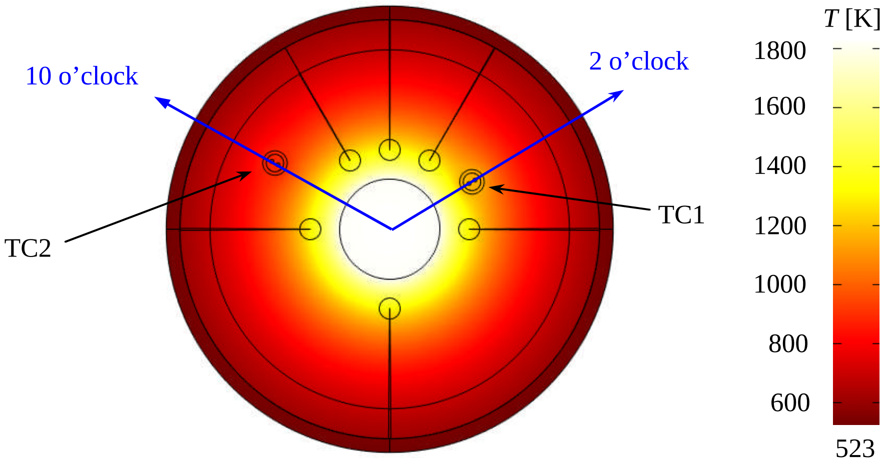

Figure 107: Out-reactor fuel element radial cross section temperature distribution plot of 1st fuel element simulator commissioning test model

The thermocouple temperature measurements of FES1, provided in Figure 106, are compared to the modeled temperatures, which are provided by the radial temperature plots in Figure 108. The measured temperature values in Figure 108 are provided with uncertainty bars, which were estimated using the temperature readings of the the two FES1 thermocouple axial planes. Specifically, the error bars are equal to the difference in the two TC readings from similar radial positions that are at two different axial planes, divided by two, plus the uncertainty of an individual type-R thermocouple, which is ±1.5 K [167], rounded up to the nearest decade, gives a total uncertainty of ±30 K. A similar result is obtained by taking one standard deviation of these two TC readings. The blue and purple curves in Figure 108 in the 2 and 10 o’clock positions, respectively (Figure 107), are the modeled radial temperatures originating from the centre of the model, passing through the inner-most thermocouple (TC1) and the intermediate thermocouple (TC2) in Figure 107. The outer thermocouple (TC3) was not modeled, since this required additional mesh design, which was not conducted. Also, although the modeled temperatures at the edges of a thermocouple in the radial direction are different in the pellet at similar radial locations when there is no thermocouple, the modeled temperature at the centre of the thermocouple is generally similar in a pellet without a thermocouple (at the same radial position). From Figure 108 the measured pellet temperatures and modeled temperatures agree within uncertainty.

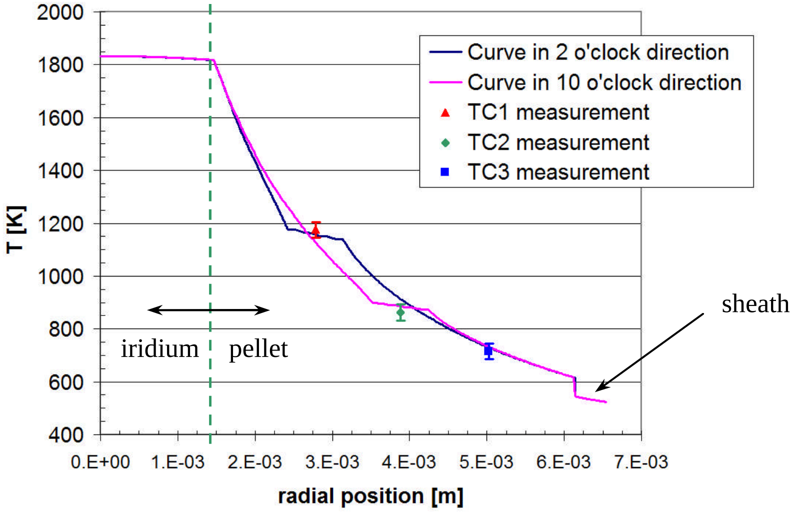

Figure 108: Model radial temperature curves through TCs at 2 and 10 o'clock positions with corresponding FES1 measured temperature values TC1, TC2 and TC3

The measured and modeled temperatures are compared in Table 35. The uncertainty of the modeled temperature was estimated by shifting the thermocouple position in the model by ±30 μm in the radial direction (to represent thermocouple location uncertainty). Note that modeling the effect of shifting the thermocouple within the thermocouple drill hole itself was not assessed in this work. This though could be another source of uncertainty.

Table 35: Measured FES1 temperature values compared to modeled values

thermocouple	measured temperatures [K]		modeled temperatures and uncertainty [K]
	plane A and plane B ±1.5 C	Average value and uncertainty	
TC1	1154.5 and 1196.5	1180±30	1157±10
TC2	851.0 and 873.0	860±30	886±6
TC3	692.0 and 737.0	710±30	718±4

As can be seen in the table above, the measured and modeled temperatures agree within uncertainty. The estimated total uncertainty in the thermocouple measurement of ±30 K could be reduced by manufacturing the out-reactor fuel pellets, the thermocouple drill holes, and the iridium bar heater to tighter tolerances. This is mentioned in the recommendations section.

4.5.2 Comparison of Fuel Oxidation Model Results to In-Reactor Measurements

The following results section provides model simulation results using the fuel oxidation model to represent an in-reactor defective fuel element and makes a comparison to coulometric titration measurements of the oxygen stoichiometric deviation levels in the defective fuel element. A model with fuel cracks running down the full length of the fuel element with fully swept mesh (where no continuity identity pair is used) is then presented and is compared to a model with the swept and free mesh with shorter cracks (in the axial direction) that includes an identity pair. This comparison is presented to show that full length axial cracks do not necessarily need to be modeled to achieve a realistic result, which saves computer resources. Finally a comparison is made between the fuel oxidation model that uses discrete fuel cracks presented in this thesis and the modeling approach used by Higgs [29]. The latter approach combines the fuel (solid) domain with steam vapour (gas) domain (fuel cracks) into a single domain using scaling parameters (or coefficients) in the diffusion PDEs, as explained in Section 1.6. Another difference between the two models is that the sheath defect surface area used in the 3D model presented in this thesis was defined as sheath defects approaching those seen in reality. I.e., not a ‘ring defect’ that is about 10-100 times larger in surface area than the actual fuel element sheath defect using Higgs [24] 2D *r*-*z* axisymmetric modeling approach (refer to Figure 13 (b)). In other words the 3D models presented in this thesis attempt to match the extent of fuel oxidation to realistically sized sheath defect surface areas.

Figure 109 (a) provides the modeled temperature distribution result and Figure 109 (b) the modeled oxygen stoichiometric deviation Xdev (or *x*) distribution result for the in-reactor defective fuel element XC9179Z-5 [29][88] with burnup, power and temperature boundary conditions defined in Table 24, after 126 days of heating (or 126 days post defect residence time).

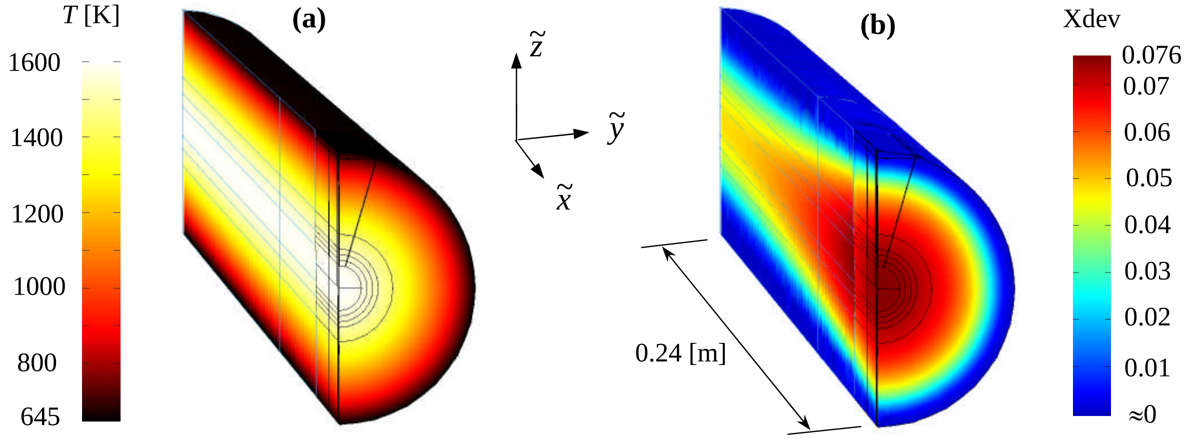

Figure 109: (a) Temperature distribution and (b) oxygen stoichiometry deviation after 126 days of simulated heating using a partial axial length cracks model

From Figure 109 (b) the highest concentration of hyperstoichiometric oxygen occurs at the fuel element radial and axial mid sections, the latter being a result of model reflection and the position of the modeled sheath breach. As the position moves away from this point in the axial direction the Xdev concentration decreases.

The effect of the hyperstoichiometric oxygen (Figure 109 (b)) introduced into the fuel on the fuel thermal conductivity (and hence the fuel temperature distribution) can be demonstrated in the following figure. In this figure the fuel element centre-line temperature at the sheath defect location (at the model axial mid section) is plotted versus time. The temperature starts at 645 K (the model’s initial temperature condition, not shown), then rises to ≈1605 K. The temperature then drops to 1590 K over the next 50 simulated days. At this point the temperature starts to increase due to fuel oxidation and reaches 1595 K at the end of the 126 simulated days. This initial temperature decrease and then increase in the modeled defective fuel temperature occurs for the reasons already explained in Section 4.2.1 in Figure 78.

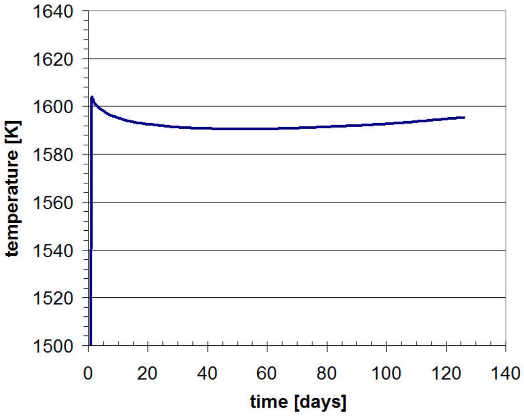

Figure 110: Modeled in-reactor XC9179Z-5 fuel element centre-line temperature at sheath defect location versus time

Hence it can be noted that the maximum oxygen deviation result of 0.076 (Figure 109 (b)) in the 3D fuel oxidation model does not substantially change the fuel thermal conductivity and thus the temperature distribution in the fuel. Only when the maximum oxygen stoichiometry deviation reaches 0.085-0.090 and above does the degraded fuel thermal conductivity start to noticeably increase the fuel temperature. This is not shown in the presented 3D model, but it was shown in Higgs axisymmetric 2D *r*-*z* fuel oxidation model, where increased fuel oxidation was computed due to the oversized modeled sheath defect surface areas [24].

The above model results are compared to coulometric titration (CT) measurements of an in-reactor defective fuel element (element number XC9179Z-5 [29]). These measurements [88] were taken by extracting powder samples from the defective fuel element, which were prepared from ≈2 mm diameter drilled holes (indicated by the ‘drill diameter’ in Figure 111) that were about 5 mm in depth. In CT the sample hyperstoichiometric oxygen content was determined by heating the samples in a reducing atmosphere (2% H_2+Ar), where a carefully controlled and monitored flow of oxygen introduced in the downstream part of the CT apparatus is used to burn off the remaining hydrogen not consumed by the sample [22][80]. As can be seen in the CT measurements, in Figure 111 (a) and (b), the highest and lowest concentrations of hyperstoichiometric oxygen in the samples occurred in the radial centre and peripheral regions of the fuel, respectively. Note that Figure 111 is not a typical histogram rather the ‘bars’ in the plots represent the CT measurement as well as the drilled hole diameter from which the CT sample was prepared.

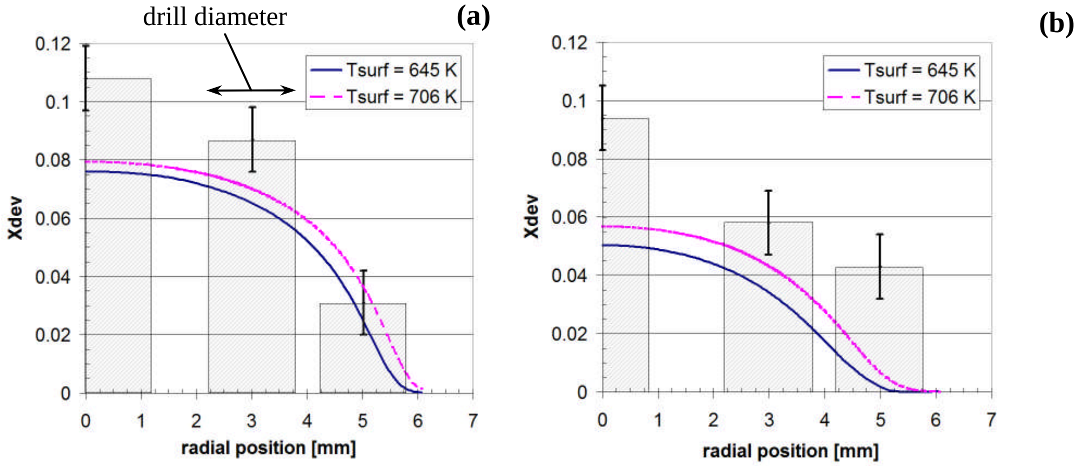

Figure 111: Modeled oxygen stoichiometric deviation radial distribution compared to actual in-reactor defective fuel element XC9179Z-5 coulometric titration measurements at (a) the fuel element mid section and (b) at 12 cm from the fuel element Non-Reference End [24][29].

Modeled Xdev (or *x*) distribution of fuel element XC9179Z-5 are given as radial profiles in Figure 111, shown as solid blue curves at (a) the fuel element midsection and (b) 12 cm from the ‘Non-Reference End’ of the fuel element [29][88] after 126 days of simulated oxidation (see Figure 112 further down for these locations). In this case the surface fuel temperature was set to 645 K. Generally the modeled oxygen stoichiometric deviation results approached the CT measurements though the experimental results were higher. Specifically it is observed that there was no agreement, within error, between the CT Xdev experimental measurements and model predictions, except at the pellet peripheral CT measurement (5 mm from pellet centre) in Figure 111 (a) where there was agreement. This discrepancy may be partly explained if the actual and modeled sheath breaches (or defects) are compared. In the actual fuel element several sheath defects were observed (see Figure 112). From the ‘Non-Reference End’ of the fuel element there was a leaking end-cap, at the fuel element mid section there was an axial sheath crack and two open blisters and at the ‘Reference End’ of the fuel element there was an open blister [29][88]. Furthermore, fuel element XC9179Z-5 [88] broke in two when it was transported from DNGS to CRL for PIE analysis, indicating that the fuel element sheath was quite brittle and probably had additional sheath breach sites. In the model on the other hand only one axial mid section sheath breach was considered. It is reasonable to suggest then that the presence of additional sheath breaches that are distributed over the fuel element have a greater oxidizing effect than a single point sheath breach. This is so even if the sum of the multiple breaches surface area is similar or less than a single modeled sheath breach surface area, which is the case for this model and defective fuel element.

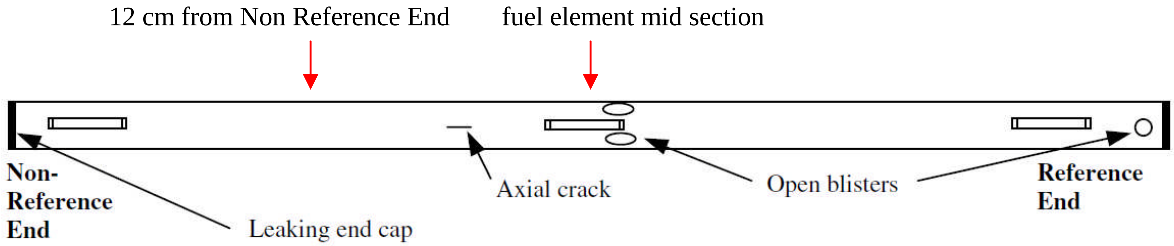

Figure 112: Sheath defect types and their locations recorded on fuel element XC9179Z-5 [29][88]

Other possible reasons for the lower modeled oxygen stoichiometry deviation results compared to the experimental measurements include: (1) the temperature selection of 1250 °C (1523 K) for the elastic-to-plastic boundary is too low and should have been set to a higher value in the current model, and (2) the CT uncertainty is not conservative enough.

Selecting a suitable fuel surface temperature in the model can also have an effect on the extent of fuel oxidation. In Figure 111 (a) and (b) the purple dashed curves represent the oxygen stoichiometric deviation radial distribution model results for when the fuel surface temperature was changed from 645 K set to 706 K, the latter temperature taken from [29] for this defective fuel element. This had the effect of raising the fuel centre line temperature from ≈1600 K to ≈1700 K. Since by doing this the fuel temperature radial profile was higher, the position of the fuel elastic-to-plastic boundary (i.e., the cracks tips or crack root) needed to moved from 1.5 mm to 2.25 mm from the pellet centre so that this boundary remained at

≈1523 K at the same power of 44 kW m^{-1}. In both Figure 111 (a) and (b), for the two axial locations in the modeled fuel element, there was a marked increase in fuel oxidation (as high as a 13% increase in certain radial locations). Thus, increasing the fuel surface temperature (which is dependent in part on the fuel-to-sheath gap distance and on the composition of the gas in the gap) directly influences fuel oxidation.

In the previous model results shown in Figure 109 and Figure 111 the radial cracks extended only 3 cm (or 6 cm actual) in the axial direction as discussed in Section 3.5.5. This was done in order conserve computer resources. Conversely in model results presented in Figure 113 (a) and (b) the radial fuel cracks were extended to the full 0.241 m axial length of the model (or 0.482 m in a full length fuel element).

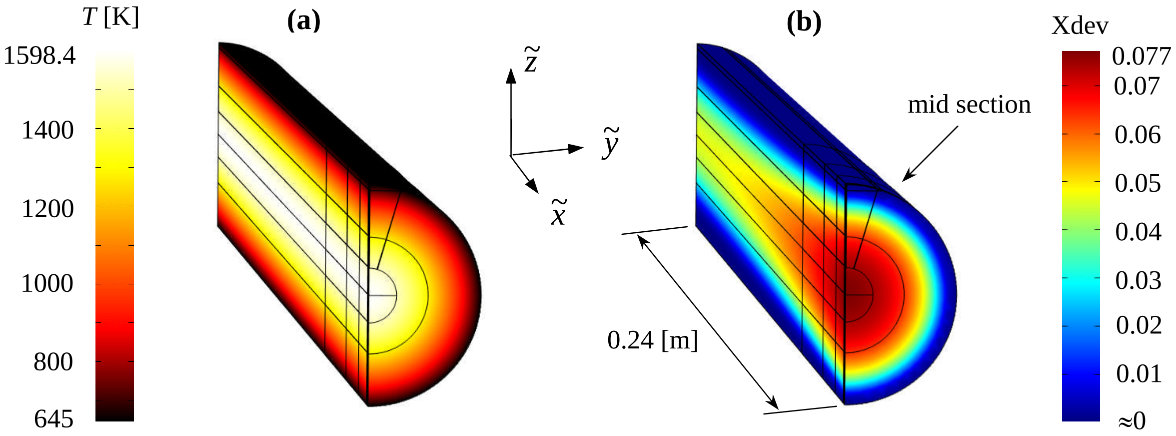

Figure 113: (a) Temperature distribution and (b) oxygen stoichiometric deviation after 126 days of simulated heating using a model with full length axial cracks with fully swept mesh

When the maximum modeled temperature and the oxygen stoichiometric deviation results in Figure 113 for defective fuel element XC9179Z-5 using the full length cracks model are compared to the partial length cracks model results in Figure 109, it can be observed that there are only slight differences between these two results. This is illustrated more clearly in Figure 114, where Xdev results are compared as radial profiles between these two models, specifically at (a) the sheath defect location (at the fuel element mid section) and at (b) 12 cm from the fuel element sheath defect.

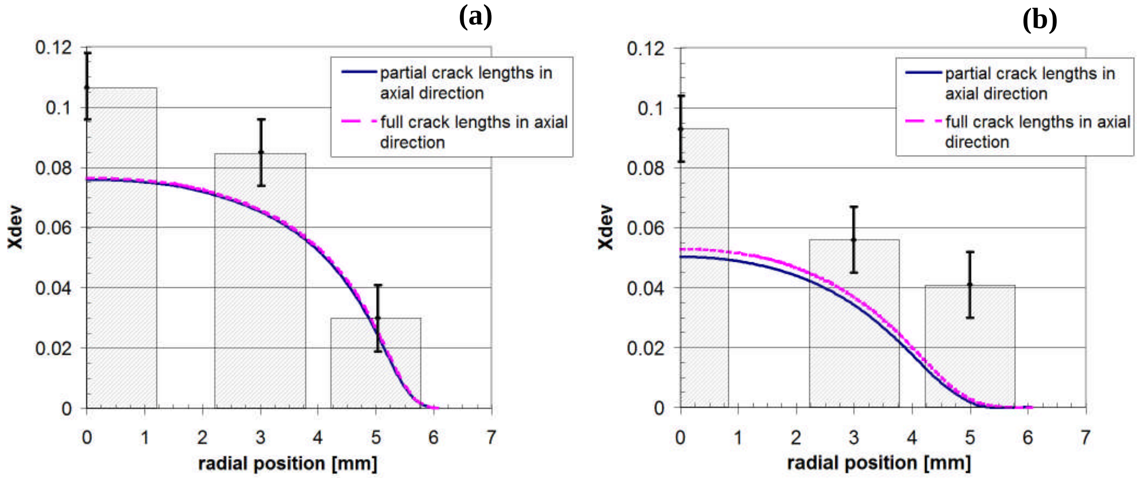

Figure 114: Modeled oxygen stoichiometric deviation radial distribution comparison between a model with partial crack lengths that are 6 cm in the axial direction and a model with full length cracks in the axial direction at (a) the fuel element mid section at the sheath defect and (b) the fuel element model middle (or 12 cm from the sheath defect)

As can be observed in Figure 114 (a) there is essentially no difference between the two Xdev profile results right at the sheath defect location, in these two models. In Figure 114 (b) there is a slightly higher concentration of hyperstoichiometric oxygen using the model with full crack lengths in the axial direction (purple dashed line) compared to the model with partial crack lengths in the axial direction (blue solid line). The difference though is small. The coulometric titration measurement results of defective fuel element XC9179Z-5 [88] seen in Figure 111 are re-plotted in Figure 114 for reference purposes.

A comparison is made between the 3D fuel oxidation model that uses discrete radial cracks running down the length of the fuel element in the axial direction (the current model in this thesis) to a model that uses the previous Higgs modeling approach [24][29]. The reader is reminded that the Higgs model does not use discrete fuel cracks but scaling parameters to represent fuel cracks (refer to Section 1.6 and to Section 3.5.5 and Figure 62 for details of the Higgs modeling approach). As can be seen in Figure 115 (a) there is a marked difference in the Xdev radial profiles (at the sheath defect location) between the two models. Specifically after 126 days of simulated oxidation the current fuel oxidation model (blue solid curve) produced Xdev values more than twice that of the model using the Higgs approach (red dashed curve). The coulometric titration measurement results of defective fuel element XC9179Z-5 [88] seen in Figure 111 are re-plotted in Figure 115 (a) for reference purposes. The reason for these different results is that the current model allows hydrogen diffusion through the discrete fuel cracks along the length of the fuel element where the Higgs model allows hydrogen diffusion only in the radial direction from the site of the sheath defect (refer to the red domain in Figure 62). In other words the fuel domains that contribute to the source term in Eq. (18) and (27) are smaller using the Higgs modeling approach.

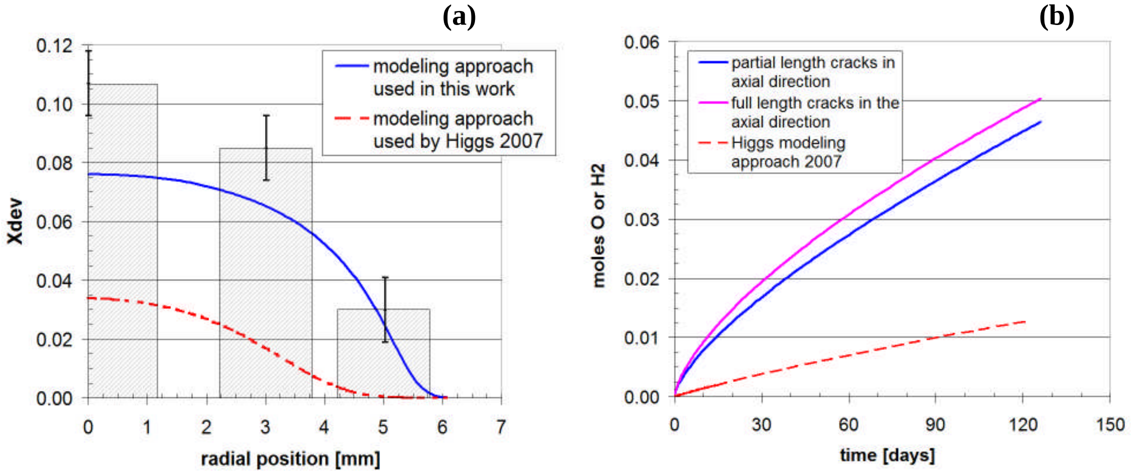

Figure 115: (a) Xdev profiles model comparison at the fuel element mid section using the current and previous modeling approaches and (b) the total computed moles of hyperstoichiometric oxygen introduced into the fuel and hydrogen gas liberated at the fuel cracks and gaps in the in-reactor fuel element

A comparison between the computed oxygen mole uptake (Eq. (165)) into the fuel element can also be made using the three different in-reactor fuel oxidation models, see Figure 115 (b). As is clearly seen from the figure the oxygen mole uptake in the two cracked fuel oxidation models (the blue and purple curves for the models with partial and full length cracks in the fuel element axial direction, respectively) after 126 simulated oxidation days are very similar and reached a value ≈0.05 moles. On the other hand using the Higgs modeling approach yielded only ≈0.012 moles of oxygen uptake in the defective fuel element after the same amount of time. It is worth noting from Figure 115 (b) that after 126 simulated oxidation days, in all three models, oxidation/reduction equilibrium has not yet been reached and that the defective fuel element models showed continued oxygen uptake.

Hence, considering the CT measured valued shown in Figure 115 (a), the fuel oxidation model using discrete fuel cracks and a sheath defect approaching realistic surface areas provides a more accurate prediction of fuel oxidation in defective fuel.

4.6 3D Out-Reactor Fuel Oxidation Simulation

High Power Case (optimal power case for experiment)

As explained earlier in the numerical implementation section for this model (Section 3.5.6) temperature boundary conditions were used on the fuel inner surface (instead of modeling the iridium bar heater) and on the fuel outer surface (instead of modeling the fuel-to-sheath gap and sheathing) of the out-reactor modeled fuel. Similar temperature values, to those computed in 2D r-θ model in Section 4.2.1 (see Table 27), were used for the boundary conditions in the current 3D model. These applied temperature boundary conditions on the modeled fuel was equivalent to approximately 23 kW of total power in the fuel element or approximately 47.7 kW m^{-1} of linear power (see Table 28) generated in both the iridium bar heater and in the fuel sheathing.

Figure 116 (a) and (b) show an isometric view of the temperature distribution and the oxygen stoichiometric deviation distribution modeled result, respectively, both after two weeks of heating. As can be seen in Figure 116 (b) the oxygen stoichiometric deviation was highest near the UO_2 heated annulus, at the axial location beneath the sheath defect, where it reached a maximum value of $x = 0.062$.

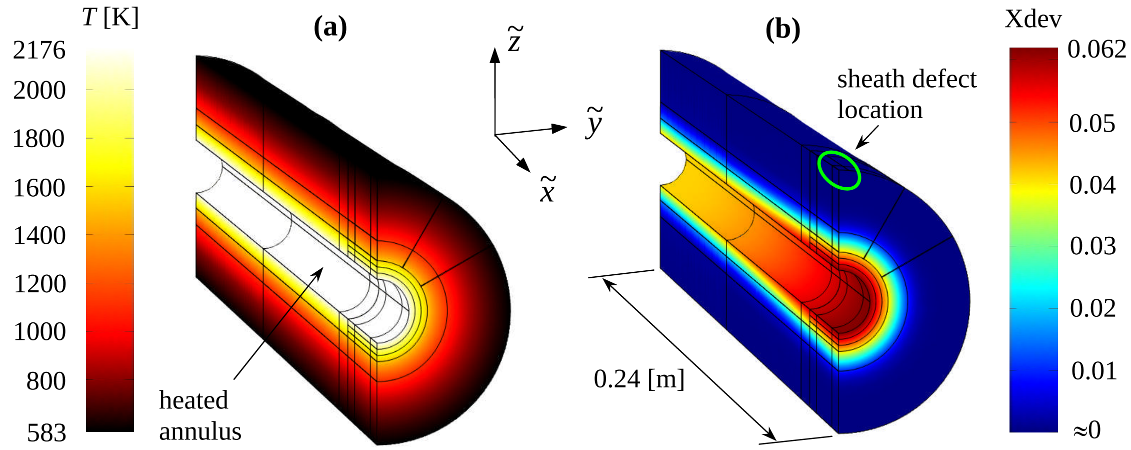

Figure 116: (a) Temperature distribution and (b) oxygen stoichiometric deviation after 2 weeks of heating in the out-reactor fuel element at 47.7 kW m^{-1} (23 kW total power)

As one moves away from the sheath defect area in the axial direction the local maximum oxygen stoichiometric deviation value drops and an axial x (or Xdev) gradient can be observed.

To view this axial gradient in x more carefully, the following figure provides radial plots of the oxygen stoichiometry deviation at three axial locations along the model: at the sheath defect location, at the centre of the model (or 12 cm away from the sheath defect location), and at the end of the model (or 24 cm away from the sheath defect location). As can be seen in Figure 117, the solid yellow curve, which gives the radial x (Xdev) values at the sheath defect axial location, shows the highest x axial and radial values in the model. The dashed purple curve provides the radial x values at the end of the model (near the fuel element end-caps, 24 cm away from the modeled sheath defect). The dashed red vertical line provides the location of the UO_2 pellet inner annulus surface.

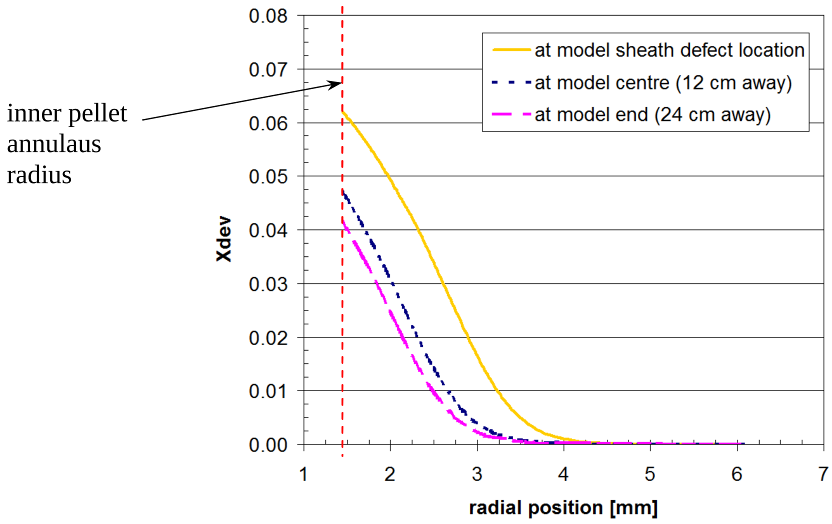

Figure 117: Radial plots of the oxygen stoichiometric deviation in modeled out-reactor fuel element at 23 kW at three axial locations after 2 weeks of simulated heating time

As can been seen there is a drop in the radial *x* values as one moves away axially from the sheath defect area at the fuel element centre to the edge 24 cm away, where the highest *x* value was 0.041.

In the current fuel oxidation model representing a defected fuel element in the out-reactor experiment the thermal conductivity of the fuel is expected to be affected by the oxidation process, which in turn can affect the temperature distribution in the fuel. Figure 118 (a) shows radial temperature plots from the pellet annulus to the pellet outer surface at three different times: at 5.5 hours, at 1 day, and at 2 weeks of simulated time. In this figure the three curves are very similar and almost coincide with one another. Figure 118 (b) is a close-up view of Figure 118 (a) near the radial position of 2.6 mm from the fuel centre, which reveals slight differences in the temperature curves. After 5.5 hours of simulated heating time the blue dashed line shows the lowest temperature value. After 1 day of simulated heating time there is a slight increase in temperature (<10 degrees K), as shown by the purple dotted curve. As the model simulation is continued the temperature increases (>21 degrees K), as shown by the solid yellow line.

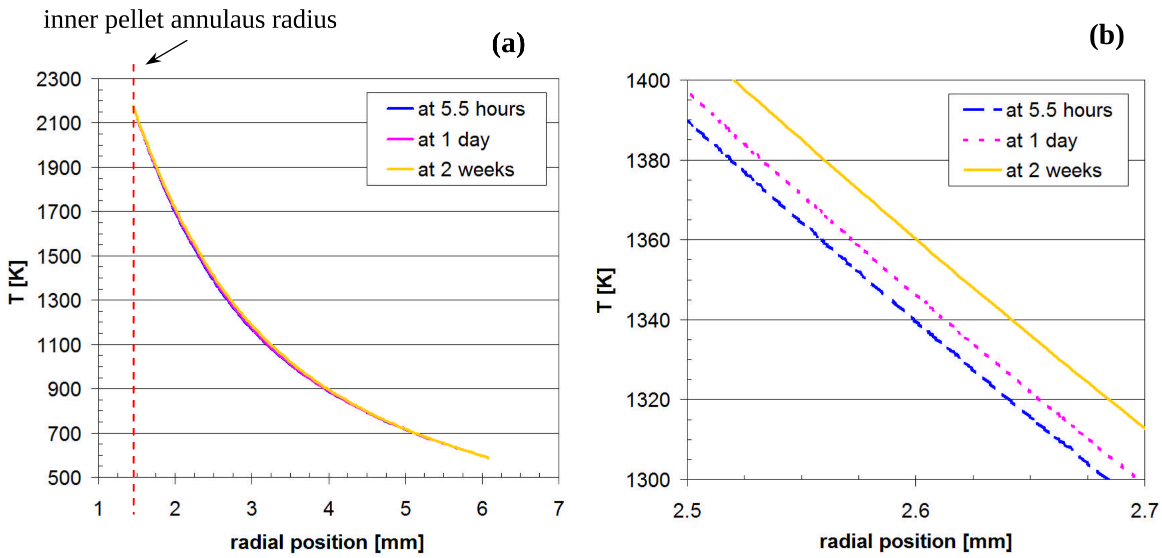

Figure 118: Radial temperature plots near the sheath defect at three different times; (a) for a complete radial span and (b) in a close-up view near the position of TC1

To demonstrate that fuel oxidation occurs at an accelerated rate at the fuel crack tips (where the temperature is highest) Figure 119 shows the oxygen stoichiometric deviation distribution in the vicinity of the fuel cracks after only 10 seconds of simulated heating.

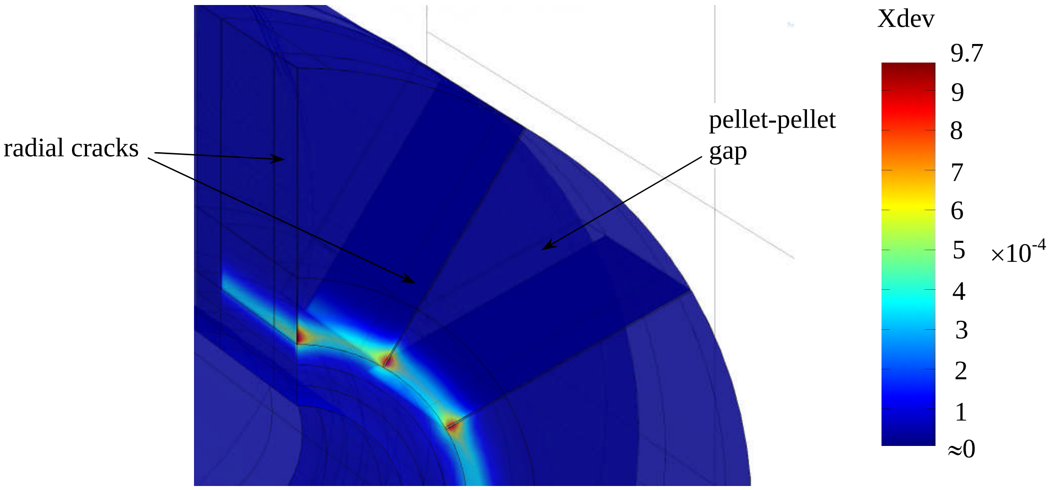

Figure 119: Oxygen stoichiometric deviation after 10 seconds of simulated heating

As can be clearly seen the highest fuel oxidation (red color) occurs at the junction between the bottom of the radial fuel crack domains and the pellet-pellet gap domains immediately under the sheath defect. The reason for the accelerated oxidation at this location in the fuel is for two reasons: (i) the steam at the crack tips is at the highest temperature and (ii) the hydrogen mole fraction is at a relatively low value due to proximity to the sheath defect. This latter point is shown in Figure 120 (a) and (b) where the blue areas indicates the lowest hydrogen mole fraction occurring in the fuel cracks, the pellet-pellet gap, and part of the fuel-to-sheath gap.

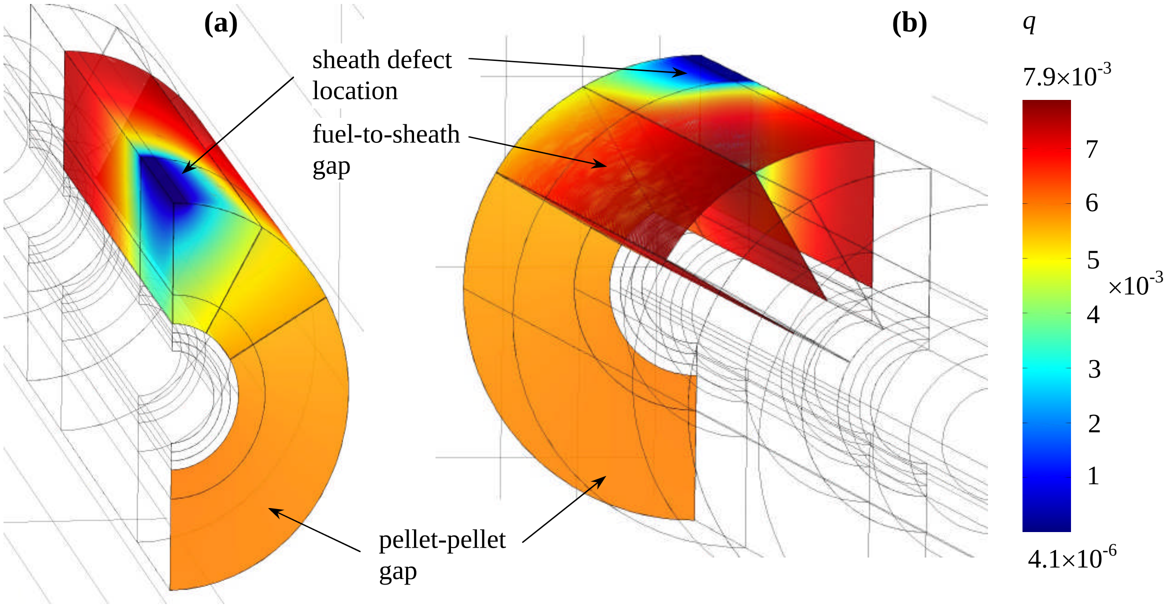

Figure 120: (a) Hydrogen mole fraction distribution seen facing the model with sheath defect (blue area) and (b) facing away from the model

In a similar model the boundary condition of the hydrogen mole fraction equation (i.e., the hydrogen diffusion equation, Eq. (27)) at the sheath defect location was set to 1.67×10^{-14}. See again Figure 63 for the sheath defect location and Table 24 for the original q_c value. This value was calculated using FactSage 6.1 Gibbs energy minimization software for pure light water at 573 K. This smaller value for q_c (essentially zero) did not change the fuel oxidation result shown earlier in Figure 116 (b). This is mentioned since the coolant of the out-reactor loop is light water, while the in-reactor coolant is heavy water with a higher q_c value.

Figure 121 shows the total hyperstoichiometric oxygen mole uptake into the fuel element after two weeks of heating by computing Eq. (165) in Section 3.5.1.

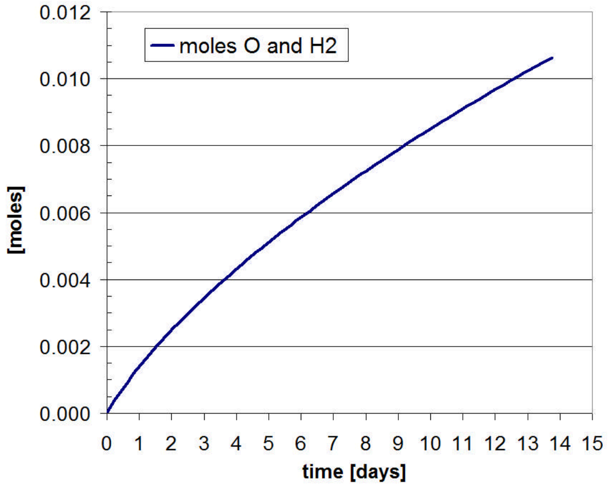

Figure 121: Total moles of hyperstoichiometric oxygen introduced into the fuel and hydrogen gas liberated at the fuel cracks and gaps for the 23 kW case

Computing the mole amount of hyperstoichiometric oxygen uptake into the fuel gives another quantity to describe the extent of fuel oxidation. For example, in the 2D r-θ closed fuel-to-sheath gap fuel oxidation model the maximum Xdev value was 0.095 (Figure 73 (b)) and the oxygen uptake n_{O} was 0.068 moles (Table 27). On the other hand in the 3D fuel oxidation model the maximum Xdev value was 0.062 (Figure 116 (b)) and the oxygen uptake n_{O} was only slightly above 0.010 moles. Thus the n_{O} computed result varies to a greater extent than the maximum Xdev value for the same amount of oxidation.

It is evident from Figure 121 that after introducing >0.010 moles (160 mg) of hyperstoichiometric oxygen, or when the maximum Xdev value in 0.062, that the oxidation process after two weeks of heating hasn’t reached equilibrium in this out-reactor defected fuel element model.

Lower Power Case

In the lower power case only 17 kW of total power, or 35.3 kW m^{-1} of linear power, was applied in the model to see the effect of the lower fuel temperature on the extent and distribution of fuel oxidation. The temperature and oxygen stoichiometric deviation distribution model result, after two weeks of heating, is shown in Figure 122. This heating power, computed from the supporting 2D r-θ model, provided a temperature boundary condition of 1816 K for the inner annular surface of the 3D fuel oxidation model. Since the fuel temperature was lower in this model the crack depth was made deeper in the pellet. Specifically, the crack depth was set to 1.874 mm from the pellet centre (or 4.201 mm from the pellet surface) to achieve a crack root temperature of 1523 K (1250 °C). It can be noted that the supporting 2D r-θ model yielded 1135 K (862 °C) at the inner most thermocouple (TC-1) location. In this 3D model the resulting maximum stoichiometric deviation was a little higher, Figure 122 (b), than in the higher powered fuel element in Figure 116 (b) after two weeks of heating, reaching a value of x (or Xdev) = 0.068. This result was initially unexpected. But if x radial plots are compared at three different axial locations in the fuel element, a steeper x gradient in the model axial direction can be observed in Figure 123, as compared to the optimal power case in Figure 117.

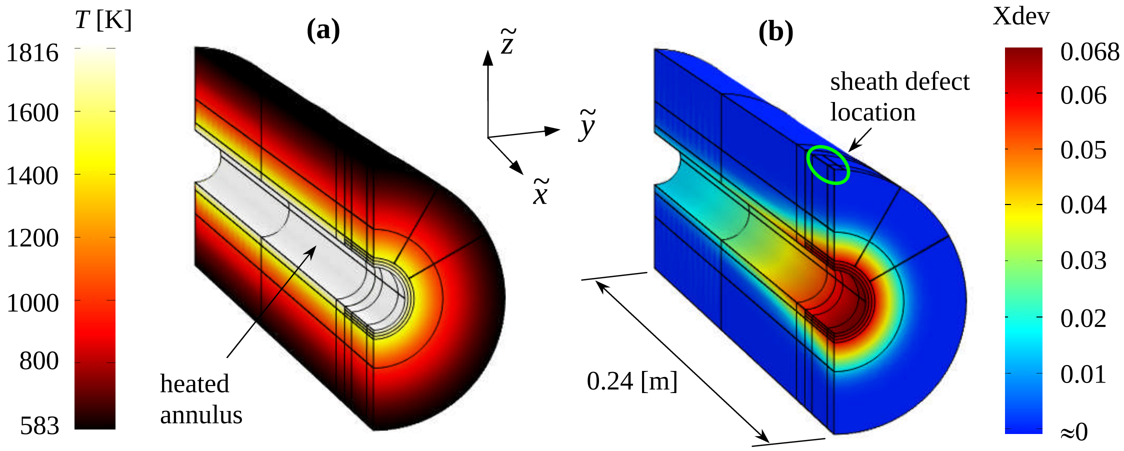

Figure 122: (a) Temperature distribution and (b) oxygen stoichiometric deviation after 2 weeks of heating, in the out-reactor fuel element at 35.3 kW m^{-1} (17 kW total power)

Specifically, for the lower power case the maximum *x* at the sheath defect (and near the heater in the radial direction) was 0.068 but drops to 0.03 when only 12 cm away from the sheath defect, unlike in the higher power case where *x* drops to just under 0.05 the same distance away from the sheath defect location. I.e., less oxygen diffusion (slower interstitial oxygen atom diffusion) occurs due to the lower internal temperature of the fuel element. This may be important to consider when interpreting the post test coulometric titration measurements.

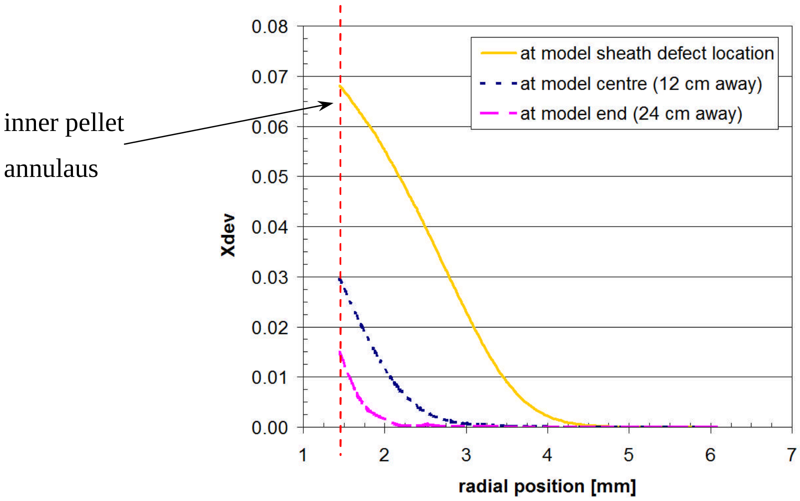

Figure 123: Radial plots of the oxygen stoichiometric deviation in the modeled out-reactor fuel element at 17 kW power at three axial locations after 2 weeks of simulated heating

The total hyperstoichiometric oxygen mole uptake into the fuel element for the lower power case after two weeks of heating is provided by Figure 124. Here, only 0.006 moles (96 mg) of hyperstoichiometric oxygen were introduced into the fuel element. Keeping in mind that the maximum oxygen stoichiometric deviation values in both the high and low power models were similar, this is ≈40% drop in the oxygen uptake compared to the high powered case (Figure 121).

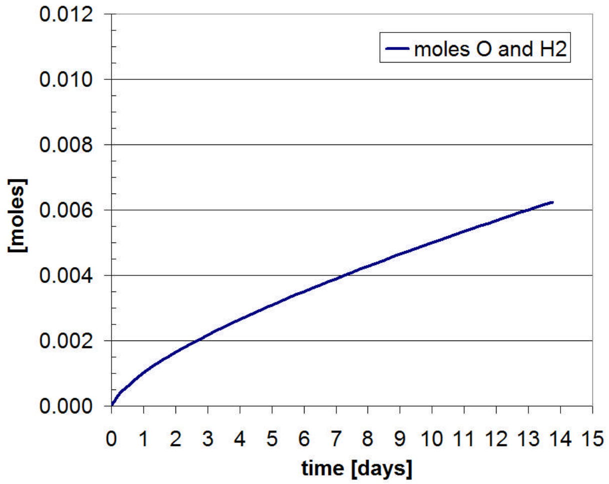

Figure 124: Total moles of hyerstoichiometric oxygen introduced into the fuel and hydrogen gas liberated at the fuel cracks and gaps for the 17 kW case

Thus, both the high powered (23 kW) and the low powered (17 kW) out-reactor fuel element modeled cases, with crack tip positions set at 1523 K (1250 °C), can generate the same maximum oxygen stoichiometric deviation in the oxidized fuel. But the higher powered fuel element model showed that more of the fuel was oxidized, and oxidized more evenly, away from the sheath defect, since interstitial oxygen diffusion is accelerated at increased temperatures. For validating the fuel oxidation model both the high and low powered cases applied in the experiment will generate enough oxygen stoichiometry deviation in the fuel to be measured in post test coulometric titration measurements. The temperature increase though in the fuel due to the fuel oxidation, for the planned experiment duration, may be too small to distinguish due to measurement uncertainty.

Summary of Chapter 4:

- A comparison was made between measured and modeled UO_2 thermal conductivity (Section 4.1). The modeled thermal conductivity comprised of a MATPRO formulation and the fuel oxidation model formulation (the latter where $x = 0$). Both model formulations were similar, however the fuel oxidation model thermal conductivity was a little higher; no more than 10% higher than the MATPRO formulation. Since the MATPRO formulation agreed more closely with experimental measurements of various investigators, a correction quantity was estimated for normal operating temperatures of the fuel and was provided for the reader. It was not used in this thesis.

- In a 2D r-θ fuel oxidation model (Section 4.2.1) with a closed fuel-to-sheath gap, it was shown that the fuel oxygen stoichiometric deviation of $x = 0.095$ resulted after two weeks of heating the defected FES. This was an overestimate of oxidation since the modeled sheath defect area was many times larger than the expected FES sheath defect.

- In a similar 2D r-θ fuel oxidation model (Section 4.2.2) the fuel-to-sheath gap dimension and then the discrete fuel crack width dimension were varied independently to demonstrate their effect on the extent of fuel oxidation. This indicated the hydrogen gas transport was sensitive to these dimensions and that it was important to select suitable values for these two dimensions in the 3D model.

- Using the J integral (Section 4.3) conditions for fuel crack propagation developing from a pellet surface flaw was computed. By analyzing the azimuthal stress in the pellet (i.e., if mode I loading occurs) the number of radial cracks was assessed.

- In a more sophisticated 2D r-θ model (Section 4.4) the fuel oxidation physics was coupled with solid mechanics physics and Arbitrary Lagrangian Eulerian (ALE) to simulate fuel oxidation and both the thermal expansion of the six preset radial fuel cracks and fuel and sheath contact using the penalty method. The model results provided the dimensions of the expanded radial fuel cracks (width and length) and also showed that the amount of fuel oxidation achieved in two weeks of heating would not affect the fuel crack dimensions.

- Initial validation of the fuel oxidation model (Section 4.5) was accomplished with two models: (i) A 2D r-θ model simulated the first prototype test (FES1) conducted at the Stern Laboratories. The modeled fuel temperatures agreed within uncertainty with measured temperatures, confirming the validity of the thermal properties of the fuel oxidation model (without oxidation). (ii) The fuel oxidation model was initially validated with a model of in-reactor defected fuel element. It was found that the oxidation model results and measurements were approaching agreement.

- With the guidance provided by the previous model results (temperature boundary conditions and fuel crack dimensions and number) a 3D out-reactor defected fuel element was modeled (Section 4.6), where a maximum oxygen stoichiometric deviation of $x = 0.062$ was achieved after two weeks of heating and oxidation.

CHAPTER 5 THE ROLE OF OXYGEN IN FUEL SHEATHING STRESS CORROSION CRACKING

5.1 Background

Pellet-cladding interaction (PCI) failures in nuclear fuel were first observed in the 1960s in Boiling Water Reactors and in CANDU type reactors. PCI occurs when the expanding and cracked fuel pellets make contact with the cladding in BWR fuel and collapsed sheathing in CANDU fuel. To reduce the effects of PCI, BWR fuel adopted a pure zirconium barrier, also called ‘liner’, in the 1980’s on the inside surfaces of the Zircaloy cladding [168]. This extra layer of pure zirconium acted as a stress reliever but it also increased susceptibility of the cladding to corrosion. Canadian reactors solved their PCI issues in the 1970’s using a thin layer of graphite, called “CANLUB”. Since then PCI has received little attention with the incorporation of strict reactor operation limits, except during times of power transient conditions and potential accident scenarios [169].

Iodine induced stress corrosion cracking (I-SCC) is usually the cause of PCI failures of unlined Zircaloy cladding containing UO_2 reactor fuel pellets. PCI failures usually occur in fuel rods with over 10 GWd tUO_2^{-1} burn-up and rapid reactor power ramps. Fission products must also be present above a local threshold concentration to cause I-SCC [61].

The following minimum conditions are required for I-SCC:

a) Critical stress (critical strain) in sheathing

b) Critical iodine concentration

c) Minimum of time and temperature

Fission product iodine in nuclear fuel is not the only corrodant that can cause SCC in Zircaloy cladding/sheathing. Cesium/cadmium vapours have also been shown to cause corrosion in the form of a liquid metal embrittlement process [30][47]. Fractographic evidence though has shown that PCI cracks in CANDU fuel is usually a mix of both integranular and transgranular cracking, whereas the cracking in cesium/cadmium vapours is always transgranular (examples of such cracking is given later in Section 5.5). Thus, evidence suggests that iodine is the main cause of SCC in Zircaloy cladding/sheathing [47].

In light water reactors as the fuel burn-up proceeds, the diameter of the fuel pellet is increased so that the pellet and the cladding contact each other typically in the third fuel cycle. In CANDU fuel, this contact occurs even sooner, since the sheathing is thinner than in BWR and PWR fuel and since sheath creep down occurs. During this time, the concentration of iodine inside the fuel rod increases. With a power ramp, the ceramic fuel additionally expands and cracks due to thermal gradients. The cladding or sheathing in contact with the fuel is put under hoop stress and the cracks allow access of corrosive fission products to the Zircaloy internal surface. With the chemical and mechanical interaction present, I-SCC failures typically occur in the cladding near fuel pellet radial cracks [55][168]. This is because the radial cracks act as conduits for gas transport that allows volatile iodine fission products to reach the fuel-to-sheath gap and make direct contact with the exposed sheathing.

The total production of cesium is about tens times that of iodine in the fuel rod [61][170]. Iodine reacts with cesium to form stable CsI. Cox *et al.* [171] and Hofmann *et al.* [172] showed that CsI on its own does not necessarily cause I-SCC in Zircaloy, but in the presence of radiation [171] or oxygen [172], CsI can be dissociated to release iodine. Thus many previous studies have focused on iodine as the main corroding agent in the SCC of Zircaloy yet new approaches to reduce or prevent I-SCC have been lacking.

Today, most new reactor builds are adopting a high burn-up operation to increase fuel economy. Future CANDU type fuel may include slightly enriched uranium for increased burn-up (up to ≈20,000 MWd/tUO$_2$). With higher burn-up and longer in-core residence times, higher fission product gas pressures are expected, which can lead to increased susceptibility to I-SCC defects. For current CANDU reactors with natural uranium fuel elements that have lower burn-ups, I-SCC of the fuel sheathing is less of a concern but increasing the fuel safety margins, especially during power ramps, would be highly beneficial to the industry. The Zircaloy sheathing corrosion problem needs to be better understood so that more effective solutions can be designed to prevent I-SCC and to find possible alternatives to CANLUB DAG154N that is currently used, especially considering current concerns for its replacement. It is believed that a slightly oxidized fuel pellet surface could provide a possible remedy or reduction of the I-SCC phenomenon in CANDU fuel.

5.2 Goal and Premise for I-SCC Experiments

The goal of the experiments conducted in this thesis is to investigate the affect of oxidized UO_2 fuel material in contact with graphite on the iodine induced stress corrosion cracking (I-SCC) process in Zircaloy sheathing (if any) and to see if it possesses any mitigation properties to this corrosion mechanism as suggested by Bruni [173] with a test apparatus briefly described by Kleczek [174], based on early I-SCC work by Wood [175]. It has been demonstrated that zirconium oxide plays a role in protecting the zirconium sheathing from I-SCC attack [61][62]. The reaction of zirconium and oxygen is highly product favoured as expressed:

$$Zr(s) + O_2(g) \rightarrow ZrO_2(s) \qquad (194)$$

with ΔG =-977 kJ per mole Zr for this reaction at 350°C . The brittle monoclinic oxide layer may crack though, at strains below 0.5% during fuel element power transients, thereby exposing the underlying zirconium to the iodine corrodants [176]. One suggested remedy to this problem is to use a surface layer of slightly oxidized fuel to repair the protective oxide on the Zircaloy sheathing [177].

Une [60] and Yang *et al.* [62] showed that a zirconium oxide layer in the sub micrometer range in thickness had protective properties to iodine corrodants. The thickness of the oxide layer can vary greatly depending on atmosphere temperature and oxygen content. At room temperature a typical Zircaloy-4 machined component exposed to air will have an oxide layer of about ≈4 nanometers [178], or about 15 monolayers. At elevated temperatures in air or in other oxygen containing atmospheres the oxide layer thickness can be increased. The zirconium oxide surface, when 5 to 250 nanometers thick, can have various colors.

Figure 125 (a) gives a coloring spectrum key for the oxide layer thicknesses, which is reinforced by submerging specimens in an anodizing 1% KOH solution [179]. The anodizing process is an electrolytic passivation process used to increase the oxide layer thickness, in this case to emphasize the colors. It is assumed that the oxide thickness in Figure 125 (a) was measured before applying the anodizing process. Figure 125 (b) gives a similar oxide thickness spectrum key (possibly without the anodizing process) [179], which shows that when the oxide is 380 nanometers in thickness and higher it is grey in color.

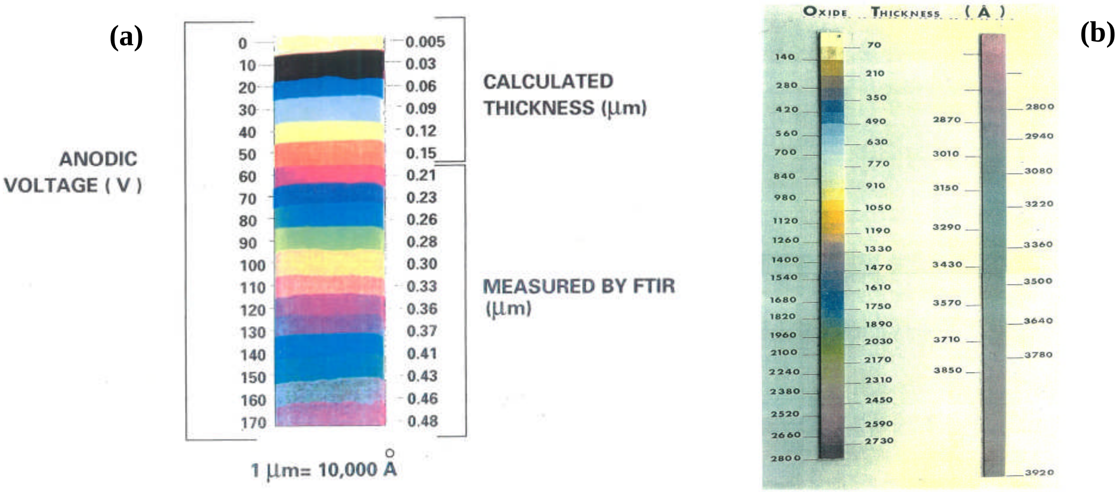

Figure 125: (a) Anodic oxide film on Zircaloy-4 spectrum key (anodized in 1% KOH) and (b) a Zircaloy oxide layer thickness spectrum key without anodizing [179]

The premise for this remedial technique considers that carbon from CANLUB graphite, when put in direct contact with UO_{2+x}, may produce carbon dioxide in a reduction reaction as shown in Eq. (195).

$$2UO_{2+x}(s) + xC(s) \rightarrow 2UO_2(s) + xCO_2(g) \qquad (195)$$

Hyperstoichiometric UO_2 can be thought of as a solid solution of UO_2 and a hypothetical form of UO_3 in the fluorite structure as expressed [24]:

$$(1-x)UO_2(s) + xUO_3(s) \rightarrow UO_{2+x}(s) \qquad (196)$$

For example, if the stoichiometric deviation in the fuel is x=0.05, one can rewrite Eq. (195) using Eq. (196) to give Eq. (197). The top right hand side of Eq. (197) can now be explored with FactSage® 6.1 Gibbs energy minimization software [21] computation. The temperature at equilibrium was set to 623 K at 1 atm. The temperature 623 K was chosen, since it is just under the calculated average fuel-to-sheath gap temperature of selected modeled fuel elements in [24]. The resulting Gibbs free energy change is computed to be $\Delta G = -2.31227\text{x}10^3$ kJ.

$$\begin{gathered} 2UO_{2.05}(s) + 0.05C(s) = 1.9UO_2(s) + 0.1UO_3(s) + 0.05C(s) \\ \rightarrow \\ 2UO_2(s) + 0.05CO_2(g) \end{gathered} \tag{197}$$

Thus, the the reaction is thermodynamically favorable and the products are basically stoichiometric UO_2 and carbon dioxide. The FactSage® 6.1 computation for Eq. (197) is provided in Appendix D-1.

Another possible outcome is the reaction between hyperstoichiometric uranium dioxide and carbon, given by Eq. (198):

$$UO_{2+x}(s) + xC(s) \rightarrow UO_2(s) + xCO(g) \tag{198}$$

This reaction gives the production of carbon monoxide if carbon dioxide does not fully form in the given time. From work by Lawrence *et al.* [69] it would seem that CO_2 is favoured over CO as a product at and below 923 K (700°C), though data at 623 K (350°C) was not provided.

The reduction of U_4O_9, the second possible phase in hyperstoichiometric uranium dioxide, at low temperatures up to $x = 2.25$ (see Figure 9) with carbon, can be written as:

$$U_4O_9(s) + C(s) \rightarrow 4UO_2(s) + 0.49938C(s) + 0.5CO_2(g) + 0.0012CO(g) \tag{199}$$

The Gibbs free energy change for this reaction was computed to be $\Delta G = -71.9$ kJ at 623 K (350°C) and 1 atm.

Since the produced carbon dioxide or carbon monoxide is a gas, it is free to move around in the fuel element via the fuel cracks, the pellet-pellet gaps, and the fuel-to-sheath gap. When it makes contact with the Zircaloy, it can oxidize any exposed/bare zirconium metal where the zirconium oxide layer has been damaged previously by cracking. Eq. (200) provides the reaction of zirconium and carbon dioxide where the Gibbs free energy change for this reaction is ΔG = -582 kJ at 623 K (350°C) and 1 atm, indicating it is a favorable reaction.

$$Zr(s) + CO_2(g) \rightarrow ZrO_2(s, \text{monoclinic}) + C(s, \text{graphite}) \qquad (200)$$

The following reaction with carbon monoxide shows a similar product favored tendency:

$$Zr(s) + CO(g) \rightarrow 1/2\ ZrO_2(s, \text{monoclinic}) + 1/2\ C(s, \text{graphite}) + 1/2\ ZrC(s) \qquad (201)$$

where the Gibbs free energy change for this latter reaction is ΔG = -417.5 kJ at 623 K and 1 atm. The reaction between zirconium and carbon dioxide though is expected to be slower than the reaction between zirconium and oxygen (Eq. (194)). But the oxidation rate of the zirconium in Eq. (200) is probably accelerated when radiolysis of CO_2 to CO + O in a gamma field and in the vicinity of metals is considered (i.e., in a reactor irradiated fuel environment) as discussed by Yoshida *et al.* [180] and Watanabe *et al.* [181].

Some important notes on the zirconium oxide should be mentioned here beyond the chemistry discussed above. The texture of the underlying Zircloy sheathing is very important in determining the crystal structure, growth rate and thickness of the protective zirconium oxide [182]. Peehs [183] showed that SCC of Zircaly sheathing (or clad) is sesnsitive to its texture. It has also been shown that the crystal structure and thickness of the zirconium oxide can be affected by fission fragment recoils while in reactor as demonstrated by Yee *et al.* [184]. This in turn may also affect the oxide's corrosion resistance to fission products. It is also possible that the CANLUB layer may offer some protection from fission fragment recoils.

Increased fuel oxygen potential has been shown to have an effect of PCI frequency in in-reactor fuel. For example, in in-reactor ramp experiments using BWR fuel with Zircaloy-2 cladding [185], that used prepared fuel pellets with average O/U ratios of 2.05 (x=0.05) resulted in no PCI failures. Although only two sectioned fuel rods with increased oxygen potential were used in these tests, regular fuel subjected to similar test conditions would fail with high probability [185]. The relatively high amounts of hyperstoichiometric oxygen in the pellets is believed to interact with the fuel cladding without pre-existing reducing agents (such as graphite in CANDU fuel) in the fuel rods. Since these fuel rods were irradiated to over 20,000 MWd tU^{-1} prior to the ramp testing it is reasonable to believe that sufficient amount of reducing agents (hydrogen, carbon or other) could have been provided as fission products.

The repair process of the zirconia layer in CANDU fuel sheathing may account in part for the effectiveness of the CANLUB layer in hindering the I-SCC phenomena. The oxygen excess in the UO_2 fuel may be occurring due to inadvertent oxidation of the fuel pellets in the current sintering process during pellet production. Superficial pellet oxidation is not currently well controlled and if the current exploratory experiments in this work show positive results, i.e., a reduction in the Zircaloy sheathing failure rate and/or corrosion extent, then this approach for mitigating I-SCC should be investigated more closely.

Thus, the fuel oxidation model can be easily modified to compute the ideal heating and oxidizing parameters needed to sufficiently oxidize the external surface of the UO_2 fuel pellets. Another benefit of slightly superficial hyperstoichiometric fuel is the possible prevention of another type of Zircaloy sheath corrosion process. During fuel oxidation at the hotter regions of the defective fuel, hydrogen is liberated from the water coolant in an oxidation reaction. If this hydrogen builds-up at the fuel-to-sheath gap to high enough levels, delayed hydride cracking of the Zircaloy sheathing may occur [186][187]. This hydrogen though could be consumed in a reduction reaction at the UO_{2+x} fuel surface producing water vapour thereby preventing a critical hydrogen-to-steam ratio from being reached (see Eq. (17)).

5.3 Experimental Setup

In the following study Zircaloy-4 slotted ring specimens were used in I-SCC experiments using a similar test setup uitilized by Wood [175], with some new experimental techniques, to investigate the effect of oxygen and oxidized UO_2 on the corrosion behavior of this material with iodine.

Zircaloy slotted ring specimens were cut out of CANDU fuel sheathing, which were then cut longitudinally so that the resulting slot could be wedged open to impart stresses in the specimens. Two types of Zircaloy wedges were used: Static wedges and impact tightened in-situ wedges. Material composition of the Zircaloy-4 impact tightened wedges [188] is provided in Appendix E. Figure 126 shows a picture of slotted ring specimens and a static wedge before they are used in an experiment.

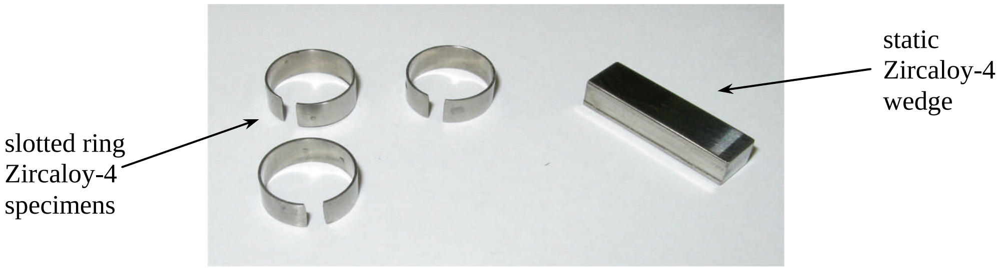

Figure 126: Zircaloy slotted rings and a static wedge prepared for I-SCC testing

Figure 127 (a) shows the sliding wedges before mounting the specimen and Figure 127 (b) shows two slotted ring specimens mounted on assembled sliding wedges.

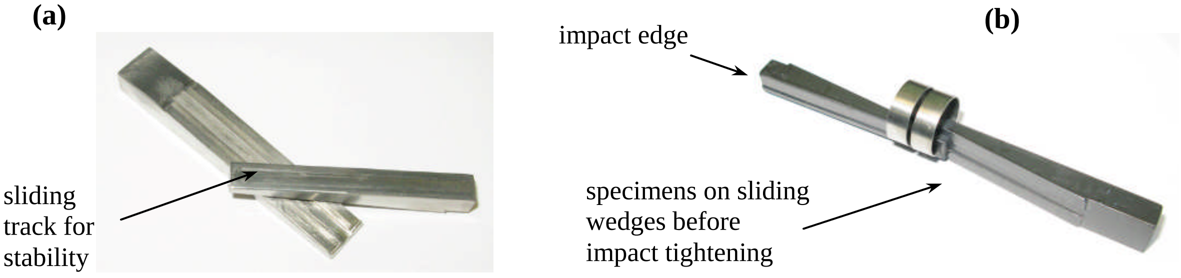

Figure 127: (a) sliding wedges before specimen mounting and (b) two slotted ring specimens mounted on sliding wedges ready for installation in a glass ampoule

The natural zirconium oxide layer that forms on Zircaloy surfaces has protective abilities against corrosion as mentioned earlier [60][61]. Thus, the purpose of the sliding wedges was to increase the susceptibility of the specimens to corrosion by disturbing the zirconium oxide layer in an oxygen free environment, so that a new oxide layer would not be formed.

5.3.1 Identification, Dimensions, and Hardness Measurements of the Zircaloy Specimens

Two types of Zircaloy specimens were available for performing the I-SCC tests: Type-1 Pickering 28-element sheath slotted ring specimens and type-2 Cameco 37-element sheath slotted rings specimens. Type-1 specimens were provided by the Chalk River Laboratories as ready made slotted rings. The type-2 specimens were prepared from current ≈480 mm long, 37-element CANDU-6 fuel sheathing, manufactured by Cameco Fuel Manufacturing. Zircaloy slotted rings were first cut from tube sheathing and were then slotted with an additional cut or two. The preparation procedure used to make the Cameco 37-element sheath slotted ring specimens (of type-2) is described in more detail in Appendix F. Table 36 provides designation and dimensional information of the two types of specimens.

Table 36: Identification and basic dimensions of Zircaloy specimens

Specimen type #	Identification number	Outside diameter [mm]	Wall thickness [mm]	Axial width [mm]
1.) Pickering 28-element type sheath (early batch)	MLI-790, 7A3-393-4A	15.50±0.25	0.40±0.01	5.0±0.1
2.) Cameco 37-element type sheath	248389-5 DAC 18787	12.50*±0.05	0.40±0.01	5.0±0.1

Note: Specimens of type-1 were provided in finished form and dimensions were taken using a Mastercraft electronic caliper. The dimensions* of the type-2 Cameco specimens were taken after the cutting procedure.

An additional specimen type was provided by Chalk River Laboratories as finished slotted rings from CANFLEX sheathing material (type-3). Since the type-3 specimens were similar in texture to the type-2 specimens it was not included in this work. However, the dimensions, hardness, and texture characterization of the type-3 specimens can be found in the appendices for reference purposes.

Hardness measurements were taken of the Zircaloy sheathing using a Rockwell Hardness indentation tester. This tester is essentially an instrument that measures hardness by determining the depth of a penetrator into a specimen. The penetrator is either a steel ball or diamond. The hardness of Zircaloy-4 sheathing falls under the Rockwell Hardness B scale where the B scales are suitable for materials of medium hardness, like low to medium carbon steels in the annealed condition [189]. Indentation tests are commonly used as an inexpensive material characterization test, since the tests are quick to perform and the hardness measurements typically correlate linearly with the tensile strength of the material. A Clark Instrument Inc. model CR-8, dial operated Rockwell Hardness indentation tester with a 1/16" diameter steel ball indenter and a 100 kg load, was used for this purpose. Slotted ring specimens for hardness measurements were cut into two pieces, one short and the other long in length. The long piece was partially flattened into a strip, which could then be loaded onto the indentation tester. Table 37 provides the hardness measurement of both types of specimens with no preliminary heat treatment in the lab (as received).

Table 37: Hardness Rockwell measurements of as received type-1 and type-2 Zircaloy sheathing specimens

hardnes scale	specimen type	mean	SD	SDOM (error)
HRB	type-1 (Pickering)	88.1	1.0043	0.3
	type-2 (Cameco)	86.3	1.1543	0.4

The average hardness of the as-received type-1 Pickering specimen was measured to be 88.1±0.3 HRB and the average hardness of the as received type-2 Cameco specimens was measured to be 86.3±0.4 HRB. From these measurements it is observed that the hardness of the two specimen types was quite similar, though the Pickering type specimens were slightly harder. The quoted hardness of Zircaloy-4 by the manufacturer ATI Wah Chang is 89 HRB averaged [190], which is slightly higher than the measured hardness of both as-received type specimens.

When both types of specimens were heat treated and stressed in the transverse direction, after which they were hardness measured, there was a slight increase in specimen hardness (about 2% on average). In other words there was a slight increase in the specimen tensile strength (and possibly a slight decrease in specimen ductility). See Appendix G for more details on specimen hardness measurements.

5.3.2 Characterization of Zircaloy Specimens - Crystallography

Zircaloy is an alloy of zirconium. The nominal Zircaloy-4 composition (as previously mentioned in Section 3.2.3) is Zr and 1.5% Sn, 0.2% Fe and 0.1% Cr with some impurities, such as 270 ppm C, 200 ppm Hf, 120 ppm Si, 100 ppm W, and 75 ppm Al [111][188]. In pure zirconium, a β-phase crystal structure exists between the temperatures 1855°C and 863°C, which is body centred cubic (bcc). Below 823°C to room temperature, the crystal structure changes to α-phase that is hexagonal close-packed (hcp). The tin additive is an α-phase stabilizer and helps increase the upper $\alpha + \beta$ to β transition temperature. The iron and the chromium additives are β-phase stabilizers, which help suppress the lower $\alpha + \beta$ to α + intermetallic compound transition temperature [191][192]. The optimal concentration of these additives achieves the desired phase concentration in the alloy, among other physical properties. Zircaloy exhibits anisotropy as a result of the hcp crystal structure.

The hcp crystal structure is depicted in Figure 128 (a) and (b).

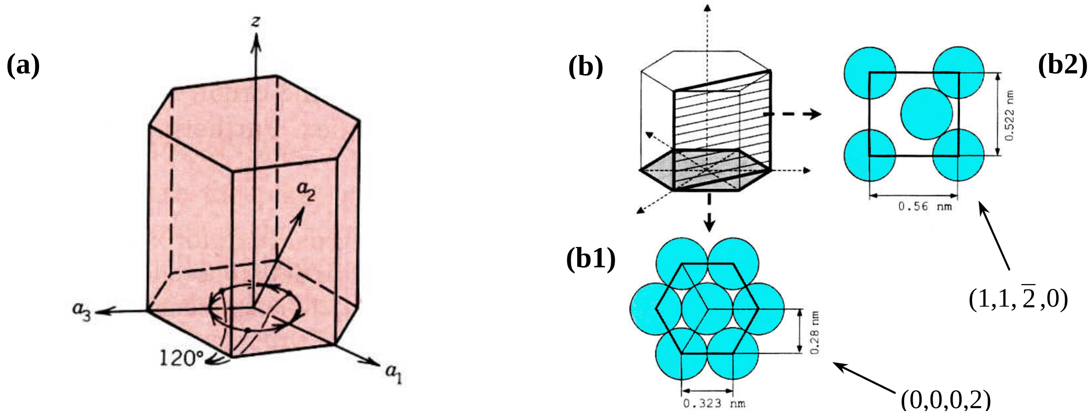

Figure 128: Schematic of the Miller-Bravais coordinate system of the hexagonal close-packed unit cell (a) and two lattice planes in the hcp unit cell; the basal plane (b1) and a prism plane (b2), adapted from [182]

It shows the four-axis in the Miller-Bravais coordinate system (a_1,a_2,a_3,c) used to describe the hcp crystal structure and two lattice planes in the hcp structure: the basal plane (0,0,0,2) in Figure 128 (b1) and a prism plane $(1,1,\bar{2},0)$ in Figure 128 (b2). There are other types of prism planes in the hcp crystal structure, such as $(1,\bar{1},0,0)$, $(1,0,\bar{1},0)$, and $(1,\bar{2},1,0)$. Generally all prism planes intercept the basal plane at 90°. Besides these two crystal planes in Figure 128, which are also slip planes (a plane in which a dislocation motion produces plastic deformation), there are also various pyramidal planes in the hcp structure. One such pyramidal plane is shown for example in Figure 129, which is also an important slip plane.

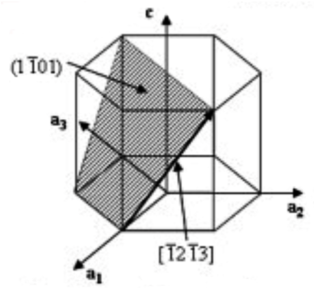

Figure 129: An example of a pyramidal crystal plane in a hcp crystal structure, taken from [193]

Slip on crystal planes other than the primary planes (i.e., (0,0,0,2), (1,0,$\bar{1}$,0), and (1,0,$\bar{1}$,1) [194]) are substantially harder to activate, making the zirconium material plastically anisotropic [195].

The hexagonal crystal deforms by both slip and twinning to produce a strong preferred orientation of the crystals (texture) during cold working. Typically, a cold rolled Zircaloy strip will have a strong normal texture where most of the basal poles of the hexagonal crystals are orientated about 35 degrees to the transverse plane of the strip. Figure 130 provides a description of the three principle crystal texture directions in fuel sheathing or the cladding.

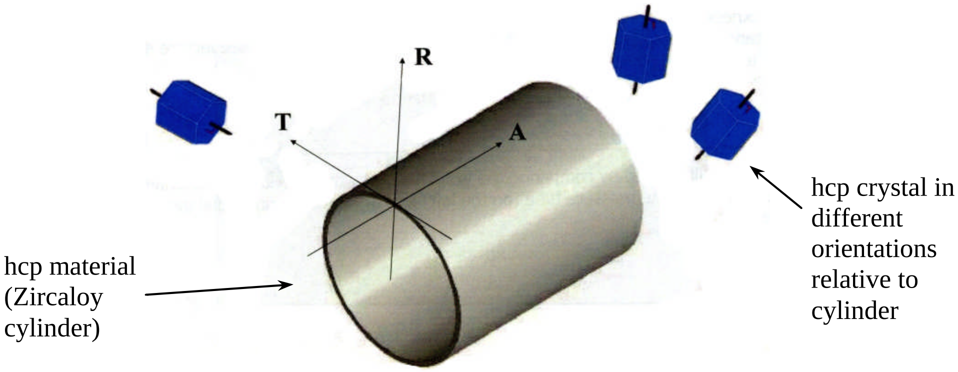

Figure 130: Schematic illustrating the principle directions used to describe the Zircaloy texture in CANDU fuel element sheathing: T for transverse, R for radial, and A for axial, taken from [192]

The anisotropic properties of a Zircaloy strip results in a significantly higher yield strength in the transverse direction. The control of crystallographic orientation allows designers to optimize material properties. Crystallographic orientation can be controlled by different manufacturing parameters. It is not possible though to manufacture a component with a completely well defined texture or of a single crystal orientation. Instead a manufactured component can have a distribution of grains with different orientations with a preference to certain orientations or texture [183].

Studies have been conducted by Knorr *et al.* [196], Peehs [183] and Wilson *et al.* [197] and discussed further by Cox [55] and Edsinger [168] that show that the majority of cracking in I-SCC experimentation were seen at positions where the basal pole of the hcp zirconium crystal structure are positioned mainly along the transverse or the hoop direction in the Zircaloy sheathing/cladding. Maximum crack density occurred at basal poles between 50° and 70° from the basal normal. It was also observed that a predominant radial texture resists I-SCC and has been observed in tubing fabricated using a high precision tube reduction process versus the normal Pilger milling [168]. Figure 131 shows the dependence of the crack intensity on the basal pole orientation. According to Peehs [183], when the basal poles are normal to the tube surface no crack initiation occurs. Furthermore, when cracks did appear they progressed slower when texture was in the radial (normal) direction and faster when texture was in tangential (transverse) direction, relative to the sheath/cladding principle directions, Knorr *et al.* [196].

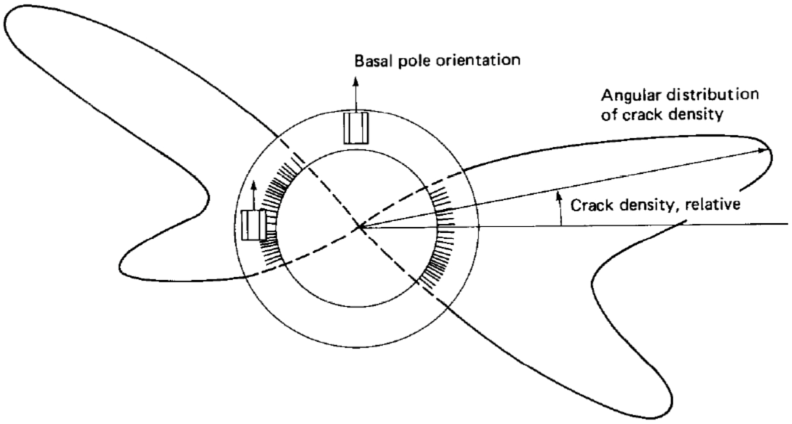

Figure 131: The influence of hcp basal pole orientation on I-SCC crack density, taken from [183]

The manufacturing processes used (such as Cold Pilge Milling processes [198][199] and other mechanical processes as well as heat treatments) to reduce the diameter and wall thickness of Zircaloy tubes into nuclear fuel clad/sheathings have been fine-tuned over the years. This resulted in optimal tube reduction procedures that minimized susceptibility of the clad/sheathings to stress corrosion cracking (as explained by Figure 131). The type-1 specimens were made using earlier tube reduction practices leading to less favorable texture, where type-2 (and type-3 Appendix H) specimens were made with more recent sheath manufacturing practices.

For the slotted ring specimens tested in this work, texture characterization was performed using the X-ray diffraction method (XRD) at the Royal Military College of Canada (RMC). For a description of the X-ray diffraction method see Appendix H.

Diffraction Pattern Measurements

The following are the diffraction pattern scans for the two types of specimens used in the I-SCC tests. Both specimens were previously-prepared slotted rings that were modified slightly by being bent into flat strips so that they could be mounted on the XRD specimen holder as shown in Figure 163 in Appendix H.

For the Pickering 28-element slotted ring material (type-1 specimen) a 29-mm long and 5-mm wide straightened strip was cut from a slotted ring and was placed face down on the specimen mount so that the outside surface of the sheath would deflect the X-rays. Furthermore, the long edge of the strip was positioned perpendicular to the path of the X-rays. This positioning ensured the greatest reflected X-ray intensity pick-up at the instrument detector. In this manner a maximum coverage of X-rays on the specimen was maintained. The XRD scan for the type-1 specimen is given in Figure 132 (a).

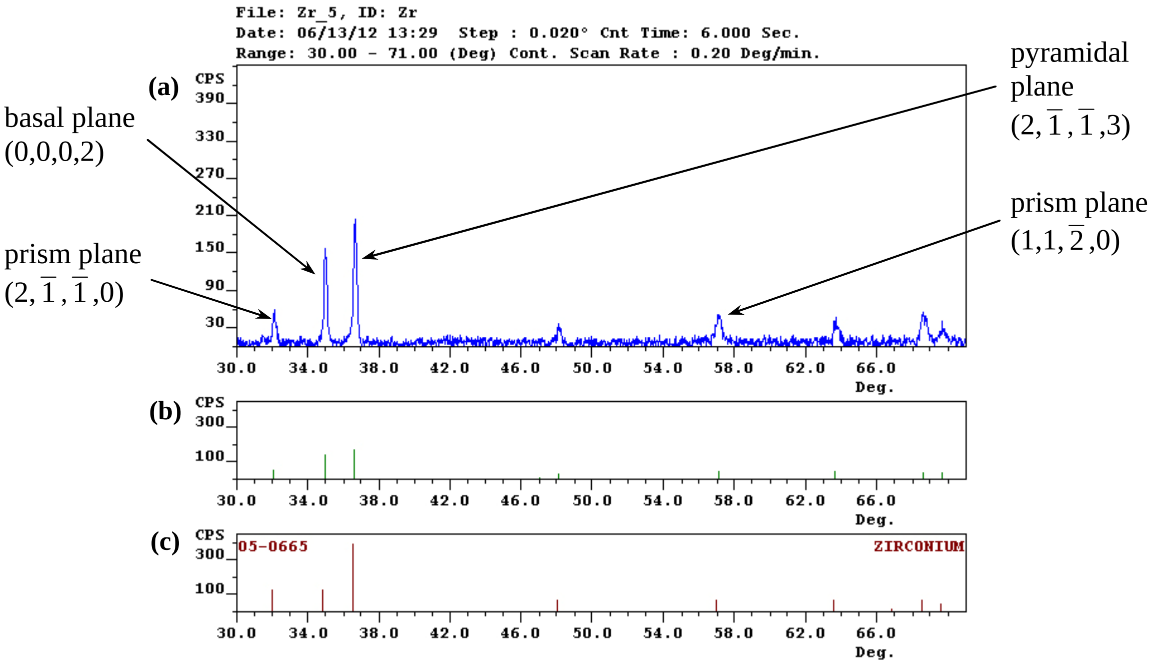

Figure 132: Diffraction pattern scan of a Pickering 28-element sheath material (type-1 specimen), inner sheath surface exposed to X-rays, perpendicular to the sheath transverse direction

The high intensity peaks are manifested when the Bragg law is satisfied. Dominant crystal planes can then be identified.

Figure 132 (b) provides the exact location and intensity of the peaks in the raw data using curve fitting and averaging software. Figure 132 (c) shows the relative intensities in a XRD scan of a zirconium crystalline powdered sample taken from the PDF (Powder Diffraction File). In essence, this scan is a database ‘finger print’ file that the scanned sample can be compared to. As can be seen all the peaks that are in the PDF file show up in the XRD scan. The difference lies in the relative intensities of the peaks. Table 38 (from the Scintag Diffractometer software package) provides a sample of the dominant existing crystal planes measured in powdered zirconium. Here the relative X-ray intensities of each peak and the Miller-Bravais coordinates of appropriate crystal planes are given. Figure 132 (c) holds some of the information in Table 38. Referring to this table, the observed peaks in Figure 132 (a) can be identified with basal and prism planes.

Table 38: Reflection angles in increasing order with corresponding X-ray signal intensity and hcp crystal plane coordinates for α zirconium

2θ	Intensity	Crystal planes: a_1, a_2, a_3, z or (u,v,t,w)
31.9594	33	$(2,\bar{1},\bar{1},0)$
34.8396	32	(0,0,0,2)
36.5103	100	$(2,\bar{1},\bar{1},3)$
47.9948	17	$(2,\bar{1},\bar{1},6)$
56.9348	17	$(1,1,\bar{2},0)$
63.5395	18	$(2,\bar{1},\bar{1},9)$
66.8154	3	$(2,\bar{1},\bar{1},0)$
68.5368	18	$(1,1,\bar{2},6)$
69.5810	12	$(2,\bar{1},\bar{1},3/2)$
73.5263	4	(0,0,0,4)

Note: Angle 2θ represents the summation of both the X-ray angle of incidence and the angle of reflection on the sample. Hence the angle of incidence for the first plane $(2,\bar{1},\bar{1},0)$ in the table is really 31.95°/2=15.97°.

Out of the eight observed peaks in Figure 132 (a), four peaks should be noted. The first is the peak at 34.83°, which is the basal plane (0,0,0,2) of the hcp crystal structure as depicted in Figure 128 (b1). The second and most dominant peak is at 36.51°, which represents a slanted plane $(2,\bar{1},\bar{1},3)$, or a pyramidal plane [200]. The third peak worth noting is the peak at 56.93°, which represents the prism plane $(1,1,\bar{2},0)$ as depicted in Figure 128 (b2). The fourth peak is another prism $(2,\bar{1},\bar{1},0)$ plane occurring at 31.95°.

A similar scan of the Pickering 28-element sheath material (type-1 specimen) is given in Appendix H where the specimen is positioned parallel to the impinging X-rays, which yields similar results.

For the Cameco 37-element sheath material (type-2 specimen, see Figure 133) a sample was taken from a slotted ring, which was 29-mm in length and 5-mm in width. The specimen was placed face up on the specimen mount so that the inside surface of the sheath was exposed to the X-rays.

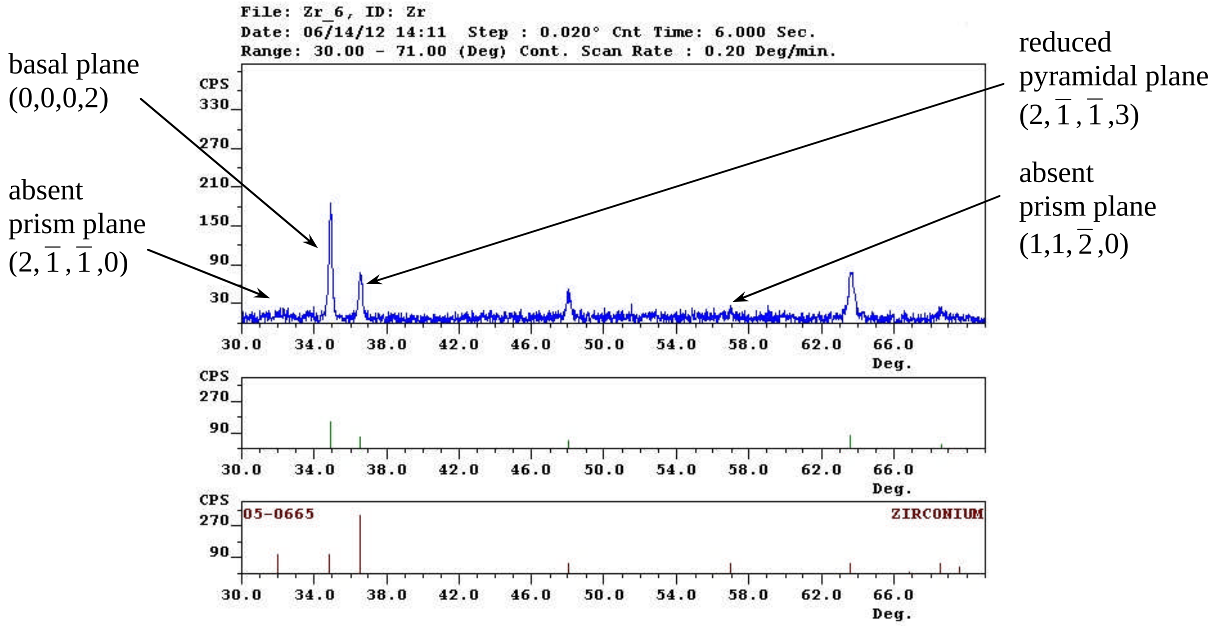

Figure 133: Diffraction pattern scan of a Cameco 37-element type material (type-2 specimen) inner sheath surface exposed to X-rays, perpendicular to the sheath transverse direction

The transverse direction of the sheath was positioned perpendicular to the X-ray direction. In this scan fewer peaks are observed compared with the scan in Figure 132 (and Figure 164 in Appendix H) discussed previously. A dominant basal plane peak is noticed at 34.83°, which is also greater than the pyramidal plane peak at 36.51° that was previously the dominant peak in the Pickering type sheathing (type-1 specimen) in Figure 132 (and Figure 164). Also noticed is the complete absence of the prism plane at 56.93° that was observed in the Pickering type sheathing. Since the XRD signal for every crystal plane in the zirconium powder PDF is not observed to be equal in intensity (refer to Figure 132 (c) and Table 38), the strong basal plane peak seen in Figure 133 relative to the other peaks indicates a strong preference for this texture, where the grain crystals have their hcp basal plane normals oriented close to the sheath radial direction.

An XRD scan of the 43-element CANFLEX sheathing was very similar to that of the 37-element Cameco type-2 specimen XRD scan in Figure 133. Hence, as explained earlier, this specimen type was not selected for in-depth I-SCC testing. An XRD scan of the CANFLEX sheathing is presented in Figure 165 in Appendix H for reference purposes. The importance of the Zircaloy crystal texture and the oxidized surfaces of the specimens on the I-SCC phenomena will become clear in the test results section.

5.3.3 Slotted Ring Analysis

Section 5.3.3.1 provides the complete form for the expression used by Wood [175] based on the work by Oding *et al.* [201] for calculating the maximum induced stress on the inside surface of the loaded ring. This equation was derived using the ‘unit load method’ [138] in Appendix I. In Section 5.3.3.2, this derivation is used to give an expression for the slotted ring deflection under a given force in order to assess the effective thickness of the specimen.

5.3.3.1 Analytical Formulation for Stress

The slotted ring is stressed by inserting a wedge in the specimen’s cut-out slot. This is a simple and effective way to impart a tensile stress near or above the yield point of the material. Figure 134 (a) shows the cross section of an unstressed slotted ring of thickness t_{sr}. The dimension b is the initial unstressed slotted ring gap equal to the width of the diamond blade that cut out the slot, or wider due to an additional cut. The dimension w_f in Figure 134 (b) is the stressed slotted ring gap.

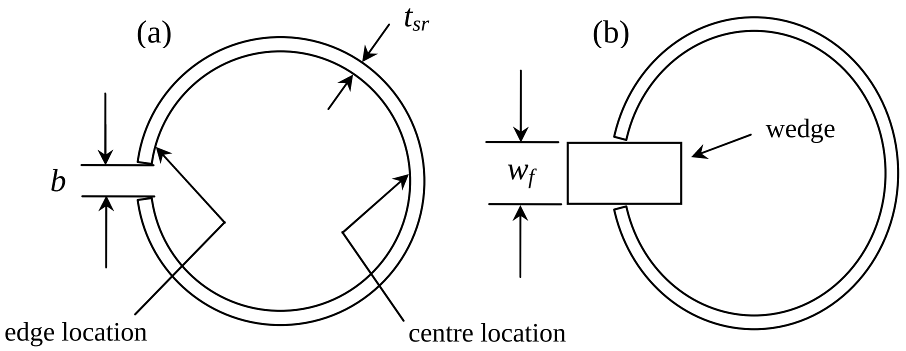

Figure 134: Slotted Zircaloy ring specimens, when (a) unstressed with slot dimension *b* and when (b) stressed with a Zircaloy wedge of width w_f

The stressed ring can be drawn as a free body diagram in Figure 135 (a).

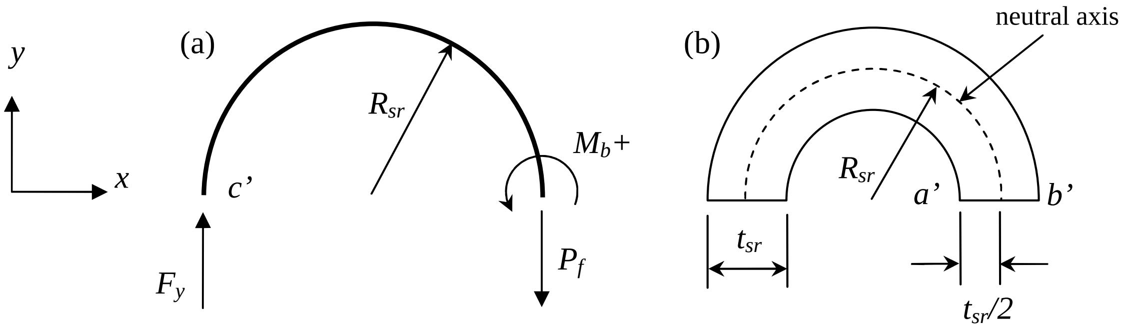

Figure 135: (a) Free body diagram of the stressed ring and (b) an exaggerated half ring thickness schematic showing the line of neutral axis

Here the ring of radius R_{sr} is cut into two and only the top half is shown. The forces P_f and F_y as well as the moment M_b are added to the free body diagram. Figure 135 (b) shows the same half ring but with an exaggerated thickness t_{sr}. This figure shows the neutral stress line in the ring that occurs at $\approx t_{sr}/2$, where the location *a'* indicates the internal surface of the ring opposite the slot and location *b'* indicates the external surface of the ring opposite the slot.

At static equilibrium $\Sigma F = F_y - P_f = 0$ and $\Sigma M = M_b - 2R_{sr} \cdot P_f = 0$. The stress distribution in the loaded ring at the location of maximum stress (point *a'* in Figure 135 (b)) is obtained by superposing the uniform stress distribution corresponding to the centric load P_f, or σ_o, and the linear distribution corresponding to the bending moment M_b, or σ_y. The stress distribution is provided by:

$$\sigma = \sigma_o - \sigma_y \Rightarrow \frac{P_f}{A_{area}} - \frac{M_b x}{I} \tag{202}$$

where A_{area} is the rectangular cross section of the ring slot, x is the distance from the neutral axis in the ring to the surface of the ring (at either point *a*' or *b*') and I is the centroidal moment of inertia [117].

At point *a'* in Figure 135 (b), both the centric load stress and the bending moment stress are tensile in Eq. (202), so that this equation can be rewritten as:

$$\sigma_{y\_axis} = \frac{P_f}{A_{area}} + \frac{M_b x}{I} \tag{203}$$

If the point of interest is the maximum tensile stress in the ring (at point *a'*) and Eq. (203) is written in terms of the force P_f, Eq. (204) is obtained where R is the radius of the ring and t_{sr} is the ring thickness.

$$\sigma_{y\_axis} = \frac{P_f}{A_{area}} + \frac{2R_{sr}P_f\frac{t_{sr}}{2}}{I} \tag{204}$$

An expression for the force F_y acting on the ring slot surfaces as a function of the displacement in the y direction at point *c'* in Figure 135 (a) is given by:

$$F_y = \frac{D_y}{\pi R_{sr}\left(\frac{3R_{sr}^2}{EI_z} + \frac{1}{EA_{area}} + \frac{k_y}{G_{sh}A_{area}}\right)} \tag{205}$$

where D_y is the displacement in the y direction, E is the Young's modulus of Zircaloy-4, A_{area} is the rectangular cross section of the ring body, k_y is the transverse shear factor, I_z is the centroidal moment of inertia about the z axis (i.e., into the page in Figure 135 (a)), R_{sr} is the radius of the ring, and G_{sh} is the shear modulus. For derivation of Eq. (205) using a 'unit load method' see Appendix I.

If Eq. (205) is substituted into Eq. (204), where $F_y=P_f$, one obtains:

$$\sigma_{y\_axis} = \frac{D_y}{\pi R_{sr} A_{area}\left(\frac{3R_{sr}^2}{EI_z}+\frac{1}{EA_{area}}+\frac{k_y}{G_{sh}A_{area}}\right)} + \frac{D_y t_{sr}}{\pi I_z\left(\frac{3R_{sr}^2}{EI_z}+\frac{1}{EA_{area}}+\frac{k_y}{G_{sh}A_{area}}\right)} \tag{206}$$

If σ_o in Eq. (202) is neglected as well as the axial force $(1/(EA_{area}))$ and the transverse shear $(k_y/(G_{sh}A_{area}))$ terms in the denominator of Eq. (206), since their contribution is small, and consider only the bending moment, one obtains:

$$\sigma_{y\_axis} = \frac{D_y E t_{sr}}{3\pi R_{sr}^2} \tag{207}$$

Here σ_{y_axis} is the stress in the y direction for the ring depicted in Figure 135. If the cut that is made in the ring is larger than half a millimeter, its dimension should be considered. If the initial unstressed slot dimension is designated as b and the final stressed width is designated as w_f as shown in Figure 134, then the deflection with the wedge in the slot is $D_y=(w_f - b)$ so that Eq. (207) can be written as [175]:

$$\sigma_{y\_axis} \approx \frac{E t_{sr}\left(w_f - b\right)}{3\pi R_{sr}^2} \tag{208}$$

An approximate equal sign is given, since the 'unit load method' used to derive Eq. (205) assumes an integration over 2π radians of the ring circumference. If however a slot is cut into the ring, the actual ring circumference is less than 2π radians. Also, the derivation in Appendix I assumes a circular geometry. Hence, stress in an excessively deformed ring will deviate from this solution.

If for example the Young's modulus of Zircaloy is E=100 GPa, t_{sr}=(0.40±0.01)×10^{-3} m, b=(2.30±0.02)×10^{-3} m, w_f =(6.00±0.02)×10^{-3} m, and R=(6.25±0.03)×10^{-3} m then the max stress is σ_{y_axis}=400±20 MPa. For an induced stress in the loaded slotted ring at room temperature. At 623 K, $E\cong$70-80 GPa [202] and the Zircaloy yield stress can drop from ≈300±15 MPa to ≈150±10 MPa (see Eq. (72)). Hence, the induced stress in the specimen at 623 K (350°C) may be as low as 150±10 MPa.

Finally it is worth noting a significant difference between the induced stresses in the slotted Zircaloy rings using a wedge and in the fuel element sheathing by thermally expanded UO_2 fuel pellets (and by sheath creep down) while in the reactor. The stress distribution in the slotted Zircaloy ring cross sections can be described by Figure 136 [117]. Tensile stress is considered positive, while compressive stress is considered negative. As can be seen in Figure 136 (a), the stress is maximum at the top and bottom regions of the beam cross section. These two extremes are also opposite in direction. Once the stress field is equal to or exceeds the material yield stress, the material plastically deforms, starting at the cross section top and bottom regions and working its way to the neutral axis in the middle of the beam.

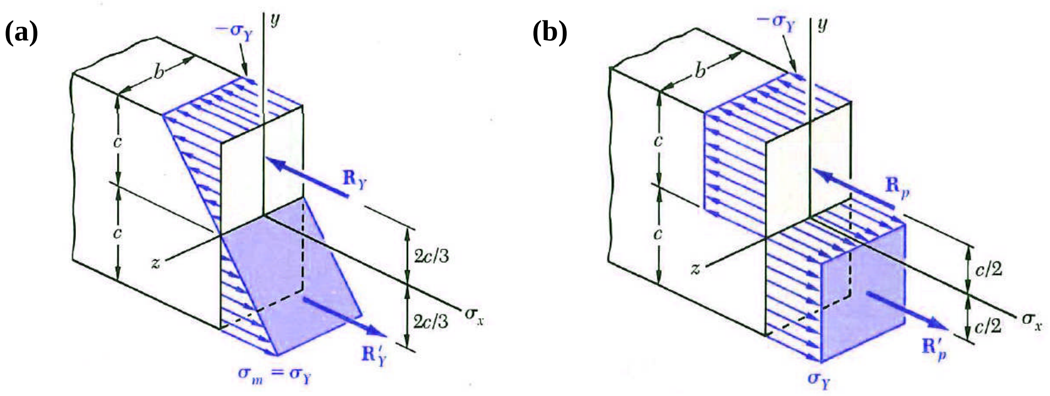

Figure 136: The stress distribution in a rectangular cross section of a beam under a load displaying (a) elastic and (b) plastic deformation, adapted from [117]

Figure 136 (b) illustrates what the stress distribution may be in a beam cross section that is completely plastically deformed, or where all the stress is at the material's yield stress. In reality though Figure 136 (b) is idealized for an elastoplastic material (a non realistic material with an infinite strain after yield), so the actual stress profile would look more like a thin *S* curve. In comparison, the stress distribution for the in-reactor sheathing would be essentially a single direction uniform stress field (like Figure 136 (b) but stress only in a single direction).

Thus, the slotted Zircaloy ring initial stress field is not representative of an in-reactor stressed sheathing. It is possible that the nature of the slotted Zircaloy ring stress field is less favorable to I-SCC attack, i.e., half of the stress is compressive and the stress diminishes as one approaches the neutral axis. A completely plastically deformed slotted Zircaloy ring though may be prone more to I-SCC attack, since the stress at the crack tips may be greater than in an only-elastically deformed ring. Lastly, for in-reactor fuel sheathing, the stress field is homogeneous and is all tensile (i.e., Mode I loading on cracks throughout sheath cross section, see Figure 30), which probably makes it more susceptible to I-SCC than the slotted rings used for these tests. Nevertheless, if iodine induced corrosion/failures are observed in the slotted ring specimens it can be expected that similar effects would also be observed in specimens that were stressed in a similar way as the fuel sheath in the reactor.

5.3.3.2 Post-Experiment Corrosion Assessment

In previous work conducted by Wood [175] and Wilson *et al.* [197], who used slotted Zircaloy rings in early I-SCC tests, there were essentially only two recorded quantitative outcomes at the end of there tests: fail or not failed. In other words, a specimen was visibly cracked usually in two sections, or not. In the current tests though it was planned that if the failure rate was very low it was thought that it might be overly simplistic to simply declare that the specimens were not affected in any manner by the iodine vapour if they were not visibly cracked. Thus, a new technique was required that could provide some quantitative assessment of the extent of corrosion in specimens that did not visibly crack.

For this purpose, a Zircaloy slotted ring deflection tester was designed and built at RMC by the author with the assistance of C. McEwen who was the departmental technologist/machinist. The slotted ring deflection tester worked on the simple premise that for a given applied force to the slotted ring in the transverse direction, an appropriate deflection can be measured. The resulting deflection distance can then be used to calculate the effective thickness of the specimen after it has been exposed to the corrosive iodine vapour (i.e., it considered both potential invisible cracks if present and the amount of eroded surface due to chemical pitting and etching).

If in Eq. (205) the axial force term ($1/(EA_{area})$) and the transverse shear term ($k_y/(G_{sh}A_{area})$) are neglected then the expression for D_y deflection becomes:

$$D_y = \frac{3R^3\pi F_y}{EI_z} \tag{209}$$

where F_y is the force opening the slotted ring and the centroidal moment of inertia I_z for the ring body cross section is given by Eq. (210), where l_{rw} is the width of the ring and t_{sr} is its thickness.

$$I_z = \frac{l_{rw}t_{sr}^3}{12} \tag{210}$$

Substituting Eq. (210) into Eq. (209) yields Eq. (211), which provides a relationship between the measured deflection of the slotted ring and the dimensions of the cross section of the ring body at maximum stress.

$$D_y = \frac{36\pi R^3 F_y}{El_{rw}t_{sr}^3} \tag{211}$$

From this equation, the deflection measurement is proportional to the inverse cube of the specimen cross section thickness and linearly proportional to its width. In other words, any surface erosion and small invisible cracks should be possible to detect. Specifically if the approximate measurement resolution is 0.025 mm then the measureable change in the specimen wall thickness, is 7.3 μm (or about 1.8% the specimen wall thickness).

If D_y is the measured quantity then the calculated value of t_{sr} can be compared to the measured value. Solving Eq. (211) for t_{sr} gives:

$$t_{sr} = R\left(\frac{36\pi F_y}{El_{rw}D_y}\right)^{1/3} \tag{212}$$

which is the effective thickness of the specimen.

The slotted ring deflection tester is depicted in Figure 137. A slotted ring specimen is placed on the lever and static jaws. The test force acting on the slotted ring is provided by a 50 g weight attached on the right hand side of the leaver.

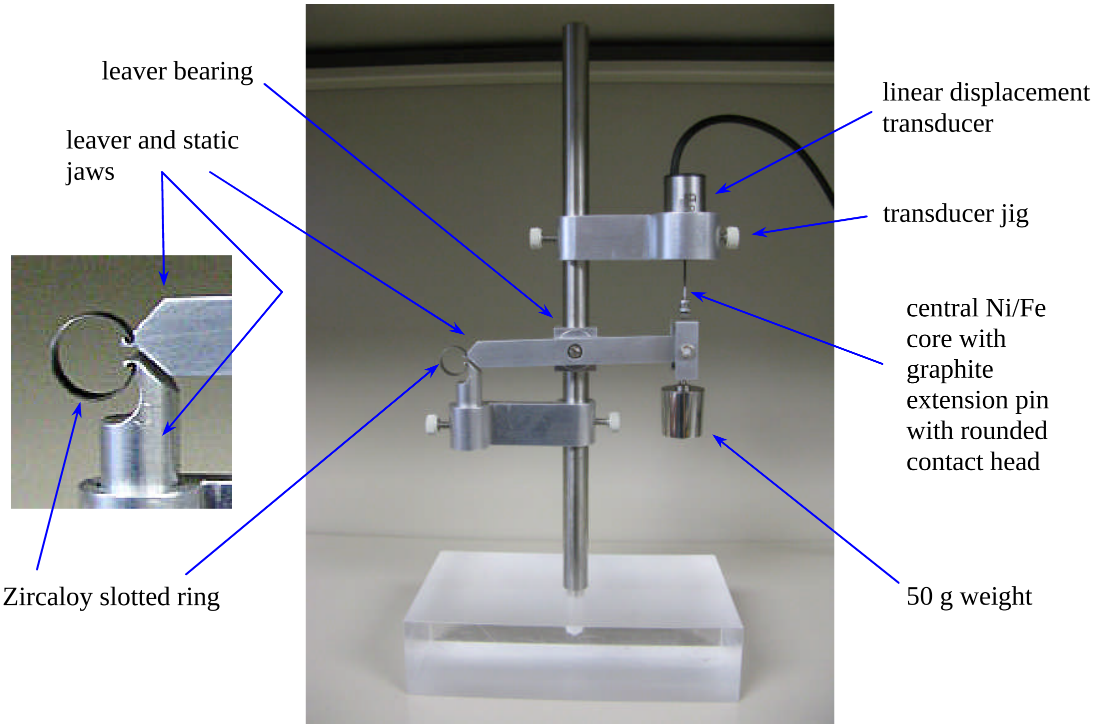

Figure 137: Zircaloy slotted ring deflection tester

By measuring the displacement of the ring under the applied weight a direct comparison can be made between various tests. For the complete details of the slotted ring deflection tester see Appendix J.

5.4 Experimental Procedure

Glass ampoule and baking procedure:

Zircaloy slotted rings described in Table 36 were pre-loaded using a Zircaloy wedge as shown in Figure 127 (b) and Figure 134 (b). The maximum applied stress in the type-1 (28-element sheath material) and in the type-2 (37 element sheath material) slotted rings specimens, using Eq. (208), was 480±10 MPa, when at room temperature. The loaded specimens of type-1 were inserted in a 2.05 cm ID Pyrex medium-walled tube that was 22-24 cm long (plus excess length) and type-2 specimens were inserted in 2.47 cm ID Pyrex thin-walled tubing that was 14-18 cm long (plus excess length), which were glass blown shut at one end. Also inserted into the glass tube was a glass vial containing iodine crystals, as shown in Figure 138. Since in the tests different specimens and different number of specimens were used and since two types of wedges were utilized, the amount of iodine used is specified in mg iodine crystals per cm^2 of Zircaloy surface area. Once these test items were inserted in the glass tube it was necked-down (ideally to a 2-3 mm internal diameter) at the indicated lengths. This made it possible to vacuum pump the tube contents to low pressures and at the same time allowed for a durable glass blown seal (that would not crack while in furnace). After necking down the glass tube, moisture would typically form inside the tube due to the cooling off of the glass. To remove this moisture an initial vacuum pump of several hours was performed on the necked-down glass tube with the intact iodine glass vial and wedged specimens using a custom built vacuum system (decribed further down and in Appendix K).

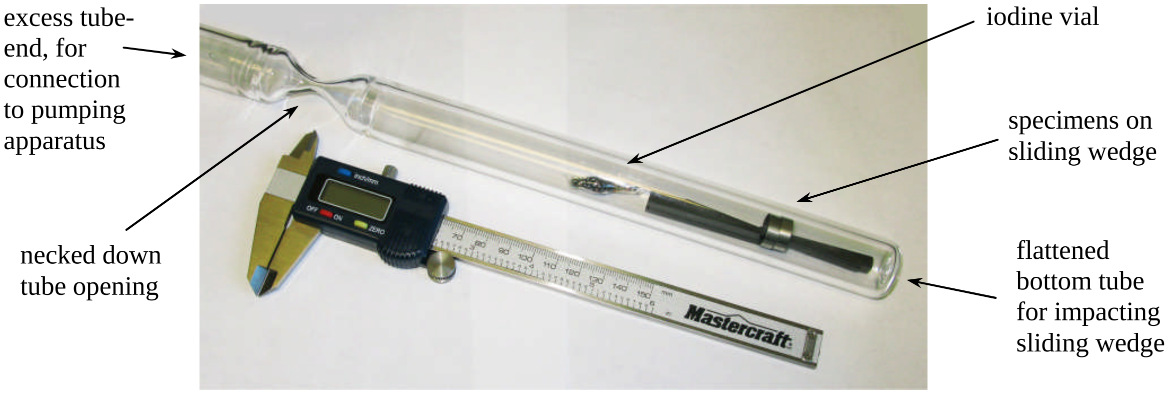

Figure 138: Glass tube with intalled 37-element type slotted ring specimens on sliding wedge with iodine glass vial before vacuum pumping.

In certain tests a mixture of UO_{2+x} and vacuum baked graphite was also introduced. The UO_{2+x} was prepared in a Setaram Instrumentation SETSYS Evolution thermogravimetric analyzer (TGA) by first reducing a non stoichiometric amount of uranium dioxide material until a stoichiometric UO_2 batch was made. Using the same instrument, but also a Zirox SGM5EL electrolysis device, this batch was then oxidized until a desired level of hyperstoichiometric uranium dioxide was produced. See Appendix D-2 for FactSage® 6.1 thermodynamic equilibrium computations for UO_2 oxidation parameters applied in the TGA and see Appendix L for explanation of the TGA and the used operation procedure. Appendix L also gives the temperature and weight-loss and gain plots of the reduction and oxidation stages. In this manner the exact amount of added oxygen to the UO_2 was known. For example in test 29 the amount of stoichiometric UO_2 material prepared was 141.523±0.001 mg. After the oxidation process, the weight of the UO_{2+x} batch increased to 142.734±0.001 mg. The difference between these two weights (1.211±0.002 mg) was the amount of hyperstoichiometric oxygen added to the UO_2 batch. To figure out the average stoichiometric deviation for this batch the moles equivalent of the oxygen atoms is calculated:

$$n_{\mathrm{O}} = \frac{1.211\times10^{-3}\,[\mathrm{g}]}{16\,[\mathrm{g/mol}]} = 7.568\times10^{-5}\,[\mathrm{mol}] \qquad (213)$$

Taking the mass of the UO_2 batch after the reduction stage and calculating its mole equivalent one gets:

$$n_{\mathrm{UO}_2} = \frac{141.523\times10^{-3}\,[\mathrm{g}]}{270.03\,[\mathrm{g/mol}]} = 5.241\times10^{-4}\,[\mathrm{mol}] \tag{214}$$

Thus, the average stoichiometric deviation of this UO_{2+x} batch is then:

$$x = \frac{n_{\mathrm{O}}}{n_{\mathrm{UO}_2}} = \frac{7.568\times10^{-5}\,[\mathrm{mol}]}{5.241\times10^{-4}\,[\mathrm{mol}]} = 0.144 \tag{215}$$

This simple computation can be expressed more concisely as [203]:

$$x = \frac{M_{\mathrm{UO}_2}}{M_{\mathrm{O}}}\frac{\Delta W}{W_{reduced}} \tag{216}$$

where M_{UO2} and M_O are the molecular weights of UO_2 and O, respectively, and ΔW and $W_{reduced}$ are the sample change in weight after oxidation and the weight of the sample after reduction (before oxidation), respectively. See sample calculation with error analysis in Appendix L.

The stoichiometric deviation achieved for these tests ranged from $x = 0.06$ to 0.16.

The dried graphite was prepared from CANLUB DAG-154N. To reproduce the baking procedure used in industry when CANLUB is applied to the internal surfaces of the fuel element sheathing, about 5 ml of CANLUB was poured into an aluminum foil boat. The boat was then baked in atmostphere at 140°C for two hours in a quartz process tube in a furnace. This drove off most of the iso-Propyl alcohol (and some water) solvent. A $\approx 5\times10^{-3}$ torr vacuum was then allied to the process tube with the CANLUB using an Alcatel mechnical rotary vane pump and the furnace temperature was increased to 350°C. Baking at this temperature took place for a duration of 2-3 hours. The dried graphite was then removed as flakes from the boats and crushed in a ceramic mortar with a pestle.

The dried graphite (255-278 mg used in these tests) was inserted into the bottom part of necked-down glass tube with the loaded specimens and iodine vial. After crushing the oxidized UO_2 (87-141 mg used in these tests), as much as possible with a long aluminum rod, the UO_{2+x} was positioned at the narrow opening of the necked-down tube (see Figure 139). The tube was then positioned in the vertical orientation to allow the oxidized fuel to slide into the tube. These two stages were done only after the glass neck-down procedure followed by an initial vacuum pumping of the tube to avoid exposure of the additives to condensed moisture and heat. The two crushed powders were then gently mixed by slowly rotating the tube.

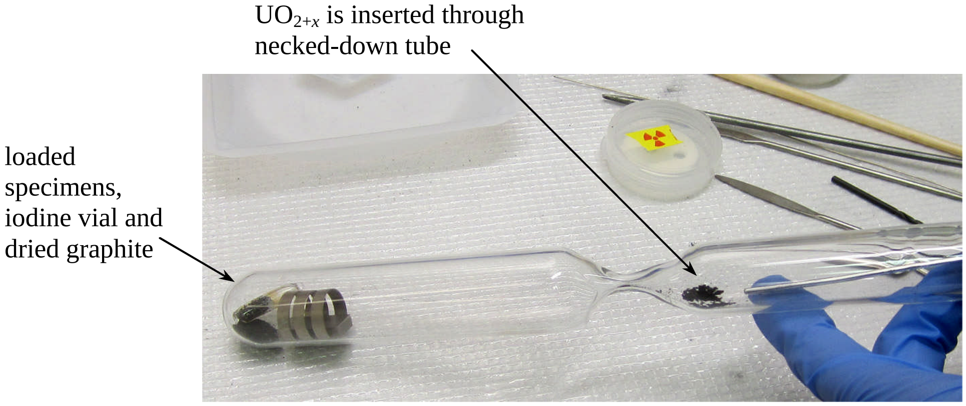

Figure 139: Prepared UO_{2+x} is positioned for insertion into tube before vacuum pumping. Here 28-element type slotted ring specimens are loaded on a static wedge.

Since oxygen in air reacts with zirconium to form a thin oxide layer [60][62] (see Eq. (194)), a custom made vacuum system was used to remove all air and moisture from inside the tube (same system as used previously to remove condensed moisture). The vacuum system consisted of a turbomolecular pump (upstream) and a roughing vacuum pump (downstream) connected in series to the vacuum chamber. The pumping time typically took between 18-24 hours to achieve a vacuum pressure of 7×10^{-6} to 3×10^{-5} torr. The glass tube was then glass blown shut with the vacuum maintained, effectively sealing in the components of the experiment in the prepared glass ampoule. Figure 140 shows a sealed glass ampoule with type-1 stress loaded Zircaloy specimens (see Table 36), iodine vial, and UO_{2+x} with dried graphite mixture.

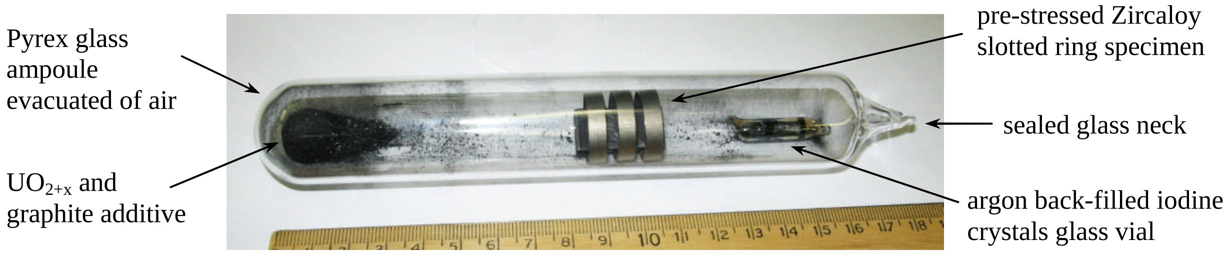

Figure 140: Sealed glass ampoule with loaded specimens, iodine crystal vial and UO_{2+x} with dried graphite mixture

Additional details on the glass ampoule vacuum pumping station and sealing procedure is given in Appendix K. In certain tests the impact tightening sliding wedges were used (see Figure 127 (b)). As mentioned earlier the purpose of the sliding wedges was to increase the susceptibility of the specimens to iodine attack (by disturbing the oxide in-situ).

At this point the iodine glass vial was broken by gentle agitation (this entailed breaking a specially prepared ‘goose neck’ on the glass vial). The purpose of the glass vial was to avoid the loss of iodine by sublimation during the vacuum pumping and glass blowing (heating) stages, which also avoided potential damage to the pumping equipment. Once the glass vial was broken the glass ampoule was inserted into a MTI OTF-1200X 2.5kW tube furnace pre-set to 350±1°C to duplicate the approximate temperature in the fuel element fuel-to-sheath gap. During the first 15 minutes to several hours the iodine crystals in the glass vial completely sublimated into a dark purple vapour. After this initial period the purple iodine vapour quickly dissipated leaving behind orange/brown ZrI_x deposits (salts). The deposits are ZrI, ZrI_2, ZrI_3 and ZrI_4, as summarized by Sidky [61]. The dominant deposit species, at room temperature and pressure, was later determined using Energy-Dispersive X-ray spectroscopy and Nuclear Activation Analysis at RMC to determine chemical element composition. The heating of the glass ampoule was continued for a five-day duration, during which the specimens were visibly inspected from time to time through the glass ampoule for signs of obvious failure.

Once the heating period was completed specimens were removed from the glass ampoule by breaking the glass ampoule at one end. Specimens were carefully removed from wedges and dropped in an ethanol filled beaker and gently stirred to remove deposits and eroded zirconium iodide materials.

For cases where the slotted ring specimens did not classically crack in-two but remained intact, a slotted ring deflection tester was designed and built to measure the extent of surface corrosion/internal cracking (Figure 137). Specifically, a slotted ring specimen was attached to the static and lever jaws, while at the other end a 50 g weight was attached to cause the specimen to deflect. A transducer placed above the lever read the vertical displacement of the leaver. A Labview program was desiged to read the linear transducer voltage readout signal, which was conveted to a displacement in mm. Each specimen deflection was measured 5-6 times. The total error in the measurement was estimated by considering the standard deviation of the mean (of the multiple deflection measurements of each specimen), the error of the transducer and the error in the specimen cut width (the l dimension in Eq. (211)). For further technical details on the deflection tester see Appendix J.

5.5 I-SCC Experimental Results

Specimens of type-1 and type-2 (see Table 36) were deflection tested and compared after they were exposed to one of three different test conditions:

A. The specimens were exposed to heat only
B. The specimens were exposed to heat and an iodine vapour, and
C. The specimens were exposed to heat, iodine vapour with a UO_{2+x} and graphite or oxygen gas additive.

Specimens of type-1 were stressed with a static wedge (ST) and specimens of type-2 were stressed with static or sliding wedges (SW), where indicated in the result figures further down.

Specimen deflection measurements

The slotted ring deflection measurement of each test between these three test conditions of type-1 specimens is provided by Figure 141. The amount of iodine used in each test is given as per surface area of Zircaloy material in the glass ampoule (i.e., specimens + wedge/s). Generally for these experiments, three specimens were placed in each glass ampoule, except for in tests 4 and 7, which contained six specimens per ampoule. In test 15 (a blank test, test condition A) where only heat was applied, the average deflection of the specimens was 0.76±0.04 mm (green bar in Figure 141). Assessing the analytical deflection using Eq. (211), where R=7.55±0.13 mm, F_y=0.441±0.001 N, E=97±2 GPa [202], l=5.0±0.1 mm, and t =0.40±0.01 mm then D_y= 0.69±0.12 mm, which agrees with test 15 measured value within error and differed only by ≈10%. In the second test condition (B), in tests 4 and 7 (orange bars in Figure 141), where heat and 4.5±0.2 mg cm^{-2} iodine were introduced, a slight increase in specimen deflection to ≈0.80±0.04 mm was recorded. Also, one out of six specimens, in test 4, failed (cracked in-two). When the iodine content was increased in test 13 to 28±1 mg cm^{-2} the deflection increased to 0.87±0.04 mm and one out of three specimens failed. Hence, ≈13% of test condition (B) specimens failed.

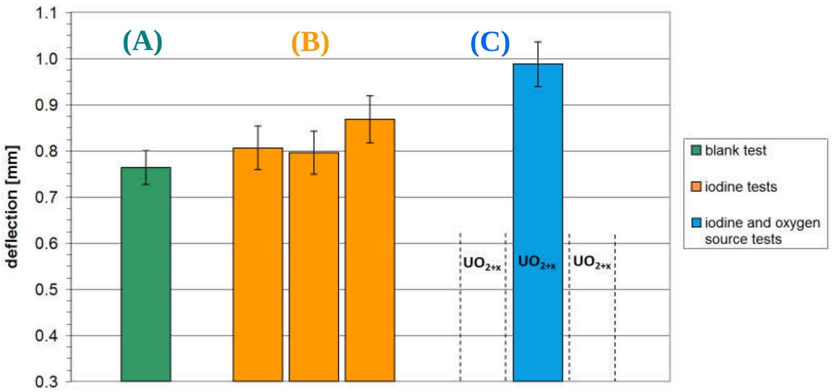

test number:	15	4	7	13	21	24	29	
iodine used mg cm^{-2}:	0	4.5	4.5	28.2	6.4	28.2	6.4	± error in text
failed specimens / total specimens:	0/3	1/6	0/6	1/3	3/3	0/3	3/3	
equivalent O_2 mol cm^{-2} added ×10^{-6}:		0	0	0	0.40	1.70	1.61	± error in text

Figure 141: Deflection measurements of type-1 sheath slotted rings

In the third test condition (C) (blue and empty bars in Figure 141), heat, iodine and a UO_{2+x} with vacuum baked graphite mixture were introduced in tests 21, 24 and 29. The amount of hyperstoichiometric oxygen in the UO_{2+x} is expressed here as available moles O_2 per Zircaloy surface area. In tests 21 and 29, that had similar iodine content equal to 6.4±0.3 mg cm^{-2} and dissimilar oxygen source content equal to $(0.40\pm0.01)\times10^{-6}$ and $(1.61\pm0.05)\times10^{-6}$ mol cm^{-2}, respectively, all specimens failed (as indicated in red figures in Figure 141). When the iodine content in test 24 was increased to 28±1 mg cm^{-2} (blue bar), none of the specimens failed, but the specimen deflection on average was the highest, at 0.99±0.05 mm in Figure 141.

An electron microscope image of the iodine induced cracked surface of the failed type-1 specimen was taken from test 13, which is shown in Figure 142. This image is taken at the axial midway point of the 5 mm wide slotted ring specimen, looking down at the fully cracked thickness of the specimen. The Zircaloy slotted ring cracking commenced from the right side of image and ended on the left side.

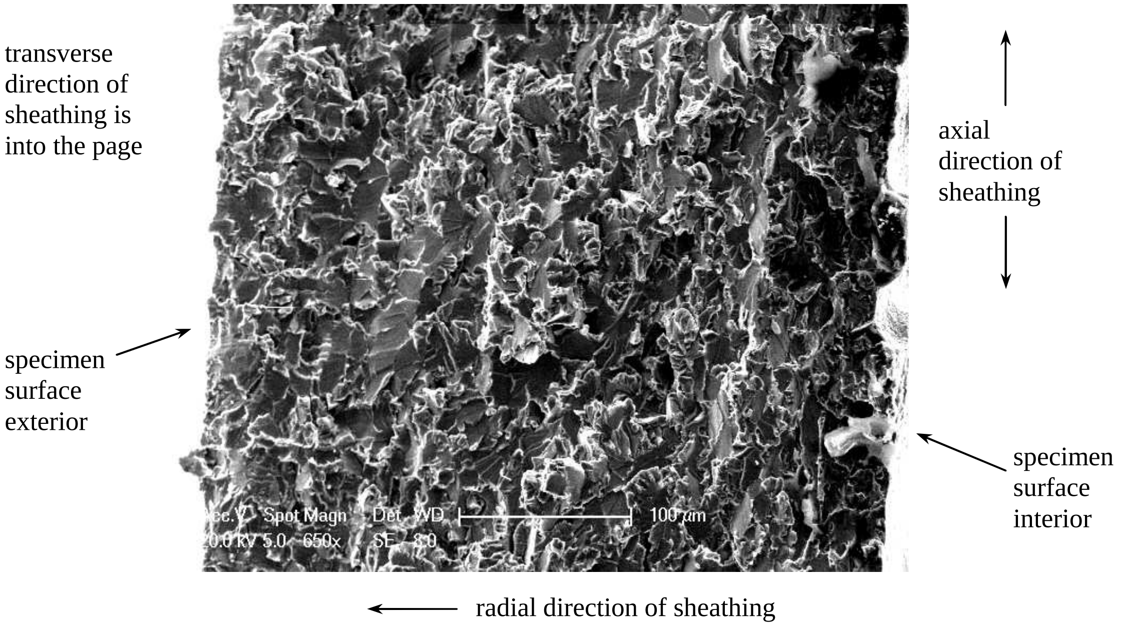

Figure 142: Electron microscope image of surface of fully cracked type-1 specimen thickness in test 13, 650× magnification

From this image and from a closer look, shown in Figure 143 (a) at 2000× and (b) at 5000× magnification, it seems that the cracking is a fully transgranular cleavage and there is very little intergranular crack initiation in the vicinity of the interior specimen surface (right side of Figure 142). For a description of intergranular and transgranular cracking see [171][204].

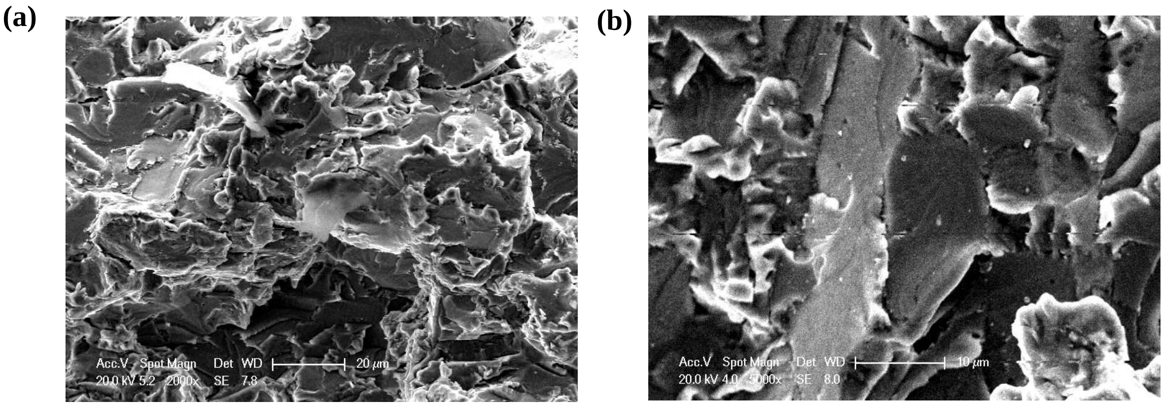

Figure 143: (a) Centre area of cracked surface at 2000× magnification and (b) 5000× magnification revealing transgranular cleavage fracture surface

The deflection measurement comparison results with type-2 slotted ring specimens between the three test conditions is provided by Figure 144. In these tests none of the specimens failed (cracked) but specimen deflection differences were observed. For the first test condition (A) (blank tests), the average deflections of tests 8 and 18, which were exposed to a temperature of 350°C, was 0.48±0.02 mm (green bars 14 Figure 144).

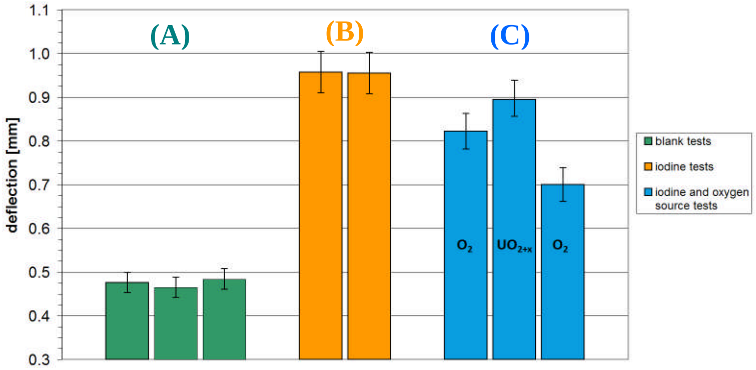

test number:	8	17	18	19	20b	20	25	30	
iodine used mg cm^{-2}:	0	0	0	30.0	30.0	22.0	30.0	35.5	± error in text
failed specimens / total specimens:	0/6	0/3	0/3	0/2	0/2	0/2	0/2	0/3	
equivalent O_2 mol cm^{-2} added $\times 10^{-6}$:	0	0	0	0	0	0.69	1.11	8.74	± error in text
type of wedge used: ST or SW	ST	ST	ST	SW	SW	SW	SW	ST	

Figure 144: Deflection measurements of type-2 sheath slotted rings

When the temperature was 300°C in test 17 the average deflection was 0.46±0.02 mm. Calculating Eq. (211), where R=6.35±0.03 mm, F=0.441±0.001 N, E=97±2 GPa [202], l=5.0±0.1 mm and t=0.40±0.01 mm the analytical deflection was D_y= 0.41±0.05 mm, which agrees within error to tests 8, 17 and 18. For the second test condition (B) (orange bars, Figure 144) 30.0±0.4 mg cm^{-2} of iodine was used in tests 19 and 20b, and the average deflections of these two tests was ≈0.96±0.05 mm. When only 4.2±0.2 and 16.0±0.2 mg cm^{-2} of iodine was used (tests 3 and 16 not shown in figure) the average deflections were 0.49±0.02 and 0.69±0.03 mm, respectively. The former result is similar to the blank test (tests 8, 17 and 18) results indicating a threshold iodine quantity (in this type of test). The latter result suggests a linear relationship between specimen deflection and iodine quantity. For the third test condition (C) (blue bars, Figure 144) two types of tests were run: Tests 20 and 30 used oxygen gas additive and test 25 used UO_{2+x} and vacuum baked graphite mixture additive. In test 30 when 35.5±0.7 mg cm^{-2} of iodine was used (the highest amount in these tests) with $(8.74\pm1.20)\times10^{-6}$ mol cm^{-2} of oxygen the specimen deflection was 0.70±0.4 mm, noting that here a static wedge was used. In test 20, although 22.1±0.3 mg cm^{-2} of iodine was used (which is lower than in the other tests in Figure 144), with a sliding wedge, the addition of $(0.69\pm0.09)\times10^{-6}$ mol cm^{-2} of oxygen gas may have also contributed to a lower average specimen deflection of 0.82±0.04 mm. Lastly, test 25 that used the UO_{2+x} and graphite additive, equivalent to $(1.10\pm0.01)\times10^{-6}$ mol cm^{-2} of oxygen, with a sliding wedge, showed a marked average reduction in specimen deflection at 0.89±0.04 mm compared to the tests that did not include an oxygen source. From these reduced specimen deflections it seemed that the addition of oxygen gas had a mitigating effect on iodine corrosion. The addition of UO_{2+x} and graphite additive seemed also to have a protective quality on type-2 specimens in an iodine environment.

To see if there were any signs of surface cracking in the type-2 specimen, which could not be seen with the naked eye, electron microscope images were taken of a test 20b specimen. Figure 145 (a) shows a 65× magnification of the inside surface of the slotted ring at the location of maximum stress (i.e., a view in the radial direction).

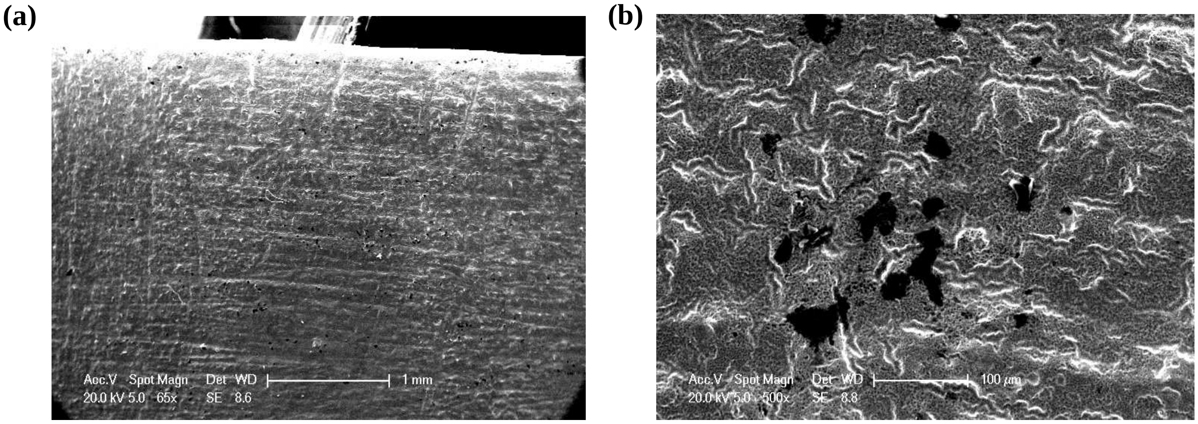

Figure 145: Electron microscope image of surface of fully cracked specimen thickness in test 13, (a) 65× and (b) 500× magnification

No deep cracks are observed but shallow grooves running vertically at the top and middle of the image can be noted. Furthermore the sharp edge of the specimen (top of image where specimen was cut with a diamond cutter) has been chemically etched/corroded away. Figure 145 (b) shows a 500× magnification of a similar area, where here the white curvy lines represent local high points on the surface and the black zones are local low points where surface pitting has occurred.

Iodine residence time

Once the iodine sufficiently reacted with the zirconium to form the ZrI_x the partial pressure of I_2 decreased to a level where the purple iodine vapour color disappeared. The time it took for this transition to be reached gives some insight on the integrity and/or the thickness of the oxide surface. This iodine residence time is plotted in the following bar charts:

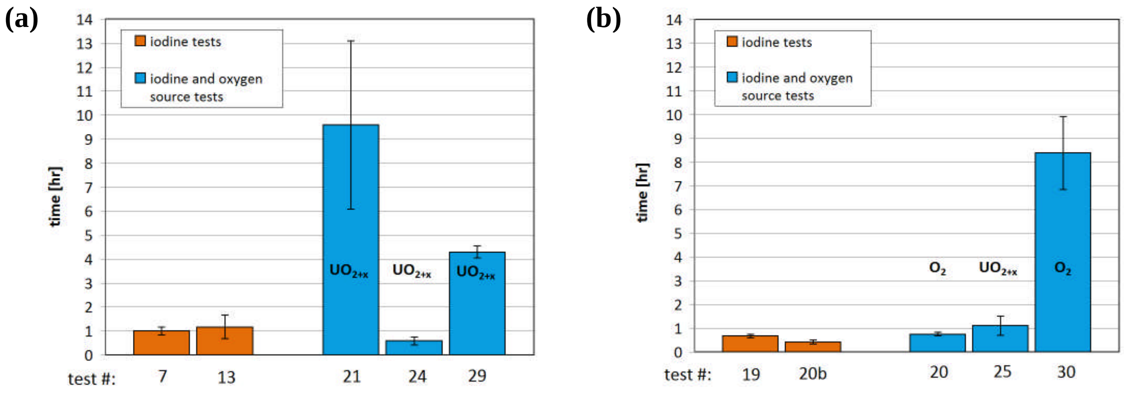

Figure 146: The visible iodine vapour residence time in glass ampoule for (a) type-1 sheath specimens and (b) type-2 sheath specimens

For the type-1 specimens, Figure 146 (a), when iodine only was used in tests 7 and 13 the iodine vapour residence time was only about an hour. When the UO_{2+x} and graphite mixture was added the iodine vapour residence time in tests 21 and 29 increased to 10±4 and 4.5±0.3 hours, respectively. In both cases only 6.4±0.3 mg cm^{-2} of iodine was used and all specimens failed. In test 24 when the iodine was increased to 28±1 mg cm^{-2} the iodine vapour residence time dropped substantially to only 0.8±0.2 hours and none of the specimens failed. These results suggests (and Figure 141) that a sufficient partial pressure of iodine is needed for a minimum amount of time to cause cracking (increased iodine residence time). When all the iodine had been visually converted to ZrI_x species cracking did not seem to occur.

For type-2 slotted ring specimens, the iodine vapour residence times were different (Figure 146 (b)) than type-1 slotted ring specimens. In test 20 when oxygen gas was added and sliding wedges were used the iodine residence time was similar to when no oxygen was present in tests 19 and 20b (0.4-0.6 hours). In test 30 the iodine residence time increased to 8.5±1.5 hours when oxygen gas was used. In test 25, which used a UO_{2+x} and graphite mixture and sliding wedges, there was a slight increase in the iodine residence time compared to tests with no oxygen source (1.1±0.4 h vs. 0.5±0.1 h). Tests 25 and 30 seem to support the deflection measurements seen earlier, indicating the presence of a protective oxide layer between the iodine corrodant and bare zirconium in the basal dominated Zircaloy texture sheath specimens. See Figure 144 for quantity of oxygen used in these tests.

A color change in the Zircaloy specimens was noticed when they were heated in the glass ampoules and exposed to an oxygen source (UO_{2+x} and graphite mixture or oxygen gas). Before the baking stage commenced with the oxygen source the Zircaloy specimens had the typical shinny silvery metallic color. But after baking was initiated a color change was observed. This observation was mode when the glass ampoules were momentarily removed from the furnace for visual inspection, after the iodine vapour subsided, but especially in cases where the iodine vial remained intact after it was intentionally agitated - when it didn't fail on the first agitation attempt but did fail on the second. For example in test 31 (a test not included in this work due divergence from test procedure) there was a ≈20 hour period delay between the glass ampoule baking initiation and the iodine vial breakage (iodine exposure), while in the other oxygen additive tests (20, 21, 24, 25, 29 and 30) the iodine vial was broken at the time the baking stage commenced. The color change was observed as a change to a yellow-gold color, see Figure 147, which is indicative of a fine oxide buildup on the Zircaloy specimens. It should be noted that this color change was not noticed in tests with no oxygen source. The oxide thickness buildup can be estimated by comparing the color of the specimens in Figure 147 to a Zircaloy oxide color scale. According to Figure 125 (a) and (b), the in-situ formed oxide thickness lies between 0.3 and 0.1 μm, respectively. Interestingly, the iodine residence time in the type-2 specimens (Figure 146) was longer in the test when a pre-build up of oxide occurred without iodine vapour present but was also longer in type-1 specimens where there was no delay in baking initiation and exposure to iodine.

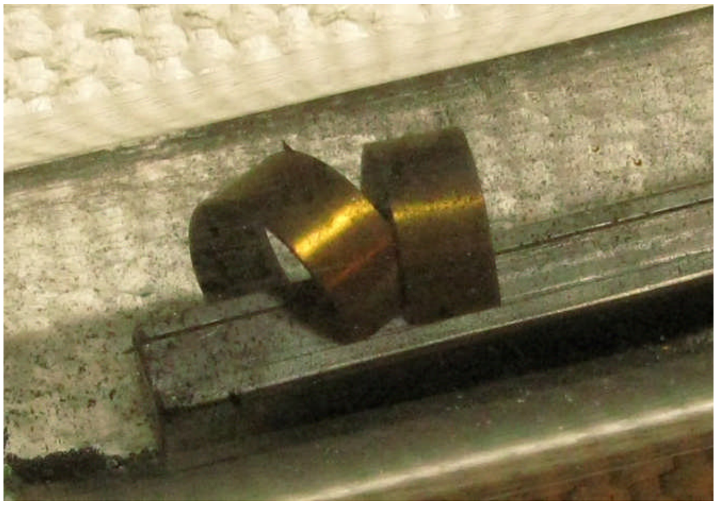

Figure 147: Zircaloy slotted ring specimens after baking for ≈20 hours before iodine exposure showing a change in surface color indicating oxide buildup

Surface etching/corrosion

The slotted ring specimen wall thickness, *t*, was measured with a digital Mastercraft (150 mm span) caliper after performing the experiment for the three test cases. Measurements were taken (and repeated) at the centre and at the edges of the specimens, see Figure 134 (a), while ensuring a minimal value was recorded. Figure 148 (a) and (b) show the wall thickness of type-1 and type-2 slotted ring specimens, respectively.

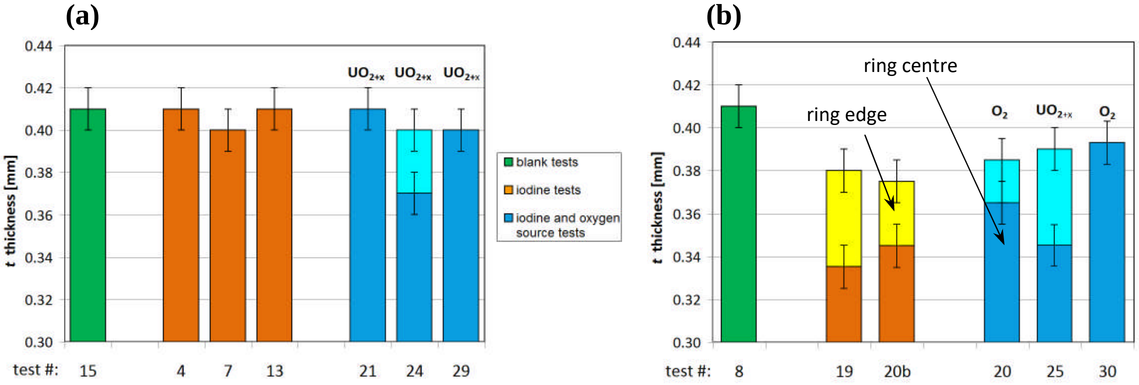

Figure 148: The slotted ring specimen wall thickness *t* vs. test number for (a) type-1 specimen and (b) type-2 specimens at specimen centres, where yellow and light blue bars indicate wall thicknesses at specimen edges.

For the type-1 specimens the thicknesses did not vary much in Figure 148 (a), equal to ≈0.40 mm, in either the iodine only tests (orange bars) or the iodine and UO_{2+x} with graphite mixture tests (blue bars). Only in test 24 there was a marked chemical erosion of the surface when more iodine was used (where the dark and light color bars represent the specimen thicknesses at the centre and at the edge of the specimen, respectively). For the type-2 specimens in Figure 148 (b) there was a marked erosion of surfaces for the iodine only experiments. Specifically, in tests 19 and 20b, where 30.0±0.4 mg cm^{-2} of iodine was used, most of the iodine induced corrosion occurred at the centre of the specimen where the stress was highest (orange bars) and less where stress was lowest (yellow bars). The chemically eroded and removed material from the specimen surfaces showed up as orange-red deposits in the glass ampoule away from the specimen and wedges. Figure 149 (a) shows some of these deposits extracted from the glass ampoule of one of the Zircaloy-iodine stress corrosion tests.

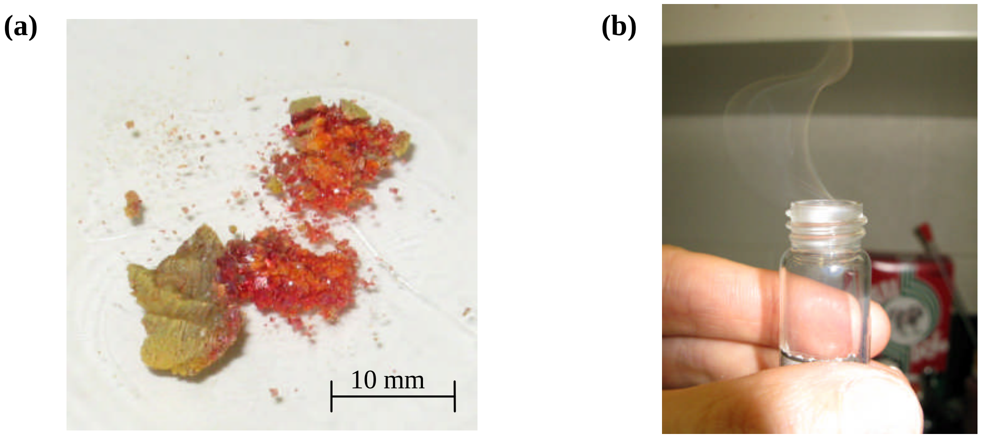

Figure 149: Collected ZrI_x deposits from a Zircaloy I-SCC test

The brown-green surfaces of the deposits seen in the same figure are surfaces that were exposed to air for twenty minutes and above. Figure 149 (b) shows a bottle that was used to store this deposit, which when opened released a visible vapour, which is possibly sublimated ZrI_x (perhaps ZrI_4(g)) or some other compound mixture of ZrI_x with oxygen from the air. These deposits were later identified (using Energy-Dispersive X-ray Spectroscopy (EDX) and Nuclear Activation Analysis (NAA)) composed of Zr and I with a Zr:I atomic ratio of about

≈1:2, indicating that the deposits were mostly $ZrI_2(s)$ (or possibly $ZrI+ZrI_3$). It can be noted that the quantity of each compound could also be analytically verified using Zr-I phase diagrams [177]. See Appendix M for the EDX and NAA scans of these deposits taken from tests 16 and 19. If the deflection of test 19 is calculated using Eq. (211) with the minimum average measured t value of 0.34±0.01 mm (from Figure 148 (b)) and where R=6.35±0.03 mm, F=0.441±0.001 N, E=97±2 GPa [202], l =5.0±0.2 mm then D_y=0.70±0.12 mm. The actual average deflection of test 19 was 0.96±0.05 mm in Figure 144, which does not agree with the theoretical value. Hence, it is possible that the specimen degradation is a combination of both external and internal corrosion (the latter possibly being cracks). In test 30, where oxygen was added, the specimen average wall thickness was 0.39±0.01 mm, and there was no increased surface chemical erosion/corrosion at specimens centre. Since the deflection in test 30 (Figure 144) was also the lowest measured, this result supports the idea that the ZrO_2 layer is protective in type-2 specimens.

Besides the specimen wall thickness comparison in certain experiments some surface peeling was observed while in the glass ampoule (tests 20 and 24) and when removing specimens from glass ampoule (test 29). This though seemed to occur when the iodine quantity was equal to or greater than 16 mg cm^{-2} and not necessarily at locations of highest tensile stress.

Specimen stress corrosion cracking in methanol solution

As shown previously, the type-2 specimens (typical of current CANDU fuel sheathing) did not classically crack and fail as the type-1 specimens did in the current experiments, although chemical etching/corrosion and thinning of the type-2 specimens at locations of maximum stress was clearly shown in Figure 145 and Figure 148 (b). To confirm that type-2 specimens can classically crack due to I-SCC, a side experiment was conducted. In this case the SCC experimental conditions were different than that provided by the evacuated and baked glass ampoules. Specifically two Zircaloy-4 type-2 slotted rings were stressed with a static Zircaloy-4 wedge and submerged in beaker containing a methanol solution of 1 wt% iodine at room temperature. Immediately after the specimens were inserted into the solution faint pinging/cracking sounds could be heard from the beaker. After 2 hours the first specimen cracked into two pieces (Figure 150 right) and after 5 hours the second specimen cracked almost right through the specimen thickness (Figure 150 left). During and after the experiment the specimens and wedge maintained their metallic sheen (i.e., besides the obvious cracking, no pitting or chemical etching could be observed with the naked eye).

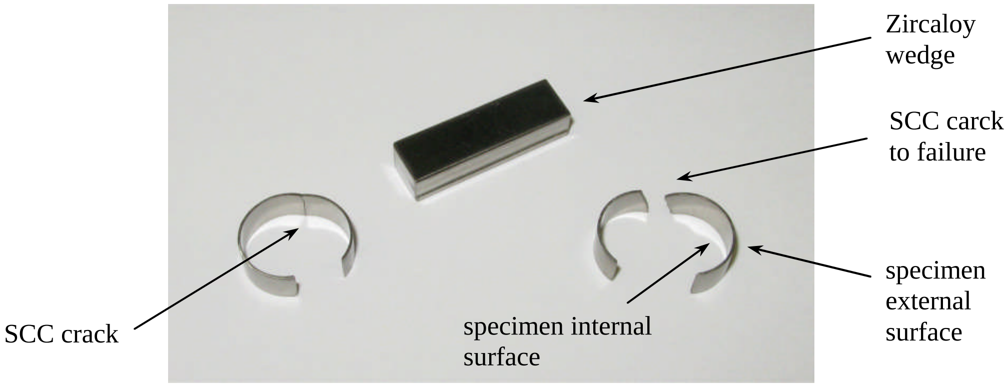

Figure 150: Failed type-2 slotted rings that were stressed and submerged in an iodine methanol solution

The cracked surfaces were scanned with an electron microscope for fractographic analysis. Figure 151 (a) shows transgranular cleavage cracking in the specimen thickness midsection in the sheath radial direction with the characteristic fluting occurring on internal grain surfaces.

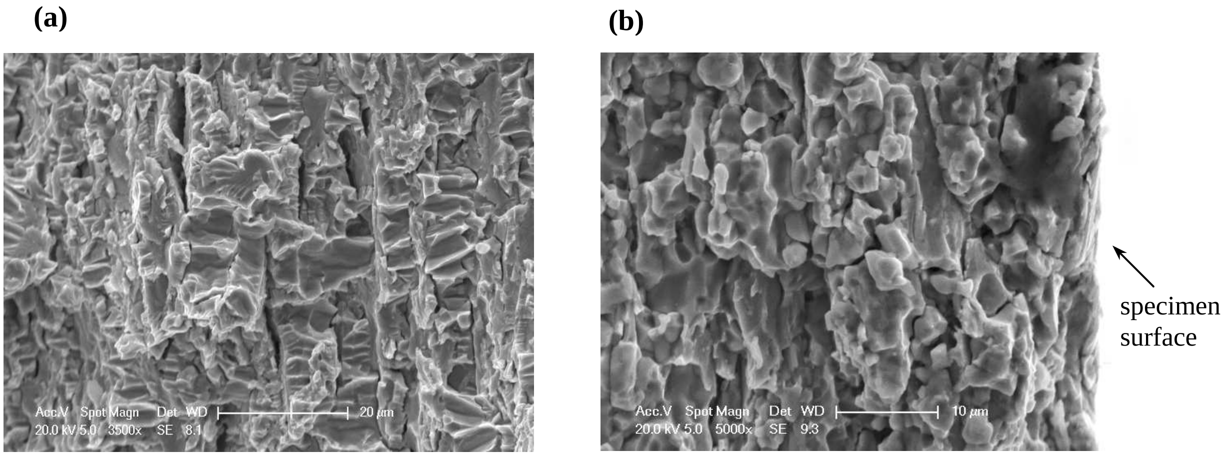

Figure 151: (a) Transgranular cleavage cracking at specimen thickness midpoint and (b) intergranular cracking at specimen internal surface, in test conducted with type-2 specimens in an iodine methanol solution

Also observed in this figure is cracking occurring in the sheath transverse direction in 4-5 locations (i.e., into the page). Figure 151 (b) shows intergranular cracking from the specimen internal surface to at least 50 μm into the specimen. The different corrosion behaviors observed between Zircaloy specimens exposed to hot gaseous iodine vapours in the glass ampoules and specimens exposed to dissolved iodine in methanol may have to do with the dissolving ability of methanol to the ZrI_x compounds that are formed when iodine reacts with the zirconium. Methanol like water is a polar molecule and is a good solvent. When the ZrI_x compound deposit, seen earlier in Figure 149 (a) (which is essentially a salt), was submerged in methanol at room temperature for a few minutes (with some agitation) it readily dissolved, as seen in Figure 152.

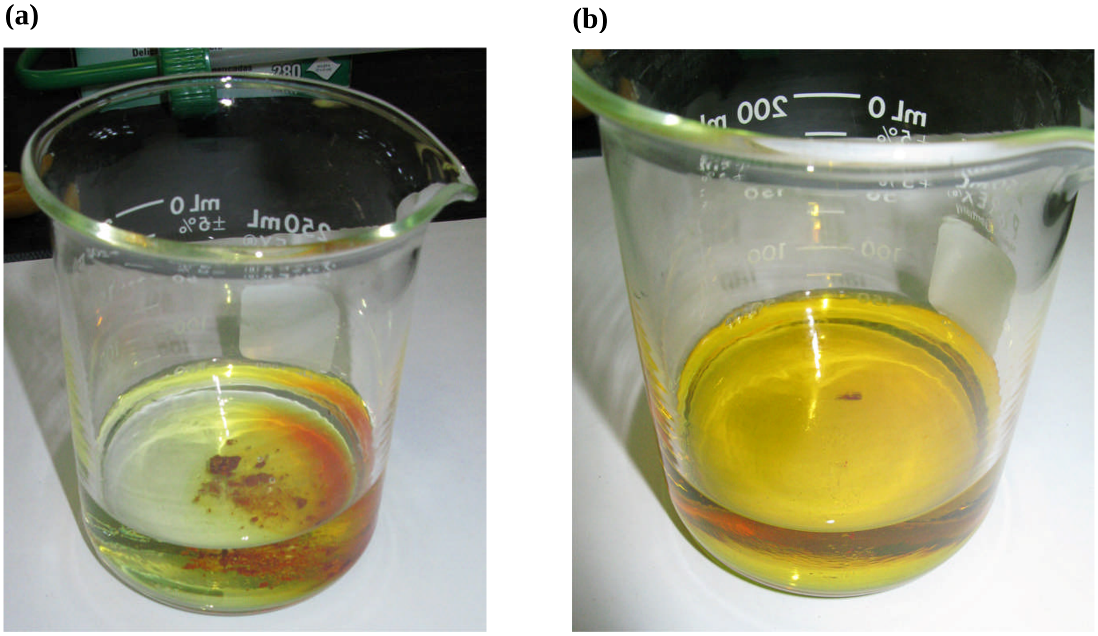

Figure 152: (a) ZrI_x deposits submerged in methanol and (b) after a few minutes duration and some agitation deposits were readily dissolved

Remembering that the reaction of zirconium with iodine produces ZrI(s), ZrI_2(s), ZrI_3(s), and ZrI_4(g) compounds, at fuel-to-sheath temperatures, only ZrI_4(g) is able to ferry away Zr from the crack tip in the sheath. But in the SCC experiment involving an iodine methanol solution all the iodides can be dissolved by the solvent and removed from the crack tip, allowing for an accelerated crack growth rate. For further reading on SCC in methanol and aqueous solutions see [205][206]. Thus, type-2 specimens may indeed crack to failure (and not just chemically corrode and etch under stress) in a hot iodine vapour environment in the lab by improving the experiment.

5.6 Use of the Fuel Oxidation Model to Introduce Superficial Oxygen

The fluid dynamics computation result of the laminar flow in the sintering furnace in shown in Figure 153. The boundary conditions of 0.4 m s^{-1} entrance velocity set at the inlet (left side) and an ambient pressure set at the outlet (right side) induces the flow. The black flow lines indicate the flow path, where the color gradient provides the flow velocity magnitude in m s^{-1}. The point where the flow meets the pellet surface head-on is referred to as the leading surface (or point) and the point on the other side of the pellet is referred to as the trailing surface (or point). As can be seen in the figure the flow velocity is at a maximum of 0.588 m s^{-1} at the model upper mid section shown in red and the flow has stagnant points at the pellet leading surfaces and trailing surfaces, as would be expected. Figure 154 shows the resulting pressure gardient, which is quite low for this case, but enough to induce gas flow.

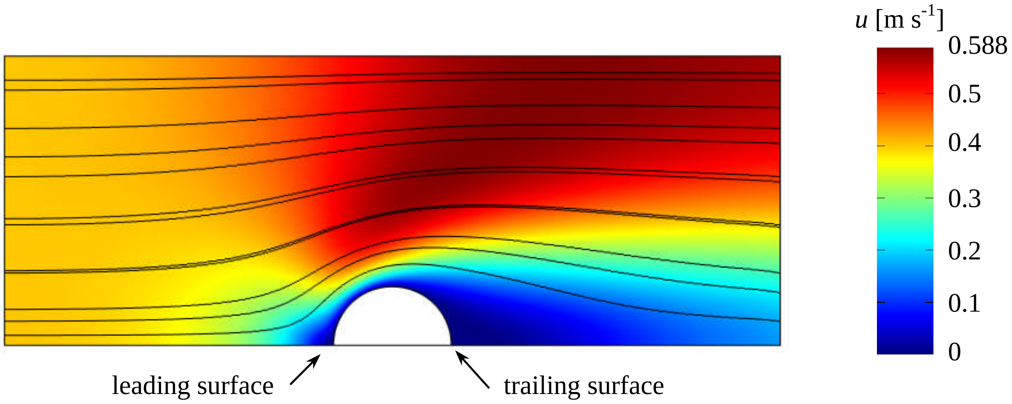

Figure 153: Laminar flow lines and color gradient for absolute velocities

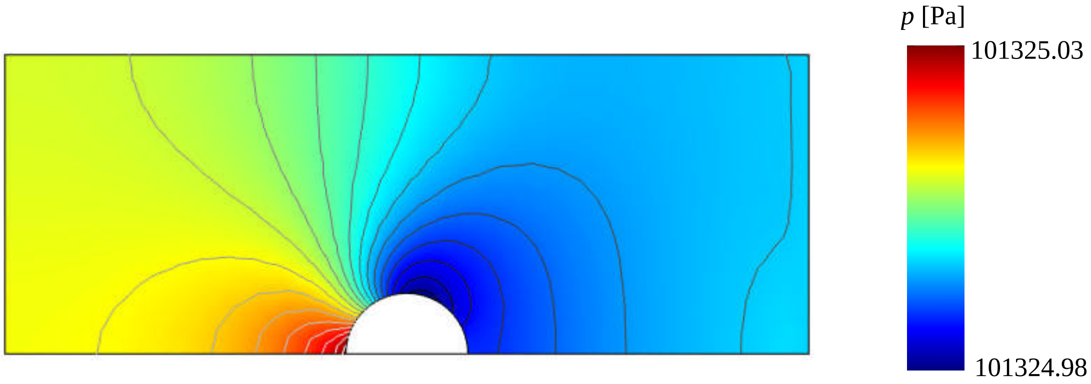

Figure 154: Pressure gradient around the sintered pellet

The hydrogen mole fraction *q* distribution is shown in Figure 155. Here one sees that the highest hydrogen mole fraction region (shown in red) is situated in the vicinity of the sintered pellet, especially at the pellet trailing surface. From comparing the flow plot in

Figure 153 to the hydrogen mole fraction plot below it becomes clear they are related, which justifies the inclusion of the fluid dynamics physics in this model, since the hydrogen mole fraction distribution affects the oxidation extent in the pellet. The pellet oxygen stoichiometric deviation distribution result, *x*, is provided in Figure 156 after 120 s of heating in the steam atmosphere, which was at 1250 °C. The maximum oxygen stoichiometric deviation that occurs on the pellet surface is about 0.0018, where the interior of the pellet remains at the oxygen stoichiometry deviation initial boundary condition at 1×10^{-5}.

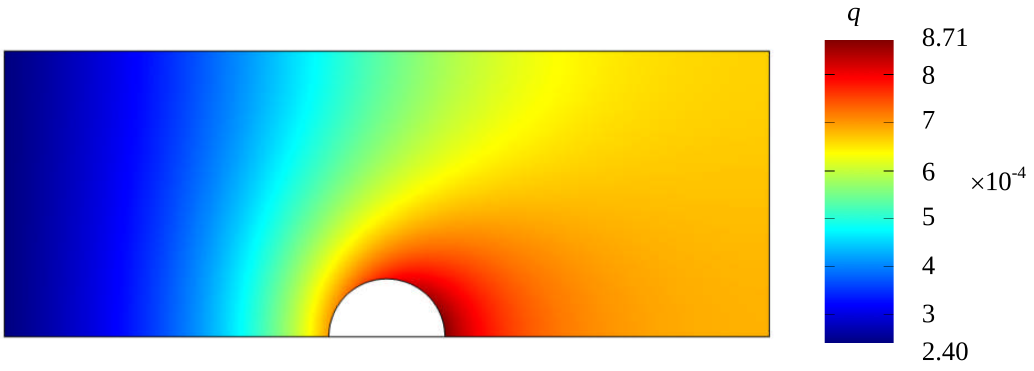

Figure 155: Hydrogen mole fraction in the flowing gas domain

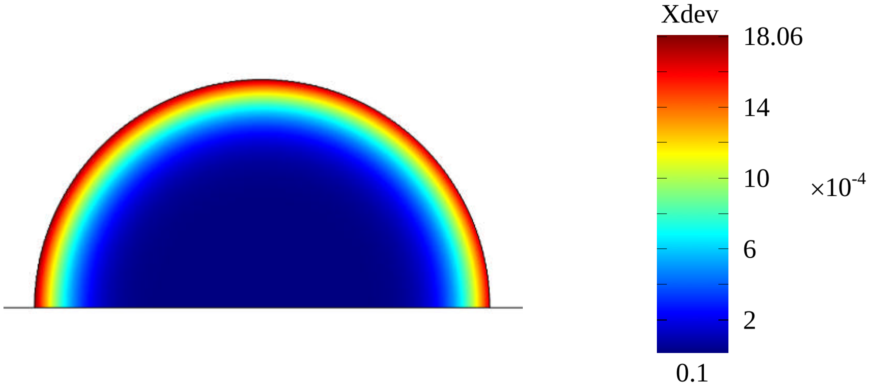

Figure 156: The oxygen stoichiometric deviation in the sintered pellet after 120 s of heating in a 1250 °C steam atmosphere

A radial *x* distribution plot is also provided through the leading and trailing surfaces of the pellet, but here after only 100 seconds of surface oxidation, in order to better describe the extent of pellet surface oxidation, as shown in the following figure:

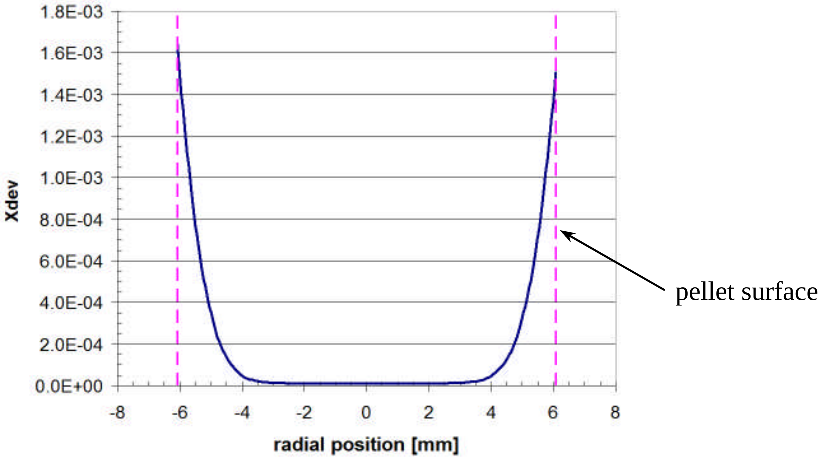

Figure 157: Radial Xdev distribution through the pellet leading and trailing surfaces after 100 s of oxidation in steam at 1250 °C and 1 atm

As can be observed in the Figure 157 the pellet surface oxidation is more or less symmetric in circumference, though increased surface oxidation in observed on the leading edge of the fuel pellet, due to the lower hydrogen mole fraction in the steam in this area. After 100 seconds of surface oxidation the O/M ratio is still close to zero up to 4 mm from the pellet interior (as is intended) and the maximum oxygen stoichiometric deviation occurring at the pellet surface is $\approx 1.6\times10^{-3}$, which is relatively low and has a negligible effect on the fuel thermal conductivity.

In Section 3.5.7 an initial target quantity for atomic oxygen molar amount uptake per CANDU fuel pellet using a modified pellet sintering process was calculated to be 2.469×10^{-5} moles (Eq. (183)). This amount of oxygen was based on Figure 144 in Section 5.5 where there was an effect of oxygen content as low as $(0.69\pm0.09)\times10^{-6}$ mol O_2 cm^{-2} on the specimen deflection measurement (to assess stress corrosion extent). The oxygen amount of 2×10^{-6} mol O_2 cm^{-2} was selected as a starting target amount of oxygen in the model (and possibly later in fuel experimentation). Figure 158 shows the atomic oxygen mole uptake in a single fuel pellet as a function of time, computed using the current model by integrating *x* (in

Figure 156) over the pellet volume. As can be seen in the figure, to achieve this target mole quantity only about 100 seconds of exposure time to steam at a temperature of 1250 °C is necessary.

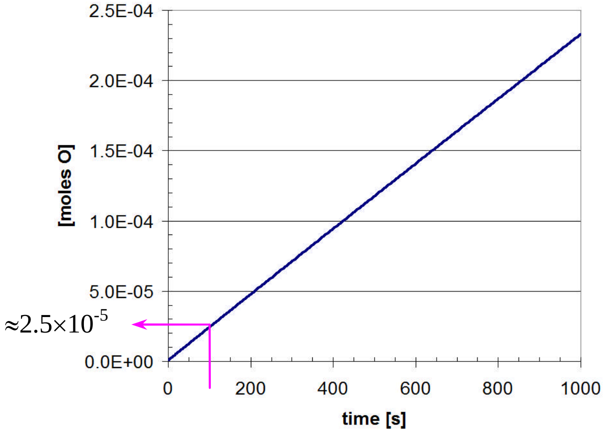

Figure 158: Computed atomic oxygen mole uptake during the oxidation process in an individual CANDU fuel pellet up to 1000 s during exposure to steam at 1250 °C and 1 atm

Having superficially oxidized the pellet surfaces to a maximum target oxygen stoichiometric deviation the question can then be asked (neglecting the possible chemical reactions between UO_{2+x} and carbon or with any other possible reactants) how long would the superficial hyperstoichiometric oxygen distribution last in the pellet once the pellets are sealed in a fuel element and placed in an operating reactor.

To answer this question a 2D r-θ fuel oxidation model based on models from Section 3.5.1 (2D r-θ model) and Section 3.5.5 (3D model) was prepared to represent an in-reactor intact fuel element, back filled with helium, heated with 44 kW m^{-1} of volumetric power, a fractional burnup of 0.5 atom%, with a temperature boundary condition (sheath outer skin) set to 573 K and with a fuel-to-sheath gap set to 3 μm. Here the superficially oxidized pellet prepared using the modified sintering process discussed earlier in this section was used as an initial condition in this model. Specifically the outer radial region of the pellet, which was 0.435 mm thick (lying between the radii 6.075 mm and 5.640 mm), was defined to have a starting oxygen stoichiometric deviation (Xdev) equal to 1.6×10^{-3}, to be inline with the maximum computed superficial Xdev value plotted in Figure 157. The oxygen stoichiometric deviation versus the radial position in the fuel element is plotted at several different times in Figure 159 (a). When the simulation time reaches 1 hour (dark blue curve) the hyperstoichiometric oxygen remains essentially in the 0.435 mm thick outer ring domain. Yet when the simulation time reaches 14 days (yellow curve) (as also represented by the 2D r-θ Xdev distribution model result in Figure 159 (b)) there is a marked decrease of Xdev in the 0.435 mm thick outer ring domain (a decrease to $\approx 1.4\times10^{-3}$) and an increase in Xdev in the fuel inner region (an increase to $\approx 5\times10^{-4}$). Note that the internal 2.9 mm diameter circle in Figure 159 (b) that previously represented the iridium bar heater is really UO_2 fuel in the current model.

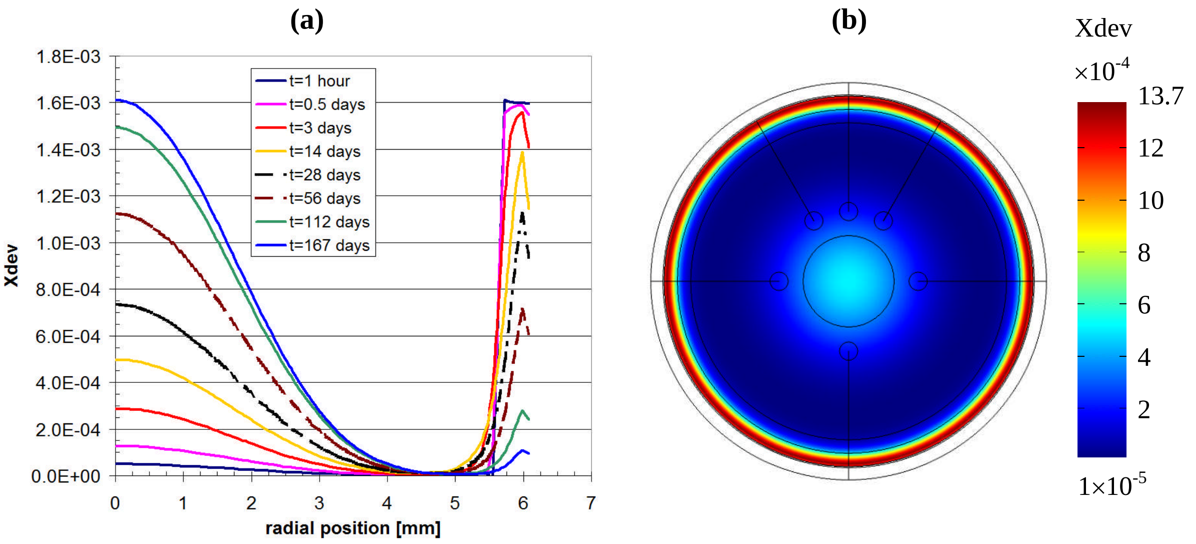

Figure 159: Oxygen stoichiometric deviation versus radial position in a in-reactor intact fuel prepared with a superficial hyperstoichiometric layer of oxygen

This net diffusion of hyperstoichiometric oxygen from the cooler outer region to the hotter inner region of the fuel is due to the initial oxygen concentration imbalance but also due to the Soret effect (Section 3.2). This interstitial oxygen diffusion trend continues as the simulation time progresses until the simulated time reaches 167 days at which point the Xdev concentration in the pellet outer region reaches a value $\approx 1\times10^{-4}$ and the inner fuel Xdev value reaches ≈1.6×10^{-3} (which has no effect on the fuel thermal conductivity). Hence, the position of the hyperstoichiometric oxygen in the fuel pellet changes from the outer region to the inner region given enough time (a few months) at reactor temperatures due to the Soret effect. This though may not be an issue, since the mitigative properties of the hyperstoichiometric oxygen and graphite (CANLUB DAG-154) may be particularly important during the first few days and weeks of the fuel residence time in the reactor core. During this early time most of the sheath deformation occurs (sheath creep down, fuel pellet expansion and cracking, fuel element hour glassing or bambooing, etc.), which can lead to the damage of protective zirconium oxide and exposure of the Zircaloy to SCC attack. Lastly the Soret effect may be less dominant than modeled here, which will be verified wth analysis of FES2 final results. Implementing this SCC mitigation technique may partially repair the sheath zirconium oxide and slow or stop this corrosion process.

Summary of Chapter 5:

- A brief outline on pellet-cladding interaction (PCI) failures was given and the solutions found in the past to PCI, in light water BWR reactors and in heavy water CANDU reactors, was described (Section 5.1).

- The goal of the SCC experiments in this thesis was then explained (Section 5.2). Specifically it was to investigate the affect of oxidized UO_2 fuel material in contact with graphite on the iodine induced stress corrosion cracking (I-SCC) process in Zircaloy sheathing, and to see if it possesses any mitigation properties to this corrosion mechanism.

- The experimental setup was then given (Section 5.3), which included the identification and characterization of the Zircaloy specimens and the slotted ring specimen stress analysis. This was followed by the experimental procedure description (Section 5.4), which detailed the slotted ring experiment performed in evacuated and sealed glass ampoules.

- In the experiment results (Section 5.5) two Zircaloy specimens were used: One dominated with prism and pyramidal plane texture and one dominated with basal plane texture. Also, two sources of oxygen were used: one from UO_{2+x} and graphite and one from oxygen gas. Results showed that both specimens were affected by the presence of an oxygen source, where in the case of specimens with basal dominated texture the source of oxygen had a protective effect against iodine induced SCC.

- Lastly, a modified pellet sintering process was modeled (Section 5.6), incorporating the fuel oxidation model. The model computed the suitable time at a specific furnace temperature to introduce a small amount of hyperstoichiometric oxygen on the outer surface of a fuel pellet without disturbing the overall O/U ratio of the fuel comparison was made between measured

CHAPTER 6 DISCUSION

6.1 General Observations of the Out-Reactor Fuel Oxidation Model

Two fuel oxidation models representing the *out-reactor instrumented defected fuel experiment* were discussed in this thesis: A 2D r-θ model and 3D model. The former required less computational resources (i.e., less time to compute) and provided a quick estimate of the radial temperature distribution. The latter required considerably more computer resources but provided a more realistic estimate of fuel oxidation.

2D r-θ Fuel Oxidation Model Results Discussion

In the 2D r-θ fuel oxidation model two scenarios were investigated: In the first scenario the fuel-to-sheath gap was ≈1 μm (model results in Section 4.2.1) and the second scenario the fuel-to-sheath gap >1 μm (model results in Section 4.2.2). This was done because the conditioning period of fuel element was planned to be relatively short so total sheath creep down was not expected occur. Hence, the fuel-to-sheath gap of the out-reactor fuel element simulator during the test was unknown and could only be estimated when the main experimental results were available (which were not available at the time this thesis was written). For the first scenario Figure 73 (b) provides the oxygen stoichiometric deviation after two weeks of heating where 12 radial cracks were considered. In this model a maximum value of x = 0.095 occurred near the fuel centre adjacent the iridium bar heater. The selection of 12 radial cracks was later found to be excessive, since the number of cracks in the fuel element is approximately equal to the fuel element linear power divided by two (see Section 1.6). This applies to an in-reactor fuel element where in the out-reactor configuration only the power dissipated by the iridium bar heater needed to be considered for radial crack number prediction. Thus, this is why the models with the open fuel-to-sheath gap in Section 4.2.2 were corrected to incorporate just six radial cracks.

The effect of fuel oxidation on fuel thermal conductivity and hence fuel temperature is simulated in the closed fuel-to-sheath gap model. Figure 77 (a) and (b) gave a radial temperature plot at 6 hours, 1 day, 4.6 days and 2 weeks of simulated defected fuel heating (where Figure 77 (b) gave the temperature plots in the vicinity of TC1). Plotting x at the same location as a function of time (Figure 78) showed an increase in x over the 14 days and a general decrease in fuel thermal conductivity (a ≈5% decrease). The maximum x and T results occurring at the inner most location of the fuel was also presented in Table 27, which showed a general increase in temperature, specifically a ≈27 degree increase after 14 days of heating. This though was not a very large temperature increase in the fuel partly because the oxidation simulation duration was relatively short, fuel burnup was not considered (since the model represents an out-reactor test configuration where there is no radiation damage or fission product generation), and the out-reactor fuel with the concave facing-up temperature profile yielded a smaller region where fuel oxidation actually occurs (at the bottom of fuel cracks).

The closed fuel-to-sheath gap in the 2D r-θ fuel oxidation model (Section 4.2.1) considered 12 radial cracks. Since modeling 12 radial fuel cracks is complicated in 2D and even more challenging in 3D, the effect of modeling only five radial cracks near the sheath defect on the extent of fuel oxidation was investigated. For the five crack model (Figure 80), the maximum oxidation result after two weeks of simulated heating was x=0.102. Referring back to when all 12 radial cracks were included in the oxidation process (Figure 73 (b)), the maximum oxidation was a little lower, at x = 0.095 (see Table 27 and Table 30 comparison). The increase in fuel oxidation for the five-crack case was caused by the reduced number of fuel cracks at remote locations from the sheath defect that were not present to act as hydrogen sinks. Hydrogen concentration increase can reduce the oxidation rate, stop, and even reverse the oxidation process. This behaviour was numerically confirmed in the model by plotting and comparing the reaction rates (for fuel oxidation and reduction) in a near and remote radial fuel crack from the sheath defect (Figure 81 and Figure 82). This explains the non-azimuthal symmetric fuel oxidation in the fuel element when plotting the oxygen deviation distribution result after the first few minutes of the heating/oxidation simulation, as seen in Figure 84.

A parametric study was conducted in the 2D r-θ fuel oxidation model that involved varying the fuel-to-sheath gap and the radial crack widths to investigate their effect on fuel oxidation. This was done because the fuel-to-sheath gap was not expected to be completely closed (i.e., to be <3 μm gap), neither were the fuel crack widths expected to remain constant, in the *out-reactor instrumented defected fuel experiment*. Hence in Section 4.2.2 an open fuel-to-sheath gap 2D r-θ fuel oxidation model was used to examine two scenarios: (i) When the fuel-to-sheath gap was varied and the fuel crack widths were held constant, and (ii) when the fuel cracks were varied and the fuel-to-sheath gap was held constant.

For the first scenario the crack tip depth and temperature were held constant while the fuel-to-sheath gap was varied in a parametric study. This was accomplished by adjusting the iridium bar heater power for each gap dimension, while maintaining the same crack depth. Table 31 showed the oxidation results for several fuel-to-sheath gaps, where increased fuel oxidation occurred when the fuel-to-sheath gap was increased. Specifically, $\mathrm{Xdev}_{\mathrm{max}}$ increased from 0.094 to 0.106 and the total oxygen uptake into the fuel increased from 0.068 to 0.129 moles, as the fuel-to-sheath gap was increased from 1 to 20 μm. It should be noted that this observed Xdev increase cannot be explained solely by the slightly warmer areas of the fuel (by ≈130 degrees) near the pellet surface as a result of the increased fuel-to-sheath gap, as seen in Figure 86. This is because most of the fuel oxidation occured at the crack tips and rapidly decreased away from the crack tip where the temperature was lower. This was due to the Arrhenius exponential behavior in the fuel oxidation reaction rate (refer to Eq. (22) and Figure 81). The increased fuel oxidation may also be due to increased interstitial oxygen diffusion in the slightly warmer fuel (with the larger gap), but it is suggested that the increased fuel oxidation in the model was a result of the increased fuel-to-sheath gap dimension, which can affect the hydrogen mass transport in the gap.

In the second scenario the crack widths were varied while the fuel-to-sheath gap was held constant in a parametric study. Holding the latter constant also meant that the power applied to iridium bar heater was held constant because there was no change in the radial thermal resistance across the fuel-to-sheath gap, which simplified the study. For the selected iridium bar heater power all simulations used the same crack tip depth and temperature. The model results summed in Table 32 showed similar oxidation dependence, but this time on crack width dimension. Specifically, $Xdev_{max}$ increased from 0.071 to 0.093 and the total oxygen uptake into the fuel increased from 0.031 to 0.070 moles, as the fuel crack width was increased from 1 to 20 μm. Hence, the second scenario parametric study showed that the models with the widest fuel cracks, where flux/source terms were also active (Eq. (25)), there was increased fuel oxidation. This was because of the greater hydrogen mass transport afforded by the wider cracks, from the crack tips (where the hydrogen is generated) to the sheath defect (where the hydrogen escapes to the coolant). This resulted in a lower hydrogen mole fraction in the cracks, which in turn increased the amount of fuel oxidation.

For the 2D r-θ fuel oxidation model a mesh sensitivity test was performed between a high density, all triangular, meshed model and a lower density, quadrilateral and triangular, meshed model (a mesh density difference greater by a factor of four). This was to show that lower density meshed case provided an accurate solution and also to show that high aspect-ratio mesh elements (such as the slender mesh in the fuel cracks and in the fuel-to-sheath gap) could be used. Results showed (refer to Table 32 and Table 33) that there was only a 0.39% difference in the maximum oxygen stoichiometric deviation between the two models, which showed model mesh independence.

The thermocouples (TCs) themselves were included in the 2D r-θ closed fuel-to-sheath gap model to investigate local heat transfer effects near and in the TCs. These TCs were considered to be in total physical contact with the fuel. The temperature radial profile through the fuel only and through the fuel with a thermocouple (inner most TC1), the latter at a different azimuthal location, were not the same at either sides of the TC hole in the fuel radial direction (i.e., at the thermocouple edges, Figure 74). However, the modeled temperature was the same at the centre of the TC. This would also be so if the fuel-to-TC gap was modeled, on condition that this gap is circumferentially equal. In reality this gap will not be circumferentially equal, so actual temperature measurements at a similar radial position but at a different axial position were not expected to be equivalent (a temperature discrepancy of at least ±30 K is initially expected). If the temperature discrepancy is greater than this value between TC at two axial positions, possibly due to movement of the TC in its hole, smaller fuel-to-TC gaps should be considered in future experiment designs.

Discussion of the 2D r-θ solid mechanics model that deals with fuel crack geometry and conditions for fuel crack propagation is provided in Section 6.3.

3D Out-Reactor Fuel Oxidation Model Results Discussion

The 3D fuel oxidation model was built, since it is a more accurate representation of the fuel element because its length and the sheath defect surface area are specifically defined. As explained in Chapter 2 and in Section 3.5.6 the 3D geometry for computing fuel oxidation is computationally more expensive, so incorporating all the 2D r-θ model features such as modeling fully cracked fuel pellets, solid mechanics thermal stresses, fuel and sheath contact, and electrical (or Joule) heating was not attempted, since it was not necessary. Instead the 3D out-reactor fuel oxidation model included only some of the pre-defined radial fuel cracks and a partial fuel-to-sheath gap, both near the site of the sheath defect. Temperature boundary conditions were used at the fuel central annulus and at the fuel outer surface, which were based on the 2D r-θ model results (refer to Sections 3.5.1 and 4.2.1).

In the model numerical implementation in Section 3.5.6, two power cases were selected for simulating the *out-reactor instrumented defected fuel experiment*: a high powered case (23 kW) and a low powered case (17 kW), both being the total power applied in the FES. This was done because it wasn't known at the time how much electrical heating power could be taken by the FES without failing prematurely. In both cases, the crack tips were positioned so that they were located at a local fuel temperature of 1523 K (1250 °C), as was also set in the 2D r-θ model. It can be noted that it is possible that this *effective* crack depth, situated between the plastic and elastic fuel zones, may have been underestimated. In reality the crack tips may have been positioned at temperatures >1673 K (1400 °C), or higher still, since the healing time of the fuel cracks in the plastic fuel zone may take considerably more time (i.e., not instantaneously as assumed in this work). As was seen in Figure 116 (b) the maximum oxygen stoichiometry deviation after two weeks of heating for the high powered case was $x = 0.062$, while for the low powered case it was a little higher at $x = 0.068$ as seen in Figure 122 (b). As the distance increased from the sheath defect area in the axial direction, the oxygen stoichiometric deviation dropped off more quickly in the low powered case compared to the high powered case, as seen in Figure 117 and Figure 123. This was also shown when the total hyperstoichiometric oxygen atoms mole uptake, n_O (or n_O in Appendix C), into the fuel elements was compared for the two power cases after two weeks of heating: In the high powered case $n_O = 0.010$ moles and in the lower powered case $n_O = 0.006$ moles, as shown in Figure 121 and Figure 124. The higher powered fuel element model showed more fuel oxidation, and the fuel oxidized more evenly in the axial direction, away from the sheath defect. For validating the fuel oxidation model, both the high and low power model cases showed enough oxygen stoichiometry deviation in the fuel so that detectable post test coulometric titration measurements of hyperstoichiometric oxygen could be taken.

The effect of fuel oxidation on the temperature distribution was noted in the 3D model. In Figure 118 (b) the temperature was plotted along the fuel radius (near the position of TC1) at three different times during a two week heating period and showed that the fuel temperature increased by about 20 °C. Comparing the 2D r-θ fuel oxidation and temperature model results (in Figure 77 (b) and tabulated results in Table 27 and Table 30 in Section 4.2.1) to the 3D oxidation and temperature model results (Figure 116 (b), Figure 117, and Figure 118 in Section 4.6) it was observed that more fuel oxidation occurred in the 2D r-θ model and yielded a larger fuel temperature increase compared to the 3D model. Specifically, in 2D r-θ model there was an increase in the inner radial fuel temperature by about 30-40 degrees °C when $\mathrm{Xdev}_{\mathrm{max}}$ reached 0.095 and above. Hence, the 2D r-θ model predicted a sufficient fuel temperature increase which should be measurable with the FES thermocouples within the two week heating period. However, the time required to reach this level of fuel oxidation in the out-reactor FES test configuration was predicted in the 3D model to be greater than two weeks of heating at the current modeled heating powers. Thus, the fuel temperature increase due to fuel oxidation achieved in the planned two week experiment may be too small to distinguish, since the thermocouple reading may be within the uncertainty of the measurement (see Section 4.2.1 for the thermocouple uncertainty estimate).

6.2 Model Validation of the Current Fuel Oxidation Model

Two models were developed to partially validate the fuel oxidation model: In Section 4.5.1 a steady state 2D r-θ model of the FES1 experiment was used to validate the heat transfer properties of the fuel oxidation model (where fuel oxidation was not simulated), and in Section 4.5.2 a time dependent full length 3D model was used to simulate an in-reactor defective fuel element (where fuel oxidation was simulated).

For validating model heat transfer properties of the fuel oxidation model Figure 106 provided the Stern Laboratories temperature readings during the FES1 commissioning test and these readings were compared to the 2D r-θ model simulation in Figure 108. As was observed, all three temperature readings (TC1, TC2, and TC3), on average, provided by the two axial thermocouple planes in the FES agreed with the model simulation result within uncertainty. Also, the temperature readings were stable and demonstrated little noise. It was also noted that in order for the 2D r-θ model to match the FES1 temperature readings and the applied total electrical current reading as close as possible, the fuel-to-sheath gap dimension was set to 5.1 μm (ftsg_thickness parameter in Table 34), indicating that the gap was probably open given the short conditioning period in the FES1 experiment. It is important to note that the total electrical current did not match exactly (i.e., experiment measurement of 930 A as compared to the modeled value of 990 A). This might be because of the slightly higher UO_2 thermal conductivity in the fuel oxidation model formulation compared to thermal conductivity measurements seen in the literature (Figure 71 and Figure 72 in Section 4.1). It might also be because the equations representing the electrical conductivity of the iridium bar heater and the Zircaloy sheath are not accurate enough. Lastly, improved modeling may be achieved if the ohmic heating physics module is utilized in computation of electrical power (Eq. (91)). Modeling the results of the *out-reactor instrumented defected fuel experiment* (FES2) (not conducted in this work) may help explain this discrepancy.

For a preliminary validation the fuel oxidation model in this work, 3D model simulation results were compared to an in-reactor defective fuel element (XC9179Z-5) where the degree of fuel oxidation was confirmed by coulometric titration measurements [29][88]. The maximum oxygen deviation of 0.076 (Figure 109 (b)) in the current model did not substantially change the fuel thermal conductivity and thus the temperature distribution in the fuel (Figure 110). It can be noted that only when the maximum oxygen stoichiometric deviation reaches 0.085-0.090 and above does the degraded fuel thermal conductivity start to noticeably increase the fuel temperature. The measured oxygen deviations in the defective fuel element were higher than the modeled values, specifically, the modeled values agreed only in one out of six measured CT values within uncertainty in Figure 111. As detailed in Section 4.5.2 this may be explained for following reasons (or other reasons not elaborated here):

1) In the in-reactor 3D model only one sheath defect location was defined. However, in the actual defective fuel element the sheath was breached at several locations along the whole length of the fuel element. It is suggested that the presence of distributed sheath breaches over the fuel element has a greater oxidizing effect than a single sheath breach, even if the sum of the multiple breaches' surface area is similar or less than a single modeled sheath breach surface area. This is because a local sheath breach has a large effect on the local hydrogen mole fraction in the fuel cracks (i.e., will be low), which accelerates fuel oxidation. It is important to note that actual defective fuel elements are usually detected once hydriding defects have been developed at various locations on the element sheath, some time after the primary sheath defect occurred (for reasons given in Section 1.4). In other words, a fuel element that first develops a primary sheath defect, followed after a certain amount of time by multiple secondary sheath defects was not considered in this in-reactor 3D fuel oxidation model. Modeling of a defective fuel element with multiple sheath breaches developed after the primary sheath defect was not attempted in this work, since it required additional computational resources.

2) The positioning of fuel crack tips where the fuel temperature is 1250 °C (1523 K) may have been incorrect. The *effective* crack tips may have needed to be set closer to 1400 °C (1673 K) in the current model. This can be justified considering that the fuel elastic-to-plastic transition zone occurs over a range of temperatures (1200-1400 °C) [15][73]. For implementing this change the radial fuel cracks could be made longer than 4.575 mm from the pellet surface (or for the crack root to be located less than 1.5 mm from of the pellet centre line, see Section 3.5.5) in this specific defective in-reactor model. Furthermore, if the fuel healing time is considered (Eq. (48) at the end of Section 3.2), fuel cracks may be present in the inner plastic fuel during its time in the reactor, especially during fuel shifting or power ramps, at which time new fuel cracks can form. Hence, accelerated fuel oxidation can occur in these plastic fuel cracks.

3) The selection of the fuel surface temperature in the model can also have an effect on the extent of fuel oxidation. The applied fuel surface temperature of 645 K in the in-reactor 3D model (Figure 109 (a)) was an estimated value, since heat transfer through the fuel-to-sheath gap and through the sheath was not included. To investigate the effect of fuel surface temperature on fuel oxidation a second case was modeled where the fuel surface temperatures was set to 706 K (a temperature boundary condition taken from [29] for fuel element XC9179Z-5). Two resulting fuel centre-line temperatures ≈1600 K to ≈1700 K were computed for these two fuel surface temperature boundary conditions. The fuel oxidation extent for these two cases was shown in Figure 111, and it was observed there was a marked increase in the modeled fuel oxidation with the increased fuel surface temperature. However, the increase in the oxygen stoichiometric deviation, as high as 13% in certain radial and axial locations in the model, did not result in modeled x values that agree with the remaining five CT measurements in Figure 111 within the measurement uncertainty.

4) The radial crack width of 30 μm may have been set too narrow. It is possible the crack width in the in-reactor defective fuel element may have been wider than this value as was shown possible in the out-reactor fuel solid mechanics expanded crack model result

(45 μm wide) in Figure 94 (a). Another related possibility is that too few cracks were modeled in the immediate vicinity of the sheath defect. It has been shown in PIEs of in- and out-reactor fuel that the number of radial cracks is approximately equal to the fuel linear fuel power divided by two as discussed in Section 1.6 and in [29][73]. The applied power in the 3D in-reactor fuel oxidation model was 44 kW m^{-1} so the estimated number of radial cracks is 22. The model on the other hand included only three radial cracks (see Figure 56 and Figure 60 (b)). Hence there should probably have been an additional two to five radial cracks in the immediate vicinity of the sheath defect, which would have increased the overall fuel oxidation result.

5) The values calculated for the hydrogen mole fraction diffusivity term (Eq. (29)) derived using Chapman-Enskog gas kinetic theory, which is used in model gaps and cracks, is possibly too small and may need reexamination.

6) The post defect residence time discussed in [24][29] in defective fuel element XC9179Z-5 is an estimate based on detected fission products (iodine-131) in the reactor primary coolant. In reality this fuel element may have been defective for a longer period of time than the modeled oxidation period (126 days), since it is possible the first detection occurred only when the secondary sheath defects developed.

The *out-reactor instrumented defected fuel experiment* addresses two of these points (1 and 6), since only one sheath defect location is present throughout the experiment and the post defect residence time is known with certainty.

To perform a sensitivity analysis on the number of participating cracks (point 4), the 2D r-θ out-reactor fuel oxidation model was used to investigate two cases: case (1) where all radial cracks participated in fuel oxidation and case (2) where only radial cracks in the immediate vicinity of the defected sheath location were defined as ‘active’ in the model (see results Section 4.2.1 and discussion Section 6.1). The results showed similar oxidation results in both cases, though there was a marked increase in the maximum oxygen stoichiometric deviation (about 7%) when fewer cracks were active. This was explained due to the absence of fuel reduction in the hydrogen rich fuel cracks that were remote from the sheath defect in case (2).

Also, a sensitivity analysis was performed in the 3D in-reactor fuel oxidation model. Specifically in the current 3D model the radial cracks extended only 3 cm (6 cm actual) in the axial direction of the fuel element in order to conserve computer resources. To show that this modeling approach can be used, an additional in-reactor 3D model was constructed where the three radial cracks were extended to the full length of the fuel element. Figure 113 (a) and (b) provided the modeled temperature and the oxygen stoichiometric deviation results, respectively, for defective fuel element XC9179Z-5, using the full axial crack length model. When both modeling approaches were compared (Figure 109 and Figure 113) it was observed that there are only slight differences in the model's maximum temperature and oxygen stoichiometric deviation results, which was illustrated more clearly in Xdev radial profiles comparison (Figure 114). Thus, partial crack lengths in the axial direction can be used.

Also, a comparison was made between the current 3D in-reactor fuel oxidation model with partial crack lengths in the axial direction to a model that used the previous Higgs modeling technique [24][29] (refer again to Section 3.5.5 and Figure 62 for a brief description on the numerical implementation of this model). It was shown that there was a marked difference in the Xdev radial profile results between the two models (Figure 115 (a)), specifically the current 3D model showed Xdev values more than twice that of Xdev values using the previous Higgs' modeling technique. The Xdev increased in the 3D model was further illustrated with a comparison made between the total computed oxygen mole uptake (Figure 115 (b)) in the three different in-reactor fuel oxidation models (the current partial length discrete fuel cracks in axial direction, the full length discrete fuel cracks in axial direction, and the previous Higgs' non-discrete fuel cracks - oxidation models). As was clearly seen in the Figure 115 (b) the oxygen mole uptake in the two discretely cracked fuel oxidation models were quite similar. Using the Higgs modeling technique yielded an oxygen mole uptake that was about four times less than the first two models. This relative increase is caused by the use of discrete fuel cracks in the current model and the application of gas diffusion constraints (anisotropic diffusion) in the Higgs' model.

From these results it would seem that modeling the fuel oxidation model with discrete fuel cracks near the sheath defect yields a solution more in-line with PIE coulometric titration oxygen measurements. Nevertheless some points should be made to explain why this is the case. The previous Higgs modeling technique [24][29] applied in a 3D fuel oxidation model (Figure 115 (a)) assumed that the hydrogen gas diffusion occurs in the fuel domain, but only in the radial direction (not in the azimuthal or axial directions) and only above the fuel elastic-to-plastic boundary (the red and blue domains in Figure 62). Axial hydrogen gas diffusion though was allowed in the fuel-to-sheath gap using *weak form* terms in the Higgs model [24][29]. However, considering the solid mechanics modeling results of expanded fuel crack geometry (Figure 88 and Figure 94 in Section 4.3), and the conditions for fuel crack propagation (both further discussed in Section 6.3), and the computation of radial cross section area of the fuel cracks (Figure 105 in Section 4.4), it can be said that in the out-reactor fuel element the total radial cross sectional area for gas diffusion through the fuel cracks is significantly greater than the cross sectional area of the closed fuel-to-sheath gap (by about ≈25 time). The same would be expected in in-reactor fuel, though this was not modeled in this work. This would mean there is more gas diffusion occurring through the cracked fuel than through the fuel-to-sheath gap. Thus, if the hydrogen gas diffusion was allowed to occur in all principle fuel directions (radial, azimuthal, and axial) in the Higgs' 3D non-discrete cracked fuel oxidation model, increased fuel oxidation would be computed. However, isotropic gas diffusion in the fuel is hard to justify, since the few cracks in the fuel relative to the fuel volume, which act as gas conduits, provide specific gas diffusion directions. In other words using isotropic gas diffusion in the fuel is not quite physical.

6.3 Modeling Crack Geometry and Conditions for Fuel Crack Propagation in Support of the Fuel Oxidation Model

The geometry (length and width) and the number of the radial fuel cracks defined in the current fuel oxidation model were initially based on previous experimental and modeling work [57][73][76]. However, these sources of information did not fully characterize the out-reactor experimental configuration. Also, considering that is was shown that the fuel crack width dimension can have an effect on fuel oxidation (Table 32 in Section 4.2.2) it became clear that fuel crack number and geometry needed to be modeled in support of the fuel oxidation model. Section 4.3 elaborated on a number of solid mechanics modeled scenarios in the out-reactor UO_2 fuel. This modeling provided predictions of the fuel crack geometry, and determined conditions for crack propagation (number of cracks).

In the first 2D r-θ solid mechanics modeling scenario it was assumed that the iridium bar heater expanded onto the UO_2 inner annulus. This was captured by applying solid continuity between the iridium bar heater and the UO_2 fuel in the model (this was also more representative of in-reactor fuel). In the same model five pre-set radial cracks 3μm wide were defined, while a sixth crack was initially a surface flaw. This model also included sheath and fuel contact modeling using a customized penalty method. Figure 89 (a) showed that when the sixth crack was still a surface flaw one of the remaining five radial cracks (at the 11 o'clock position) was as wide as 100 μm (much wider than the fuel-to-sheath gap in CANDU fuel). When the six cracks was fully extended this crack width decreased to ≈45 μm, a significant decrease but still relatively large compared to the fuel-to-sheath gap. Plotting the radial and azimuthal components of stress in the fuel pellet, at the fuel crack tip as well as in the sheath, gave a better depiction of internal stresses than could be visualized with a von Mises distribution plot (the latter giving no information on stress directions). Figure 91 showed that when the developing crack was still a surface flaw the azimuthal stress was positive in most of the pellet outer regions, which fulfilled one of the conditions for Mode I cracking. For determining the second condition for Mode I cracking, stress intensity values K_I were computed using the J integral and compared to analytically calculated and measured fracture toughness values K_{Ic} in Figure 93. As could be seen in the figure K_I values were higher than K_{Ic} values throughout the whole length of the crack, in a model with five pre-set radial cracks. When the developing crack was fully opened in Figure 92 the azimuthal stress at the crack tip was zero but then jumped to a very high tensile value beyond the crack tip and further into the pellet. This large stress increase though is a fictitious value, since in this region the fuel will behave plastically (which is not considered in this model), effectively relieving the stress field. Figure 92 also showed that the UO_2 radial stress in the model is not zero near the iridium bar heater but tensile. In other words the UO_2 pellet was being ‘pulled’ by the iridium domain, which is not physically possible. This indicated that the UO_2 pellet was thermally expanding more than the iridium bar heater. Hence a second modeling scenario, where no solid mechanics physics was applied to the iridium bar heater domain, was investigated.

In the second 2D r-θ solid mechanics modeling scenario the iridium bar heater was removed from the solid mechanics physics computation. Like in the first scenario the stress components in the radial and azimuthal directions were plotted through the fuel pellet but this time at two azimuthal directions, one through the developing crack and one through uncracked fuel (Figure 96 and Figure 98). Additionally, two cases were modeled for the second scenario. One case where there was one surface flaw and five pre-set radial cracks, and a second case where there was only one surface flaw and only one radial crack. With the stress component plots the relation between the number of pre-set radial cracks and the azimuthal stresses in the out-reactor fuel pellet was observed. When there was only one pre-set radial crack the azimuthal stress was tensile (i.e., positive) from the pellet surface all the way to a ≈3 mm depth. But when there were five pre-set radial cracks the azimuthal stress was shown to be compressive (i.e., negative) at the fuel pellet outer surface. Thus, in this latter case it could initially be deduced that the surface flaw would not develop into a sixth full length radial fuel crack, since it is not Mode I cracking.

The computation of the stress intensity factor for the two cases (Figure 99) showed that K_I was greater in the one pre-set crack case (two cracks in all) compared to the five pre-set crack case (six cracks in all), since the radial cracks relieve stress in the fuel pellet. In both cases K_I was greater than the calculated or the measured K_{Ic} values, indicating that the number of radial cracks could be five, if the assumption is made that fuel radial cracks only develop from fuel surface flaws. However, this assumption is probably overly simplistic, since fuel radial cracks (or fuel cracks in general) can also develop from internal fuel flaws, considering as well that the internal out-reactor fuel azimuthal stress is tensile from a depth of ≈1 to ≈3.9 mm (see blue curve in Figure 96). Thus, if cracks can develop from internal fuel flaws the number of radial cracks (in the current model with the specific heating power applied) may be greater than five.

A sensitivity analysis of the *J* integral line integration contour was conducted to show contour shape and size independence. Two contour shapes were used - a circular and a rectangular shaped contour. Model results showed that the *J* integral values (and hence the stress intensity factor values) were independent of the contour shape (Figure 101) and size (Figure 102). It was also shown that the *J* integral results were independent of the applied mesh (Figure 100); be it quadrilateral or triangular mesh. However increased model stability during convergence was noticed when the quadrilateral mesh was used.

In certain situations thermal gradients can have an effect on the computation of the *J* integral, i.e., the *J* integral can become path dependent (Section 3.4.2). Although path dependence was not noticed in the *J* integral computation using the two contour shapes and sizes, this work also included the *J** integral computation. For the less relevant case of homogeneous materials (Eq. (134)) when the temperature is uniform the stress intensity factor KI_star was computed, and for the more relevant case of non-homogeneous materials (Eq. (135)) when material properties depend on temperature and when the temperature is not uniform the stress intensity factor KI_star_2 was computed. Figure 101 showed that the solution of the regular *J* integral was essentially the same as *J** for the homogenous case. For the non-homogeneous material case *J** was slightly higher than *J* but not by much (≈30% higher). *J** values were shown to be contour shape and size independent for the homogeneous case and almost independent for the non-homogeneous case (Figure 101 and Figure 102).

Additional modeling involving *J** computations for homogeneous and non-homogeneous cases should be conducted to make more definitive deductions. For the current model both the *J* and *J** integrals can be computed to determine the conditions for the onset of crack growth in a developing surface crack. The *J* integral is simpler to implement in the model as well as to post process than the *J** integral. Hence the *J* integral should be sufficient for determining conditions for crack growth in non-isothermal expanded fuel pellets.

Section 4.4 showed that the 2D r-θ solid mechanics plane strain pre-set cracked fuel model (with fuel and sheath contact modeling) can be coupled to the fuel oxidation model, using the Arbitrary Lagrangian Eulerian (ALE) moving mesh method (or a deformed mesh). This method allowed the use of the fuel cracks and the fuel-to-sheath gap domains (which were typically inactive in the solid mechanics only model) for computing the hydrogen gas diffusion more realistically (since the cracks are wedge like and change dimensions in the simulation). The dimensional change of the fuel cracks and the fuel-to-sheath gap is important to consider, since it affects the hydrogen mass transport. In other words had ALE not been used the cracks would remain only 3 μm wide, reducing the extent of fuel oxidation. The maximum oxygen stoichiometry deviation result in this model (Figure 103 (b)) was $x = 0.088$ after two weeks of heating, which is consistent with the results of the 2D r-θ fuel oxidation static model Section 4.2. The crack depth (which is dependent on the fuel linear power and on fuel oxidation) was held spatially constant in this time dependent model. It is possible to make the fuel cracks grow or retract using the deformed mesh method. However, considering that the current fully coupled 2D r-θ model required several days to converge to a solution, modeling crack growth in a time dependent model was not attempted in this work. It can be noted that this discrete crack modeling method could also be used in simulating some aspects of fission gas release or stress corrosion cracking in fuel where the effects of fuel crack dimensions need to be considered.

6.4 Stress Corrosion Cracking of Fuel Sheathing and its Relation to Oxygen and Oxidized Fuel

It was shown in experimental results in Section 5.5, in the Zircaloy slotted ring specimen defection measurements, that the Zircaloy specimens can form an increased resistance to corrosion when in the presence of an oxygen source, as a result of the growth and fortification of the protective zirconium oxide layer. These tests involved exposure of stressed Zircaloy specimens to hot iodine vapour (as low as 4.5±0.2 mg cm^{-2}) in evacuated glass ampoules (Figure 141 for type-1 specimens and Figure 144 for type-2 specimens) while heated in a furnace. In tests with type-1 specimens where no oxygen source was present about 13% of the specimens failed. In tests with type-1 specimens and an oxygen source, from UO_{2+x} and vacuum baked graphite mixture or oxygen gas, more specimens failed and increased specimen deflection was measured is specimens that did not fail. This was a result of the less favorable type-1 specimen texture, which is believed to produce a fast growing oxide layer over the Zircaloy surface in the presence of an oxygen source, but where this oxide is believed to be uneven with various growth planes [182] that does not afford good protection from I-SCC attack. This was supported from the increased iodine residence times in the glass ampoules (Figure 146) and from the post experiment specimen thickness measurements after exposure to iodine (Figure 148). The oxide build-up was visually observed in one experiment with an oxygen source, where the specimens were observed to have an initial shinny silvery metallic color that changed to a gold-yellow-brown color (Figure 147), indicating surface oxidation due to the presence the UO_{2+x} and graphite mixture.

The UO_{2+x} and graphite additive, providing an oxygen source as high as $(1.61\pm0.05)\times10^{-6}$ mol O_2 cm^{-2} of Zircaloy surface (or CO_2 equivalent), was more obvious to have affected the type-1 specimens with prism, pyramidal and basal plane texture, causing all the specimens to fail when exposured to 6.4±0.3 mg cm^{-2} iodine vapour at 350°C. When the iodine vapour was increased (28±1 mg cm^{-2}) the iodine reacted more quickly with the zirconium to form ZrI_x species (<0.8±0.2 hours). In this test specimen, failures did not occur, but increased surface corrosion at the specimen point of highest stress was measured. Surface peeling was also observed in some tests when the iodine content was ≥ 16 mg cm^{-2}, leading to further exposure of the zirconium and accelerated reaction with the iodine.

The oxygen gas additive was obvious with type-2 specimens when exposed to 22.1±0.3 to 35.5±0.7 mg cm^{-2} iodine (providing more protection to the specimens as shown by less specimen deflection). The hyperstoichiometric fuel with graphite additive may have also reduced corrosion in the type-2 specimens but more tests are needed to confirm this result. The seemingly opposite effect of the oxygen source additive (promoting SCC failures in type-1 specimens but providing protection in type-2 specimens) may be explained by work by Kim *et al.* [182] who showed that when the zirconium texture contains basal and prism planes in the transverse direction (as was demonstrated with XRD scans in the type-1 specimens in Section 5.3.2) there are two or more oxide growth planes present, causing rapid but discontinuous oxide growth. When the texture is basal dominated in the sheath transverse direction (or the basal normal is in the sheath radial direction, as was similarly demonstrated in XRD scan of type-2 specimens) there is only one oxide growth plane on which the oxide layer grows and grows more slowly. The latter texture type provides a thicker and more continuous ‘columnar’ oxide layer in zirconium oxide, which is more resistant to corrosion.

In Section 5.6 the fuel oxidation model was modified to superficially oxidize sintered fuel pellets (heated isothermally in a sintering furnace) as a mitigation approach to stress corrosion cracking in CANDU fuel. It is believed that the increased oxygen potential at the fuel periphery as hyperstoichiometric oxygen can be reduced by graphite (CANLUB internal sheath coating), which is in close-intimate contact with the fuel pellet after sheath creep-down and pellet thermal expansion. To achieve 2.469×10^{-5} moles of atomic hyperstoichiometric oxygen uptake in a single CANDU fuel pellet (this value was based on an initial target oxygen amount of 2×10^{-6} moles O_2 cm^{-2} of Zircaloy sheathing, given the explanation in Section 3.5.7 (Eq. (183)) and the experimental measurements in Section 5.5), a pellet was modeled in a 1250 °C and 1 atm steam flow in a 2D model. The resulting modeled oxygen stoichiometric deviation was shown in Figure 157 in Section 5.6 as a radial cross section of the sintered pellet after 100 s duration in the steam flow. As was seen the highest oxygen stoichiometric deviation achieved was Xdev = 1.6×10^{-3} at the fuel periphery. When this radial distribution of hyperstoichiometric oxygen was integrated over the volume of the pellet using Eq. (165), the result being plotted in Figure 158, the quantity of $\approx 2.5\times10^{-5}$ moles of atomic hyperstoichiometric oxygen uptake in a single CANDU fuel pellet was achieved after a 100 simulated seconds. This is approximately the target of oxygen amount intended for the repair of any damaged zirconium oxide on the internal surface of the Zircaloy sheath. A lower steam temperature could also have been modeled in order to slow the oxidation process, to suit the process design. It should also be mentioned that Xdev = 1.6×10^{-3} oxygen deviation may be a relatively low initial value to set on the fuel periphery (in future experimentation), since it is probably within fresh fuel oxygen deviation tolerance specifications such as O/U = $2.000\pm^{0.010}_{0.005}$[†]. In other words the fuel periphery could be intentionally oxidized (to Xdev = 0.010) while still being within the O/U specification tolerance requirements for the fuel. The O/U tolerance specifications in manufactured fuel provides additional support for the idea that CANLUB graphite acts as a reducing agent (as explained at the end of Section 1.4) for hyperstoichiometric oxygen, which in turn mitigates SCC in fuel sheathing.

It should be noted that not all the oxygen that oxidized the exposed zirconium of the type-1 and type-2 slotted ring specimens in experiments, involving hyperstoichiometric uranium dioxide and vacuum baked CANLUB graphite (which in turn affected SCC behavior in the experiments), necessarily originated from the hyperstoichiometric uranium dioxide. This is because the vacuum baked graphite itself has the ability to absorb and adsorb gases such as oxygen, and carbonaceous molecules as well as organic molecules, from exposure to the air or from CANLUB dilutants and binders. Graphite with its large surface area can store some of these gases. Hence, the graphite can potentially act as a modest reservoir for oxygen. Most of these molecules are thermally desorbed from the graphite at temperatures typical of fuel-to-sheath gap temperatures (≈350 °C). So in the current glass ampoule I-SCC experiments it can be expected that some of the oxygen or oxygen containing molecules came

---

[†] The exact technical specification of the oxygen deviation tolerances in CANDU fuel is not shown here due to information proprietary considerations, but is close to these values.

from the graphite. The same may also be happening in CANDU fuel elements. Absorbed and adsorbed oxygen and oxygen containing molecules on the graphite coating in CANDU fuel (introduced before sealing the fuel element) would be liberated once inserted into the reactor core. These liberated gases would oxidize the uranium dioxide fuel and the Zircaloy sheathing surface, affording some buildup and repair of the zirconium oxide on the latter. The suggested use of UO_{2+x} and graphite as mitigation approach for SCC would provide a larger reservoir of oxygen liberated in the fuel element over a greater amount of time after being put in the reactor (days and even weeks, even with the slow diffusion of hyperstoichiometric oxygen from the fuel periphery to the fuel centre as modeled in Figure 159), affording increased protection to the Zircaloy sheath surface when the corrodant concentration in the fuel-to-sheath gap becomes significant.

6.5 Limitations and Challenges of the Fuel Oxidation Model with Discrete Fuel Cracks and its Validation

At the time this thesis was being written the *out-reactor instrumented fuel oxidation experiment* and post experiment coulometric titration as well as X-ray diffraction measurements (that were used to determine the oxidation extent) were in the process of being conducted. Thus, the initial validation of the fuel oxidation model was not done directly in this thesis by specifically comparing the out-reactor experimental results with model results. Instead the validation was conducted indirectly by: (1) Comparing the FES1 commissioning test temperature measurements, which included heating an intact instrumented fuel element for a short duration in the loop (see Section 4.5.1) with a 2D r-θ steady-state out-reactor model that validated the model’s heat transfer correlations and with no fuel oxidation, and (2) Comparing PIE of an in-reactor defective fuel element XC9179Z-5 coulometric titration oxidation measurements with a 3D transient fuel oxidation model results (Section 4.5.2). Hence, the model validation work presented here is based on available measurements and experimental analysis that were completed to date and made available to the candidate. Further validation and benchmarking of the fuel oxidation model (in an out-reactor configuration) can be performed once post test measurements and analysis are complete and documented in a future COG report as a COG deliverable to industry.

The current fuel oxidation model with discrete fuel cracks (be it an in- or out-reactor reactor model configuration) has essentially the same governing equations as the previous fuel oxidation model [24] (with the exception of using flux terms rather than source terms in the solid state oxygen diffusion equation in the fuel and in the gas diffusion equation in the fuel cracks). Since these equations are based on experimental measurements up to temperatures of 2200 °C [24] and since defective fuel operating under normal operating conditions is unlikely to melt at its centre line [43], it is expected that the fuel oxidation model validated to date is representative of defective fuel during normal operating conditions. In accident conditions the fuel temperature can be substantially higher (due to dry out) leading to accelerated fuel oxidation rates, which may not be accurately captured in the current model. To improve the model's accuracy material properties such as fuel thermal conductivities, fuel specific heat, oxidation rates, and oxygen diffusion rates may need to be measured at tempertures >2200 K so that the model correlations cover these higher temperature conditions.

Another limitation of the current fuel oxidation model with discrete fuel cracks is that the root of the cracks was specifically positioned so as to be at a temperature of 1250 °C. This arbitrarily selected temperature was set to be the fuel effective elastic-to-plastic boundary (refer to Sections 1.5 and 3.2). This though is an over simplification, since this transition does not occur abruptly but over a range of temperatures (1200-1400 °C). With final validation of the out-reactor fuel oxidation model a more suitable crack root temperature (i.e., an effective crack root position) could be selected. An additional related limitation of the presented model is that the radial crack root position does not change with time, where in reality it would, especially in highly oxidized fuel. Lastly, the current model doe not consider the likely possibility that the plastic region of the fuel contains fuel cracks that have not yet healed (see the end of Section 3.2). In other words fuel sites in the defected/defective fuel element with increased fuel oxidation (in the fuel plastic regions) were not considered in the presented fuel oxidation models.

The main challenge of the 3D fuel oxidation model with discrete fuel cracks is the construction of the model. As shown in the numerical implementations detailed in Sections 3.5.5 and 3.5.6 and discussed at the end of Section 6.2, the construction of the 3D model involves detailed geometry building and assembly ground work using COMSOL's CAD tools, followed by incorporation of applicable physics and boundary conditions. The number or surfaces and domains in the current model with discrete fuel cracks compared to the previous model [24][29] that used a 'smeared crack' approach was much greater. Furthermore just as the geometry construction is more complex so is also the mesh construction. Both of these differences mean that a greater effort was required to set up the fuel oxidation model with discrete cracks.

6.6 Fuel Oxidation Model Applications

Once the current fuel oxidation model is validated using the results of the out-reactor instrumented defected fuel experiment the model can then be incorporated into fuel performance and licensing codes to assess operational safety margins. The current fuel oxidation model though would not be the sole input into these fuel performance codes, since this model was validated only for an out-reactor case (i.e., no radiation effects were considered in the validated out-reactor model as would otherwise be considered in an in-reactor case by applying the correction or contributing factors κ_{1d} κ_{1d} and κ_{4r} in the fuel thermal conductivity equation, refer to Eq. (35)). An accompanying in-reactor defected fuel experiment would provide the remaining validated fuel oxidation model input. Additionally, COMSOL® version 5.0 and above offers Application Builder software that allows the modeler to make simplified stand-alone model applications that can be provided to a client (such as the reactor regulator or operator) to run various cases of interest (such as linear powder, burnup, post defect residence time, and sheath defect size) without in-depth knowledge of the model.

The fully coupled fuel oxidation and the solid mechanics model, that includes thermally expanded fuel cracks and fuel and sheath contact (model results discussed in Section 4.4), demonstrated that this type of model is possible to build and solve in a 2D r-θ configuration. Such a model would be quite useful in simulating in-reactor high powered defective fuel elements in normal and possibly in accident conditions, where temperature distribution and hence crack number and geometry can change with time. The 2D r-θ model could be used to study this phenomenon while conserving computer resources.

Prior to the onset of a primary sheath defect (i.e., intact fuel), a stress corrosion cracking model of fuel sheathing (similar to that discussed in [177]), especially near fuel radial crack openings where sheath defects typically occur, could be coupled to a fission gas release model using the same model configuration as the 2D r-θ fuel oxidation model coupled with the solid mechanics model. In other words the chemistry part of SCC in fuel sheathing could be coupled with the solid mechanics physics of the sheath (sheath stress and strains induced by the thermally expanded fuel pellets and sheath creep down), thus providing a more realistic simulation to SCC. A mesoscale or mesoscopic physics scale model, to simulate SCC crack propagation at the micron length level, could be implemented as a coupled model (using the same model geometry) or as a separate coupled model (using separate model geometry).

CHAPTER 7 CONCLUSIONS

Conclusions involving the fuel oxidation model validated to an out-reactor instrumented defected fuel experiment

Generally two fuel oxidation models representing the *out-reactor instrumented defected fuel experiment* were analyzed: a 2D r-θ model and 3D model. The presented models used the discrete fuel cracks as paths for radial (and axial in the 3D model) gas diffusion transport. Also, in both models the hydrogen and hyperstoichiometric oxygen generation were provided by flux terms on common gas and solid domain boundaries in the modeled fuel, i.e., at the discrete radial fuel crack surfaces. The 2D r-θ model, which included modeling the fuel element sheath, provided an estimate of the radial temperature distribution. It also provided an overestimate for the fuel oxidation extent but required only modest computer resources. The 3D model required considerably more computer resources but provided a more realistic estimate of fuel oxidation in the out-reactor experiment. Given the possible applied electric heating powers and the expected duration of the FES2 final test it was predicted with the models that sufficient fuel oxidation would occur to be detectable in post test CT measurements. Also, it was predicted that the fuel temperature rise due to fuel oxidation would be relatively small if the test duration was two weeks or less, considering as well that the measurement would depend largely on the sensitivity of the thermocouples. Initial validation of the fuel oxidation was accomplished by comparing a 2D r-θ model temperature results to the FES1 commissioning test temperature measurements, and by comparing 3D in-reactor fuel oxidation model results to an actual defective fuel element oxidation measurements. Final validation of the fuel oxidation model will be conducted at CNL when all the post test measurements of the FES2 (the *out-reactor instrumented defected fuel experiment*) have been completed and analyzed.

The current fuel oxidation models in this thesis assumed discrete fuel cracks of a specific number and of specific dimensions. It was shown in the oxidation models that fuel geometry can have an effect on fuel oxidation. Hence to compliment the fuel oxidation model development, conditions for fuel crack propagation using the *J* integral and predictions of full length radial fuel crack geometry in thermally expanded UO_2 fuel were modeled in a plane strain 2D r-θ solid mechanics model.

Since thermally induced fuel cracking is an intrinsic component of fuel oxidation in defective fuel, a model coupling of the plane strain solid mechanics model (with thermally expanded fuel cracks) to the fuel oxidation model was included in this work as a 2D r-θ model. Solving the model with all physics fully coupled was shown to be possible but was computationally demanding.

Conclusions involving SCC experiments with sources of oxygen (UO_{2+x} and graphite or O_2) and the use of the fuel oxidation model to mitigate SCC

In this study, results from I-SCC tests with Zircaloy sheathing material showed that when Zircaloy-4 specimens had prism, pyramidal and basal plane texture in the sheath transverse direction (type-1 specimens) this led to some specimen failures (≈13%). However, when UO_{2+x} and graphite mixture additives were introduced in the tests the iodine residence time increased substantially and all the specimens failed (cracked in-two). This suggested that the increased thickness of the formed zirconium oxide layer, due to the UO_{2+x} and graphite mixture, prevented contact of the iodine corrodant to most of the zirconium below the oxide. This further suggested that a sufficient partial pressure of iodine for a minimum amount of time was needed to cause cracking (increased iodine residence time). Since the oxide layer formed in type-1 specimen texture was believed to have irregularities [182], increased specimen failures were observed. In tests with specimens that had mostly basal plane texture in the sheath transverse direction (type-2 specimens), none of the specimens failed but increased specimen deflections were measured. Specimen reduced thicknesses at points of highest stress also showed that external and possibly internal corrosion (crack initiation) may have taken place, since the theoretical specimen deflection was less than the actual measurement. The introduction of pure oxygen gas additive (leading to oxide layer build-up and repair) was shown to be an effective additive in protecting the Zircaloy specimens, even when the highest amount of iodine was used. When UO_{2+x} and graphite mixture additive was introduced there was a slight decrease in the average specimen deflection and a slight increase in iodine residence time, indicating this additive may also have surface oxide repairing properties on type-2 specimens (very similar to CANDU fuel sheathing) against iodine induced stress corrosion cracking.

Hyperstoichiometric fuel at low amounts in conjunction with the currently used CANLUB sheath coating, essentially graphite, may have mitigative properties against SCC in the CANDU fuel. A modified fuel oxidation model in 2D showed how to compute the time and temperature needed to add a specific amount of oxygen to the outside surface of a fuel pellet (in a steam oxidizing environment), without changing the overall fuel pellet oxygen stoichiometry. These conditions could then be applied to the final stage of fuel pellet manufacturing process. The change to fuel pellet design is relatively minimal and could be achieved at a low cost - potentially making CANDU fuel more resistant to SCC failures, and thus increasing the fuel’s operation safety margins, especially if higher fuel burnups are desired in the near future.

CHAPTER 8 RECOMENDATIONS

1) Based on the fuel oxidation model results discussed in Section 6.1, in order to validate the fuel oxidation model for higher oxidation levels, which would be confirmed by measuring fuel temperature and hence the changing fuel thermal conductivity due to oxidation, it is recommended to manufacture the FES fuel pellets and the iridium bar heater to closer radial dimensions. This is because as the gap between the fuel and the iridium bar heater is reduced there is a drop in the operating temperatures of the iridium bar heater (as discussed in Section 4.2.1). With a smaller initial gap between these two materials the heater operating lifespan can be extended, allowing increased fuel oxidation. Manufacturing the pellets to closer and tighter tolerances includes placing the thermocouple and thermocouple drill holes in the pellet with increased geometric precision. This will reduce the total thermocouple measurement uncertainty allowing for better detection of fuel oxidation. Also, better expressions for the iridium and Zircaloy electrical conductivities (Eq. (82) and Eq. (86)) may be needed, since these quantities determine the fuel temperature. These expressions should be determined with in-lab testing. Lastly, consideration should be given to utilizing a shorter fuel element simulator, such as a 24.1 cm length rather than a full length 48.2 cm fuel element, in order to maximize fuel oxidation.

2) One of the limitations in the 2D r-θ and 3D fuel oxidation models with discrete fuel cracks was that the position of the radial crack roots did not change with time. This could be corrected by including an Arbitrary Lagrangian Eulerian (ALE) moving mesh (or a deformed mesh method). In this manner the root of the crack could be made to shift position (to a shallower depth) as the temperature of the fuel increases due to fuel oxidation with deterioration of the fuel thermal conductivity, or by an increase in the fuel linear power. Another limitation that may need to be considered is that fuel crack healing takes a specific amount of time. In other words, the model may need to consider the probable situation where the radial fuel cracks initially penetrate right to the centre of the fuel pellet in the in-reactor fuel and to the iridium heater element in the out-reactor fuel, and then slowly heal to the

elastic-to-plastic transition boundary. During this time it is expected that the fuel element will experience accelerated fuel oxidation below the fuel elastic-to-plastic boundary.

3) The 2D r-θ plane strain solid mechanics model that was used to predict the fuel crack geometry and crack number can be improved by also considering fuel internal flaws (rather than just fuel surface flaws). Like in the current model the stress intensity factor could be computed using the J integral but this time at crack tips of internal fuel flaws. Fuel plasticity beneath the fuel elastic-to-plastic boundary could also be included allowing for a more realistic computation of the fuel stress and strain fields. As with the current model a steady state solver would be employed for the solution of this quasi-dynamic crack propagation model.

4) A similar model to the 2D r-θ plane strain solid mechanics model coupled with discrete cracks to the fuel oxidation model would be quite useful in simulating in-reactor high powered defective fuel elements in normal and possibly in accident conditions, where crack number and geometry can change.

5) In the I-SCC experimental results a strong link was found between sheath surface oxidation (from an oxygen source such as UO_{2+x} and graphite mixtures or pure oxygen gas additives) and susceptibility of the sheath specimens to I-SCC phenomenon. The former additive is applicable to CANDU fuel. Section 5.6 modeled how the fuel oxidation model could be modified and used to introduce a small and controlled amount of hyperstoichiometric oxygen to a fuel pellet surface applied in a modified pellet manufacturing process. This I-SCC mitigation approach should be investigated further with lab experimentation leading to in-reactor tests.

6) Fuel reduction in a steam environment occurs at a faster rate than fuel oxidation [94][95]. This is not reflected in the current model. It is recommended to modify the fuel reduction term (Eq. (23)) as discussed in [94][95] so that is better represents experimental data.

BIBLIOGRAPHY

[1] J.R. Lamarsh and A.J. Baratta, Introduction to Nuclear Engineering 3rd Ed., Prentice Hall 2001.

[2] Canadian Nuclear Association, https://cna.ca/technology/energy/, accessed May 3 2014.

[3] Ontario's Long Term Energy Plan, The Ontario Ministry of Energy, http://www.energy.gov.on.ca/en/ltep/, accessed Aug 14 2012.

[4] Jacques Leclercq, The Nuclear Age, Published by Le Chêne, 1986.

[5] CANDU reactor, http://en.wikipedia.org/wiki/CANDU_reactor, accessed Aug 2012.

[6] R.E. Sonntag and G.J. Van Wylen, Introduction to thermodynamics classical and statistical 3rd Ed., John Wiley and Sons 1991.

[7] S. Glasstone and A. Seasonske, Nuclear Reactor Engineering 3rd Ed., Van Nostrand Reinhold Company, New York 1981.

[8] A.C. Morreale, D.R. Novog and J.C. Luxat, "A strategy for intensive production of molybdenum-99 isotopes for nuclear medicine using CANDU reactors", *Applied Radiation and Isotopes*, 70(2012)p. 20-34.

[9] Risk-based life cycle management of engineering systems, Waterloo University, www.civil.uwaterloo.ca/watrisk/research.html, accessed Sep 3 2012.

[10] C.S. Rim, "Korean nuclear fuel program", *Journal of Nuclear Science and Technology*, 35, no. 7(1998)p. 467-472.

[11] A.K. Sengupta, R. Agarwal, H.S. Kamath, "Carbide Fuel", *Comprehensive Nuclear Materials*, 3(2012)p. 55-86.

[12] J. Zakova and J. Wallenius, "Fuel residence time in BWRs with nitride fuels", *Annals of Nuclear Energy* 47(2012)p. 182-191.

[13] D. LeBlanc, "Molten salt reactors: A new beginning for an old idea", *Nuclear Engineering and Design*, 240(2010)p. 1644-1656.

[14] J.J. Katz and Eugene Rabinowitch, The Chemistry of Uranium: The Element, its Binary and Related Compounds, Dover Publications Inc., New York, 1951.

[15] D.R. Olander, Fundamental Aspects of Nuclear Reactor Fuel Elements, University of California, Technical Information Center, Energy Research and Development Administration, 1976, US Department of Energy, Prepared for Publishing by HP, reprint from the University of Michigan Libraries Collection.

[16] G.C. Allen and P.A. Tempest, "The accommodation of oxygen clusters in hyperstoichiometric uranium dioxide and its effects on crystal structures", *Journal of Chemical Society, Dalton Transactions*, 12(1983)p. 2673-2677.

[17] H. Matzke, "Atomic transport properties in UO_2 and mixed oxides $(U,Pu)O_2$", *Journal of the Chemical Society, Faraday Transactions* 2 83(1987)p. 1121-1142.

[18] B.E. Schaner, "Metallographic determination of the UO_2-U_4O_9 phase diagram", *Journal of Nuclear Materials* 2 no.2(1960)p. 110-120.

[19] L. Lynds, W.A. Young, J.S. Mohl and G.G. Libowitz, X-ray and density study of nonstoichiometry in uranium oxides, A symposium on non-stoichiometric compounds,

American Chemical Society, Advances in Chemistry, Series 39, Washington, D.C. March 21-23, 1962, p. 58-65.

[20] John C. Kotz and Paul Treichel Jr., Chemistry & Chemical Reactivity 3rd Ed., Saunders College Sunburst Series 1996.

[21] C.W. Bale, P. Chartrand, S.A. Degterov, G. Eriksson, K. Hack, R. Ben Mahfoud, J. Melancon, A.D. Pelton and S, Petersen, “FactSage thermochemical software and databases”, Calphad, 26, No. 2 (2002) 189-228.

[22] E.C. Corcoran, Thermochemical Modeling of Advanced CANDU Reactor Fuel, PhD thesis, The Royal Military College of Canada, March 2009.

[23] Allen M. Alper, Phase diagrams – Material Science and Technology, Refractory Materials, Volume 1 – Theory, Principles and Techniques of Phase Diagrams, Academic Press, London, 1970.

[24] J.D. Higgs, Modelling Oxidation Behaviour in Operating Defective Nuclear Reactor Fuel Elements, PhD thesis, Royal Military College of Canada, January 2006.

[25] J.M. Prausnitz, Molecular Thermodynamics of Fluid-Phase Equilibria, Prentice Hall, New Jersey, 1969.

[26] M.B. King, Phase Equilibrium in Mixtures, Pergamon Press, Oxford, 1969.

[27] J.M. Prausnitz, R.N. Litchtenthaler and E.G. de Azevedo, Molecular Thermodynamics of Fluid-Phase Equilibria 3rd Ed., Prentice Hall, New Jersey, 1999.

[28] J.C. Bailar, H.J. Emelóus, Sir Ronald Nyholm, A.F. Trotman-Dickenson, Comprehensive Inorganic Chemistry, Vol 5 Actinides, Pergamon Press, Oxford 1973.

[29] J.D. Higgs, B.J. Lewis, W.T. Thompson and Z. He, “A conceptual model for the fuel oxidation of defective fuel”, *Journal of Nuclear Materials*, 366(2007)p. 99-128.

[30] S.H. Shann and D.R. Olander, “Stress corrosion cracking of Zircaloy by cadmium, iodine and metal iodides”, *Journal of Nuclear Materials*, 113(1983)p. 234-248.

[31] C. Powers, P. Dewes-Erlangen, M. Billaux, R. Perkins, E. Ruzauskas, E. Armstrong, R. Ralph, G. Blomberg, G. Lysell, B. Cheng, Hot cell examination of PCI failures, Proc. Water React. Fuel Perf. Meet., Kyoto 2005.

[32] Review of Fuel Failures in Water Cooled Reactors, IAEA Technical Reports, IAEA No. TR-NF-T-2 1, Vienna 2010.

[33] P. Mishra, V.P. Jathar, J.L. Singh, D.N. Sah, P.K. Shah, S. Anantharaman, “In-reactor degradation of fuel and cladding in fuel pins operated with weld defects”, *Journal of Nuclear Materials* 439(2013)p. 217–223.

[34] J.A.L. Robertson, Learning from history: A case study in nuclear fuel, Zirconium in the nuclear industry: Eleventh International Symposium, ASTM STP 1295, E.R. Bradley and G.P. Sabol, Eds., American Society for Testing and Materials, 1996, p. 3-11.

[35] Ian Crossland, Nuclear Fuel Cycle Science and Engineering, Woodhead Publishing Series in Energy: Number 37, 2012.

[36] Kenneth D. Kok, Nuclear Engineering Handbook, CRC Press 2009.

[37] B.J. Lewis, F.C. Iglesias, D.S. Cox and E. Gheorghiu, “A model for fission gas release and fuel oxidation behaviour for defected UO_2 fuel elements”, *Nuclear Technology*, 92(1990)p. 353-362.

[38] B.J. Lewis, R.D. MacDonald, N.V. Ivanoff and F.C. Iglesias, “Fuel performance and fission product release studies for defected fuel elements”, *Nuclear Technology*, 103(1992)p. 220-232.

[39] L.A. Goldsmith and J.A.M. Douglas, “Measurements of the thermal conductivity of uranium dioxide at 670-1270 K”, *Journal of Nuclear Materials*, 47(1973)p. 31-42.

[40] P.G. Lucuta, Hj. Matzke, R.A. Verrall, “Thermal conductivity of hyperstoichiometric SIMFUEL”, *Journal of Nuclear Materials*, 223(1995)p. 51-60.

[41] D.R. Olander, Y.S. Kim, W. Wang and S.K. Yagnik, “Steam oxidation of fuel in defective LWR rods”, *Journal of Nuclear Materials*, 270(1999)p. 11-20.

[42] B.J. Lewis, B. Szpunar and F.C. Iglesias, “Fuel oxidation and thermal conductivity model for operating defective fuel rods”, *Journal of Nuclear Materials*, 306(2002)p. 30-43.

[43] B.J. Lewis, W.T. Thompson, F. Akbari, D.M. Thompson, C. Thurgood and J. Higgs, “Thermodynamic and kinetic modelling of the fuel oxidation behaviour in operating defective fuel”, *Journal of Nuclear Materials*, 328(2004)p. 180-196.

[44] K. Une, M. Imamura, M. Amaya and Y. Korei, “Fuel oxidation and irradiation behaviours of defective BWR fuel rods”, *Journal of Nuclear Materials*, 223(1995)p. 40-50.

[45] D.R. Olander, “Oxidation of UO_2 by High-Pressure Steam”, *Nuclear Technology*, 74 (1986)p. 215-217.

[46] H. Matzke, “Gas release mechanisms in UO_2 - A critical review”, *Radiation Effects*, 53(1980)p. 219-242.

[47] B. Cox, “Stress corrosion cracking of zirconium alloys”, *American Chemical Society* 3(1987)p. 867-873.

[48] A. Viktorov and M. Couture, Regulatory Activities in the Area of Fuel Safety and Performance, Fuelling A Clean Future, 9th International CNS Conference on CANDU Fuel, Location, 2005 September p. 18-21.

[49] P.E. Macdonald and R.H. Smith, “An empirical model of the effects of pellet cracking on the thermal conductivity of UO_2 light water reactor fuel”, *Nuclear Engineering and Design* 61(1980)p. 163-177.

[50] F.R. Campbell, L.R. Bourque, R. DesHaies, H. Sills and M.J.F. Notley, In-reactor measurement of fuel-to-sheath heat transfer coefficient between UO_2 and stainless steal, AECL-5400, Chalk River Laboratories May 1977.

[51] W. Hüttig, H. Enker and M. Forberg, “In-Core surveillance of defective PWR fuel elements in the case of fuel-to-water contact”, *Journal of Nuclear Materials*, 175 (1990)p. 147-157.

[52] J. Karlsson, G. Lysell, H. Pettersson and G. Rönnberg, In-pile testing of liner cladding and pellet performance in failed fuel rods, Proceedings of the 2004 International Meeting on LWR Fuel Performance, paper 1046, Orlando, Florida, September 19-22 2004, p. 377-383.

[53] M. Limbäck, M. Dahlbäck, L. Hallstadius, P.M. Dalene, H. Devold, C. Vitanza, W. Wiesennack, H. Jenssen, B.C. Oberländer, I. Matsson and T. Andersson, Test-reactor study of the phenomena involved in secondary fuel degradation, Paper 1045,

Proceedings of the 2004 International Meeting on LWR Fuel Performance, Orlando, Florida, September 19-22 2004, p. 54-68.

[54] B. Cheng, B.C. Oberländer, W. Weisenack, S. Yagnik and J. Turnbull, An in-reactor simulation test to evaluate root cause of secondary degradation of defective BWR fuel rod, Zirconium in the nuclear industry: 13th International Symposium, ASTM STP 1423(2002)p. 616-633.

[55] B. Cox, "Pellet-clad interaction (PCI) failures of zirconium alloy fuel cladding - A review", *Journal of Nuclear Materials,* 172(1990)p. 249-292.

[56] J.C. Wood, D.G. Hardy and A.S. Bain, Power ramping performance of water reactor fuel, AECL-6676, August 1979.

[57] J.C. Wood, B.A. Surette and I. Aitchison, "Pellet cladding interaction - Evaluation of lubrication by graphite", *Journal of Nuclear Materials,* 88 (1980)p. 81-94.

[58] D.G. Hardy, A.S. Bain and R.R. Meadowcroft, Performance of CANDU development fuel in the NRU reactor loops, AECL-5785, 1977.

[59] P.K. Chan, K.G. Irving and J.R. Mitchell, "The role of Zr_xI_yC compounds in minimizing stress corrosion cracking in fuel cladding", 3rd International Conference on CANDU Fuel Performance, 7-24/7-40, 1992.

[60] Katsumi Une, "Stress corrosion cracking of Zircaloy-2 cladding in iodine vapor", *Journal of Nuclear Science and Technology* 14(6)(1977)p. 443-451.

[61] P.S. Sidky, "Iodine stress corrosion cracking of Zircaloy reactor cladding: iodine chemistry (a review)", *Journal of Nuclear Materials,* 256(1998)p. 1-17.

[62] T. Yang and C. Tsai, "On the susceptibility to stress corrosion cracking of zircaloy in an iodine containing environment", *Journal of Nuclear Materials*, 166(1989)p. 252-264.

[63] X. Ma, C. Toffolon-Masclet, T. Guilbert, D. Hamon, J.C. Brachet, "Oxidation kinetics and oxygen diffusion in low-tin Zircaloy-4 up to 1523 K", *Journal of Nuclear Materials*, 377(2008)p. 359-369.

[64] I.G. Ritchie and A. Atrens, "The diffusion of oxygen in alpha-zirconium", *Journal of Nuclear Materials,* 67(1977)p. 254-264.

[65] N. Lakshmi, H.-I. Yoo and M. Martin, "Oxidation kinetics of zirconium examined by in situ X-ray diffraction", *Journal of the Electrochemical Society,* 160,3,(2013)p. C136-C141.

[66] E.A. Schaefer and J.O. Hibbits, "Determination of oxygen-to-uranium ratios in hypo- and hyperstoichiometric uranium dioxide and tungsten-uranium diode", *Analytical Chemistry* 41(1969)p. 254-259.

[67] Hj. Matzke, "Oxygen potential measurements in high burnup LWR UO_2 fuel", *Journal of Nuclear Materials* 223(1995)p. 1-5.

[68] S. Nicoll, Hj. Matzke, R.W. Grimes, C.R.A Catlow, "The behaviour of single atoms of molybdenum in urania", *Journal of Nuclear Materials* 240(1997)p. 185-195.

[69] J.J. Lawrence and D.J. O'Connar, "Some studies of gas evolution from graphite and uraniummoxide/graphite compacts at temperatures up to 1250 °C", *Journal of Nuclear Materials,* 4, No. 1(1961)p. 79-89.

[70] F.R. Campbell, Interaction between graphite and UO_2 in operating nuclear fuel elements, Chalk River Laboratories AECL-5301, 1976.

[71] COMSOL Multiphysics home page, www.comsol.com, accessed Sep 2009-Nov 2015.

[72] R.F. Canon, J.T.A. Roberts and R.J. Beals, “Deformation of UO_2 at high temperature”, *American Ceramic Society* 54(1971)p. 105-112.

[73] M. Oguma, “Cracking and relocation behaviour of nuclear fuel pellets during rise to power”, *Nuclear Engineering and Design*, 76(1983)p. 35-45.

[74] J.H. Gittus, “Theoretical analysis of the strains produced in nuclear fuel cladding tubes by expansion of cracked cylindrical fuel pellets”, *Nuclear Engineering and Design* 18(1972)p. 69-82.

[75] D. Olander, “Nuclear fuels – present and future”, *Journal of Nuclear Materials*, 389 (2009)p. 1-22.

[76] R.E. Williford, “A cracked constitutive equation”, *Nuclear Technology* 67(1984)p. 208-220.

[77] K. Shaheen, A.D. Quastel, J.S. Bell, B.J. Lewis, W.T. Thompson and E.C. Corcoran, “Modelling CANDU fuel element and bundle behavior for in- and out-reactor performance of intact and defective fuel”, 11th International Conference on CANDU Fuel, Sheraton Fallsview Hotel Conference Centre, Ont. Canada Oct 17-20 2010.

[78] O. Dahlblom and N.S. Ottosen, “Smeared crack analysis using a generalized fictitious crack model”, *Journal of Engineering Mechanics*, 116(1990)p. 55-76.

[79] T.L. Anderson, Fracture Mechanics Fundamentals and Applications, 3rd Ed., Taylor and Francis Group, 2005.

[80] R.A. Verrall, Z. He and J. Mouris, “Characterization of Fuel Oxidation in Rods with Clad-Holes”, *Journal of Nuclear Materials*, 344 (2005)p. 240-245.

[81] Z. He, R. Verrall, J. Mouris and C. Buchannan, “Characterization of Fuel Pellet Oxidation in Defected Fuel Elements Using O/U Ratio Measurements and Optical Microscopy”, COG-03-2011, 2002 December.

[82] F. Abbasian, Test procedure for out-reactor instrumented defected fuel experiment, Stern Laboratories, SLTP-195 Rev. 1, October 2012.

[83] P. Villars, editor-in-chief, H. Okamoto and K. Cenzual, section editors, ASM Alloy Phase Diagram Center, ASM International, Materials Park, OH, USA, www.1asminternational.org/AsmEnterprise/APD, accessed Feb 6 2013.

[84] J. Mastroianni, Out-Reactor Instrumented Defected Fuel Experiment Internal Assembly drawing provided by Farzin Abbasian at Stern Labs, July 11 2012.

[85] Personal email communication, F. Abbasian of Stern Labs to A.D. Quastel, Sep 6 2011.

[86] F. Abbasian, E. Ritchie and A. Shanahan, Out-reactor instrumented defected fuel experiment, COG WP-22331, March 2011.

[87] C. Thiriet, E. Corcoran, A. Quastel, B. Lewis, G. Hadaller, Test Plan for Out-Reactor Instrumented Defected Fuel Experiment, OP-09-2043, AECL 153-124520-COG-001, Aug 2009.

[88] Z. He and J. Mouris, Oxidation characterization of fuel pellets from defected DNGS element XC9179Z-5, COG TN-05-2002, Jul 2005.

[89] V.A. Alekseyev, L.A. Anan’yeva, and R.P. Rafal’skiy, “Effects of composition on lattice parameter of UO_{2+x}”, *Geology Review* 23(no.19)(1979)p. 1229-1235.

[90] Y. Sumi, L.M. Keer and S. Nemat-Nasser, “Thermally induced radial cracking in fuel element pellets”, *Journal of Nuclear Materials* 96(1981)p. 147-159.

[91] C. Bernaudat, “Mechanical behaviour modelling of fractured nuclear fuel pellets”, *Nuclear Engineering and Design*, 156(1995)p. 373-381.

[92] M. Imamura and K. Une, “High temperature steam oxidation of UO2 fuel pellets”, *Journal of Nuclear Materials*, 247(1997)p. 131-137.

[93] D.W. Oxtoby and N.H. Nachtrieb, Principles of Modern Chemistry, Saunders College Publishing, New York, 1986.

[94] B.J. Lewis, W.T. Thompson, J. Higgs, F. Akbari, and M.H. Kaye, Fuel oxidation model for defective fuel, COG-05-2095 (WP22324), Jul 2006.

[95] B.J. Lewis *et al*., State-of-the-Art Report on Multi-scale Modelling of Nuclear Fuels, Nuclear Science, NEA/NSC/R/(2015)5, www.oecd-nea.org, September 2015.

[96] Lennart Råde and Bertil Westergren, Mathematics Handbook for Science and Engineering, Studentlitteratur, Lund, 2008.

[97] P.G. Lucuta, Hj. Matzke and I.J. Hastings, “A pragmatic approach to modelling thermal conductivity of irradiated UO_2 fuel”: review and recommendations, *Journal of Nuclear Materials* 232 (1996)p.166-180.

[98] W.E. Ellis, J.D. Porter, T.L. Shaw, The Effect of Oxidation, Burnup and Poisoning on the Thermal Conductivity of UO_2: A Comparison of Data with Theory, in: Proc. International Topical Meeting on Light Water Reactor Fuel Performance, Park City, Utah, April 10–13, 2000, p. 715.

[99] D.G. Martin, “The thermal expansion of solid UO_2 and (U, Pu) mixed oxides - A review and recommendations”, *Journal of Nuclear Materials*, 152(1988)p. 94-101.

[100] J.J. Carbajo, G.L. Yoder, S.G. Popov and V.K. Ivanov, “A review of the thermophysical properties of MOX and UO_2 fuel”, *Journal of Nuclear Materials*, 299(2001)p. 188-198.

[101] Su Chieng Shu Faya, A survey on fuel pellet cracking and healing phenomena in reactor operation, Centro De Engenharia Nuclear - CEN, San Paulo, Brazil, October 1981.

[102] J.B. Ainscough and F. Rigby, “Measurements of crack sintering rates in UO_2 pellets”, *Journal of Nuclear Materials* 47(1973)p. 246-250.

[103] K. Shaheen, A Semi-Empirical Oxidation Model for Defective Nuclear Fuel, M.A.Sc. thesis, Royal Military College of Canada, 2007.

[104] U. Grigull, J. Straub and Peter Schiebener, Steam Tables in SI-units Wasserdampftafeln 3rd Ed., Springer-Verlag 1990.

[105] L. Haar, J.S. Gallagher and G.S. Kell, NBS/NRC Steam Tables: Thermodynamic and Transport and Computer Programs for Vapor and Liquid States of Water in SI units, McGraw Hill 1984.

[106] J.P. Holman, Heat Transfer in SI Units, 7th Ed., McGraw-Hill, 1990.

[107] Y.M Savitskii, Handbook of Precious Metals, Hemisphere Pub, November 1989.

[108] PGM Database, Johnson Matthey Public Limited Company, http://www.pgmdatabase.com/jmpgm/index.jsp, accessed August 12 2012.

[109] D.R. Lide Editor-in-Chief, CRC Handbook of Chemistry and Physics, 77th Ed., CRC Press, 1996.

[110] SCDAP/RELAP5 Development Team, Mode3.2 Code Manual, Volume IV:MATPRO, A library of materials properties for light water reactor accident analysis, Idaho National Engineering and Environmental Laboratory, Idaho, 1997.
[111] Standard Specification for: Hot-Rolled and Cold-Finished Zirconium and Zirconium Alloy Bars, Rod, and Wire for Nuclear Applications, ASTM B351/B351M-13.
[112] A. Chopelas, "Thermal Expansion, heat capacity, and entropy of MgO at mantle pressures", *Physics and Chemistry of Minerals* 17(1990)p. 142-148.
[113] J.C. Bailar, H.J. Emelóus, Sir Ronald Nyholm, A.F. Trotman-Dickenson, Comprehensive Inorganic Chemistry, Vol 1, Pergamon Press, Oxford 1973.
[114] J.C. Bailar, Jr. Therald Moeller, Jacob Kleinberg, Cyrus O. Guss, Mary E. Castellion and Clyde Metz, Chemistry, Academic Press, 1989.
[115] W.B.J. Zimmerman, Multiphysics Modelling with Finite Element Methods, World Scientific Publishing Co. Pte. Ltd., London, 2006.
[116] Nuclear Engineering International, www.neimagazine.com, September 2010.
[117] Ferdinand P. Beer and E. Russell Johnson, Jr., Mechanics of Materials 2nd Ed., McGraw Hill Inc., 1992.
[118] J.E. Talia and F. Povolo, "Tensile properties of Zircaloy-4", *Journal of Nuclear Materials* 67(1977)p. 198-206.
[119] I.D. Peggs and D.P. Godin, "The yield strength - hot hardness relationship of Zircaloy-4", *Journal of Nuclear Materials* 57(1975)p. 246-248.
[120] K.M. Lee, M.Y. Ohn, H.S. Lim, J.H. Choi and S.T. Hwang, "Study on models for gap conductance between fuel and sheath for CANDU reactors", *Annals of Nuclear Energy* 22(1995)p. 601-610.
[121] UK Steam Tables in SI Units 1970, United Kingdom Committee on the Properties of Steam, Edward Arnold (Publishers) Ltd., London 1970.
[122] Tamas I. Gombosi, Gaskinetic Theory, Cambridge University Press 1994.
[123] Carl Nording and Jonny Österman, Physics Handbook for Science and Engineering, Studentlitteratur, 2006.
[124] E.G. Price, "Thermal conductivity, electrical resistivity, and specific heat of CANDU constructional zirconium alloys and AISI type 403 end fitting", TDVI-368, AECL-Sheridan Park Research Community, November 1980.
[125] M. Benedict, T.H. Pigford and H.W. Hans, Nuclear Chemical Engineering, McGraw-Hill, 1981.
[126] F. Abbasian, E. Ritchie and A. Shanahan, Out-reactor instrumented fuel experiment design, Stern Labs, COG WP-22331, March 2011.
[127] B. Schulz (Rudolf Keim Editor), Electrical and Magnetic Properties, U-Uranium, Supplement Volume C5 Uranium Dioxide UO_2, Gmelin Handbook of Inorganic and Organometallic Chemistry - 8th edition, Volume U/A-E/C/5 1986.
[128] D.E. Johnson, J.L. Hilburn, J.R. Johnson, Basic Electric Circuit Analysis, Prenstice-Hall, New Jersey 1978.
[129] Structural Mechanics Module User's Guide, COMSOL Multiphysics, Version 4.2a.
[130] A.F. Bower, Applied Mechanics of Solids, CRC Press Taylor and Francis Group, Boca Raton, Florida, USA 2010.

[131] B. Hari, S. Bakalis and P. Fryer, Computational modeling and simulation of the human duodenum, Excerpt from the Proceedings of the 2012 COMSOL Conference in Milan, www.comsol.com/papers/13008, accessed Dec 13 2012.

[132] G.L. Narasaiah, Finite Element Analysis, CRC Press LLC, Boca Raton, Florida, USA 2009.

[133] William D. Callister, Material Science and Engineering, An Introduction, 4th Ed., John Wiley & Sons 1997.

[134] T. Tachibana, H. Furuya and M. Koizumi, "Dependence on strain rate and temperature shown by yield stress of uranium dioxide", *Journal of Nuclear Science and Technology* 13[9](1976)p. 497-502.

[135] T.R.G. Kutty, K.N. Chandrasekharan, J.P. Panakkal, J.K. Ghosh, "Fracture toughness and fracture surface energy of sintered uranium dioxide fuel pellets", *Journal of Materials Science Letters* 6(1987)p. 260-262.

[136] Rajan Tandon, Andrew Wereszczak and Edgar Lara-Curzio, Mechanical Properties and Performance of Engineering Ceramics and Composites II, Wiley and Sons Inc, New Jersey, 2007.

[137] C. Ganguly and R.N. Jayaraj, Characterization and Quality Control of Nuclear Fuel, Allied Publishers Pvt. Ltd., New Delhi, India, 2004.

[138] Robert D. Cook and Warren C. Young, Advanced Mechanics of Materials, 2nd Ed., Prentice Hall New Jersey 1999.

[139] M. Janssen, J. Zuidema and R.J.H. Wanhill, Fracture Mechanics 2nd Ed., Spon Press 2000.

[140] D.P. Rooke and D.J. Cartwright, Compendium of Stress Intensity Factors, Her Majesty's Stationary Office, The Hillington Press, London, 1976.

[141] T.Y. Kam and C.D. Lu, "Thermal stress fracture analysis of brittle bodies", *Engineering Fracture Mechanics* 32(1989)p. 827-832.

[142] X.R. Wu, Application of weight function method for crack analysis in thermal stress fields, G.A. Schneider and G. Petzow (editors), Proceedings of the NATO advanced research workshop on thermal shock and thermal fatigue behavior of advanced ceramics, Munich Germany, Nov 3-13(1992)p. 119-141.

[143] X.R. Wu, Stress intensity factors for circumferentially cracked hollow cylinder with thermal stresses, Proceedings of the international conference on fracture and fracture mechanics, Shanghai, April 21-24(1987)p. 638-642.

[144] J.R. Rice, "A path independent integral and the approximate analysis of strain concentration by notches and cracks", *Journal of Applied Mechanics Transactions,* ASME Series E, 35(2)(1968)p. 379-386.

[145] W.K. Wilson and I.W. Yu, "The use of the *J*-integral in thermal stress crack problems", *International Journal of Fracture*, Vol. 15, No. 4 August 1979, p. 377-387.

[146] S. Aoki, K. Kishimoto and M. Sakata, "Elastic-plastic analysis of crack in thermally-loaded structures", *Engineering Fracture Mechanics* 16(3)(1982)p. 405-413.

[147] R.A. Ainsworth, B.K. Neale and R.H. Prince, Fracture behaviour in the presence of thermal strains, Proc. Inst. Mech. Engng. Conf. on Tolerance of Flaws in Pressurized Components, pp. 197-204, London, May 1978.

[148] K. Kishimoto, S. Aoki and M. Sakata, “On the path independent integral-*J*”, *Engineering Fracture Mechanics* 13(1980)p. 841-850.

[149] MatWeb Material Property Data, on-line, http://www.matweb.com/search/QuickText.aspx?SearchText=zircaloy%204, accessed September 15 2012.

[150] E.B. Schwenk, K.R. Wheeler, G.D. Shearer and R.T. Webster, “Poisson's ratio in zircaloy-4 between 24° and 316°C”, *Journal of Nuclear Materials*, 78(1978)p. 129-131.

[151] C.L. Whitmarsh, Review of Zircaloy-2 and Zircaloy-4 properties relevant to N.S. Savannah reactor design, www.ornl.gov/info/reports/1962/3445605716311.pdf, accessed Jan 16 2013.

[152] Reactor Grade Zirconium Alloys for Nuclear Waste Disposal, Technical Data Sheet, www.atimetals.com/pages/default.aspx, accessed on Jan 16 2013.

[153] D.O. Hobson, The collapse behavior of Zircaloy fuel cladding, Metals and Ceramics Division, Oak Ridge National Laboratory, Oak Ridge Tennessee 37830, March 1976, accessed from DOE-OSTI: http://www.osti.gov/bridge/product.biblio.jsp?osti_id=7290923, Jan 16 2013.

[154] S.C. Chapra and R.P. Canale, Numerical Methods for Engineers 5th Ed., McGraw Hill International Edition 2006.

[155] K.H. Huebner, The Finite Element Method for Engineers, John Wiley and Sons, Toronto, 1975.

[156] S. Venit and W. Bishop, Elementary Linear Algebra, 4th Ed., Brooks/Cole Publishing Company, Pacific Grove, CA, 1996.

[157] D. Laux, B. Cros, G. Despaux and D. Baron, “Ultrasonic study of UO_2: effects of porocity and grain size on ultrasonic attenuation and velocities”, *Journal of Nuclear Materials* 300(2002)p. 192-197.

[158] K.W. Song, K.S. Kim, Y.M. Kim, K.W. Kang and Y.H. Jung, “Reduction of the open porosity of UO_2 pellets through pore structure control”, *Journal of Nuclear Materials*, 279(2000)p. 253-258.

[159] ‘What does degrees of freedom (DOFs) mean in COMSOL Multiphysics’, www.comsol.com/support/knowledgebase/875/, accessed Feb 20 2014.

[160] Frank M. White, Fluid Mechanics, 5th Ed., McGraw Hill, 2003.

[161] John C. Slattery, Momentum, energy and mass transfer in continua, Krieger Publishers, 1981.

[162] J.K. Fink, “Thermophysical properties of uranium dioxide”, *Journal of Nuclear Materials*, 279(2000)p. 1-18.

[163] Z. Zhu, L. Wang, B. Mohanty, C. Huang, “Stress intensity factor for a cracked specimen under compression”, *Engineering Fracture Mechanics* 73(2006)p. 482-489.

[164] Personal email correspondence with Farzin Abbasian of Stern Labs, Jul 11 2013.

[165] N.B. Vargaftik, Tables on the Thermalphysical Properties of Liquids and Gases in Normal and Dissociated States, 2nd Ed., Hemisphere Publishing Corporation, Washington, 1975.

[166] W.M. Haynes Editor-in-Chief, CRC Handbook of Chemistry and Physics, 92nd Ed., CRC Press 2011.

[167] Omega Engineering Technical Reference, site accessed: http://www.omega.ca/prodinfo/thermocouples.html, Feb 15 2015.

[168] Kurt Edsinger and K. Linga Murty, "LWR Pellet-Cladding Interactions: Materials Solutions to SCC", JOM *Journal of the Minerals and Materials Society*, July 2001, p. 9-13.

[169] L. Fournier, A. Serees, Q. Auzoux, D. Leboulch and G.S. Was, "Proton irradiation effect on microstructure, strain localization and iodine-induced stress corrosion cracking in Zircaloy-4", *Journal of Nuclear Materials* 384(2009)p. 38-47.

[170] K. Minato, "Thermodynamic analysis of cesium and iodine behavior in severe light water reactor accidents", *Journal of Nuclear Materials* 185(1991)p. 154-158.

[171] B. Cox, B.A. Surette and J.C. Wood, "Stress corrosion cracking of Zircaloys in unirradiated and irradiated CsI", *Journal of Nuclear Materials*, 138(1986)p. 89-98.

[172] P. Hofmann and J. Spino, "Conditions under which CsI can cause SCC failure of Zircaloy tubing", *Journal of Nuclear Materials*, 127(1985)p. 205-220.

[173] Gino. M.F. Bruni, Framework for sheath hydriding model for defective nuclear fuel, Masters thesis, Royal Military College of Canada, May 2010.

[174] Monika R. Kleczek, Thermodynamic and Kinetic Modelling of Iodine Induced Stress Corrosion Cracking in Nuclear Fuel Sheathing, Masters thesis, Royal Military College of Canada, April 2010.

[175] J.C. Wood, "Factors affecting stress corrosion cracking on Zircaloy in iodine vapor", *Journal of Nuclear Materials* 45(1972/73)p. 105-122.

[176] J.T.A. Jones, R.L. Jones, D. Cubicciotti, A.K. Miller, H.F. Wachob, E. Smith and F.L. Yaggee, A stress corrosion cracking model for pellet cladding interaction failures in light water reactor fuel rods, Zirconium in the Nuclear Industry (4th conference), ASTM STP 681, 1979, p. 285-305.

[177] B.J. Lewis, W.T. Thompson, M.R. Kleczek, K. Shaheen, M. Juhas and F.C. Iglesias, "Modeling of iodine-induced corrosion cracking in CANDU fuel", *Journal of Nuclear Materials*, 408 (2011)p. 209-223.

[178] R. Kaufmann, H. Klewe-Nebenius, H. Moers, G. Pfennig, H. Jennet and H.J. Ache, XPS "Studies of the Thermal Behaviour of passivated Zircaloy-4 surfaces", *Surface and Interface Analysis*, 11(1988)p. 502-509.

[179] Bernie A. Surette, private communication RMC to AECL-CRL, Sep 30 2012.

[180] T. Yoshida, T. Tanabe, Y. Okabe, T. Sawasaki and A. Chen, "Decomposition of CO_2 by metals during gamma irradiation", *Radiation Research* 164(2005)p. 332-335.

[181] D. Watanabe, T. Yoshida, C. Allen, T. Tanabe, "Enhancement of gamma-ray radiolysis of carbon dioxide with the assistance of solid materials", *Journal of Radioanalytical and Nuclear Chemistry* Vol. 272, No. 3(2007)p. 461-465.

[182] H.G. Kim, T.H. Kim and Y.H. Jeong, "Oxidation characteristics of basal (0002) plane and prism $(1,1,\bar{2},0)$ plane in HCP Zr", *Journal of Nuclear Materials*, 306(2002)p. 44-53.

[183] M. Peehs, H. Stehle and E. Steinberg, Out-of-pile testing of iodine stress corrosion cracking in Zircaloy tubing in relation to pellet-cladding interaction phenomenon, Zirconium in the Nuclear Industry 4th Conference, ASTM STP 681, Philadelphia, PA, 1979, p. 244-260.

[184] W.C. Yee and G.H. Jenks, “Fission fragments recoil effects on zirconium oxidation”, *Journal of the Electrochemical Society*, Vol. 109, No. 3 (March 1962)p. 198-204.

[185] J.H. Davies, E.V. Hoshi, D.L. Zimmerman, “Ramp test behavior of high O/U fuel”, *Journal of Nuclear Materials*, 270(1999)p. 87-95.

[186] G.A. McRae, C.E. Coleman and B.W. Leitch, “The first step for delayed hydride cracking in zirconium alloys”, *Journal of Nuclear Materials* 396(2010)p. 130-143.

[187] D.H. Locke, “The behavior of defective reactor fuel”, *Nuclear Engineering and Design* 21(1972)p. 318-330.

[188] Teledyne Wah Chang Albany, Zircaloy-4 plate ingot material analysis test report, provided by B.A Surette at AECL-CRL, 2011.

[189] E. Oberg, F.D. Jones, H.L. Norton and H.H. Ryffel, 27th Machinery's Handbook, Industrial Press Inc., New York, 2004.

[190] ATI Wah Chang, Reactor grade zirconium alloys for nuclear waste disposal, Technical data sheet, www.atimetals.com/pages/default.aspx, accessed Sep 1 2012.

[191] S.L. Chawla and R.K. Gupta, Materials Selection for Corrosion Control, ASM International, OH, USA, 1993.

[192] R. Holt, Nuclear Materials - Mech 483/883 class notes, Queens University, Kingston Ontario, Canada, 2008.

[193] G. Venkataramani, K. Kirane, and S Ghosh, “Microstructural parameters affecting creep induced load shedding in Ti-6242 by a size dependent crystal plasticity FE model”, *International Journal of Plasticity*, 24, Issue 3 (2008)p. 428-454.

[194] E. Tenckhoff, Deformation Mechanism, Texture and Anisotropy in Zirconium and Zircaloy, ASTM, STP-966, ASTM, 1988.

[195] K.L. Murty and I. Charit, “Texture development and anisotropic deformation in zircaloys (a review)”, *Progress in Nuclear Energy*, 48(2006)p. 325- 359.

[196] D. B. Knorr, J.M. Peltier and R.M. Pelloux, Influence of crystallographic texture and test temperature on the initiation and propagation of iodine stress-corrosion cracks in Zircaloy, Zirconium in the Nuclear Industry, 6th International Symposium, ASTM STP 824, 1984, p. 627-652.

[197] H.W. Wilson, K.K. Yoon and D.L. Baty, The effect of fuel rod design on SCC susceptibility, in Proceedings, American Nuclear Society Topical Meeting on Light Water Reactor Fuel Performance, Portland, Oregon 1979, p. 246-254.

[198] K.L. Murty and I. Charit, “Texture development and anisotropic deformation in Zircaloys, a review”, Progress in Nuclear Industry 48(2006)p. 325-359.

[199] C.S. Cook, G.P. Sabol, K.R. Sekera and S.N. Randall, Texture control in Zircaloy tubing through processing, Zirconium in the Nuclear Industry: Ninth International Symposium, ASTM STP 1132 (1991)p. 80-95.

[200] P.G. Partridge, “The crystallography and deformation modes of hexagonal close-packed metals”, *Metallurgical Reviews*, 12(1967)p. 169-194.

[201] I.A. Oding, V.V. Ivanova and V.N. Geminov, Creep and Stress Relaxation in Metals, Oliver and Boyd, Edinburgh, 1965.

[202] H.E. Rosinger, “The elastic properties of zirconium alloy fuel cladding and pressure tubing materials”, *Journal of Nuclear Materials*, 79(1979)p. 170-179.

[203] J.T. White and A.T. Nelson, “Thermal conductivity of UO_{2+x} and U_4O_{9-y}, *Journal of Nuclear Materials*, 443(2013)p. 342-350.

[204] S.Y. Park, J.H. Kim, M.H. Lee, Y.H. Jeong, “Effects of the microstructure and alloying elements on the iodine-induced stress-corrosion cracking behavior of nuclear fuel claddings”, Journal of Nuclear Materials, 376(2008)p. 98-107.

[205] S.B. Farina, G.S. Duffo, and J.R. Galvele, Stress corrosion cracking of hexagonal close-packed metals and alloys in solutions of iodine in methanol, Corrosion vol.61, no.6(2005)p. 847-855.

[206] S.B. Farina, G.S. Duffo, and J.R. Galvele, Stress corrosion cracking of zirconium and Zircaloy-4 in halide aqueous solution, Corrosion Science 45(2003)p. 2497-2512.

[207] Company literature, ‘Chapter 7: Basics of X-Ray Diffraction’, Scintag Inc., 10040 Bubb Road, Cupertino, CA 95014, USA, 1990.

[208] Private communication with Nelson Garcia, SETARAM Inc., Valley Business Park, 216 State highway 206, Suite 22, Hillsborough, NJ 08844, USA, May 29 2013.

APPENDIX A: The 2D *r*-θ Fuel Oxidation Model Report

The 2D *r*-θ fuel oxidation COMSOL 3.5a model

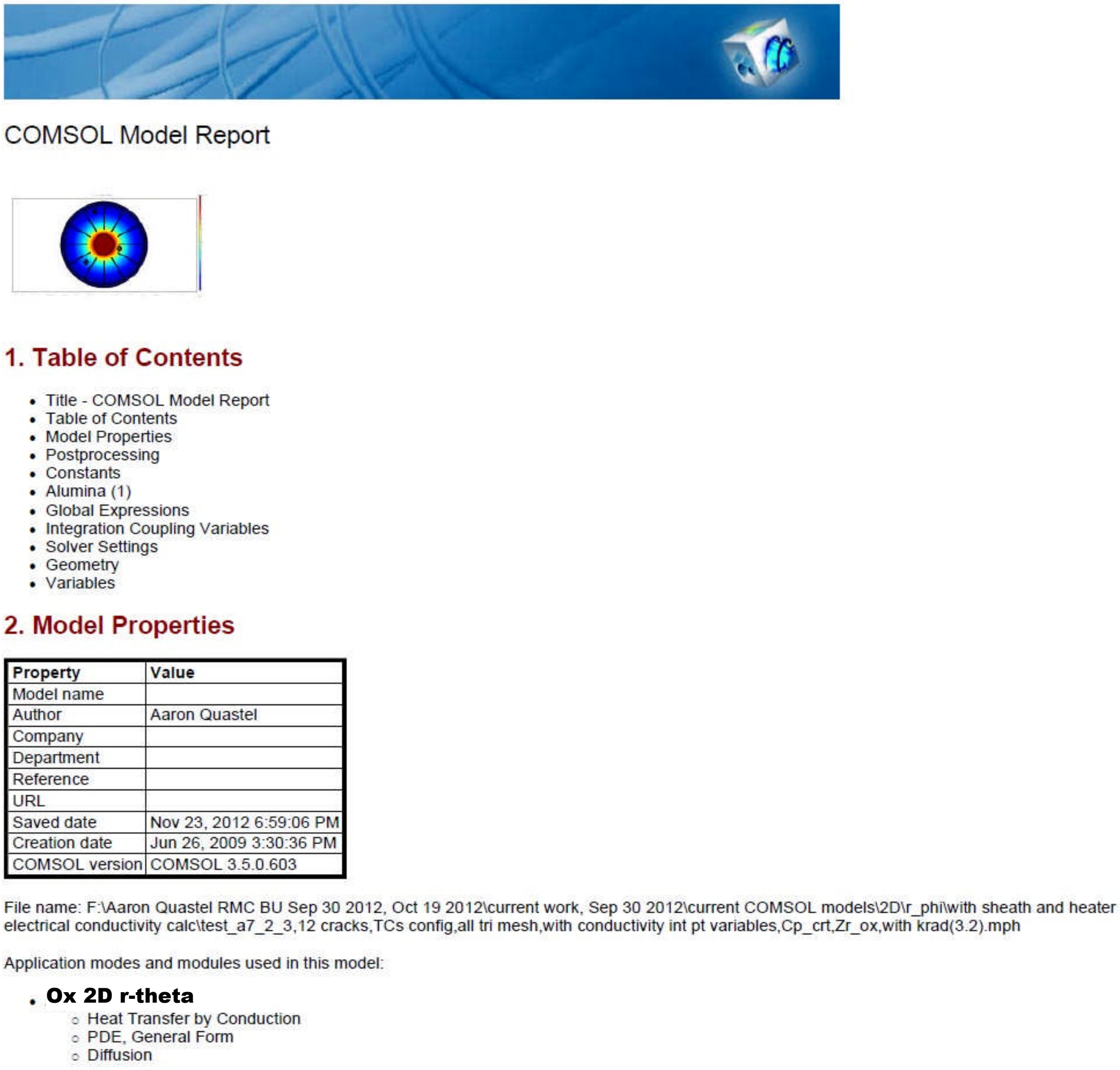

COMSOL Model Report

1. Table of Contents

2. Model Properties

Property	Value
Model name	
Author	Aaron Quastel
Company	
Department	
Reference	
URL	
Saved date	Nov 23, 2012 6:59:06 PM
Creation date	Jun 26, 2009 3:30:36 PM
COMSOL version	COMSOL 3.5.0.603

File name: F:\Aaron Quastel RMC BU Sep 30 2012, Oct 19 2012\current work, Sep 30 2012\current COMSOL models\2D\r_phi\with sheath and heater electrical conductivity calc\test_a7_2_3,12 cracks,TCs config,all tri mesh,with conductivity int pt variables,Cp_crt,Zr_ox,with krad(3.2).mph

Application modes and modules used in this model:

- **Ox 2D r-theta**
  - Heat Transfer by Conduction
  - PDE, General Form
  - Diffusion

2. Postprocessing

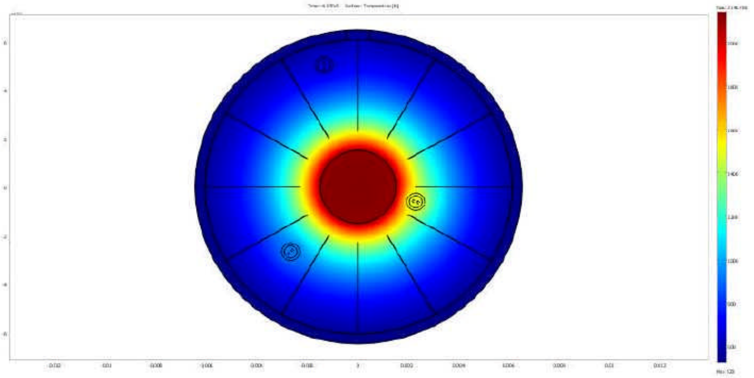

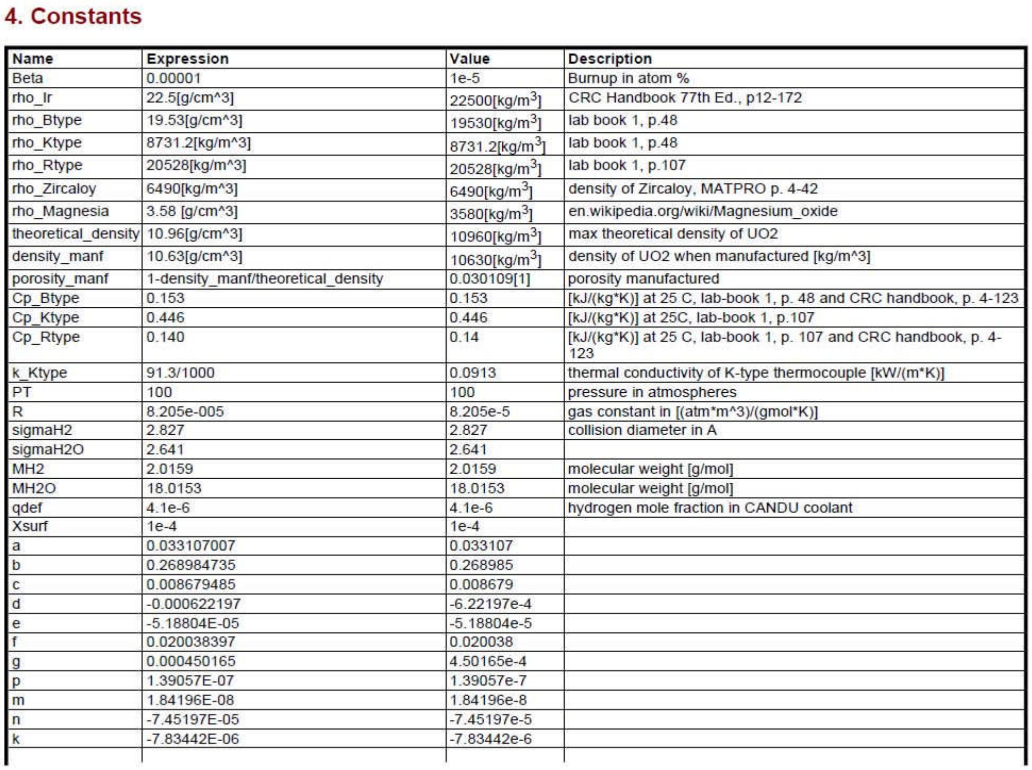

4. Constants

Name	Expression	Value	Description
Beta	0.00001	1e-5	Burnup in atom %
rho_Ir	22.5[g/cm^3]	22500[kg/m^3]	CRC Handbook 77th Ed., p12-172
rho_Btype	19.53[g/cm^3]	19530[kg/m^3]	lab book 1, p.48
rho_Ktype	8731.2[kg/m^3]	8731.2[kg/m^3]	lab book 1, p.48
rho_Rtype	20528[kg/m^3]	20528[kg/m^3]	lab book 1, p.107
rho_Zircaloy	6490[kg/m^3]	6490[kg/m^3]	density of Zircaloy, MATPRO p. 4-42
rho_Magnesia	3.58 [g/cm^3]	3580[kg/m^3]	en.wikipedia.org/wiki/Magnesium_oxide
theoretical_density	10.96[g/cm^3]	10960[kg/m^3]	max theoretical density of UO2
density_manf	10.63[g/cm^3]	10630[kg/m^3]	density of UO2 when manufactured [kg/m^3]
porosity_manf	1-density_manf/theoretical_density	0.030109[1]	porosity manufactured
Cp_Btype	0.153	0.153	[kJ/(kg*K)] at 25 C, lab-book 1, p. 48 and CRC handbook, p. 4-123
Cp_Ktype	0.446	0.446	[kJ/(kg*K)] at 25C, lab-book 1, p.107
Cp_Rtype	0.140	0.14	[kJ/(kg*K)] at 25 C, lab-book 1, p. 107 and CRC handbook, p. 4-123
k_Ktype	91.3/1000	0.0913	thermal conductivity of K-type thermocouple [kW/(m*K)]
PT	100	100	pressure in atmospheres
R	8.205e-005	8.205e-5	gas constant in [(atm*m^3)/(gmol*K)]
sigmaH2	2.827	2.827	collision diameter in A
sigmaH2O	2.641	2.641	
MH2	2.0159	2.0159	molecular weight [g/mol]
MH2O	18.0153	18.0153	molecular weight [g/mol]
qdef	4.1e-6	4.1e-6	hydrogen mole fraction in CANDU coolant
Xsurf	1e-4	1e-4	
a	0.033107007	0.033107	
b	0.268984735	0.268985	
c	0.008679485	0.008679	
d	-0.000622197	-6.22197e-4	
e	-5.18804E-05	-5.18804e-5	
f	0.020038397	0.020038	
g	0.000450165	4.50165e-4	
p	1.39057E-07	1.39057e-7	
m	1.84196E-08	1.84196e-8	
n	-7.45197E-05	-7.45197e-5	
k	-7.83442E-06	-7.83442e-6	

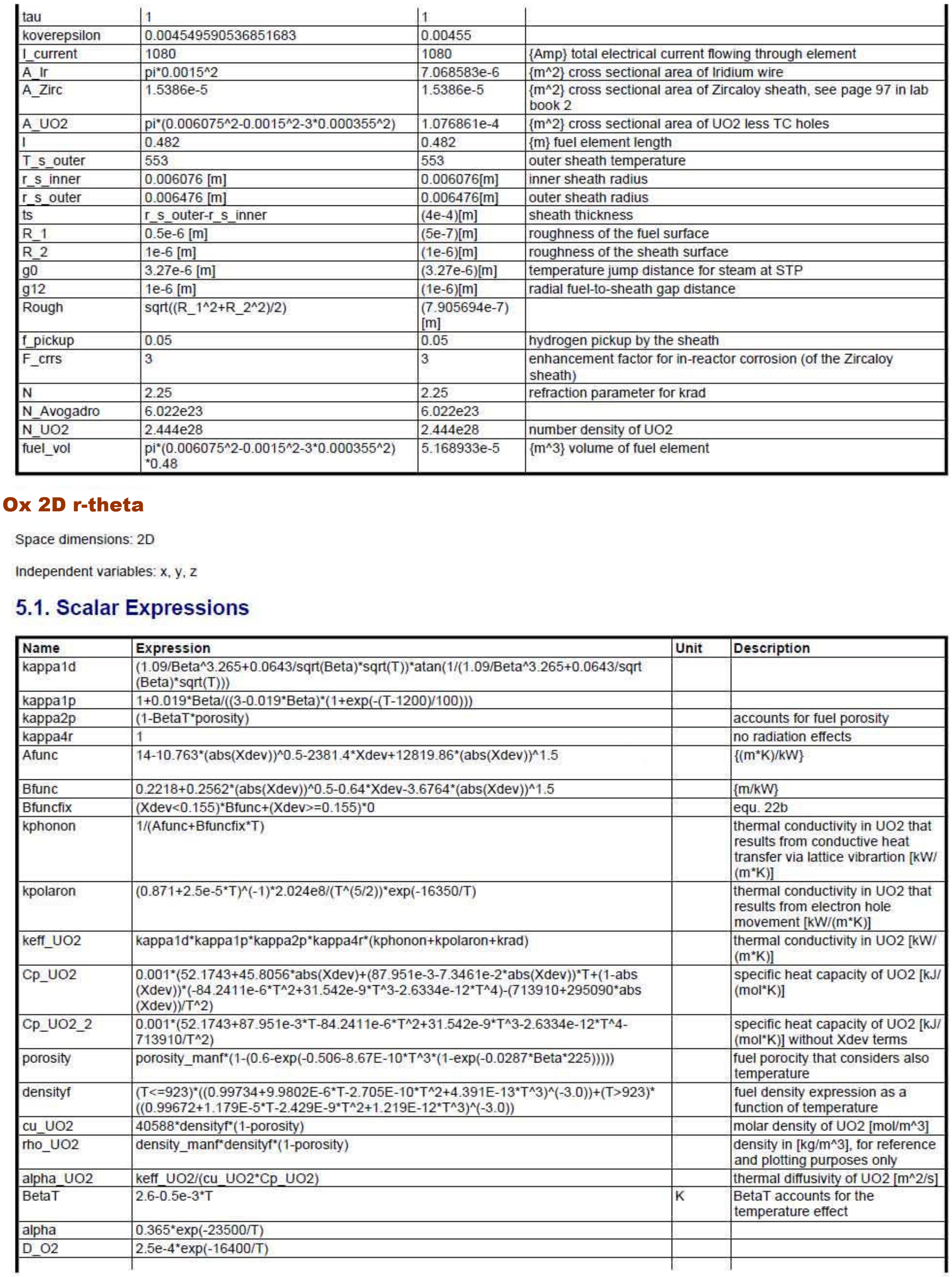

tau	1	1	
koverepsilon	0.004549590536851683	0.00455	
I_current	1080	1080	{Amp} total electrical current flowing through element
A_Ir	pi*0.0015^2	7.068583e-6	{m^2} cross sectional area of Iridium wire
A_Zirc	1.5386e-5	1.5386e-5	{m^2} cross sectional area of Zircaloy sheath, see page 97 in lab book 2
A_UO2	pi*(0.006075^2-0.0015^2-3*0.000355^2)	1.076861e-4	{m^2} cross sectional area of UO2 less TC holes
l	0.482	0.482	{m} fuel element length
T_s_outer	553	553	outer sheath temperature
r_s_inner	0.006076 [m]	0.006076[m]	inner sheath radius
r_s_outer	0.006476 [m]	0.006476[m]	outer sheath radius
ts	r_s_outer-r_s_inner	(4e-4)[m]	sheath thickness
R_1	0.5e-6 [m]	(5e-7)[m]	roughness of the fuel surface
R_2	1e-6 [m]	(1e-6)[m]	roughness of the sheath surface
g0	3.27e-6 [m]	(3.27e-6)[m]	temperature jump distance for steam at STP
g12	1e-6 [m]	(1e-6)[m]	radial fuel-to-sheath gap distance
Rough	sqrt((R_1^2+R_2^2)/2)	(7.905694e-7)[m]	
f_pickup	0.05	0.05	hydrogen pickup by the sheath
F_crrs	3	3	enhancement factor for in-reactor corrosion (of the Zircaloy sheath)
N	2.25	2.25	refraction parameter for krad
N_Avogadro	6.022e23	6.022e23	
N_UO2	2.444e28	2.444e28	number density of UO2
fuel_vol	pi*(0.006075^2-0.0015^2-3*0.000355^2)*0.48	5.168933e-5	{m^3} volume of fuel element

Ox 2D r-theta

Space dimensions: 2D

Independent variables: x, y, z

5.1. Scalar Expressions

Name	Expression	Unit	Description
kappa1d	(1.09/Beta^3.265+0.0643/sqrt(Beta)*sqrt(T))*atan(1/(1.09/Beta^3.265+0.0643/sqrt(Beta)*sqrt(T)))		
kappa1p	1+0.019*Beta/((3-0.019*Beta)*(1+exp(-(T-1200)/100)))		
kappa2p	(1-BetaT*porosity)		accounts for fuel porosity
kappa4r	1		no radiation effects
Afunc	14-10.763*(abs(Xdev))^0.5-2381.4*Xdev+12819.86*(abs(Xdev))^1.5		{(m*K)/kW}
Bfunc	0.2218+0.2562*(abs(Xdev))^0.5-0.64*Xdev-3.6764*(abs(Xdev))^1.5		{m/kW}
Bfuncfix	(Xdev<0.155)*Bfunc+(Xdev>=0.155)*0		equ. 22b
kphonon	1/(Afunc+Bfuncfix*T)		thermal conductivity in UO2 that results from conductive heat transfer via lattice vibrartion [kW/(m*K)]
kpolaron	(0.871+2.5e-5*T)^(-1)*2.024e8/(T^(5/2))*exp(-16350/T)		thermal conductivity in UO2 that results from electron hole movement [kW/(m*K)]
keff_UO2	kappa1d*kappa1p*kappa2p*kappa4r*(kphonon+kpolaron+krad)		thermal conductivity in UO2 [kW/(m*K)]
Cp_UO2	0.001*(52.1743+45.8056*abs(Xdev)+(87.951e-3-7.3461e-2*abs(Xdev))*T+(1-abs(Xdev))*(-84.2411e-6*T^2+31.542e-9*T^3-2.6334e-12*T^4)-(713910+295090*abs(Xdev))/T^2)		specific heat capacity of UO2 [kJ/(mol*K)]
Cp_UO2_2	0.001*(52.1743+87.951e-3*T-84.2411e-6*T^2+31.542e-9*T^3-2.6334e-12*T^4-713910/T^2)		specific heat capacity of UO2 [kJ/(mol*K)] without Xdev terms
porosity	porosity_manf*(1-(0.6-exp(-0.506-8.67E-10*T^3*(1-exp(-0.0287*Beta*225)))))		fuel porocity that considers also temperature
densityf	(T<=923)*((0.99734+9.9802E-6*T-2.705E-10*T^2+4.391E-13*T^3)^(-3.0))+(T>923)*((0.99672+1.179E-5*T-2.429E-9*T^2+1.219E-12*T^3)^(-3.0))		fuel density expression as a function of temperature
cu_UO2	40588*densityf*(1-porosity)		molar density of UO2 [mol/m^3]
rho_UO2	density_manf*densityf*(1-porosity)		density in [kg/m^3], for reference and plotting purposes only
alpha_UO2	keff_UO2/(cu_UO2*Cp_UO2)		thermal diffusivity of UO2 [m^2/s]
BetaT	2.6-0.5e-3*T	K	BetaT accounts for the temperature effect
alpha	0.365*exp(-23500/T)		
D_O2	2.5e-4*exp(-16400/T)		

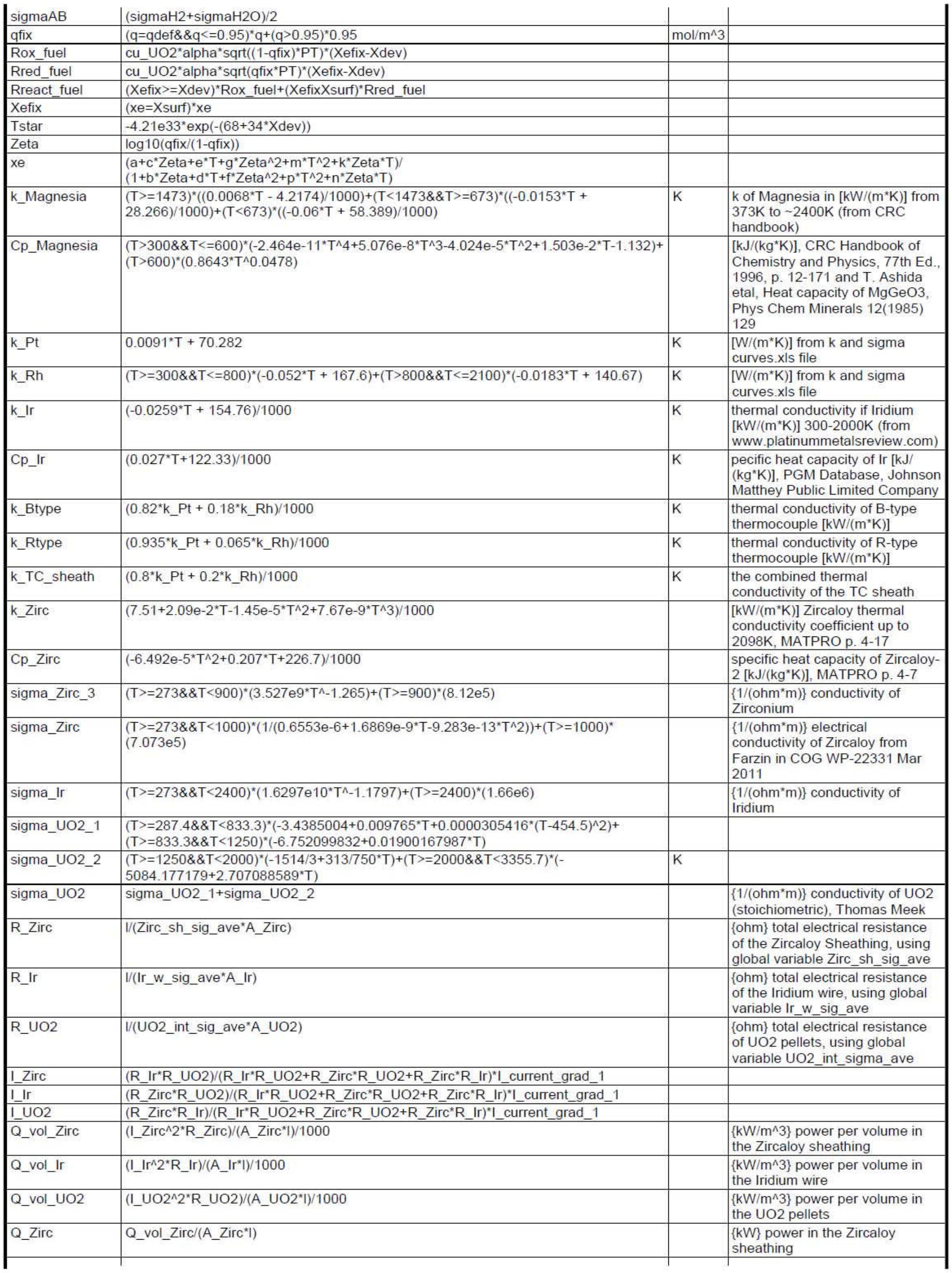

sigmaAB	(sigmaH2+sigmaH2O)/2		
qfix	(q=qdef&&q<=0.95)*q+(q>0.95)*0.95	mol/m^3	
Rox_fuel	cu_UO2*alpha*sqrt((1-qfix)*PT)*(Xefix-Xdev)		
Rred_fuel	cu_UO2*alpha*sqrt(qfix*PT)*(Xefix-Xdev)		
Rreact_fuel	(Xefix>=Xdev)*Rox_fuel+(XefixXsurf)*Rred_fuel		
Xefix	(xe=Xsurf)*xe		
Tstar	-4.21e33*exp(-(68+34*Xdev))		
Zeta	log10(qfix/(1-qfix))		
xe	(a+c*Zeta+e*T+g*Zeta^2+m*T^2+k*Zeta*T)/ (1+b*Zeta+d*T+f*Zeta^2+p*T^2+n*Zeta*T)		
k_Magnesia	(T>=1473)*((0.0068*T - 4.2174)/1000)+(T<1473&&T>=673)*((-0.0153*T + 28.266)/1000)+(T<673)*((-0.06*T + 58.389)/1000)	K	k of Magnesia in [kW/(m*K)] from 373K to ~2400K (from CRC handbook)
Cp_Magnesia	(T>300&&T<=600)*(-2.464e-11*T^4+5.076e-8*T^3-4.024e-5*T^2+1.503e-2*T-1.132)+ (T>600)*(0.8643*T^0.0478)		[kJ/(kg*K)], CRC Handbook of Chemistry and Physics, 77th Ed., 1996, p. 12-171 and T. Ashida etal, Heat capacity of MgGeO3, Phys Chem Minerals 12(1985) 129
k_Pt	0.0091*T + 70.282	K	[W/(m*K)] from k and sigma curves.xls file
k_Rh	(T>=300&&T<=800)*(-0.052*T + 167.6)+(T>800&&T<=2100)*(-0.0183*T + 140.67)	K	[W/(m*K)] from k and sigma curves.xls file
k_Ir	(-0.0259*T + 154.76)/1000	K	thermal conductivity if Iridium [kW/(m*K)] 300-2000K (from www.platinummetalsreview.com)
Cp_Ir	(0.027*T+122.33)/1000	K	pecific heat capacity of Ir [kJ/ (kg*K)], PGM Database, Johnson Matthey Public Limited Company
k_Btype	(0.82*k_Pt + 0.18*k_Rh)/1000	K	thermal conductivity of B-type thermocouple [kW/(m*K)]
k_Rtype	(0.935*k_Pt + 0.065*k_Rh)/1000	K	thermal conductivity of R-type thermocouple [kW/(m*K)]
k_TC_sheath	(0.8*k_Pt + 0.2*k_Rh)/1000	K	the combined thermal conductivity of the TC sheath
k_Zirc	(7.51+2.09e-2*T-1.45e-5*T^2+7.67e-9*T^3)/1000		[kW/(m*K)] Zircaloy thermal conductivity coefficient up to 2098K, MATPRO p. 4-17
Cp_Zirc	(-6.492e-5*T^2+0.207*T+226.7)/1000		specific heat capacity of Zircaloy-2 [kJ/(kg*K)], MATPRO p. 4-7
sigma_Zirc_3	(T>=273&&T<900)*(3.527e9*T^-1.265)+(T>=900)*(8.12e5)		{1/(ohm*m)} conductivity of Zirconium
sigma_Zirc	(T>=273&&T<1000)*(1/(0.6553e-6+1.6869e-9*T-9.283e-13*T^2))+(T>=1000)* (7.073e5)		{1/(ohm*m)} electrical conductivity of Zircaloy from Farzin in COG WP-22331 Mar 2011
sigma_Ir	(T>=273&&T<2400)*(1.6297e10*T^-1.1797)+(T>=2400)*(1.66e6)		{1/(ohm*m)} conductivity of Iridium
sigma_UO2_1	(T>=287.4&&T<833.3)*(-3.4385004+0.009765*T+0.0000305416*(T-454.5)^2)+ (T>=833.3&&T<1250)*(-6.752099832+0.01900167987*T)		
sigma_UO2_2	(T>=1250&&T<2000)*(-1514/3+313/750*T)+(T>=2000&&T<3355.7)*(-5084.177179+2.707088589*T)	K	
sigma_UO2	sigma_UO2_1+sigma_UO2_2		{1/(ohm*m)} conductivity of UO2 (stoichiometric), Thomas Meek
R_Zirc	l/(Zirc_sh_sig_ave*A_Zirc)		{ohm} total electrical resistance of the Zircaloy Sheathing, using global variable Zirc_sh_sig_ave
R_Ir	l/(Ir_w_sig_ave*A_Ir)		{ohm} total electrical resistance of the Iridium wire, using global variable Ir_w_sig_ave
R_UO2	l/(UO2_int_sig_ave*A_UO2)		{ohm} total electrical resistance of UO2 pellets, using global variable UO2_int_sigma_ave
I_Zirc	(R_Ir*R_UO2)/(R_Ir*R_UO2+R_Zirc*R_UO2+R_Zirc*R_Ir)*I_current_grad_1		
I_Ir	(R_Zirc*R_UO2)/(R_Ir*R_UO2+R_Zirc*R_UO2+R_Zirc*R_Ir)*I_current_grad_1		
I_UO2	(R_Zirc*R_Ir)/(R_Ir*R_UO2+R_Zirc*R_UO2+R_Zirc*R_Ir)*I_current_grad_1		
Q_vol_Zirc	(I_Zirc^2*R_Zirc)/(A_Zirc*l)/1000		{kW/m^3} power per volume in the Zircaloy sheathing
Q_vol_Ir	(I_Ir^2*R_Ir)/(A_Ir*l)/1000		{kW/m^3} power per volume in the Iridium wire
Q_vol_UO2	(I_UO2^2*R_UO2)/(A_UO2*l)/1000		{kW/m^3} power per volume in the UO2 pellets
Q_Zirc	Q_vol_Zirc/(A_Zirc*l)		{kW} power in the Zircaloy sheathing

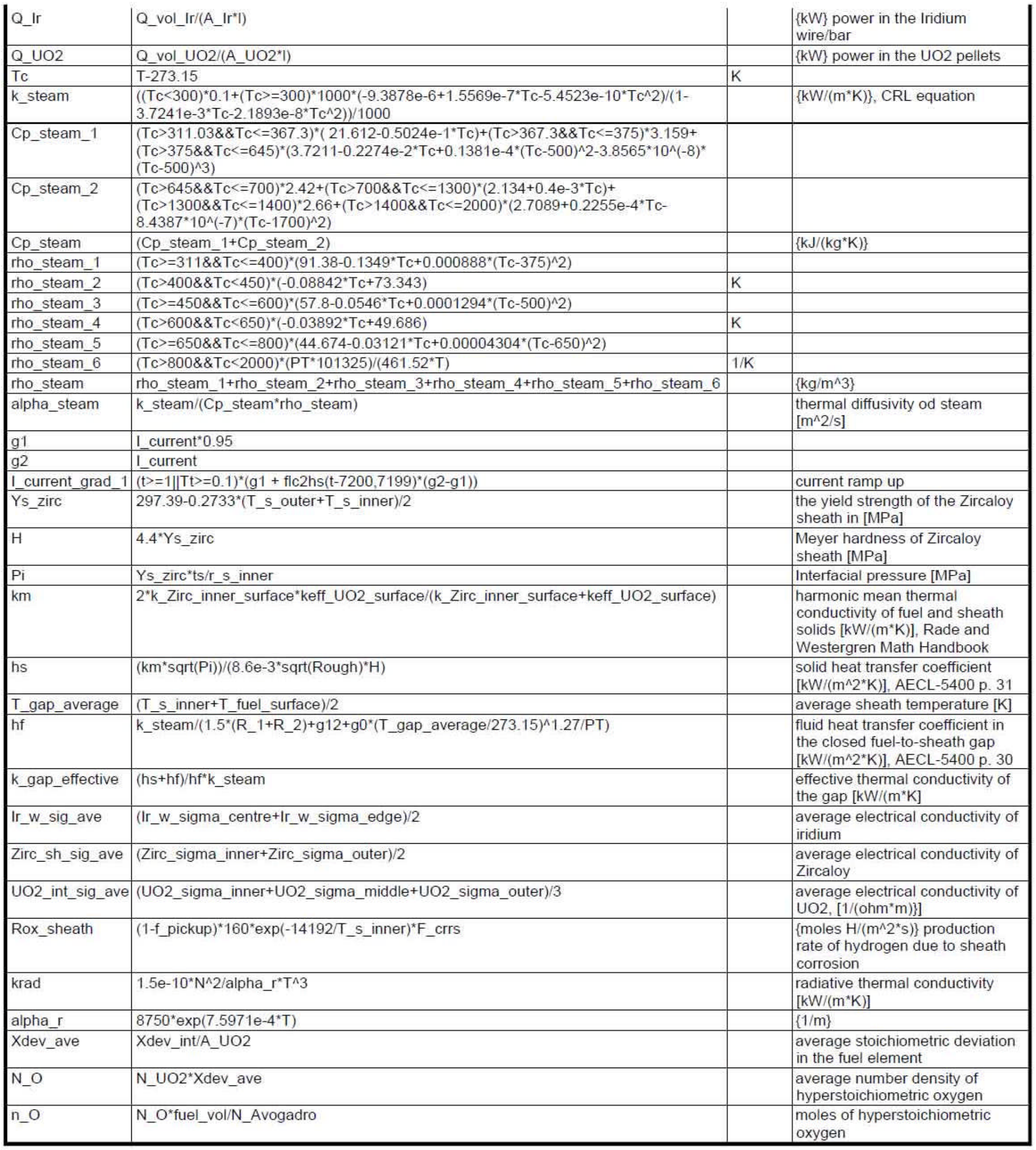

Q_Ir	Q_vol_Ir/(A_Ir*l)		{kW} power in the Iridium wire/bar
Q_UO2	Q_vol_UO2/(A_UO2*l)		{kW} power in the UO2 pellets
Tc	T-273.15	K	
k_steam	((Tc<300)*0.1+(Tc>=300)*1000*(-9.3878e-6+1.5569e-7*Tc-5.4523e-10*Tc^2)/(1-3.7241e-3*Tc-2.1893e-8*Tc^2))/1000		{kW/(m*K)}, CRL equation
Cp_steam_1	(Tc>311.03&&Tc<=367.3)*(21.612-0.5024e-1*Tc)+(Tc>367.3&&Tc<=375)*3.159+(Tc>375&&Tc<=645)*(3.7211-0.2274e-2*Tc+0.1381e-4*(Tc-500)^2-3.8565*10^(-8)*(Tc-500)^3)		
Cp_steam_2	(Tc>645&&Tc<=700)*2.42+(Tc>700&&Tc<=1300)*(2.134+0.4e-3*Tc)+(Tc>1300&&Tc<=1400)*2.66+(Tc>1400&&Tc<=2000)*(2.7089+0.2255e-4*Tc-8.4387*10^(-7)*(Tc-1700)^2)		
Cp_steam	(Cp_steam_1+Cp_steam_2)		{kJ/(kg*K)}
rho_steam_1	(Tc>=311&&Tc<=400)*(91.38-0.1349*Tc+0.000888*(Tc-375)^2)		
rho_steam_2	(Tc>400&&Tc<450)*(-0.08842*Tc+73.343)	K	
rho_steam_3	(Tc>=450&&Tc<=600)*(57.8-0.0546*Tc+0.0001294*(Tc-500)^2)		
rho_steam_4	(Tc>600&&Tc<650)*(-0.03892*Tc+49.686)	K	
rho_steam_5	(Tc>=650&&Tc<=800)*(44.674-0.03121*Tc+0.00004304*(Tc-650)^2)		
rho_steam_6	(Tc>800&&Tc<2000)*(PT*101325)/(461.52*T)	1/K	
rho_steam	rho_steam_1+rho_steam_2+rho_steam_3+rho_steam_4+rho_steam_5+rho_steam_6		{kg/m^3}
alpha_steam	k_steam/(Cp_steam*rho_steam)		thermal diffusivity od steam [m^2/s]
g1	I_current*0.95		
g2	I_current		
I_current_grad_1	(t>=1||Tt>=0.1)*(g1 + flc2hs(t-7200,7199)*(g2-g1))		current ramp up
Ys_zirc	297.39-0.2733*(T_s_outer+T_s_inner)/2		the yield strength of the Zircaloy sheath in [MPa]
H	4.4*Ys_zirc		Meyer hardness of Zircaloy sheath [MPa]
Pi	Ys_zirc*ts/r_s_inner		Interfacial pressure [MPa]
km	2*k_Zirc_inner_surface*keff_UO2_surface/(k_Zirc_inner_surface+keff_UO2_surface)		harmonic mean thermal conductivity of fuel and sheath solids [kW/(m*K)], Rade and Westergren Math Handbook
hs	(km*sqrt(Pi))/(8.6e-3*sqrt(Rough)*H)		solid heat transfer coefficient [kW/(m^2*K)], AECL-5400 p. 31
T_gap_average	(T_s_inner+T_fuel_surface)/2		average sheath temperature [K]
hf	k_steam/(1.5*(R_1+R_2)+g12+g0*(T_gap_average/273.15)^1.27/PT)		fluid heat transfer coefficient in the closed fuel-to-sheath gap [kW/(m^2*K)], AECL-5400 p. 30
k_gap_effective	(hs+hf)/hf*k_steam		effective thermal conductivity of the gap [kW/(m*K]
Ir_w_sig_ave	(Ir_w_sigma_centre+Ir_w_sigma_edge)/2		average electrical conductivity of iridium
Zirc_sh_sig_ave	(Zirc_sigma_inner+Zirc_sigma_outer)/2		average electrical conductivity of Zircaloy
UO2_int_sig_ave	(UO2_sigma_inner+UO2_sigma_middle+UO2_sigma_outer)/3		average electrical conductivity of UO2, [1/(ohm*m)}]
Rox_sheath	(1-f_pickup)*160*exp(-14192/T_s_inner)*F_crrs		{moles H/(m^2*s)} production rate of hydrogen due to sheath corrosion
krad	1.5e-10*N^2/alpha_r*T^3		radiative thermal conductivity [kW/(m*K)]
alpha_r	8750*exp(7.5971e-4*T)		{1/m}
Xdev_ave	Xdev_int/A_UO2		average stoichiometric deviation in the fuel element
N_O	N_UO2*Xdev_ave		average number density of hyperstoichiometric oxygen
n_O	N_O*fuel_vol/N_Avogadro		moles of hyperstoichiometric oxygen

5.2. Expressions

5.2.1. Subdomain Expressions

Subdomain		1, 4, 6-9, 12-15, 18, 20-22, 25-31, 34, 38	2-3, 10-11, 16-17, 23-24, 32-33, 35-37	41, 46, 51
cDg		0.0022646*sqrt(T*(1/MH2+1/MH2O))/ (sigmaAB^2*omega)	0.0022646*sqrt(T*(1/MH2+1/MH2O))/ (sigmaAB^2*omega)	0.0022646*sqrt(T*(1/MH2+1/MH2O))/ (sigmaAB^2*omega)
cg	1/K	PT/(R*T)	PT/(R*T)	PT/(R*T)
omega		0.45776+0.80674*(koverepsilon*T)^(-0.45859)	0.45776+0.80674*(koverepsilon*T)^(-0.45859)	0.45776+0.80674*(koverepsilon*T)^(-0.45859)

5.3. Mesh

5.3.1. Mesh Statistics

Number of degrees of freedom	38428
Number of mesh points	5161
Number of elements	10178
Triangular	10178
Quadrilateral	0
Number of boundary elements	1334
Number of vertex elements	171
Minimum element quality	0.003
Element area ratio	0

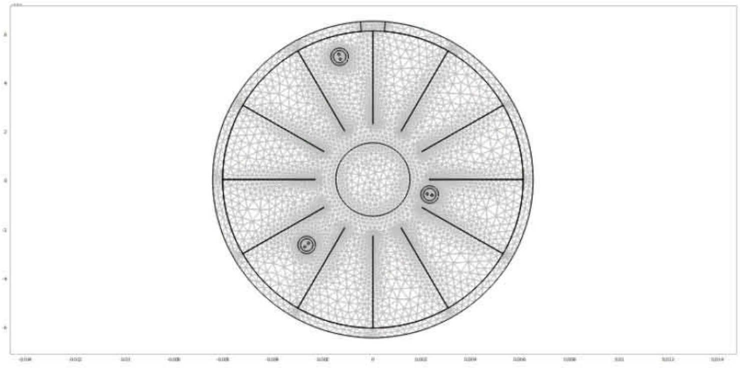

5.4. Application Mode: Heat Transfer by Conduction (ht)

Application mode type: Heat Transfer by Conduction

Application mode name: ht

5.4.1. Application Mode Properties

Property	Value
Default element type	Lagrange - Quadratic
Analysis type	Transient
Frame	Frame (ref)
Weak constraints	Off
Constraint type	Ideal

5.4.2. Variables

Dependent variables: T

Shape functions: shlag(2,'T')

Interior boundaries not active

5.4.3. Boundary Settings

Boundary		51-52, 129, 136, 144, 150
Type		Temperature
Temperature (T0)	K	**T_s_outer**

5.4.4. Subdomain Settings

Subdomain		1, 4, 6-9, 12-15, 18, 20-22, 25-31, 34, 38	2-3, 10-11, 16-17, 23-24, 32-33, 35-37	5
Thermal conductivity (k)	W/(m·K)	**k_steam**	**k_gap_effective**	**keff_UO2**
Density (rho)	kg/m^3	**rho_steam**	**rho_steam**	**cu_UO2**
Heat capacity at constant pressure (C)	J/(kg·K)	**Cp_steam**	**Cp_steam**	**Cp_UO2**
Heat source (Q)	W/m^3	0	0	**Q_vol_UO2**

Subdomain		19	39, 43, 48	40, 44, 49
Thermal conductivity (k)	W/(m·K)	**k_Zirc**	**k_TC_sheath**	**k_Magnesia**
Density (rho)	kg/m^3	**rho_Zircaloy**	**rho_Rtype**	**rho_Magnesia**
Heat capacity at constant pressure (C)	J/(kg·K)	**Cp_Zirc**	**Cp_Rtype**	**Cp_Magnesia**
Heat source (Q)	W/m^3	**Q_vol_Zirc**	0	0

Subdomain		41-42, 46-47, 50-51	45
Thermal conductivity (k)	W/(m·K)	**k_Rtype**	**k_Ir**
Density (rho)	kg/m^3	**rho_Rtype**	**rho_Ir**
Heat capacity at constant pressure (C)	J/(kg·K)	**Cp_Rtype**	**Cp_Ir**
Heat source (Q)	W/m^3	0	**Q_vol_Ir**

Subdomain initial value		1, 4, 6-9, 12-15, 18, 20-22, 25-31, 34, 38	2-3, 10-11, 16-17, 23-24, 32-33, 35-37	5	19	39, 43, 48	40, 44, 49	41-42, 46-47, 50-51	45
Temperature (T)	K	573.15	573.15	573.15	573.15	573.15	573.15	573.15	573.15

5.5. Application Mode: PDE, General Form (ox)

Application mode type: PDE, General Form

Application mode name: ox

5.5.1. Application Mode Properties

Property	**Value**
Default element type	Lagrange - Quadratic
Wave extension	Off
Frame	Frame (ref)
Weak constraints	Off

5.5.2. Variables

Dependent variables: Xdev, Xdev_t

Shape functions: shlag(2,'Xdev')

Interior boundaries active

5.5.3. Boundary Settings

Boundary		1-2, 5-6, 9-10, 13-14, 17-18, 21-23, 26, 29-30, 41-86, 89-93, 95, 99, 101-108, 111-116, 119, 121, 124-160, 166, 168-169, 171-204	87-88, 94, 96-98, 100, 109-110, 117-118, 120, 122-123, 161-165, 167, 170	3-4, 7-8, 11-12, 15-16, 19-20, 24-25, 27-28, 31-40
Type		Neumann boundary condition	Neumann boundary condition	Neumann boundary condition
(g)		0	**sigma*Rreact_fuel/cu_UO2**	**Rreact_fuel/cu_UO2**

5.5.4. Subdomain Settings

Subdomain		5
Source term (f)		**0**
Conservative flux source term (ga)		**{{-D_O2*(Xdevx+Xdev*Tstar/T^2*Tx);-D_O2*(Xdevy+Xdev*Tstar/T^2*Ty)}}**

Subdomain initial value		5
Xdev		Xsurf/10

5.6. Application Mode: Diffusion (hm)

Application mode type: Diffusion

Application mode name: hm

5.6.1. Application Mode Properties

Property	**Value**
Default element type	Lagrange - Quadratic
Analysis type	Transient
Frame	Frame (ref)
Weak constraints	Off
Constraint type	Ideal

5.6.2. Variables

Dependent variables: q

Shape functions: shlag(2,'q')

Interior boundaries active

5.6.3. Boundary Settings

Boundary		1-2, 5-6, 9-10, 13-14, 17-18, 22-23, 26, 29, 41-52, 57-58, 63-64, 67-68, 75-76, 79-80, 85-86, 89-93, 95, 99, 107-108, 111-116, 119, 121, 124, 132, 135-136, 138, 140-141, 143, 150, 155-156, 166, 171-178, 181-182, 189-190, 193-194, 201-202	3-4, 7-8, 11-12, 15-16, 19-20, 24-25, 27-28, 31-40	21, 30, 59-60, 71-72, 83-84, 101-106, 125-128, 130, 133-134, 139, 142, 146-148, 151-154, 157-160, 168-169, 185-186, 197-198
Type		Continuity	Flux	Insulation/Symmetry
Inward flux (N)	mol/(m^2·s)	0	**Rreact_fuel**	0
Concentration (c0)	mol/m^3	0	0	0

Boundary		87-88, 94, 96-98, 100, 109-110, 117-118, 120, 122-123, 161-165, 167, 170	129, 144	53-56, 61-62, 65-66, 69-70, 73-74, 77-78, 81-82, 131, 137, 145, 149, 179-180, 183-184, 187-188, 191-192, 195-196, 199-200, 203-204
Type		Continuity	Concentration	Flux
Inward flux (N)	mol/(m^2·s)	**sigma*Rreact_fuel**	0	**Rox_sheath**
Concentration (c0)	mol/m^3	0	**qdef**	0

5.6.4. Subdomain Settings

Subdomain		1-4, 6-18, 20-38
Diffusion coefficient (D)	m^2/s	**cDg/tau^2**
Time-scaling coefficient (Dts)	1	**cg**

Subdomain initial value		1-4, 6-18, 20-38
Concentration, q (q)	mol/m^3	qdef

6. Global Expressions

Name	**Expression**	**Unit**	**Description**
n_O_global	n_O		

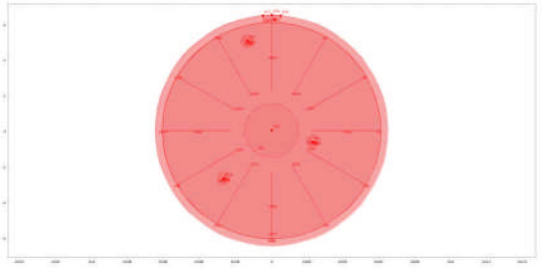

2D Ox r-theta model

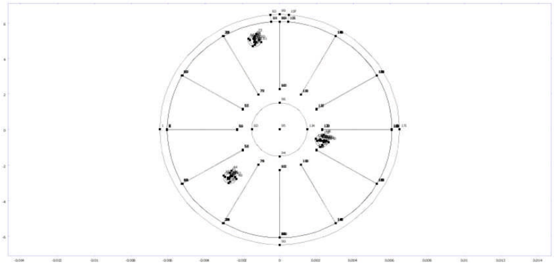

Point mode

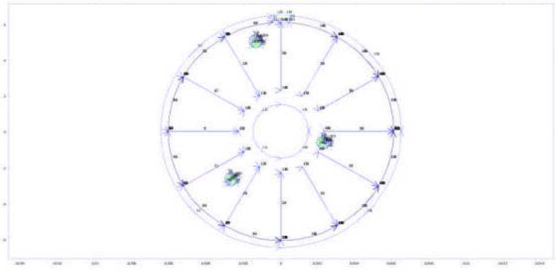

Boundary mode

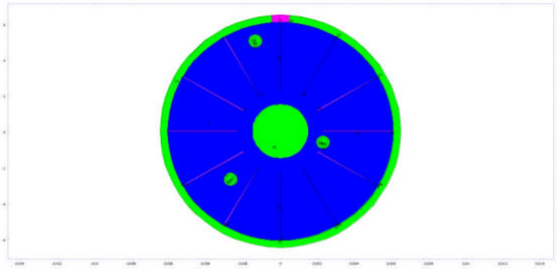

Subdomain mode

APPENDIX B: The 2D r-θ Plane Strain Solid Mechanics Model Report

2D Plane Strain Solid Mechanics Model: r Phi,j Integral Thermal,larger Round Contour 4,quad Mesh,PC.mph

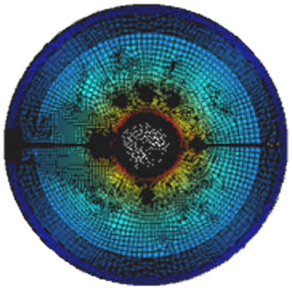

Date: Jan 31, 2014 1:35:56 PM

1 Global Definitions:

1.1 Parameters:

Name	**Expression**	**Description**
Density_Manf	10.6[g/cm^3]	UO2 fuel density
theo_density	10.96[g/cm^3]	UO2 theoretical fuel density
UO2_frac_theo_dens	Density_Manf/theo_density	UO2 fractional theoretical density
porosity_manf	1 - Density_Manf/theo_density	fractional porosity
Xdev	0.000001	
delta_zirc	0.0001	average oxygen concentration
cold_work_zirc	0.001	unitless ratio of areas
phi_fluence	1	fast neutron fluence [n/m^2]
rho_zircaloy	6.44[g/cm^3]	
Cp_zirc_2	325/1000	specific heat of zircaloy at 300C in [kJ/(kg*K)]
T_ref	300[K]	strain reference temperature
T_surf	573	
Beta	0.001	fractional burnup in atom %
rho_Ir	22.5[g/cm^3]	CRC Handbook 77th Ed., p12-172
alpha_Ir	6.4e-6	Iridium coefficient of linear expansion at 25C in [1/K], CRC Handbook 77th Ed., p. 12-172
E_Ir	528e9	Young's modulus of Ir in [Pa], Wikipedia
nu_UO2	1.32*(1 - 0.26*porosity_manf) - 1	UO2 Poisson's ratio using Equ. 16.2 in Olander
nu_Ir	0.27	Ir Poisson's radio, PGM database
nu_zirc	0.37	Poisson's ratio of Zircaloy-4, Wah Chang information sheet on Zircaloy-4
Q_vol_Ir	3.5e6	Iridium wire power in [kW/m^3]
coolant_p	10e6[Pa]	coolant pressure [Pa]
ftsg_thickness	3e-6 [m]	

Name	Expression	Description
pellet_radius	0.006075 [m]	
Ir_radius	0.00145[m]	
w_1	pellet_radius - Ir_radius	FES pellet thickness
sheath_wall	0.0004 [m]	sheath wall thickness
sheath_R_inner	0.006116 [m]	
sheath_R_outer	sheath_R_inner + sheath_wall	
crack_depth	0.00229 [m]	
lower_crk_mesh_den	14	
lower_crk_mesh_den_botm	7	
crack_time	0[s]	
V_Rw	2580 [m/s]	Raleigh wave speed in UO2, D. Laux etal JNM 300(2002)192
crack_speed	V_Rw	
crack_tip	-0.0059[m]	
crack_tip_dyna	crack_speed*crack_time+crack_tip	the crack tip location, material coordinates
Q_frack	1590[J/mole]	MATPRO, p. 2-125
R_gas	8.314	gas constant
Y_factor_2	0.126	stress intensity configuration correction calculated using T.R.G. Kutty's work [Journal of Materials Science Letter 6(1987)260], see also p. 32 in Lab book #4.
s_yield_zirc_initial	150e6[Pa]	yield stress at ≈300C
angle_degree_1	180	
angle_1	angle_degree_1*pi/180 [rad]	
crack_length_a_2	20e-6[m]	UO2 pore size, Olander
crack_domain_width	15e-4	
contour_side	5e-4[m]	
contour_offset_centre	0.0002[m]	
contour_radius	2.5e-4[m]	
outer_crack_disp	10	fuel upper mesh density

2 Model 1 (mod1)

2.1 Definitions

2.1.1 Variables

Variables 1 (thermal and mechanical)

Selection

Geometric entity level	Entire model

Name	**Expression**	**Description**
alpha_exp_1	9.828e-6 - 6.39e-10*T + 1.33e-12*T^2 - 1.757e-17*T^3	UO2 coefficient for thermal expansion when 273<=T<923 K, D.G. Martin JNM 152(1988)94
alpha_exp_2	1.1833e-5 - 5.013e-9*T + 3.756e-12*T^2 - 6.125e-17*T^3	UO2 coefficient for thermal expansion when 923<=T<=3120 K, D.G. Martin JNM 152(1988)94
alpha_exp_UO2	(T>=273&&T<923)*alpha_exp_1 + (T>=923&&T<=3120)*alpha_exp_2	UO2 coefficient for thermal expansion as a function of temperature
densityf	(T<=923)*((0.99734 + 9.9802E-6*T - 2.705E-10*T^2 + 4.391E-13*T^3)^(-3.0)) + (T>923)*((0.99672 + 1.179E-5*T - 2.429E-9*T^2 + 1.219E-12*T^3)^(-3.0))	density multiplier that accounts for temperature, JNM 366(2007)99
porosity	porosity_manf*(1 - (0.6 - exp(-0.506 - 8.67E-10*T^3*(1 - exp(-0.0287*Beta*225)))))	
cu	40588*densityf*(1 - porosity)	UO2 molar density [mol/m^3]
rho_UO2	0.27003*cu	UO2 density [kg/m^3]
fractional_density	rho_UO2/theo_density	
ES_UO2	2.334e11*(1 - 2.752*(1 - fractional_density))*(1 - 1.0915e-4*T)	Young's modulus of elasticity for stoichiometric UO2, [N/m^2], MATPRO p. 2-58
Afunc	14 - 10.763*(abs(Xdev))^0.5 - 2381.4*Xdev + 12819.86*(abs(Xdev))^1.5	

Name	Expression	Description
Bfunc	0.2218 + 0.2562*(abs(Xdev))^0.5 - 0.64*Xdev - 3.6764*(abs(Xdev))^1.5	
kphonon	1/(Afunc + Bfunc*T)	[kW/(m*K)]
kpolaron	(0.871 + 2.9e-5*T)^(-1)*2.024e8/(T^(5/2))*exp(-16350/T)	[kW/(m*K)]
BetaT	2.6 - 0.5e-3*T	
kappa2p	(1 - BetaT*porosity)	fuel porosity factor
keff_UO2	kappa2p*(kphonon + kpolaron)	UO2 effective thermal conductivity, [kW/(m*K)]
Cp_UO2	0.001*(52.1743 + 45.8056*abs(Xdev) + (87.951e-3 - 7.3461e-2*abs(Xdev))*T + (1 - abs(Xdev))*(-84.2411e-6*T^2 + 31.542e-9*T^3 - 2.6334e-12*T^4) - (713910 + 295090*abs(Xdev))/T^2)	[kJ/(mol*K)]
k_zirc	(7.51 + 2.09e-2*T - 1.45e-5*T^2 + 7.67e-9*T^3)/1000	Zircaloy thermal conductivity coefficient [kW/(m*K)], MATPRO p. 4-17
Cp_zirc	(-6.492e-5*T^2 + 0.207*T + 226.7)/1000	[kJ/(kg*K)] heat capacity of Zircaloy-2 for the temperatures 300 to 1090 K
E_alpha_zirc	(1.088e11 - 5.475e7*T + K1_zirc + K2_zirc)/K3_zirc	Zircaloy Young's modulus alpha phase, [Pa]. MATPRO p. 4-44, till 1083K, Wah Chang information sheet on Zircaloy-4
E_beta_zirc	9.21e10 - 4.05e7*T	Zircaloy Young's modulus beta phase, [Pa]. MATPRO p. 4-44, from 1253K, Wah Chang information sheet on Zircaloy-4
K1_zirc	(6.61e11 + 5.912e8*T)*delta_zirc	
K2_zirc	-2.6e10*cold_work_zirc	
K3_zirc	0.88 + 0.12*exp(-phi_fluence/1e25)	

Name	Expression	Description
epsilon_alpha11_zirc	4.95e-6*T - 1.485e-3	linear thermal expansion coefficient of Zircaloy in the circumferential direction, for 300K<T<1083K, MATPRO p. 4-26
epsilon_alpha33_zirc	1.26e-5*T - 3.78e-3	linear thermal expansion coefficient of Zircaloy in the axial direction, for 300K<T<1083K, MATPRO p. 4-26
G_zirc	(4.04e10 - 2.168e7*T + K1_zirc + K2_zirc)/K3_zirc	Zircaloy shear modulus for alpha phase, isotropic, MATPRO p. 4-45
alpha11_zirc	epsilon_alpha11_zirc/(T - T_ref)	thermal expansion coefficient of Zircaloy in the circumferential direction
alpha33_zirc	epsilon_alpha33_zirc/(T - T_ref)	thermal expansion coefficient of Zircaloy in the axial direction
k_Ir	(-0.0259*T + 154.76)/1000	thermal conductivity of Iridium [kW/(m*K)] 300-2000K (from www.platinummetalsreview.com)
Cp_Ir	(0.027*T + 122.33)/1000	specific heat of iridium [kJ/(kg*K)]
Tc	T - 273.15	
Cp_steam_1	(Tc>311.03&&Tc<=367.3)*(21.612 - 0.5024e-1*Tc) + (Tc>367.3&&Tc<=375)*3.159 + (Tc>375&&Tc<=645)*(3.7211 - 0.2274e-2*Tc + 0.1381e-4*(Tc - 500)^2 - 3.8565*10^(-8)*(Tc - 500)^3)	
Cp_steam_2	(Tc>645&&Tc<=700)*2.42 + (Tc>700&&Tc<=1300)*(2.134 + 0.4e-3*Tc) + (Tc>1300&&Tc<=1400)*2.66 + (Tc>1400&&Tc<=2000)*(2.7089 + 0.2255e-4*Tc - 8.4387*10^(-7)*(Tc - 1700)^2)	
Cp_steam	Cp_steam_1 + Cp_steam_2	Steam Tables in SI-Units, Wasserdampftafelm, Ulrich

Name	Expression	Description
		Grigull, Johannes Straub, Peter Schiebener, Springer-Verlag, 1990, [kJ/(kg*K)]
k_steam	((Tc<300)*0.1 + (Tc>=300)*1000*(-9.3878e-6 + 1.5569e-7*Tc - 5.4523e-10*Tc^2)/(1 - 3.7241e-3*Tc - 2.1893e-8*Tc^2))/1000	CRL equation, [kW/(m*K)]
rho_steam_1	(Tc>=311&&Tc<=400)*(91.38 - 0.1349*Tc + 0.000888*(Tc - 375)^2)	
rho_steam_2	(Tc>400&&Tc<450)*(-0.08842*Tc + 73.343)	
rho_steam_3	(Tc>=450&&Tc<=600)*(57.8 - 0.0546*Tc + 0.0001294*(Tc - 500)^2)	
rho_steam_4	(Tc>600&&Tc<650)*(-0.03892*Tc + 49.686)	
rho_steam_5	(Tc>=650&&Tc<=800)*(44.674 - 0.03121*Tc + 0.00004304*(Tc - 650)^2)	
rho_steam_6	(Tc>800&&Tc<2000)*(PT*101325)/(461.52*T)	
rho_steam	rho_steam_1 + rho_steam_2 + rho_steam_3 + rho_steam_4 + rho_steam_5 + rho_steam_6	Steam Tables in SI-Units, Wasserdampftafelm, Ulrich Grigull, Johannes Straub, Peter Schiebener, Springer-Verlag, 1990, p. 41, till 1100C, and the ideal gass law from 1100C, [kg/m^3]
calangle	atan2(y, x)	sector azimuthal position on the contact surface [rad]
sectorangle	((sin(calangle)>=0)*calangle+(sin(calangle)<0)*(2*pi + calangle))	provides an ascending azimuthal angle of 0-2*pi on the contact surface [rad]
R1	sqrt(x^2 + y^2)	radial distance of surface
relative_distance	sheath_inner_surface(R1) - pellet_surface(R1) - ftsg_thickness	relative diatance between the sheath and fuel pellet

Name	Expression	Description
relative_distance_d	d(relative_distance, TIME)	time derivative of relative distance
contact_damping	relative_distance_d*1e15[Pa*s/m]	for helping time dependent solver convergence
contact_pressure	-(relative_distance<0)*relative_distance*2e14[Pa/m]	pressure [Pa]
ave_relative_distance	aveop1(relative_distance_2)	average relative diatance between the sheath and fuel pellet
ave_pellet_surface_disp	aveop1(pellet_surface(R1)) - pellet_radius	average radial pellet displacement
average_contact_pressure	aveop1(contact_pressure)	
relative_distance_2	sheath_inner_surface(R1) - pellet_surface_2(R1) - ftsg_thickness	meant for plotting purposes only
E_Tiso	E_alpha_zirc/10	isotropic tangent modulus, Hobson, Oak Ridge
calangle2	atan(y/x)	

Variables 2a (fracture mechanics)

Selection

Geometric entity level	Entire model

Name	Expression	Description
W_1	intop1(ts.Ws*Nx1)	ts.Ws is the strain energy density
Tdudx_1	intop1(-((ts.sx*Nx1 + ts.sxy*Ny1)*uX + (ts.sxy*Nx1 + ts.sy*Ny1)*vX))	ts.sx*Nx is the traction vector
J_1	W_1 + Tdudx_1	the J integral quantity
ES_UO2_crack	aveop2(ES_UO2/(1 - nu_UO2^2))	Young's modulus at the crack tip, [N/m^2]
KI_1	sqrt(ES_UO2_crack*abs(J_1))	stress intensity factor [Pa*m^0.5]
sig_frack	1.7e8*(1 - 2.62*(1 - UO2_frac_theo_dens))^0.5*exp(-	fracture stress MATPRO, p. 2-125 [Pa]

Name	**Expression**	**Description**
	Q_frack/R_gas/T)[Pa]	
sig_frack_tip	intop2(sig_frack)	fracture stress at crack tip
crack_length_a	abs(intop3(x) - intop2(x))	the crack length, spacial coordinates distance
A	crack_length_a/w_1	relative crack length
Y_factor_1	-0.836*A^3 + 0.359*A^2 - 0.149*A + 1.125	SIF for cylinder external crack at steady state thermal stress from work by Wu
KI_c	Y_factor_1*sig_frack_tip*sqrt(pi*crack_length_a_2)	fracture toughness of UO2 using Y correction factor provided by Wu
KI_c_deduced	Y_factor_2*sig_frack_tip*sqrt(pi*crack_length_a_2)	fracture toughness of UO2, W.D. Callister 4th Ed., using deduced Y correction factor from results by Kutty
crack_speed_1	V_Rw*(1 - 1.75e-4/crack_length_a)	crack speed using Freund's treatment, T.L. Anderson, Fracture Mechanics, 3rd Ed. 2005
sigma_r	ts.sx*0.5*(1 + cos(2*angle_1)) + ts.sy*0.5*(1 - cos(2*angle_1)) + 2*ts.sxy*sin(angle_1)*cos(angle_1)	stress in the radial direction
sigma_theta	ts.sx*0.5*(1 - cos(2*angle_1)) + ts.sy*0.5*(1 + cos(2*angle_1)) - 2*ts.sxy*sin(angle_1)*cos(angle_1)	stress in the azimuthal direction
area_integral	intop4(alpha_exp_UO2*(ts.Sl11 + ts.Sl22 + ts.Sl33)*ts.gradTX)	
J_star	J_1 + area_integral	
area_integral_2	intop4((ts.Sl11 + 2*ts.Sl12 + 2*ts.Sl13 + ts.Sl22 + 2*ts.Sl23 + ts.Sl33)*d((ts.eel11 + 2*ts.eel12 + 2*ts.eel13 + ts.eel22 + 2*ts.eel23 + ts.eel33), X))	
J_star_2	Tdudx_1 + area_integral + area_integral_2	
KI_1_star	sqrt(ES_UO2_crack*abs(J_star))	
KI_1_star_2	sqrt(ES_UO2_crack*abs(J_star_2))	

top circ

Selection

Geometric entity level	Boundary
Selection	Boundaries 85, 87

Name	Expression	Description
Nx1	nx	
Ny1	ny	

bottom circ

Selection

Geometric entity level	Boundary
Selection	Boundaries 84, 86

Name	Expression	Description
Nx1	nx	
Ny1	ny	

2.1.2 Model Couplings

Integration 1

Coupling type	Integration
Operator name	intop1

Integration 2

Coupling type	Integration
Operator name	intop2

Integration 3

Coupling type	Integration
Operator name	intop3

Integration 4

Coupling type	Integration
Operator name	intop4

Average 1

Coupling type	Average
Operator name	aveop1

Average 2

Coupling type	Average
Operator name	aveop2

General Extrusion 1

Coupling type	General extrusion
Operator name	pellet_surface

General Extrusion 2

Coupling type	General extrusion
Operator name	sheath_inner_surface

General Extrusion 3

Coupling type	General extrusion
Operator name	pellet_surface_2

2.1.3 Selections

Section 1

Section 2

Section 3

Section 4

2.1.4 Coordinate Systems

Boundary System 1

Coordinate system type	Boundary system
Identifier	sys1

2.2 Geometry 1

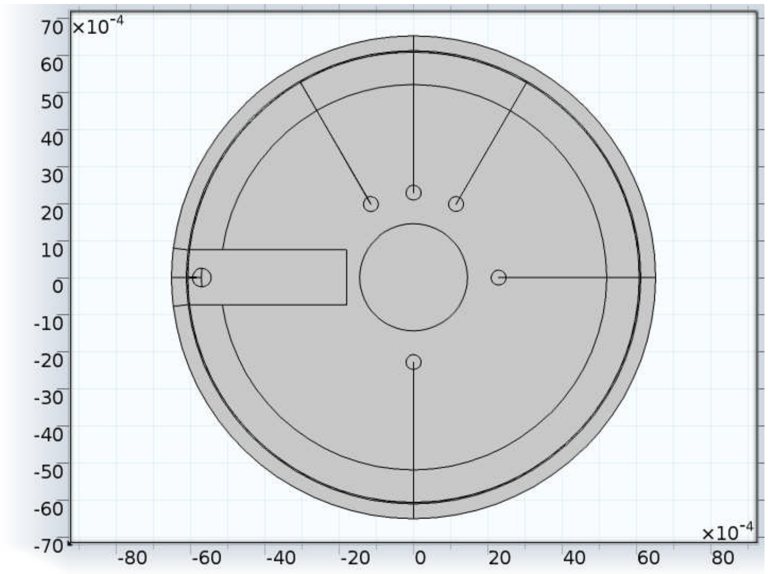

Geometry 1

Units

Length unit	m
Angular unit	deg

2.3 Materials

2.3.1 UO2

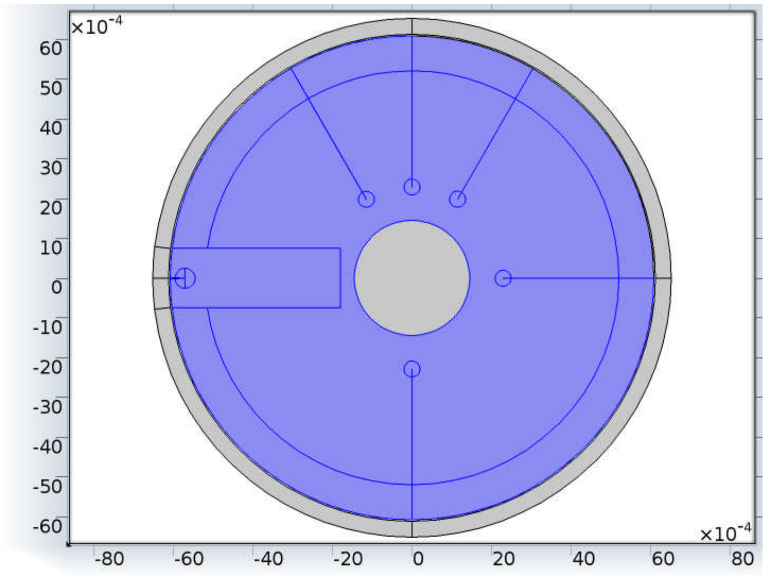

UO2 domain

Selection

Geometric entity level	Domain
Selection	Domains 8, 12–14, 16–18, 20, 22–25, 27–34, 39–40, 42–45, 48–49

Material parameters

Name	**Value**	**Unit**
Young's modulus	ES_UO2	Pa
Poisson's ratio	nu_UO2	1
Density	rho_UO2	kg/m^3
Coefficient of thermal expansion	alpha_exp_UO2	1/K
Thermal conductivity	keff_UO2	W/(m*K)
Heat capacity at constant pressure	Cp_UO2	J/(kg*K)

Basic settings

Description	**Value**
Young's modulus	ES_UO2
Poisson's ratio	nu_UO2
Density	rho_UO2
Coefficient of thermal expansion	{{alpha_exp_UO2, 0, 0}, {0, alpha_exp_UO2, 0}, {0, 0, alpha_exp_UO2}}
Thermal conductivity	{{keff_UO2, 0, 0}, {0, keff_UO2, 0}, {0, 0, keff_UO2}}
Heat capacity at constant pressure	Cp_UO2

2.3.2 Iridium

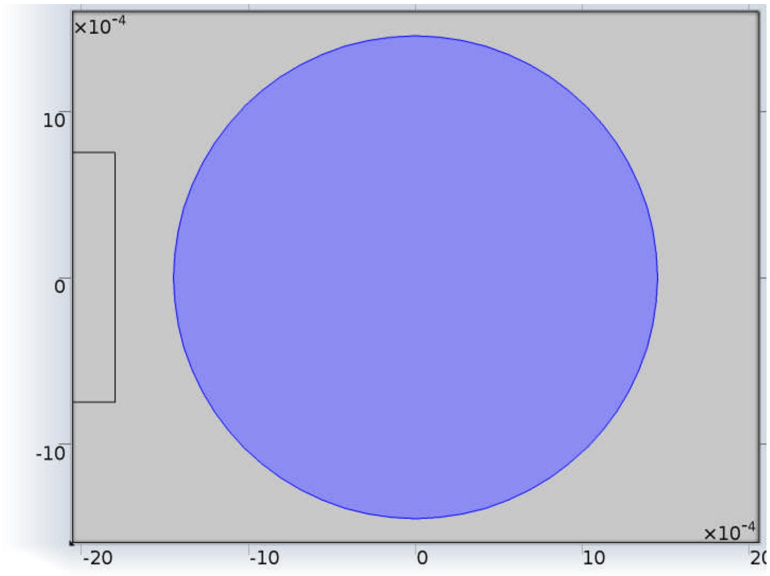

Iridium doamin

Selection

Geometric entity level	Domain
Selection	Domain 54

Material parameters

Name	**Value**	**Unit**
Heat capacity at constant pressure	Cp_Ir	J/(kg*K)
Density	rho_Ir	kg/m^3
Thermal conductivity	k_Ir	W/(m*K)

Basic settings

Description	**Value**
Heat capacity at constant pressure	Cp_Ir
Density	rho_Ir
Thermal conductivity	{{k_Ir, 0, 0}, {0, k_Ir, 0}, {0, 0, k_Ir}}
Young's modulus	E_Ir
Poisson's ratio	nu_Ir

Description	Value
Coefficient of thermal expansion	{{alpha_Ir, 0, 0}, {0, alpha_Ir, 0}, {0, 0, alpha_Ir}}

2.3.3 Zircaloy

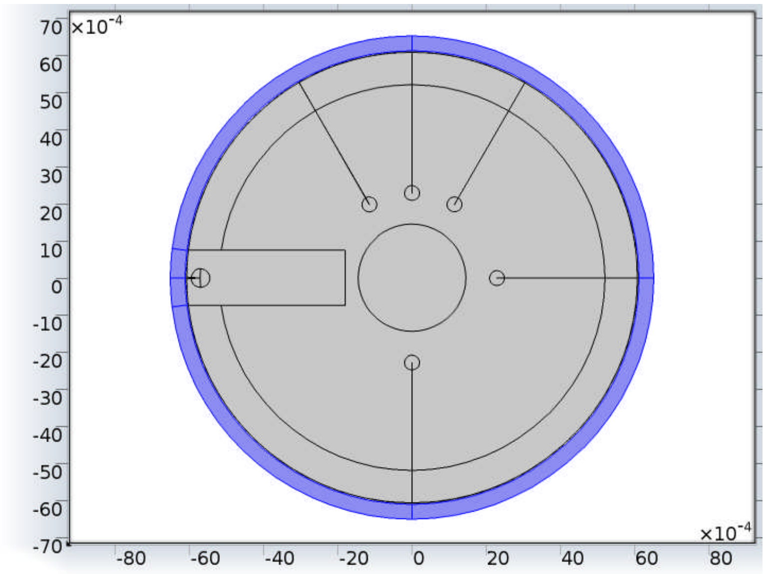

Zircaloy domain

Selection

Geometric entity level	Domain
Selection	Domains 1–4, 36–37

Material parameters

Name	Value	Unit
Young's modulus	E_alpha_zirc	Pa
Coefficient of thermal expansion	alpha11_zirc	1/K
Heat capacity at constant pressure	Cp_zirc	J/(kg*K)
Density	rho_zircaloy	kg/m^3
Thermal conductivity	k_zirc	W/(m*K)
Poisson's ratio	nu_zirc	1
Initial yield stress	s_yield_zirc_initial	Pa
Isotropic tangent modulus	E_Tiso	Pa

Basic settings

Description	Value
Young's modulus	E_alpha_zirc
Coefficient of thermal expansion	{{alpha11_zirc, 0, 0}, {0, alpha11_zirc, 0}, {0, 0, alpha11_zirc}}
Heat capacity at constant pressure	Cp_zirc
Density	rho_zircaloy
Thermal conductivity	{{k_zirc, 0, 0}, {0, k_zirc, 0}, {0, 0, k_zirc}}
Poisson's ratio	nu_zirc

Elastoplastic material model Settings

Description	Value
Initial yield stress	s_yield_zirc_initial
Isotropic tangent modulus	E_Tiso
Kinematic tangent modulus	

2.3.4 steam

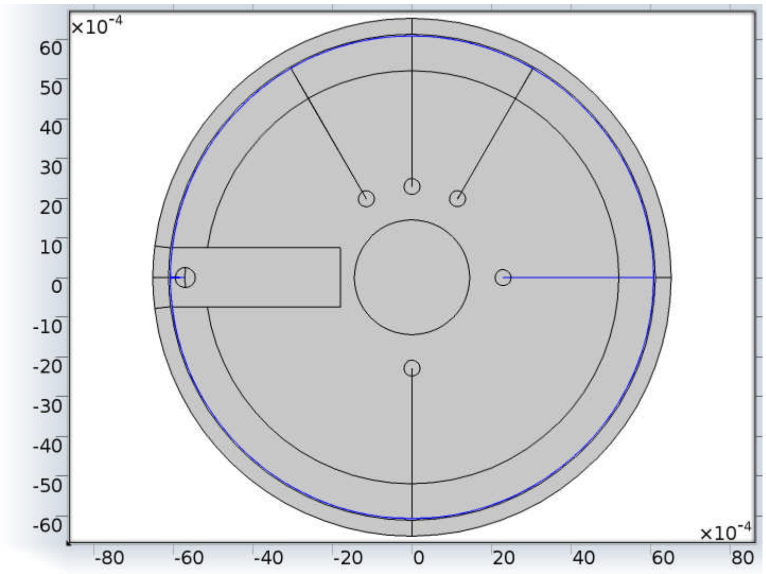

Steam domains

Selection

Geometric entity level	Domain
Selection	Domains 5–7, 9–11, 15, 19, 21, 26, 35, 38, 41, 46–47, 50–53

Material parameters

Name	**Value**	**Unit**
Heat capacity at constant pressure	Cp_steam	J/(kg*K)
Thermal conductivity	k_steam	W/(m*K)
Density	rho_steam	kg/m^3

Basic settings

Description	**Value**
Heat capacity at constant pressure	Cp_steam
Thermal conductivity	{{k_steam, 0, 0}, {0, k_steam, 0}, {0, 0, k_steam}}
Density	rho_steam
Young's modulus	
Poisson's ratio	
Coefficient of thermal expansion	{{, 0, 0}, {0, , 0}, {0, 0, }}

2.4 Thermal Stress (ts)

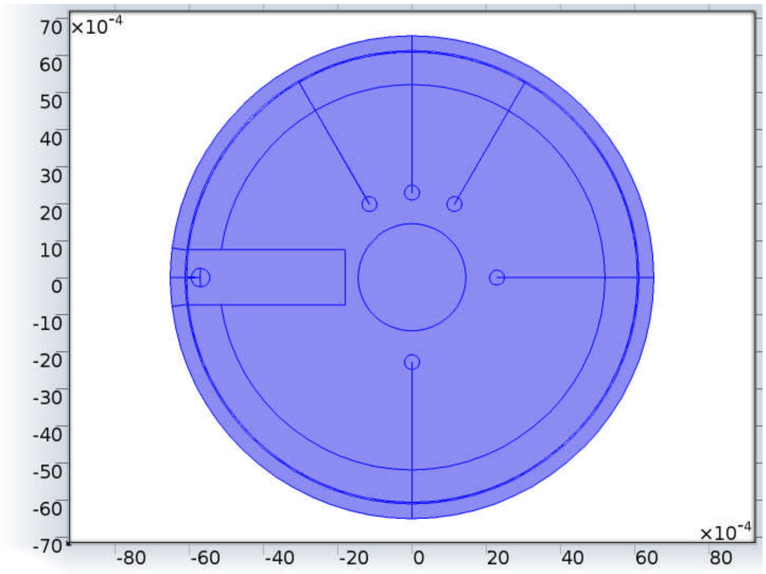

Thermal Stress

Features

Thermal Linear Elastic 1
Free 1
Thermal Insulation 1
Initial fuel temperature
Initial shieth temperature
Iridium wire heat source
outside surface temperature of shiething
Fixed Constraint 1
Prescribed Displacement 3 (fuel x only)
Prescribed Displacement 5 (fuel y only)
Prescribed Displacement 1 (sheath x only)
Prescribed Displacement 2 (sheath y only)
Boundary Load 1 (coolant pressure)
Heat Transfer in Solids 1 (steam regions)
inner sheath surface temperature
Boundary Load 2 (on sheath inner surface)
Boundary Load 3 (on pellet surface)
Heat Transfer in Solids 2 (iridium)

2.5 Moving Mesh (ale)

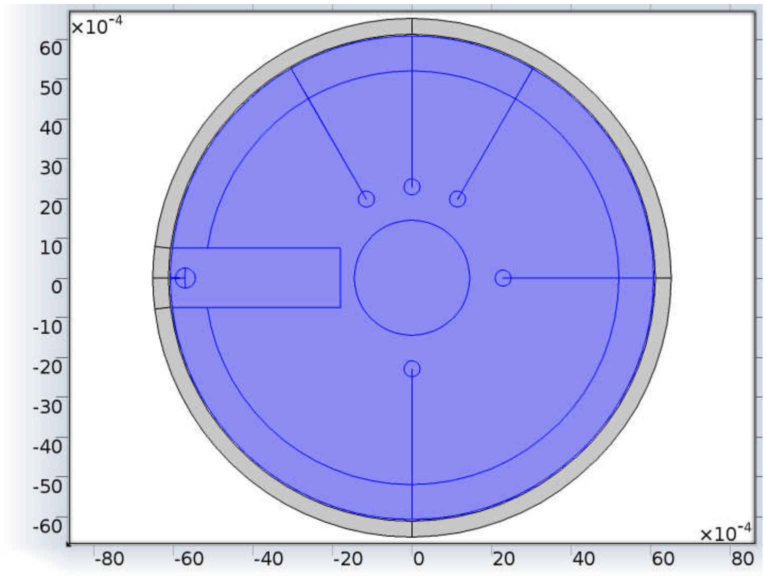

Moving Mesh

Features

Fixed Mesh 1
Prescribed Mesh Displacement 1
Free Deformation 1
Prescribed Mesh Displacement 2

2.6 Mesh 1

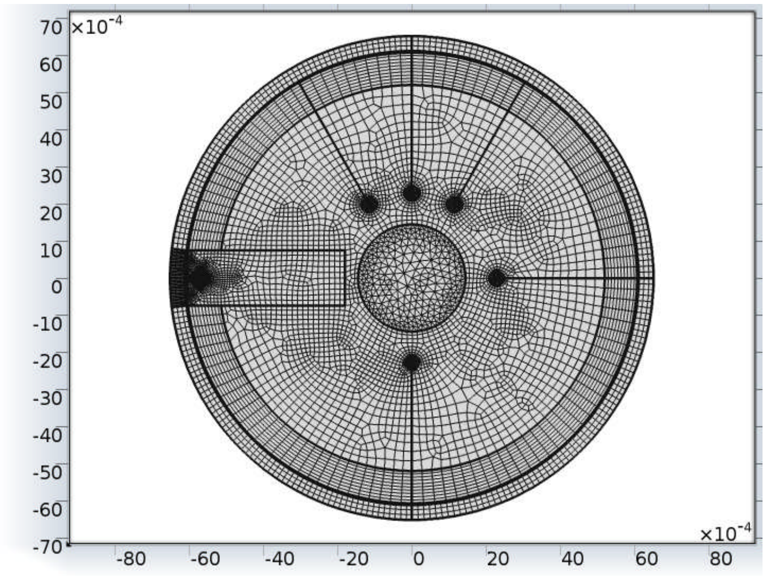

Mesh 1

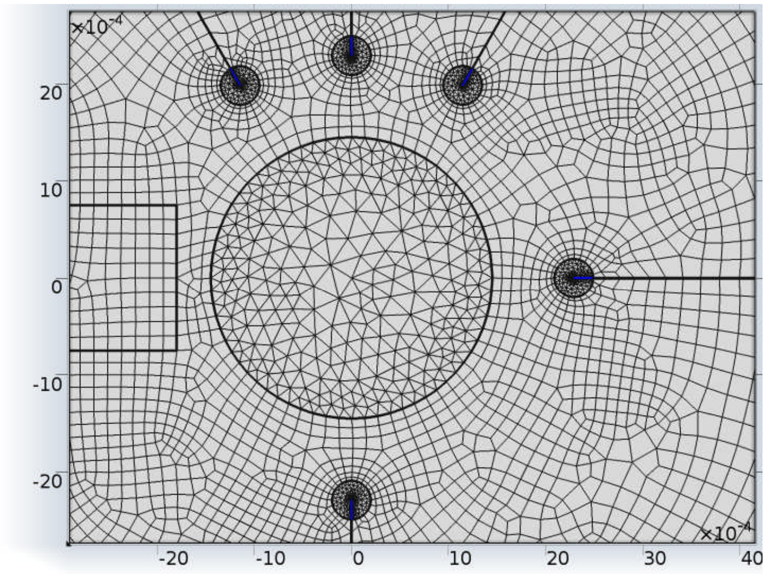

inner cracks, bottom

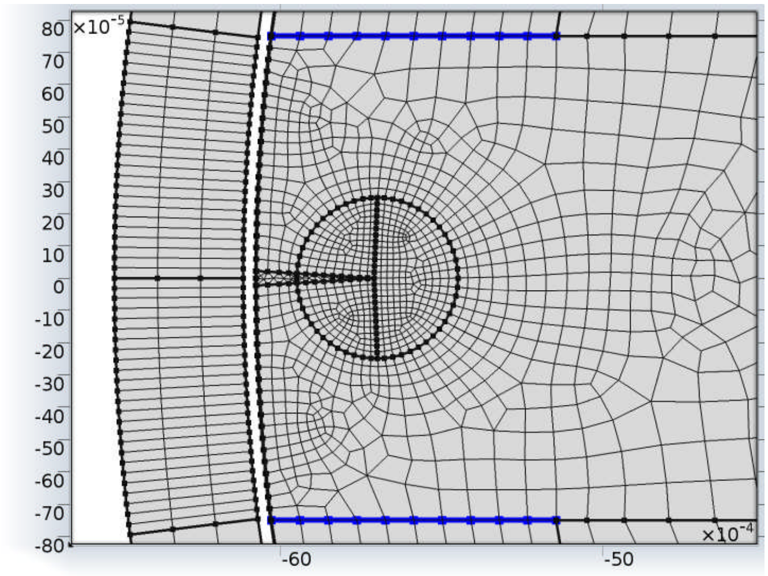

Distribution 1

3 Study 1

3.1 Parametric Sweep

Parameter name: crack_time

Parameters:

3.2 Stationary

Study settings

Property	**Value**
Include geometric nonlinearity	On

Mesh selection

Geometry	**Mesh**
Geometry 1 (geom1)	mesh1

Physics selection

Physics	**Discretization**
Thermal Stress (ts)	physics
Moving Mesh (ale)	physics

4 Results

4.1 Data Sets

4.1.1 Solution 1

Selection

Geometric entity level	Domain
Selection	Geometry geom1

Solution

Name	**Value**
Solution	Parametric 1
Model	Save Point Geometry 1

4.1.2 Cut Line 2D 4 (steady state)

Data

Name	**Value**
Data set	Solution 1

Advanced

Name	**Value**
Space variable	cln4x

4.2 Derived Values

4.2.1 Global Evaluation 1

Data

Name	**Value**
Data set	Solution 1

Expression

Name	**Value**
Expression	crack_length_a

Name	Value
Unit	m
Description	the crack length, spacial coordinates distance

4.2.2 KI_c

Data

Name	Value
Data set	Solution 1

Expression

Name	Value
Expression	KI_c
Description	fracture toughness of UO2 using Y correction factor provided by Wu

4.2.3 sig_frack_tip

Data

Name	Value
Data set	Solution 1

Expression

Name	Value
Expression	sig_frack_tip
Description	fracture stress at crack tip

4.2.4 Y_factor_1

Data

Name	Value
Data set	Solution 1

Expression

Name	Value
Expression	Y_factor_1
Unit	1
Description	SIF for cylinder external crack at steady state thermal stress from work by Wu

4.3 Tables

4.3.1 Table 1

Point Evaluation 1 (ts.mises)

Table 1

crack_time	von Mises stress (MPa), Point: 29
0	686.558923
2e-7	1428.048752
4e-7	2460.111763
6e-7	3831.396382
8e-7	5675.332339

4.3.2 Table 2

Global Evaluation 1 (crack_tip_dyna)

Table 2

crack_time	**crack_tip_dyna**
0	-0.0059
2e-7	-0.00542
4e-7	-0.00494
6e-7	-0.00446
8e-7	-0.00398

4.3.3 Table 3

Global Evaluation 2 (crack_speed_2)

Table 3 (crack speed calculated for reference)

crack_time	**crack speed using Freund's treatment, T.L. Anderson, Fracture Mechanics, 3rd Ed. 2005 (1/s)**
0	8.710499
2e-7	1893.371288
4e-7	2183.919143
6e-7	2301.75167
8e-7	2365.59204

4.3.4 Table 4

Point Evaluation, intop2(x) (intop2(x))

Table 4

crack_time	**intop2(x) (m), Point: 29**
0	-0.005972
2e-7	-0.005491
4e-7	-0.005009
6e-7	-0.004527
8e-7	-0.004045

4.3.5 Table 5

Global Evaluation 1 (crack_length_a)

Table 5

crack_time	the crack length, spacial coordinates distance (m)
0	1.756114e-4
1.75e-7	6.289911e-4
3.5e-7	0.001083
5.25e-7	0.001537
7e-7	0.001991

4.3.6 Table 6

KI_c (KI_c)

Table 6

crack_time	fracture toughness of UO2 using Y correction factor provided by Wu
0	1.065926e6

4.3.7 Table 7

sig_frack_tip (sig_frack_tip)

Table 7

crack_time	fracture stress at crack tip
0	1.20085e8

4.3.8 Table 8

sig_frack_tip (sig_frack_tip)

Table 8

crack_time	fracture stress at crack tip
1.4e-6	1.433987e8

4.3.9 Table 9

Y_factor_1 (Y_factor_1)

Table 9 (begin)

crack_time	**SIF for cylinder external crack at steady state thermal stress from work by Wu (1)**
0	1.11982

4.3.10 Table 10

Y_factor_1 (Y_factor_1)

Table 10 (end)

crack_time	**SIF for cylinder external crack at steady state thermal stress from work by Wu (1)**
1.4e-6	0.77782

4.4 Plot Groups

4.4.1 Stress (ts), steady state, parametric

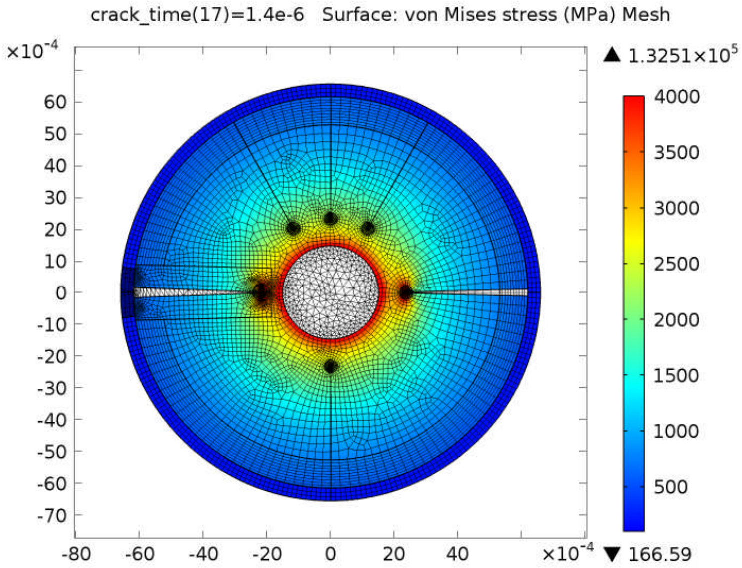

crack_time(17)=1.4e-6 Surface: von Mises stress (MPa) Mesh

4.4.2 Temperature (ts), last parametric

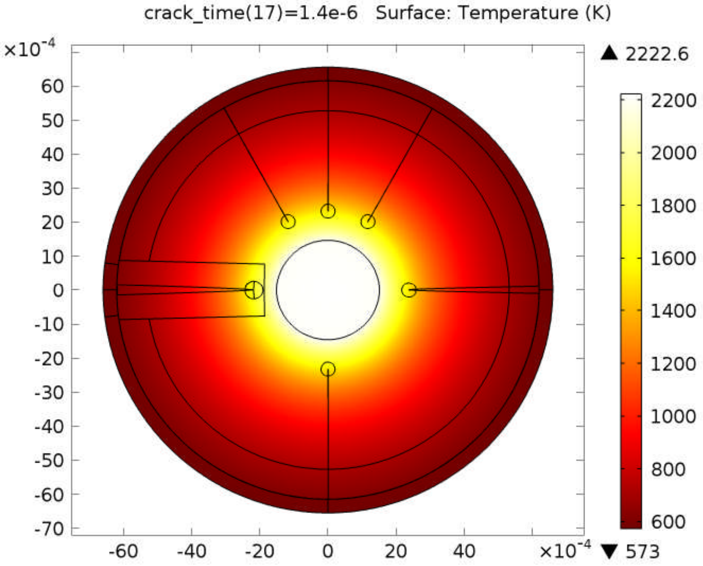

crack_time(17)=1.4e-6 Surface: Temperature (K)

4.4.3 radial temperature profile (steady state)

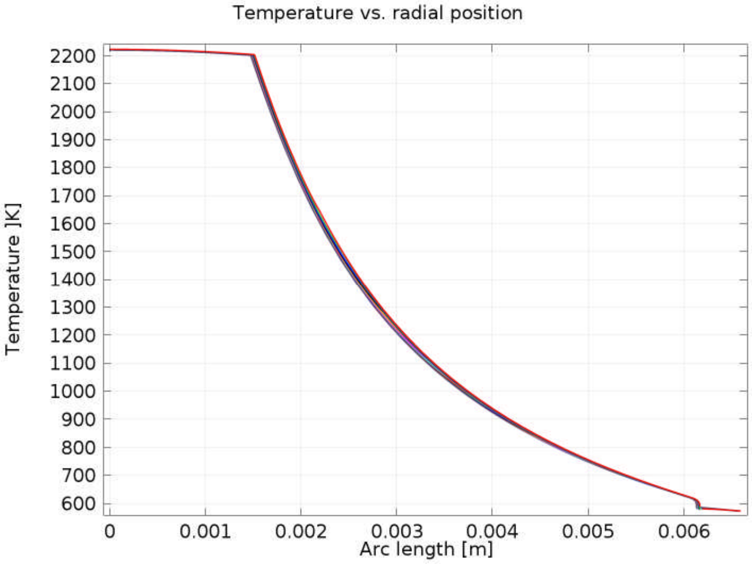

Temperature vs. radial position in out-reactor fuel pellet

4.4.4 J, J* and components

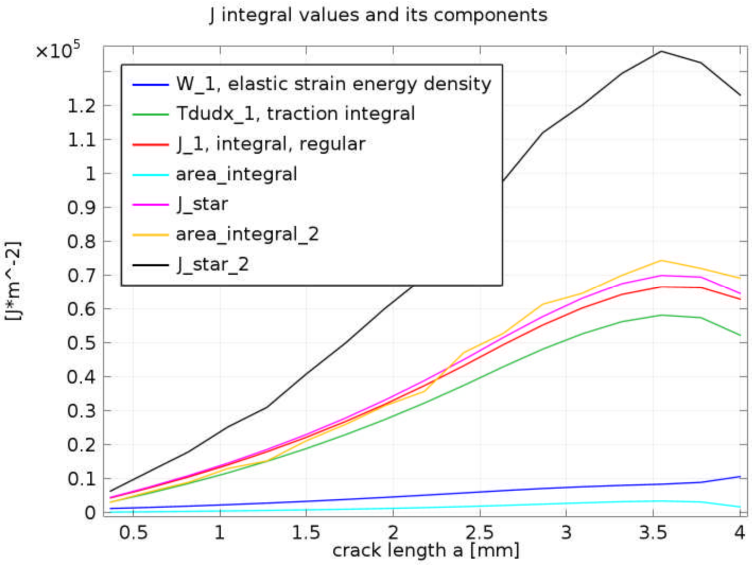

J and J* integral values and their components for growing crack lengths

4.4.5 KI_1

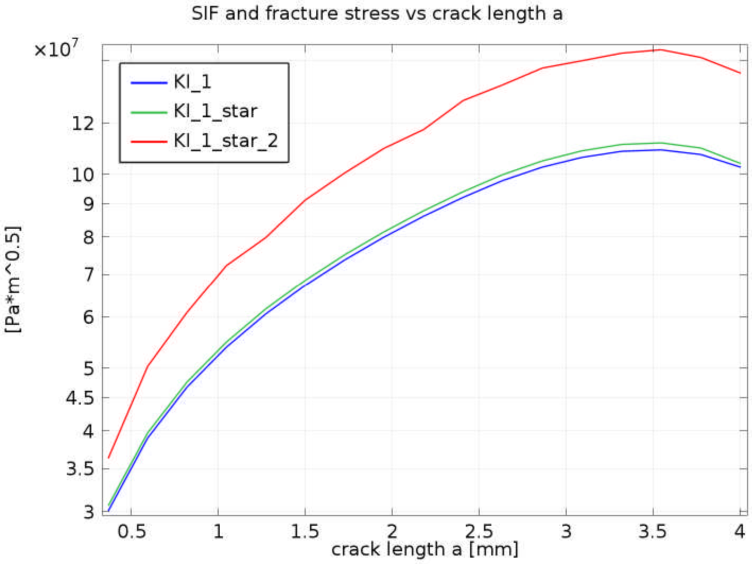

SIF and fracture stress vs crack length a

4.4.6 Youngs modulus at crack tip

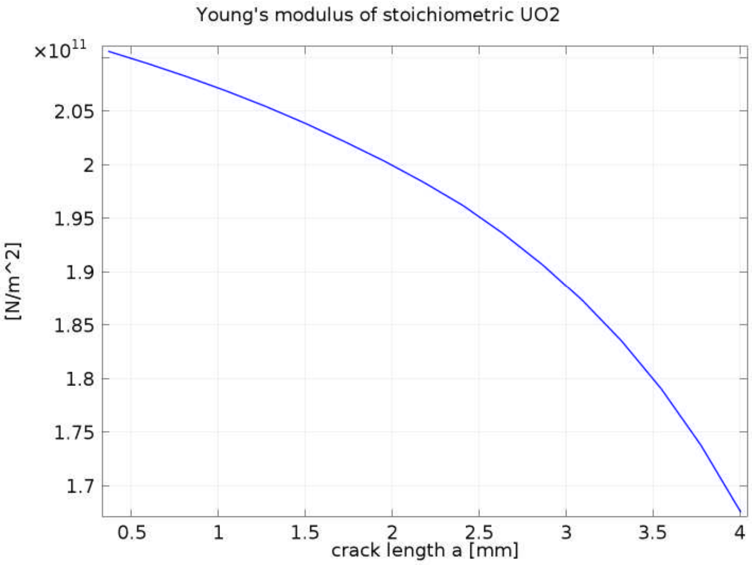

Young's modulus of stoichiometric UO2 for various crack lengths (or for different radial pellet positions)

4.4.7 fracture stress at crack tip

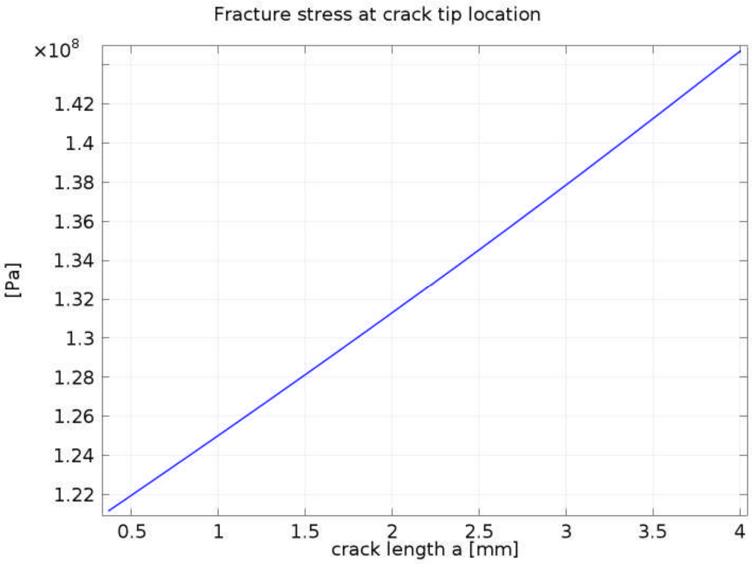

Fracture stress at crack tip location at various crack lengths

4.4.8 crack length a vs time

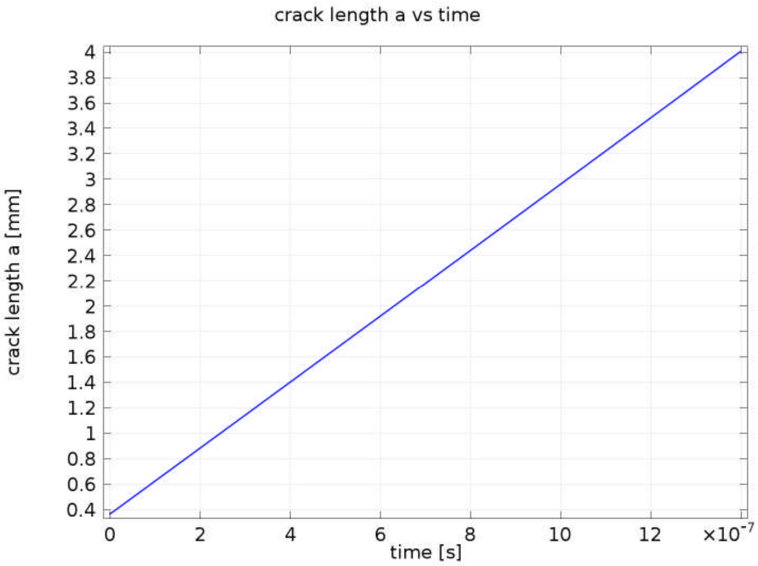

crack length a vs time [s]

4.4.9 Y_factor_1

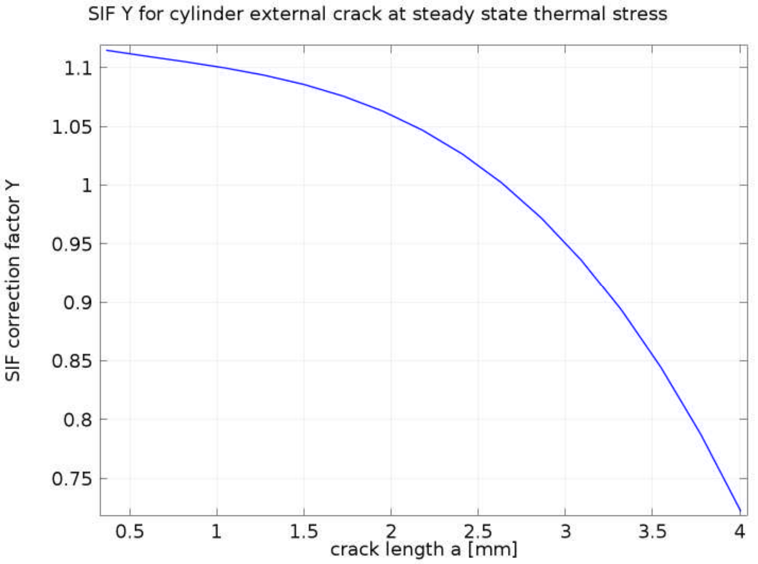

SIF Y for cylinder external crack at steady state thermal stress for increasing crack lengths

4.4.10 Freund crack speed

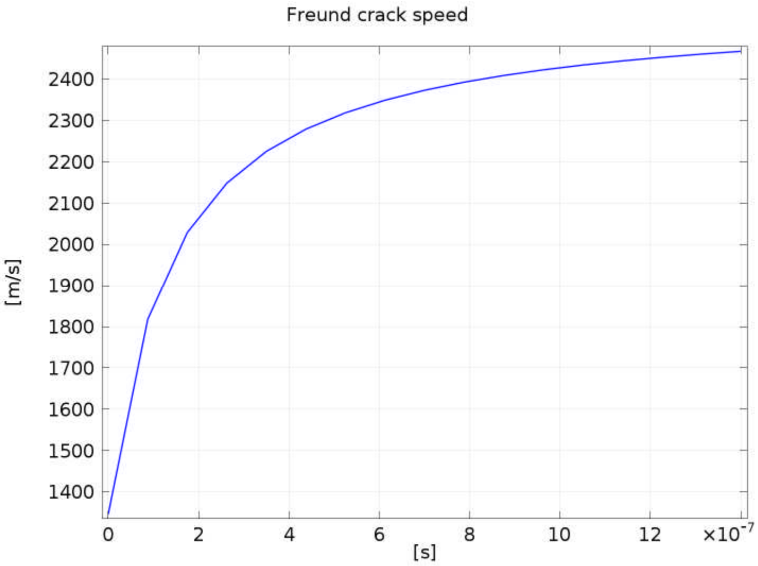

Freund crack speed (reference calculation only)

4.4.11 von Mises stress radial plot

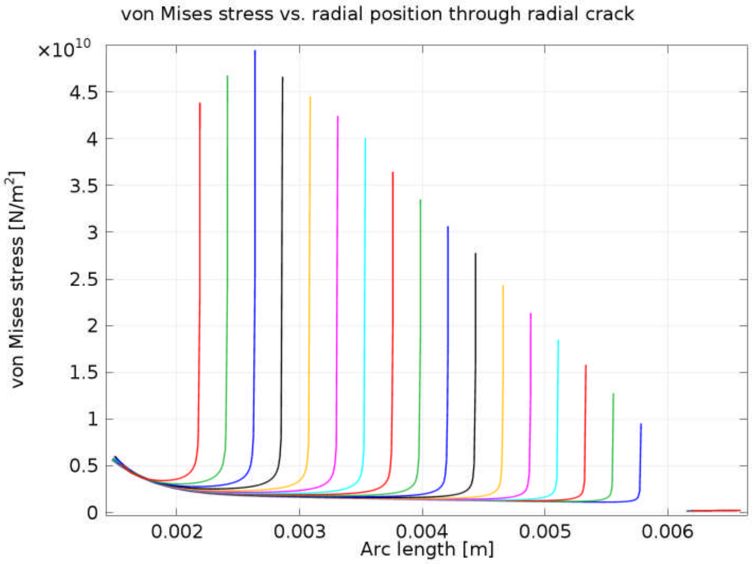

von Mises stress vs. radial position through radial crack as the crack grows in length

4.4.13 contact pressure

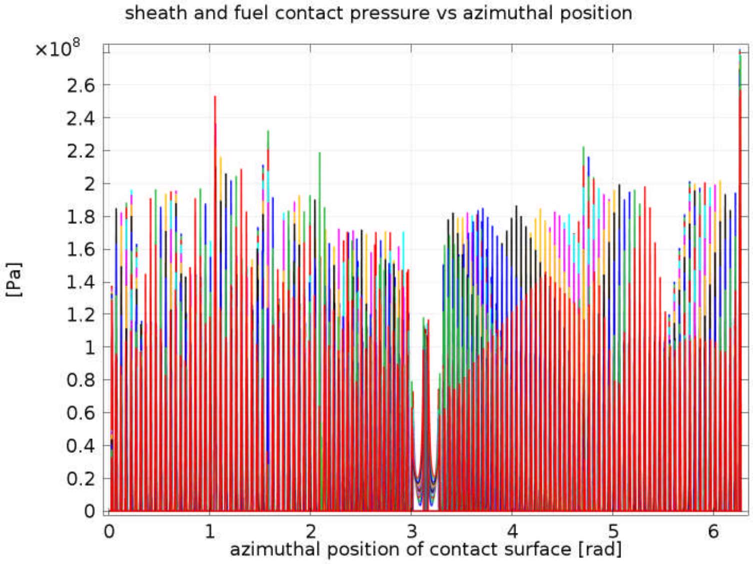

sheath and fuel surface contact pressure vs. azimuthal position

4.4.14 calangle

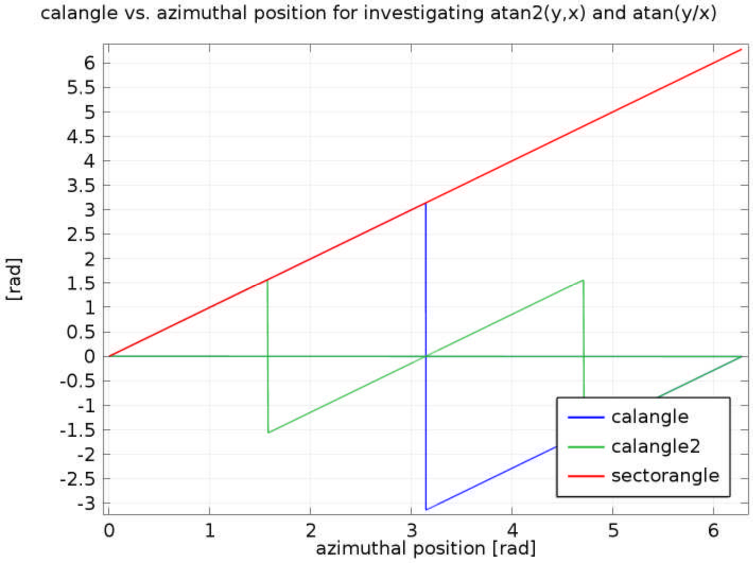

calangle vs. azimuthal position for investigating atan2(y,x) and atan(y/x) values

APPENDIX C: The 3D Fuel Oxidation Model Report

3D Fuel Oxidation Model: Model 6 5 Regular Cracks(3.2)

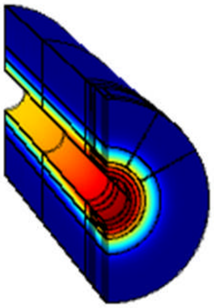

Date: Jan 31, 2013 3:48:59 PM

Contents: page:

1 Global Definitions

1.1 Parameters 1

Name	**Expression**	**Description**
kappa	110	inverse neutron diffusion length [1/m]
sigmaH2	2.827	collision diameter [A]
sigmaH2O	2.641	collision diameter [A]
MH2	2.01594	hydrogen gas molecular weight
MH2O	18.01594	light water molecular weight
Rgas	8.205e-005	
PT	100	atm pressure [atm]
koverepsilon	0.004549590536851683	
tau	1	tortuosity factor
qdef	4.1e-6	
Xsurf	1e-4	
a	0.033107007	
b	0.268984735	
c	0.008679485	
d	-0.000622197	
e	-5.18804E-05	
f	0.020038397	
g	0.000450165	
k	-7.83442E-06	
m	1.84196E-08	
n	-7.45197E-05	
p	1.39057E-07	
Density_Manf	10.6	fuel density [Mg/m^3]
porosity_manf	1 - Density_Manf/10.96	
Beta	0.00001	burnup atom%
T_surf_sheath_int	573	temperature of top of ftsg or sheath internal surface
T_surf	583	temperature of outer fuel-to-

Name	Expression	Description
		sheath gap
T_end	750	edge effect temperature
T_heater	2176	temperature at the 1.5mm radius inner surface of pellet
crack_tip_radius	0.00229[m]	
radius_2	(crack_tip_radius - Ir_radius)/3 + Ir_radius	2nd radius, above r=0.00145
radius_3	(crack_tip_radius - Ir_radius)/3*2 + Ir_radius	3rd radius, above r=radius_2
fuel_element_vol	pi*(pellet_radius^2 - Ir_radius^2)*0.24*2	total fuel volume, less iridium
N_UO2	2.444e28	UO2 particles per m^3
ppg	25e-6[m]	pellet-pellet gap
crack_width	25e-6[m]	radial crack width
defect_length	0.0074[m]	the defect length is twice this value
first_section	0.025[m]	
Ir_radius	0.00145[m]	iridium wire/hole radius
ftsg	1e-6[m]	fuel to sheath gap
pellet_radius	6.075e-3[m]	
N_Avogadro	6.022e23	
N	2.25	

2 Surface heated Out-Reactor fuel (mod1)

2.1 Definitions

2.1.1 Variables

Variables 1

Selection

Geometric entity level	Entire model

Name	Expression	Description
kappa1d	(1.09/Beta^3.265 + 0.0643/sqrt(Beta)*sqrt(T))*atan(1/(1.09/Beta^3.265 + 0.0643/sqrt(Beta)*sqrt(T)))	

Name	Expression	Description
kappa1p	1 + 0.019*Beta/((3 - 0.019*Beta)*(1 + exp(-(T - 1200)/100)))	
kappa2p	(1 - BetaT*porosity)	accounts for fuel porosity
kappa4r	1	no radiation effects
Afunc	14 - 10.763*(abs(Xdev))^0.5 - 2381.4*Xdev + 12819.86*(abs(Xdev))^1.5	{(m*K)/kW}
Bfunc	0.2218 + 0.2562*(abs(Xdev))^0.5 - 0.64*Xdev - 3.6764*(abs(Xdev))^1.5	{m/kW}
Bfuncfix	(Xdev<0.155)*Bfunc + (Xdev>=0.155)*0	equ. 22b
kphonon	1/(Afunc + Bfuncfix*T)	thermal conductivity in UO2 that results from conductive heat transfer via lattice vibrartion [kW/(m*K)]
kpolaron	(0.871 + 2.9e-5*T)^(-1)*2.024e8/(T^(5/2))*exp(-16350/T)	thermal conductivity in UO2 that results from electron hole movement [kW/(m*K)]
keff_UO2	kappa1d*kappa1p*kappa2p*kappa4r*(kphonon + kpolaron + krad)	thermal conductivity in UO2 [kW/(m*K)]
Cp_UO2	0.001*(52.1743 + 45.8056*abs(Xdev) + (87.951e-3 - 7.3461e-2*abs(Xdev))*T + (1 - abs(Xdev))*(-84.2411e-6*T^2 + 31.542e-9*T^3 - 2.6334e-12*T^4) - (713910 + 295090*abs(Xdev))/T^2)	specific heat of UO2 [kJ/(mol*K)]
Cp_UO2_2	0.001*(52.1743 + 87.951e-3*T - 84.2411e-6*T^2 + 31.542e-9*T^3 - 2.6334e-12*T^4 - 713910/T^2)	specific heat capacity of UO2 [kJ/(mol*K)] without Xdev terms
porosity	porosity_manf*(1 - (0.6 - exp(-0.506 - 8.67E-10*T^3*(1 - exp(-0.0287*Beta*225)))))	fuel porocity that considers also temperature

Name	Expression	Description
densityf	(T<=923)*((0.99734 + 9.802E-6*T - 2.705E-10*T^2 + 4.391E-13*T^3)^(-3.0)) + (T>923)*((0.99672 + 1.179E-5*T - 2.429E-9*T^2 + 1.219E-12*T^3)^(-3.0))	fuel density expression as a function of temperature
cu_UO2	40588*densityf*(1 - porosity)	molar density of UO2 [mol/m^3]
rho_UO2	density_manf*densityf*(1 - porosity)	density in [kg/m^3], for reference purposes
BetaT	2.6 - 0.5e-3*T	BetaT accounts for the temperature effect
alpha	0.365*exp(-23500/T)	
D_O2	2.5e-4*exp(-16400/T)	
sigmaAB	(sigmaH2 + sigmaH2O)/2	
qfix	(q<qdef)*(qdef) + (q>=qdef&&q<=0.95)*q + (q>0.95)*0.95	
Rox_fuel	cu_UO2*alpha*sqrt((1 - qfix)*PT)*(Xefix - Xdev)	
Rred_fuel	cu_UO2*alpha*sqrt(qfix*PT)*(Xefix - Xdev)	
Rreact_fuel	(Xefix>=Xdev)*Rox_fuel + (Xefix<Xdev&&Xdev>Xsurf)*Rred_fuel	
Xefix	(xe<Xsurf)*Xsurf + (xe>=Xsurf)*xe	
Tstar	-4.21e33*exp(-(68 + 34*Xdev))	
Zeta	log10(qfix/(1 - qfix))	
xe	(a + c*Zeta + e*T + g*Zeta^2 + m*T^2 + k*Zeta*T)/(1 + b*Zeta + d*T + f*Zeta^2 + p*T^2 + n*Zeta*T)	
Tc	T - 273.15	
k_steam	((Tc<300)*0.1 + (Tc>=300)*1000*(-9.3878e-6 + 1.5569e-7*Tc - 5.4523e-10*Tc^2)/(1 - 3.7241e-3*Tc - 2.1893e-8*Tc^2))/1000	{kW/(m*K)}, CRL equation
Cp_steam_1	(Tc>311.03&&Tc<=367.3)*(21.612 - 0.5024e-1*Tc) + (Tc>367.3&&Tc<=375)*3.159 + (Tc>375&&Tc<=645)*(3.7211 - 0.2274e-2*Tc + 0.1381e-4*(Tc - 500)^2 - 3.8565*10^(-8)*(Tc - 500)^3)	between temperatures 311K and 645K
Cp_steam_2	(Tc>645&&Tc<=700)*2.42 + (Tc>700&&Tc<=1300)*(2.134 + 0.4e-3*Tc) + (Tc>1300&&Tc<=1400)*2.66 +	between temperatures

Name	**Expression**	**Description**
	(Tc>1400&&Tc<=2000)*(2.7089 + 0.2255e-4*Tc - 8.4387*10^(-7)*(Tc - 1700)^2)	645K and 2000K
Cp_steam	(Cp_steam_1 + Cp_steam_2)	[kJ/(kg*K)]
rho_steam_1	(Tc>=311&&Tc<=400)*(91.38 - 0.1349*Tc + 0.000888*(Tc - 375)^2)	
rho_steam_2	(Tc>400&&Tc<450)*(-0.08842*Tc + 73.343)	
rho_steam_3	(Tc>=450&&Tc<=600)*(57.8 - 0.0546*Tc + 0.0001294*(Tc - 500)^2)	
rho_steam_4	(Tc>600&&Tc<650)*(-0.03892*Tc + 49.686)	
rho_steam_5	(Tc>=650&&Tc<=800)*(44.674 - 0.03121*Tc + 0.00004304*(Tc - 650)^2)	
rho_steam_6	(Tc>800&&Tc<2000)*(PT*101325)/(461.52*T)	
rho_steam	rho_steam_1 + rho_steam_2 + rho_steam_3 + rho_steam_4 + rho_steam_5 + rho_steam_6	[kg/m^3]
cDg	0.0022646*sqrt(T*(1/MH2 + 1/MH2O))/(sigmaAB^2*omega)	diffusivity [moles/(m*s)]
cg	PT/(Rgas*T)	total molar concentration of the gas [moles/m^3]
omega	0.45776 + 0.80674*(koverepsilon*T)^(-0.4585)	the collision integral
Xdev_average	aveop1(Xdev)	averge Xdev value
N_O	N_UO2*Xdev_average	the average oxygen excess atom density in the fuel (m^-3)
n_O	N_O*fuel_element_vol/N_Avogadro	moles of oxygen atoms absorbed by fuel
n_H	n_O	moles of hydrogen molecules liberated to ftsg and coolant
alpha_r	8750*exp(7.5971e-4*T)	[1/m]

Name	**Expression**	**Description**
krad	1.5e-10*N^2/alpha_r*T^3	radiative thermal conductivity [kW/(m*K)]

2.1.2 Model Couplings

Average 1

Coupling type	Average
Operator name	aveop1

2.1.3 Selections

Section 1, Section 2, Section 3, Section 4, Section 5, Section 6, Section 7, Section 8, Section 9, Section 10

2.1.4 Pairs

Identity Pair 1

Pair type	Identity pair
Pair name	p1

2.1.5 Coordinate Systems

Boundary System 1

Coordinate system type	Boundary system
Identifier	sys1

2.2 Geometry 1

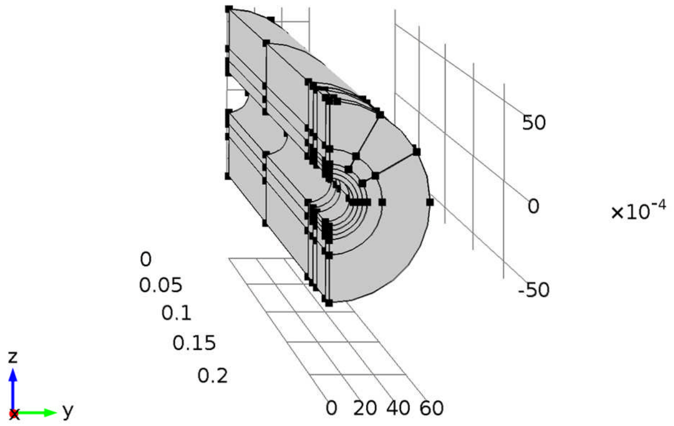

Geometry 1

Units

Length unit	m
Angular unit	deg

2.3 Materials

2.3.1 Gas

Selection

Geometric entity level	Domain
Selection	Domains 31–33, 36–38, 40, 42–46, 53–55, 58–60, 62, 64–71, 75–90

2.3.2 UO2

Selection

Geometric entity level	Domain
Selection	Domains 1–30, 34–35, 39, 41, 47–52, 56–57, 61, 63, 72–74

2.4 Heat Transfer (Heat)

Features

Heat Transfer in Solids 1

Thermal Insulation 1
Initial Values 1
Temperature 1(outside fuel)
Temperature 2(inside)
Thermal Insulation 2
Symmetry 1
Heat Continuity 1

2.5 Transport of Diluted Species (Hdif)

Features

Diffusion
No Flux 1
Initial Values 1
Reactions 1
Concentration 1
Flux 1

2.6 PDE (Ox)

Features

General Form PDE 1
Zero Flux 1
Initial Values 1
Flux/Source 1
Continuity 1

2.7 Mesh 1

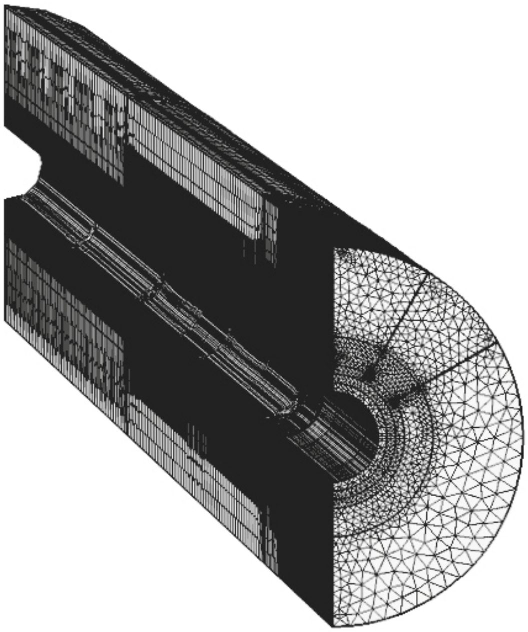

2.7.1 Size (size)

Settings

Name	Value
Maximum element size	0.024
Minimum element size	0.00432
Resolution of curvature	0.6
Resolution of narrow regions	0.5
Maximum element growth rate	1.5

Note: For in-depth mesh details an *intermediate* or *complete* report in COMSOL$^{®}$ Multiphysics version 4.3b can be generated.

3 Study 1

3.1 Time Dependent

Compile Equations: Time Dependent (st1)

Study settings

Property	**Value**
Include geometric nonlinearity	Off

Times: range(0,0.1,0.9) range(1,1,19) range(20,5,75) range(80,0.25*86400,14*86400)

Mesh selection

Geometry	**Mesh**
Geometry 1 (geom1)	mesh1

Physics selection

Physics	**Discretization**
Heat Transfer (ht)	physics
Transport of Diluted Species (chds)	physics
PDE (g)	physics

3.2 Solver Configurations

3.2.1 Solver 1

Compile Equations: Time Dependent (st1)

Study and step

Name	**Value**
Use study	Study 1
Use study step	Time Dependent

Dependent Variables 1 (v1)

General

Name	**Value**
Defined by study step	Time Dependent

Initial values of variables solved for

Name	**Value**
Solution	Zero

Direct (dDef)

General

Name	**Value**
Solver	PARDISO

Fully Coupled 1 (fc1)

General

Name	**Value**
Linear solver	Direct

4 Results

4.1 Data Sets

4.1.1 Solution 1

Selection

Geometric entity level	Domain
Selection	Geometry geom1

Solution

Name	**Value**
Solution	Solver 1
Model	Save Point Geometry 1

4.1.2 Cut Line 3D 1 (at defect)

Data

Name	**Value**
Data set	Solution 1

Advanced

Name	**Value**
Space variable	cln1x

Coordiantes [m]

Point	x	y	z
1	0.239	20e-6	1.45e-3
2	0.239	20e-6	0.007

4.1.3 Cut Line 3D 2 (at fuel element end)

Data

Name	Value
Data set	Solution 1

Advanced

Name	Value
Space variable	cln2x

Coordiantes [m]

Point	x	y	z
1	0.001	20e-6	1.45e-3
2	0.001	20e-6	0.007

4.1.4 Cut Line 3D 3 (middle of fuel element)

Data

Name	Value
Data set	Solution 1

Advanced

Name	Value
Space variable	cln3x

Coordiantes [m]

Point	x	y	z
1	0.12	20e-6	1.45e-3
2	0.12	20e-6	0.007

4.2 Tables

4.2.1 Evaluation 3D

Interactive 3D values

Evaluation 3D

x	**y**	**z**	**Value**
0.24	6.091e-7	0.00145	7.31893e-5

APPENDIX D: FactSage Thermoequilibrium Computations

FactSage® 6.1 thermoequilibrium computations:

D-1: Carbothermal reduction of hyperstoichiometric fuel:

```
   1.9 UO2 +  0.1 UO3 +  0.05 C =

  5.0000E-02 mol   gas_ideal
  (2.2005 gram, 5.0000E-02 mol, 2.5561 litre, 8.6087E-04 g/ml)
      (623.00 K, 1 atm,     a=1.0000)
      ( 0.99998         CO2                          FACT
      + 2.2950E-05      CO                             FACT)

+ 2.0000     mol   Fluorite
  (540.06 gram, 2.0000 mol)
      (623.00 K, 1 atm,     a=1.0000)
      ( 1.0000          UO2                          RMCS
      + 5.7376E-07      UO3                             RMCS)

      System component       Mole fraction  Mass fraction
      U                      0.33333        0.88150
      O                      0.66667        0.11850

+ 0.00000    mol   U4O9_solid(s)                     RMCB
      (623.00 K, 1 atm, S1, a=6.2364E-04)
+ 0.00000    mol   U3O7_solid(s)                     RMCB
      (623.00 K, 1 atm, S1, a=2.5226E-04)
+ 0.00000    mol   C_graphite                        FACT
      (623.00 K, 1 atm, S1, a=8.6978E-05)
+ 0.00000    mol   C_diamond                          FACT
      (623.00 K, 1 atm, S2, a=3.8754E-05)
+ 0.00000    mol   UO3_alpha_solid(s)                RMCB
      (623.00 K, 1 atm, S1, a=1.6046E-07)
+ 0.00000    mol   U3O8_solid(s)                     RMCB
      (623.00 K, 1 atm, S1, a=3.1434E-09)

The cutoff concentration has been specified to 1.0000E-20
*****************************************************************
     H              G               V               S         Cp
    (J)            (J)            (litre)          (J/K)     (J/K)
*****************************************************************
-2.14102E+06 -2.31227E+06  2.55610E+00  2.74879E+02  1.61735E+02

Total mass/gram = 542.26
Total mass/gram excluding gas = 540.06
~~~~~~~~~~~~~~~~~~~~~~~~~~~~~~~~~~~~~~~~~~~~~~~~~~~~~~~~~~~~~~~~~~~~~~~~~~~~~~~~~~
T = 623.00 K
```

```
P = 1.00000E+00 atm
V = 2.55610E+00 dm3

STREAM CONSTITUENTS       AMOUNT/mol
UO2                        1.9000E+00
UO3                        1.0000E-01
C                          5.0000E-02

                 EQUIL AMOUNT  MOLE FRACTION     FUGACITY
PHASE: gas_ideal           mol                   atm
CO2_FACT              4.9999E-02    9.9998E-01    9.9998E-01
CO_FACT               1.1475E-06    2.2950E-05    2.2950E-05
TOTAL:                5.0000E-02    1.0000E+00    1.0000E+00
PHASE: Fluorite            mol      MOLE FRACTION    ACTIVITY
UO2                   2.0000E+00    1.0000E+00    1.0000E+00
UO3                   1.1475E-06    5.7376E-07    2.5942E-12
UO                    1.8740E-32    9.3699E-33    9.3699E-33
TOTAL:                2.0000E+00    1.0000E+00    1.0000E+00

                  mol                  ACTIVITY

U4O9_solid(s)_RMCB       0.0000E+00              6.2364E-04
U3O7_solid(s)_RMCB       0.0000E+00              2.5226E-04
C_graphite(s)_FACT       0.0000E+00              8.6978E-05
C_diamond(s2)_FACT       0.0000E+00              3.8754E-05
UO3_alpha_solid(s)_RMCB  0.0000E+00              1.6046E-07
U3O8_solid(s)_RMCB       0.0000E+00              3.1434E-09
*******************************************************************
  Cp_EQUIL      H_EQUIL      S_EQUIL      G_EQUIL      V_EQUIL
   J.K-1           J           J.K-1          J            dm3
*******************************************************************
 1.61735E+02  -2.14102E+06   2.74879E+02  -2.31227E+06   2.55610E+00

Mole fraction of system components:
           gas_ideal    Fluorite
U          4.3731E-33   0.33333
O          0.66666      0.66667
C          0.33334      0.00000

The cutoff limit for phase or gas constituent activities is 1.0000E-20
```

D-2: Thermogravimetric analyzer (TGA) thermodynamic equilibrium computations:

To achieve a stoichiometric deviation of $x=0.1$ in a sample that has a mass of 107 mg (test #25):

```
T = 1273.00 K
P = 1.00000E+00 atm
```

3.963E-4 UO2 + 2E-5 O2 =

```
  0.00000    mol   gas_ideal
        (1273.00 K, 1 atm,     a=1.9940E-08)
        ( 1.9712E-08      O2
        + 2.1368E-10      UO3
        + 1.5010E-11      O
        + 1.1225E-16      UO2
        + 9.8805E-22      O3
        + 1.3225E-29      UO
        + 1.8259E-42      U)

+ 3.9630E-04 mol   Fluorite
  (0.10765 gram, 3.9630E-04 mol)
        (1273.00 K, 1 atm,     a=1.0000)
        ( 0.89907         UO2
        + 0.10093         UO3
        + 1.2605E-17      UO)

        System component       Mole fraction  Mass fraction
        U                      0.32248        0.87626
        O                      0.67752        0.12374

The cutoff concentration has been specified to 1.0000E-75

Data on 1 product species identified with "T" have been extrapolated

*******************************************************************
     H           G           V           S          Cp
    (J)         (J)       (litre)      (J/K)       (J/K)
*******************************************************************
-4.04696E+02 -5.05277E+02  0.00000E+00  7.90117E-02  3.58981E-02

Total mass/gram = 0.10765
~~~~~~~~~~~~~~~~~~~~~~~~~~~~~~~~~~~~~~~~~~~~~~~~~~~~~~~~~~~~~~~~~~~~~~~~~~~~~~~~~~~~~~~~~~
T = 1273.00 K
P = 1.00000E+00 atm
V = 0.00000E+00 dm3

STREAM CONSTITUENTS        AMOUNT/mol
UO2                        3.9630E-04
O2                         2.0000E-05

                       EQUIL AMOUNT  MOLE FRACTION     FUGACITY
PHASE: gas_ideal            mol                        atm
O2                      0.0000E+00     9.8853E-01     1.9712E-08
UO3                     0.0000E+00     1.0716E-02     2.1368E-10
O                       0.0000E+00     7.5273E-04     1.5010E-11
UO2                     0.0000E+00     5.6293E-09     1.1225E-16
O3                      0.0000E+00     4.9550E-14     9.8805E-22
UO                      0.0000E+00     6.6321E-22     1.3225E-29
U                       0.0000E+00     9.1566E-35     1.8259E-42
```

```
TOTAL:                 0.0000E+00     1.0000E+00     1.9940E-08
PHASE: Fluorite             mol       MOLE FRACTION     ACTIVITY
UO2                  3.5630E-04     8.9907E-01     8.7593E-01
UO3                  4.0000E-05     1.0093E-01     1.6935E-06
UO                   4.9953E-21     1.2605E-17     3.9147E-17
TOTAL:                 3.9630E-04     1.0000E+00     1.0000E+00
PHASE: Liquid               mol       MOLE FRACTION     ACTIVITY
UO2                  0.0000E+00     9.9006E-01     1.7622E-02
UO3                  0.0000E+00     9.9427E-03     1.7104E-06
UO                   0.0000E+00     1.6183E-18     2.8544E-20
U                   0.0000E+00     3.8176E-52     1.2186E-28
TOTAL:                 0.0000E+00     1.0000E+00     1.7807E-02
                        mol                    ACTIVITY
U4O9_solid(s)            0.0000E+00                  4.7563E-01
U3O7_solid(s)          T 0.0000E+00                  1.6953E-01
U3O8_solid(s)            0.0000E+00                  1.8624E-02
UO3_alpha_solid(s)        0.0000E+00                  4.5319E-03
U_solid-c_cubic(s3)       0.0000E+00                  1.3134E-28
U_beta-solid_tetrago(s2)   0.0000E+00                  1.1932E-28
U_alpha-solid_orthorh(s)   0.0000E+00                  1.0983E-28
*******************************************************************
  Cp_EQUIL      H_EQUIL      S_EQUIL      G_EQUIL      V_EQUIL
    J.K-1          J          J.K-1          J           dm3
*******************************************************************
 3.58981E-02  -4.04696E+02   7.90117E-02  -5.05277E+02   0.00000E+00

Mole fraction of system components:
              Fluorite
U             0.32248
O             0.67752

The cutoff limit for phase or gas constituent activities is 1.0000E-75

Data on 1 constituent marked with 'T' are extrapolated outside their valid
temperature range
```

~~~~~~

To achieve a stoichiometric deviation of *x*=0.01 in a sample that have a mass of 107 mg:

3.963E-4 UO2 + 2E-6 O2 =

```
  0.00000    mol   gas_ideal
        (1273.00 K, 1 atm,     a=8.9627E-11)
        ( 7.3920E-11      O2
        + 1.4787E-11      UO3
        + 9.1916E-13      O
        + 1.2685E-16      UO2
        + 2.2690E-25      O3
        + 2.4404E-28      UO
        + 5.5021E-40      U)
```
~~~~~~

```
+ 3.9630E-04 mol   Fluorite
  (0.10708 gram, 3.9630E-04 mol)
        (1273.00 K, 1 atm,     a=1.0000)
        ( 0.98991         UO2
        + 1.0093E-02      UO3
        + 6.4409E-16      UO)

        System component       Mole fraction  Mass fraction
        U                      0.33222        0.88097
        O                      0.66778        0.11903


The cutoff concentration has been specified to 1.0000E-75

Data on 1 product species identified with "T" have been extrapolated

*****************************************************************
     H           G           V           S          Cp
    (J)         (J)       (litre)      (J/K)       (J/K)
*****************************************************************
-3.99573E+02 -4.96311E+02  0.00000E+00  7.59916E-02  3.40258E-02

Total mass/gram = 0.10708
~~~~~~~~~~~~~~~~~~~~~~~~~~~~~~~~~~~~~~~~~~~~~~~~~~~~~~~~~~~~~~~~~~~~~~~~~~~~~~~~~~~~~~~~~~~~~

T = 1273.00 K
P = 1.00000E+00 atm
V = 0.00000E+00 dm3

STREAM CONSTITUENTS        AMOUNT/mol
UO2                        3.9630E-04
O2                         2.0000E-06

                         EQUIL AMOUNT  MOLE FRACTION     FUGACITY
PHASE: gas_ideal             mol                         atm
O2                       0.0000E+00     8.2475E-01     7.3920E-11
UO3                        0.0000E+00     1.6499E-01     1.4787E-11
O                        0.0000E+00     1.0255E-02     9.1916E-13
UO2                        0.0000E+00     1.4153E-06     1.2685E-16
O3                       0.0000E+00     2.5316E-15     2.2690E-25
UO                        0.0000E+00     2.7229E-18     2.4404E-28
U                        0.0000E+00     6.1389E-30     5.5021E-40
TOTAL:                     0.0000E+00     1.0000E+00     8.9627E-11
PHASE: Fluorite              mol       MOLE FRACTION     ACTIVITY
UO2                        3.9230E-04     9.8991E-01     9.8985E-01
UO3                        4.0000E-06     1.0093E-02     1.1719E-07
UO                        2.5525E-19     6.4409E-16     7.2241E-16
TOTAL:                     3.9630E-04     1.0000E+00     1.0000E+00
PHASE: Liquid                mol       MOLE FRACTION     ACTIVITY
UO2                        0.0000E+00     9.9933E-01     1.9914E-02
UO3                        0.0000E+00     6.7095E-04     1.1836E-07
UO                        0.0000E+00     2.7885E-17     5.2674E-19
U                        0.0000E+00     6.2309E-50     3.6723E-26
```

```
TOTAL:                  0.0000E+00     1.0000E+00     1.9927E-02
                       mol                       ACTIVITY
U4O9_solid(s)            0.0000E+00                4.7501E-02
U3O7_solid(s)          T 0.0000E+00                 1.4982E-02
UO3_alpha_solid(s)        0.0000E+00                 3.1362E-04
U3O8_solid(s)            0.0000E+00                1.0079E-04
U_solid-c_cubic(s3)        0.0000E+00                 3.9578E-26
U_beta-solid_tetrago(s2)   0.0000E+00                  3.5956E-26
U_alpha-solid_orthorh(s)   0.0000E+00                  3.3098E-26
********************************************************************
  Cp_EQUIL      H_EQUIL      S_EQUIL      G_EQUIL       V_EQUIL
    J.K-1           J           J.K-1          J             dm3
********************************************************************
 3.40258E-02  -3.99573E+02   7.59916E-02  -4.96311E+02   0.00000E+00

Mole fraction of system components:
             Fluorite
U             0.33222
O             0.66778

The cutoff limit for phase or gas constituent activities is 1.0000E-75

Data on 1 constituent marked with 'T' are extrapolated outside their valid
temperature range

~~~~~~~~~~~~~~~~~~~~~~~~~~~~~~~~~~~~~~~~~~~~~~~~~~~~~~~~~~~~~~~~~~~~~~~~~~~~~~~~~~~~~
```

Carrier gas from gas bottle calculation:

The achieve $x=0.1$ the oxygen partial pressure of the gas needs to be 1.9712E-08 (page 380) at T=1273 K over the UO_2 batch.
Setting this partial pressure in the gas products, the initial partial pressure of oxygen in the reactants, at room temperature, was calculated:

```
 1E6 Ar +  2000 H2 +  2 H2O +  999.65 O2 =

  1.0020E+06 mol   gas_ideal
  (3.9984E+07 gram, 1.0020E+06 mol, 1.0468E+08 litre, 3.8196E-04 g/ml)
         (1273.15 K, 1 atm,     a=1.0000)
         ( 0.99800         Ar
         + 1.9972E-03      H2O
         + 7.4789E-07      H2
         + 1.9910E-08      O2
         + 1.9526E-08      OH
         + 6.1458E-10      H
         + 1.5128E-11      O
         + 5.9851E-14      HOO
         + 1.2449E-14      HOOH
         + 1.0046E-21      O3)

 The cutoff concentration has been specified to 1.0000E-75
```

```
*****************************************************************
     H           G           V           S          Cp
    (J)         (J)       (litre)      (J/K)       (J/K)
*****************************************************************
 1.98579E+10 -2.16332E+11  1.04681E+08  1.85516E+08  2.08758E+07

Total mass/gram = 3.9984E+07

~~~~~~~~~~~~~~~~~~~~~~~~~~~~~~~~~~~~~~~~~~~~~~~~~~~~~~~~~~~~~~~~~~~~~~~~~~~~~~~~~~~~~~~~~~~~

T = 1273.15 K
P = 1.00000E+00 atm
V = 1.04681E+08 dm3

STREAM CONSTITUENTS        AMOUNT/mol
Ar                        1.0000E+06
H2                        2.0000E+03
H2O                       2.0000E+00
O2                        9.9965E+02

                       EQUIL AMOUNT  MOLE FRACTION     FUGACITY
PHASE: gas_ideal             mol                        atm
Ar                        1.0000E+06     9.9800E-01     9.9800E-01
H2O                       2.0012E+03     1.9972E-03     1.9972E-03
H2                        7.4939E-01     7.4789E-07     7.4789E-07
O2                        1.9950E-02     1.9910E-08     1.9910E-08
OH                        1.9565E-02     1.9526E-08     1.9526E-08
H                         6.1581E-04     6.1458E-10     6.1458E-10
O                         1.5158E-05     1.5128E-11     1.5128E-11
HOO                       5.9970E-08     5.9851E-14     5.9851E-14
HOOH                      1.2474E-08     1.2449E-14     1.2449E-14
O3                        1.0067E-15     1.0046E-21     1.0046E-21
TOTAL:                    1.0020E+06     1.0000E+00     1.0000E+00
********************************************************************
  Cp_EQUIL       H_EQUIL       S_EQUIL       G_EQUIL       V_EQUIL
    J.K-1           J           J.K-1           J           dm3
********************************************************************
 2.08758E+07   1.98579E+10   1.85516E+08  -2.16332E+11   1.04681E+08

Mole fraction of system components:
             gas_ideal
Ar            0.99403
O             1.9894E-03
H             3.9801E-03

The cutoff limit for phase or gas constituent activities is 1.0000E-75

~~~~~~~~~~~~~~~~~~~~~~~~~~~~~~~~~~~~~~~~~~~~~~~~~~~~~~~~~~~~~~~~~~~~~~~~~~~~~~~~~~~~~~~~~~~~
```

Now the oxygen partial pressure is calculated that is required at the SGM5EL electrolysis cell at *T*=1023.15 K:

1E6 Ar + 2000 H2 + 2 H2O + 999.65 O2 =

```
  1.0020E+06 mol   gas_ideal
 (3.9984E+07 gram, 1.0020E+06 mol, 8.4126E+07 litre, 4.7529E-04 g/ml)
        (1023.15 K, 1 atm,     a=1.0000)
        ( 0.99800         Ar
        + 1.9973E-03      H2O
        + 6.9861E-07      H2
        + 2.7033E-11      OH
        + 3.4525E-12      H
        + 2.3585E-13      O2       (=2.35×10^-7 ppm reading reqired on the SGM5EL electrolysis cell)
        + 1.5099E-16      O
        + 3.5459E-18      HOOH
        + 7.1175E-19      HOO
        + 1.4813E-30      O3)

 The cutoff concentration has been specified to 1.0000E-75

 ******************************************************************
     H           G           V           S          Cp
    (J)         (J)       (litre)      (J/K)       (J/K)
 ******************************************************************
  1.46398E+10 -1.70503E+11  8.41256E+07  1.80953E+08  2.08692E+07

 Total mass/gram = 3.9984E+07


 ~~~~~~~~~~~~~~~~~~~~~~~~~~~~~~~~~~~~~~~~~~~~~~~~~~~~~~~~~~~~~~~~~~~~~~~~~~~~~~~~~~~~~~

 T = 1023.15 K
 P = 1.00000E+00 atm
 V = 8.41256E+07 dm3

 STREAM CONSTITUENTS        AMOUNT/mol
 Ar                         1.0000E+06
 H2                          2.0000E+03
 H2O                          2.0000E+00
 O2                          9.9965E+02

                         EQUIL AMOUNT  MOLE FRACTION     FUGACITY
 PHASE: gas_ideal              mol                         atm
 Ar                         1.0000E+06     9.9800E-01     9.9800E-01
 H2O                          2.0013E+03     1.9973E-03     1.9973E-03
 H2                          7.0001E-01     6.9861E-07     6.9861E-07
 OH                           2.7087E-05     2.7033E-11     2.7033E-11
 H                          3.4594E-06     3.4525E-12     3.4525E-12
 O2                          2.3633E-07     2.3585E-13     2.3585E-13
 O                          1.5130E-10     1.5099E-16     1.5099E-16
 HOOH                          3.5530E-12     3.5459E-18     3.5459E-18
```

```
HOO                     7.1317E-13    7.1175E-19    7.1175E-19
O3                    1.4843E-24    1.4813E-30    1.4813E-30
TOTAL:                  1.0020E+06    1.0000E+00    1.0000E+00
*******************************************************************
  Cp_EQUIL     H_EQUIL     S_EQUIL     G_EQUIL     V_EQUIL
    J.K-1          J          J.K-1          J          dm3
*******************************************************************
 2.08692E+07   1.46398E+10   1.80953E+08  -1.70503E+11   8.41256E+07

Mole fraction of system components:
            gas_ideal
Ar            0.99403
O             1.9894E-03
H             3.9801E-03

The cutoff limit for phase or gas constituent activities was set to 1.0000E-75
```

APPENDIX E: Test Report of Zircaloy-4 Material

Test report for Zircaloy-4 material used to make the impact tightened sliding wedges [188].

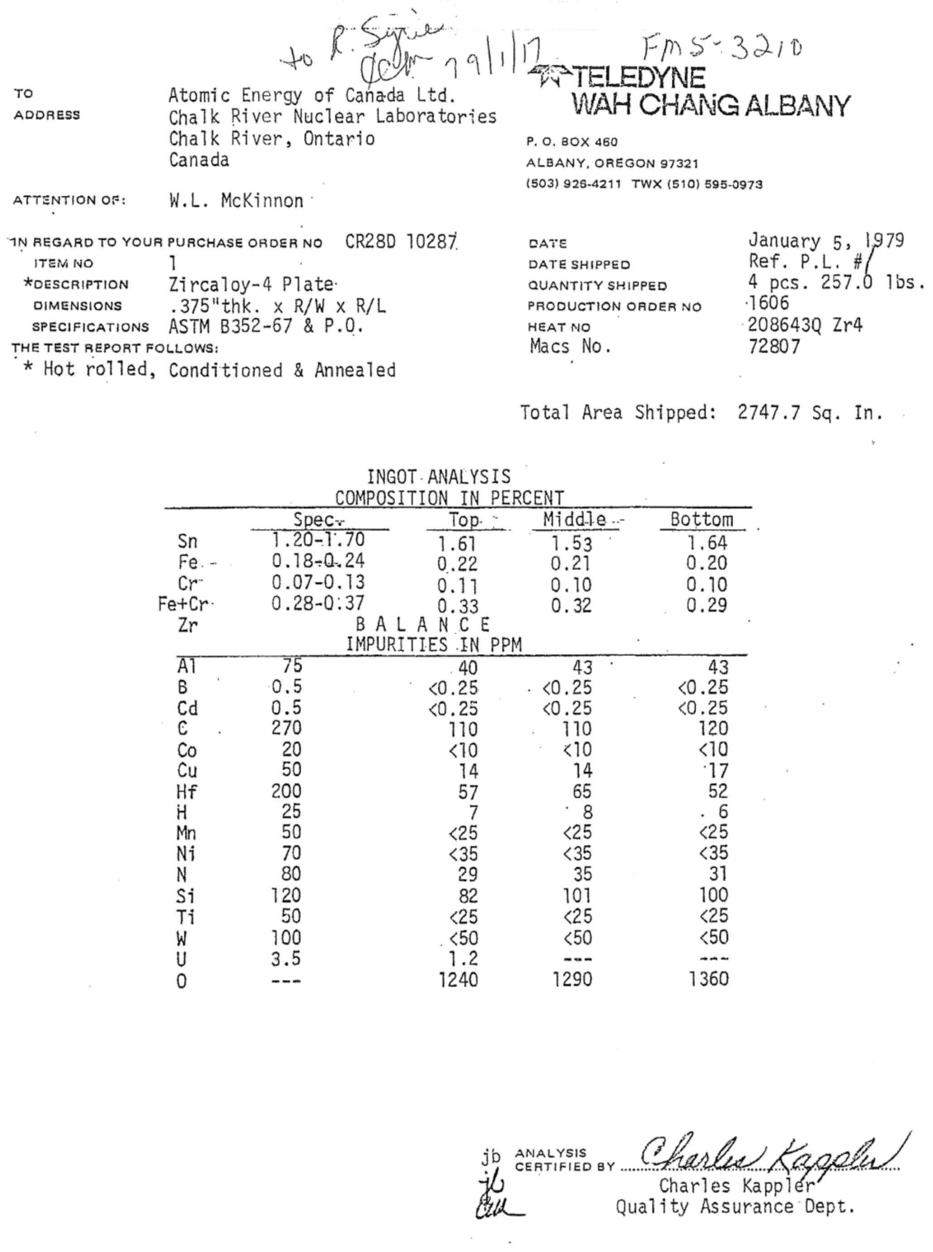

to R. Sigie 79/1/17

FMS-3210

TELEDYNE
WAH CHANG ALBANY

P. O. BOX 460
ALBANY, OREGON 97321
(503) 926-4211 TWX (510) 595-0973

TO
ADDRESS: Atomic Energy of Canada Ltd.
Chalk River Nuclear Laboratories
Chalk River, Ontario
Canada

ATTENTION OF: W.L. McKinnon

IN REGARD TO YOUR PURCHASE ORDER NO: CR28D 10287
ITEM NO: 1
*DESCRIPTION: Zircaloy-4 Plate
DIMENSIONS: .375"thk. x R/W x R/L
SPECIFICATIONS: ASTM B352-67 & P.O.

DATE: January 5, 1979
DATE SHIPPED: Ref. P.L. #/
QUANTITY SHIPPED: 4 pcs. 257.0 lbs.
PRODUCTION ORDER NO: 1606
HEAT NO: 208643Q Zr4
Macs No.: 72807

THE TEST REPORT FOLLOWS:
* Hot rolled, Conditioned & Annealed

Total Area Shipped: 2747.7 Sq. In.

INGOT ANALYSIS
COMPOSITION IN PERCENT

	Spec.	Top	Middle	Bottom
Sn	1.20-1.70	1.61	1.53	1.64
Fe	0.18-0.24	0.22	0.21	0.20
Cr	0.07-0.13	0.11	0.10	0.10
Fe+Cr	0.28-0.37	0.33	0.32	0.29
Zr	B A L A N C E			

IMPURITIES IN PPM

	Spec.	Top	Middle	Bottom
Al	75	40	43	43
B	0.5	<0.25	<0.25	<0.25
Cd	0.5	<0.25	<0.25	<0.25
C	270	110	110	120
Co	20	<10	<10	<10
Cu	50	14	14	17
Hf	200	57	65	52
H	25	7	8	6
Mn	50	<25	<25	<25
Ni	70	<35	<35	<35
N	80	29	35	31
Si	120	82	101	100
Ti	50	<25	<25	<25
W	100	<50	<50	<50
U	3.5	1.2	---	---
O	---	1240	1290	1360

jb
ANALYSIS CERTIFIED BY Charles Kappler
Charles Kappler
Quality Assurance Dept.

APPENDIX F: Slotted Ring Specimen Preparation Procedure

Each Zircaloy slotted ring specimen was specified to be 5.0±0.1 mm wide with a 2-2.5 mm slot cut in its axial direction so that a wedge could be used to apply a stress in the specimen’s transverse direction.

The following materials were required for the cutting of the Zircaloy sheathing:

1. Zircaloy sheath
2. Fine sandpaper (Silicon Carbide 600 grit)
3. Diamond blade cutting oil
4. Wrench
5. Diamond saw blade
6. Precision diamond saw (shown in Figure 160)
7. Saw clamp and allen key
8. Calipers for measuring specimen width and slot width

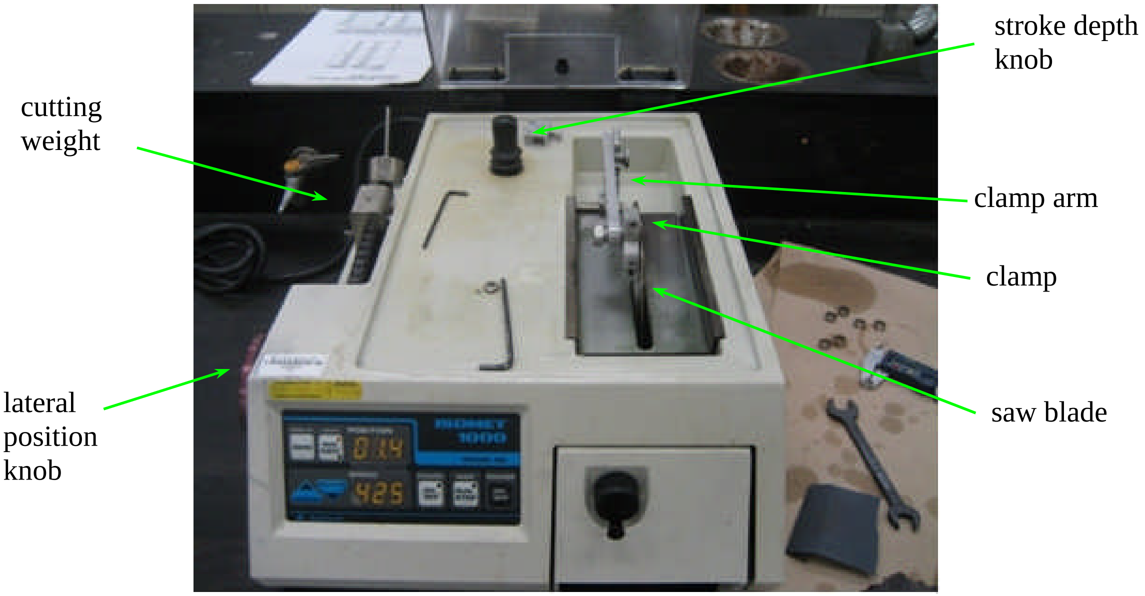

Figure 160: Zircaloy sheathing cutting apparatus; the Buehler ISOMET 1000 Precision Saw

For cutting CAMECO 37-element fuel sheathing into individual specimens, an UKAM Industrial 6”x0.032”x0.5” diamond wafering blade was attached to a Buehler ISOMET 1000 precision saw. The UKAM blade was then tightened between two metal spacers. Cutting oil was used for this job. The sheath tube was then held in position by a clamp so individual rings could be cut off (see Figure 161 (a)). The clamp screws were tightened enough to hold the tube in place but not tight enough to plastically deform it.

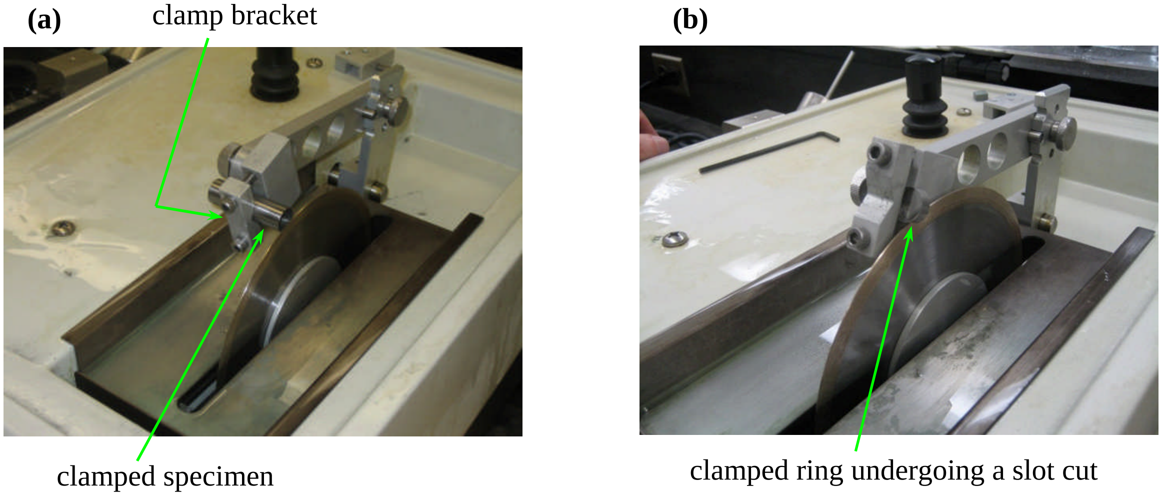

Figure 161: (a) Cutting a ring from a sheath tube and (b) cutting a slot in a ring

For the cutting process a saw speed of 425 RPM and a cutting weight of a 100 grams were selected (Figure 160). Once a specimen ring was cut from a sheath-tube the cut edges were smoothed and deburred by hand using 600 grit sandpaper. The Zircaloy ring was then repositioned in the saw clamp and the clamp bracket was reversed as shown in Figure 161 (b) so that a slot was cut out in the ring axial direction.

The prepared slotted ring specimens were then wiped with kim-wipe paper to remove cutting oil and dirt. For final cleaning the specimens were then inserted in an ethanol filled beaker, which was inserted into an ultrasonic water bath set at 45°C for duration of 30 minutes. The specimens were then removed and allowed to dry.

APPENDIX G: Specimen Hardness Measurements

(i) *As received specimens*

A ready made slotted ring of a Pickering type sheath (type-1) was cut into three pieces and partially flatted so they could be loaded onto the indentation tester. Table 39 provides the hardness test results for this specimen type.

Table 39: Hardness Rockwell measurements of Pickering type sheathing

	measured value	mean	SD	SDOM (error)
HRB	88.55, 87.45, 87.80, 88.70, 86.20, 87.00, 88.00, 88.10, 90.30, 88.40, 88.60, 88.00	88.1	1.0043	0.3

A slotted ring prepared in-house from Cameco type sheathing (type-2) (see specimen preparation detailed in Appendix F) was cut into two pieces for the hardness test: one short and one long. The long piece was partially flattened into a strip, which was loaded onto the indentation tester. Table 40 provides the hardness measurement results of a Cameco sheath specimen.

Table 40: Hardness Rockwell measurements of Cameco type sheathing

	measured value	mean	SD	SDOM (error)
HRB	85.00, 85.80, 86.20, 86.50, 85.40, 86.90, 88.50	86.3	1.1543	0.4

The third sheathing type that was available was CANFLEX fuel sheathing. It was provided as ready made slotted ring specimens. A specimen was cut into three pieces that were not flattened and were loaded onto the indentation tester. Table 41 provides the hardness measurements of a CANFLEX sheath specimen.

Table 41: Hardness Rockwell measurements of CANFLEX type sheathing

	measured value	mean	SD	SDOM (error)
HRB	90.00, 90.60, 89.30, 90.50, 89.60, 89.80, 90.60, 89.30	90.0	0.5528	0.2

(ii) *Stressed and heat treated specimens*

Indentation hardness tests were also performed on specimens that were exposed to 623 K (350°C) temperature and ≈489 MPa of transverse stress (when initially at room temperature) for 5 days. Table 42 provides the hardness measurements of a Pickering type sheath material (type-1) after this heat and stress treatment.

Table 42: Hardness Rockwell measurements of a Pickering type sheathing after exposure to 623 K temperature and 489 MPa of transverse stress

	measured value	mean	SD	SDOM (error)
HRB	90.45, 90.40, 90.50, 90.80	90.4	0.3276	0.2

A similar measurement was made on a Cameco type sheath specimen that was exposed to 623 K (350°C) heat and ≈500 MPa of transverse stress (when initially at room temperature) for 5 days. Table 43 shows the hardness measurements of a Cameco sheath specimen (type-2):

Table 43: Hardness Rockwell measurements of a Cameco type sheathing after exposure to 623 K temperature and 500 MPa of transverse stress

	measured value	mean	SD	SDOM (error)
HRB	87.60, 87.50, 87.90, 87.00, 87.20	87.4	0.3507	0.2

APPENDIX H: XRD Basic Operation

In XRD, when a beam of X-rays impinges on a solid material, a portion of the beam will be scattered in all directions by the electrons associated with each atom or ion that lies within the path of the beam [133]. In Figure 162 the necessary conditions for diffraction of X-rays by a periodic arrangement of atoms is considered.

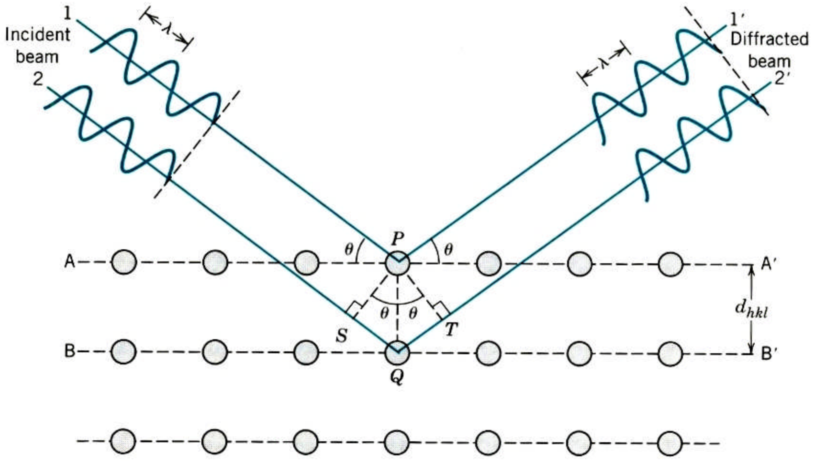

Figure 162: Diffraction of X-rays by planes of atoms in a crystal structure, taken from [133]

In the figure, two atom planes are considered: A-A' and B-B'. Incident on these two atom planes are parallel, monochromatic and coherent (in-phase) beams of X-rays of wavelength λ at an angle θ to the surface. The two rays in this figure that are labeled 1 and 2 are scattered by atoms P and Q. Constructive interference of the scattered rays 1' and 2' only occurs at the angle θ if the path length difference between 1-*P*-1' and 2-*Q*-2' is equal to a whole number n_{or} of X-ray wavelengths. In other words, $n_{or}\lambda = SQ + QT$. Expressing this relationship in terms of the angle θ gives us the so-called Bragg's law:

$$n_{or}\lambda = d_{hkl}\sin\theta + d_{hkl}\sin\theta = 2d_{hkl}\sin\theta \qquad (217)$$

In this equation, n_{or} is the order of reflection, which may be any integer (1,2,3,....). Thus, this simple expression relates the X-ray wavelength and interatomic spacing d_{hkl} to the angle of the diffracted beam. If the Bragg law is not fulfilled then the interference will be non-constructive and will yield a very low intensity diffracted beam [133].

In XRD, crystalline substances have to have a minimum crystallite size, somewhere between 0.002 to 0.005 mm. XRD is used on single crystal substances (when there are no grain boundaries) and on polycrystalline materials or powdered crystalline substances (i.e., materials constructed from numerous grains or where each powdered particle is a grain). Having a large number of grains with random orientations ensures that some particles are properly oriented so that every possible crystallographic plane will be available for diffraction. XRD cannot be used to determine structure in an amorphous material such as glass. An instrument called a diffractometer uses the Bragg relationship to determine and analyze an average bulk structure of long-range ordered materials.

A Scintag X-ray diffractometer at the RMC was used for this purpose. In the θ-θ method, the sample positioned on the sample holder is maintained constant in the horizontal direction (see Figure 163) and both the X-ray source and the X-ray detector are moved by a goniometer and maintained at an angle θ so that the angle of incidence (from the X-ray source) and the angle of reflection (to the X-ray detector) are always equal.

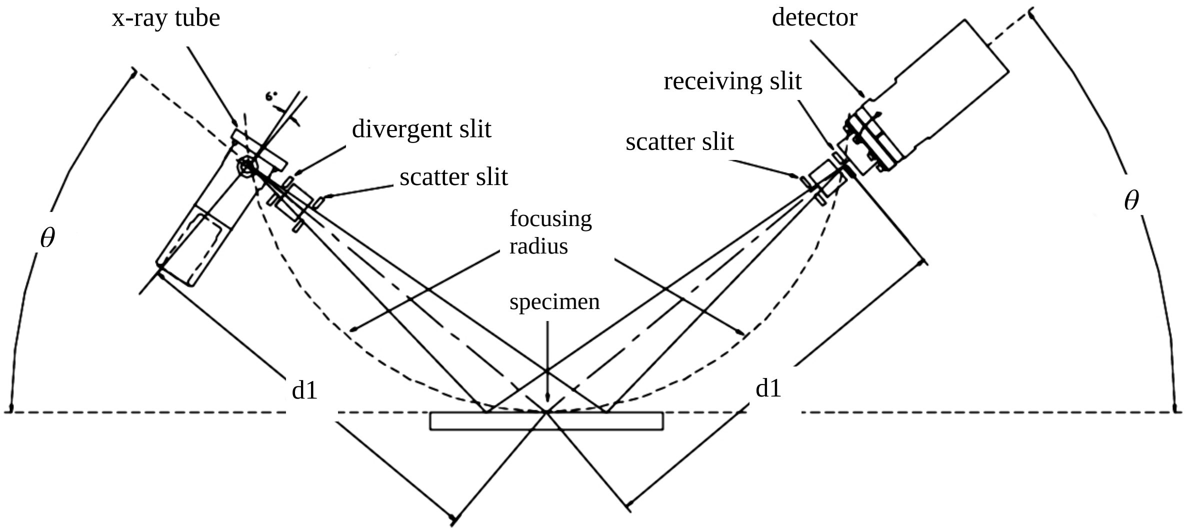

Figure 163: Goniometer in θ-θ configuration used in the XRD, taken from [207]

As the goniometer moves the X-ray tube and counter at constant angular velocity, a recorder automatically reads the diffracted beam intensity. High intensity counts or peaks on the plot result when the Bragg diffraction condition is satisfied by crystallographic planes in the suitable orientation.

Figure 164 provides a second XRD scan of the Pickering 28-element sheath material (type-1 specimen) but this time the outside surface of three 15-mm long, 5-mm wide, flattened sheathing pieces were laid one next to each other parallel to the direction of the X-rays. In other words, the sheath transverse direction was positioned parallel to the X-rays.

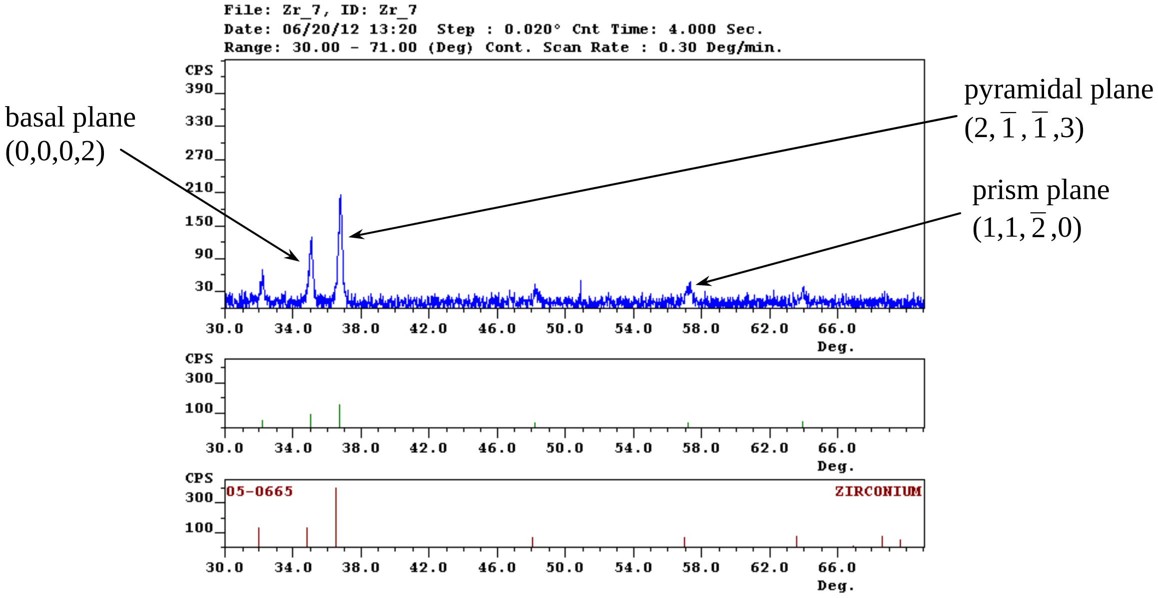

basal plane (0,0,0,2)

pyramidal plane (2,$\bar{1}$,$\bar{1}$,3)

prism plane (1,1,$\bar{2}$,0)

Figure 164: Diffraction pattern scan of a Pickering slotted ring sheath material (type-1) when specimen outer surface, exposed to X-rays, is positioned parallel to the sheath transverse direction

If the two Pickering sheath material scans, Figure 132 and Figure 164 above, are compared it is observed they are very similar. Specifically, the first three peaks on the left side (at angles 31.95°, 34.83°, 36.51°) are almost identical in location and in relative intensities to one another. The next three peaks (at angles 47.99°, 56.93° and 63.53°) agree in peak location but are a little lower in intensity in Figure 164. It is also observed there is a noticeable difference between the two scans. Specifically, the scan in Figure 164 almost lacks the peaks at 68.53° and 69.58° that show up in the scan in Figure 132. This may suggest that the texture in these samples differs slightly in the sheath axial and transverse directions or that the orientation of the samples on the XRD in the Figure 164 scan was exposed less to the X-rays.

The last XRD scan presented is the scan of CANFLEX sheathing (type-3 sheathing material). Table 44 provides the designation and dimensional information of the type-3 specimens.

Table 44: Identification and basic dimensions of type-3 Zircaloy specimen

Specimen type #	Identification number	Outside diameter [mm]	Wall thickness [mm]	Axial width [mm]
3.) CANFLEX 43-element type sheath	PO# 188909, QA# 328168	11.00±0.05	0.40±0.01	5.0±0.1

From Figure 165 the XRD scan of the type-3 specimen looks very similar to the Cameco type-2 sheathing scan (as see in Figure 133) in both the number of observed peaks and their relative intensities, especially a strong basal plane signal.

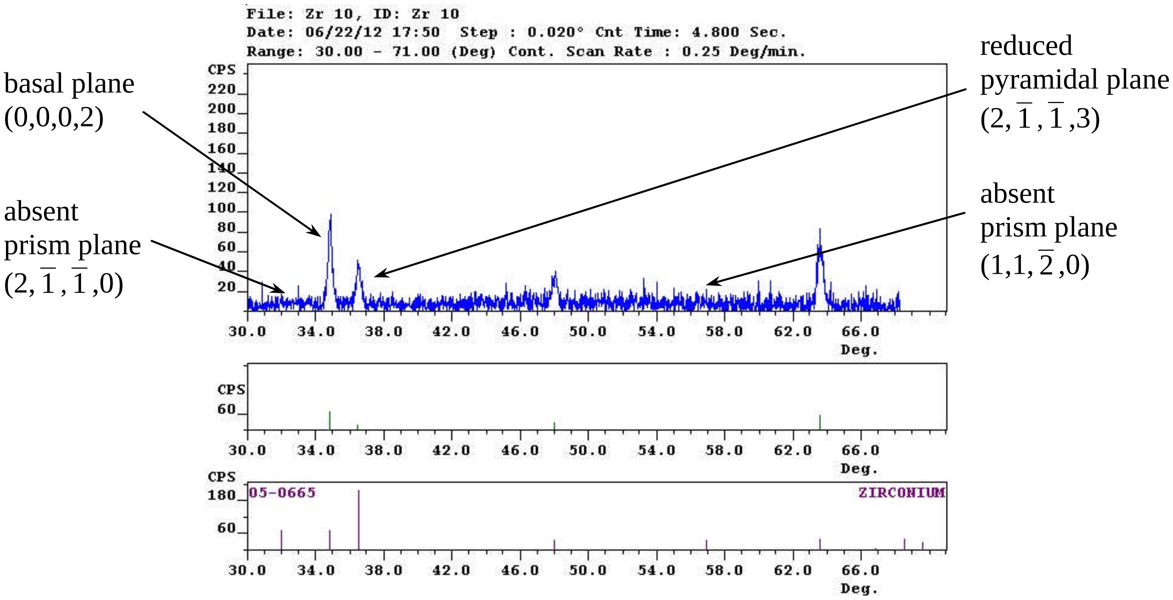

Figure 165: Diffraction pattern scan of a CANFLEX slotted ring sheath material, inner sheath surface exposed to X-rays, perpendicular to the sheath transverse direction

Hence, the crystal texture of the Cameco and CANFLEX Zircaloy materials are quite similar. This is not surprising since these two sheath materials where probably manufactured with the more current and similar manufacturing processes. The Pickering sheath material (type-1) on the other hand may have been manufactured some 30-40 years earlier (the exact date is not known).

APPENDIX I: The Unit Load Method

The unit load method [138] is used to derive the expressions for force and stress vs. displacement (or opening displacement) of the slotted Zircaloy ring. The unit load method is a convenient way of calculating deflections and it is particularly well suited to problems involving rings and arches. Usually the arc is less than a complete circle and its cross section dimensions are small in comparison with the radius of the arc. Let D_y represent the desired deflection, be it translation or rotation. For a beam or arc of length L the deflection is given by Eq. (218), where from left to right the first and second terms are the bending moment contributions, the third term is the torque contribution, the forth term is the axial force contribution and the fifth and six terms are the transverse shear force contribution[†].

$$D_y = \int_0^L \left(\frac{M_y m_y}{EI_y} + \frac{M_z m_z}{EI_z} + \frac{Tt}{GJ} + \frac{Nn}{EA} + \frac{k_y V_y v_y}{GA} + \frac{k_z V_z v_z}{GA} \right) dx \qquad (218)$$

More specifically M, T and N are the bending moment, torque, and axial force, respectively, due to the actual load and m, t and n are the bending moment, torque and axial force, respectively, due to the unit load. E is the Young's modulus, I_y and I_z are the moments of inertia about the y and z axes, respectively, G is the shear modulus, J is the polar moment of inertia, A is the cross section of the ring and k_y and k_z are the transverse shear factors. Figure 166 (a) shows the slotted ring placed in the xy plane where a force F_y is acting in the vertical direction to open the ring at the slotted surface a distance or deflection D_y.

Internal actions are determined from conditions of static equilibrium, by summing forces and moments with reference to radial, axial and z directions at a 'cut' part of the ring. Figure 166 (b) provides a free body diagram of the relevant forces acting on a 'cut' part of the ring body from points p to point q, where N is the axial force acting through the ring cross

---

[†] For the stated variables please refer to the descriptions of the abbreviations/symbols provided in this appendix text, since theses abbreviations/symbols don't have the added subscripts as used in the body of the thesis or in the abbreviations/symbols tables at the beginning of the thesis.

section, V_R is the radial force acting in the plane of the ring cross section, M_z is an out-of-plane moment and C_x, C_y, and C_z are corresponding reaction moments to maintain static equilibrium.

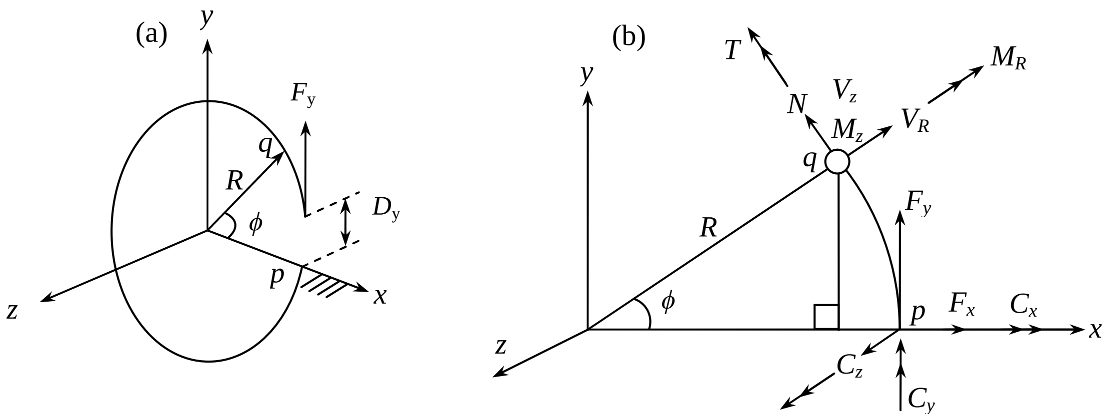

Figure 166: (a) Slotted ring with applied force and resulting deflection and (b) free body forces to point *q* on the slotted ring (b)

The double headed arrows indicate a bending moment or a torque. The static equilibrium equations of the forces depicted in Figure 166 (b) are summed up in Eq. (219) [138].

$$\begin{aligned}
N &= F_x \sin\phi - F_y \cos\phi \\
V_R &= -F_x \cos\phi - F_y \sin\phi \\
V_z &= -F_z \\
M_R &= F_z R \sin\phi - C_x \cos x - C_y \sin\phi \\
M_z &= -F_x R \sin\phi - F_y R(1-\cos\phi) - C_z \\
T &= -F_z R(1-\cos\phi) + C_x \sin\phi - C_y \cos\phi
\end{aligned} \tag{219}$$

Some of the forces depicted in Figure 166 (b) for the current problem are redundant, specifically, $F_x = F_z = C_x = C_y = 0$, hence Eq. (219) simplifies to Eq. (220).

$$\begin{aligned} N &= -F_y \cos\phi \\ V_R &= -F_y \sin\phi \\ M_z &= -F_y R(1-\cos\phi) - C_z \end{aligned} \tag{220}$$

The bending moment *m*, torque *t*, axial force *n*, and radial force *v* due the unit load seen in Eq. (218), are essentially the rates of change of *M*, *T*, *N* and *V* with respect to the reaction forces F_i. By applying Castigliano's theorem [138], the unit load forces can be derived by using Eq. (221), where Δ_i represents the rates of change and U^* is the generic force or bending moment.

$$\Delta_i = \frac{\partial U^*}{\partial F_i} \tag{221}$$

Thus, the values *n*, v_R and m_z are derived in Eqs. (222).

$$\begin{aligned} n &= \frac{\partial N}{\partial F} = \frac{\partial}{\partial F_y}\left(-F_y \cos\phi\right) = -\cos\phi \\ v_y = v_R &= \frac{\partial V_R}{\partial F_y} = \frac{\partial}{\partial F_y}\left(-F_y \sin\phi\right) = -\sin\phi \\ m_z &= \frac{\partial M_z}{\partial F} = \frac{\partial}{\partial F_y}\left(-F_y R(1-\cos\phi)\right) = -R(1-\cos\phi) \end{aligned} \tag{222}$$

Substituting these expressions into Eq. (218), taking $dx = Rd\phi$ and integrating from 0 to 2π for the circumference of the slotted ring (assuming a small slot width), one can write out the slotted ring deflection expression as:

$$\begin{aligned} D_y = \int_0^{2\pi} -\frac{F_y R}{EI_z}(1-\cos\phi)(-R(1-\cos\phi))Rd\phi + \\ \int_0^{2\pi} -\frac{F_y}{EA}\cos\phi(-\cos\phi)Rd\phi + \int_0^{2\pi}\frac{k_y V_R v_R}{GA}Rd\phi \end{aligned} \tag{223}$$

which is equivalent to:

$$D_y = \frac{F_y R^3}{EI_z}\int_0^{2\pi}(1-\cos\phi)^2\,d\phi + \frac{F_y R}{EA}\int_0^{2\pi}\cos^2\phi\,d\phi + \frac{k_y F_y R}{GA}\int_0^{2\pi}\sin^2\phi\,d\phi \qquad (224)$$

Solving Eq. (224) one obtains Eq. (225), which is rewritten as Eq. (205) in the body of the thesis.

$$D_y = \pi F_y R\left(\frac{3R^2}{EI_z} + \frac{1}{EA} + \frac{k_y}{GA}\right) \qquad (225)$$

The moment of inertia of the ring cross section about the *z* axis can be calculated using Eq. (210).

APPENDIX J: The Specimen Deflection Tester

Hardware

An OMEGA LD400-1 linear displacement transducer (Figure 137) with a Ni/Fe central core pin (centred ±1 mm at the middle of the transducer) was used to detect the vertical displacement of the specimen by the movement of the displacement pin riding on the deflection tester lever. The transducer was powered by an HP 6236B power supply; the red wire was connected to +20 terminal and the black wire to a COM terminal, with the transducer ground wire connected to the HP 6236B ground terminal. The power supply was connected to an APC uninterrupted power supply in order to filter out any noise and line source frequencies. The HP 6236B power supply was set using the fine tuning knob to a 22 VDC excitation voltage (not exceeding 24 V) for the transducer, which was maintained at this voltage for all measurements.

A National Instruments NI 9205 data acquisition card (Figure 167) was used to acquire the analog transducer voltage signal. The transducer wires were connected to card channels AI0 and AI8.

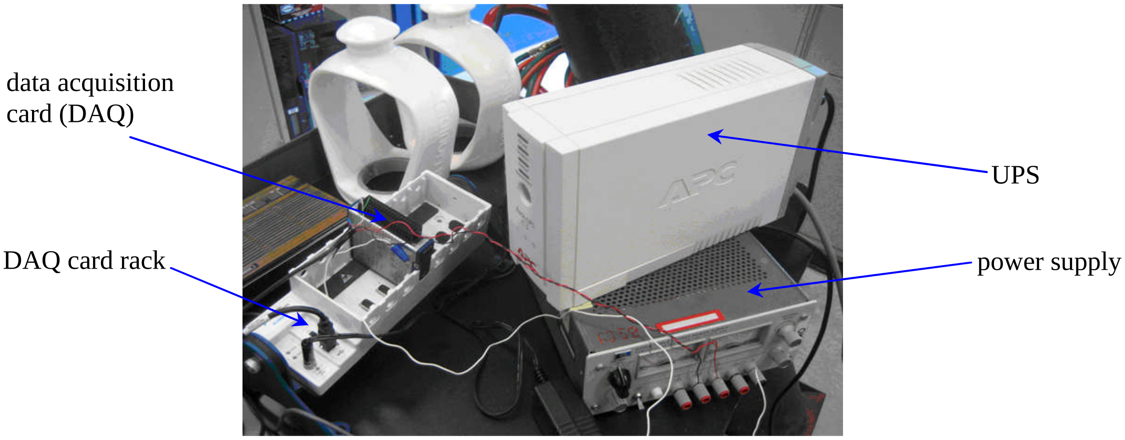

Figure 167: Deflection tester data acquisition card in the card rack and power supply connected to an APC uninterruptable power supply (UPS)

Specifically, the transducer green wire was connected to pin 1 and the white wire was connected to pin 19. The card was installed in a NI cDAG-9172 data acquisition card rack and the rack was connected via USB cable to a computer running Windows XP running LabView version 2011, which recorded and transformed the transducer voltage signal to a deflection distance.

Software

Software interface was provided with a custom made Labview program for reading the deflection tester output. The control panel is shown in the following figure:

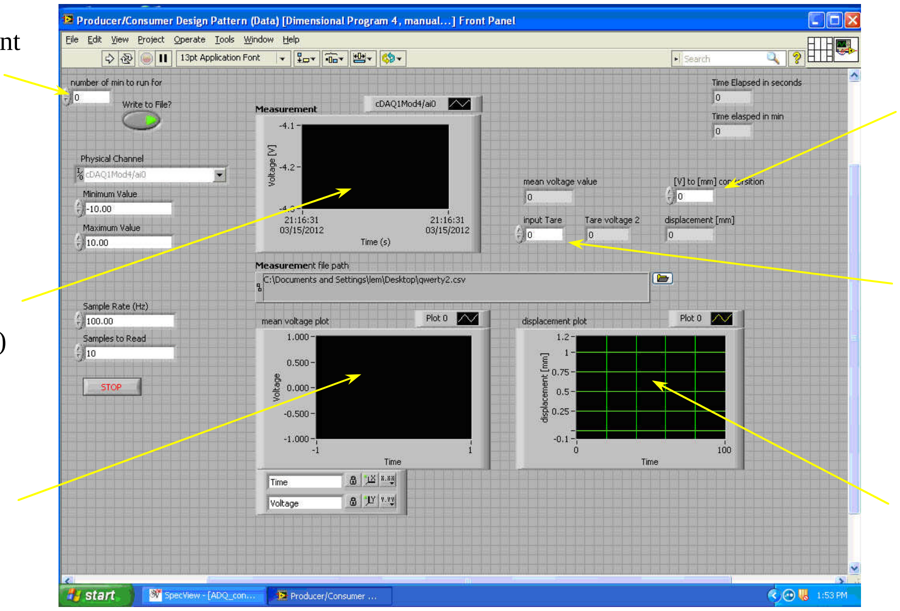

number of min to run for: 0
Physical Channel: cDAQ1Mod4/ai0
Minimum Value: -10.00
Maximum Value: 10.00
Sample Rate (Hz): 100.00
Samples to Read: 10
Measurement file path: C:\Documents and Settings\lem\Desktop\qwerty2.csv
Time Elapsed in seconds: 0
Time elasped in min: 0
mean voltage value: 0
[V] to [mm] conversition: 0
input Tare: 0
Tare voltage 2: 0
displacement [mm]: 0
Time
Voltage

measurement time [min]

transducer voltage [V] (raw signal)

transducer mean voltage [V]

voltage to distance conversion factor

maual tare entry field

deflection output in [mm]

Figure 168: LabView slotted ring deflection tester control window

The deflection output of the slotted ring specimen is provided in the bottom right window in Figure 168. The Labview program file was named ‘Dimensional Program 4, manual tare.vi’.

Use

To execute the program the indicated file name within Labview was opened. The desired measurement time in “number of minutes to run for” the value (typically 30 minutes) was set. The voltage V-to-mm conversion factor of 1.65 was entered and the Labview run-button (arrow icon) was clicked.

Before placing the specimen on the deflection tester the *b* dimension (see Figure 134 (a)) was noted. A slotted ring specimen was installed on the deflection tester jaws (see Figure 137). A 5 gram weight was installed on deflection tester for calibration and taring. The transducer mean voltage value was allowed to settle. To tare the system a negative transducer mean voltage value was inputted into the manual tare entry field. The mean voltage value field was observed; a value close to zero was desired. The tare procedure was repeated until the system stabilized near zero. The displacement scrolling chart was checked to read zero. At this point the 5 gram weight was replaced with a 50 gram weight and the slotted ring specimen displacement was noted down. The corresponding weight and force for this displacement test was hence 45 g and 0.44 N, respectively.

This procedure was repeated once or twice for additional deflection measurements using the 50 g (45 g net) mass. The slotted ring specimen was then vertically reversed in the deflection tester’s lever and static jaws and additional two-three deflection measurements of the specimen were taken with the same weight. Mean specimen deflections were then calculated.

Lastly, the slotted ring specimen was removed from the deflection tester apparatus and a measurement of the specimen slot distance (the final *b* value in Figure 134 (a)) with calipers was taken to confirm that the specimen did not plastically deform (i.e., that the *b* gap distance did not increase after the deflection test was conducted).

The procedure outlined above was repeated for every slotted ring specimen.

APPENDIX K: The Vacuum Pumping Station for Preparing Evacuated Glass Ampoules

A vacuum pumping station shown in Figure 169 was used for preparing evacuated glass ampoules containing stressed Zircaloy slotted rings with sealed iodine vials. In Figure 169 (a) the vacuum pumping station is setup to evacuate the air and then introduce a specific amount of gas additive, specifically oxygen, to the evacuated glass ampoule. The mole amount of the gas added was calculated by knowing the glass ampoule volume and pressure; the pressure measured with a diaphragm pressure gauge, and applying the ideal gas law. The reason a diaphragm pressure gauge was used was because it is insensitive to the type of gas measured. A needle value was used between the gas bottle and glass ampoule volume in order to introduce small amounts of the additive gas in a controlled manner. Figure 169 (b) shows the vacuum pumping station setup for preparing evacuated glass ampoules containing stressed Zircaloy slotted and sealed iodine vials, with no gas additive capability. Vacuum pressure in this case was measured with an Inverted Magnetron and Pirani vacuum gauge, suitable for measuring air gas pressures between atmosphere and 1×10^{-8} torr. In the current vacuum setup a Varian V70D turbo molecular pump was connected to the glass ampoule volume via NW25 (1” internal diameter) vacuum tubing and fittings, which had a pumping speed of about 70 L s^{-1} in vacuum (Figure 169 (a) and (c)). The pressure gauge displays and controllers as well as the vacuum pump controller are shown in Figure 169 (c).

Connected downstream to the turbo pump was an Alcatel 2005 Pascal Dual Stage rotary vane mechanical vacuum pump, which had a pumping speed of 1.8 L s^{-1} in vacuum (Figure 170). The oil vapour trap and the mist eliminator reduced

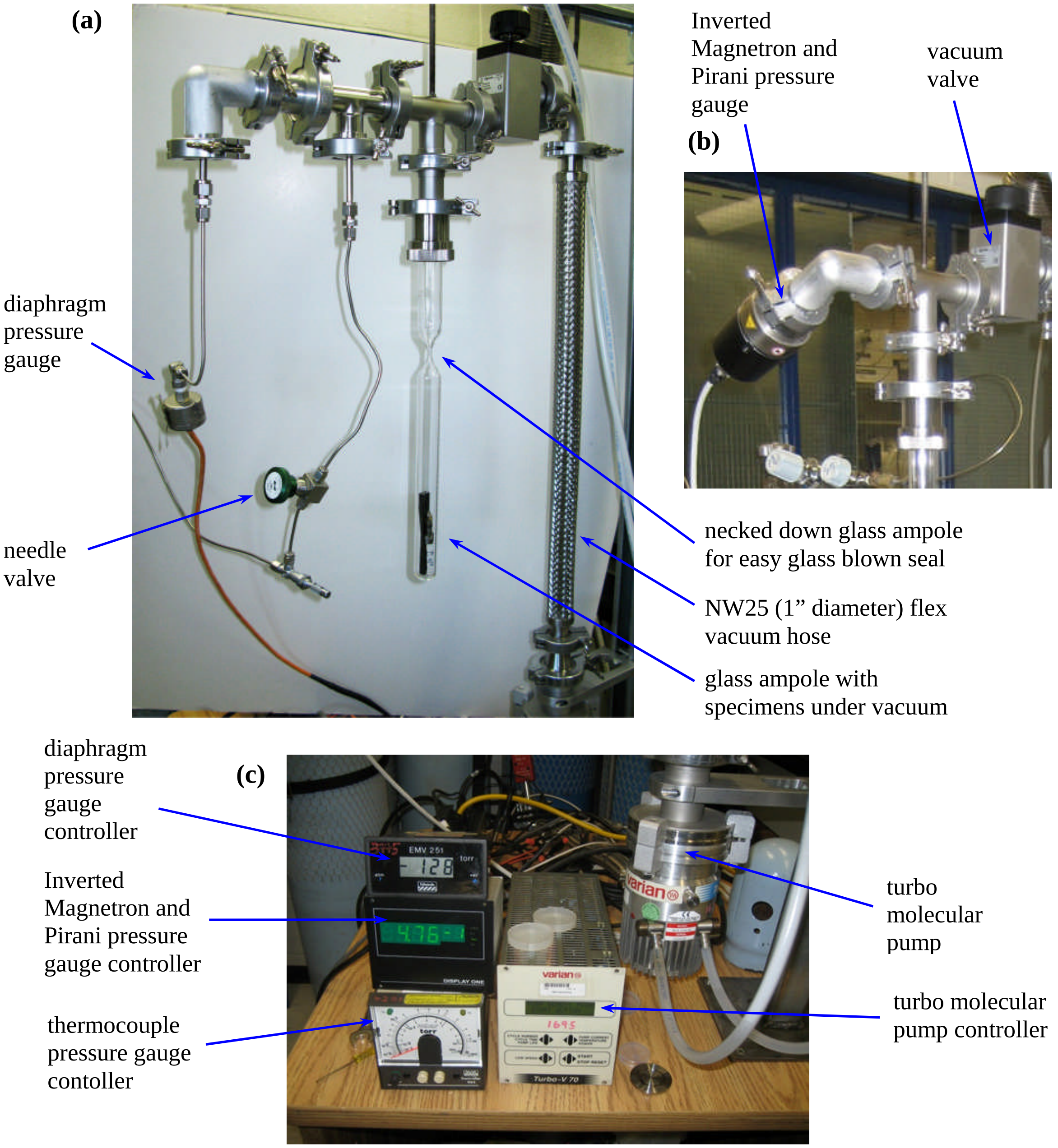

Figure 169: Glass ampoule vacuum pumping and sealing station that holds specimens, (a) to evacuate air and to introduce a controlled amount of oxygen, (b) to evacuate air only. (c) Shows the turbo pump and various controllers.

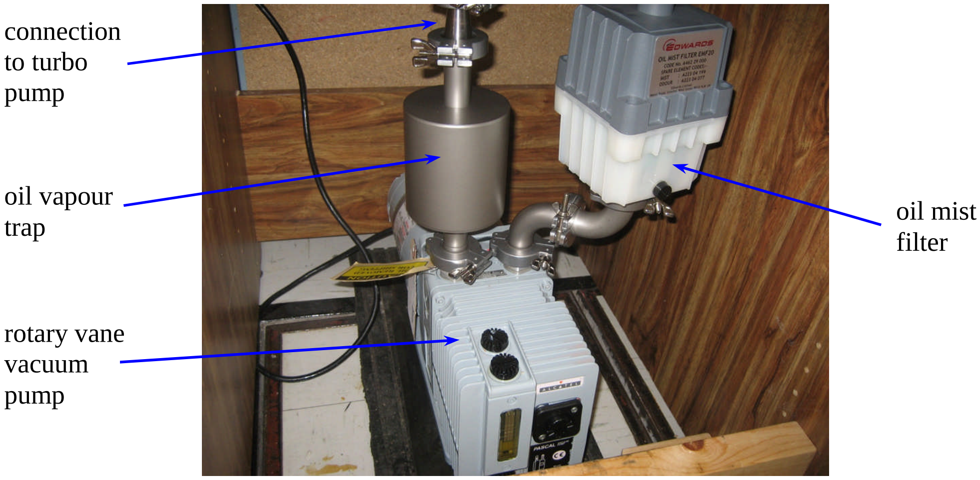

Figure 170: An Alcatel 2005 Pascal Dual Stage rotary vane vacuum roughing pump

Vacuum pressures of 7×10^{-6} torr to 3×10^{-5} torr was achieved in glass ampoules using the current setup after about 24 hours of vacuum pumping. It is worth noting that with increased system vacuum conductance by using larger NW40 (1.5” internal diameter) vacuum tubing and fittings, and with increased vacuum pump speeds, using a larger turbo molecular pump such as a 300 L s^{-1} pump, a reduced pumping time can be achieved. Also, using conflat copper seals and fittings instead of quick flange elastomer seals and fittings will reduce vacuum chamber outgassing times.

Before vacuum pumping was conducted on the glass tube containing the stressed Zircaloy slotted rings, the sealed iodine vials and any additive (if included), a pre vacuum pumping tube neck-down was conducted. It was not possible to glass blow the initial 1” outside diameter medium walled glass tube, while vacuum pumping, and achieving a good seal in a one-step procedure. This is because experience showed that a one-step sealed glass ampoule would fail while being baked in the tube furnace. Instead a two-step glass blowing sealing procedure was adopted. This involved inserting the specimens and iodine vial in the glass tube with one end already glass blown shut and then glass blowing the tube down in diameter at a selected point along the tube until a 2-4 mm inside diameter neck was achieved. See again Figure 139 for a neck-down glass ampoule with specimens and iodine vial before sealing under vacuum. This was them fitted onto the vacuum pumping station and the pumps turned on. When a suitable pressure was achieved the vacuum valve, seen in Figure 169 (b), was closed. Next, the necked-down glass was heated equally from all sides with the glass blowing torch (Figure 171 (a) and (b)), so that with increased glass temperature and the atmospheric pressure acting on the outside surfaces, the glass tube collapsed on itself and a seal was created. It was important to remember to close the vacuum valve (Figure 169 (b)), as mentioned above, since any fracture of the glass at this stage could expose the turbomolecular pump to atmospheric pressure, which would cause damage to the pump. While this was done the glass ampoule below was gently twisted until it was detached from the top glass portion of the tube. The last stage of the process was the gentle and equal heating of the glass seal vicinity by applying a flame with a reduced temperature (a yellow flame instead of a blue flame by adjusting the fuel to oxygen ratio) for an additional 30-60 seconds. This important last step eliminated/reduced the internal stresses in the glass seal and reduced the chances a failure of the glass ampoule when it was later baked in the furnace.

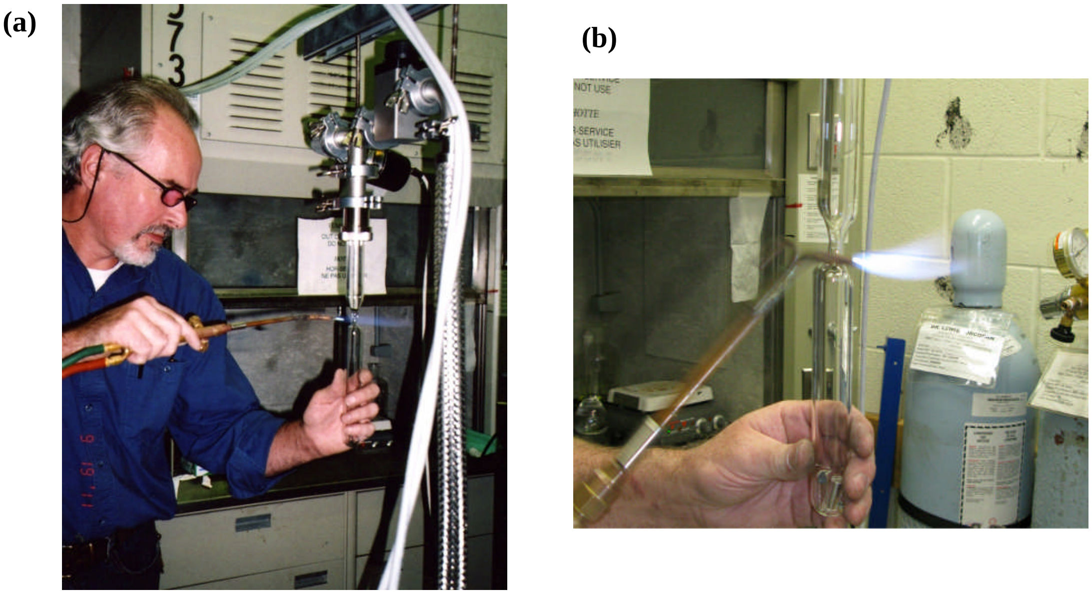

Figure 171: The final stage of preparing the evacuated glass ampoule is (a) glass blowing shut the pre necked-down glass portion (as conducted by Tim Nash in the picture) by (b) constantly moving the flame back and forth equally across the glass neck.

APPENDIX L: TGA Setup for Oxidizing UO_2 Specimens

Reduction and oxidation of UO_2 batches was achieved by using a thermogravimetric analyzer (TGA) and one coulometric titration (CT) electrolysis cell as shown in the following figure. The instrumentation used in this apparatus includes one upstream Zirox SGM5EL electrolysis cell (shown in blue), a precision balance scale with a position laser and sensor (shown in green) and a furnace with alumina tube (shown in red). The term ‘titration’ is applicable only when a down stream cell is also used [22], which was not the case here. The advertised resolution of the balance in the ±2 g range setting is about 0.02 μg. The noise RMS in this setting is 0.3 μg and according to [208] the actual uncertainty of the scale is ±1 μg. So a typical 120 mg sample will have a measurement uncertainty of ±0.001 mg.

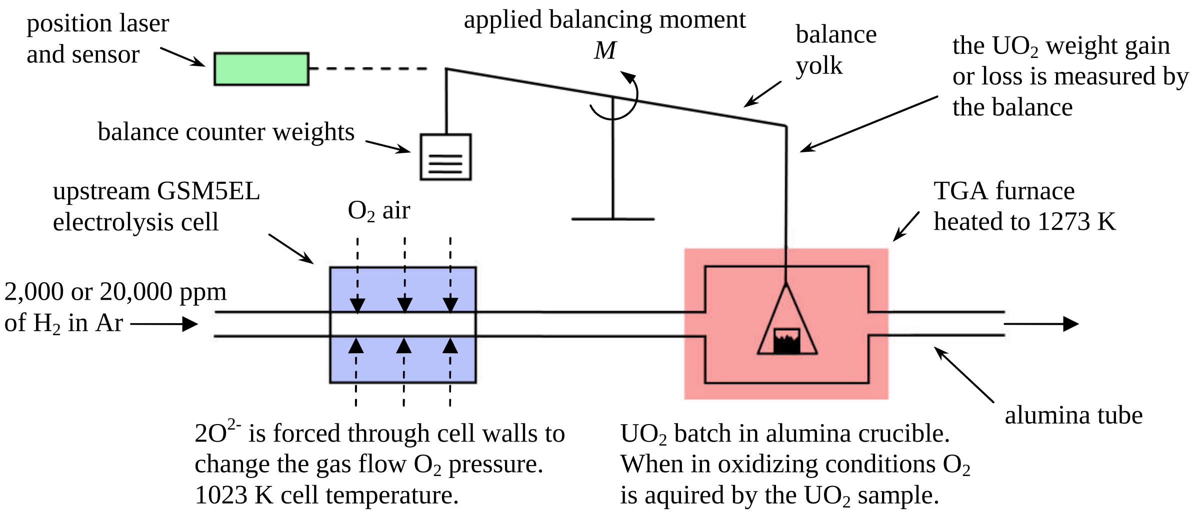

Figure 172: thermogravimetric analyzer (TGA) and coulometric titration (CT) electrolysis cell

Before taring the balance the TGA yolk was allowed to freely tilt around its central axis while holding an empty crucible. Counter weights were added or subtracted to achieve a near even balance on each side of the yolk. The instrument was then tared (zeroed) and the crucible was filled with sample material (UO_2/U_4O_9). With the loaded crucible the balance was no longer ‘balanced’ but the position of the yolk was maintained in a more or less unchanged horizontal position due to a counter acting moment *M* on the balance provided by the precision acting solenoid. This proportional moment was determined by the position of the yolk, measured by the position laser and sensor. The mass of the sample was thus determined by the direct conversion of the applied moment force to weight. As the mass of the sample decreased (when reduced) or increased (when oxidized) the instrument applied decreasing or increasing amounts of electrical current to the solenoid, respectively, which was interpreted as a mass change.

The CT cell (shown in blue in Figure 172) uses a given H_2 to H_2O ratio to create stable oxygen partial pressures at a given temperature. The equilibrium reaction of water and its constituents can be written as:

$$2H_2(g) + O_2(g) \leftrightarrow 2H_2O(g) \tag{226}$$

The oxygen partial pressure in this equilibrium system can be found by calculating [22]:

$$p_{O_2} = \left(\frac{p_{H_2}}{p_{H_2O}} \right)^{-2} e^{\frac{\Delta G^o}{RT}} \tag{227}$$

where $\Delta G°$ is the standard Gibbs energy change for Eq. (226) at temperature *T* (the Zirox SGM5EL CT cell operated at a temperature is 1023 K). Generally, in the CT cell oxygen from the air is reduced at the outer surface of a ceramic tube made of ZrO_2 doped with 8% Y_2O_3, which acts as a solid electrolyte. The electrical current flowing across the tube wall is proportional to the number of moles of O^{2-} ions transferred. The oxygen ions making it to the internal surface of the zirconia tube are then oxidized with the hydrogen flowing with the carrier gas through the tube. The oxygen reacts with virtually all the hydrogen in the carrier gas mixture to create water vapour with a small amount of O_2 left over. The current across the cell wall continues (due to a control voltage across the cell), and is adjusted, until a preset target partial pressure of O_2 is reached in the gas flow.

Reduction

For the purpose of demonstration the preparation of UO_2 batch #29 was selected. Here UO_2/U_4O_9 powder was gently packed into a 50 μl (50 mm^3) alumina crucible and mounted in the TGA. The tared weight of UO_2/U_4O_9 powder recorded before the reduction run was 162.266±0.001 mg, as shown in Figure 173.

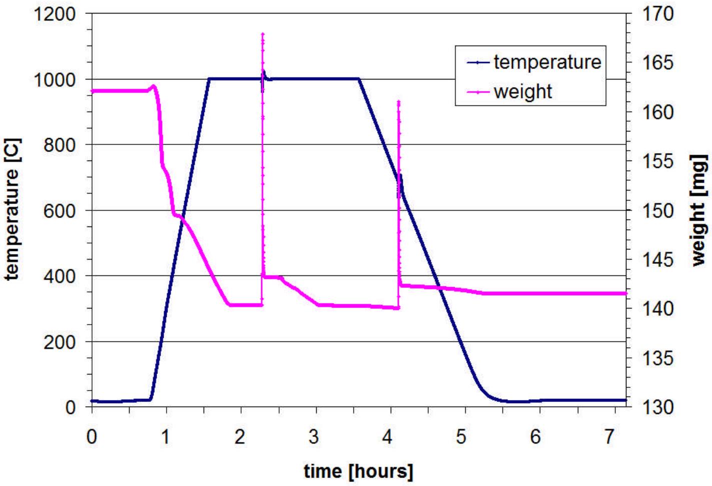

Figure 173: Reduction run temperature and weight of UO_{2+x} batch prepared for test 29

Argon gas with 2% (20,000 ppm) hydrogen was used as a carrier gas, which flowed over the crucible. For this stage of the process the upstream CT electrolysis cell was kept off so that no oxygen from the air was introduced to the gas flow, i.e., the oxygen partial pressure was dependent only on the feed gas composition. In this case the oxygen partial pressure (p_{O2}) in the gas flow was $\approx 2\times10^{-19}$ atm (which constitutes is a reducing environment for the UO_2/U_4O_9 batch). The TGA furnace was ramped to a temperature of 1273 K (1000°C) and the UO_2/U_4O_9 batch was held there for approximately 2 hours. As one can see from the weight plot in purple the weight dropped and stabilized at approximately 140 mg during this time. The recorded spikes in the weight measurement (at about 2.3 and 4.2 hours) were due to momentary adjustments of the carrier gas flow but this did not interfere with the overall process. Once the reduction run was complete, which produced a stoichiometric UO_2 batch, the recorded weight was 141.523±0.001 mg (a drop of 20.743±0.001 mg).

Oxidation

The next step of the process was the oxidation of the UO_2 batch to a target stoichiometric deviation x (or UO_{2+x}). Here the carrier gas bottle was switched to a bottle containing Argon gas with 0.2% (2000 ppm) hydrogen (this bottle had a higher level partial pressure of oxygen than the previous bottle with the Argon 2% H_2, hence it was used). For this step in the process the upstream Zirox SGM5EL electrolysis CT cell was switched on. In this case the partial pressures of oxygen (p_{O2}) was increased to $\approx 2\times10^{-8}$ atm over the UO_2 batch (constituting an oxidizing environment).

For achieving the desired level of oxidation two oxidation runs was applied on the sample. The first oxidation run had a heating duration of approximately 12 hours at a temperature of 1273 K (1000°C). To achieve a target oxygen stoichiometric deviation in the UO_2 batch of x=0.1 the required oxygen partial pressure in the furnace was computed to be 2×10^{-8} atm. Since the CT electrolysis cell operated at a lower temperature than the furnace (at 1023 K), the gas flowing over the UO_2 batch had the target oxygen partial pressure of 2.36×10^{-13} atm. The flow rate of the carrier gas was set to approximately 23 cc min^{-1} and the CT cell current (I_e) was set to approximately 2.6 mA. See Appendix D-2 for FactSage® thermodynamic equilibrium computations for this case. As one sees in Figure 174 the weight of the UO_2 batch was stable in the first two hours of the oxidation process, after which the weight started to increase. The final weight at the end of the first oxidation run was 141.890±0.001 mg, so the weight gain at this point was 0.367±0.002 mg, which was below the target weight gain of about 1 mg. Note that he weight at the beginning of this oxidation run (or the final weight measured in Figure 173) was 141.523±0.001 mg, which is a bit lower than the initial weight measurement of 141.797±0.001 mg before the first oxidation run in Figure 174. This difference may have to do with the intermission time between the two runs (a few hours to 1-2 days), which allowed for some measurement drift. One possibility is that during this intermission time some air entered the system replacing the argon fill gas, effectively changing the buoyancy of the system and allowing for a higher weight reading.

But once the gas flow and furnace were reactivated, so the system was fully purged, this interim discrepancy was believed to be insignificant.

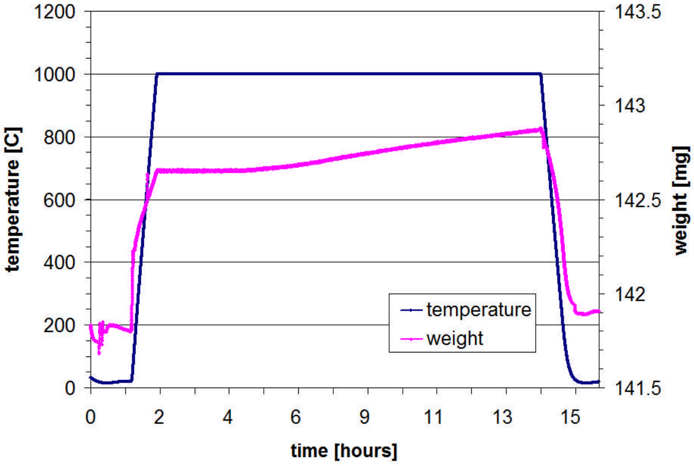

Figure 174: First oxidation run temperature and weight of UO_{2+x} batch prepared for test 29

In a second oxidation run a similar temperature profile was used as in the first oxidation run. The carrier gas was set to 22.5 cc min^{-1} and the CT electrolysis cell current was set to 2.5 mA. In Figure 175 the initial measured weight was 141.994±0.001 and the final measured weight was 142.734±0.001, which shows an additional weight gain, after the extra 12 hours of heating, equal to 0.844±0.001 mg. Note that this last quoted measurement is after the furnace was turned off and was at room temperature and the carrier gas flow was turned off.

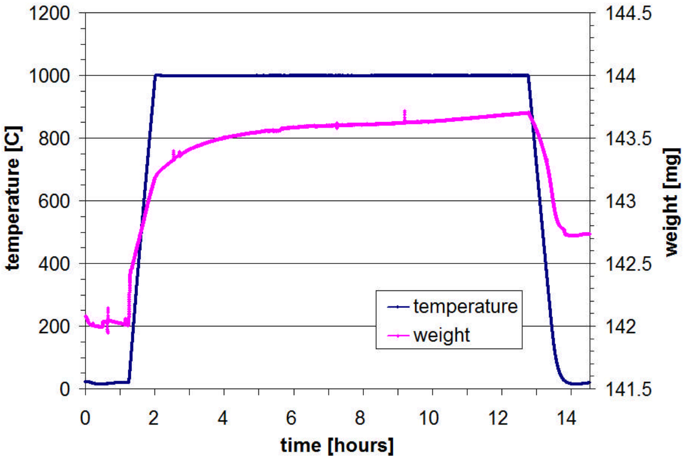

Figure 175: Second oxidation run temperature and weight of UO_{2+x} batch prepared for test 29

Thus, the total weight gain for this UO_2 batch is the weight gain of both oxidation runs, which was 1.211±0.002 mg. Table 45 sums up these weight measurements.

Table 45: UO_2 batch weights before and after reduction and oxidation runs

	Reduction run	Oxidation run #1	Oxidation run #2
Initial weight [mg]	162.266±0.001	141.797±0.001	141.994±0.001
Final weight [mg]	141.523±0.001	141.890±0.001	142.734±0.001
Δm of final oxidation and reduction weights [mg]		0.367±0.002	1.211±0.002

This weight gain is then used to calculate the average stoichiometric deviation in the UO_{2+x} batch using Eq. (216) in Section 5.4:

$$x = \frac{270.03\,[\text{g mol}^{-1}]}{16\,[\text{g mol}^{-1}]} \cdot \frac{1.211 \pm 0.002\,[\text{mg}]}{141.523 \pm 0.001\,[\text{mg}]} = 16.8769 \cdot \frac{1.211 \pm 0.1652\%}{141.523 \pm 0.0007\%} = 0.1444 \pm 0.0002$$

Since there may be other sources of error that were not considered the result is rounded up to be conservative:

$$x = 0.144 \pm 0.001$$

APPENDIX M: EDX and Neutron Activation Analysis of ISCC Experiment Deposits

EDX analysis of deposits from experiment 16 and 19:

Microanalysis Report

Prepared for: *Aaron Quastel*

Prepared by: *Dr. J.L. Snelgrove* *14-May-12*

Deposit sample from test 16

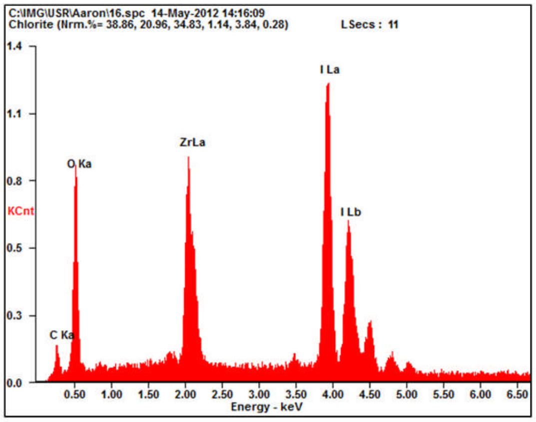

Element	***Wt %***	***At %***
C K	05.51	21.28
O K	16.22	47.03
ZrL	21.51	10.94
I L	56.76	20.75

EDAX ZAF QUANTIFICATION STANDARDLESS SEC TABLE : DEFAULT

KV:20.00 TILT: 0.00 TAKE-OFF:35.00 AMPT:12.8 DETECTOR TYPE :SDD APOLLO X RESOLUTION :127.40

Note: The carbon signal is thought to come from the carbon based double-sided tape, which secured the sample.

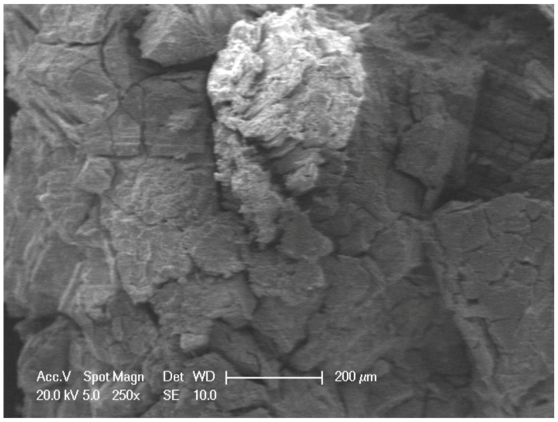

Image of scanned deposit sample

Microanalysis Report

EDAX®
AMETEK®

Prepared for: *Aaron Quastel*

Prepared by: *Dr. J.L. Snelgrove* *14-May-12*

Deposit sample from test 19 (1st sample)

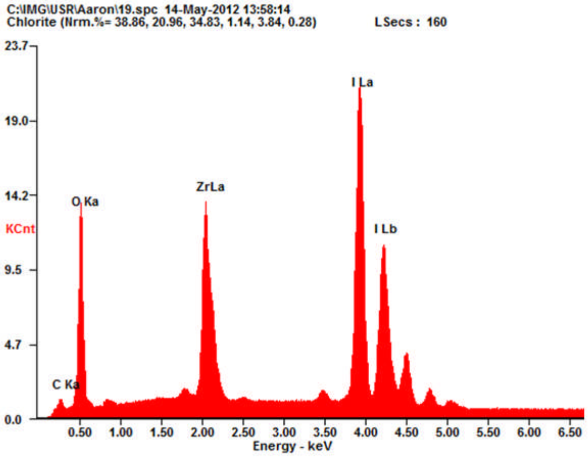

Element	***Wt %***	***At %***
C K	02.73	11.89
O K	15.58	51.00
ZrL	21.08	12.10
I L	60.61	25.01

EDAX ZAF QUANTIFICATION STANDARDLESS SEC TABLE : DEFAULT

KV:20.00 TILT: 0.00 TAKE-OFF:34.07 AMPT:12.8 DETECTOR TYPE :SDD APOLLO X RESOLUTION :127.40

Microanalysis Report

Prepared for: *Aaron Quastel*

Prepared by: *Dr. J.L. Snelgrove* *14-May-12*

Deposit sample from test 19 (2nd sample)

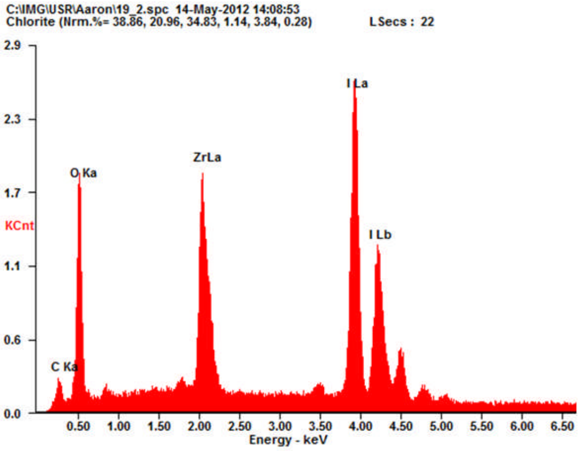

Element	*Wt %*	*At %*
C K	04.78	18.36
O K	17.41	50.25
ZrL	21.58	10.92
I L	56.24	20.46

EDAX ZAF QUANTIFICATION STANDARDLESS SEC TABLE : DEFAULT

Note: A second deposit sample from the same experiment (19) was scanned.

KV:20.00 TILT: 0.00 TAKE-OFF:35.00 AMPT:12.8 DETECTOR TYPE :SDD APOLLO X RESOLUTION :127.40

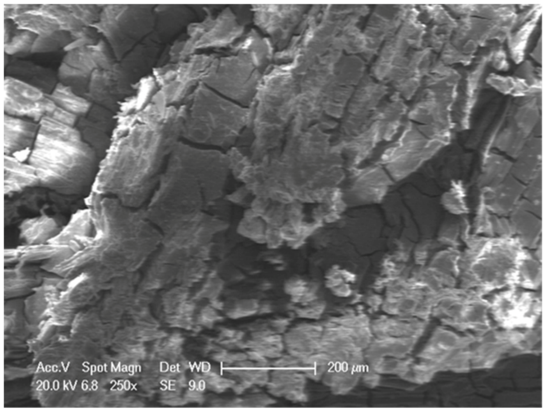

Image of scanned deposit sample

Neutron Activation Analysis of deposits:

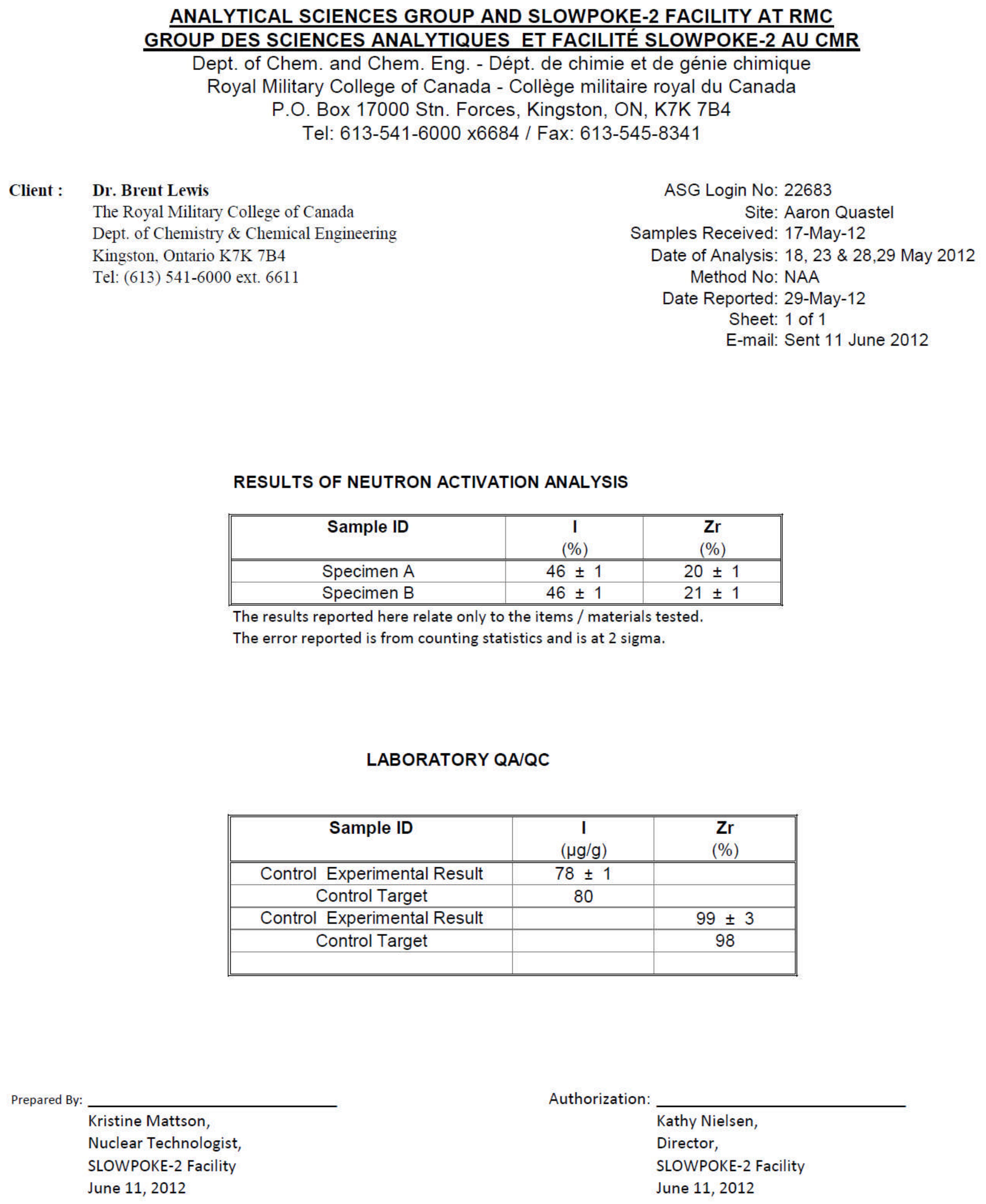

ANALYTICAL SCIENCES GROUP AND SLOWPOKE-2 FACILITY AT RMC
GROUP DES SCIENCES ANALYTIQUES ET FACILITÉ SLOWPOKE-2 AU CMR
Dept. of Chem. and Chem. Eng. - Dépt. de chimie et de génie chimique
Royal Military College of Canada - Collège militaire royal du Canada
P.O. Box 17000 Stn. Forces, Kingston, ON, K7K 7B4
Tel: 613-541-6000 x6684 / Fax: 613-545-8341

Client : **Dr. Brent Lewis**
The Royal Military College of Canada
Dept. of Chemistry & Chemical Engineering
Kingston, Ontario K7K 7B4
Tel: (613) 541-6000 ext. 6611

ASG Login No: 22683
Site: Aaron Quastel
Samples Received: 17-May-12
Date of Analysis: 18, 23 & 28,29 May 2012
Method No: NAA
Date Reported: 29-May-12
Sheet: 1 of 1
E-mail: Sent 11 June 2012

RESULTS OF NEUTRON ACTIVATION ANALYSIS

Sample ID	I (%)	Zr (%)
Specimen A	46 ± 1	20 ± 1
Specimen B	46 ± 1	21 ± 1

The results reported here relate only to the items / materials tested.
The error reported is from counting statistics and is at 2 sigma.

LABORATORY QA/QC

Sample ID	I (µg/g)	Zr (%)
Control Experimental Result	78 ± 1	
Control Target	80	
Control Experimental Result		99 ± 3
Control Target		98

Prepared By: ________________________
Kristine Mattson,
Nuclear Technologist,
SLOWPOKE-2 Facility
June 11, 2012

Authorization: ________________________
Kathy Nielsen,
Director,
SLOWPOKE-2 Facility
June 11, 2012